Liming Dai · Reza N. Jazar *Editors*

Nonlinear Approaches in Engineering Applications

Energy, Vibrations, and Modern Applications

Springer

Nonlinear Approaches in Engineering Applications

Liming Dai • Reza N. Jazar
Editors

Nonlinear Approaches in Engineering Applications

Energy, Vibrations, and Modern Applications

Springer

Editors
Liming Dai
Xiamen University of Technology
Xiamen, China

Industrial Systems Engineering
University of Regina
Regina, SK, Canada

Reza N. Jazar
Xiamen University of Technology
Xiamen, China

School of Engineering RMIT University
Melbourne, VIC, Australia

ISBN 978-3-319-69479-5 ISBN 978-3-319-69480-1 (eBook)
https://doi.org/10.1007/978-3-319-69480-1

Library of Congress Control Number: 2018930145

Printed on acid-free paper

This Springer imprint is published by Springer Nature
The registered company is Springer International Publishing AG
The registered company address is: Gewerbestrasse 11, 6330 Cham, Switzerland

Dedicated to Xinming and Mojgan.
The one who knows where to go cannot be stopped.

Preface

This book is based on the same concept used in the previous volumes of the series *Nonlinear Approaches in Engineering Applications*, organized by the editors. Nonlinear analysis and approaches have been developed alongside the development and modelling of natural dynamic phenomena. Although the main approaches in the analysis of dynamic phenomena are still linear approaches, depending on the required level of accuracy, linear analyses reach their limits, and nonlinear approaches become necessary. The beauty of nonlinearity is that every single system will be treated as a unique system such that a general solution and classification cannot be found. Every nonlinear system needs its own unique method of modelling and analysis.

Considering that modelling of nonlinear systems is as important as development of solution methods, we selected topics to cover both, modelling and solution methods. The book is divided into four sections; Section 1, Energy Applications; Section 2, Vibrations and Automotive Applications; Section 3, Modern Engineering Applications; and Section 4, Analytical-Numerical Analysis Applications. Every section includes a few selected topics which are very interesting to investigators and researchers working in the area of nonlinear approaches in dynamic system analysis.

Level of the Book

This book is aimed at engineers, scientists, researchers and engineering and physics graduate students, together with the interested individuals in engineering, physics and mathematics. The book focuses on the application of nonlinear approaches representing a wide spectrum of disciplines of engineering and science. Throughout the book, great emphasis is placed on engineering applications, the physical meaning of the nonlinear systems and methodologies of the approaches in analysing and solving for the systems. Topics that have been selected are of high

interest in engineering and physics. An attempt has been made to expose the engineers and researchers to a broad range of practical topics and approaches. The topics contained in the present book are of specific interest to engineers who are seeking expertise in vehicle- and automotive-related technologies as well as engines and alternative fuels, mathematical modelling of complex systems, biomechanical engineering approaches to robotics and artificial muscles, nonclassical engineering problems and modern mathematical treatments of nonlinear equations.

The primary audience for this book are; researchers, graduate students and engineers in mechanical engineering, engineering mechanics, electrical engineering, civil engineering, aerospace engineering, mathematics and science disciplines. In particular, the book can be used for training graduate students as well as senior undergraduate students to enhance their knowledge by taking a graduate or advanced undergraduate course in the areas of nonlinear science, dynamics and vibration of discreet and continuous system, structure dynamics and engineering applications of nonlinear science. It can also be utilized as a guide to readers' fulfilment in practices. The covered topics are also of interest to engineers who are seeking to expand their expertise in these areas.

Organization of the Book

The main structure of the book consists of 4 parts, energy applications, vibrations and automotive applications, modern engineering applications and analytical-numerical analysis applications, including 15 chapters. Each chapter covers an independent topic along the line of nonlinear approach and engineering applications of nonlinear science. The main concepts in nonlinear science and engineering applications are explained fully with necessary derivatives in detail. The book and each of the chapters are intended to be organized as essentially self-contained. All necessary concepts, proofs, mathematical background, solutions, methodologies and references are supplied except for some fundamental knowledge well known in the general fields of engineering and physics. The readers may therefore gain the main concepts of each chapter with as less as possible the need to refer to the concepts of the other chapters and references. Readers may hence start to read one or more chapters of the book for their own interests.

Method of Presentation

The scope of each chapter is clearly outlined, and the governing equations are derived with an adequate explanation of the procedures. The covered topics are logically and completely presented without unnecessary overemphasis. The topics are presented in a book form rather than in the style of a handbook. Tables, charts, equations and references are used in abundance. Proofs and derivations are

emphasized in such a way that they can be straightforwardly followed by the readers with fundamental knowledge of engineering science and university physics. The physical model and final results provided in the chapters are accompanied with necessary illustrations and interpretations. Specific information that is required in carrying out the detailed theoretical concepts and modelling processes has been stressed.

Prerequisites

The readers should be familiar with the fundamentals of dynamics, calculus and differential equations associated with dynamics in engineering and physics, as well as have a basic knowledge of linear algebra and numerical methods. The presented topics are given in a way to establish as conceptual framework that enables the readers to pursue further advances in the field. Although the governing equations and modelling methodologies will be derived with adequate explanations of the procedures, it is assumed that the readers have a working knowledge of dynamics, university mathematics and physics together with theory of linear elasticity.

Acknowledgements

This book is made available under the close and effective collaborations of all the enthusiastic chapter contributors who have the expertise and experience in various disciplines of nonlinear science and engineering applications. They deserve sincere gratitude for the motivation in creating such book, encouragement in completing the book, scientific and professional attitude in constructing each of the chapters of the book and the continuous efforts toward improving the quality of the book. Without the collaboration and consistent efforts of the chapter contributors, the completion of this book would have been impossible. What we have at the end is a book that we have every reason to be proud of.

It has been gratifying to work with the staff of Spinger through the development of this book. The assistance provided by the staff members has been valuable and efficient. We thank Spinger for their production of an elegant book.

This book has been supported by the National High-End Foreign Experts Project (GDT20163600003), Republic of China.

Regina, SK, Canada — Liming Dai
Melbourne, VIC, Australia — Reza N. Jazar

Contents

List of Figures

List of Tables

Part I
Energy Applications

Chapter 1
Nonlinear Behaviour Diagnosis for Horizontal-Axis Wind Turbine Blades Subjected to Inconstant Wind Excitations

Dandan Xia, Liming Dai, Changping Chen, and Pan Fang

Nomenclature

$\boldsymbol{\Omega}$	Speed of the blade
$\boldsymbol{\Omega}_0$	Average angular velocity
$\boldsymbol{A}$	Amplitude for blade rotation
$\boldsymbol{\omega}$	Frequency for blade rotation
$\boldsymbol{V}_{\mathbf{v}}$	Varying velocity of the fluctuating wind
$\boldsymbol{V}_0$	Average wind speed
$\boldsymbol{V}(\boldsymbol{t})$	Fluctuating wind speed
$\boldsymbol{S}$	Area of the wind wing blade
$\boldsymbol{C}_{\mathbf{L}}$	Lift coefficient of the wing
$\boldsymbol{V}_{\mathbf{a}}$	Wind speed on the hub
$\boldsymbol{f}_x^{\boldsymbol{a}}$	Centrifugal force on the x direction
$\boldsymbol{f}_y^{\boldsymbol{a}}$	Centrifugal force on the y direction
$\boldsymbol{u}$	Displacement along the x direction
$\boldsymbol{v}$	Displacement along the y direction
$\boldsymbol{\varepsilon}_0$	Extensional strain of the blade in axial direction
$\boldsymbol{\varepsilon}_1$	Ending strain from the central axis of the blade
$\boldsymbol{E}$	Elastic modulus

(continued)

D. Xia • L. Dai (✉)
Sino-Canada Research Center for Noise and Vibration Control, Xiamen University of Technology, Xiamen, China

Industrial Systems Engineering, University of Regina, Regina, SK, Canada
e-mail: liming.dai@uregina.ca

C. Chen
Sino-Canada Research Center for Noise and Vibration Control, Xiamen University of Technology, Xiamen, China

P. Fang
School of Mechanical Engineering, Southwest Petroleum University, Chengdu, China

L. Dai, R.N. Jazar (eds.), *Nonlinear Approaches in Engineering Applications*,
https://doi.org/10.1007/978-3-319-69480-1_1

A'	Section area
I	Moment of inertia
μ	Damping coefficient
m	Mass of blade
ρ_{air}	Density of air

1.1 Background

As a clean and renewable energy source, wind energy has attracted more and more attentions from the countries in the world. The potential of wind energy is enormous. As it is anticipated that the total wind energy can be 2.7×10^9 MW in the world; and among which, about 2×10^7 MW can be implemented for electricity generation. This is about ten times of that of the hydraulic energy that can be developed and used on the earth. The wind power becomes an important energy source for the human society in striving to reduce the dependence of fossil fuels. As can be seen from Fig. 1.1, which was reported by Global Wind Energy Council (GWEC) (2015), the wind power cumulative capacity has been increased dramatically in the past two decades, and one may anticipate that the increase of the wind power capacity will follow the exponential trend as shown in the figure.

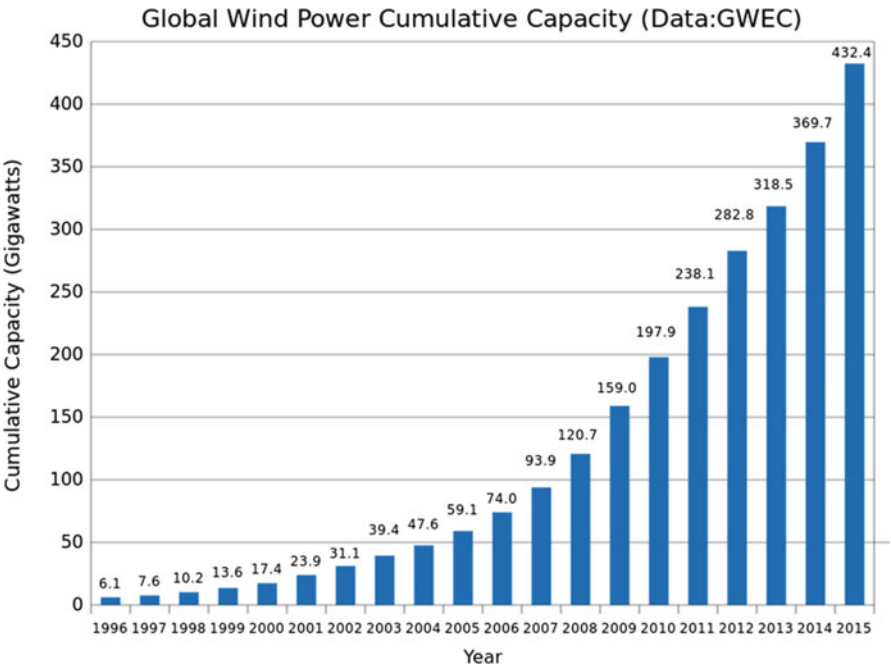

Fig. 1.1 Global wind power cumulative capacity reported by Global Wind Energy Council (GWEC)

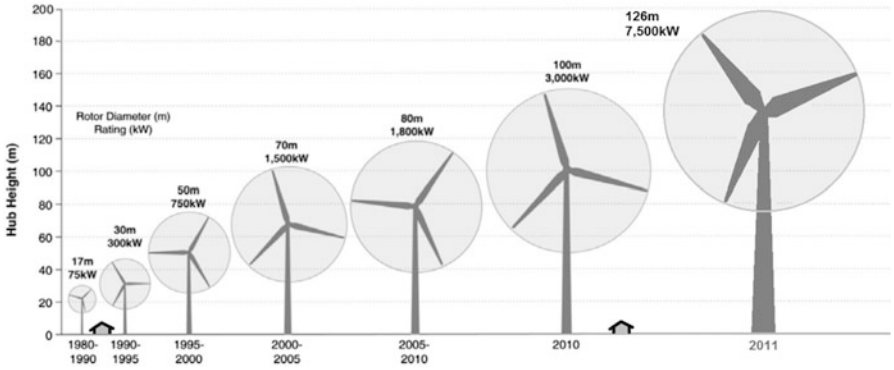

Fig. 1.2 Evolution of HAWT in size and capacity

To utilize the wind energy, wind turbines play an important role. A wind turbine, also known as an aerofoil-powered generator, is a device that converts the wind energy into kinetic energy of the turbine blades and then into electrical power. Among all types of wind turbines implemented in the world, horizontal-axis wind turbines (HAWT) are probably the most popular ones, and they are becoming an increasingly important source of green and renewable energy and have attracted great attention from researchers and engineers in their development and applications. As shown in Figs. 1.2 and 1.3, a horizontal-axis wind turbine usually has three blades and designed to point into the wind. This is usually achieved by motors controlled by computers, particularly for large-scale wind turbines.

In the past decades, in fact, the HAWT have been built larger and larger in size, in the attempt to collect more wind energy and generate electricity with high efficiency. As per the report by Pentland (2014), shown in Fig. 1.2 with the data up to 2011, the capacity of the maximum HAWT has been increased from 75 kW to 7500 kW, and the hub height of the wind turbine with maximum capacity has been increased from 17 m to 140 m, whereas the maximum HAWT has a rotor diameter of 126 m, increased from 17 m in the 1980s. Recently, the wind turbine with a nominal capacity of 8 MW was installed in Denmark and has an overall height of 220 m, a rotor diameter of 164 m (Wittrup 2014).

Indeed, high-power HAWT start to play an increasingly influential role in the electricity market. Figure 1.3a, b show the wind turbines in 1980 and 2005, respectively (Larsen 2005). At the early stage of the wind turbine development, the power of the turbine is relatively small, as shown in Fig. 1.3a, where the power of the turbine is 30 KW. When the high-power HAWT are implemented in the market, arrays of the HAWT turbines, known as wind farms, are applied. This is true especially for the huge wind turbines established at the shores, as shown in Fig. 1.3b.

As the wind turbines become larger and larger, the blades of the wind turbines become lighter, longer, and more flexible, as can be seen from Fig. 1.4. Large-sized wind turbine with large blades has a massive effect on the surrounding flow fields

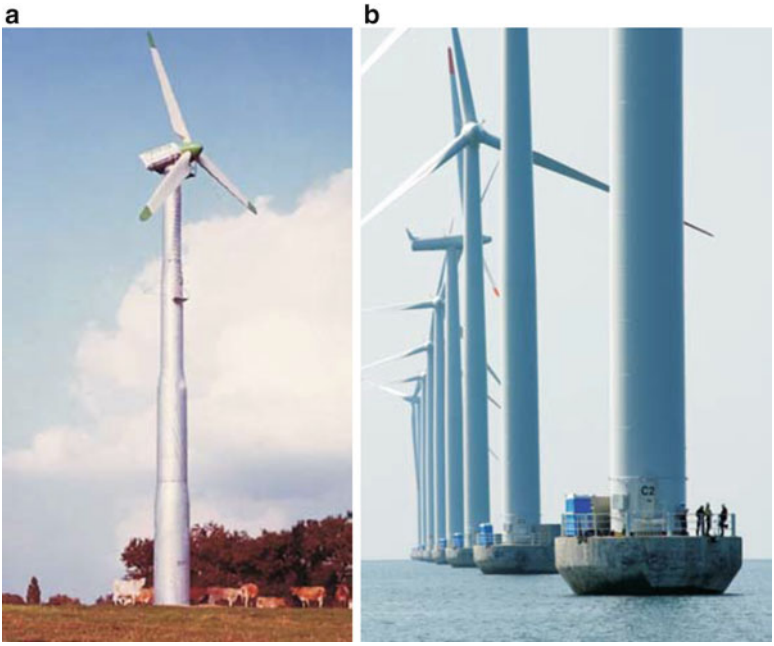

Fig. 1.3 (**a**) Single wind turbine of 30 KW used in the 1980s (Larsen 2005). (**b**) Arrays of HAWT of 2.3 MW each at the shores (Larsen 2005)

Fig. 1.4 Wind turbine blade in transportation (Statkraft 2012)

especially for the turbulence phenomena due to vortex shedding of the blades. Other effects such as rotation of the blades, the aerodynamics of the rotor blades, and the vibrations of the rotors also play a significant role in the dynamics of wind turbine blades, therefore affecting the operation and service life of the wind turbines. Moreover, with the consideration of cost of the turbines, the blades installed are becoming increasingly flexible. This causes the concerns of nonlinear vibrations of the blades, as the nonlinear vibrations may lead to large deflections or fatigue failures of the blades and gear boxes of the turbines.

1.2 Nonlinear Investigations of Wind Turbine Blades

The nonlinear vibrations described above produce instability of the wind turbine blades and therefore cause difficulties in controlling their operations and bring negative effects on the quality of the electricity generated by the wind turbines. The dynamics and nonlinear responses of the wind turbine blades therefore need to be studied and comprehended for designing and operating the wind turbines and their blades. Conventionally, the nonlinear structural dynamics of wind turbine blades were investigated considering the decoupling of tower and blade system. The entire wind blade was regarded as a rigid body which was studied as a Bernoulli-Euler beam. In 1983, Krenk (1983a) developed a linear theory for the blades simplified as pretwisted elastic beams which were considered as under general loads. The cross-sectional deformation in the longitudinal direction was investigated. Further research developed an explicit asymptotic formula for the torsion-extension coupling for the blades simplified as pretwisted elastic beams which had arbitrary homogeneous cross section (Krenk 1983b). Esmailzadeh and Jalili (1998) developed a linear model for the blades considered as non-rotating cantilever Timoshenko beams. Nevertheless, the study only considered the first mode of vibration. The results obtained showed that the increase of tip mass would almost always reduce the stable region. From the study of model established, it was concluded that purely flexural or even the Euler-Bernoulli model rather than Timoshenko would produce an incorrect periodic region. Kane et al. (1987) investigated the dynamics of a cantilever beam attached to a moving base. The stretching and bending in shear and warping directions were considered. Later on, Dwivedy and Kar (1999a, b) studied both the steady-state response and stability of a blade modelled as a slender beam with an attached mass retaining up to cubic nonlinearities. Hanagud and Sarkar (1989) redefined the stretch in studying a blade simplified as a cantilever beam attached to a moving support. The research was considered valid for large displacement. In 2004, Yang et al. (2004) studied the flexible motion of a blade considered as a uniform Euler-Bernoulli beam attached to a rotating rigid hub and developed a set of fully coupled nonlinear-differential equations to describe the axial, transverse, and rotational motions of the beam. The centrifugal stiffening effect was included without the restriction concerning angular velocity. The structural nonlinearities were found significant in studying the dynamic characteristics of the blade.

However, with the increase of the wind wing size, the large displacement of the wing in both edgewise and blade direction can no longer be considered as the second derivative of the elastic displacement. Larsen and Nielsen (2007) analysed the nonlinear dynamic responses of rotating wind turbine wings with considerations of the modal interactions due to parametric and additive excitation from the motions of a support point. In their study, the interaction between the nacelle and the wings is introduced as a support point motion of the wings (Larsen and Nielsen 2006). A Galerkin reduced degrees-of-freedom model was derived for analysing various nonlinear phenomena. Moreover, the important nonlinear coupling between the fundamental blade mode and the fundamental edgewise modes is identified by the reduced system.

With the increasing demand for large-scale wind turbines and for the high efficiency and controllability of the operations of the turbines, comprehension of the nonlinear behaviour of the wind turbine blades becomes all the time important. Several theoretical and numerical investigations on the nonlinear behaviour of the blades are seen in the current literature (Larsen and Nielsen 2006; Liu et al. 2015; Huang 2001). However, due to the complexities of the wind turbine blades under dynamic wind loads, not many systematic studies on nonlinear behaviour of the blades are found in the field, and a thorough comprehension of nonlinear behaviour of the blades is still lacking. The research presented in this chapter intends to study the nonlinear behaviour of the HAWT blades under fluctuating wind loads and to characterize these nonlinear behaviour. The influences of different external excitations due to the wind loads on the nonlinear responses of the blade are to be examined. With implementation of the newly developed periodicity-ratio (P-R) method, the nonlinear responses of the blade are quantitatively characterized, and the results are compared with that of the Lyapunov exponent method, which is probably the most popular method in the field in diagnosing nonlinear behaviour of a dynamic system. With the approach described in this chapter, the global responses of the wind turbine blades can be quantified and accurately diagnosed corresponding to large ranges of system parameters, geometric dimensions, and loading conditions. A periodic-nonperiodic-quasiperiodic-chaotic region diagram is to be created with the approach for quantitatively and graphically evaluating the nonlinear behaviour of the blades. This research is significant for HAWT blade designs with considerations of nonlinear vibrations of the blades. In analysing and characterizing the nonlinear responses of the HAWT blades, the approach described in this chapter shows efficiency and accuracy, in comparing with the other approaches used in the field.

1.3 HAWT Modelling

Figure 1.5 shows a sketch of HAWT considered in this chapter. The blade of the turbine is illustrated in Fig. 1.6. For the sake of clarity, the blade is considered as a cantilever beam. In Fig. 1.5, OX_0Y_0 represents the inertial coordinate system for the

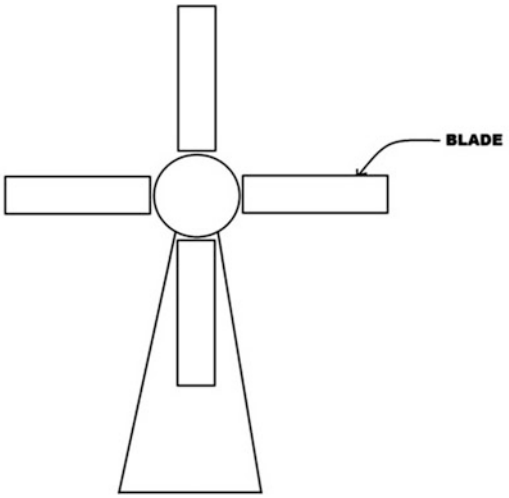

Fig. 1.5 Sketch of horizontal-axis wind turbines (HAWT)

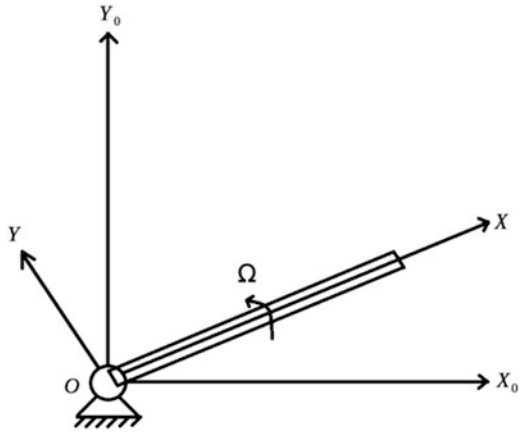

Fig. 1.6 Blade of turbine

blade, and the *OXY* is the rotating coordinate system moving with the blade under the wind load.

The speed of the blade is considered as varying with time and can be expressed as

$$\Omega = \Omega_0 + A\cos\omega t \tag{1.1}$$

where Ω_0 is the average angular velocity, A is amplitude, and ω is the frequency for blade rotation.

The wind speed can be divided into the long period and short period part (Wang and Zhang 2003). The varying velocity of the fluctuating wind applied on the turbine blade is assumed as

$$V_{\mathrm{v}} = V_0 + V(t) \tag{1.2}$$

where V_0 is the average wind speed and $V(t)$ is a function reflecting the fluctuating wind. According to the aerodynamic principle (Wang and Zhang 2003; Huang 2001), the wind force on any point of wind wing blade in the rotated plane can be written as

$$F(x) = \frac{1}{2}\rho S C_{\mathrm{L}}\left[(\Omega x)^2 + \left(\frac{2}{3}V_{\mathrm{h}}\right)^2\right] \tag{1.3}$$

where S is the area of the wind wing blade, C_{L} is the lift coefficient of the wing, and V_{h} is the wind speed on the hub.

For the sake of analysis, take the infinitesimal as an example, as shown in Fig. 1.4; the displacement can be ignored comparing with the length of the beam.

The centrifugal force on the X and Y direction can be written as in Eqs. (1.4a) and (1.4b):

$$f_x^a = f_{lx} + f_{kx} + f_{qx} = m\begin{bmatrix}(\Omega_0 + \Omega_{00}\cos\Omega_1 t)^2 x\\ +2(\Omega_0 + \Omega_{00}\cos\Omega_1 t)\dot{v}\\ -\Omega_{00}\Omega_1 \sin(\Omega_1 t)v\end{bmatrix} dx = f_x dx \tag{1.4a}$$

$$f_y^a = f_{ly} - f_{qy} = \left[m(\Omega_0 + \Omega_{00}\cos\Omega_1 t)^2 v + m\Omega_{00}\Omega_1 \sin(\Omega_1 t)x\right] dx = f_y dx. \tag{1.4b}$$

The equation of internal force of the infinitesimal can be written as in Eq. (1.4a), with the assumption that the beam is made of homogeneous material and the axis will not change after deformation as shown in the Fig. 1.7.

Therefore, the displacement of end **F** is obtained as follows:

$$\Delta\mathbf{F} = \mathbf{F}\mathbf{F}' = u(x,t)\mathbf{i} + v(x,t)\mathbf{j}, \tag{1.5}$$

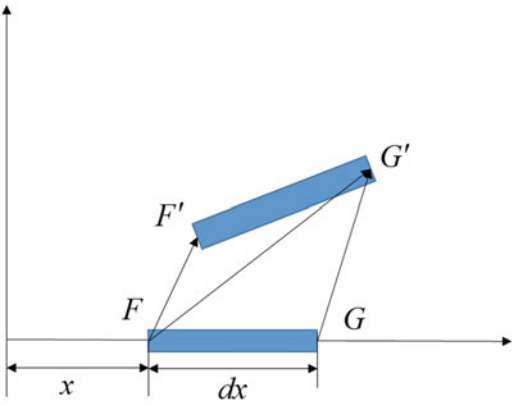

Fig. 1.7 Model of beam after deformation

and the displacement of end **G** is obtained by

$$\Delta\mathbf{G} = (u + u_x dx)\mathbf{i} + (v + v_x dx)\mathbf{j}. \tag{1.6}$$

F and G are two boundaries of the beam, and F' and G' are the two boundaries after deformation; the following equation can be obtained:

$$\Delta\mathbf{F} + \Delta\mathbf{F}'\mathbf{G}' = \Delta\mathbf{G} + dx\mathbf{i}, \tag{1.7}$$

where $\Delta\mathbf{F}$ is the displacement of the F and $\Delta\mathbf{G}$ is the displacement of the G. Therefore, the displacement of $\Delta\mathbf{F}'\mathbf{G}'$ can be acquired as

$$\Delta\mathbf{F}'\mathbf{G}' = \Delta\mathbf{G} + dx\mathbf{i} - \Delta\mathbf{F} = (u_x + 1)dx\mathbf{i} + v_x dx\mathbf{j}. \tag{1.8}$$

The length of the infinitesimal after deformation can be written as

$$|\Delta\mathbf{F}'\mathbf{G}'| = ds = \sqrt{(u_x + 1)^2 + v_x^2}. \tag{1.9}$$

And the extensional strain of the beam in axial direction can be calculated with

$$\varepsilon_0 = \frac{ds - dx}{dx} = \sqrt{(1 + u_x)^2 + v_x^2} - 1. \tag{1.10}$$

The bending strain from the central axis of the beam can be given as

$$\varepsilon_1 = y\left\{\frac{\partial^2 v}{\partial x^2}\left[1 + \left(\frac{\partial v}{\partial x}\right)^2\right]^{-3/2}\right\}. \tag{1.11}$$

Applying Taylor series expansion for above-mentioned equations, to obtain

$$\varepsilon_0 = \frac{ds - dx}{dx} = u_x + \frac{1}{2}v_x^2 + \cdots\cdots \tag{1.12}$$

$$\varepsilon_1 = y\left\{\frac{\partial^2 v}{\partial x^2}\left[1 + \left(\frac{\partial v}{\partial x}\right)^2\right]^{-\frac{3}{2}}\right\} = y\frac{\partial^2 v}{\partial x_2} + \cdots\cdots \tag{1.13}$$

According to Eqs. (1.12) and (1.13), strain ε is obtained by

$$\varepsilon = \varepsilon_0 + \varepsilon_1 = u_x + \frac{1}{2}v_x^2 + y\frac{\partial^2 v}{\partial x_2}. \tag{1.14}$$

In the cross section of the beam that is asymmetrical related to plane xz, one can have

$$E\iint_A y\frac{\partial^2 v}{\partial x_2}dA = 0. \tag{1.15}$$

In this case, the axial force of the deformation section along the vector $\Delta\mathbf{F}'\mathbf{G}'(\boldsymbol{\delta})$ is expressed with

$$N(x,t)\boldsymbol{\delta} = EA'\left[\frac{\partial u}{\partial x} + \frac{1}{2}\left(\frac{\partial v}{\partial x}\right)^2\right]\boldsymbol{\delta} = E\mathrm{A}'\frac{ds-dx}{dx}\boldsymbol{\delta}. \tag{1.16}$$

And the bending moment of the section in the beam is equal to

$$M(x,t) = \iint \sigma y d\mathrm{A}' = E\iint \varepsilon(x,y,t) y d\mathrm{A}' = EI\frac{\partial^2 v}{\partial x^2}. \tag{1.17}$$

Then, the shear force in the beam section is given by

$$Q = \frac{\partial M}{\partial x}\mathbf{j} = EIv'''\mathbf{j}. \tag{1.18}$$

Considering the aerodynamic force and inertia force and per the Newton's law, the dynamic equation of system can be given by

$$N(x,t)\boldsymbol{\delta} + F(x)\mathbf{j} + f_x\mathbf{i} + f_y\mathbf{j} = m\ddot{u}\,\mathbf{i} + m\ddot{v}\,\mathbf{j}. \tag{1.19}$$

In the above equation,

$$N(x,t)\boldsymbol{\delta} = \frac{u_x+1}{\sqrt{(u_x+1)^2+v_x^2}}\mathbf{i} + \frac{v_x}{\sqrt{(u_x+1)^2+v_x^2}}\mathbf{j}. \tag{1.20}$$

The governing equation along the X and Y directions can be expressed as

$$\frac{\partial}{\partial x}\left\{EA'\left\{1-\left[(1+u_x)^2+v_x^2\right]^{-0.5}\right\}(1+u_x)\right\} + f_x = m\ddot{u} \tag{1.21a}$$

$$\frac{\partial}{\partial x}\left\{EA'\left(1-\left[(1+u_x)^2+v_x^2\right]^{-0.5}\right)v_x\right\} - EIv'''' + F(x) + f_y = m\ddot{v} \tag{1.21b}$$

Assume $f(u_x, v_x) = \left[(1+u_x)^2+v_x^2\right]^{-0.5}$, Taylor series expansion of $f(u_x, v_x)$ can be implemented,

$$f(0,0) = 1, \tag{1.22}$$

$$\frac{\partial f}{\partial u_x} = (1+u_x)\left[(1+u_x)^2+v_x^2\right]^{-\frac{3}{2}}, \text{ thus } \left.\frac{\partial f}{\partial u_x}\right|_{\substack{u_x=0\\v_x=0}} = -1 \tag{1.23}$$

$$\frac{\partial f}{\partial v_x} = -v_x\left[\left(1+u_x^2\right)^2+v_x^2\right], \text{and therefore } \left.\frac{\partial f}{\partial v_x}\right|_{\substack{u_x=0\\v_x=0}} = 0 \tag{1.24}$$

$$\frac{\partial^2 f}{\partial u_x \partial \omega_x} = 3\omega_x(1+u_x)\left[(1+u_x)^2+\omega_x^2\right]^{-\frac{5}{2}}, \text{and } \left.\frac{\partial^2 f}{\partial u_x \partial \omega_x}\right|_{\substack{u_x=0\\ v_x=0}} = 0 \tag{1.25}$$

$$\frac{\partial^2 f}{\partial u_x^2} = -\left[(1+u_x)^2+\omega_x^2\right]^{-\frac{3}{2}} + 3(1+u_x)^2\left[(1+u_x)^2+\omega_x^2\right]^{-\frac{5}{2}}, \text{and} \left.\frac{\partial^2 f}{\partial u_x^2}\right|_{\substack{u_x=0\\ v_x=0}} = 2 \tag{1.26}$$

$$\frac{\partial^2 f}{\partial \omega_x^2} = -\left[(1+u_x)^2+\omega_x^2\right]^{-\frac{3}{2}} + 3\omega_x^2\left[(1+u_x)^2+\omega_x^2\right]^{-\frac{5}{2}}, \text{and thus} \left.\frac{\partial^2 f}{\partial \omega_x^2}\right|_{\substack{u_x=0\\ v_x=0}} = -1. \tag{1.27}$$

Then, $f(u_x, v_x)$ can be expressed by

$$f(u_x, v_x) = 1 - u_x + u_x^2 - \frac{1}{2}v_x^2. \tag{1.28}$$

Equation (1.21a) can be rewritten as

$$u_{xx} + \frac{\partial\left[\frac{1}{2}v_x^2 + \frac{1}{2}u_x v_x^2 - u_x^3\right]}{\partial x} + \frac{f_x}{EA'} = \frac{m}{EA'}\ddot{u}. \tag{1.29}$$

Neglecting the third-order nonlinear and inertia terms, applying the integral operation, Eq. (1.29) can be rearranged by

$$u_x = e(t) - \frac{1}{2}v_x^2 - \frac{1}{EA'}\int_0^x f_x dx. \tag{1.30}$$

Sequentially, with Taylor expansion for Eq. (1.21b) and retaining the second-order term, one may have

$$EA'\frac{\partial}{\partial x}\{u_x v_x\} - EIv'''' + F(x) + f_y = m\ddot{v}. \tag{1.31}$$

Substitute Eq. (1.25) into Eq. (1.26) to obtain

$$m\ddot{v} + EIv'' - EA'e(t)v''' - F(x) + \frac{\partial\int_0^x f_x dx}{\partial x}v' - f_y = 0. \tag{1.32}$$

Substituting the interrelated formulas into Eq. (1.32), one may obtain

$$\begin{aligned} &m\ddot{v} + EIv'' - EA'e(t)v''' - \rho_{\text{air}}SC_{\text{L}}\left[(\Omega_0+\Omega_{00}\cos\Omega_1 t)^2 x^2 + \frac{4}{9}(V_0+V_1\cos\Omega_2 t)\right] \\ &+\frac{\partial}{\partial x}\left\{\int_0^x\left[(\Omega_0+\Omega_{00}\cos\Omega_1 t)^2 x + 2(\Omega_0+\Omega_{00}\cos\Omega_1 t)\dot{v} - \Omega_{00}\Omega_1\sin(\Omega_1 t)v\right]v' dx\right\} \\ &-\left[(\Omega_0+\Omega_{00}\cos\Omega_1 t)^2 v + \Omega_{00}\Omega_1\sin(\Omega_1 t)x\right] = 0 \end{aligned} \tag{1.33}$$

with boundary conditions

$$\begin{aligned} x = 0: \quad & v = 0, \quad \frac{\partial v}{\partial x} = 0, \\ x = l: \quad & \frac{\partial^2 v}{\partial x^2} = 0, \quad \frac{\partial^3 v}{\partial x^3} = 0. \end{aligned} \tag{1.34}$$

Introduce the following dimensionless parameters into Eq. (1.33):

$$\begin{aligned} & x^* = \frac{x}{l}, v = \frac{v}{l}, g = \frac{Al^2}{2I}, p = \frac{\rho_{\text{air}} S C_{\text{L}} l^3}{2m}, t^* = \sqrt{\frac{EI}{ml^4}} t, V_0^* = \sqrt{\frac{EI}{ml^4}} V_0, V_1^* = \sqrt{\frac{EI}{ml^4}} V_1, \\ & \Omega_0^* = \sqrt{\frac{ml^4}{EI}} \Omega_0, \Omega_{00}^* = \sqrt{\frac{ml^4}{EI}} \Omega_{00}, \Omega_1^* = \sqrt{\frac{ml^4}{EI}} \Omega_1, \Omega_2^* = \sqrt{\frac{ml^4}{EI}} \Omega_2. \end{aligned} \tag{1.35}$$

The dimensionless form (3.24) of the partial differential Eq. (1.34) can be obtained as shown below:

$$\begin{aligned} & \ddot{v} + 2\mu\dot{v} + v'''' - g\int_0^1 v'' v'^2 dx - p\left[(\Omega_0 + A\cos\omega t)^2 x^2 + \frac{4}{9}(V_0 + V_1\cos\omega_1 t)^2\right] \\ & + \frac{\partial}{\partial x}\left\{\int_0^1 \left[(\Omega_0 + A\cos\omega t)^2 x + 2(\Omega_0 + A\cos\omega t)\dot{v} - A\omega\sin(\omega t) v\right] v' dx\right\} \\ & - \left[(\Omega_0 + A\cos\omega t)^2 v + A\omega\sin(\omega t) x\right] = 0 \end{aligned} \tag{1.36}$$

where μ is the damping coefficient and ω_1 is the frequency of the wind fluctuation. Apply Galerkin method to discretize Eq. (1.36), and assume that the solution of Eq. (1.36) can be expressed as

$$v(x) = y_1(t)^* Y_1(x) \tag{1.37}$$

where y_1 is a weight function of time and Y_1 is the mode function of the blade. Assume that the mode function takes the following form:

$$Y_j(x) = \cos h(r_j x) - \cos(r_j x) + \frac{\cos hr_j + \cos r_j}{\sin hr_j + \sin r_j}\left[\sin hr_j - \sin r_j\right]. \tag{1.38}$$

Substituting the solution and the mode function into Eq. (1.36), the following governing equation for the beam can thus be obtained as the following:

$$\begin{aligned} & \ddot{y}_1 + 2\mu_1\dot{y}_1 + \omega_0^2 y_1 - a y_1^3 - bp(\Omega_0 + A\cos\omega t)^2 + \frac{4}{9}cp(V_0 + V_1\cos\omega_1 t)^2 \\ & - (\Omega_0 + A\cos\omega t)^2 y_1 - A\omega d\sin(\omega t) = 0 \end{aligned} \tag{1.39}$$

where

$$a = -g\lambda_r^2 \int_0^1 Y_1''(x)dx, \quad b = \int_0^1 Y_1(x)x^2 dx$$
$$c = \int_0^1 Y_1(x)dx, \quad d = \int_0^1 xY_1(x)dx.$$

1.4 Implementation of Periodicity-Ratio in Characterizing Nonlinear Dynamic Responses

1.4.1 Concept of Periodicity-Ratio Method

The periodicity-ratio method or P-R method is an efficient method for diagnosing nonlinear behaviour of dynamic systems. The P-R method considers the geometry of Poincare maps of nonlinear response. An index named P-R value is developed to describe the periodicity of a system through an examination of the overlapping points in a Poincare map with respect to the total number of points generated by Poincare sections (Nayfeh and Mook 1979; Dai 2008; Dai and Wang 2008). Consider a general dynamic system subjected to an external excitation of period T; for a solution of a considered system $x(t)$, the following expression must be satisfied if it is a periodic solution:

$$x(t_0 + jT) = x(t_0), \tag{1.40}$$

where t_0 denotes a random time and j is the number of visible points in the corresponding Poincare map and T is the period of the system. For a completely periodic system, all the points in a Poincare map must be overlapping points, regardless of how large the time rang is. For a real dynamical system, there is a finite number of j points in the Poincare map. To define whether a point in the Poincare map is an overlapping point or not can be judged by the following equations (Dai 2008; Dai and Wang 2008):

$$X_{ki} = |X(t_0 + kT) - X(t_0 + iT)|, \tag{1.41}$$
$$\dot{X}_{ki} = \left|\dot{X}(t_0 + kT) - \dot{X}(t_0 + iT)\right|, \tag{1.42}$$

where k is an integer in the range $1 \le k \le j$ and i is an integer in the range $1 \le i \le n$ in which n is the total number of points generated for the Poincare map over the time range considered. Equation (1.41) and Eq. (1.42) are to define whether the displacements and velocities of the two points i and k are identical receptively. With these definitions, the following conclusions can be obtained:

1. As the points in the Poincare map are represented by displacement and velocity indicated as $(x_i, \dot{x}_i)$ for the ith points, if the ith point $(x_i, \dot{x}_i)$ is an overlapping

point of the kth point $(x_k, \dot{x}_k)$, the velocity and displacement of the kth point should be identical with the ith point. The two points can be concluded as overlapping points.

2. The point $(x_i, \dot{x}_i)$ is considered to be an overlapping point of $(x_k, \dot{x}_k)$ if and only if the expressions of Eqs. (1.41) and (1.42) satisfy the following conditions:

$$X_{ki} = 0; \dot{X}_{ki} = 0. \tag{1.43}$$

If the above conditions are satisfied, the two points can be regarded as overlapped points with each other. The total number of the points overlapping the kth point can be calculated by

$$\zeta(k) = \left\{\sum\nolimits_{i=k}^{n} \left[Q(X_{ki})Q\left(\dot{X}_{ki}\right)\right]\right\} P\left(\sum\nolimits_{i=k}^{n} \left[Q(X_{ki})Q\left(\dot{X}_{ki}\right)\right] - 1\right), \tag{1.44}$$

where $Q(y)$ and $P(z)$ are step functions expressed in the following form:

$$Q(y) = \begin{cases} 1, & \text{if } y = 0; \\ 0, & \text{if } y \neq 0; \end{cases} \tag{1.45}$$

$$P(z) = \begin{cases} 1, & \text{if } z = 0; \\ 0, & \text{if } z \neq 0. \end{cases} \tag{1.46}$$

The total number of overlapping points can be expressed as

$$N = \zeta(1) + \sum\nolimits_{k=2}^{n} \zeta(k)\, P\left(\prod\nolimits_{i=1}^{k-1} \left\{X_{ki} + \dot{X}_{ki}\right\}\right). \tag{1.47}$$

For a perfect periodic case,

$$N = \sum\nolimits_{k=1}^{j} \zeta(k). \tag{1.48}$$

1.4.2 Further Development in Determining for P-R Values

Overlapping points are not necessarily periodically appearing in a Poincare map. To determine the number of the periodic points in a Poincare map, assume that there are M sets of visible points in a Poincare map and j sets among these contain overlapping points.

Consider the average time span of the overlapping points:

$$\tau = \frac{t_{k,q} - t_{k,1}}{q - 1}, \tag{1.49}$$

where q represents the number of the overlapping points in the kth set and $t_{k,q}$ indicates the time when the qth overlapping point appears. In the kth set, each overlapping point may appear in every τ time units named periodic overlapping

points. Consider the following variance for determining how periodic overlapping points may occur:

$$p^2 = \frac{\sum_i^{q-1} (t_{k,i+1} - t_{k,i} - \tau)^2}{q-1}. \tag{1.50}$$

If p^2 equals to 0 or is small enough, the overlapping points in the kth set are completely periodic overlapping points.

Considering the kth set of overlapping points among the j sets, the time span between the ith point in the kth set and the $i+1$th point in the same set can be defined as

$$T_{k,i} = t_{k,i+1} - t_{k.i}. \tag{1.51}$$

And the time span between the $(i+2)th$ point and the $(i+1)th$ point can be described:

$$T_{k,i+1} = t_{k,i+2} - t_{k,i+1}. \tag{1.52}$$

If the overlapping points in the kth set satisfy the following equation:

$$T_{k,i} - T_{k,i+1} = 0 \tag{1.53}$$

then the $i, i+1, i+2$ points are periodic points. The number of periodic points with an identical time span in the kth group can be determined by employing the following formula:

$$\xi(i) = \left\{ \sum_{h=i}^{q-1} Q(T_{k,h} - T_{k,h+1}) \right\} P\left(\sum_{h=i}^{q-1} Q(T_{k,h} - T_{k,h+1}) - 1 \right) + P\left(Q\left(\sum_{h=i}^{q-1} Q(T_{k,h} - T_{k,h+1}) \right) \right). \tag{1.54}$$

The total number of periodic points in the kth set can be given by

$$\phi(k) = \xi(1) + \sum_{i=2}^{q-1} \xi(i) P\left(\prod_{h=1}^{i-1} \{T_{k,h} - T_{k,h+1}\} \right). \tag{1.55}$$

The total number of periodic overlapping points (NPP) is expressible as

$$\text{NPP} = \sum_{k=1}^{j} \phi(k). \tag{1.56}$$

Thus, the P-R value can be defined as

$$\gamma = \lim_{n \to \infty} \frac{\text{NPP}}{n}. \tag{1.57}$$

The P-R value therefore quantifies the periodicity of a response of a dynamic system. If the dynamic system is completely periodic, all the points in the Poincare

map are overlapping points, and the P-R value should equal to 1. If a system is completely nonperiodic, γ equals 0, the system will be quasiperiodic or chaotic. The quasiperiodic cases can then be distinguished from chaos by the other means such as least square method. Also, as one may notice that there may exist infinite number of different types of response with different P-R values in between zero and one, it should be noticed that the P-R value is calculated based on the infinitely large number of n and the time range considered should be $t \in [0, \infty)$.

1.5 Lyapunov Exponent

1.5.1 Concept of Lyapunov Exponent

In order to understand the characteristics of the Lyapunov exponent method, it may need to review the definition and application of the method. Lyapunov exponent of a dynamical system is used to measure the sensitive dependence upon initial conditions that is a characteristic of chaotic behaviour. The exponent actually indicates the average exponential rate of divergence or convergence of nearby trajectories in a phase diagram.

For a system evolving from two slightly differing initial conditions, say x and $x + \varepsilon$, where ε is a small quantity, after n iterations of a numerical simulation, the divergence of the two systems can be characterized approximately as

$$\varepsilon(n) \approx \varepsilon e^{\lambda n}, \tag{1.58}$$

where λ is defined as the Lyapunov exponent.
Considering a nonlinear dynamic described by a general equation

$$x_{n+1} = f(x_n) \tag{1.59}$$

after n iterations, the difference between two initially nearby states can be written as

$$f^n(x + \varepsilon) - f^n(x) \approx \varepsilon \mathrm{e}^{\lambda n}, \tag{1.60}$$

where $f^n(x) = f\{f[\ldots f[f(x)]\ldots]\}$.
Taking the natural logarithm of the equation, it can be obtained as

$$\ln\left[\frac{f^n(x + \varepsilon) - f^n(x)}{\varepsilon}\right] \approx n\lambda. \tag{1.61}$$

For small ε, the general expression of the Lyapunov exponent can be given by

$$\lambda \approx \frac{1}{n} \ln\left|\frac{df^n}{dx}\right|, \tag{1.62}$$

or

$$\lambda = \lim_{n\to\infty} \frac{1}{n} \sum_{i=0}^{n-1} \ln \left| f'(x_i) \right|. \tag{1.63}$$

From the definitions above, it can be seen that when $\lambda < 0$, the system is periodic, while if $\lambda > 0$, nearby trajectories diverge, and the evolution is sensitive to initial conditions and is therefore chaotic. However, the divergence of chaotic trajectories can only be locally exponential. Therefore, to obtain the Lyapunov exponents, one must average the local exponential growth over a long time. Lyapunov exponents have been defined in terms of the principal axes of an *n*-dimensional ellipsoid in an n-dimensional phase space. Similarly, the behaviour of the volume of the ellipsoid is related to the sum of Lyapunov exponents. The relative rate of change of an n-dimensional volume *V* in *n*-dimensional phase space under the action of flow is given by the 'Lie derivative' (Rong et al. 2002; Shahverdian and Apkarian 2007; Kim and Choe 2010).

For an *n*-dimensional system, there are *n* Lyapunov exponents, since stretching can occur for each axis. An *n*-dimensional initial volume is developed as (Henon 1976; Wolf et al. 1985)

$$V = V_0 e^{(\lambda_1+\lambda_2+\lambda_3)n}. \tag{1.64}$$

For the continuous time dynamic system, the *n*-dimensional initial volume developed as

$$V = V_0 e^{(\lambda_1+\lambda_2+\lambda_3)t}. \tag{1.65}$$

For a dissipative system, the sum of the exponents must be negative. If the system is chaotic, then at least one of the exponents is positive.

Taking a driven pendulum system as an example, three Lyapunov exponents should be used to describe the three dimensions of the phase space $(\theta, \omega, \varphi)$ where θ is the phase angle, ω is the phase velocity, and φ is the initial phase angle. Since the orbits of the pendulum are the solutions to a set of differential equations governing the dynamic system, the calculation for the Lyapunov exponents is rather complicated. On a chaotic attractor, the directions of divergence and contraction are locally defined, and the calculation must be constantly adjusted. Despite this difficulty, many computer programs have been developed for calculating Lyapunov exponents. The Lyapunov exponent approach is not valid for diagnosing whether or not this system is periodic or chaotic if it cannot determine an expression for a dynamic system. The usual test for chaos with the utilization of the Lyapunov exponent is the calculation for the largest Lyapunov exponent. The largest positive Lyapunov exponent of a system is believed to indicate the corresponding system is chaotic. As an example, for a three-dimensional dissipative system, (0, −, −) of the Lyapunov exponents implies stable limit cycle; (0, 0, −) implies quasiperiodic oscillation, and (+, 0, −) suggests a strange attractor of chaos (Carbajal-Gómez et al. 2013). For a four-dimensional dissipate dynamical system, (+,+,0,−),

(+,0,0,−), and (+,0,−,−) of the Lyapunov exponent indicate strange attractors, and the first cases represent hyperchaos, as indicated in hyper-Rossler system (Shin and Hammond 1998; Liao 2016). Currently, Lyapunov exponent is the only method to diagnose hyperchaos.

1.5.2 Calculation of Lyapunov Exponent Spectrum

There are several different methods to calculate the Lyapunov exponent, such as the whole Lyapunov exponent, global and local Lyapunov exponent, and Lyapunov spectrum. The method of whole Lyapunov exponent also known as the maximum Lyapunov exponent is suitable for the discrete differential system, whereas the Lyapunov spectrum is more suitable for continuous differential systems (Castanier and Pierre 1995; Yang and Wu 2011). The global Lyapunov exponent, on the other hand, gives a measure for the total predictability of a system, whereas the local Lyapunov exponent estimates the local predictability around a given point in phase space.

Considering an n-dimensional continuous dynamical system

$$\frac{dX}{dt} = F(X) \tag{1.66}$$

$X(t)$ such as $X\ (t = 0) = X_0(t)$ represents a trajectory of the system from $X_0(0)$, and $X\ (t)$ is another trajectory, let define

$$\check{X}\ (t) = X(t) - X_0(t). \tag{1.67}$$

It can be obtained that

$$\frac{d\check{X}}{dt} = \mathrm{DF}(X_0(t), t)\check{X} \tag{1.68}$$

where DF is the Jacobian matrix with time-dependent coefficients. If we consider an initial deviation of $X_0(t)$, then

$$\check{X}\ (t) = M(t)\tilde{X}_0 \tag{1.69}$$

where $M(t)$ is the fundamental (transition) matrix solution of Eq. (1.67) associated with the trajectory $X_0(t)$ and the evolution equation of M(t) can be obtained as

$$\frac{dM(t)}{dt} = \mathrm{DF}(X_0(t), t)M(t). \tag{1.70}$$

For an appropriately chosen $X_0(t)$, the rate of the exponential expansion or contraction in the direction of $X_0(t)$ on the trajectory passing through X_0 can be expressed as

$$\lambda_i = \lim_{t\to\infty} \frac{1}{t} \ln \left(\frac{\|X_0(t)\|}{\|X_0(0)\|} \right. \tag{1.71}$$

where the symbol $\|\|$ represents the vector norm and λ_i is the calculated Lyapunov exponent.

To obtain the Lyapunov exponent spectrum for a continuous dynamical system, a set of linearly independent vectors $x_1, x_2, x_3 \ldots x_n$ may form the basis of the n-dimensional state space. Choosing an initial deviation along each of these n factors, n Lyapunov exponent λ_i can be determined, and this set of Lyapunov exponent can be defined as Lyapunov exponent spectrum. For each initial vector, the Eq. (1.70) can be integrated for a finite time T, and a set of vectors $X_1(T)$, $X_2(T), \ldots X_n(T)$ can be obtained. The new set of vectors is orthonormalized by the application of Gram-Schmidt procedure as follows:

$$\hat{X}_1 = \frac{X_{1(T)}}{\|X_1(T)\|} \tag{1.72}$$

$$\hat{X}_n = \frac{X_n(T) - \sum_{i=1}^{n-1} \left[X_n(T)\hat{X}_i\right]\hat{X}_i}{\left\|X_n(T) - \sum_{i=1}^{n-1} \left[X_n(T)\hat{X}_i\right]\hat{X}_i\right.}. \tag{1.73}$$

Subsequently, using $X(t = T)$ as an initial condition for Eq. (1.70) and using each of the $\hat{X}_i$ as an initial condition for Eq. (1.69), Eqs. (1.69) and (1.70) can be integrated again for a finite time and carry out the Gram-Schmidt procedure to obtain a new set of orthonormal vectors. The norm in the denominator can be denoted by N_j^k. Thus, after repeating the integrations and the processes of Gram-Schmidt orthonormalization r times, the Lyapunov exponent can be obtained from

$$\widehat{\lambda}_i = \frac{1}{rT} \sum_{k=1}^{r} \ln N_j^k \tag{1.74}$$

The Lyapunov exponent spectrum can be obtained as a consequence.

Numerous numerical methods are proposed to estimate the spectrum of the Lyapunov exponent (Odavic et al. 2017) base on the numerical integration of vibrational equation, aiming to improve the accuracy and efficiency of algorithms. The Lyapunov exponent is also applied in diagnosing the dynamic of the system in engineering applications (Czolczynski et al. 2017). Moreover, numerous researches have been conducted for the development of Lyapunov exponent. For instance, it has shown its efficiency in differentiating the hyperchaotic system in a four-dimensional vibrational system (Yang and Liu 2013; Li et al. 2014).

Although the spectrum of the Lyapunov exponent has been proven to be one of the most theoretically sound methods which can be used to obtain a measure of the sensitive dependence upon initial conditions and has been proven as a powerful tool in characterizing the nonlinear behaviour of dynamic systems (Kim and Choe 2010; Wolf et al. 1985; Castanier and Pierre 1995), it should be noticed, however, although the Lyapunov exponent method is developed on a solid theoretical

basis, the actual determination of the Lyapunov exponents is rather time-consuming and relying on numerical calculations. The numerical method used and the numerical computations themselves may bring unavoidable errors in determining the Lyapunov exponents.

1.6 Analyses and Diagnosis of the Nonlinear Behaviour of the Wind Turbine Blade

The behaviour of the HAWT blade governed by the model described in Sect. 1.3 is nonlinear and complex. With the utilization of the model, the nonlinear behaviour of the HAWT blade can be examined numerically. For diagnosing the nonlinear behaviour of the blade, the P-R method can be implemented.

Numerical simulations based on fourth-order Runge-Kutta method can be conducted to demonstrate the nonlinear motions of the considered system, though the other numerical methods can also be considered. In order to demonstrate the types of the nonlinear responses of the system governed by the model established in Sect. 1.3, phase diagrams and Poincare maps of are plotted for various cases. Figures 1.8 and 1.9 show the phase diagram and Poincare map, respectively, for a periodic case with a specific set of parameters. The P-R value corresponding to this case is indeed equal to 1, i.e. all the overlapping points in the corresponding Poincare map are periodic, as expected.

Many cases are found irregular, i.e. neither perfectly chaotic nor perfectly periodic. Figures 1.10 and 1.11 indicate the phase diagram and Poincare map for such an irregular case of which the P-R equals to 0.34.

Quasiperiodic cases of the nonlinear system considered are also found in the numerical simulations. Figures 1.12 and 1.13 illustrate the phase diagram and Poincare map for a quasiperiodic case of which the P-R value is zero.

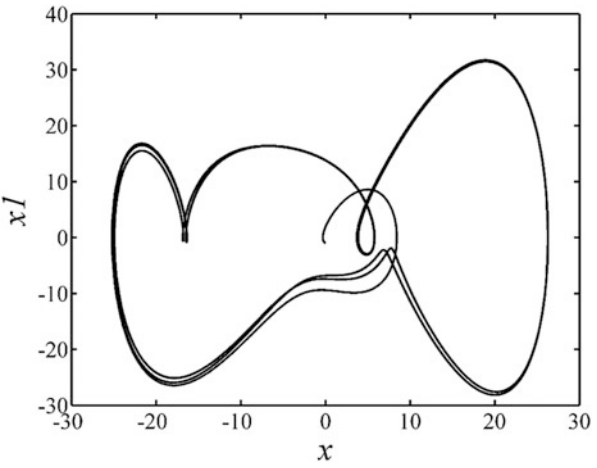

Fig. 1.8 Phase diagram $\Omega = 1.2, V_1 = 1$

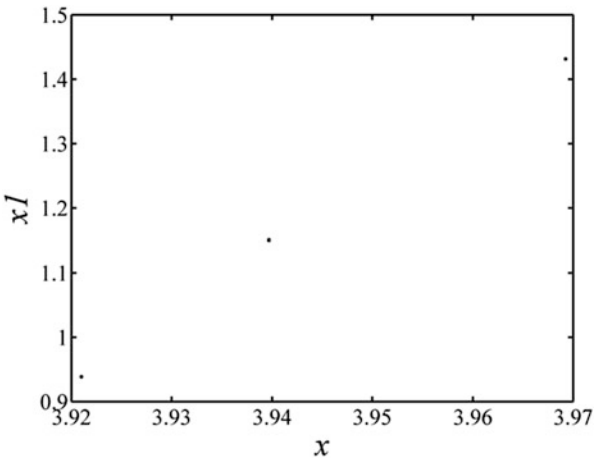

Fig. 1.9 Poincare map $\Omega = 1.2$, $V_1 = 1$

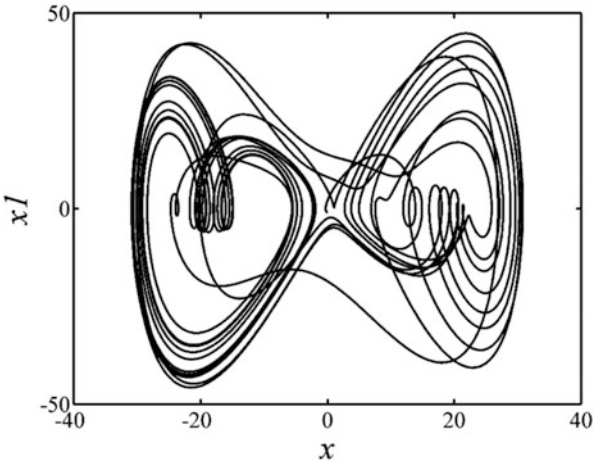

Fig. 1.10 Phase diagram $\Omega = 2.4$, $V_1 = 3$

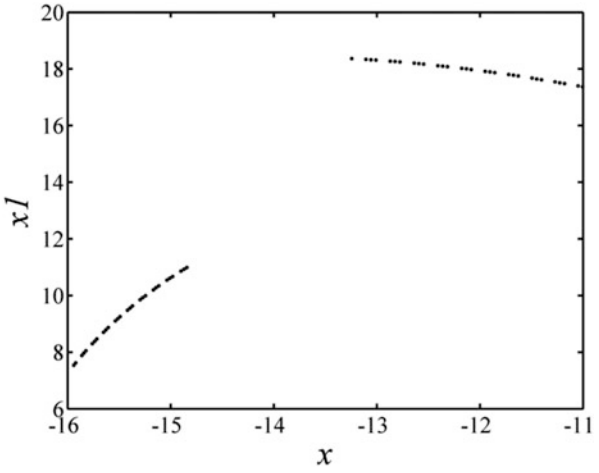

Fig. 1.11 Poincare map $\Omega = 2.4$, $V_1 = 3$

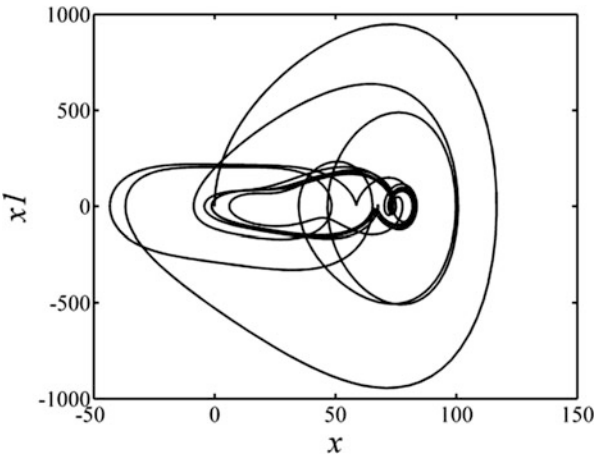

Fig. 1.12 Phase diagram $\Omega = 3, V_1 = 16$

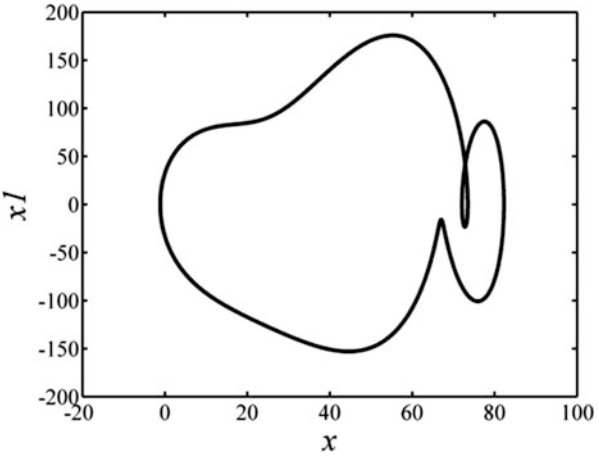

Fig. 1.13 Poincare map $\Omega = 3, V_1 = 16$

The system considered has chaotic responses as well. Figures 1.14 and 1.15 show the phase diagram and Poincare map for a chaotic case of this system. In this case, the P-R equal is zero as expected.

In considering that the P-R value can be used as a single value index to describe the periodicity for infinite types of responses of a nonlinear system, the nonlinear behaviour of the system can be quantitatively diagnosed by the P-R method without physically plotting a single diagram, and large ranges of system parameters can be considered as desired. With the P-R values, therefore, a diagram named periodic-quasiperiodic-chaotic region diagram can be conveniently constructed for graphically demonstrating the nonlinear behaviour of the turbine blade considered over the ranges of system parameters needed. Two of such diagrams are shown in Figs. 1.16 and 1.17, for analysing the nonlinear responses of the blade under various wind speed and turbine rotation speed. In the diagrams, blue diamonds are used for

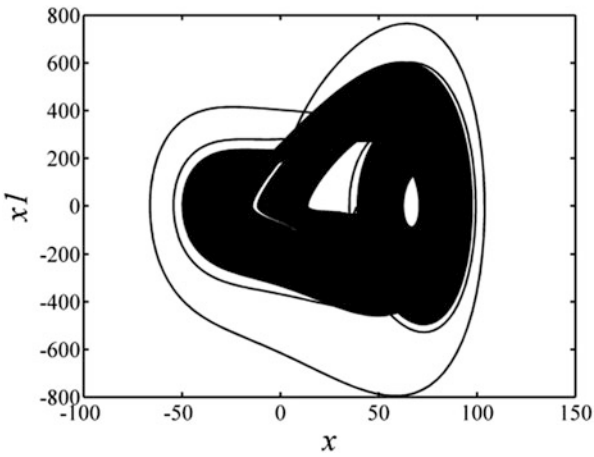

Fig. 1.14 Phase diagram $\Omega = 4$, $V_1 = 10$

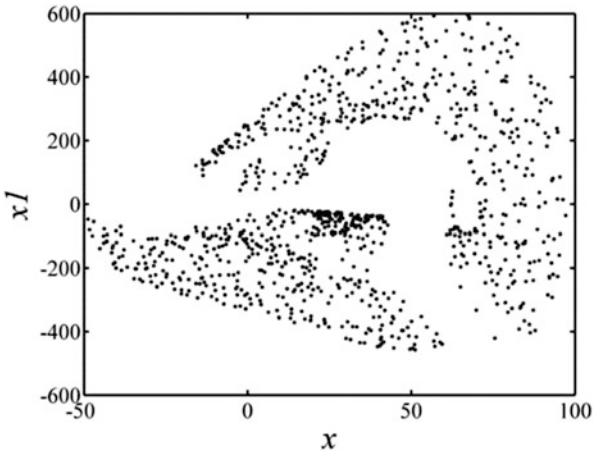

Fig. 1.15 Poincare map $\Omega = 4$, $V_1 = 10$

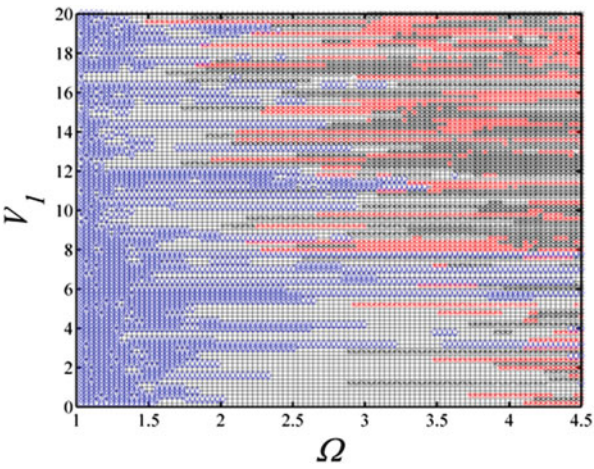

Fig. 1.16 Nonlinear behaviour region diagram (V_1 vs. Ω)

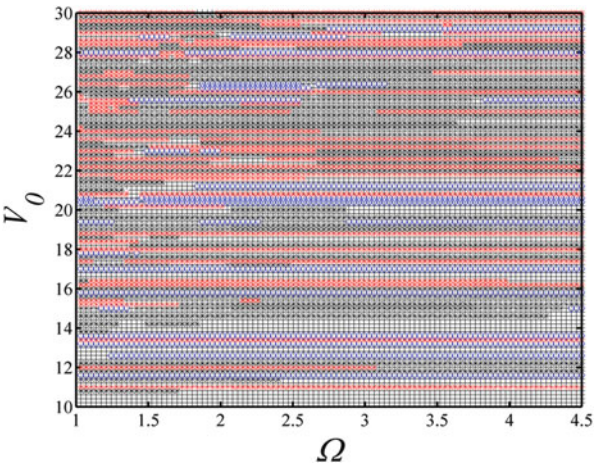

Fig. 1.17 Nonlinear behaviour region diagram (V_0 vs. Ω)

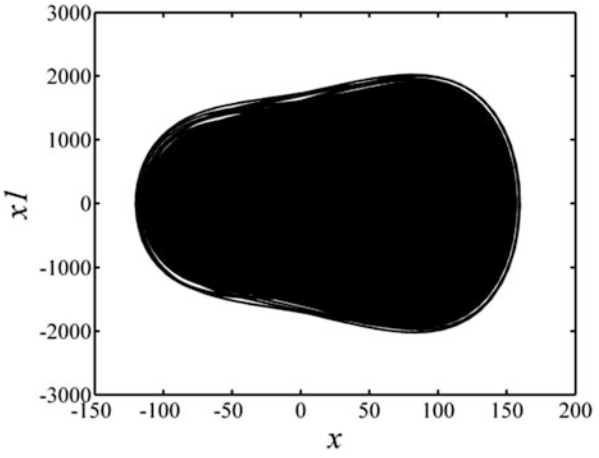

Fig. 1.18 Phase diagram $\Omega = 4.5$, $V_0 = 20$

illustrating the periodic responses of the blade, red stars for chaos, and black stars for quasi-periodic motions. As found in the present research, some of the responses of the system are not falling into the well-categorized characteristics; they can be nonperiodic, i.e. not periodic, or quasiperiodic or chaotic, though they may show certain level of periodicity. They are therefore named irregular motions and plotted with black plus symbols (+'s) as shown in Figs. 1.16 and 1.17.

As can be seen from Fig. 1.16, various responses may occur with respect to different wind speed and turbine rotation speed. The nonlinear behaviour can be identified from the region diagram within a large range of parameters. When wind speed and turbine rotation speed become larger, chaotic response of the blade may occur as can be seen from Figs. 1.18 and 1.19. Moreover, Figs. 1.20, 1.21, 1.22, and 1.23 show the quasiperiodic and periodic selected cases from Fig. 1.17 considering the parameters Ω and V_0.

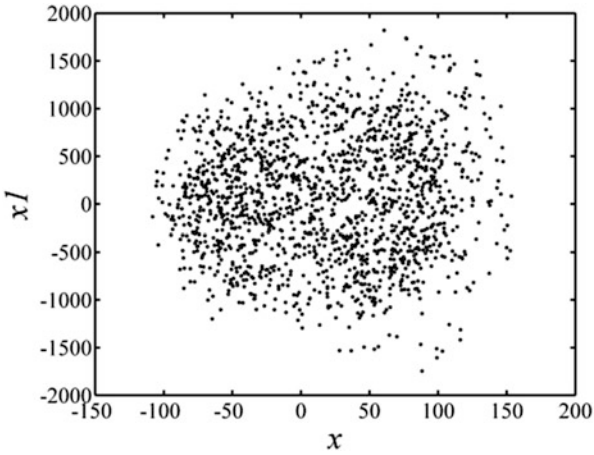

Fig. 1.19 Poincare map $\Omega = 4.5$, $V_0 = 20$

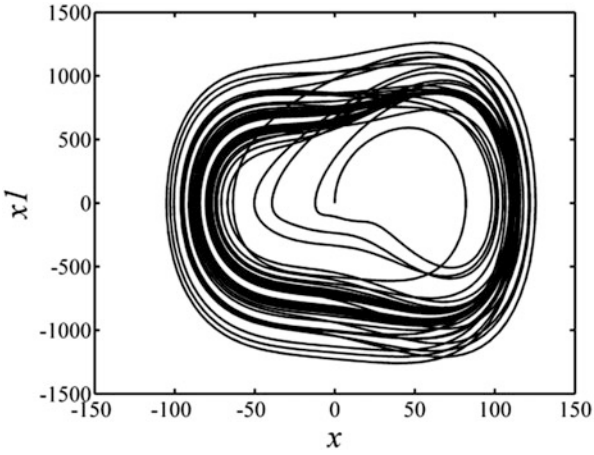

Fig. 1.20 Phase diagram $\Omega = 3.5$, $V_0 = 15$

It can be seen, from the region diagram, the dynamical behaviour varies with a tiny change of parameters. Figures 1.24 and 1.25 show the phase diagram and Poincare map of a chaotic case with P-R value 0. Figures 1.26 and 1.27 represent a periodic case with P-R equal to 1. It can be seen that, with the Ω change from 2.7 to 3.2, the system changes from chaos to a periodic case.

The Lyapunov exponent method is probably the most popular method used in the field for diagnosing the nonlinear behaviour of a dynamic system. Lyapunov exponent determines convergence or divergence of a system. Convergent cases are usually considered as periodic cases. However, as recognized by the researchers in the field, not all the converged cases are periodic cases (Henon 1976). As found in the present research, the Lyapunov exponent approach is less reliable for some cases especially when its maximum value is around zero. One case, in comparing with the approach of P-R method, is shown in Figs. 1.28 and 1.29. As can be seen

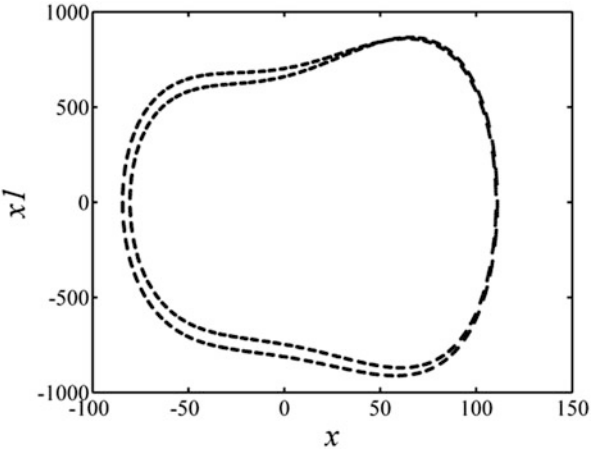

Fig. 1.21 Poincare map $\Omega = 3.5$, $V_0 = 15$

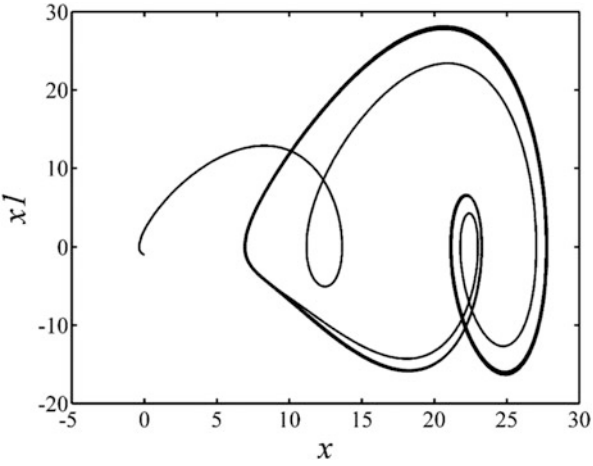

Fig. 1.22 Phase diagram $\Omega = 1.2$, $V_0 = 10.8$

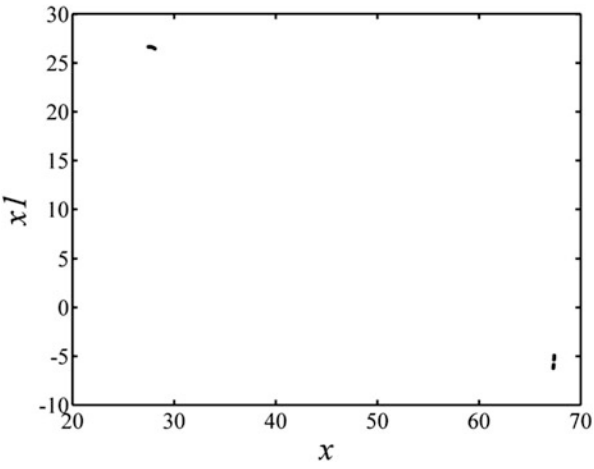

Fig. 1.23 Phase diagram $\Omega = 1.2$, $V_0 = 10.8$

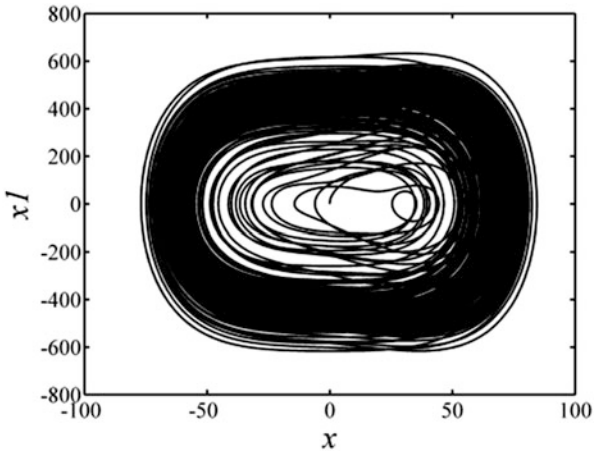

Fig. 1.24 Phase diagram $V_1 = 12, \Omega = 3.2$

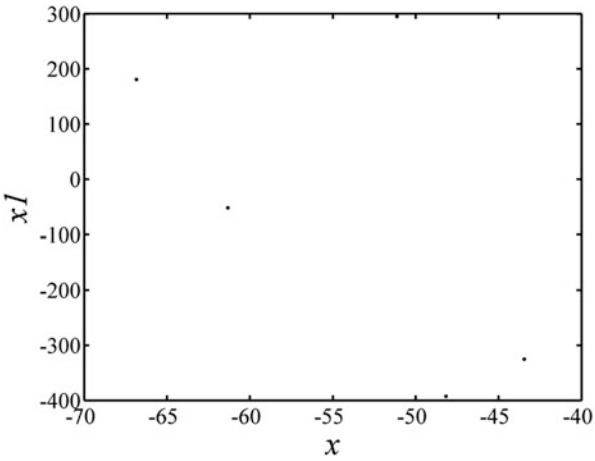

Fig. 1.25 Poincare map $V_1 = 12, \Omega = 3.2$

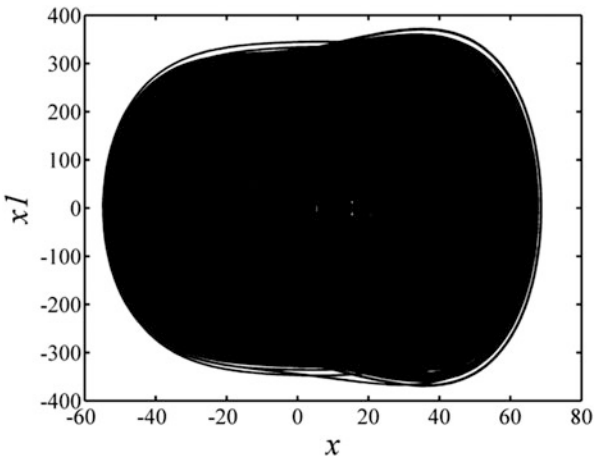

Fig. 1.26 Phase diagram $V_1 = 12, \Omega = 2.7$

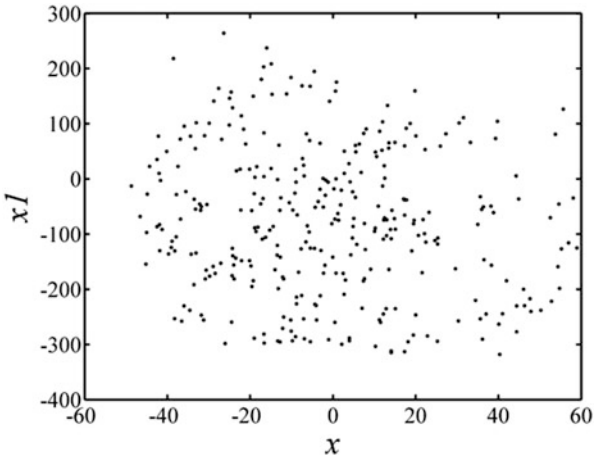

Fig. 1.27 Poincare map $V_1 = 12$, $\Omega = 2.7$

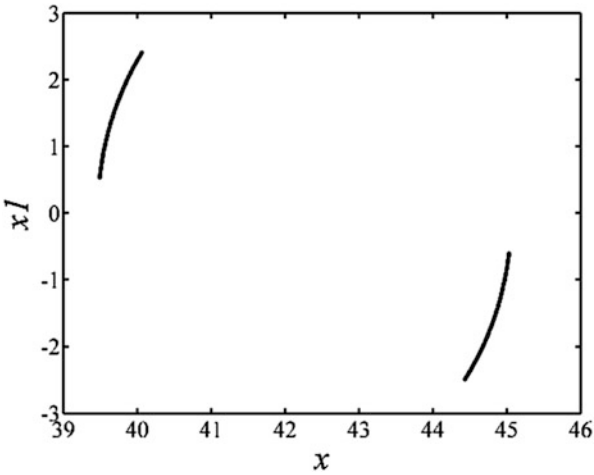

Fig. 1.28 Poincare map $\Omega = 14$, $V_1 = 10$

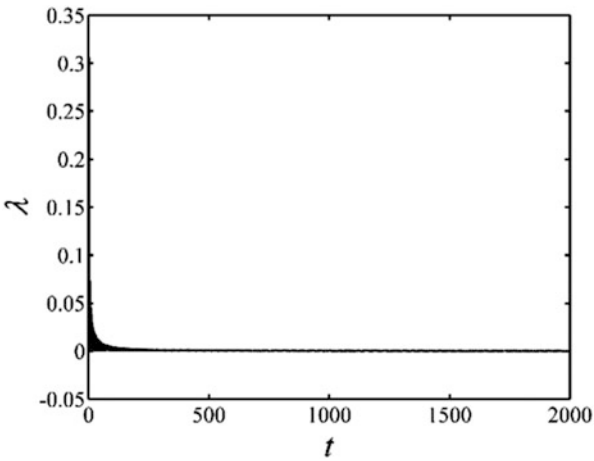

Fig. 1.29 Lyapunov exponent $\Omega = 14$, $V_1 = 10$

from the figures, the Lyapunov exponent is positive which is 0.0014, but the response of the blade is obviously not chaotic though Lyapunov exponent indicates divergence of the system. Nevertheless, the P-R value in this case is 0.64 that implies certain periodicity but not perfectly periodic. Indeed, the response of the blade in this case is nonperiodic and shows irregular behaviour.

Also, based on the computations for diagnosing the nonlinear behaviour of the blade, P-R method is more efficient and uses much less time for the diagnosis in comparing with that of Lyapunov method. In generating the P-R value, the CPU time used is about 2.1 s, while the time used by Lyapunov method is about 5.3 s for each case. Actually, as indicated in the literature, in generating the periodic-quasiperiodic-chaotic region diagram, the CPU time used by the P-R method is about 1/3 of that of the Lyapunov method (Xia 2016).

1.7 Conclusions

Horizontal-axis wind turbines (HAWT) are becoming popular in people's efforts of implementing green power in the electric power market. The HAWT, especially those constructed at the shores, are getting larger and more powerful with longer and more flexible wind turbine blades, which are subjected to inconstant wind loads. These cause the concerns of the researchers and engineers for the nonlinear vibratory responses of the blades and the effects of the nonlinear responses on the operation, service life, and reliability of the structures of the HAWT. Analysis of the nonlinear behaviour of the HAWT is therefore crucial to the design, manufacturing, and application of the blades and the turbines themselves. This chapter provides the development of an analytical model for HAWT blades and an approach to quantitatively characterize the nonlinear behaviour of the HAWT blades. With the descriptions and concepts provided in the chapter, the following can be summarized:

1. The behaviour of HAWT blades can be very complex, and a powerful and practically sound tool is needed not only for analysing nonlinear behaviour of the blades but also for diagnosing the complex behaviour of the blade systems.
2. In analysing the behaviour of the HAWT blades, the effects of aerodynamic forces, elastic forces, and inertia forces including Coriolis forces acting on the blades are the essential loads on the blades and needed to be taken into consideration in establishing the mode governing the motion of the blades. The blade geometric nonlinearity and the nonlinear rotation of the blade subjected the inconstant wind loads may also need to be counted in modelling the HAWT blades as described in the context.
3. The periodicity-ratio approach and the P-R value described in the chapter show efficiency and accuracy in quantitatively describing the periodicity of the responses of a dynamic system and can be implemented to reliably characterize the nonlinear behaviour of a dynamic system.

4. With implementation of the periodicity-ratio approach, a perfect periodic motion can be identified as the case of which its P-R value is one, whereas a perfectly chaotic case can be identified as perfectly nonperiodic with P-R value equals to zero.
5. As the P-R value described the periodicity of the nonlinear response, there can be infinite types of responses corresponding to different levels of periodicity i.e. different P-R values.
6. With application of the P-R method, the irregular motions in between perfect periodic and chaotic motions can be diagnosed for research and engineering application purpose.
7. The periodic-quasiperiodic-chaotic region diagrams provided in this chapter are significant for analysing the nonlinear behaviour of a HAWT blade as they provide visible regions of different types of nonlinear responses of the blade. Such diagram can also be used as a powerful tool in designing and manufacturing the blades. It should be noticed, however, although three system parameters are used for generating the two diagrams provided, more system parameters can be conveniently considered if so desire.
8. As per the numerical simulations conducted with implementation of the model established, the HAWT blade considered shows periodic responses when the wind speed and blade rotation speed are both not very high.
9. Quasiperiodic and chaotic responses of the blade are related to initial conditions and also related to the system parameters, in addition to the wind speed and blade rotation speed.
10. In comparing the Lyapunov exponent method, as a single value index, P-R method is more efficient in terms of calculation time for diagnosing the nonlinear characteristics.
11. The approach described in this chapter provides a practically sound tool for quantifying and diagnosing the vibratory responses of HAWT blade and is significant for turbine and turbine blade designs with considerations of nonlinear vibrations of the blades.

Acknowledgements The authors would like to acknowledge with great appreciation for the support provided by the Natural Sciences and Engineering Research Council of Canada (NSERC) to the research described in the chapter. The authors are also grateful for the supports, encouragements, and helps provided by the colleagues at the Sino-Canada Research Center for Noise and Vibration Control at Xiamen University of Technology and those at the University of Regina.

Appendix A

This appendix provides the main code for calculating phase diagram, Poincare map, P-R value, region diagrams and Lyapunov exponents. The numerical simulation is based on the fourth-order Runge-Kutta method. Main process of the calculation is provided in the Appendix, and implementations are added in each line as well.

Code for Poincare map plotting

```
[x,x1,t]=RKwindwing3(x0,x10,omega0,omega00,omega1,miu,omega2,w1,f1,a,b,c,d
,hh,n,V0,V1);
 figure; plot(t(1:n),x(1:n),'k','linewidth',2);hold on;  %wave diagram
 xlabel('\fontname{Times New
Roman}\fontsize{30}\it{t}');ylabel('\fontname{Times New
Roman}\fontsize{30}\it{x}');
 set(gca,'FontName','Times New Roman','FontSize',20,'linewidth',2);
%set(gca,'XTick', [800  1000 1200]);
%print(gcf,'-dpng','-r350','1.png');
 figure; plot(x(1:n),x1(1:n),'k','linewidth',2);hold on;  %wave diagram
  xlabel('\fontname{Times New
Roman}\fontsize{30}\it{x}');ylabel('\fontname{Times New
Roman}\fontsize{30}\it{x1}');
  set(gca,'FontName','Times New Roman','FontSize',20,'linewidth',2);
  %print(gcf,'-dpng','-r350','2.png');
n2=floor((n-n1)/(aa));xx=zeros(1,n2);xx1=zeros(1,n2);
%prepare for poincare map
 figure;
 for i=1:n2
      xx(i)=x(n1+round((i-1)*(aa)));
      xx1(i)=x1(n1+round((i-1)*(aa)));
      plot(xx(i),xx1(i),'.k','markersize',10);hold on;
end
%poincare map
 xlabel('\fontname{Times New Roman}\fontsize{30}\it{x}');
 ylabel('\fontname{Times New Roman}\fontsize{30}\it{x1}');
 %set xlabal and y label
 set(gca,'FontName','Times New Roman','FontSize',20,'linewidth',2);
 print(gcf,'-dpng','-r350','3.png');
```

Code for region diagram plotting

```
[x,x1,t]=RKwindwing3(x0,x10,omega0,omega00,omega1,miu,omega2,w1,f1,a11,c11
1,c211,k11,lamad11,b1,d1,hh,n,V0,V1,g);
figure; plot(t(1:n),x(1:n),'k','linewidth',2);hold on;  %wave diagram
xlabel('\fontname{Times New Roman}\fontsize{30}\it{t}');
ylabel('\fontname{Times New Roman}\fontsize{30}\it{x}');
set(gca,'FontName','Times New Roman','FontSize',20,'linewidth',2);
set(gca,'XTick', [800  1000 1200]);
 figure; plot(x(1:n),x1(1:n),'k','linewidth',2);hold on;  %wave diagram
   xlabel('\fontname{Times New Roman}\fontsize{30}\it{x}');
ylabel('\fontname{Times New Roman}\fontsize{30}\it{x1}');
   set(gca,'FontName','Times New Roman','FontSize',20,'linewidth',2);

n2=floor((n-n1)/(aa));xx=zeros(1,n2);xx1=zeros(1,n2);
%prepare for poincare map
  figure;
  for i=1:n2
       xx(i)=x(n1+round((i-1)*(aa)));
       xx1(i)=x1(n1+round((i-1)*(aa)));
       plot(xx(i),xx1(i),'.k','markersize',10);hold on;
end
xlabel('\fontname{Times New
Roman}\fontsize{30}\it{x}');ylabel('\fontname{Times New
Roman}\fontsize{30}\it{x1}'); %set xlabal and y label
  set(gca,'FontName','Times New Roman','FontSize',20,'linewidth',2);
%set size of coordinate
nnn1=100;nnn2=100;
 nV0=zeros(1,nnn1);nomega1=zeros(1,nnn2);pr=zeros(nnn1,nnn2);
 for jj=1:nnn1
     for jjj=1:nnn2
         nV0(jj)=0.2*jj+10;
         nomega1(jjj)=0.035*jjj+1;
         V0=nV0(jj);
         omega1=nomega1(jjj);
         omega2=omega1;
         aa=2*3.14159265/omega1/hh;

[x,x1,t]=RKwindwing3(x0,x10,omega0,omega00,omega1,miu,omega2,w1,f1,a1,b1,c
1,d1,hh,n,V0,V1);
         n2=floor((n-n1)/(aa));xx=zeros(1,n2); xx1=zeros(1,n2);
         for i=1:n2
             xx(i)=x(n1+round((i-1)*(aa)));
             xx1(i)=x1(n1+round((i-1)*(aa)));
         end
         z=zeros(n2,n2);
         for i=1:n2
             for j=i:n2
                 z(i,j)=sqrt((xx(i)-xx(j))^2+(xx1(i)-xx1(j))^2);
           if z(i,j)<0.0001              %value for calculation
                  z(i,j)=1;
                else
                    z(i,j)=0;
                end
            end
         end
```

Code for Lyapunov exponent calculations

```
        for ii=1:n2-2
            zz=z(ii,ii+1:n2);
            zza=find(zz==1);
            if length(zza)>=1
                for t=1:length(zza)
                    z(zza(t)+ii,zza(t)+ii+1:n2)=0;
                end
            end
        end
        for k1=3:n2
            a=z(1:k1-1,k1);
            b=find(a==1);
            if length(b)>1
           z(b(1)+1:k1-1,k1)=0;
            end
        end
        e=zeros(1,n2);
        for t=1:n2
            c=z(t,:);
            d=find(c==1);
            if length(d)>1
                e(t)=length(d);
            else
                e(t)=0;
            end
        end
        sum=0;
        for t=1:n2
            sum=sum+e(t);
        end
        pr(jj,jjj)=sum/n2;                    %need to find it in
workspace
     end
 end
 for jj=1:nnn1
    for jjj=1:nnn2
        if pr(jj,jjj)>=0.9
            plot(nV0(jj),nomega1(jjj),'dk');hold on;
        end
        if (pr(jj,jjj)<0.9)&(pr(jj,jjj)>0.001)
            plot(nV0(jj),nomega1(jjj),'+k');hold on;
        end
        if pr(jj,jjj)==-1
           plot(nV0(jj),nomega1(jjj),'*k');hold on;
        end
    end
 end
 xlabel('\fontname{Times New
Roman}\fontsize{30}\it{f2}');ylabel('\fontname{Times New
Roman}\fontsize{30}\it{\omega}');
 set(gca,'FontName','Times New Roman','FontSize',16,'linewidth',2);
 %set(gca,'XTick', [-4 -3 -2 -1 0 1 2 3 4]);
%set coordinate value for xlabel
 %set(gca,'YTick', [-10 -5 0 5 10]);
 %axis([0.2,2.05,-0.01,0.21]);
 %print(gcf,'-dpng','-r350','Region diagram of f2 to omiga.png');
toc
```

```
[x,x1,t]=RKwindwing3(x0,x10,omega0,omega00,omega1,miu,omega2,w1,f1,a11,c11
1,c211,k11,lamad11,b1,d1,hh,n,V0,V1,g);
  x=x(50000:10:100000);
  N=length(x);
    m=3;
    dt=1;
    N=N-(m-1)*dt;
    Y=chonggou(x,m,N,dt);
     xP=abs(fft(x)).^2;
    N1=floor(length(xP)/2);
    xP(1)=[];
    xP=xP(1:N1);
    [maxP,T]=max(xP);
   dmin=inf;
    for i=1:(N-1)
        for j=i+1:N
            d(i,j)=sqrt(sum((Y(:,i)-Y(:,j)).^2));
            if dmin>d(i,j)
                dmin=d(i,j);
            end
        end
    end
    davg=2*sum(sum(d))/(N*(N-1));
    deps=(davg-dmin)*0.02;
    epsmin=dmin+deps/2;
    epsmax=dmin+2*deps;

    lmdsum=0 ;
    for i=1:(N-1)
              if i==1
            L=inf;
            for j=(T+1):(N-1)
d=sqrt(sum((Y(:,j)-Y(:,i)).^2));
            if (d<L)&&(d>epsmin)
                L=d;
                n=j;
            end
            end
        end
            if i>1
            L1=sqrt(sum((Y(:,i)-Y(:,n+1)).^2));
            oldn=n;
             if (L1~=0)&&(L~=0)
                lmdsum=lmdsum+log(L1/L);
            end
            lmd(i-1)=lmdsum/(i-1);
              num=0;
            cth=0;
            kznum=0;
            while (num==0)
                for j=1:(N-1)
                    if abs(j-i)<T
                        continue;
                    end
 d=sqrt(sum((Y(:,i)-Y(:,j)).^2));
                    if (d<epsmin)||(d>epsmax)
                        continue;
                    end
```

```
            dd=sum((Y(:,i)-Y(:,j)).*(Y(:,i)-Y(:,oldn+1)));
CTH=dd/(d*L1);
                    if acos(CTH)>(pi/4)
                        continue;
                    end
                    if CTH>cth
                        cth=CTH;
                        n=j;
                    L=d;
                    end
                    num=num+1;
                end
                        if num<2
                    epsmax=epsmax+deps;
                    kznum=kznum+1;
                    if kznum>5
                        L=inf;
                        for j=1:(N-1)
                            if abs(i-j)<T-1
                                continue;
                            end
                            d=sqrt(sum((Y(:,i)-Y(:,j)).^2));
                            if (d<L)&&(d>epsmin)
                                L=d;
                                n=j;
                            end
                        end
                        break;
                    end
                    num=0;
                    cth=0;
                end
            end
        end
    end
maxlambda=sum(lmd)/length(lmd)
toc
.
```

References

Carbajal-Gómez, V. H., Tlelo-Cuautle, E., Trejo-Guerra, R., & Muñoz-Pacheco, J. M. (2013). Simulating the synchronization of multi-scroll chaotic oscillators. *IEEE International Symposium on Circuits and Systems. IEEE*,1773–1776.

Castanier, M. P., & Pierre, C. (1995). Lyapunov exponents and localization phenomena in multi-coupled nearly periodic systems. *Journal of Sound and Vibration, 183*(3), 493–515.

Czolczynski, K., Okolewski, A., & Blazejczyk, B. (2017). Lyapunov exponents in discrete modelling of a cantilever beam impacting on a moving base. *International Journal of Non-Linear Mechanics, 88*, 74–84.

Dai, L. (2008). *Nonlinear dynamics of piecewise constant systems and implementation of piecewise constant arguments*. Singapore/Hackensack: World Scientific Publishing.

Dai, L., & Wang, G. (2008). Implementation of periodicity ratio in analyzing nonlinear dynamic systems: A comparison with Lyapunov exponent. *Journal of Computational and Nonlinear Dynamics, 3*(1), 112–113.

Dwivedy, S. K., & Kar, R. C. (1999a). Dynamics of a slender beam with an attached mass under combination parametric and internal resonances, part ii: Periodic and chaotic responses. *Journal of Sound and Vibration, 222*(2), 281–305.

Dwivedy, S. K., & Kar, R. C. (1999b). Dynamics of a slender beam with an attached mass under combination parametric and internal resonances part I: Steady state response. *Journal of Sound and Vibration, 222*(2), 281–305.

Esmailzadeh, E., & Jalili, N. (1998). Parametric response of cantilever Timoshenko beams with tip mass under harmonic support motion. *International Journal of Non-Linear Mechanics, 33*(5), 765–781.

Global Wind Energy Council. (2015). *Global wind report annual market update*. http://www.gwec.net/wp-content/uploads/vip/GWEC-Global-Wind-2015-Report_April-2016_19_04.pdf.

Hanagud, S., & Sarkar, S. (1989). Problem of the dynamics of a cantilever beam attached to a moving base. *Journal of Guidance, Control, and Dynamics, 13*(3), 438–441.

Henon, M. A. (1976). Two-dimensional mapping with a strange attractor. *Communications in Mathematical Physics, 50*, 69–77.

Huang, B. (2001). *Analysis principle and application of wind – Resistant structure*. Shanghai: Tongji University Press.

Kane, T., Ryan, R., & Bannerjee, A. (1987). Dynamics of a cantilever beam attached to a moving base. *Journal of Guidance, Control and Dynamics, 10*, 139–151.

Kim, B. J., & Choe, G. H. (2010). High precision numerical estimation of the largest Lyapunov exponent. *Communication in Nonlinear Science and Numerical Simulation, 15*, 1378–1384.

Krenk, S. (1983a). A linear theory for pretwisted elastic beams. *Journal of Applied Mechanics, 105*, 137–142.

Krenk, S. (1983b). The torsion-extension coupling in pretwisted elastic beams. *International Journal of Solids and Structures, 19*(1), 67–72.

Larsen, J. W. (2005). *Nonlinear dynamics of wind turbine wings*. Thesis of Aalborg University.

Larsen, J. W., & Nielsen, S. R. K. (2006). Non-linear dynamics of wind turbine wings. *International Journal of Non-Linear Mechanics, 41*(5), 629–643.

Larsen, J. W., & Nielsen, S. R. K. (2007). Nonlinear parametric instability of wind turbine wings. *Journal of Sound and Vibration, 299*(1–2), 64–82.

Li, Q., Zeng, H., & Li, J. (2014). Hyperchaos in a 4D memristive circuit with infinitely many stable equilibria. *Nonlinear Dynamics, 79*, 2295–2308.

Liao, H. (2016). Novel gradient calculation method for the largest Lyapunov exponent of chaotic systems. *Nonlinear Dynamics, 85*(3), 1–16.

Liu, X., Lu, C., Liang, S., Godbole, A., & Chen, Y. (2015). Influence of the vibration of large-scale wind turbine blade on the aerodynamic load. *Energy Procedia, 75*, 873–879.

Nayfeh, A. H., & Mook, D. T. (1979). *Nonlinear oscillations*. New York: Wiley.

Odavic, J., Mali, P., Tekic, J., Pantic, M., & Hrvojevic, M. P. (2017). Application of largest exponent analysis on the studies of dynamic under external forces. *Communications in Nonlinear Science and Numerical Simulation, 47*, 100–108.

Pentland, W. (2014). Micro-windmills may one day power your smart phone. *Forbes*.

Rong, H., Meng, G., Wang, X., Xu, W., & Fang, T. (2002). Invariant measures and Lyapunov-exponents for stochastic Mathieu system. *Nonlinear Dynamics, 30*, 313–321.

Shahverdian, A. Y., & Apkarian, A. V. (2007). A difference characteristic for one-dimensional deterministic systems. *Communications in Nonlinear Science and Numerical Simulation, 12*(3), 233–242.

Shin, K., & Hammond, J. K. (1998). The instantaneous Lyapunov exponent and its application to chaotic dynamical systems. *Journal of Sound and Vibration, 218*(3), 389–403.

Statkraft. (2012). *Wind turbines on their way*. http://www.statkraft.com/media/news/News-archive/2012/wind-turbines-on-their-way/

Wang, C., & Zhang, Y. (2003). *Wind-power generation*. Beijing: China Electric Power Press.
Wittrup, S. (2014). Power from Vestas' giant turbine (in Danish, English translation). *Ingenioren*.
Wolf, A., Swift, J. B., & Swinney, H. L. (1985). Determining Lyapunov exponents from a time series. *Physica D: Nonlinear Phenomena, 16*(3), 285–317.
Xia, D. (2016). *Nonlinear behaviors analysis and nonlinear characteristics diagnosing of mechanical vibration systems*. MASc Thesis, University of Regina.
Yang, N., & Liu, C. (2013). A novel fractional-order hyperchaotic system stabilization via fractional sliding-mode control. *Nonlinear Dynamics, 74*, 721–732.
Yang, C., & Wu, C. (2011). A robust method on estimation of Lyapunov exponents from a noisy time series. *Nonlinear Dynamics, 64*, 279–292.
Yang, J. B., Jiang, L. J., & Chen, D. C. (2004). Dynamic modelling and control of a rotating Euler-Bernoulli beam. *Journal of Sound and Vibration, 274*, 863–875.

Chapter 2
Concentrated Solar Power Plants Capacity Factors: A Review

Albert Boretti

Symbols

η	Efficiency
ε	Capacity factor
E	Electric energy
P	Electric power
Q	Thermal energy

Acronyms

CSP	Concentrated solar power
CCGT	Combined cycle gas turbine
GT	Gas turbine
ISEGS	Ivanpah Solar Electric Generating System
MS	Molten salt
NG	Natural gas
PT	Parabolic troughs
PV	Photovoltaic
SEGS	Solar Energy Generating Systems
SPT	Solar power tower
TES	Thermal energy storage

A. Boretti (✉)
Department of Mechanical and Aerospace Engineering, Benjamin M. Statler College of Engineering and Mineral Resources, West Virginia University, Morgantown, WV, USA

Military Technological College, Muscat, Oman
e-mail: alboretti@mail.wvu.edu; a.a.boretti@gmail.com

L. Dai, R.N. Jazar (eds.), *Nonlinear Approaches in Engineering Applications*,
https://doi.org/10.1007/978-3-319-69480-1_2

2.1 Introduction

Concentrated solar power (CSP) systems collect sunlight energy at high temperature and transfer heat to a power cycle that produces electricity. Lenses or mirrors are used in CSP systems to concentrate the solar thermal energy on a small area. The concentrated light is converted to heat, which ultimately produces superheated steam which drives a Rankine steam turbine cycle. The basic principles of CSP systems are covered in reference works such as Romero-Alvarez and Zarza (2007) and are not repeated here.

Concentrators differ in tracking of the sun and focusing the light. Concentrating technologies exist in different optical types, the most popular parabolic trough (PT), and solar power tower (SPT). Solar concentrators are simple. Nevertheless, the concentrators are still far from achieving the theoretical maximum concentration of sun energy. Different concentrators produce different receiver temperatures and different peak temperatures of the steam for the power cycle, with correspondingly varying thermal efficiency of the power cycle. In addition to the type of receiver and the solar field feeding this receiver, also the receiver fluid plays a role in the peak temperatures of the steam. The receiver fluid may be oil, molten salt (MS), or directly water/steam. In the first case, intermediate heat exchangers are needed between oil or MS and water/steam. MS permits thermal energy storage (TES) in hot and cold reservoir to decouple in some extent the electricity production from the availability of sunlight, have a quicker start-up at sunrise, or prolongate the electricity production after sunset.

An additional MS circuit has been proposed as an addition to existing CSP plants with oil as the receiver fluid. However, MS better replaces the oil as the receiver fluid. Replacement of oil with MS in existing PT CSP plants has translated in operation at higher temperatures translating in higher steam temperature for higher efficiency in power generation and additionally in lower-cost TES.

Direct use of water/steam has a receiver fluid that has the advantage of simplicity, cost, and, possibly, in some extent, efficiency, but this limits the production of electricity to the sun availability. Condensation of steam usually occurs in air-cooled towers.

Boost by combustion of fossil fuels, typically natural gas (NG), drastically improves the match between production and demand of CSP plants in every configuration. However, boost by NG burners is reasonable only if performed in minimal extent, for efficiency of energy use and regulations concerning emissions of carbon dioxide. The use of NG in a combined cycle gas turbine (CCGT) plant occurs with a fuel conversion efficiency that may be almost double the efficiency of a CSP plant operated NG only (fuel conversion efficiency above 60% vs. fuel conversion efficiencies around 30%). The spreading in between the fuel conversion efficiency of CSP and NG plant is even larger in case of cogeneration, where the gas turbine plant also features production of process heat, for heating, cooling, desalination, or other activities.

Despite the largest CSP plant uses the SPT technology, the global market is dominated by PT plants. About 90% of all the CSP plants are designed with the PT technology. The SPT technology offers theoretically higher efficiency because of the higher temperature. However, the technology is also more demanding from the economic and technical view point, reason why SPT developments are less advanced than PT systems. The two largest CSP projects in the world are the Ivanpah Solar Electric Generating System (ISEGS) SPT facility and the Solar Energy Generating Systems (SEGS) facility which uses PT.

Figure 2.1 presents a Google Map image of the central tower and heliostats of the Ivanpah CSP SPT facility.

The net capacity of Ivanpah 1-3 is 377 MW, while the net capacity of SEGS II-IX is 340 MW. Both facilities use NG to boost the electricity production, in a

Fig. 2.1 Google Map image of the Ivanpah CSP SPT facility. https://www.google.com/maps/@35.5572423,-115.4705938,703m/data=!3m1!1e3?hl=en

greater extent the Ivanpah facilities, in a minor extent the SEGS facilities, and both lack of TES capabilities. As discussed later, the actual capacity factors (ε) of both installations (electricity produced in a year divided by the product of net capacity by 365 days by 24 h a day) are about 20%, even with the benefit of the boost by combustion of NG not included in the computation.

The CSP technologies presently do not compete on price with photovoltaics (PV) solar panels that have come through enormous progress in recent years because of the decreasing prices of the PV panels and the much smaller operating costs. While the total solar electricity generation (2015) is 253.0 TW·h, or 1.05% of the total, CSP plants represent (2015) less than 2% of the worldwide installed capacity of solar electricity plants, for a total CSP contribution to the global energy mix of about 0.02%.

2.2 Solar Power Tower (SPT)

A solar power tower concentrates the sunlight from a field of heliostats on a central tower. The heliostats are dual-axis tracking reflectors. Heliostats are grouped in arrays. They concentrate sunlight on a relatively small central receiver that is located at the top of the tower. As the sunlight is much more concentrated, the working fluid in the receiver may be heated to temperatures of 500–1000 °C depending on the fluids and the solar concentration. This heat is the hot source driving the power generation cycle.

The field of heliostats focuses the light on top of the tower with typically a 500× to 1000× concentration. Light is absorbed by metal tubes and delivered to the receiver fluid, either water/steam or nitrate salt. Not all the incident light is collected by the receiver fluid because the light may be shaded, blocked, absorbed, or spilled. All these losses account for more than 40% of the incident light. Receiver, piping, and tank thermal losses further reduced the amount of energy transferred to the power cycle. The power cycle then rejects the most of this energy as waste heat to the air-cooled condenser. Peak steam temperature is about 550 °C. Condenser temperature in desert installations with high solar exposure is 40 °C. The gross electric energy production is about 23–24% of the incident light. The net electric energy production, depurated by the energy to pumps and other auxiliaries, is finally 21–22% of the incident light. The above figures are based on the 565 °C molten nitrate salt SPT with Rankine power cycle of Reilly and Kolb (2001).

Figure 2.2 presents a scheme of a CSP SPT with TES having MS as the receiver fluid and steam as the power cycle fluid. An auxiliary NG heater is included in the scheme to boost production.

Reference SPT specifications change if the receiver fluid is water/steam or MS (nitrate salt) as follows (data from Reilly and Kolb 2001; Margolis et al. 2012; Radosevich 1988): for nitrate salt as the receiver fluid, the receiver temperature is 565 °C, the peak flux on receiver is 1000 kW/m^2, the hot storage temperature is 565 °C, the cold storage temperature is 290 °C, and condenser temperature is 40 °C

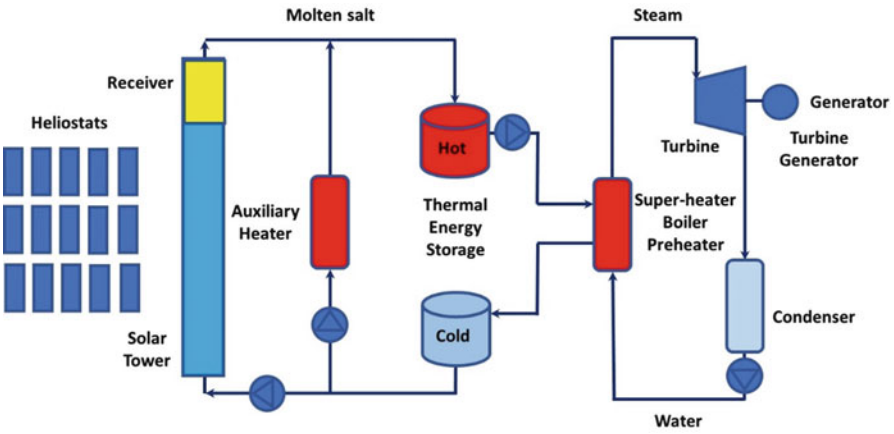

Fig. 2.2 Simplified scheme of a CSP SPT with TES having MS as the receiver fluid and steam as the power cycle fluid. An auxiliary NG heater is included in the scheme to boost production

for heat rejection. In the case of water/steam as the receiver fluid, the receiver temperature is 550 °C; the peak flux on receiver is >300 kW/m^2. The hot and cold storage tanks are not available in this case, all the other parameters being unchanged.

Supercritical steam power cycles (Pacheco et al. 2013) and supercritical carbon dioxide power cycles (Turchi et al. 2013) are presently considered to improve the conversion efficiency thermal electric. Higher temperature receiver fluids and higher temperature MS and water/steam towers are also considered. Materials and manufacturing improvements are however the focus to reduce the cost of the solar thermal plant, still the major downfall of CSP SPT.

2.3 Parabolic Troughs (PT)

A parabolic trough (PT) is made up of a linear parabolic reflector concentrating the sunlight onto a tubular receiver located along the focal line of the reflector. The tubular receiver is filled with a working fluid that may be oil, nitrate salt, or water/steam. The reflector follows the sun. The tracking operates along a single axis. The working fluid is usually heated to 390–500 °C, depending on the fluid, as it flows through the receiver. If oil or MS, this fluid is then used as the heat driving the production of steam for the power cycle.

The shaped mirrors of a PT focus the sunlight on a tube running along the focus line with an 80× concentration. The sunlight is absorbed by tube often in a glass vacuum and delivered to the receiver fluid. While PT may be less efficient than SPT, they are much simpler and less expensive to build and operate.

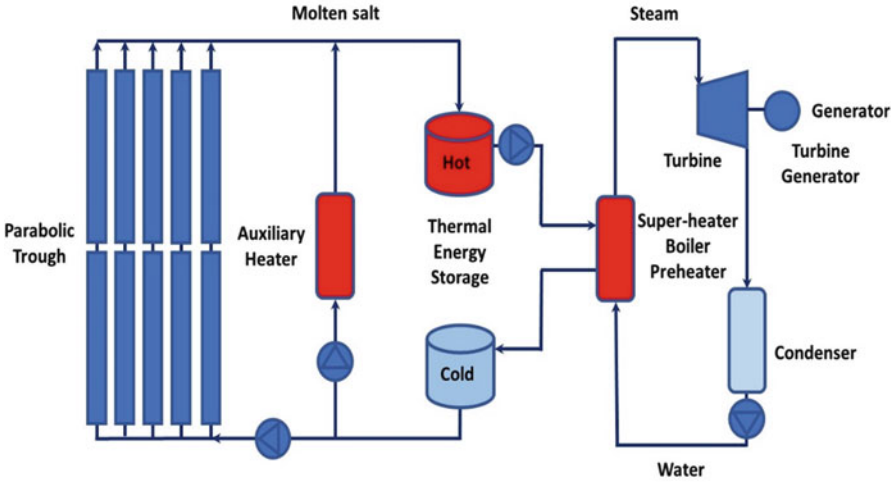

Fig. 2.3 Simplified scheme of a CSP PT with TES having MS as the receiver fluid and steam as the power cycle fluid. An auxiliary NG heater is included in the scheme to boost production

Figure 2.3 presents a scheme of a CSP PT with TES having MS as the receiver fluid and steam as the power cycle fluid. An auxiliary NG heater is included in the scheme to boost production.

Reference PT specifications change if fluid is water/steam, oil, or MS (nitrate salt) as follows (data from Margolis et al. 2012; Kearney and Herrmann 2006; Feldhoff et al. 2012; Bendt et al. 1979): for oil as the receiver fluid, the receiver temperature is 390 °C. The peak flux on receiver is 25 kW/m^2. The hot storage temperature is 390 ° C, the cold storage temperature is 290 °C, and condenser temperature is 40 ° C for heat rejection. For nitrate salt as the receiver fluid, the receiver temperature is 500 °C, the peak flux on receiver is 25 kW/m^2, the hot storage temperature is 500 °C, and the cold storage temperature is 300 ° C. The condenser temperature is unchanged. In the case of steam as the receiver fluid, the receiver temperature is 500 °C; the peak flux on receiver is 25 kW/m^2. The hot and cold storage tanks are not available in this case, all the other parameters being unchanged.

Supercritical steam power cycles (Pacheco et al. 2013) and supercritical carbon dioxide power cycles (Turchi et al. 2013) are being considered to improve the conversion efficiency thermal electric. Higher temperature receiver fluids. Materials and manufacturing improvements to reduce costs are also the major area of concern for CSP PT.

2.4 Capacity Factors and Boost by Natural Gas

Plant level data of electricity production and NG consumption of CSP plants with NG boost in the United States are provided in (Energy Information Administration 2017).

The capacity factor (ε) is presently defined as the ratio of the actual electricity produced in a year E [MW·h] vs. the product of net capacity P [MW] by 365 days by 24 h.

$$\varepsilon_1 = \frac{E}{P \cdot 365 \cdot 24}$$

This capacity factor does not account for the consumption of NG to boost production. Hereafter, we refer to this capacity factor as ε_1.

Data of Energy Information Administration (2017) includes the energy input from both the sun and the NG. A first opportunity to account for the NG consumption is to multiply the above capacity factor by the ratio of the solar energy input Q_{Sun} to the total sun and NG energy input $Q_{\text{Sun}} + Q_{\text{NG}}$, all in [MW·h]. Hereafter, we refer to this capacity factor as ε_2.

$$\varepsilon_2 = \frac{E}{P \cdot 365 \cdot 24} \cdot \frac{Q_{\text{Sun}}}{Q_{\text{Sun}} + Q_{\text{NG}}}$$

Two other capacity factors are here defined. These capacity factors help to understand the value the NG has in a GT or CCGT plant vs. the CSP plant value.

A third capacity factor, ε_3 hereafter, is defined as the ratio of the actual electricity produced reduced of the electricity produced by burning the NG in a GT plant, estimated by using a reference thermal conversion efficiency $\eta_{\text{GT}} = 30\%$ vs. the product of net capacity by 365 days by 24 h.

$$\varepsilon_3 = \frac{E - Q_{\text{NG}} \cdot \eta_{\text{GT}}}{P \cdot 365 \cdot 24}$$

A fourth capacity factor, ε_4 hereafter, is defined as the ratio of the actual electricity produced reduced of the electricity produced by burning the NG in a CCGT plant, estimated by using a reference thermal conversion efficiency $\eta_{\text{CCGT}} = 60\%$ vs. the product of net capacity by 365 days by 24 h.

$$\varepsilon_4 = \frac{E - Q_{\text{NG}} \cdot \eta_{\text{CCGT}}}{P \cdot 365 \cdot 24}$$

These other capacity factors permit to better assess the actual efficiency of the CSP plants that use boost by NG.

Finally, an important parameter not accounted for in the present review is the electricity generation profile requested from a specific facility. The largest is the

Table 2.1 Capacity factors of the three largest CSP projects

Time window for average and way to account for the NG boost	Ivanpah 1	Ivanpah 2	Ivanpah 3	SEGS IX	Solana
Years 2014, 2015, and 2016, NG not accounted for (ε_1)	19.43%	16.29%	18.42%	22.85%	29.89%
Years 2014, 2015, and 2016, NG accounted for with η actual plant (ε_2)	16.09%	13.55%	15.08%	20.02%	29.89%
Years 2014, 2015, and 2016, NG accounted for with $\eta = 30\%$ (ε_3)	16.15%	13.56%	15.37%	20.33%	29.89%
Years 2014, 2015, and 2016, NG accounted for with $\eta = 60\%$ (ε_4)	12.88%	10.82%	12.32%	17.81%	29.89%
Jul 2016 to Jun 2017, NG not accounted for (ε_1)	22.98%	21.59%	23.67%	22.54%	32.65%
Jul 2016 to Jun 2017, NG accounted for with η actual plant (ε_2)	19.20%	18.04%	20.12%	19.91%	32.65%
Jul 2016 to Jun 2017, NG accounted for with $\eta = 30\%$ (ε_3)	19.40%	18.19%	20.37%	20.22%	32.65%
Jul 2016 to Jun 2017, NG accounted for with $\eta = 60\%$ (ε_4)	15.83%	14.80%	17.07%	17.91%	32.65%

departure of the electricity generation profile from the sun energy profile during a day, the more difficult is to achieve a large capacity factor.

The availability of TES is indeed a key factor to reduce NG boost or complement by burning natural gas, however, requiring extra costs.

Table 2.1 presents the capacity factors of the three largest CSP projects, Ivanpah, SEGS, and Solana, described later in the manuscript.

2.5 Ivanpah Solar Electric Generating System (ISEGS)

Information on CSP projects including ISEGS is provided in (National Renewable Energy Laboratory 2017). The CSP technology is SPT. Ivanpah consists of three separate units. Ivanpah 1 has gross capacity 126 MW (121 MW net), while Ivanpah 2 and 3 have gross capacity 133 MW each (128 MW net). Location is Primm, NV, California, United States. The total turbine capacity is 377 net and 392 gross. The plant is operational since January 2014. The land area is 14,164,000 m^2. The solar resource is 2717 kW·h/m^2/year. The planned electricity generation is 1,079,232 MW·h/year, corresponding to a capacity factor ε_1 from the 377 MW net power of 33%. The approximate cost of the project is about 2200 USD million (2014 values), corresponding to about 2272 USD million in August 2017.

The solar field is characterized by a heliostat solar field aperture area of 2,600,000 m^2. The number of heliostats is 173,500. Every heliostat is made of

two mirrors and has an aperture area of 15.0 m^2. The tower height is 140 m. The receiver fluid is water/steam with inlet temperature 249 °C and outlet temperature 566 °C. The power cycle is steam Rankine with pressure 160 bar. Cooling method is dry cooling. The planned annual gross solar-to-electricity efficiency is 28.72%. Fossil boost (or backup) is by NG. The facility has no TES.

Data of electricity production and NG consumption of the Ivanpah CSP plant are provided in (Energy Information Administration 2017).

Figure 2.4 presents the energy input to the solar plant, either solar or NG: the efficiency of the plant, as ratio of electricity out to energy input; the electricity out, from the actual plant and from a reference GT or CCGT plant burning the NG; and finally the capacity factors, ε_1 to ε_4 defined before, for the Ivanpah 1 facility, of net capacity 121 MW. The missing data of NG consumption in (Energy Information Administration 2017) are interpolated from the neighboring months. ε_2 and ε_3 are very close each other. The peak CSP plant efficiency is well above 30%. The capacity factors are those of Table 2.1 column 1. The capacity factors are improving after 3 years from commissioning. The average July 2016 to June 2017, NG not accounted for, is 22.98%. In the case of NG accounted with η actual plant, it drops to 19.20%. In the case of NG accounted for with $\eta = 60\%$, it reduces to 15.83%.

Figure 2.5 presents the electricity produced month by month in the Ivanpah 2 plant, the electricity produced burning the NG in a GT plant, and the electricity produced burning the NG in a CCGT plant, plus the capacity factors, ε_1, ε_3, and ε_4. The net capacity is 128 MW.

The capacity factors are those of Table 2.1 column 2. The capacity factors are improving also here. The average July 2016 to June 2017, NG not accounted for, is 21.59%. In the case of NG accounted with η actual plant, it drops to 18.04%. In the case of NG accounted for with $\eta = 60\%$, it reduces to 14.80%.

Figure 2.6 presents the electricity produced month by month in the Ivanpah 3 plant, the electricity produced burning the NG in a CSP plant and the electricity produced burning the NG in a CCGT plant, plus the three capacity factors, ε_1, ε_3, and ε_4. The net capacity is 128 MW.

In the case of Ivanpah 3, with net capacity 128 MW net, the capacity factors are those of Table 2.1 column 3. The capacity factors are improving the same of Ivanpah 1 and 2. The average July 2016 to June 2017, NG not accounted for, is 23.67%. In the case of NG accounted with η actual plant, it drops to 20.12%. In the case of NG accounted for with $\eta = 60\%$, it reduces to 17.17%.

Ivanpah 3 is the best performing plant of the Ivanpah installations over the last 12 months.

The actual capacity factors for the three installations are much smaller than the planned values, 23.67% of the latest best performing Ivanpah 3 vs. the planned 33%, without accounting for the consumption of NG. Accounting for the NG contribution at actual plant efficiency, the capacity factor is reduced to a 15%. In the case of NG accounted for with $\eta = 60\%$, it reduces to another 15%.

The interested reader may find working models of SPT and PT plants including the Ivanpah and the SEGS facilities in between the examples of Thermoflow

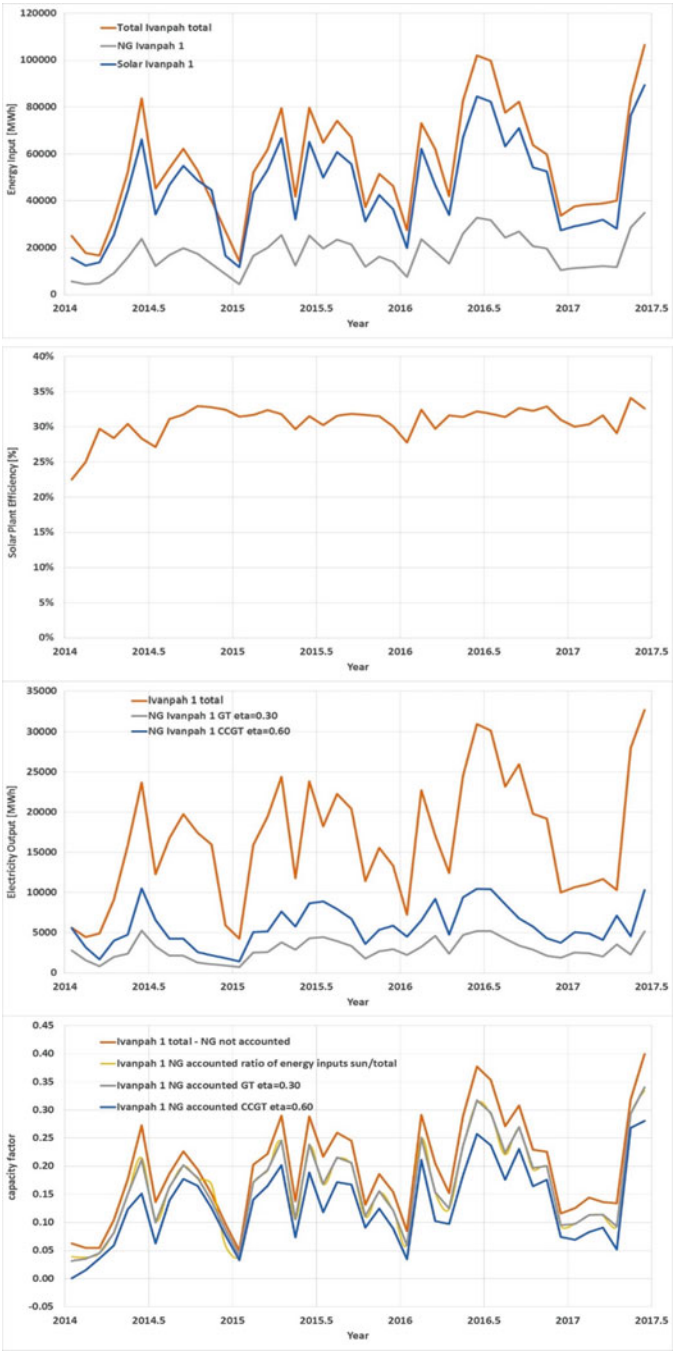

Fig. 2.4 Energy input to the solar plant, either solar or NG; the efficiency of the plant, as ratio of electricity out to energy input; the electricity out, from the actual plant and from a reference GT or CCGT plant burning the NG; and finally the capacity factors ε_1 to ε_4 defined above for the Ivanpah 1 CSP SPT plant

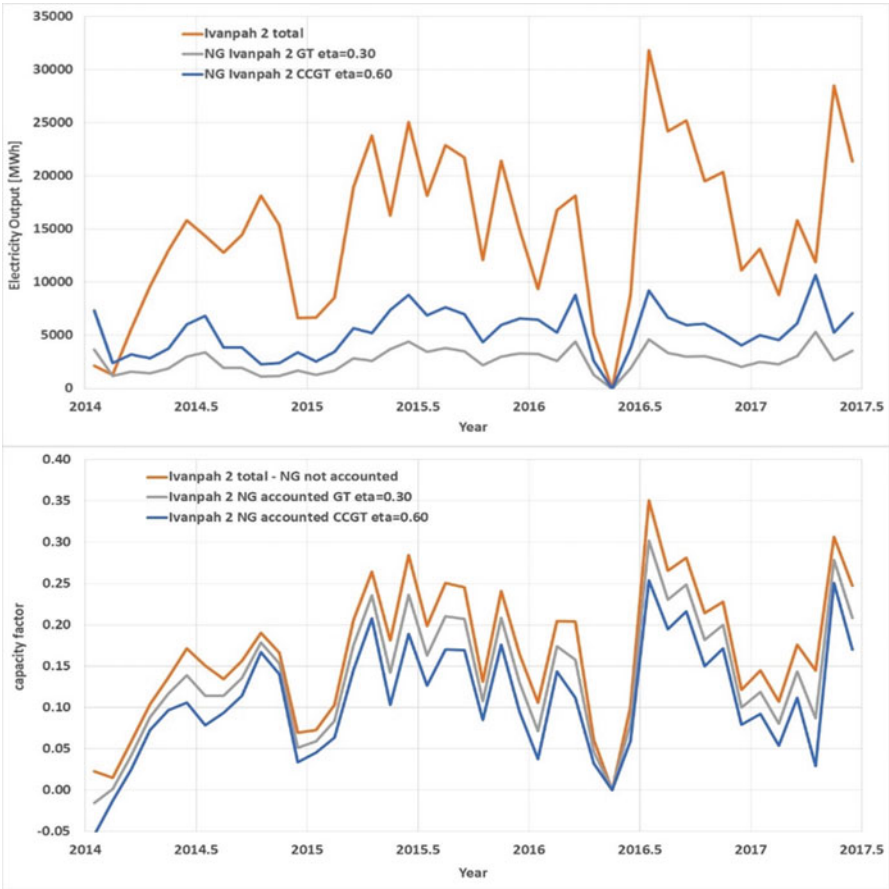

Fig. 2.5 Electricity produced month by month in the Ivanpah 2 plant, the electricity produced burning the NG in a CSP plant, and the electricity produced burning the NG in a CCGT plant, plus the three capacity factors ε_1, ε_3, and ε_4

(Thermoflow, Inc 2017, 2012; Martin 2017), the leading multi-physics CSP system simulation software.

A scheme of the Ivanpah 1 facility, design point operation, is provided in Fig. 2.7, courtesy of Thermoflow, www.thermoflow.com (Thermoflow, Inc 2017, 2012).

A working model of another SPT installation, the 150 MW Rice Solar Energy Project, proposed for Rice Valley, California, United States, and put on indefinite hold in 2014, is provided in between the sample applications available with the free trial software THERMOFLEX 23 by Thermoflow. Rice is featuring a much more sophisticated design with MS as the receiver fluid and a double-tank TES on the MS circuit permitting extended operation without any NG boost.

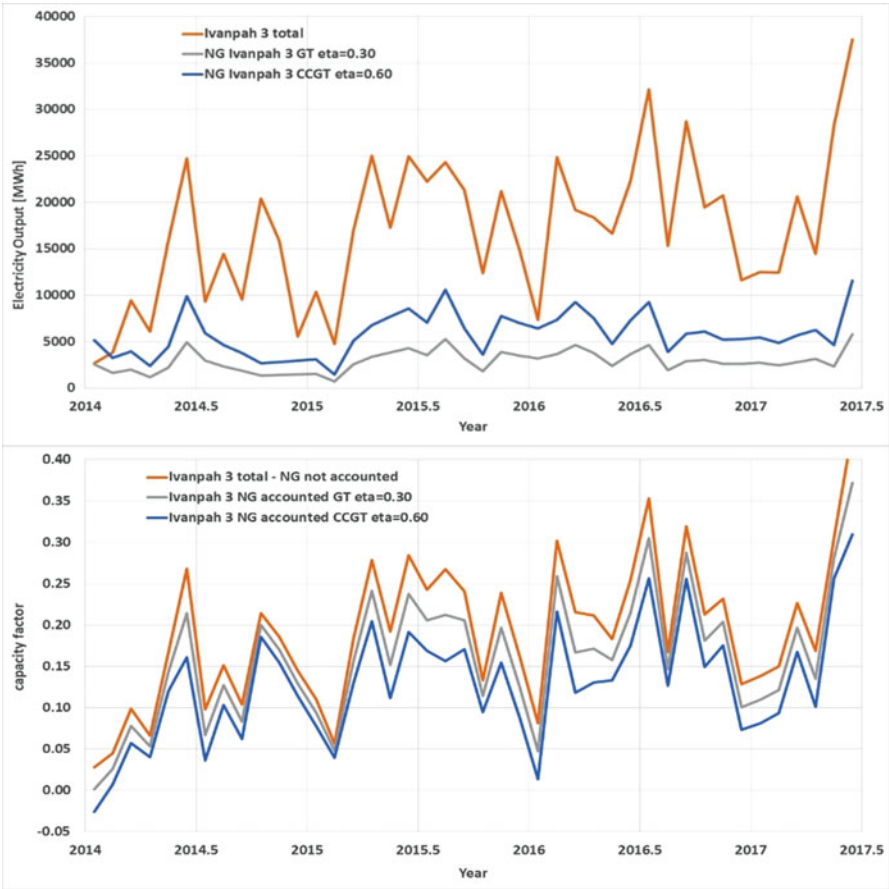

Fig. 2.6 Electricity produced month by month in the Ivanpah 3 plant, the electricity produced burning the NG in a CSP plant and the electricity produced burning the NG in a CCGT plant, plus the three capacity factors, ε_1, ε_3, and ε_4

A scheme of the Rice facility, design point operation, is provided in Fig. 2.8, courtesy of Thermoflow, www.thermoflow.com (Thermoflow, Inc 2017, 2012).

2.6 Solar Energy Generating Systems (SEGS) Plants

Information on CSP projects including SEGS is provided in (National renewable Energy Laboratory 2017). The CSP technology is PT. The 340 MW net, 376 MW gross, SEGS facility, located in the California's Mojave Desert, United States, is the second largest CSP facility in the world and uses eight PT solar power fields. Construction began in 1983, and the first unit was commissioned in 1984.

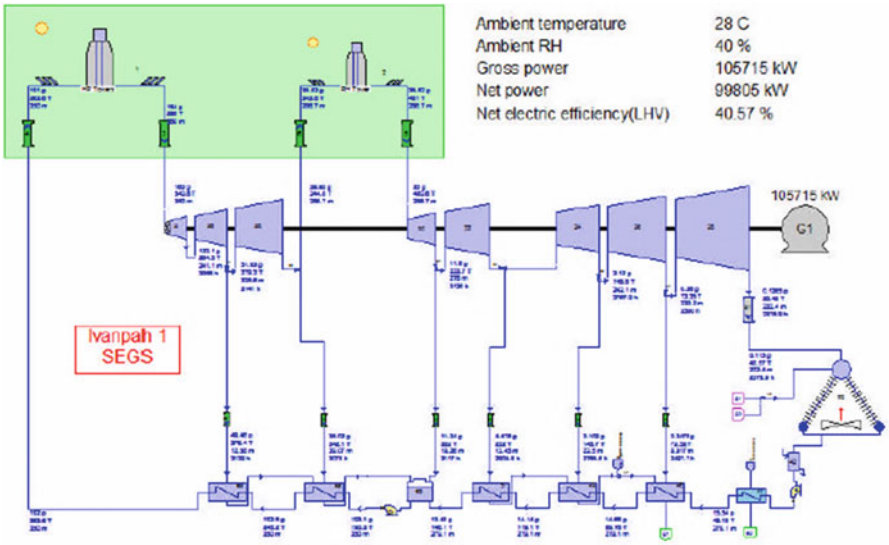

Fig. 2.7 Thermoflow scheme of the Ivanpah 1 facility. Design point balance (Courtesy of Thermoflow, www.thermoflow.com. All data extracted from public available sources, California Energy Commission)

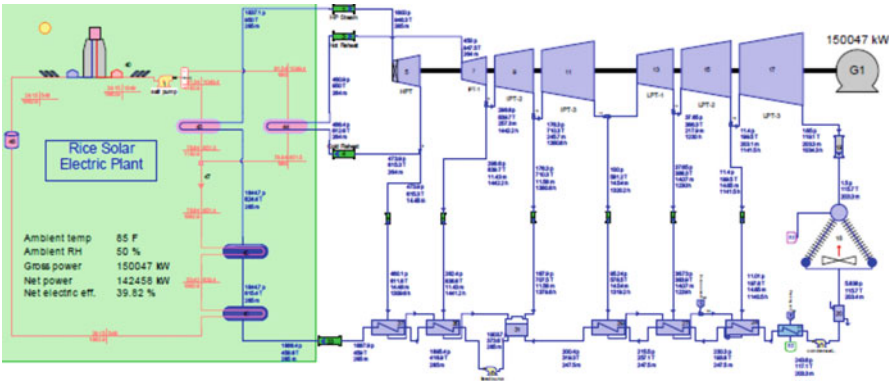

Fig. 2.8 Thermoflow scheme of the Rice facility. Design point balance (Courtesy of Thermoflow, www.thermoflow.com. All data extracted from public available sources, California Energy Commission)

Constructions of the other units followed. In addition to the eight units still operational (SEGS II-IX), two units were canceled, one unit was not completed, and one unit, SEGS I, has been decommissioned.

The total number of collectors, including the decommissioned unit, is 936,384. The total land area is 6,474,970 m^2. The solar resource is 2725 kW·h/m^2/year. The total solar field aperture area of SEGS II to SEGS IX is 2,232,018 m^2.

SEGS I, now decommissioned, had installed a 3 h TES. This TES was intended for producing electricity during peak periods. The TES was damaged by a fire in 1999 and never restored. The other facilities, SEGS II to SEGS IX, do not have TES.

The receiver fluid is Therminol. The power cycle is steam Rankine. The synthetic oil is heated up to 400 °C in the receivers. There is fossil fuel backup (or boost) by NG in all the facilities.

As an example of cost, one of the 33 MW Kramer Junction facilities required 90 USD million to build (1999 values). The approximate cost of a project delivering the same net capacity of Ivanpah on PT technology would be 1569 USD million in August 2017.

Solar Electric Generating Station II (SEGS II) is in Daggett, California. The start year was 1985. The solar resource is 2725 kWh/m^2/year. The solar field has an aperture area of 190,338 m^2. The solar field outlet temperature is 316 °C. The power block is characterized by a turbine capacity of 30 MW net and 33 MW gross, the power cycle pressure is 40 bar, and the turbine efficiency is 29.4%. There is fossil fuel backup (or boost) by NG.

Solar Electric Generating Station III (SEGS III) is in Kramer Junction, California. The start year was 1985. The solar resource is 2725 kWh/m^2/year. The solar field has an aperture area of 230,300 m^2. The solar field outlet temperature is 349 °C. The power block is characterized by a turbine capacity of 30 MW net and 33 MW gross, the power cycle Pressure is 40 bar, and the turbine efficiency is 30.6%. There is fossil fuel backup (or boost) by NG.

Solar Electric Generating Station IV (SEGS IV) is also located in Kramer Junction. Start year was 1989. The solar field has an aperture area of 230,300 m^2. The other characteristics are same of SEGS III.

Solar Electric Generating Station V (SEGS V) is also located in Kramer Junction. Start year was 1989. The solar field has an aperture area of 250,500 m^2. The other characteristics are the same of SEGS III.

Solar Electric Generating Station VI (SEGS VI) is also located in Kramer Junction. Start year was 1989. The solar field aperture area is 188,000 m^2. The solar field outlet temperature is now 390 °C. The power block is characterized by a turbine capacity of 30 MW net and 35 MW gross, the power cycle pressure is 100 bar, and the turbine efficiency is 37.5%. There is fossil fuel backup (or boost) by NG.

Solar Electric Generating Station VII (SEGS VII) is also located in Kramer Junction. Start year was 1989. The solar field aperture area is 194,280 m^2. The other characteristics are the same of SEGS VI.

Solar Electric Generating Station VIII (SEGS VIII) is in Harper Dry Lake, California. The start year was 1989. The solar resource is 2725 kWh/m^2/year. The solar field aperture area is 464,340 m^2. The solar field outlet temperature is 390 °C. The power block is characterized by a turbine capacity of 80 MW net and 89 MW gross, the power cycle pressure is 100 bar, and the turbine efficiency is 37.6%. There is fossil fuel backup (or boost) by NG.

Solar Electric Generating Station IX (SEGS IX) is also located in Harper Dry Lake. The start year was 1990. The solar field aperture area was 483,960 m^2. The other characteristics are the same of SEGS VIII.

Data of electricity production and NG consumption of the SEGS II to IX CSP plants are provided in (Energy Information Administration 2017).

Figure 2.9 presents the energy input to the solar plant, either solar or NG; the efficiency of the plant, as ratio of electricity out to energy input; the electricity out, from the actual plant and from a reference GT or CCGT plant burning the NG; and finally the capacity factors, ε_1 to ε_4 defined above of SEGS IX. The net capacity is 80 MW.

ε_2 and ε_3 are still very close each other, however, with larger differences vs. the Ivanpah 1 facility. The peak CSP plant efficiency is above 35%. The capacity factors are those of Table 2.1 column 4. The capacity factors are about constant or even slightly reducing, as these plants are operating since many years. The average July 2016 to June 2017, NG not accounted for, is 22.54%. In the case of NG accounted with η actual plant, it drops to 19.91%. In the case of NG accounted for with $\eta = 60\%$, it reduces to 17.91%. Only without accounting for the NG consumption, Ivanpah is marginally better than SEGS IX.

When compared to the Ivanpah 3 facility, the latest 12 months' capacity factor for the SEGS IX facility is 1.1% lower if NG is not accounted for, 22.54% vs. 23.67%. Accounting for the NG contribution at actual plant efficiency, the capacity factor is only 0.2% lower, 19.91% vs. the 20.12% of Ivanpah 3, reflecting the larger use of NG to boost production of the Ivanpah facility.

To be noted, the SEGS facilities have significantly different net and gross capacity values, while in the Ivanpah facilities, net and gross capacity values are much closer.

The operation of the SEGS VI plant is also discussed in Lippke (1995) and Griffin et al. (2009). A scheme of the SEGS VI facility, design point operation, is provided in Fig. 2.10, courtesy of Thermoflow, www.thermoflow.com (Thermoflow, Inc 2017, 2012). A working model of SEGS VI is also provided in between the sample applications available with the free trial software THERMOFLEX 23 by Thermoflow.

2.7 Solana Generating Station

Information on CSP projects including Solana is provided in (National renewable Energy Laboratory 2017). The 280 MW gross Solana CSP PT plant is the largest single location CSP PT project in the world. It is in Gila Bend, Arizona, United States. Solana features TES, in the form of a MS system that is coupled to the otherwise traditional oil receiver fluid circuit. The TES system provides up to 6 h of generating capacity after sunset. The net turbine capacity is 250 MW; the gross turbine capacity is 280 MW. The start year is 2013. The land area is 7,800,000 m^2.

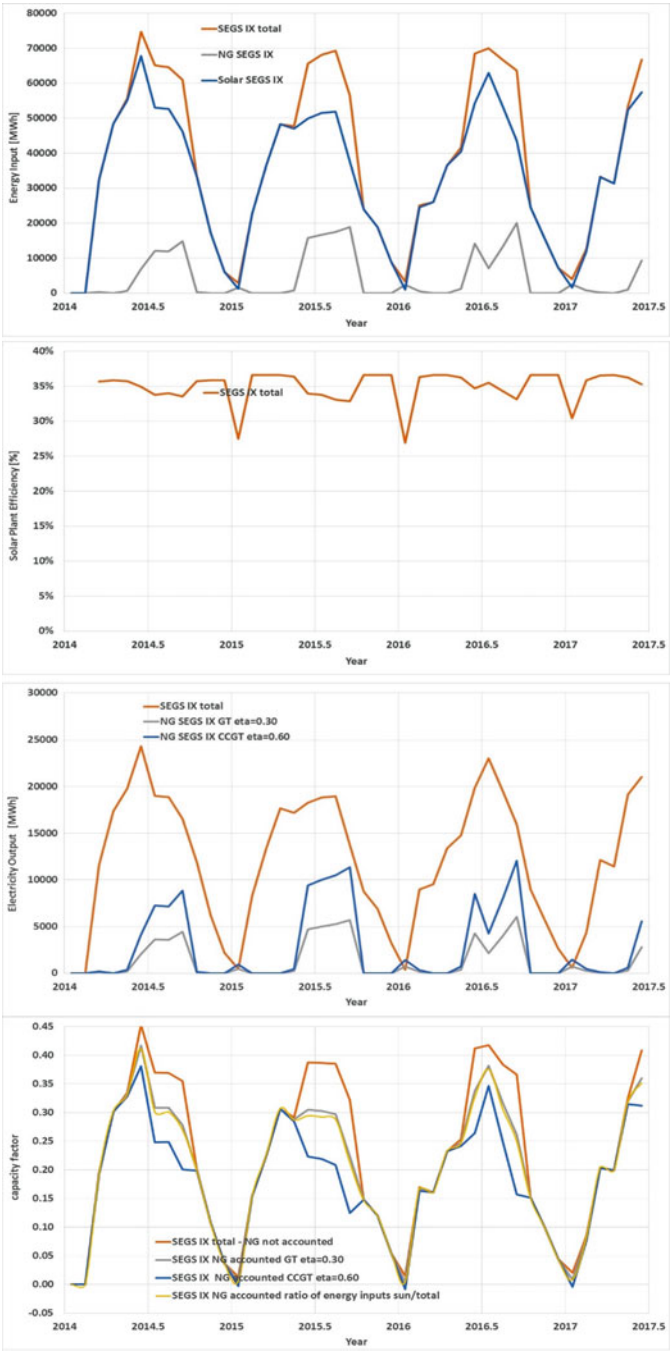

Fig. 2.9 Energy input to the solar plant, either solar or NG; the efficiency of the plant, as ratio of electricity out to energy input; the electricity out, from the actual plant and from a reference GT or CCGT plant burning the NG; and finally the capacity factors ε_1 to ε_4 defined above for the SEGS IX CSP PT plant

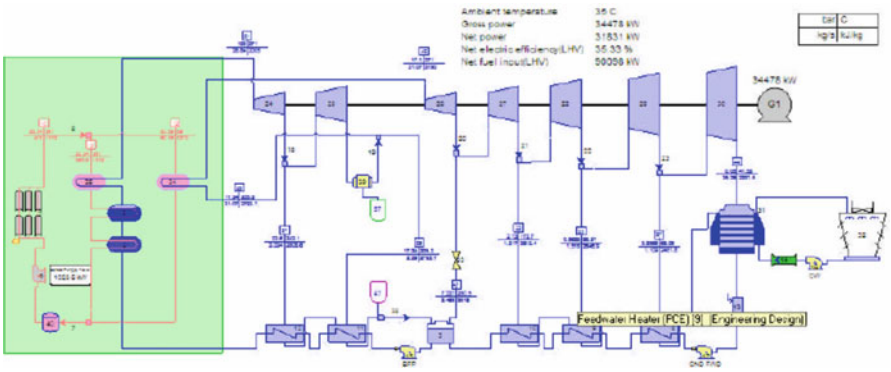

Fig. 2.10 Thermoflow scheme of the SEGS VI facility. Design point balance (Courtesy of Thermoflow, www.thermoflow.com. All data extracted from public available sources, California Energy Commission)

The planned electricity generation is 944,000 MW·h/year. The planned capacity factor from the net capacity of 250 MW is therefore 43%.

The cost is approximately 2 USD billion, 10% less than the Ivanpah facility that was completed only 2 months later, however, for 34% less net capacity.

The solar field aperture area is 2200,000 m^2. Therefore, Solana has a solar field aperture area per MW of gross capacity 44% larger than SEGS IX. (SEGS IX only has a solar field aperture area of 483,960 m^2 for a gross capacity of 89 MW.)

The number of solar collector assemblies (SCAs) is 3232. The number of loops is 808. There are four SCAs per loop. Every SCA is made of ten modules. The receiver fluid is Therminol VP-1. The TES fluid is Xceltherm MK1. The solar field inlet temperature is 293 °C, while the solar field outlet temperature is 393 °C. The power block is characterized by two turbines of gross power 280 MW (net power is 250 MW). The power cycle is steam Rankine, of maximum pressure 100.0 bar.

The cooling method is wet cooling. This permits better performances than the dry cooling of the other plant located in desert areas but at the expenses of using water. A fossil backup type based on NG is mentioned in (National renewable Energy Laboratory 2017). However, no NG consumption data is given in (Energy Information Administration 2017).

TES is by two-tank indirect (there is a separate circuit of MS fitted through a heat exchanger to the oil circuit that also includes the receiver and the heat exchanger for steam production). The storage capacity is 6 h.

Data of electricity production of the Solana CSP plant are provided in (Energy Information Administration 2017).

Figure 2.11 presents the solar energy input to the plant; the efficiency of the plant, as ratio of electricity out to energy input; the electricity out; and finally the capacity factor ε_1 for Solana. The net capacity is 250 MW. The capacity factors are those of Table 2.1 column 5. The capacity factors are increasing, as this plant is also relatively new. The average July 2016 to June 2017 is 32.65%. This capacity factor

is much better than those of SEGS II to IX or Ivanpah 1 to 3, even if much lower than the planned values of 43%.

A scheme of a smaller but similar PT installation, featuring oil as the receiver fluid and a double-tank MS TES added the oil circuit, the 50 MW Andasol 1 plant, located in Aldeire (Granada), Spain, is shown in Figs. 2.12 and 2.13, courtesy of Thermoflow, www.thermoflow.com (Thermoflow, Inc 2017, 2012). Figure 2.12 presents a scheme of the Andasol 1 heat balance design point operation, while Fig. 2.13 presents a scheme of the molten salt thermal energy storage system of the facility.

A working model of Andasol 1 is also provided in between the sample applications available with the free trial software THERMOFLEX 23 by Thermoflow.

2.8 Discussion and Conclusions

The NG boost of CSP plants is controversial. In principle CSP plants should not use NG, as otherwise they do not qualify as carbon-free plants. If CSP plants use NG boost, this should be accounted for in the computation of the capacity factor.

The actual contribution to the total energy output by NG in a CSP with boost by NG is also controversial. As the fuel energy conversion efficiency of the CSP thermal plant is lower than the fuel conversion efficiency of a CCGT plant, it may be argued that the splitting between solar and NG contributions to the produced electricity in the specific plant is incorrect and the use of the NG in a CCGT plant operated in parallel should be preferred.

We proposed different capacity factors to account for the NG boost and compare CSP plants with and without NG boost. We analyzed the three world's largest CSP plants, Ivanpah, SEGS, and Solana.

Ivanpah SPT uses steam as the receiver fluid and has no TES. SEGS PT has oil as the receiver fluid and steam produced in a heat exchanger oil-water/steam, but no TES. Both Ivanpah and SEGS make use of NG boilers to boost their solar energy output to match the contractual outputs. The Ivanpah and SEGS facilities are limited by rules in the use of this NG, as this impacts on the monitored carbon dioxide emission of the facilities. However, Ivanpah has used so far much more boost by NG than SEGS to meet the contractual daily output. The recent Ivanpah does not perform better than the old SEGS, delivering very close capacity factors with or without the NG accounted for. Solana PT does not use NG boost, it has oil as the receiver fluid and steam produced in a heat exchanger oil-water/steam featuring a MS TES connected to the oil circuit. Even if other aspects affect the capacity factor, nevertheless, the TES drives significantly up the capacity factor. Within the limit of an analysis that does not include the actual daily generation profile, Solana has a capacity factor 33% better than Ivanpah and SEGS also without considering the help by NG boost for Ivanpah and SEGS.

Not considered in the present analysis, the daily generation profile may be different for Ivanpah and SEGS.

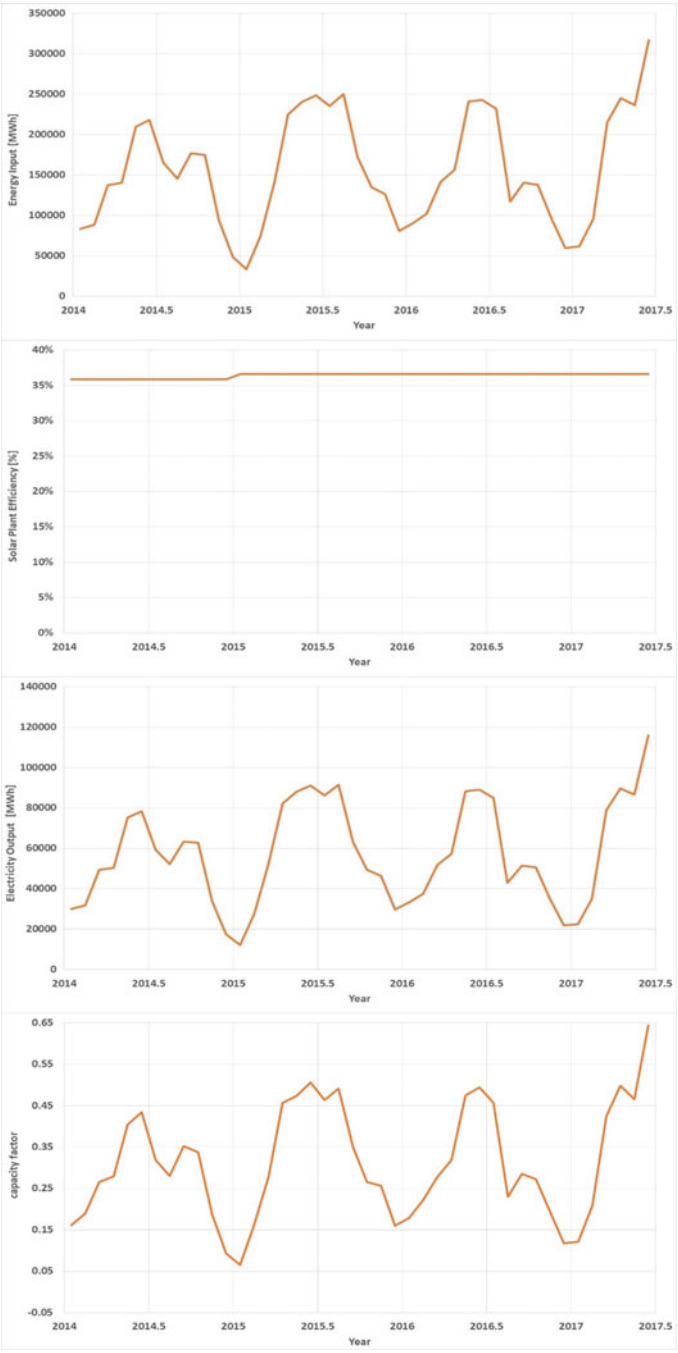

Fig. 2.11 Solar energy input to the plant; the efficiency of the plant, as ratio of electricity out to energy input; the electricity out; and finally ε_1. The actual capacity factor is still far from the planned value

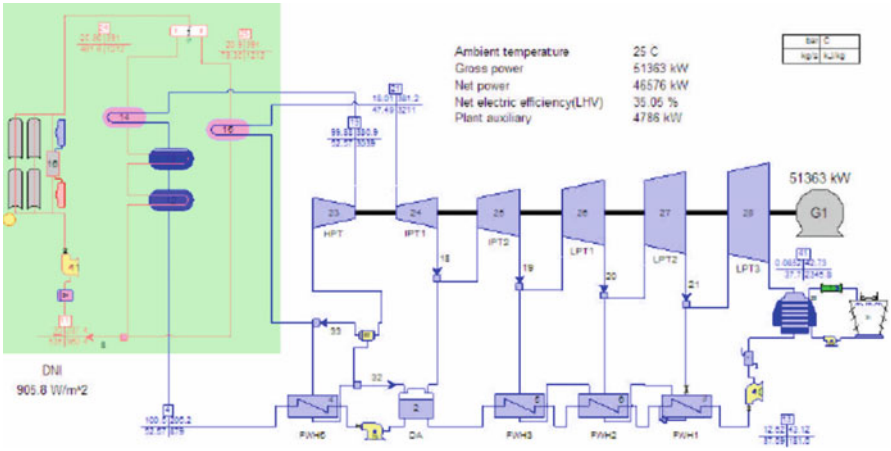

Fig. 2.12 Thermoflow scheme of the Andasol 1 facility. Design point balance (Courtesy of Thermoflow, www.thermoflow.com)

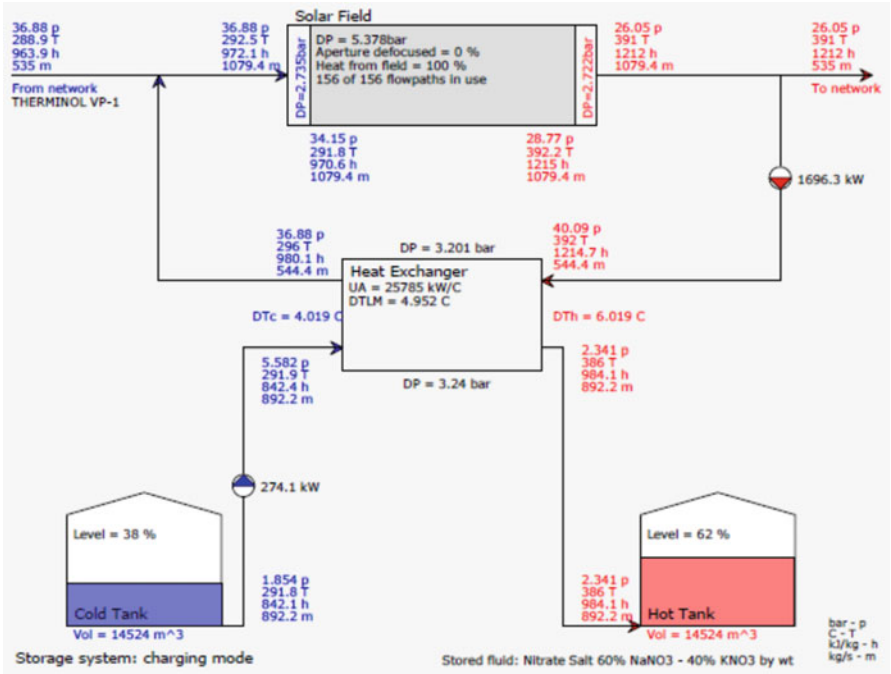

Fig. 2.13 Thermoflow scheme of the thermal energy storage of the Andasol 1 facility (Courtesy of Thermoflow, www.thermoflow.com)

We found TES is a key factor to achieve high capacity factors and avoid NG boost. MS TES technology appears as the best avenue to generate nonintermittent electricity with CSP and achieve high capacity factors. A 10 h TES eliminates the need for a fossil fuel backup or boost of electricity production at sunrise and in the evening peak hours. Next-generation CSP plants will very likely consist of three major units, PT or SPT MS receivers to convert the solar energy into thermal energy, TES section to store thermal energy using the MS, and finally power block generating electricity through a steam turbine. While costs are expected to further increase, the capacity factors may possibly rise well above the 40% mark.

References

Bendt, P., Rabl, A., Gaul, H. W., & Reed, K. A. (1979). *Optical analysis and optimization of line focus solar collectors* (No. NREL/TR-34-92). Golden: National Renewable Energy Laboratory (NREL).

Energy Information Administration. (2017). *Electricity data browser – Plant level data*. https://www.eia.gov/electricity/data/browser/. Retrieved 28 Aug 2017.

Feldhoff, J. F., Schmitz, K., Eck, M., Schnatbaum-Laumann, L., Laing, D., Ortiz-Vives, F., & Schulte-Fischedick, J. (2012). Comparative system analysis of direct steam generation and synthetic oil parabolic trough power plants with integrated thermal storage. *Solar Energy, 86* (1), 520–530.

Griffin, P., Huschka, K., & Morin, G. (2009). Software for design, simulation, and cost estimation of solar Thermal power and heat cycles. In *Proceedings of the SolarPACES 2009 Conference in Berlin*. https://www.thermoflow.com/images/SolarPACES2009%20Thermoflow.pdf. Retrieved 28 Aug 2017.

Kearney, D., & Herrmann, U. (2006). *Engineering evaluation of a molten salt HTF in a parabolic trough solar field*. Golden, CO: National Renewal Energy Laboratoy (NREL Contract No. NAA-1-30441-04).

Lippke, F. (1995). *Simulation of the part-load behavior of a 30 MWe SEGS plant* (No. SAND--95-1293). Albuquerque: Sandia National Labs.

Margolis, R., Coggeshall, C., & Zuboy, J. (2012). *SunShot vision study*. US Dept. of Energy, chapter 2. https://energy.gov/sites/prod/files/2014/01/f7/47927_chapter2.pdf

Martin, I. (2017). Webinar: Modeling solar thermal systems in THERMOFLEX, July 27, 2017. https://www.thermoflow.com/ppt/Feature%20Webinars/Webinar%207%20-%20Modelling%20Solar%20Thermal%20Systems.pdf. Retrieved 28 Aug 2017.

National renewable Energy Laboratory. (2017). Concentrating solar power projects by project name. https://www.nrel.gov/csp/solarpaces/by_project.cfm. Retrieved 28 Aug 2017.

Pacheco, J. E., Wolf, T., & Muley, N. (2013). *Incorporating supercritical steam turbines into advanced molten-salt power tower plants: Feasibility and performance*. Albuquerque: Sandia National Laboratories, Report No. SAN2013-1960.

Radosevich, L. G. (1988). *Final report on the power production phase of the 10 MWe solar thermal central receiver pilot plant*, SAND87-8022. Albuquerque: Sandia National Laboratories.

Reilly, H. E., & Kolb, G. J. (2001). *An evaluation of molten-salt power towers including results of the solar two project* (No. SAND2001–3674). Albuquerque/Livermore: Sandia National Labs.

Romero-Alvarez, M., & Zarza, E. (2007). Concentrating solar thermal power. In D. Y. Goswami & F. Kreith (Eds.), *Handbook of energy efficiency and renewable energy* (pp. 21–21). Boca Raton, FL: CRC Press.

Thermoflow, Inc. (2012). *Spotlight on solar thermal modelling*. https://www.thermoflow.com/images/Solar%20Thermal%20Pamphlet%202012.pdf. Retrieved 28 Aug 2017.
Thermoflow, Inc. (2017). *Thermoflow*. https://www.thermoflow.com/. Retrieved 28 Aug 2017.
Turchi, C. S., Ma, Z., Neises, T. W., & Wagner, M. J. (2013). Thermodynamic study of advanced supercritical carbon dioxide power cycles for concentrating solar power systems. *Journal of Solar Energy Engineering, 135*(4), 041007.

Chapter 3
Diagnosis of Nonlinear Stochastic Dynamics of Active Slider in Nanometer Spacing

Y.F. Wang, Y. Lu, and G. Chen

3.1 Introduction

Storage of 10 Tb/in^2 has been used to estimate the flying height signal. Recently, hard disk drives requires a physical spacing in the level of 0.25 nm at the read-write transducer location. A lot of physical and tribology issues exist to such a low flying height. At such a small spacing intermittent contact of solid-solid and solid-liquid between the slider and disk surface becomes inevitable.

At first, the current MEMS-based thermal fly-height control (TFC) technology needs further improvement to satisfy the future needs. How to control slider to reduce touchdown instability and eventually eliminate bouncing has been a pressing and challenging research topic. There are much research dedicated to address this complex problem, including the effects of hysteresis, the influence of surface roughness and waviness, and the lubricant modulation and uncertainty (Hua et al. 2016; Eguchi 2016; Canchi and Bogy 2010; Tagawa et al. 2007; Ono 2008; Xu et al. 2007, Sheng and Xu 2011; Hua et al. 1999, 2009; Wang et al. 2000). Basically, the contact dynamics of slider involves strong nonlinearity and stochastic properties. The existing research has clarified many nonlinear dynamic phenomena using the FFT spectrum; however, many more complicated phenomena such as narrowband and wideband frequency spectrum and the stochastic features of system response have yet been clarified. The existing analytical and numerical research has been centered on deterministic model analysis. The widely observed random properties of roughness and waviness of solid surfaces and modulation of lubricant have not been fully reflected in the analysis.

Y.F. Wang • Y. Lu
School of Mechanical Engineering and Automation Northeastern University, Shenyang, China

G. Chen (✉)
College of IT and Engineering, Marshall University, Huntington, WV, USA
e-mail: chenga@marshall.edu

L. Dai, R.N. Jazar (eds.), *Nonlinear Approaches in Engineering Applications*,
https://doi.org/10.1007/978-3-319-69480-1_3

Secondly, in order to improve the capacity of HDD, a higher areal density and accordingly higher track density in tracks per inch (TPI) are required. This poses a big challenge for the servo-mechanical system to support the positioning of the R/W head with a standard deviation of a few nanometers. Thus, accurately positioning the read/write head through the voice coil motor (VCM) actuator becomes more critical to sustaining the recording density growth. One disk side was dedicated to servo information to generate the position error signal (PES) between the read/write head and the desired track Yang et al. 2001. The rotary actuator was composed of a voice coil motor (VCM) and the bearing-supported actuator arm with the read/write head and its suspension system. Head-disk interface-induced vibrations are mixed with the position error signal (PES). Therefore, the rejection of these kinds of disturbances is critical to improving the positioning accuracy of the R/W head.

In this paper, we characterize the complex dynamics of active slider and then develop the fuzzy rules from PES signal data and use these fuzzy rules to identify noise type. A novel fuzzy median-mean filter is proposed which is capable of removing large amounts of mixed Gaussian and impulsive noise. It can be showed from the result of the test and the theoretical analysis that the proposed signal filter provides superior results in the mixed noise environment when compared to conventional median filters and mean filter.

3.2 Dynamics of Thermal Fly-Height Control Slider

The current slider technology uses thermal fly-height control (TFC) to bring the read-write sensors of the slider closer to the disk by resistive heating-induced thermal deformation/protrusion. While sub-nanometer level spacing has been achieved using the TFC, slider stability and head-disk interface (HDI) reliability at very small spacing remain to be fully understood. The TFC slider touchdown dynamics with clearance from sub-3 nanometer to sub-nanometer involves in varied interface effects in nanometer clearance regime including nonlinear air-bearing force, intermolecular force, electrostatic force, and solid-solid and solid-lubricant contact forces influenced by the uncertain effect of lubricant surface profile and disk topographic effect which possess underlying fractal structure. The nonlinear dynamics of TFC slider has been widely studied. The drawback of the results lies in the limit of conventional nonlinear dynamic methods used, which are majorly based on assumptions of small nonlinearity and being deterministic. In our investigation, the data from well-known models and measured real data are used for the diagnosis. Figures 3.1 and 3.2 are the typical FFT spectrum and spectrogram of the responses of two TFC sliders in touchdown and near-contact process.

Thermal fly-height control is used in a static manner in todays' disk drives, i.e., a constant power is applied to the heater during writing and reading, respectively. Dynamic flying height variations of a slider over a disk are composed of repeatable and non-repeatable contributions. As the name suggests, repeatable variations of

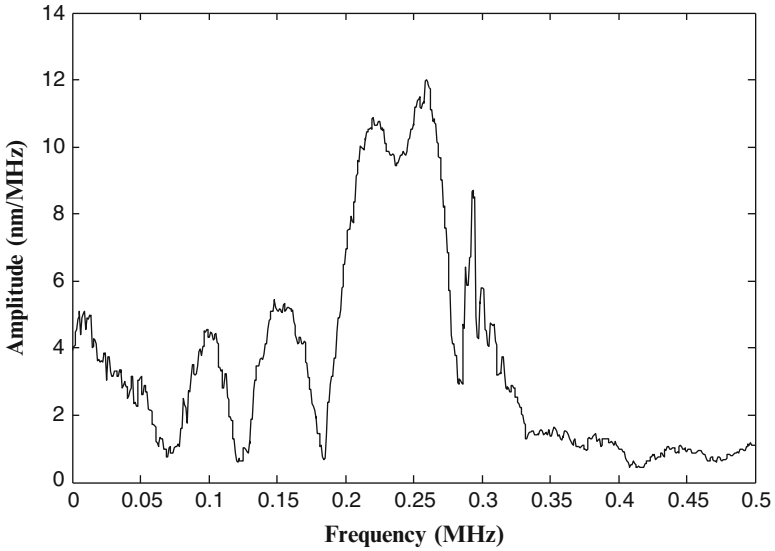

Fig. 3.1 FFT of response of TFC active slider in nanometer spacing touchdown

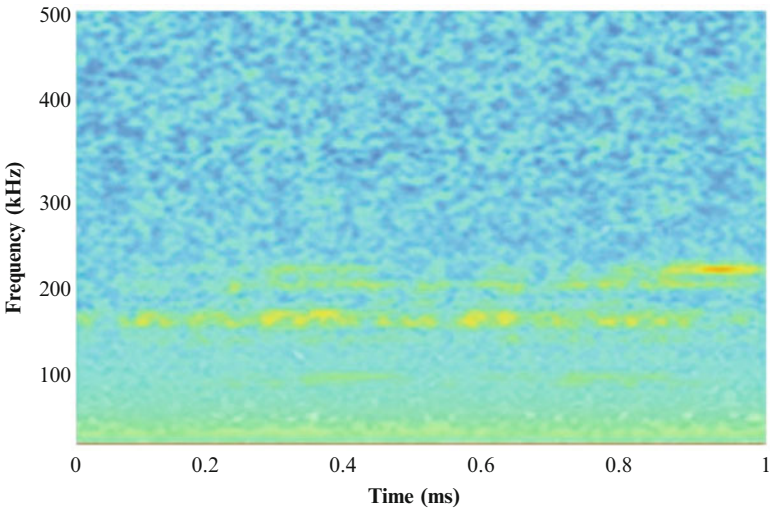

Fig. 3.2 FFT of response of TFC active slider in nanometer spacing touchdown

flying height occur at the same angular and radial position of the slider above the disk at each revolution. Thus, the question arises as to whether a thermal fly-height control slider can be used to dynamically control the repeatable flying height variations between slider and disk. One of the first approaches to dynamic flying height has been shown in Shiramatsu et al. (2008) where time domain and frequency domain data have been used to estimate the flying height signal.

Recently, a novel method of measuring the relative head-medium spacing based on a measurement in the servo sectors is developed and simulated using a read-back signal model by following Eqs.3.1 and 3.2 in Boettcher et al. (2011).

$$\Delta z = -\frac{\lambda}{2\pi} \ln\left(\frac{\Phi_A(\lambda, z) + \Phi_B(\lambda, z)}{\Phi_A(\lambda, z_{\text{ref}}) + \Phi_B(\lambda, z_{\text{ref}})}\right) \tag{3.1}$$

$$\text{PES} = \frac{A - B}{A + B} \tag{3.2}$$

Therefore, the exact PES signal is critical to improving the accuracy of the TFC and positioning control (PC).

3.3 Noise Properties of PES Signal

A HDD consists of a voice coil motor (VCM), several magnetic heads, several disks, and a spindle motor. The head-positioning control system in HDDs is illustrated in Fig. 3.3. The position error signal (PES) in the current hard disk drives

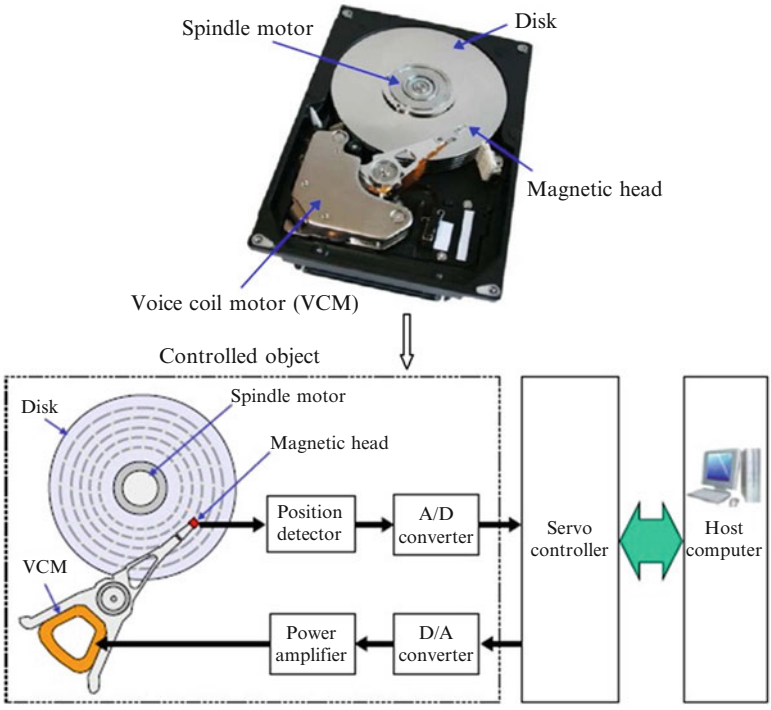

Fig. 3.3 Schematic diagram of HDD

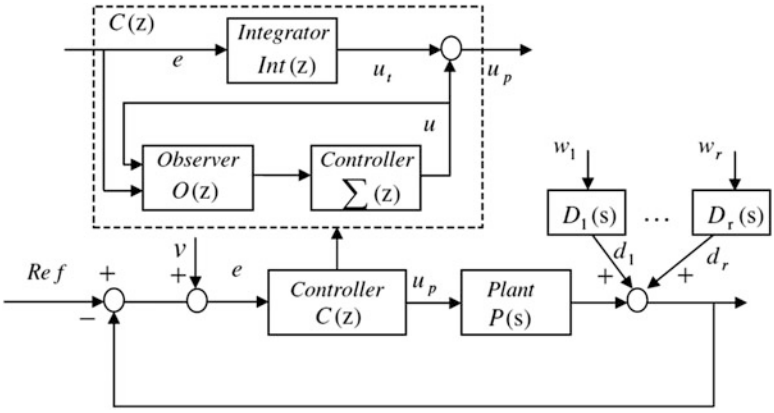

Fig. 3.4 Servo control loop with injected disturbances and measurement noise

is generated from the embedded servo data and used as the input for the track-following controller. It is well known that the PES often be contaminated by noise disturbances in hard disk drives. The control system for the micro-actuator loop is shown in Fig. 3.4, where P (s) is the VCM actuator model, $C(z)$ is the feedback controller, and e is the measurement or the position error signal (PES) in HDDs. $D_i(s)$, $i = 1, 2,. .., r$ are disturbance models and w_i are white noises with unity variances. v is the measurement noise with its standard deviation given in Du et al. (2009). PES is the relative position between the R/W head and the disk track.

A hard disk drive position error signal (PES) can be decomposed in the frequency domain into three components in Bramovitch et al. (1997).

This is typically due to the rotation of the spindle and therefore synchronous with it or one of the spindle orders. While synchronous excitation may be large, it is already a standard practice in the disk drive industry to use feedforward cancellers to dramatically attenuate its effect: nonsynchronous or non-repeatable spectral excitation. While this excitation does not correspond to any of the spindle orders, it does have sharp spectral peaks due to cage orders. Typical sources of this excitation are disk or arm resonances (which are less sharp but still narrowband), often stimulated by synchronous or broadband excitation. Again, this can have a significant effect on PES; however, it has become recently apparent that such phenomena as disk resonances can be considerably reduced by the use of damped substrates: broadband or baseline noise. This is the broad baseline level of the noise that remains when all the narrowband components have been removed.

In order to achieve very high track densities, each of these sources of PES must be reduced considerably. These noises are displayed in the form of useless information, reduce the signal quality, and impact the successive work.

There are two popular kinds of noises studied: one is the Gaussian noise in Lin et al. (2000) and the other is impulse noise in Gao et al. (2009). These effort approaches for PES signal restoration are aimed at removing either Gaussian or

impulsive noise. However, in many situations, practical PES signal seldom only contains single noise (Gaussian or impulse noise), and it is often contaminated by more than one type of noises, such as mixed noise. The mixed noise corruption often happens in some complex environment, for example, a signal with Gaussian noise is transmitted through a disturbed communication channel. As such it is important to design a filter to remove mixed noise in a PES signal-processing environment without blurring the signal details.

3.4 Advanced Diagnosis of Noise Properties

Generally, data mining is the process of analyzing data from different perspectives and summarizing it into useful information. In Wang et al. (2011), an off-line data mining method with completeness and robustness to extract the fuzzy rules of the friction force model was developed. In this section, we will improve that data mining method so that it can be used to online identify the noise types and filtering for PES signal. The scheme is described as follows:

3.4.1 Define Fuzzy Variables

Let $e(k)$ denote the position error signal in this normal case. When the normal position error signal is corrupted by $d(k)$, the contaminated position error signal is given by

$$\tilde{e}(k) = e(k) + d(k) \tag{3.3}$$

where $d(k)$ may be the disturbance noise, or the measurement noise, or a mix of the disturbance noise and measurement noise.
We calculate the mean value of the contaminated position error signal as follows:

$$x(k) = \frac{1}{k}\sum_{j=0}^{k} |\tilde{e}(k)| \tag{3.4}$$

Assume e_l and e_u be some lower and upper bounds for e. Define the contaminated position error signal $\tilde{e}(k)$ composed of three discrete signal levels, denoted by $\{r_1, r_2, r_3\}$. The probability density function (PDF) of r_i is defined as

$$p(r_i) = \frac{n_i}{k}, \quad i = 1, 2, 3 \tag{3.5}$$

where n_1 is the number of lower signal ($\tilde{e}(n) > e_\mathrm{l}$, $n = 0,..., k$), n_2 is the number of middle signal ($e_\mathrm{l} < \tilde{e}(n) < e_\mathrm{u}$, $n = 0,..., k$), and n_3 is the number of upper signal

($e\tilde{}(n) > e_u$, $n = 0,..., k$). Based on the PDF, the feature variable y using identification of the mixed noise is defined as

$$y(k) = \frac{\text{Min}\{p(r_1), p(r_3)\}}{\text{Max}\{(p(r_1), p(r_3)\}} \tag{3.6}$$

3.4.2 Online Identify Noise Types

To identify the noise type by the use of fuzzy rules, our proposed approach consists of the following steps:

Step 1. Divide the input and output spaces into fuzzy regions

Assume that the domain intervals of $x(k)$ and $y(k)$ are $[x_-, x_+]$ and $[y_-, y_+]$, respectively, where the domain interval of a variable means that most probably, this variable will lie in this range. The sets of linguistic labels are denoted by $A = \{A_1, A_2, A_3\}$ for $x(k)$ and $B = \{B_1, B_2, B_3\}$ for $y(k)$, where each linguistic label is associated with a fuzzy membership function. We use the fuzzy sets and membership functions as shown in Fig. 3.5.

Step 2. Calculate degree of support

From a data mining perspective, the degree of support is the percentage of records where the rule holds. If a fuzzy rule has practical meaning, it must have a large enough degree of support from PES signal online data. Therefore, the degree of support for a specific fuzzy input space is a good indicator for extraction of fuzzy rules from numerical data. The degree of support for a fuzzy rule is defined as follows:

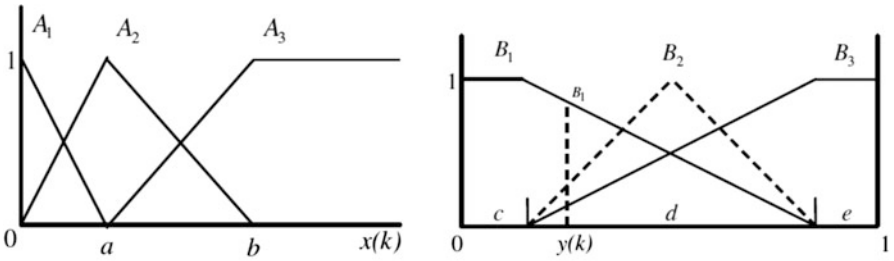

(a) Fuzzy sets of x variable (b) Fuzzy sets of y variable

Fig. 3.5 Fuzzy sets and membership functions

$$\mathrm{Sup}_{x\Rightarrow y}(k) = \frac{\sum_{p=0}^{k} \mu B_l(y(p))\mu_{A_j}(x(p))}{\sum_{p=0}^{k} \mu_{(A_j)p}(x(p))}, \tag{3.7}$$

where the $\mu_{Aj}(x(p))$ and the $\mu_{Bl}(y(p))$ are values of membership functions for the p-th record, respectively, and k is the PES sample, $l, j \in \{1, 2, 3\}$.
For simplicity, we can use the following formula to calculate the degree of support:

$$\mathrm{Sup}_{x\Rightarrow y}(k) = \frac{1}{(k+1)} \sum_{p=0}^{k} \mu_{B_l}(y(p))\mu_{A_j}(x(p)) \tag{7.8}$$

Step 3. Generate a fuzzy rule base

Details of the data mining algorithm can be found in Fig. 3.6. We show the process for a fuzzy rule-base generation. Design $A = \{A_1, A_2, A_3\}$ is a set of linguistic labels

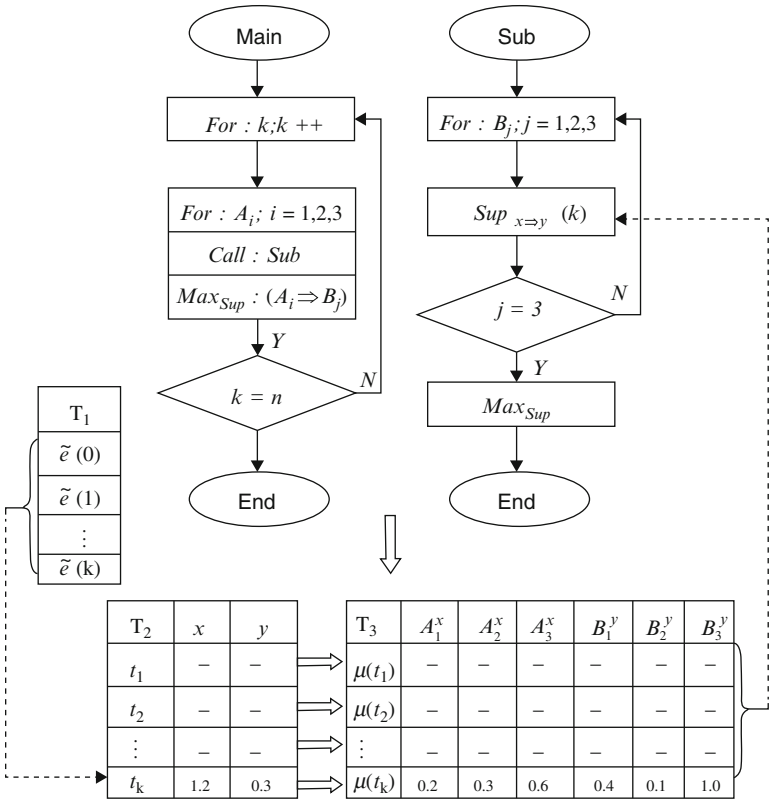

Fig. 3.6 Process of the data mining algorithm for PES signal noise

for attribute $x(k)$, and $B = \{B_1, B_2, B_3\}$ is another set of linguistic labels for attribute $y(k)$. For $\{A_1\}$, we first calculate the respective degrees of support for pairs $\{A_1, B_1\}$, $\{A_1, B_2\}$, and $\{A_1, B_3\}$. Then, we select a fuzzy subspace with the maximum degree of support for this column. Repeating this process for $\{A_2\}$ and $\{A_3\}$, we can obtain one of the following fuzzy rules $R(1)$, $R(2)$, and $R(3)$ in Step 4.

Step 4. Decide noise type using fuzzy rule base

Focusing on the $R(1)$ rule base, i.e., the group of rules having B_1 as the consequent, we conclude that the noise type is a Gaussian noise. Similarly, if we obtain the $R(2)$ rule base, i.e., the group of rules having B_3 as the consequent, the noise type is generally considered as impulsive noise.

$$R(1) : \text{IF } (x(k), A_i) \quad \text{THEN} \quad (y(k), B_1), \quad i = 1, 2, 3 \tag{3.9}$$

$$R(2) : \text{IF } (x(k), A_i) \quad \text{THEN} \quad (y(k), B_3), \quad i = 1, 2, 3 \tag{3.10}$$

When the consequents of the fuzzy rules are not identical, i.e., various combinations of B_1, B_2, and B_3 (except $R(1)$and $R(2)$) appear in the THEN part, we define the type of noise as a mixed one.

In such a case, the proposed fuzzy mean-median filter will be applied to remove noises from PES signal.

$$R(3) : \begin{cases} \text{IF } (x(k), A_1) & \text{THEN} & (y(k), B_i) \\ \text{IF } (x(k), A_2) & \text{THEN} & \big(y(k), B_j\big), \\ \text{IF } (x(k), A_3) & \text{THEN} & (y(k), B_l) \end{cases} \quad i, j, l = 1, 2, 3. \tag{7.11}$$

3.5 Advanced Filtering of Noise Properties

3.5.1 Knowledge on Filter Selection

In signal processing, the most common methods are median filter and mean filter, which are representations of nonlinear filter and linear filter, respectively. The principles of the two techniques are different. The median filter and mean filter fit for deferent kinds of noise. Mean filter has been applied to restrain Gaussian noise, while median filter has been applied to restrain impulse noise.

In a mixed noise environment, where both Gaussian and impulsive noises are present, new filtering techniques must be used. Hybrid filters have been suggested as a method of solving this problem. In this paper, we combined both mean filter and median filter together with an adjustment parameter. This adjustment parameter is just equal to the fuzzy membership function B_1 in Sect. 3.3. The flow chart of the image denoising process is given in Fig. 3.7.

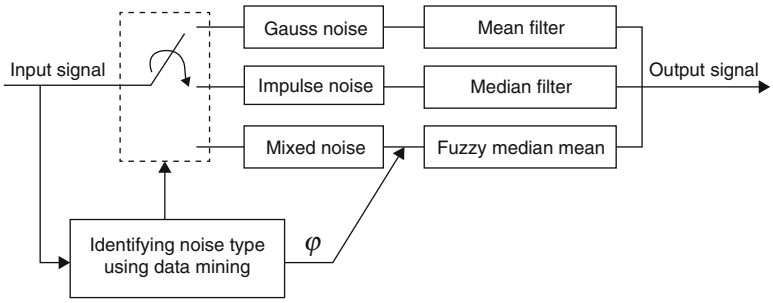

Fig. 3.7 The flow chart of noise removal

3.5.2 *Fuzzy Media-Mean Filter*

In the following, a novel filter, fuzzy media-mean (FMM) filter, is developed to remove the mixed noise. The fuzzy media-mean filter operates on a filtering window. The proposed method operates as follows:

$$\phi = \mu B_1(y(k)) \tag{3.12}$$

at first, weighted average fuzzy membership function is defined according to the following relationship:

$$\begin{cases} e(k) = \varphi m_1 + (1-\varphi)m_2 \\ m_1 = \text{median}[e(k-1), \tilde{e}(k), e(k-2)],\ M = 1 \\ m_2 = \text{mean}[e(k-1), \tilde{e}(k), e(k-2)], M = 1 \end{cases} \tag{3.13}$$

secondly, the final fuzy media-mean filter is obtained by means of the following relationship,

$$\begin{cases} e(k) = \varphi m_1 + (1-\varphi)m_2 \\ m_1 = \text{median}[e(k-1), \tilde{e}(k), \text{RRO}_e(k)],\ M > 1 \\ m_2 = \text{mean}[e(k-1), \tilde{e}(k), \text{RRO}_e(k)],\ M > 1 \end{cases} \tag{3.14}$$

where m_1 is the mean filter and m_2 is the median filter in Eq. 3.15. RRO, which is synchronous to the rotational speed of the spindle motor, is also included in the feedback servo loop. If PES is assumed to be ergodic and the average of PES NRRO converges to zero, PES RRO can be calculated as in Eq. 3.15 with M rows of data composed of n measured PESs from sector number 0 in Eq.3.17.

$$\text{RRO}_e(k) = \frac{1}{M}\sum_{i=1}^{M} \text{PES}_i(k) \tag{3.15}$$

where k means the index of PES sample and i means the index of PES data row.

3.5.3 Simulation Results

The reliability of the signal which was used for this purpose can be evaluated by signal-to-noise ratio (SNR) which is given in Eq. 3.16. When the signal ratio of a PES signal is high and the noise ratio is low, this PES signal is considered to be good quality. Therefore, in the analysis of a PES signal, SNR value should absolutely be examined. The parameters used for the following experiments are specified as follows: $a = 0.03$, $b = 0.1$, $c = 0.2$, $d = 0.5$, and $e = 0.85$ in Fig. 3.5. The lower bound $e_{\mathrm{l}} = -0.12$, and the upper bound $e_{\mathrm{u}} = 0.12$.

$$\mathrm{SNR} = 10\lg \frac{\sum_{k=1}^{N} (e(k) - \tilde{e})^2}{\sum_{k=1}^{N} (e(k) - \tilde{e}(k))^2} \tag{3.16}$$

The corrupted and the normal PES signal (200 sector/revolution) is shown in Fig. 3.8. The noise PES signal is corrupted by white Gaussian noise and impulse noise. And the experiment results using mean filter, median filter, and our proposed filter are shown in Figs. 3.9, 3.10, and 3.11, respectively. The mean filter and median filter using the following relations are indicated in (Gao et al. 2009).

$$\begin{cases} e(k) = \mathrm{median}[e(k-1), \tilde{e}(k), \mathrm{RRO}_e(k)] \\ e(k) = \mathrm{mean}[e(k-1), \tilde{e}(k), \mathrm{RRO}_e(k)] \end{cases} \tag{3.17}$$

It is obviously seen that FMM filter using Eqs. 3.13 and 3.14 has a better performance aiming at mix noise especially the last few revolutions.

We can make a further comparison of SNR value of the FMM filter with mean filter and median filter as shown in Table 3.1. The RRO values in the first revolution equal to $\tilde{e}(k)$, so the filtered result $e(k)$ using median filter equal to $\tilde{e}(k)$, which

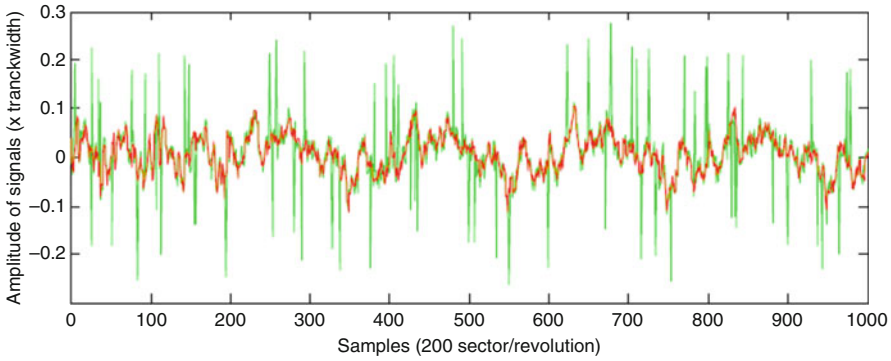

Fig. 3.8 Comparison of normal signal and corrupted signal

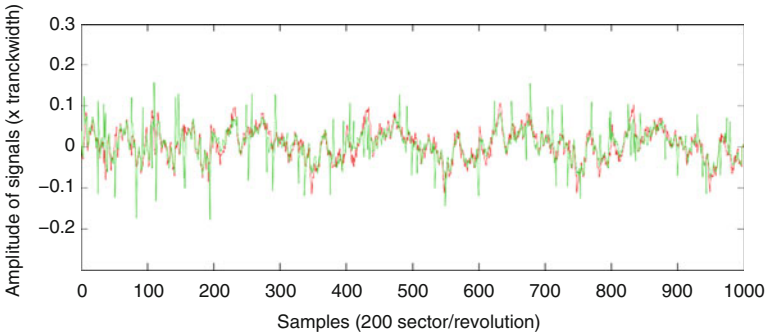

Fig. 3.9 Comparison of normal signal and filtered signal using mean filter

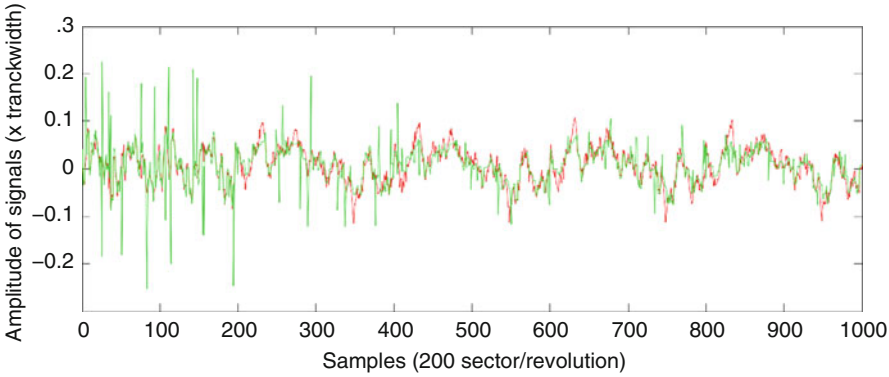

Fig. 3.10 Comparison of normal signal and filtered signal using median filter

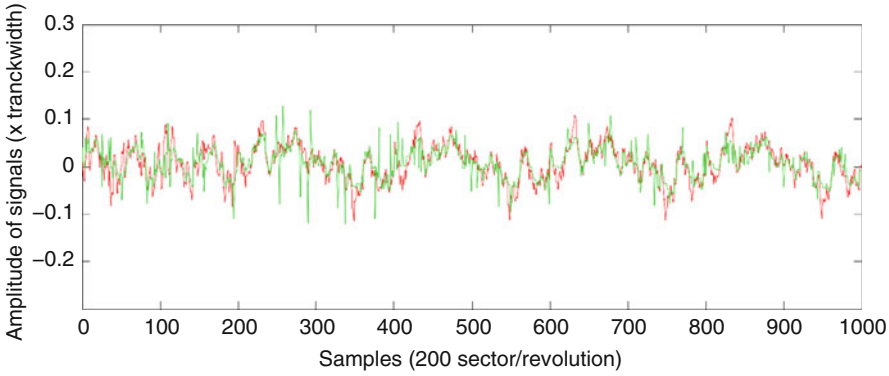

Fig. 3.11 Comparison of normal signal and filtered signal using FMM filter

Table 3.1 Comparison of SNR for different filters

SNR	Filter type		
	Mean	Median	Fuzzy median-mean
All 5 revolutions	2.1023	1.5229	3.2788
Last 4 revolutions	2.8145	3.7932	4.0929

means the result is actually not filtered in the first revolution. Therefore, a comparison of the last four revolutions of three filters is also shown in Table 3.1.

3.6 Conclusion

In this paper, the nonlinear stochastic dynamics of active slider are characterized. A novel noise classifier and fuzzy median-mean filter using data mining techniques for removing mixed noise from corrupted PES signal are proposed. The fuzzy median-mean filter combining a median-type filter with a mean filter is able to recover PES signal corrupted by Gaussian plus impulsive noise. The performance of the proposed method is evaluated and compared with the classical median filter, mean filter, and fuzzy filter algorithms for both impulsive noise and Gaussian noise removal tasks. The quantitative and qualitative results on test PES signal demonstrate that the proposed method can remove the noise effectively while preserving the PES signal local features.

Acknowledgments This work was supported in part by the Natural Science Foundation of China under Grant 51275085 and 61273177, the Science and Technology Foundation of Shenyang City under Grant F12-175-9-00 and F14-231-1-06, and the State Key Laboratory Foundation of Synthetical Automation for Process Industries, Northeastern University.

References

Boettcher, U., Lacey, C. A., & Li, H. (2011). Servo signal processing for flying height control in hard disk drives. *Microsystem Technol, 17*, 937–944.

Bramovitch, D., Hurst, T., & Henze, D. (1997). Decomposition of baseline noise sources in hard disk position error signals using the PES pareto method. In *Proceedings of the American control conference* 2901–2905.

Canchi, S. V., & Bogy, D. (2010). Slider dynamics in the lubricant-contact regime. *IEEE Transactions on Magnetics, 46*, 764–769.

Du, C., Xie, L., & Lewis, F. L. (2009). Multi-frequency disturbance rejection via blending control technique for hard disk drives. *Automatica, 45*, 2244–2249.

Eguchi, T. (2016). On the relationship of natural frequency, damping, and feedforward acceleration with transient vibrations of track-seek control. *Microsystem Technologies, 22*(6), 1257–1265.

Gao, T., Du, C., & Ye, Z. (2009). Smoothing position error signal corrupted by impulsive disturbances. *IEEE Trans Magnetics, 45*, 5082–5087.

Hua, W., Liu, B., Sheng, G., & Zhu, Y. (1999). Probability model for slider-disk interaction. J Info Storage Proc. *Syst., 1*, 273–280.

Hua, W., Liu, B., Yu, S., & Zhou, W. (2009). Nanoscale roughness contact in a slider-disk Interface. *Nanotechnology, 20*, 1–7.

Hua, W., Yu, S. K., Zhou, W. D., & Myo, K. S. (2016). Investigation of slider out-of-plane and in-plane vibrations during the track-seeking process. *Microsystem Technologies, 22*(6), 1189–1197.

Lin, C., Guo, G., & Chen, B. M. (2000). Servo signal processing for flying height control in hard disk drives. In *Proceedings of the 6th international workshop* on 502–505.

Ono, K. (2008). Dynamic instability of flying head slider and stabilizing design for near-contact magnetic recording. *Journal of Magnetism and Magnetic Materials, 320*, 3174–3182.

Sheng, G., & Xu, J. (2011). A parameter identification method for thermal flying-height control sliders. *Microsystem Technologies, 17*, 1409–1415.

Shiramatsu, T., Atsumi, T., Kurita, M., Shimizu, Y., & Tanaka, H. (2008). Dynamically controlled thermal flying-height control slider. *IEEE Trans on Magn, 44*, 3695–3697.

Tagawa, N., Mori, A., & Senoue, K. (2007). Effects of molecularly thin liquid lubricant films on slider hysteresis behavior in hard disk drives. *Journal of Tribology, 129*, 579–585.

Wang, G., Li, Y., & Lee, H. J. (2000). The effect of air-bearing surface roughness on avalanche test. *Journal of Applied Physics, 87*, 6176–6178.

Wang, Y. F., Wang, D. H., & Chai, T. Y. (2011). Extraction and adaptation of fuzzy rules for friction modeling and control compensation. *IEEE Trans Fuzzy System, 19*, 682–693.

Xu, J., Kiely, J. D., Hsia, Y. T., & Talke, F. E. (2007). Dynamic of ultra low flying sliders during contact with a lubricated disk. *Microsystem Technologies, 13*, 1371–1375.

Yang, H. S., Jeong, J., & Park, C. H. (2001). Identification of contributors to HDD servo errors by measuring PES only. *IEEE Trans Magnetics, 37*, 883–887.

Chapter 4
Formation Control of Nonholonomic Mobile Robots Using an Acoustic Sensor

Michael Hegedus, Mehran Mehrandezh, and Raman Paranjape

4.1 Introduction

4.1.1 Leader-Follower Formation Controller

Everyday tasks that humans easily perform are extremely difficult for autonomous robots. For example, an individual driving a vehicle can follow another automobile at a relatively constant range. This person maintains a simple formation without knowing his/her or the other vehicle's location on Earth, travelling speed, and angular velocity. Additionally, two drivers do not need to communicate with each other to follow in formation; a driver only needs his vision to determine the relative range and bearing of the other vehicle.

This research investigates the development of leader-follower formation controllers for a team of mobile robots. The set of formation controllers proposed assumes no communication between the leader and following robot. To maintain formation, a position sensor is mounted on the follower. This sensor measures local information: relative distance and bearing between the follower and a target. Targets can include stationary objects in the environment and fixed points on the leader. Global information relating to the leader and follower, such as world

M. Hegedus (✉)
School of Engineering Science, Simon Fraser University, Burnaby, BC, Canada
e-mail: mikehegedus@hotmail.com

M. Mehrandezh
Faculty of Engineering and Applied Science, Industrial Systems Engineering, University of Regina, Regina, SK, Canada
e-mail: Mehran.Mehrandezh@uregina.ca

R. Paranjape
Faculty of Engineering and Applied Science, Electronic Systems Engineering, University of Regina, Regina, SK, Canada
e-mail: Raman.Paranjape@uregina.ca

L. Dai, R.N. Jazar (eds.), *Nonlinear Approaches in Engineering Applications*,
https://doi.org/10.1007/978-3-319-69480-1_4

coordinates, linear velocity, and angular velocity, are unknown and need to be estimated using only local range and bearing measurements.

List of Symbols

Sensor model for leader-follower configuration	
(X_O, Y_O)	Position of object "o" in the world frame, where "a" can be the leader (l), follower (f), or landmark (w)
$({}^{O}X, {}^{O}Y)$	Coordinate frame (X-axis, Y-axis) attached to object "o" in the world frame
$({}^{f}X_O, {}^{f}Y_O)$	Position of an object "o" in the follower's coordinate frame
$({}^{f}r_O, {}^{f}\emptyset_O)$	Pose (range, bearing) to an object "o" in the follower's coordinate frame
Mobile robot kinematic model	
(a, b)	Position away from a robot's center of rotation, offset along its X-axis and Y-axis
Θ_O	Bearing of object "o," with respect to the world frame
(v_O, ω_O)	Linear and angular velocity of object "o"
Relative leader-follower kinematics	
$\mathbf{q}$	Position vector of the leader's center of rotation in the world frame, $\mathbf{q}\epsilon\mathbb{R}^3$
$\mathbf{V}$	Linear velocity vector of the leader, $\mathbf{V}\epsilon\mathbb{R}^3$
$\mathbf{\Omega}$	Angular velocity vector of the leader, $\mathbf{\Omega}\epsilon\mathbb{R}^3$
$(\mathbf{R_O}, \mathbf{T_O})$	Rotation and translation vector of object "o" in the world frame, $(\mathbf{R_O}, \mathbf{T_O})\epsilon SE(3)$
$\mathbf{u}_f$	Control input (law) for the following robot, $\mathbf{u}_f = (v_f, \omega_f)^T \epsilon\ \mathbb{R}^2$
(k_1, k_2)	Positive control gains
Relative leader-follower kinematics	
T_{MN}	Time delay for sound to travel from microphone "M" to "N"
$\widehat{T}_{MN}$	Time-delay measurement of sound travelling from microphone "M" to "N"
L_{MN}	Distance between microphone "M" and "N," $L_{MN} = D_{MIC}$
c	Speed of sound travelling in dry air at room temperature
β_{MN}	Bearing to a sound source w.r.t the microphone pair "M" and "N"
(R, Θ)	Range and bearing to a sound source w.r.t the center of the acoustic array

4.1.2 Leader-Follower Configuration

A position sensor is equipped on a follower travelling behind a leader. This sensor is simultaneously observing a point on the leader, and a stationary object located in the environment (see Fig. 4.1). Coordinate frames are attached to a point on the leader, follower, landmark, and world. Superscripts identify an object's coordinate system (or reference frame), and subscripts identify other objects located in that coordinate system. The parameter $i = \{l,f,w\}$ represents the following objects: leader (l), follower (f), and landmark (w). By convention, no superscripts are used to identify objects located in the world frame. For example, (X_l,Y_l) is the coordinate of the origin of the leader's reference frame in the world frame, while $({}^{f}X_l, {}^{f}Y_l)$ is the coordinate of the origin of the leader's reference frame with respect to the follower's coordinate frame. The kinematic model of the formation is derived in the next section using these depictions.

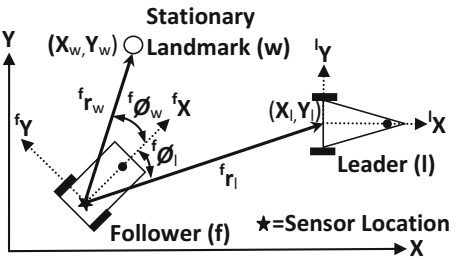

Fig. 4.1 Sensor model for simple leader-follower configuration

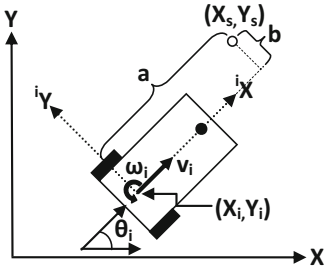

Fig. 4.2 Mobile robot kinematics model

4.1.3 Kinematic Model for Nonholonomic Mobile Robots

In order to derive the kinematic of the formation, one needs to derive the kinematic model of each individual robot in the team. Here we assume a *differential-drive* model in the wheeled mobile robots used in the team. The kinematics model (Fig. 4.2) for each robot travelling on a plane perpendicular to the z-axis, with respect to their rotational center, is described as:

$$\begin{bmatrix} \dot{X}_i \\ \dot{Y}_i \\ \dot{\theta}_i \end{bmatrix} = \begin{bmatrix} v_i \cos\theta_i \\ v_i \sin\theta_i \\ \omega_i \end{bmatrix} \tag{4.1}$$

where v_i, ω_i, and θ_i represent the linear velocity, angular velocity, and orientation of a robot, $i = \{l,f\}$, with respect to the world frame.

4.1.4 Kinematic Model for a Point Attached to a Nonholonomic Mobile Robot

In this section, the kinematics of a point attached to the robot with an offset with respect to its center of rotation is derived. The velocity of a point $\mathbf{q}_s = (X_s,Y_s)^{\mathrm{T}} \in \mathbb{R}^2$

attached to a robot, located at displacement $(a,b)^{\mathrm{T}} \epsilon\ \mathbb{R}^2$ from a robot's rotational center, is described as (see Fig. 4.2):

$$\begin{bmatrix} \dot{X}_s \\ \dot{Y}_s \end{bmatrix} = \begin{bmatrix} v_i \cos\theta_i \\ v_i \sin\theta_i \end{bmatrix} + \begin{bmatrix} -a\sin\theta_i - b\cos\theta_i \\ a\cos\theta_i - b\sin\theta_i \end{bmatrix} \dot{\theta}_i \tag{4.2}$$

4.1.5 Leader-Follower Kinematics for a Position Sensor

A model must be created that defines the motion between the leader and follower before a formation control law for the follower can be defined. Specifically, a model must be defined that describes the motion of a point observed by a follower, while it is undergoing both translation and rotation. For this model, a position sensor that observes a point on the leader's center of rotation is mounted on the follower's center of rotation so that the coordinate frames attached to the follower and position sensor are identical.

4.1.6 Relative Leader-Follower Kinematics

Consider the simplest case where one follower is travelling behind a leader, and the follower is observing a target point $\mathbf{q} = (X,Y,Z)^{\mathrm{T}} \epsilon\ \mathbb{R}^3$ attached to the leader. While travelling on the XY-plane, a mobile robot undergoes linear velocity $\mathbf{V} \epsilon \mathbb{R}^3$ and angular velocity $\mathbf{\Omega} \epsilon \mathbb{R}^3$. An observed target point $\mathbf{q} = (X,Y,Z)^{\mathrm{T}} \epsilon\ \mathbb{R}^3$ evolves in the sensor's coordinate frame (identical to the robot's coordinate frame). However, this reference frame is affected by the relative angular and linear velocity $({}^f\mathbf{\Omega}_l, {}^f\mathbf{V}_l)$ occurring between the leader and follower. To discover the motion of the leader in the follower's reference frame $({}^f\mathbf{\Omega}_l, {}^f\mathbf{V}_l)$, the pose of each robot is represented by its rotation ($\mathbf{R}$) and translation ($\mathbf{T}$) at time "t," with respect to a fixed reference frame. The pose is defined as $(\mathbf{R_i},\mathbf{T_i}) \epsilon\ SE(3)$, where $\mathbf{R}_i$ is 3×3, $\mathbf{T}_i$ is 3×1, and $i = \{l,f\}$ (see Fig. 4.3).

A point $\mathbf{q} \epsilon \mathbb{R}^3$ on the leader, observed in the follower's reference frame, is expressed as:

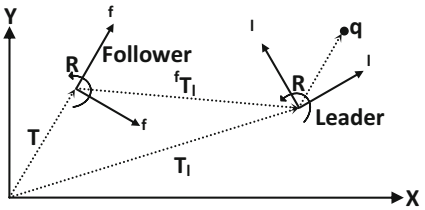

Fig. 4.3 Relative leader-follower kinematics model

$$^{f}\mathbf{q}(\mathrm{t}) = {}^{f}\mathbf{R}_{l}(\mathrm{t})^{l}\mathbf{q} + {}^{f}\mathbf{T}_{l}(t) \tag{4.3}$$

Where the leader's pose $(\mathbf{R}_l,\mathbf{T}_l)$ ϵ $SE(3)$ in the follower's frame is given by (see Fig. 4.3):

$$^{f}R_{l} \triangleq \left(\mathbf{R}_{f}\right)^{\mathrm{T}}\mathbf{R}_{l} \qquad {}^{f}\mathbf{T}_{l} \triangleq \left(\mathbf{R}_{f}\right)^{\mathrm{T}}\left(\mathbf{T}_{l} - \mathbf{T}_{f}\right) \tag{4.4}$$

Therefore, a point observed on the leader with respect to the follower is calculated as (Vidal et al. 2002, 2003):

$$^{f}\mathbf{q}(t) = \mathbf{R}_{f}^{\mathrm{T}}(t)\mathbf{R}_{l}(t)^{l}\mathbf{q} + \mathbf{R}_{f}^{\mathrm{T}}(t)\left[\mathbf{T}_{l}(t) - \mathbf{T}_{f}(t)\right] \tag{4.5}$$

Differentiating Eq. 4.5 yields the rate of change of the leader's pose (i.e., angular velocity and linear velocity) in the follower's reference frame (Vidal et al. 2002, 2003).

$$\frac{d^{f}\mathbf{q}}{dt} = {}^{f}\dot{\mathbf{q}} = \left[\dot{\mathbf{R}}_{f}^{\mathrm{T}}\mathbf{R}_{l} + \mathbf{R}_{f}^{\mathrm{T}}\dot{\mathbf{R}}_{l}\right]{}^{l}\mathbf{q} + \dot{\mathbf{R}}_{f}^{\mathrm{T}}\left[\mathbf{T}_{l} - \mathbf{T}_{f}\right] + \mathbf{R}_{f}^{\mathrm{T}}\left[\dot{\mathbf{T}}_{l} - \dot{\mathbf{T}}_{f}\right] \tag{4.6}$$

Isolating ${}^{l}\mathbf{q}$ from Eq. 4.5 and substituting it into Eq. 4.6 produces:

$$^{f}\dot{\mathbf{q}} = \left[\dot{\mathbf{R}}_{f}^{\mathrm{T}}\mathbf{R}_{f} + \mathbf{R}_{f}^{\mathrm{T}}\dot{\mathbf{R}}_{l}\mathbf{R}_{l}^{\mathrm{T}}\mathbf{R}_{f}\right]{}^{f}\mathbf{q} + \mathbf{R}_{f}^{\mathrm{T}}\left[\dot{\mathbf{T}}_{l} - \dot{\mathbf{T}}_{f} - \dot{\mathbf{R}}_{l}\mathbf{R}_{l}^{\mathrm{T}}\left(\mathbf{T}_{l} - \mathbf{T}_{f}\right)\right] \tag{4.7}$$

$[\mathbf{\Omega}]_{\mathrm{x}}\epsilon\, SO(3)$ is a skew-symmetric matrix of the vector $\mathbf{\Omega}\epsilon\mathbb{R}^{3}$ to generate the cross product $\mathbf{\Omega}\mathrm{x}\mathbf{q} = [\mathbf{\Omega}]_{\mathrm{x}}\mathbf{q}$ for all values of $\mathbf{q}$. Since $\dot{\mathbf{R}}_{i}\mathbf{R}_{i}^{\mathrm{T}}\epsilon\, SO(3)$, the following identities exist (Vidal et al. 2002, 2003):

$$\dot{\mathbf{R}}_{i}^{\mathrm{T}}\mathbf{R}_{i} = -\mathbf{R}_{i}^{\mathrm{T}}\dot{\mathbf{R}}_{i}\mathbf{R}_{i}^{\mathrm{T}}\mathbf{R}_{i} \qquad \left[\mathbf{R}_{i}^{\mathrm{T}}\mathbf{\Omega}_{\mathrm{j}}\right]_{\times} = \mathbf{R}_{i}^{\mathrm{T}}\left[\mathbf{\Omega}_{\mathrm{j}}\right]_{\times}\mathbf{R}_{i} \tag{4.8}$$

where the angular velocity $\mathbf{\Omega_i}$ for each robot is defined as (Vidal et al. 2002, 2003):

$$[\mathbf{\Omega}_{i}]_{\times} = \dot{\mathbf{R}}_{i}\mathbf{R}_{i}^{\mathrm{T}}, \quad i = \{l,f\} \tag{4.9}$$

Equations 4.8 and 4.9 simplify Eq. 4.7 to the following form:

$$\begin{aligned}
^{f}\dot{\mathbf{q}} &= \left[\left(-\mathbf{R}_{f}^{\mathrm{T}}\dot{\mathbf{R}}_{f}\mathbf{R}_{f}^{\mathrm{T}}\mathbf{R}_{f}\right) + \mathbf{R}_{f}^{\mathrm{T}}\dot{\mathbf{R}}_{l}\mathbf{R}_{l}^{\mathrm{T}}\mathbf{R}_{f}\right]{}^{f}\mathbf{q} + \mathbf{R}_{f}^{\mathrm{T}}\left[\dot{\mathbf{T}}_{l} - \dot{\mathbf{T}}_{f} - \dot{\mathbf{R}}_{l}\mathbf{R}_{l}^{\mathrm{T}}\left(\mathbf{T}_{l} - \mathbf{T}_{f}\right)\right] \\
^{f}\dot{\mathbf{q}} &= \left[-\mathbf{R}_{f}^{\mathrm{T}}\left[\mathbf{\Omega}_{f}\right]_{\times}\mathbf{R}_{f} + \mathbf{R}_{f}^{\mathrm{T}}\left[\mathbf{\Omega}_{\mathrm{l}}\right]_{\times}\mathbf{R}_{f}\right]{}^{f}\mathbf{q} + \mathbf{R}_{f}^{\mathrm{T}}\left[\dot{\mathbf{T}}_{l} - \dot{\mathbf{T}}_{f} - \left[\mathbf{\Omega}_{\mathrm{l}}\right]_{\times}\left(\mathbf{T}_{l} - \mathbf{T}_{f}\right)\right] \\
^{f}\dot{\mathbf{q}} &= \left[\left[\mathbf{R}_{f}^{\mathrm{T}}\mathbf{\Omega}_{l}\right]_{\times} - \left[\mathbf{R}_{f}^{\mathrm{T}}\mathbf{\Omega}_{f}\right]_{\times}\right]{}^{f}\mathbf{q} + \mathbf{R}_{f}^{\mathrm{T}}\left[\dot{\mathbf{T}}_{l} - \dot{\mathbf{T}}_{f} - \left[\mathbf{\Omega}_{\mathrm{l}}\right]_{\times}\left(\mathbf{T}_{l} - \mathbf{T}_{f}\right)\right] \\
^{f}\dot{\mathbf{q}} &= \left[\mathbf{R}_{f}^{\mathrm{T}}\left(\mathbf{\Omega}_{l} - \mathbf{\Omega}_{f}\right)\right] \times {}^{f}\mathbf{q} + \mathbf{R}_{f}^{\mathrm{T}}\left[\dot{\mathbf{T}}_{l} - \dot{\mathbf{T}}_{f} - \left[\mathbf{\Omega}_{\mathrm{l}}\right]_{\times}\left(\mathbf{T}_{l} - \mathbf{T}_{f}\right)\right] \triangleq \left[{}^{f}\mathbf{\Omega}_{l}\right]_{\times}{}^{f}\mathbf{q} + {}^{f}\mathbf{V}_{l}
\end{aligned} \tag{4.10}$$

Therefore, the relative angular and translational velocity (${}^f\mathbf{\Omega}_l$,${}^f\mathbf{V}_l$) of the leader in the follower's reference frame can be calculated as:

$$ {}^f\mathbf{\Omega}_l \triangleq \mathbf{R}_f^{\mathrm{T}}\left(\mathbf{\Omega}_l - \mathbf{\Omega}_f\right) \tag{4.11} $$

$$ {}^f\mathbf{V}_l \triangleq \mathbf{R}_f^{\mathrm{T}}\left[\dot{\mathbf{T}}_l - \dot{\mathbf{T}}_f - [\mathbf{\Omega}_l]_\times\left(\mathbf{T}_l - \mathbf{T}_f\right)\right] \tag{4.12} $$

The motion of a point $(X,Y,0) \in \mathbb{R}^3$ on the leader observed in the follower's reference frame, located at $(X_f,Y_f,0) \in \mathbb{R}^3$, is numerically calculated from Eqs. 4.11 and 4.12 by substituting $\mathbf{T}_i = (X_i,Y_i,0)^{\mathrm{T}} \in \mathbb{R}^3$, $\dot{\mathbf{T}}_i = \left(\dot{X}_i,\dot{Y}_i,0\right)^{\mathrm{T}} \in \mathbb{R}^3$, $\mathbf{\Omega_i} = \left(0,0,\dot{\theta}_i\right)^{\mathrm{T}} \in \mathbb{R}^3$, and $\mathbf{R}_i = \mathbf{R}_z(\theta_i) \in SO(3)$; $\mathbf{R}_z(\theta_i)$ is a 3×3 matrix that rotates an object around its z-axis and $i = \{l,f\}$:

$$ {}^f\mathbf{\Omega}_l \triangleq \begin{bmatrix} 0 \\ 0 \\ \dot{\theta}_l - \dot{\theta}_f \end{bmatrix}, \qquad {}^f\mathbf{V}_l \triangleq \begin{bmatrix} \cos\theta_f & \sin\theta_f & 0 \\ -\sin\theta_f & \cos\theta_f & 0 \\ 0 & 0 & 1 \end{bmatrix} \left\{ \begin{bmatrix} \dot{X} - \dot{X}_f \\ \dot{Y} - \dot{Y}_f \\ 0 \end{bmatrix} + \begin{bmatrix} \left(Y - Y_f\right) \\ -\left(X - X_f\right) \\ 0 \end{bmatrix} \dot{\theta}_l \right\} \tag{4.13} $$

Assuming the leader and follower can move freely in any direction, Eq. 4.13 describes the relative motion occurring between a point on the leading and following robot. To incorporate the nonholonomic constraints of each robot, the kinematic Eqs. 4.1 and 4.2 are substituted into Eq. 4.13. Considering the case when the observed point on the leader is offset a displacement $(a,b)^{\mathrm{T}} \in \mathbb{R}^2$ from the leader's rotational center, the observed point $\mathbf{q}$ becomes $\mathbf{q}_s = (X_s,Y_s,0)^{\mathrm{T}} \in \mathbb{R}^3$, and its motion in the follower's reference frame is calculated by substituting Eq. 4.2, where $i = l$, into Eq. 4.13:

$$ {}^f\mathbf{\Omega}_s \triangleq {}^f\mathbf{\Omega}_l, {}^f\mathbf{V}_s \triangleq \begin{bmatrix} \cos\theta_f & \sin\theta_f & 0 \\ -\sin\theta_f & \cos\theta_f & 0 \\ 0 & 0 & 1 \end{bmatrix} \times \left\{ \begin{bmatrix} v_l\cos\theta_l - \omega_l(a\sin\theta_l + b\cos\theta_l) - v_f\cos\theta_f \\ v_l\sin\theta_l + \omega_l(a\cos\theta_l - b\sin\theta_l) - v_f\sin\theta_f \\ 0 \end{bmatrix} + \begin{bmatrix} \left(Y_s - Y_f\right) \\ -\left(X_s - X_f\right) \\ 0 \end{bmatrix} \omega_l \right\} \tag{4.14} $$

The kinematics of a source offset from the leader's rotational center, observed by the follower, reduces to the following:

$$ {}^f\mathbf{\Omega}_s \triangleq {}^f\mathbf{\Omega}_l = \begin{bmatrix} 0 \\ 0 \\ \omega_l - \omega_f \end{bmatrix}, \qquad {}^f\mathbf{V}_s \triangleq - \begin{bmatrix} 1 \\ 0 \\ 0 \end{bmatrix} v_f + \begin{bmatrix} {}^f\mathbf{F}_l \\ 0 \end{bmatrix} $$

$$
{}^{f}\mathbf{F}_s = \begin{bmatrix} \cos\left(\theta_l - \theta_f\right) \\ \sin\left(\theta_l - \theta_f\right) \end{bmatrix} v_l - \begin{bmatrix} \sin\left(\theta_l - \theta_f\right) & \cos\left(\theta_l - \theta_f\right) \\ -\cos\left(\theta_l - \theta_f\right) & \sin\left(\theta_l - \theta_f\right) \end{bmatrix} \begin{bmatrix} a \\ b \end{bmatrix} \omega_l
$$
$$
- \begin{bmatrix} \cos\theta_f & \sin\theta_f \\ -\sin\theta_f & \cos\theta_f \end{bmatrix} \begin{bmatrix} -\left(Y_s - Y_f\right) \\ \left(X_s - X_f\right) \end{bmatrix} \omega_l \tag{4.15}
$$

Considering the case when the source is located on the leader's center of rotation, i.e., $(a,b)^{\mathrm{T}} = (0,0)^{\mathrm{T}}$, point $\mathbf{q}$ becomes $\mathbf{q}_l$ and Eq. 4.15 becomes:

$$
{}^{f}\boldsymbol{\Omega}_l \triangleq \begin{bmatrix} 0 \\ 0 \\ \omega_l - \omega_f \end{bmatrix}, \qquad {}^{f}\mathbf{V}_l \triangleq - \begin{bmatrix} 1 \\ 0 \\ 0 \end{bmatrix} v_f + \begin{bmatrix} {}^{f}\mathbf{F}_l \\ 0 \end{bmatrix}
$$
$$
{}^{f}\mathbf{F}_l = \begin{bmatrix} \cos\left(\theta_l - \theta_f\right) \\ \sin\left(\theta_l - \theta_f\right) \end{bmatrix} v_l - \begin{bmatrix} \cos\theta_f & \sin\theta_f \\ -\sin\theta_f & \cos\theta_f \end{bmatrix} \begin{bmatrix} -\left(Y_l - Y_f\right) \\ \left(X_l - X_f\right) \end{bmatrix} \omega_l \tag{4.16}
$$

Therefore, combining Eq. 4.10 with Eq. 4.16 describes the motion of a source, on the leader's rotational center, observed by the follower moving along an *XY*-plane. This is represented in Cartesian and polar coordinates, respectively.

$$
\begin{bmatrix} {}^{f}\dot{X}_l \\ {}^{f}\dot{Y}_l \end{bmatrix} = \begin{bmatrix} -1 & {}^{f}\mathbf{Y}_l \\ 0 & -{}^{f}\mathbf{X}_l \end{bmatrix} \begin{bmatrix} v_f \\ \omega_f \end{bmatrix} + \begin{bmatrix} 1 & 0 & -{}^{f}Y_l \\ 0 & 1 & {}^{f}X_l \end{bmatrix} \begin{bmatrix} {}^{f}\mathbf{F}_l \\ \omega_l \end{bmatrix} \tag{4.17}
$$
$$
\begin{bmatrix} {}^{f}\dot{r}_l \\ {}^{f}\dot{\phi}_l \end{bmatrix} = \begin{bmatrix} -\cos{}^{f}\phi_l & 0 \\ \dfrac{\sin{}^{f}\phi_l}{{}^{f}r_l} & -1 \end{bmatrix} \begin{bmatrix} v_f \\ \omega_f \end{bmatrix} + \begin{bmatrix} \cos{}^{f}\phi_l & \sin{}^{f}\phi_l & 0 \\ -\dfrac{\sin{}^{f}\phi_l}{{}^{f}r_l} & \dfrac{\cos{}^{f}\phi_l}{{}^{f}r_l} & 1 \end{bmatrix} \begin{bmatrix} {}^{f}\mathbf{F}_l \\ \omega_l \end{bmatrix} \tag{4.18}
$$

Simplifying the two previous equations yields:

$$
\begin{bmatrix} {}^{f}\dot{X}_l \\ {}^{f}\dot{Y}_l \end{bmatrix} = \mathbf{H}\left({}^{f}X_l, {}^{f}Y_l\right)\mathbf{u}_f + \mathbf{G}\left({}^{f}X_l, {}^{f}Y_l\right){}^{f}\mathbf{d}_l \tag{4.19}
$$
$$
\begin{bmatrix} {}^{f}\dot{r}_l \\ {}^{f}\dot{\phi}_l \end{bmatrix} = \mathbf{H}\left({}^{f}r_l, {}^{f}\phi_l\right)\mathbf{u}_f + \mathbf{G}\left({}^{f}r_l, {}^{f}\phi_l\right){}^{f}\mathbf{d}_l \tag{4.20}
$$

For both Eqs. 4.19 and 4.20, the control input of the follower $\mathbf{u}_f = (v_f, \omega_f)^{\mathrm{T}} \in \mathbb{R}^2$ is separated from the state and control inputs of the leader $\mathbf{G}({}^{f}X_l, {}^{f}Y_l){}^{f}\boldsymbol{d}_l \in \mathbb{R}^2$, where ${}^{f}\boldsymbol{d}_l = ({}^{f}\boldsymbol{F}_l, \omega_l) \in \mathbb{R}^3$ represents the control input of the leader and current state of both the leader and follower. Note that both $\mathbf{H}({}^{f}X_l, {}^{f}Y_l)/\mathbf{H}({}^{f}r_l, {}^{f}\varnothing_l)$ and $\mathbf{G}({}^{f}X_l, {}^{f}Y_l)/\mathbf{G}({}^{f}r_l, {}^{f}\varnothing_l)$ are 2×2 and 2×3 matrices, respectively, and only contain position measurements gathered by the follower's position sensor.

4.2 Follower Control Law

Given the leader-follower configuration shown in Fig. 4.1, the following robot is set to follow behind the leader at a desired range (${}^{f}r_{d}$) and bearing (${}^{f}\emptyset_{d}$). The kinematic equations that describe this two-robot system are defined by Eq. 4.19 in Cartesian or by Eq. 4.20 in polar coordinates. These equations isolate the control input of the follower and treat the state of the leader as an exogenous input. By applying input-output feedback linearization, the control law of the follower becomes:

$$\mathbf{u}_f = -\mathbf{H}\left({}^{f}X_l, {}^{f}Y_l\right)^{-1}\left(\mathbf{G}\left({}^{f}X_l, {}^{f}Y_l\right)^{f}\mathbf{d}_l + \begin{bmatrix} k_1\left({}^{f}X_l - {}^{f}X_d\right) \\ k_2\left({}^{f}Y_l - {}^{f}Y_d\right) \end{bmatrix}\right) \tag{4.21}$$

$$\mathbf{u}_f = -\begin{pmatrix} -1 & -\dfrac{{}^{f}Y_l}{{}^{f}X_l} \\ 0 & -\dfrac{1}{{}^{f}X_l} \end{pmatrix}\left(\mathbf{G}\left({}^{f}X_l, {}^{f}Y_l\right)^{f}\mathbf{d}_l + \begin{bmatrix} k_1\left({}^{f}X_l - {}^{f}X_d\right) \\ k_2\left({}^{f}Y_l - {}^{f}Y_d\right) \end{bmatrix}\right)$$

$$\mathbf{u}_f = -\mathbf{H}\left({}^{f}r_l, {}^{f}\phi_l\right)^{-1}\left(\mathbf{G}\left({}^{f}r_l, {}^{f}\phi_l\right)^{f}\mathbf{d}_l + \begin{bmatrix} k_1\left({}^{f}r_l - {}^{f}r_d\right) \\ k_2\left({}^{f}\phi_l - {}^{f}\phi_d\right) \end{bmatrix}\right) \tag{4.22}$$

$$\mathbf{u}_f = -\begin{pmatrix} -\dfrac{1}{\cos{}^{f}\phi_l} & 0 \\ -\dfrac{\sin{}^{f}\phi_l}{{}^{f}r_l\cos{}^{f}\phi_l} & -1 \end{pmatrix}\left(\mathbf{G}\left({}^{f}r_l, {}^{f}\phi_l\right)^{f}\mathbf{d}_l + \begin{bmatrix} k_1\left({}^{f}r_l - {}^{f}r_d\right) \\ k_2\left({}^{f}\phi_l - {}^{f}\phi_d\right) \end{bmatrix}\right)$$

The positive control gains (k_1,k_2) are user selected while Eq. 4.23 is an auxiliary control input.

$$\begin{bmatrix} k_1\left({}^{f}X_l - {}^{f}X_d\right) \\ k_2\left({}^{f}Y_l - {}^{f}Y_d\right) \end{bmatrix} \qquad \begin{bmatrix} k_1\left({}^{f}r_l - {}^{f}r_d\right) \\ k_2\left({}^{f}\phi_l - {}^{f}\phi_d\right) \end{bmatrix} \tag{4.23}$$

The nonlinear control law defined for $\mathbf{u}_f$ stabilizes the closed-loop system when $k_1 > 0$ and $k_2 > 0$. It exponentially reduces the error between the leader's current and desired position (${}^{f}r_d$,${}^{f}\emptyset_d$) to zero(Vidal al. 2003); this remains true only if (v_l, ω_l) are constant, $v_l \neq 0$, and $\omega_l = 0$. Under these conditions, the leader is travelling a constant speed along a line, while the follower is approaching its desired position. When (v_l, ω_l) are constant, $v_l \neq 0$, and $\omega_l \neq 0$, the steady-state tracking error will remain constant but will not decay to zero. Under these conditions, the leader is travelling a constant speed along a circle, and the follower can only approach its desired position while maintaining a stable formation. If $v_l = 0$ and $\omega_l \neq 0$, a zero dynamics condition occurs because the follower cannot tell whether the leader is stationary or purely rotating. Under these conditions, the follower will stop until $v_l \neq 0$.

Equations 4.21 and 4.22 guarantee that the following robot will approach the desired position as long as ${}^{f}r_l \neq 0$ and ${}^{f}\emptyset_l \neq \pm\pi/2$ (or ${}^{f}X_l \neq 0$). The first case is trivial since it indicates that the leader and follower occupy the same physical space. However, when the second constraint is violated, the source attached to the leader

crosses the follower's y-axis. As a result, the controller will become singular, and $\mathbf{u}_f$ will saturate. This also infers that the desired formation cannot be selected as ${}^f r_d = 0$ or ${}^f \emptyset_d = \pm\pi/2$ because the controller will become unstable if the following robot reaches its desired position. Since it is likely that the leader will cross the follower's y-axis, a pseudo-feedback-linearization control law is proposed to avoid this degeneracy (Vidal et al. 2003):

$$\mathbf{u}_f = -\begin{pmatrix} -\cos{}^f\phi_l & 0 \\ -\dfrac{\sin{}^f\phi_l \cos{}^f\phi_l}{{}^f r_l} & -1 \end{pmatrix} \left(\mathbf{G}\left({}^f r_l, {}^f\phi_l\right)^f \mathbf{d}_l + \begin{bmatrix} \mathrm{k}_1\left({}^f r_l - {}^f r_d\right) \\ \mathrm{k}_2\left({}^f\phi_l - {}^f\phi_d\right) \end{bmatrix} \right) \tag{4.24}$$

The new control law, defined by Eq. 4.24, does not become singular when ${}^f\emptyset_l \neq \pm\pi/2$ and takes advantage of the position sensor providing measurements in polar coordinates. However, a degeneracy condition still exists when ${}^f\emptyset_l = \pm\pi/2$ due to the robot's nonholonomic constrains; if ${}^f\emptyset_l = \pm\pi/2$ and the tracking error does not equal zero, the follower cannot maintain formation because it cannot translate along its y-axis.

4.2.1 Estimating the State of the Leader

Unfortunately, the control laws defined by Eqs. 4.22 and 4.24 cannot be solved explicitly because the follower has no knowledge of the state and control input of the leader $\mathbf{G}({}^f r_l, {}^f\emptyset_l)^f\mathbf{d}_l$—nor is this information communicated from the leader to the follower. To estimate $\mathbf{G}({}^f r_l, {}^f\emptyset_l)^f\mathbf{d}_l$, the following robot takes advantage of observing a stationary landmark (Vidal et al. 2002; Das et al. 2001), where $v_w = \omega_w = 0$ for all stationary sources. Using Eq. 4.20, the motion of the observed landmark in the follower's reference frame is defined by:

$$\begin{bmatrix} {}^f\dot{r}_w \\ {}^f\dot{\phi}_w \end{bmatrix} = \mathbf{H}\left({}^f r_w, {}^f\phi_w\right)\mathbf{u}_f \tag{4.25}$$

If the follower is observing the leader at the same time, the motion of the leader in the follower's reference frame is known as:

$$\begin{bmatrix} {}^f\dot{r}_l \\ {}^f\dot{\phi}_l \end{bmatrix} = \mathbf{H}\left({}^f r_l, {}^f\phi_l\right)\mathbf{u}_f + \mathbf{G}\left({}^f r_l, {}^f\phi_l\right)^f\mathbf{d}_l \tag{4.26}$$

Combining these two equations, the state and control input of the leader can be estimated using only measurements gathered by the position sensor.

$$\mathbf{G}\left({}^f r_l, {}^f\phi_l\right)^f\mathbf{d}_l = \begin{bmatrix} {}^f\dot{r}_l \\ {}^f\dot{\phi}_l \end{bmatrix} - \mathbf{H}\left({}^f r_l, {}^f\phi_l\right)\mathbf{H}\left({}^f r_w, {}^f\phi_w\right)^{-1}\begin{bmatrix} {}^f\dot{r}_w \\ {}^f\dot{\phi}_w \end{bmatrix} \tag{4.27}$$

4.3 Compensating for Zero Dynamics

4.3.1 Zero Dynamics Problem

By mounting the source at the center of rotation on the leader, a zero dynamics state exists when the leader is stationary. If the leading robot does not move, the follower is unable to determine if it is stationary or undergoing pure rotation. Assuming the follower has reached its desired position $({}^{f}r_{d}, {}^{f}\emptyset_{d})$ and the leader undergoes pure rotation, the control output will be $(v_f,\omega_f)^{\mathrm{T}} = (0,0)^{\mathrm{T}}$. As a result, the desired position's tracking error will not accumulate, while the leader is purely rotating.

4.3.2 Observing Any Point on the Leading Robot

To resolve this zero dynamics problem, the source $(X_s,Y_s)^{\mathrm{T}} \epsilon\, \mathbb{R}^2$ on the leading robot is offset a displacement $(a,b)^{\mathrm{T}} \epsilon\, \mathbb{R}^2$ from the robot's center of rotation $(X_l,Y_l)^{\mathrm{T}} \epsilon\, \mathbb{R}^2$ (see Fig. 4.4). If the robot is stationary with an offset source, the control output will be $(v_f,\omega_f)^{\mathrm{T}} = (0,0)^{\mathrm{T}}$, but if leader is purely rotating, the control action of the follower will be non-zero $(v_f,\omega_f)^{\mathrm{T}} \neq (0,0)^{\mathrm{T}}$.

4.3.3 Leader-Follower Dynamics and Control Law with Offset Source Position

The motion of an observed source attached to any point $\mathbf{q} \epsilon \mathbb{R}^3$ on the leader in the follower's coordinate frame is determined from Eq. 4.15.

$$ {}^{f}\boldsymbol{\Omega}_{s} \triangleq \begin{bmatrix} 0 \\ 0 \\ \omega_l - \omega_f \end{bmatrix}, \qquad {}^{f}\mathbf{V}_{s} \triangleq - \begin{bmatrix} 1 \\ 0 \\ 0 \end{bmatrix} v_f + \begin{bmatrix} {}^{f}\mathbf{F}_{s} \\ 0 \end{bmatrix} $$

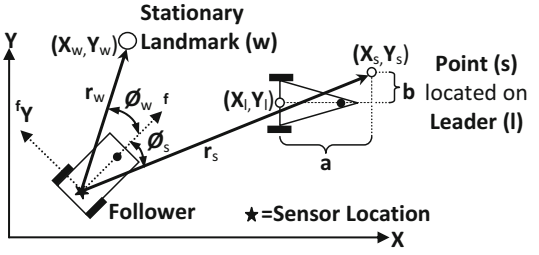

Fig. 4.4 Leader-follower configuration

$$
{}^{f}\mathbf{F}_s = \begin{bmatrix} \cos(\theta_l - \theta_f) \\ \sin(\theta_l - \theta_f) \end{bmatrix} v_l - \begin{bmatrix} \sin(\theta_l - \theta_f) & \cos(\theta_l - \theta_f) \\ -\cos(\theta_l - \theta_f) & \sin(\theta_l - \theta_f) \end{bmatrix} \begin{bmatrix} a \\ b \end{bmatrix} \omega_l
$$
$$
- \begin{bmatrix} \cos\theta_f & \sin\theta_f \\ -\sin\theta_f & \cos\theta_f \end{bmatrix} \begin{bmatrix} -({}^{f}Y_S - {}^{f}Y_f) \\ ({}^{f}X_S - {}^{f}X_f) \end{bmatrix} \omega_l
$$

Therefore, combining Eq. 4.10 with Eq 4.15 describes the motion of a source, offset from the leader's rotational center, observed by the follower moving along an *XY*-plane.

$$
\begin{bmatrix} {}^{f}\dot{r}_s \\ {}^{f}\dot{\phi}_s \end{bmatrix} = \begin{bmatrix} -\cos{}^{f}\phi_s & 0 \\ \dfrac{\sin{}^{f}\phi_s}{{}^{f}r_s} & -1 \end{bmatrix} \begin{bmatrix} v_f \\ \omega_f \end{bmatrix} + \begin{bmatrix} \cos{}^{f}\phi_s & \sin{}^{f}\phi_s & 0 \\ -\dfrac{\sin{}^{f}\phi_s}{{}^{f}r_s} & \dfrac{\cos{}^{f}\phi_s}{{}^{f}r_s} & 1 \end{bmatrix} \begin{bmatrix} {}^{f}\mathbf{F}_s \\ \omega_s \end{bmatrix}
$$
$$
{}^{f}\mathbf{F}_S
$$
$$
= \begin{bmatrix} \cos(\theta_l - \theta_f) \\ \sin(\theta_l - \theta_f) \end{bmatrix} v_l - \begin{bmatrix} \sin(\theta_l - \theta_f) & \cos(\theta_l - \theta_f) \\ -\cos(\theta_l - \theta_f) & \sin(\theta_l - \theta_f) \end{bmatrix} \begin{bmatrix} a \\ b \end{bmatrix} \omega_l
$$
$$
- \begin{bmatrix} \cos\theta_f & \sin\theta_f \\ -\sin\theta_f & \cos\theta_f \end{bmatrix} \begin{bmatrix} -{}^{f}\mathbf{Y}_s \\ {}^{f}\mathbf{X}_s \end{bmatrix} \omega_l \tag{4.28}
$$

While the control law and leader's state estimation remains unchanged.

$$
\mathbf{u}_f = -\left(\begin{bmatrix} -\cos{}^{f}\phi_s & 0 \\ -\dfrac{\sin{}^{f}\phi_s \cos{}^{f}\phi_s}{{}^{f}r_s} & -1 \end{bmatrix} \left(\mathbf{G}({}^{f}r_s, {}^{f}\phi_l)\,{}^{f}\mathbf{d}_s + \begin{bmatrix} k_1({}^{f}r_s - {}^{f}r_d) \\ k_2({}^{f}\phi_d - {}^{f}\phi_d) \end{bmatrix} \right) \right)
$$
$$
\mathbf{G}({}^{f}r_s, {}^{f}\phi_s)\,{}^{f}\mathbf{d}_s = \begin{bmatrix} {}^{f}\dot{r}_s \\ {}^{f}\dot{\phi}_s \end{bmatrix} - \mathbf{H}({}^{f}r_s, {}^{f}\phi_s)\mathbf{H}({}^{f}r_w, {}^{f}\phi_w)^{-1} \begin{bmatrix} {}^{f}\dot{r}_w \\ {}^{f}\dot{\phi}_w \end{bmatrix}
$$

4.4 Sensory Model for Acoustic Array

To estimate the leader's pose, a passive acoustic array is mounted onto the follower that simultaneously listens to two sound sources: one stationary in the environment, while the other is fixed on the leader. The array is comprised of five microphones that share a common center (Fig. 4.5). To estimate the bearing of a source between any pair of spatially separated microphones, a coherent signal is assumed to be emitted by the source, and its incoming wave front passes across the receivers at two different moments in time. The source's bearing, relative to a microphone pair, is estimated by using the ratio of time-delay estimate ($\widehat{T}_{42}$) and maximum achievable time-delay T_{42_MAX} between receivers (Eq. 4.29) (Julián et al. 2004). Here, the two-digit subscripts denote the microphone pair used for localization. The time-delay estimate is discovered by applying the generalized cross-correlation method (Charles and Carter 1976; Carter 1987, 1992). This estimate assumes receivers are close together, relative to the range of the source, and the source is sufficiently

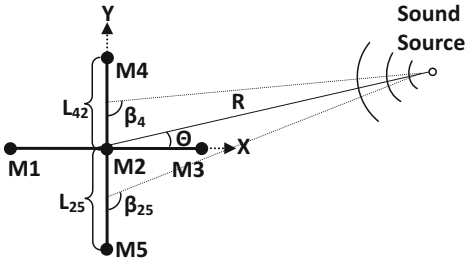

Fig. 4.5 Acoustic array configuration

distant for the curvature of its wave fronts to flatten upon reaching the receivers. The accuracy of this model is dependent on the source's position. If the source is located broadside to the receivers, this model provides an exact solution for estimating the bearing to the source. However, as the source moves toward $\beta = \pm 45^{\circ}$ of the receivers' baseline (or axis), a small error associated with the bearing estimate increases.

$$\widehat{\beta}_{42} \cong \cos^{-1}\left(\frac{\widehat{T}_{42}}{T_{42\_MAX}}\right) \quad , \quad \widehat{\alpha}_{42} = \frac{\pi}{2} - \widehat{\beta}_{42} \tag{4.29}$$

- Subscript "42" denotes information pertaining to the microphone pair M_4 and M_2
- $\widehat{T}_{42}$ is the measured time delay
- $T_{42\_MAX} = L_{42}/c$ is the maximum achievable time delay between receivers
- $c \approx 345$ m/s is the speed of sound travelling in dry air at room temperature

As shown in Fig. 4.5, an array of three microphones is needed to estimate position in 2-D because two bearing estimates are linearly projected into space; the point where these two projections intersect is the estimated position of the source. In Cartesian coordinates, this can be achieved by relating a microphone's bearing estimate to the slope of a line passing through the center of the microphone pair. To estimate the source's bearing and range precisely, the time delay between microphone pairs must be measured accurately. This becomes increasingly important for estimating range because as the source moves further away from the array, small errors associated with the time-delay measurement result in large errors associated with the position estimate (Bangs and Schultheiss 1973; Hahn 1975; Carter 1978, 1981). The variance of range error linearly depends on time-delay variance between microphone pairs and exponentially depends on the ratio of true range over effective half array length. To minimize the variance of range error for a passive array, time delay between receivers needs to be measured with a high degree of precision, effective distance between receivers must be large, or the source needs to be close to the array.

4.5 Simulation Experimental Setup

Five types of simulations are conducted for the leader-follower pair to analyze the proposed controller when implemented with instruments that have position error associated with their measurements. Each simulation compares the output of an acoustic array to a laser range finder with ±1 cm accuracy. Overlaid on top of each output is the controller output if it received ideal position estimates. The acoustic array's parameters are initially set to have a microphone separation of 36 cm (L) and sampling rate of 20 × 48 kHz. These parameters are doubled to show the performance of the controller when the accuracy of the sensor is increased. The follower is set to maintain a desired distance $r_d = 1.0$ m and bearing $\emptyset_d = 180°$ directly behind the leader. For all simulations, controller gains are set to $k_1 = 0.8$ and $k_2 = 1.6$. The laser range finder and acoustic array processes position estimates at a rate of 10 Hz.

In each simulation, the leader moves along a predetermined path; these paths include a straight trajectory ($v_l \neq 0$, $\omega_l = 0$), turning trajectory ($v_l \neq 0$, $\omega_l \neq 0$), and making a 90° turn ($v_l = 0$, $\omega_l \neq 0$). When making a 90° turn, two additional simulations are added: one shows the effects of the controller when the source on the leader is moved $(a,b)^{\mathrm{T}} = (0.5\text{ m},0.0\text{ m})^{\mathrm{T}}$ from its center of rotation. The last simulation shows how the landmark's placement affects the controller's stability. In all simulations, the landmark is placed in the environment to cross the *Y*-axis of the follower at least once. The landmark is represented with the "*" symbol while the target being observed on the leader is represented with "+."

4.5.1 Travelling Along a Straight Trajectory

The following is an example of a leader travelling along a straight trajectory and the follower maintaining a 1.0 m distance behind the follower. The source on the leader is located at its rotational center which is being observed by a follower using measurements from a laser range finder or acoustic array (Figs. 4.6 and 4.7).

4.5.2 Travelling Along a Turning Trajectory

The following is an example of a leader always turning and the follower maintaining a 1.0 m distance behind the follower. The source on the leader is located at its rotational center which is being observed by a follower using measurements from a laser range finder or acoustic array

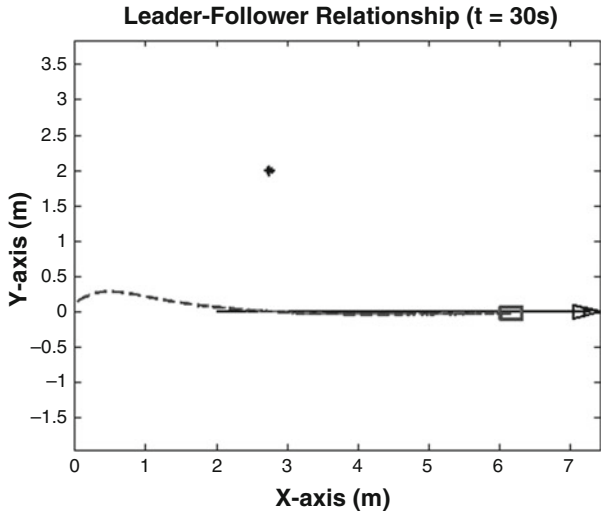

Fig. 4.6 Follower's path along a straight trajectory

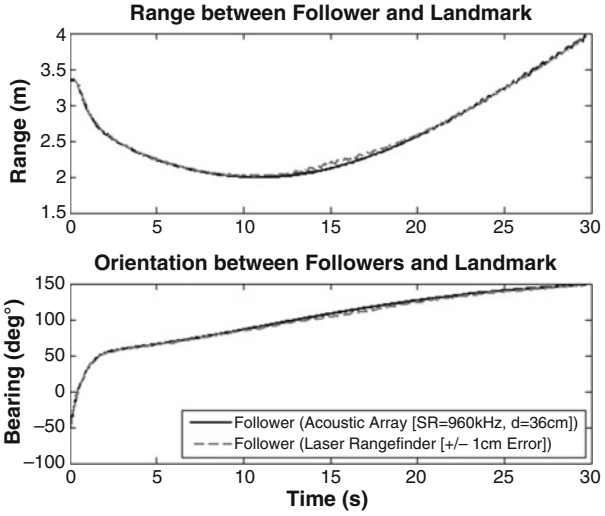

Fig. 4.7 Pose between the follower landmark

4.5.3 Travelling Along a Straight Path and Turning 90° (Source not Offset)

The following is an example of a leader travelling along a straight path, stopping, purely rotating 90°, and resuming a new straight path. The source on the leader is located at its rotational center which is being observed by a follower using measurements from a laser range finder or acoustic array

4.5.4 *Travelling Along a Straight Path and Turning 90° (With an Offset Source)*

The following is an example of a leader travelling along a straight path, stopping, purely rotating 90°, and resuming a new straight path. The source on the leader is located offset 0.5 m ahead of the robot which is being observed by a follower using measurements from a laser range finder or acoustic array

4.5.5 *Travelling Along a Straight Path and Turning 90° (With an Offset Source and Landmark Moved)*

This simulation is exactly like the previous except the landmark is moved to a new location to show how its arbitrary placement affects the controller

4.6 Controller Discussion

When utilizing an acoustic array or laser range finder, the controller's steady-state tracking error converges to a constant value when the follower is travelling along straight ($v_l \neq 0$, $\omega_l = 0$) or circular ($v_l \neq 0$, $\omega_l \neq 0$) path (Figs. 4.8, 4.9, 4.10, 4.11, 4.12, 4.13, 4.14, 4.15, 4.16, and 4.17). This tracking error is only reduced to zero when the leader is travelling along a straight trajectory. However, the performance of the controller is affected by the landmarks' placement. Observing Figs. 4.9 and

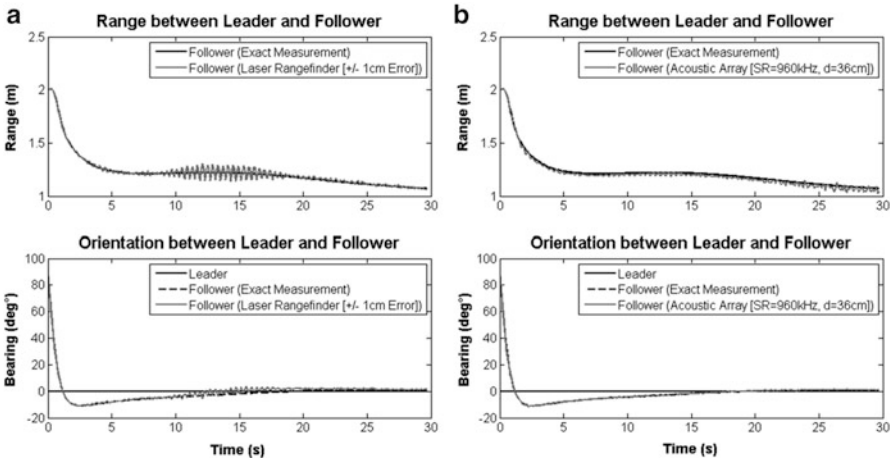

Fig. 4.8 Pose between follower leader, using **(a)** a laser range finder and (**b**) an acoustic array

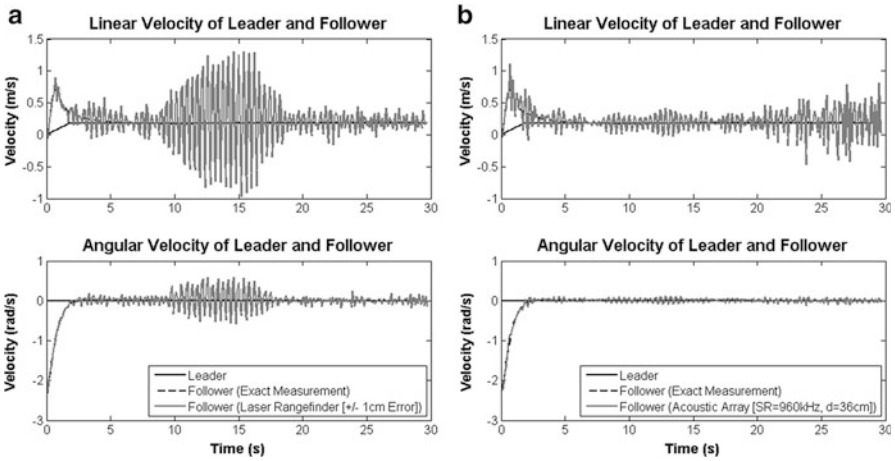

Fig. 4.9 Control output of follower and leader, using (**a)** a laser range finder and (**b**) an acoustic array

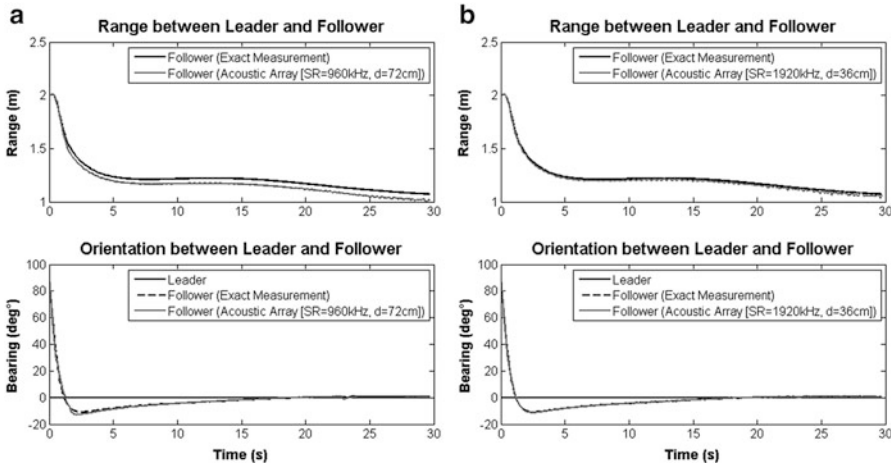

Fig. 4.10 (**a**) Pose between follower leader, (**b**) doubling the sample rate and D_{MIC} of acoustic array

4.15, the landmark causes the follower's controller to destabilize (break formation) when it crosses the y-axis of the follower. While travelling along a straight trajectory, this occurs at $t \approx 15$ s and along a turning trajectory, it occurs at $t \approx 14$ s. Formation is regained afterwards, but the controller destabilizes if the landmark is observed to be $\emptyset_w = \pm 90°$.

Due to the nature of error associated with each type of sensor, sensor selection and error also have an impact on the performance of the controller. A laser range finder with a constant ± 1 cm error associated with its measurements causes its

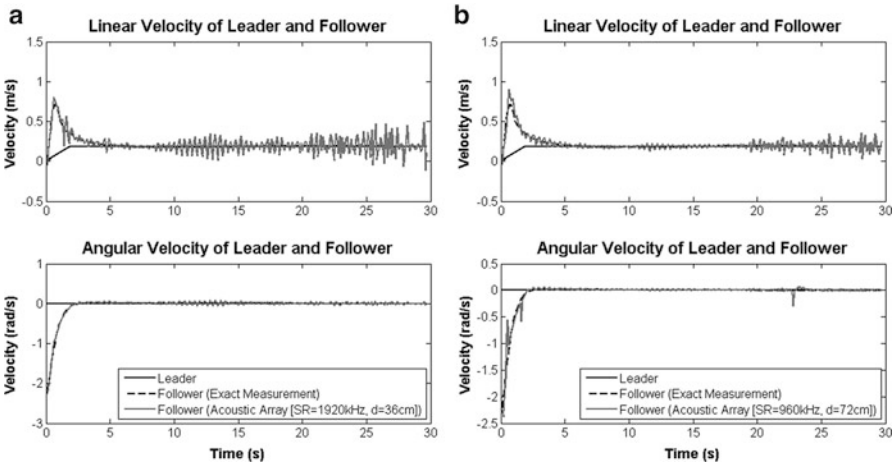

Fig. 4.11 (**a**) Control output of follower and leader, (**b**) doubling the sample rate and D_{MIC} of acoustic array

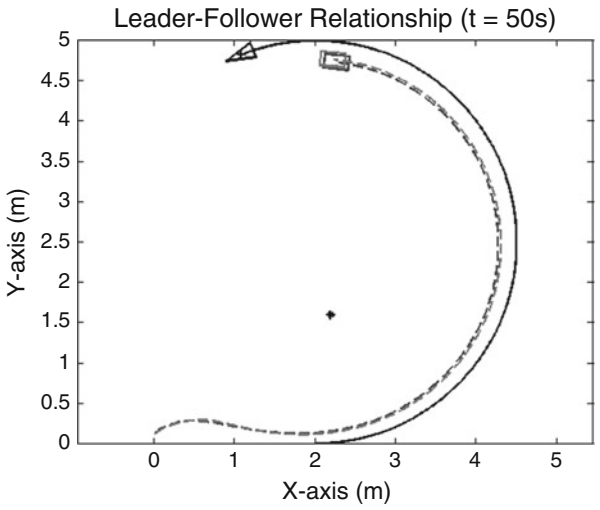

Fig. 4.12 Follower's path along a turning trajectory

output to oscillate at a constant variance (excluding any instance when the landmark crosses the *y*-axis of the follower). Since an acoustic array's accuracy is dependent on the distance of a target, its performance excels when the leader and landmark are within close proximity to the array. When the array moves further away from the landmark ($t \approx 25$ s in Fig. 4.10), the controller's oscillation increases due to larger measurement error.

When the leader is purely rotating (Figs. 4.18 and 4.19), the system experiences a zero dynamics condition if the leader's speaker is attached to its rotational center. If the speaker is offset from the leader's center of rotation, zero dynamics is

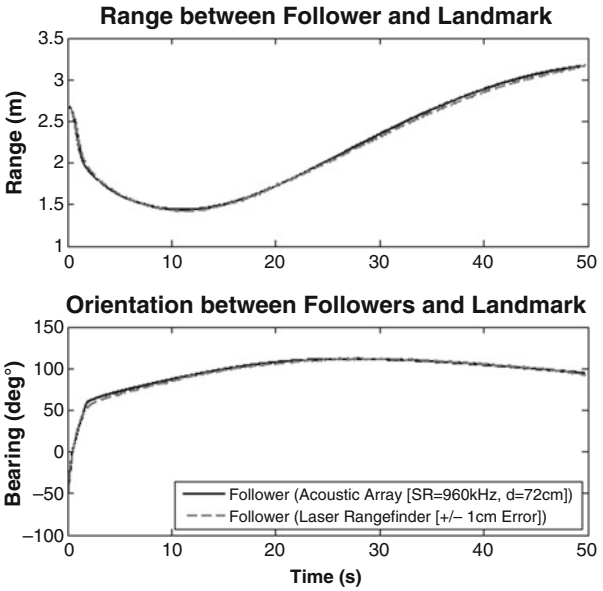

Fig. 4.13 Pose between the follower landmark

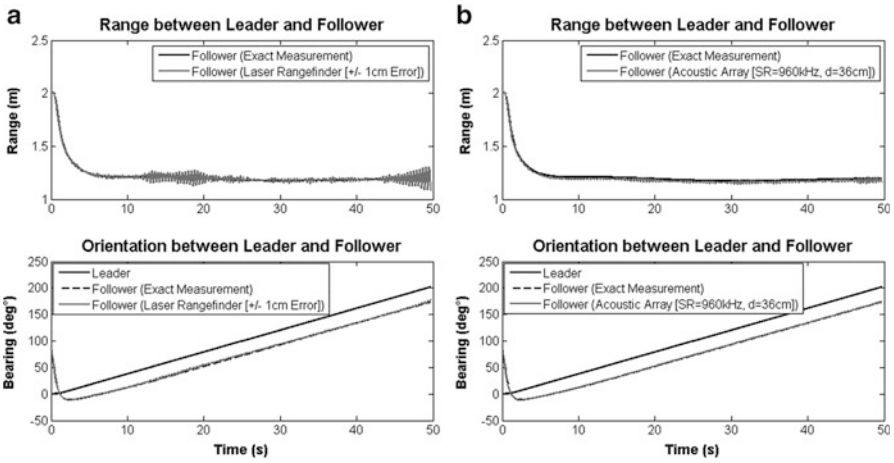

Fig. 4.14 Control output of follower and leader, using (**a**) a laser range finder and (**b**) an acoustic array

avoided, and the follower responds appropriately to the leader purely rotating ($v_l = 0$, $\omega_l \neq 0$). As a result, the follower reaches its desired formation quicker when zero dynamics is avoided (Figs. 4.20, 4.21, 4.22, 4.23, 4.24, 4.25, 4.26, 4.27, 4.28, 4.29, 4.30, 4.31, 4.32 , 4.33 and 4.34).

For all simulations, the acoustic array and laser range finder follow the same response as a sensor that provides ideal position estimates. As in the first two

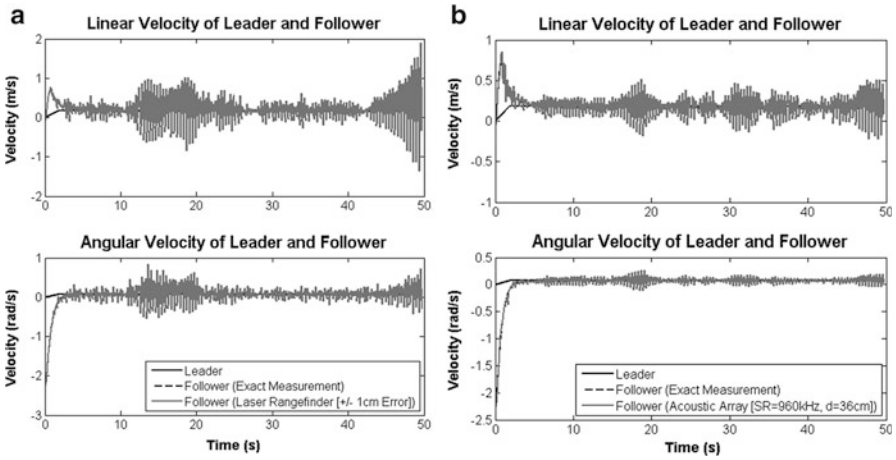

Fig. 4.15 Pose between follower leader, using (**a**) a laser range finder and (**b**) an acoustic array

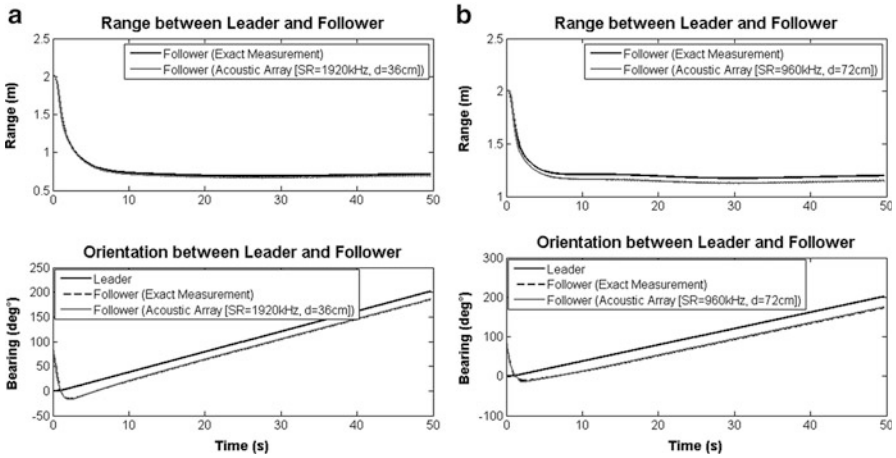

Fig. 4.16 (**a**) Pose between follower leader, doubling the sample rate and D_{MIC} of acoustic array

simulations, the controller using data from the acoustic array performs the worse when it is furthest away from the landmark. In Figs. 4.20 and 4.29, this can be observed at $t \approx 0$ s and $t \approx 30$s. By either doubling the sampling rate or increasing the microphone distance of the array, the sensor accuracy increases which improves the controller result. From these two options, doubling the microphone distance yields the best performance. However, when doubling the microphone distance of the array, the target source (from the leader or landmark) is more likely to move into the array's near field. When this occurs, position error occurs which causes the controller to output a transient response. These transients are shown in Figs. 4.11,

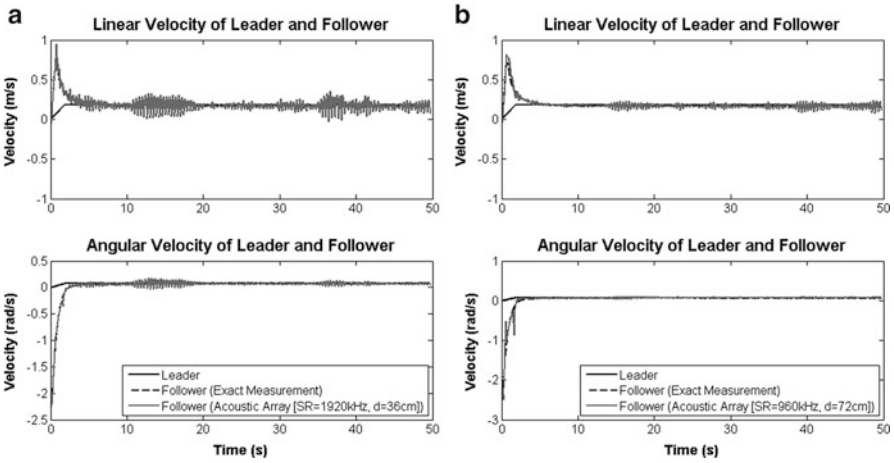

Fig. 4.17 (**a**) Control output of follower and leader, (**b**) doubling the sample rate and D_{MIC} of acoustic array

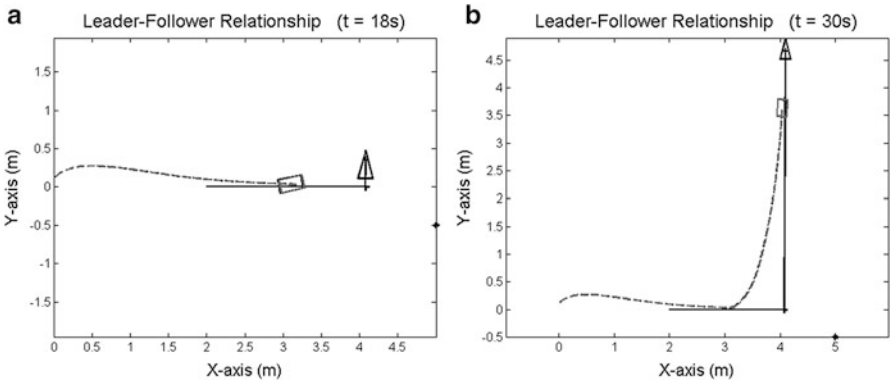

Fig. 4.18 Follower's path turning 90°. (**a**) after 18 s , (**b**) after 30 s

4.17, 4.23, 4.29, and 4.35 when doubling the microphone distance; at the time of the transient, the landmark or leader was within the microphone's near field.

The last simulation shows how much the landmark's location affects the controller's stability. When the landmark is placed closer to the follower (Fig. 4.30), the magnitude of the controller's oscillation increases whenever the landmark crosses the follower's *y*-axis. In the last simulation, the landmark crosses the follower's *Y*-axis at $t \approx 5$ s, $t \approx 13$ s, and $t \approx 26$ s. This almost leaves a contradiction for the placement of a landmark. The landmark placement should be close to improve sensor accuracy, but if it is close, the landmark cannot cross the *y*-axis of the follower. If the *y*-axis of the follower is crossed, it is best that the landmark is located away from the follower because this placement destabilizes the controller less.

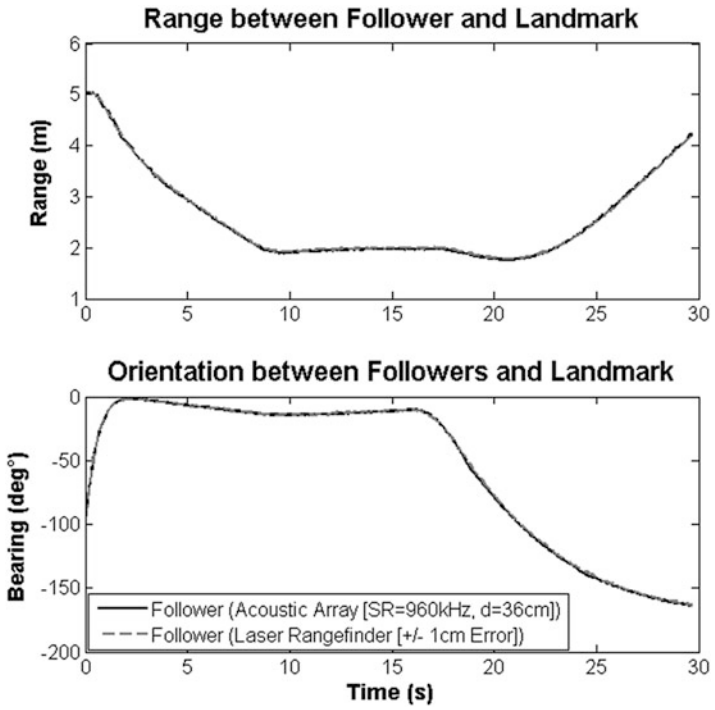

Fig. 4.19 Pose between the follower landmark

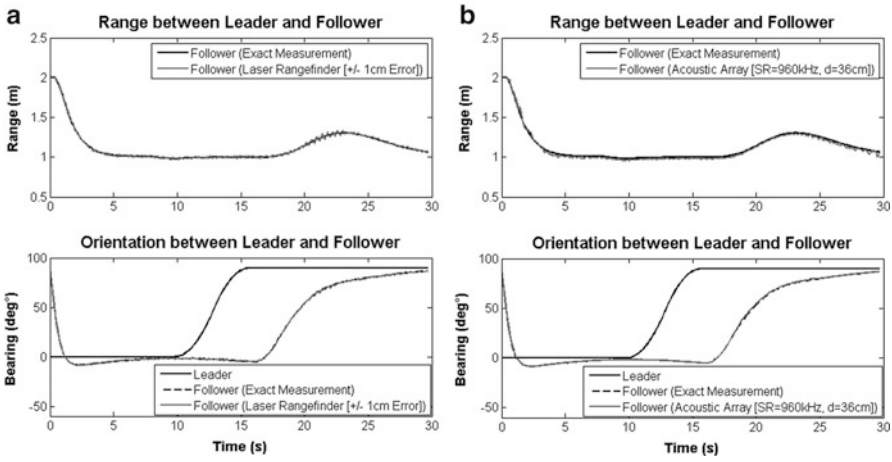

Fig. 4.20 Control output of follower and leader, using (**a**) a laser range finder and (**b**) an acoustic array

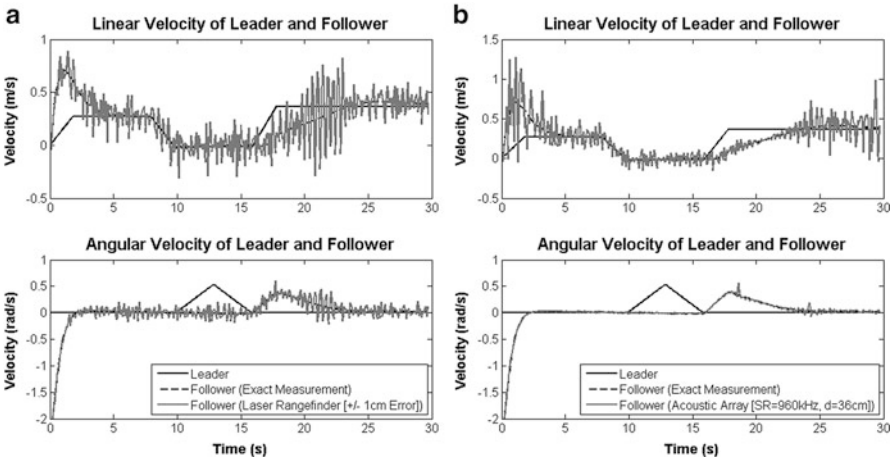

Fig. 4.21 Pose between follower leader, using (**a**) a laser range finder and (**b**) an acoustic array

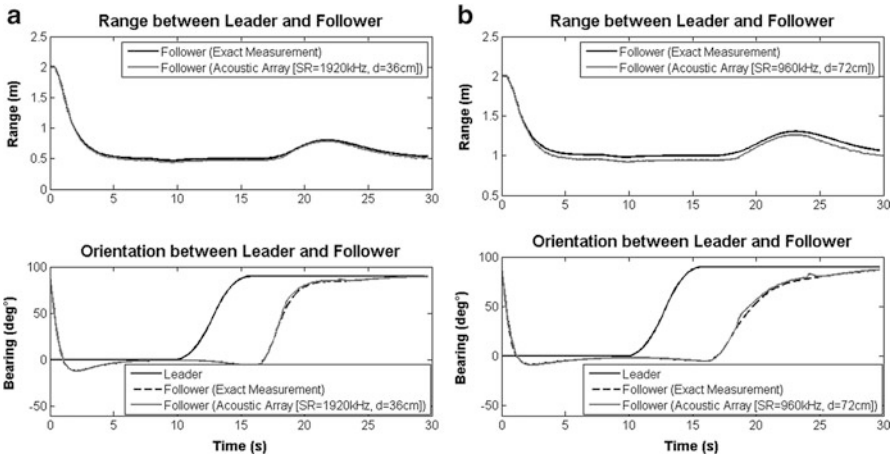

Fig. 4.22 (**a**) Pose between follower leader, (**b**) doubling the sample rate and D_{MIC} of acoustic array

4.7 Conclusions and Future Work

A leader-follower formation controller is proposed that allows a follower to maintain a desired position behind a leader by viewing one point on a leader (i.e., source) and a stationary landmark in the environment. The nonlinear nature of formation kinematics necessitates the design of a nonlinear controller. An exact feedback-linearization strategy was used. This approach involves deriving a transformation of

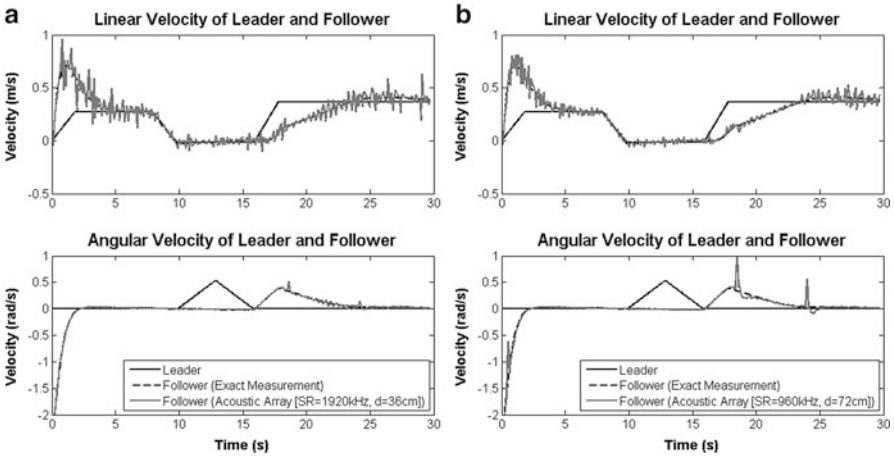

Fig. 4.23 (**a**) Control output of follower and leader, (**b**) doubling the sample rate and D_{MIC} of acoustic array

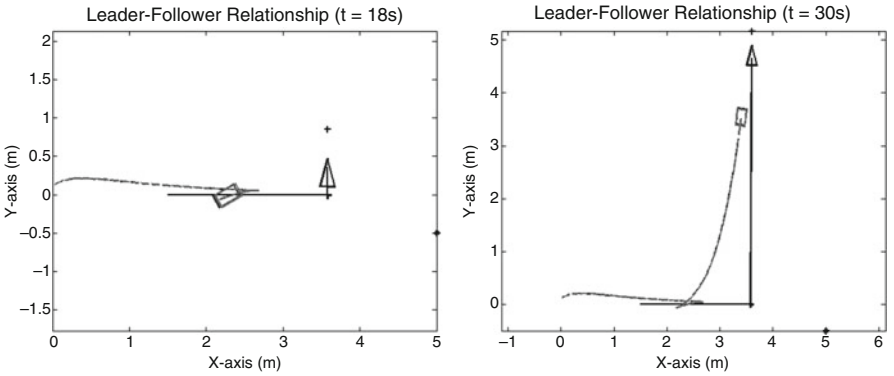

Fig. 4.24 Follower's path turning 90° (offset source). (**a**) after 18 s, (**b**) after 30 s

the nonlinear equations into an equivalent linear system by choosing a suitable nonlinear control input. However, one drawback of this approach is that global stability can be obtained over observable states only (i.e., systems with no zero dynamics). We proposed a novel way to avoid zero dynamics by placing the source with an offset of the center of rotation of the leading robot. Due to the nonholonomic constraints of the wheeled robots used in this study, the source movement will remain observable all the time (no zero dynamics).

By using either an acoustic array or laser range finder, the proposed leader-follower formation controller allows a follower to maintain a desired position behind a leader. Simulations show that the controller can exponentially reduce the tracking error to a steady-state value, and zero dynamics can be compensated by observing a point offset from the leader's center of rotation. To avoid singularities,

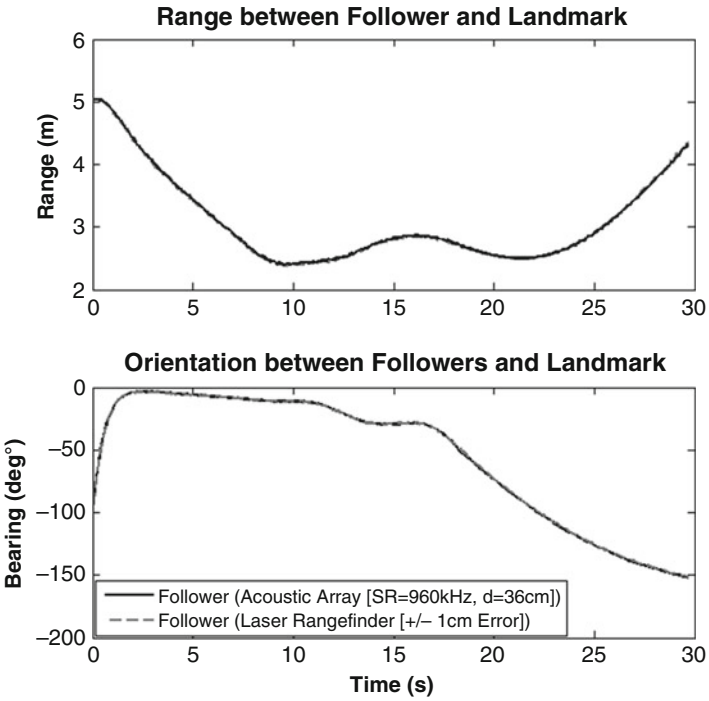

Fig. 4.25 Pose between the follower landmark

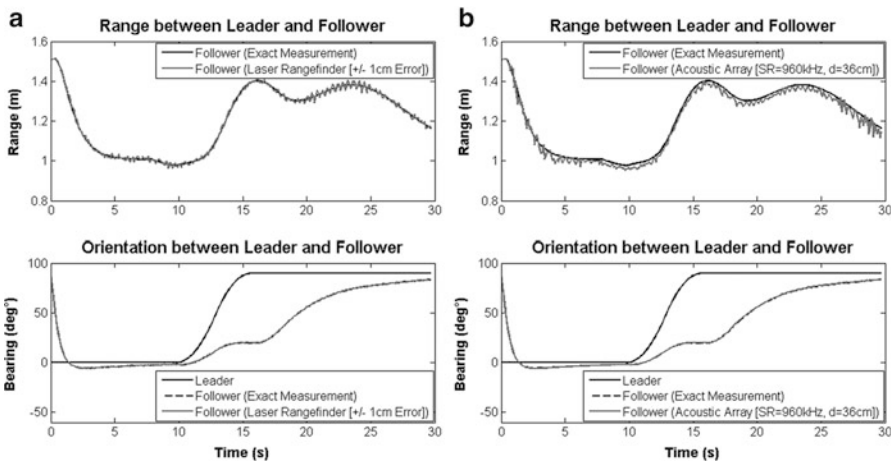

Fig. 4.26 Control output of follower and leader, using (**a**) a laser rangefinder and (**b**) an acoustic array

the nonholonomic constraints ($\emptyset \neq \pm\pi/2$) of the mobile robots must not be violated, and the positioning sensor mounted on the follower must accurately locate

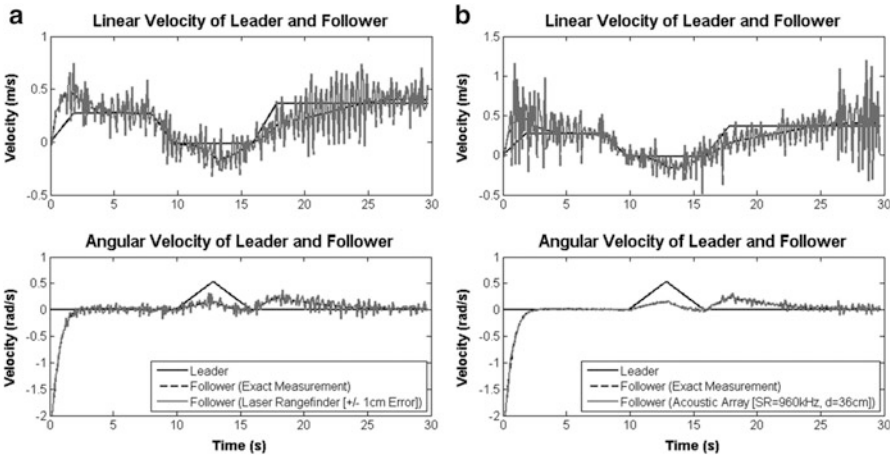

Fig. 4.27 Pose between follower leader, using (**a**) a laser range finder and (**b**) an acoustic array

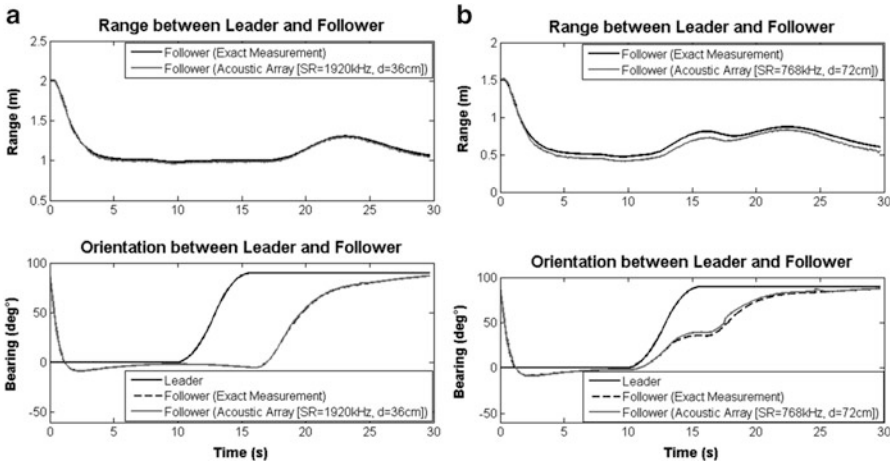

Fig. 4.28 (**a**) Pose between follower leader, (**b**) doubling the sample rate and D_{MIC} of acoustic array

both the landmark and follower within ± 1 cm. An acoustic array's having a microphone separation of 36 cm and sampling rate of 20×48 kHz is shown to maintain a desired position behind the leader if the leader and stationary landmark are within 5 m of the microphone array mounted on the follower. This range can increase by either increasing the microphone distance of the array or sampling rate of the sensor.

Implementing this on real robots moving in formation in environments cluttered with obstacles is underdevelopment. Development of a predictive motion planning

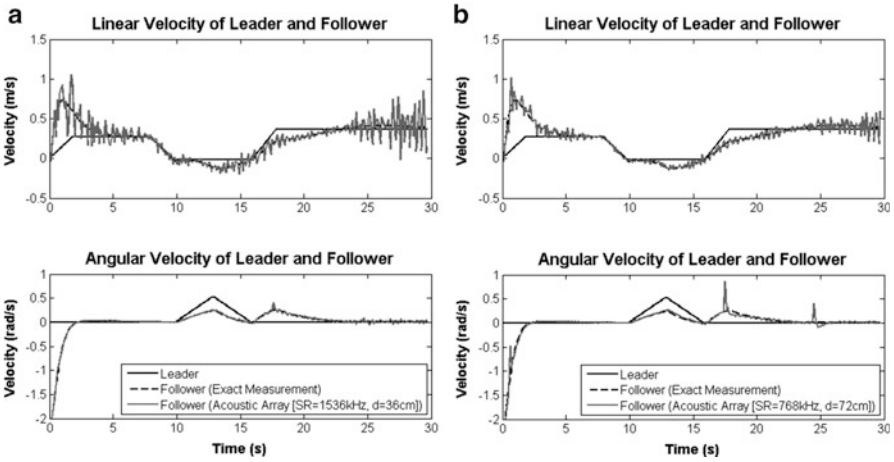

Fig. 4.29 (**a**) Control output of follower and leader, (**b**) doubling the sample rate and D_{MIC} of acoustic array

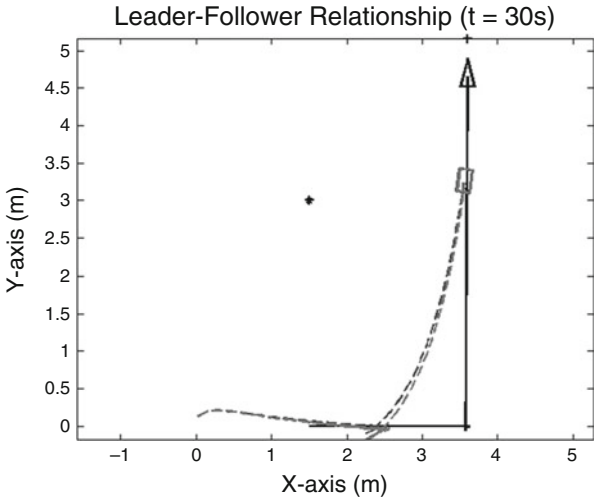

Fig. 4.30 Follower's path turning 90° with the landmark moved

and control strategy to avoid collision between the robots in the team and their colliding with physical obstacles while maintaining the formation is currently under investigation.

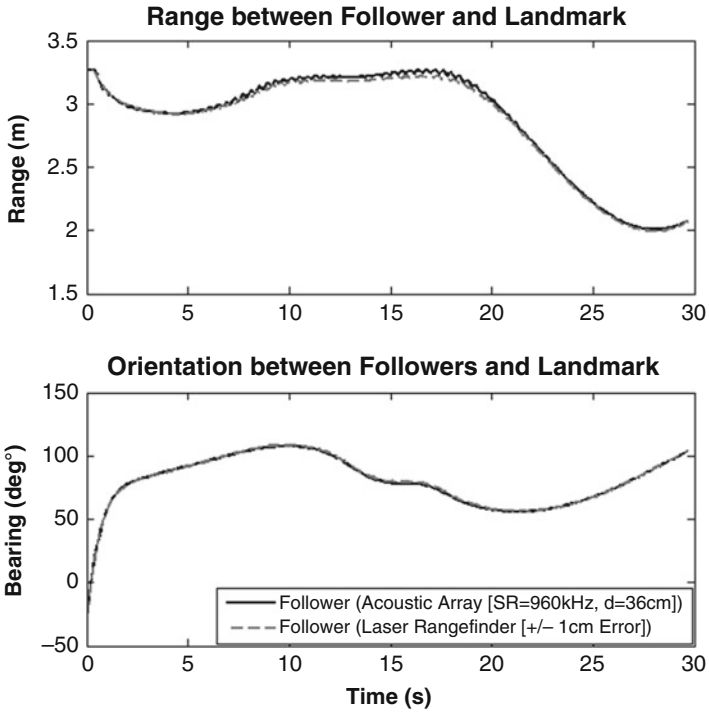

Fig. 4.31 Pose between the follower landmark

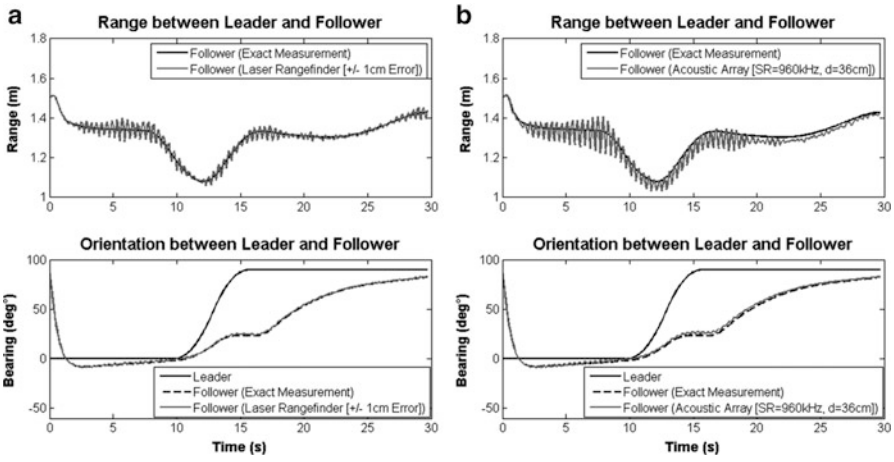

Fig. 4.32 Control output of follower and leader, using (**a**) a laser range finder and (**b**) an acoustic array

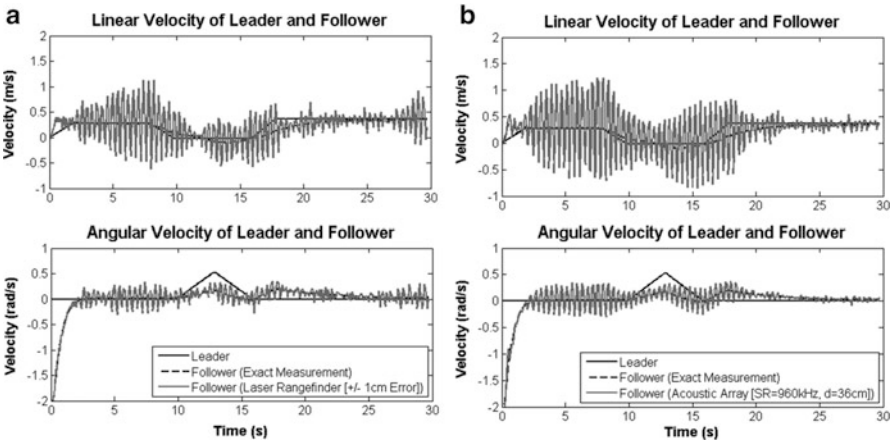

Fig. 4.33 Pose between follower leader, using (**a**) a laser range finder and (**b**) an acoustic array

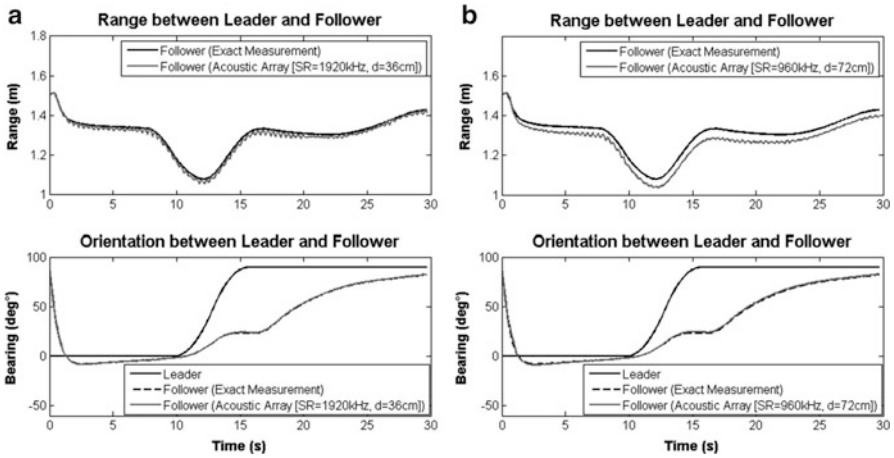

Fig. 4.34 (**a**) Pose between follower leader, (**b**) doubling the sample rate and D_{MIC} of acoustic array

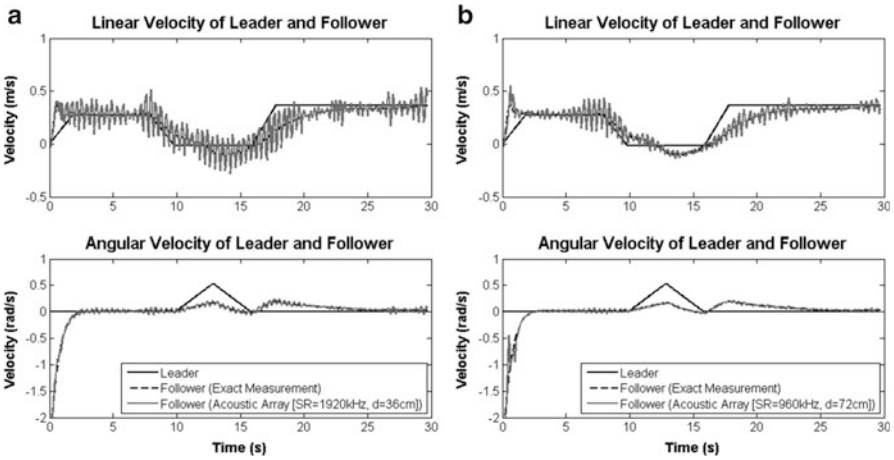

Fig. 4.35 (**a**) Control output of follower and leader, (**b**) doubling the sample rate and D_{MIC} of acoustic array

References

Bangs, W. J., & Schultheiss, P. M. (1973). Space time processing for optimal parameter estimation. In J. W. R. Griffiths, P. L. Stocklin, & C. V. Schooneveld (Eds.), *Signal processing* (pp. 577–590). Academic Press: New York.

Carter, G. C. (1978). Optimum element placement for passive bearing estimation in unequal signal-to-noise ratio environments. *IEEE Transactions on Acoustics, Speech, and Signal Processing, 26*(4), 365–366.

Carter, G. C. (1981). Time delay estimation for passive sonar signal processing. *IEEE Transactions on Acoustics, Speech, and Signal Processing, 29*(3), 463–470.

Carter, G. C. (1987). Coherence and time delay estimation. *Proceedings of the IEEE, 75*(2), 236–255.

Carter, G. C. (1992). *Time delay estimation.* In W. Perkins (Ed.) *Coherence and time delay estimation: An applied tutorial for research, development, test, and evaluation Engineers,* Chapter 1, (pp. 12–19). New York: IEEE Press.

Charles, K. H., & Carter, G. C. (1976). the generalized correlation method for estimation of time delay. *IEEE Transactions on Acoustics, Speech, and Signal Processing, 24*(4), 320–327.

Das, A. K., et al. (2001). Real-time vision-based control of a Nonholonomic Mobile Robot. In *Proceedings of the IEEE International Conference on Robotics and Automation*, (pp. 1714–1719). Seoul.

Hahn, W. R. (1975). Optimum signal processing for passive sonar range and bearing estimation. *The Journal of the Acoustical Society of America, 58*(1), 201–207.

Julián, P., et al. (2004). A comparative study of sound localization algorithms for energy aware sensor network nodes. *IEEE Transactions on Circuits and Systems, 5*(4), 640–647.

Vidal, R., Shakernia O., & Sastry S. (2002). Omnidirectional vision-based formation control. In *Annual Allerton Conerence on Communication, Control and Computing*, (pp. 1637–1646). Monticello.

Vidal, R., Shakernia, O., & Sastry, S. (2003). Formation control of Nonholonomic Mobile Robots with omnidirectional visual Servoing and motion segmentation. In *IEEE International Conference on robotics and automation, vol. 1.* (pp. 584–589). Taipei.

Chapter 5
Nonlinear Size-Dependent Instability of Hybrid FGM Nanoshells

S. Sahmani and M.M. Aghdam

5.1 Introduction

Piezoelectricity plays a useful role within a variety of applications involving the production and detection as well as fine focusing. On the other hand, as a special class of composite materials, the functionally graded material (FGM) includes a mixture of homogenous materials with continuous change in mechanical properties along with a specific direction. As a consequence, in order to develop smart structures having adaptive characteristics, joining of FGM efficient features with smart responses of piezoelectricity has attracted increasing attraction.

Several engineering applications of hybrid FGM materials with piezoelectric face sheets such as active vibration control (Liew et al. 2004; Selim et al. 2011), monomorph actuator (Chen et al. 2004), efficient sensors (Es'haghi et al. 2011), and structures with more creep resistance (Dai et al. 2013) have led to various investigations for this type of smart material. For instance, Shen (Shen 2005) investigated the postbuckling behavior of FGM plates with piezoelectric actuators subjected to thermo-electromechanical loading condition. Shariyat (Shariyat 2008) predicted the dynamic buckling characteristics of FGM cylindrical shells including surface-bonded piezoelectric layers under combined thermo-electromechanical loads. Sofiyev et al. (Sofiyev et al. 2009) studied the buckling of hydrostatic pressurized thin FGM hybrid truncated conical shells to present the related stability and compatibility equations. Meng et al. (Meng et al. 2010) reported the local buckling for the delimitation of an elliptic shape in the vicinity of the surface of piezoelectric laminated shells. Sheng and Wang (Sheng and Wang 2010) investigated the thermoelastic vibration and buckling responses FGM piezoelectric cylindrical shells. Duc et al. (Duc et al. 2016) analyzed the nonlinear dynamic response of

S. Sahmani • M.M. Aghdam (✉)
Department of Mechanical Engineering, Amirkabir University of Technology, Tehran, Iran
e-mail: aghdam@aut.ac.ir

L. Dai, R.N. Jazar (eds.), *Nonlinear Approaches in Engineering Applications*,
https://doi.org/10.1007/978-3-319-69480-1_5

FGM plates reinforced by piezoelectric stiffeners under electromechanical load in conjunction with thermal environments. Li and Pan (Li and Pan 2015) anticipated the size-dependent static bending and free vibration behaviors of FGM piezoelectric microplate on the basis of modified couple stress elasticity theory within the framework of sinusoidal shear deformation plate theory. Wang and Luo (Wang and Luo 2016) presented an exact solution in terms of Bessel functions for radial vibration response of FGM piezoelectric ring transducers. Wu and Lim (Wu and Lim 2016) used Reissner's mixed variational theorem to predict dynamic behavior of thick FGM piezoelectric hollow cylinders incorporating electromechanical effects. Liu and Zhang (Liu and Zhang 2016) studied numerically the electromechanical response of an FGM system coating with piezoelectric material subjected to axisymmetric conducting indenter.

In the modern engineering applications, the use of smart FGM structures at nanoscale seems to be attractive. In such range of application, small-scale effect plays a vital role in mechanical characteristics. Due to the lack of generality of the classical continuum theory to characterize the size dependency in mechanical response of nanostructures, several higher-order continuum elasticity theories have been proposed and utilized during the past decade. Among the different proposed nonclassical continuum theories, the nonlocal continuum elasticity (Eringen 1972) has the capability as well as convenience to capture the size effect through addition of only one material length scale parameter. In accordance with this nonconventional elasticity theory, it is supposed that the stress tensor at a reference point of body is related not only to strain components of that position but also to all other points in the continuum. In the last decade, the nonlocal continuum mechanics have been utilized in several studies to capture size-dependent behavior of nanostructures. Hao et al. (Hao et al. 2010) predicted size effect on the torsional buckling of carbon nanotubes based on nonlocal multi-shell model. Reddy (Reddy 2010) reformulated different classical beam and plate theories based on nonlocal continuum mechanics for nonlinear bending analysis of nanobeams and nanoplates. Ansari et al. (Ansari et al. 2010) established an efficient nonlocal plate model to predict the free vibration response of graphene sheets, the results of which were compared by those of molecular dynamics simulations. K. Kiani (Kiani 2010) applied the meshless method to investigate nonlocal free transverse vibration of carbon nanotubes resting on elastic matrix modeled by various beam theories. Ansari et al. (Ansari et al. 2011) implemented nonlocal continuum theory to study axial buckling behavior of carbon nanotubes in thermal environments using Rayleigh-Ritz solving process. Şimşek (Şimşek 2011) studied analytically the forced vibration of two CNTs connected elliptically with each other on the basis of nonlocal continuum theory. Narendar and Gopalakrishnan (Narendar and Gopalakrishnan 2011) analyzed thermal buckling of carbon nanotubes resting in elastic medium based on nonlocal Timoshenko beam model. Ansari and Sahmani (Ansari and Sahmani 2012) obtained the fundamental frequencies of carbon nanotubes via different nonlocal beam model and calibrated them with molecular dynamics simulations. Juntarasaid et al. (Juntarasaid et al. 2012) obtained size-dependent bending deformation and buckling compression of shear deformable

nanorods with the aid of nonlocal elasticity theory. Yang and Lim (Yang and Lim 2012) proposed a novel analytical solution to obtain the vibrational frequencies of Timoshenko nanobeams using nonlocal elastic theory. Shen (Shen 2013) analyzed torsional buckling and postbuckling of microtubules under temperature change based on Eringen's nonlocal continuum. Ansari and Sahmani (Ansari and Sahmani 2013) studied size-dependent biaxial buckling of graphene sheets on the basis of nonlocal plate model, and then the results were compared with molecular dynamics simulations. Zhang et al. (Zhang et al. 2014) examined the dispersion of elastic waves in a piezoelectric nanoplate incorporating the influence of nonlocality. Li et al. (Li et al. 2015) presented the nonlinear frequencies of graphene/piezoelectric laminated films subjected to electric field based on the nonlocal continuum theory. Sari (Sari 2015) predicted the free vibration response of annular sector plates through implementation of nonlocal continuum elasticity into the Mindlin plate theory.

More recently, Yang et al. (Yang et al. 2016) analyzed the dynamic pull-in instability of FGM nanocomposite nano-actuators including simultaneously the nonlocal stress and strain gradients in conjunction with Casimir force. Wang et al. (Wang et al. 2016) employed the theory of nonlocal piezoelectricity to predict the free and forced vibration response of circular nanoplates made of piezoelectric ceramic. Zhang et al. (Zhang et al. 2016) provided an element on the basis of kp-Ritz method to investigate the buckling behavior of graphene sheets surrounded by elastic medium. Jun Yu et al. (Jun Yu et al. 2016) reported the critical buckling loads of nanobeams used in nano-electromechanical systems under nonuniform temperature change based on the nonlocal thermoelasticity. Khorshidi and Fallah (Khorshidi and Fallah 2016) evaluated the critical buckling loads of FGM nanoplates via nonlocal elasticity theory in the form of exponential shear deformation plate theory. Sahmani and Aghdam (Sahmani and Aghdam 2017a) analyzed size-dependent radial postbuckling behavior of hybrid FGM nanoshells on the basis of the nonlocal continuum mechanics. Liu et al. (Liu et al. 2017) analyzed the transverse vibration of double-nanoplate system made of viscoelastic FGM using Eringen's nonlocal elasticity. Sahmani and Aghdam (Sahmani and Aghdam 2017b) employed nonlocal elasticity theory to analyze the size dependency in axial postbuckling response of hybrid FGM nanoshells. Mercan and Civalek (Mercan and Civalek 2017) reported the size-dependent critical buckling loads of silicon carbide nanotubes via surface and nonlocal elasticity theories. Sahmani and Aghdam (Sahmani and Aghdam 2017c) presented temperature-dependent axial postbuckling behavior of hybrid FGM nanoshells under through-thickness heat conduction on the basis of the nonlocal continuum theory. Farajpour et al. (Farajpour et al. 2017) explored the nonlocal vibration, buckling, and smart control of microtubules with the aid of piezoelectric nanoshells.

In the current study, the nonlocal nonlinear instability of hybrid FGM nanoshells embedded in elastic medium is examined corresponding to two loading cases: axial compression combined with lateral electric field and hydrostatic pressure combined with lateral electric field. To this end, nonlocal theory of elasticity is implemented into a refined exponential shear deformable shell theory to develop a size-

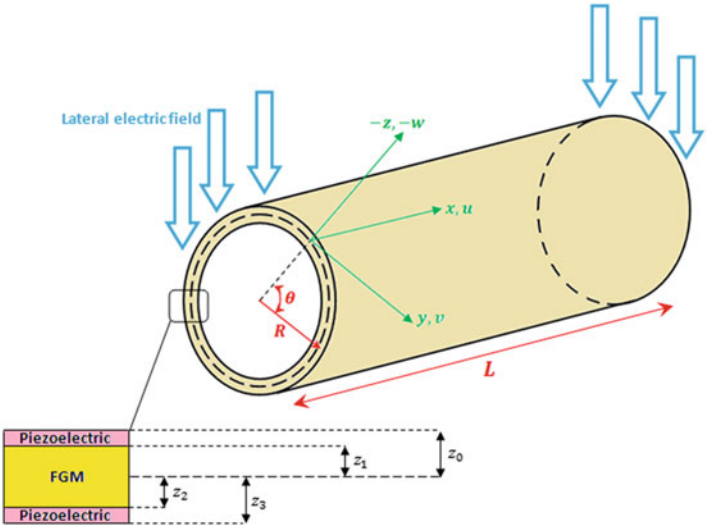

Fig. 5.1 Schematic representation of an embedded hybrid FGM nanoshell in an elastic medium

dependent shell model. Afterward, the boundary layer theory of shell buckling in conjunction with a two-stepped perturbation technique is utilized to propose explicit analytical expressions for nonlocal stability curves of hybrid FGM nanoshells relevant to both loading cases.

5.2 Nonlocal Exponential Shear Deformable Hybrid FGM Shell Model

In Fig. 5.1, a hybrid FGM cylindrical nanoshell embedded in an elastic medium is illustrated with length L, radius R, and thickness h composed of an FGM substrate of thickness h_f, and piezoelectric surface layers of thickness h_p completely bonded the substrate.

The hybrid FGM is a type of hybrid composite materials. In contrast to the traditional composite materials in which the combination of structural units yields a material with composite properties similar to the separate state, the mixture of units in the hybrid composites emerges a new property which causes multiple structural functionalities. Herein, by adding two piezoelectric face sheets to the FGM substrate, a hybrid composite material, namely, as hybrid FGM, is obtained which contains the new piezoelectricity property. The FGM substrate of nanoshell is assumed to be metal-rich and ceramic-rich at the top surface ($z = -h_f/2$) and the bottom surface ($z = h_f/2$), respectively. The effective material properties including Young's modulus, Poisson's ratio, and thermal expansion coefficient for the FGM substrate are considered temperature dependent which can be estimated as below:

$$E_f(z) = (E_c - E_m)V_f(z) + E_m \tag{5.1a}$$

$$\nu_f(z) = (\nu_c - \nu_m)V_f(z) + \nu_m \tag{5.1b}$$

in which the subscripts m and c denote the metal and ceramic phases, respectively. Furthermore, in accordance with the power law function, the volume fraction can be expressed as (Fares et al. 2009)

$$V_f(z) = \left(\frac{1}{2} + \frac{z}{h_f}\right)^k \tag{5.2}$$

where k represents the material gradient index.

In accordance with the exponential shear deformation theory (Hosseini-Hashemi et al. 2010), the displacement components of a nanoshell can be presented as

$$u_x(x,y,z) = u(x,y) - z\frac{\partial w(x,y)}{\partial x} + ze^{-\frac{2z^2}{h^2}}\psi_x(x,y) \tag{5.3a}$$

$$u_y(x,y,z) = v(x,y) - z\frac{\partial w(x,y)}{\partial y} + ze^{-\frac{2z^2}{h^2}}\psi_y(x,y) \tag{5.3b}$$

$$u_z(x,y,z) = w(x,y) \tag{5.3c}$$

in which u, v, and w in order are the midplane displacements along x, y, and z axes, ψ_x and ψ_y are, respectively, the rotations of the midplane normal about the y- and x-axis. Using the exponential shear deformation theory has two main advantages. Firstly, in contrast to the first-order shear deformation theory, there is no need for a shear correction factor which is hard to find its value as it depends on various parameters. Secondly, in contrast to the third-order shear deformation theory, for the in-plane and transverse displacements, the bending components do not contribute toward shear components and vice versa.

Based upon the kinematics of nonlinearity in von Kármán-Donnell-type form (Donnell 1976), the kinematical strain-displacement equations can be written as

$$\begin{Bmatrix} \varepsilon_{xx} \\ \varepsilon_{yy} \\ \gamma_{xy} \end{Bmatrix} = \begin{Bmatrix} \varepsilon^0_{xx} \\ \varepsilon^0_{yy} \\ \gamma^0_{xy} \end{Bmatrix} + \begin{Bmatrix} \varepsilon^E_{xx} \\ \varepsilon^E_{yy} \\ \gamma^E_{xy} \end{Bmatrix} + z\begin{Bmatrix} \kappa^{(1)}_{xx} \\ \kappa^{(1)}_{yy} \\ \kappa^{(1)}_{xy} \end{Bmatrix} + ze^{-\frac{2z^2}{h^2}}\begin{Bmatrix} \kappa^{(2)}_{xx} \\ \kappa^{(2)}_{yy} \\ \kappa^{(2)}_{xy} \end{Bmatrix} = \begin{Bmatrix} \frac{\partial u}{\partial x} + \frac{1}{2}\left(\frac{\partial w}{\partial x}\right)^2 \\ \frac{\partial v}{\partial y} - \frac{w}{R} + \frac{1}{2}\left(\frac{\partial w}{\partial y}\right)^2 \\ \frac{\partial u}{\partial y} + \frac{\partial v}{\partial x} + \frac{\partial w}{\partial x}\frac{\partial w}{\partial y} \end{Bmatrix}$$
$$+ \begin{Bmatrix} \frac{d_{31}\mathcal{V}}{h_p} \\ \frac{d_{32}\mathcal{V}}{h_p} \\ 0 \end{Bmatrix} - z\begin{Bmatrix} \frac{\partial^2 w}{\partial x^2} \\ \frac{\partial^2 w}{\partial y^2} \\ 2\frac{\partial^2 w}{\partial x \partial y} \end{Bmatrix} + ze^{-\frac{2z^2}{h^2}}\begin{Bmatrix} \frac{\partial \psi_x}{\partial x} \\ \frac{\partial \psi_y}{\partial y} \\ \frac{\partial \psi_x}{\partial y} + \frac{\partial \psi_y}{\partial x} \end{Bmatrix} \tag{5.4}$$

$$\begin{Bmatrix} \gamma_{xz} \\ \gamma_{yz} \end{Bmatrix} = \left(1 - \frac{4z^2}{h^2}\right) e^{-\frac{2z^2}{h^2}} \begin{Bmatrix} \psi_x \\ \psi_y \end{Bmatrix}$$

where $(\varepsilon_{ij}^0 \ ; \ i,j = x,y)$ denote the strain components in midplane, $(\kappa_{ij}^{(1)} \ ; i,j = x,y)$ are the first-order curvature components, and $(\kappa_{ij}^{(2)} \ ; i,j = x,y)$ represent the higher-order curvature components. Moreover, $\boldsymbol{d}_{31}, \boldsymbol{d}_{32}$ stand for the piezoelectric constants, and $\mathcal{V} = E_z h$ is the value of voltage related to the applied lateral electric field.

In contrast to the local (classical) continuum theory, in the nonlocal continuum elasticity, the stress at a reference point is dependent on the strain components of all other point of the continuum in addition to that of the reference point. Accordingly, one will have (Eringen 1972)

$$\sigma'_{ij} = \int_{\Omega} \{\varrho(|\mathcal{X}' - \mathcal{X}|)\sigma_{ij}(\mathcal{X}')\} d\Omega \tag{5.5}$$

in which $\mathcal{X}$ and $\mathcal{X}'$ in order are a point and any point else in the body, σ_{ij} and σ'_{ij} are the local (classical) and nonlocal stress components, respectively. Also, $\varrho(|\mathcal{X}' - \mathcal{X}|)$ represent the nonlocal kernel function associated with internal characteristic length of material. For a two-dimensional material, it yields

$$\left(1 - e_0^2\theta^2\nabla^2\right)\sigma'_{ij} = \sigma_{ij} \tag{5.6}$$

where $e_0\theta$ denotes the nonlocal parameter in such a way that θ is an internal characteristic constant and e_0 is a constant related to the selected material. Also, ∇^2 represents the Laplacian operator. Thereby, the nonlocal constitutive relations for a hybrid FGM nanoshell are in the following form

$$\begin{aligned} \left(1 - e_0^2\theta^2\nabla^2\right) \begin{Bmatrix} \boldsymbol{\sigma'_{xx}} \\ \boldsymbol{\sigma'_{yy}} \\ \boldsymbol{\sigma'_{xy}} \\ \boldsymbol{\sigma'_{xz}} \\ \boldsymbol{\sigma'_{yz}} \end{Bmatrix} &= \left(\left[Q_{p1}\right] + \left[Q_f\right] + \left[Q_{p2}\right]\right) \begin{Bmatrix} \varepsilon_{xx} \\ \varepsilon_{yy} \\ \gamma_{xy} \\ \gamma_{xz} \\ \gamma_{yz} \end{Bmatrix} \\ &\quad - \left(\left[Q_{p1}\right] + \left[Q_{p2}\right]\right) \begin{bmatrix} \dfrac{\mathcal{V}}{h_p} & 0 \\ 0 & \dfrac{\mathcal{V}}{h_p} \\ 0 & 0 \\ 0 & 0 \\ 0 & 0 \end{bmatrix} \{\boldsymbol{d}_{31}\, \boldsymbol{d}_{32}\} \end{aligned} \tag{5.7}$$

where

$$\left[Q^{p1}\right]=\left[Q^{p2}\right]=\begin{bmatrix}\lambda_p+2\mu_p & \lambda_p & 0 & 0 & 0\\ \lambda_p & \lambda_p+2\mu_p & 0 & 0 & 0\\ 0 & 0 & \mu_p & 0 & 0\\ 0 & 0 & 0 & \mu_p & 0\\ 0 & 0 & 0 & 0 & \mu_p\end{bmatrix}$$

$$\left[Q^{f}\right]=\begin{bmatrix}\lambda_f(z)+2\mu_f(z) & \lambda_f(z) & 0 & 0 & 0\\ \lambda_f(z) & \lambda_f(z)+2\mu_f(z) & 0 & 0 & 0\\ 0 & 0 & \mu_f(z) & 0 & 0\\ 0 & 0 & 0 & \mu_f(z) & 0\\ 0 & 0 & 0 & 0 & \mu_f(z)\end{bmatrix} \tag{5.8}$$

in which $\lambda_f(z)=\frac{\nu_f(z)E_f(z)}{\left(1-\nu_f(z)\right)\left(1+2\nu_f(z)\right)}, \mu_f(z)=\frac{E_f(z)}{2\left(1+\nu_f(z)\right)}$ are the Lame's constants for the FGM substrate, and $\lambda_p=\frac{\nu_pE_p}{\left(1-\nu_p\right)\left(1+2\nu_p\right)}, \mu_p=\frac{E_p}{2\left(1+\nu_p\right)}$ represent the Lame's constants for piezoelectric layers of hybrid FGM nanoshell.

For the hydrostatic pressure loading case, the work Π_P done by the external hydrostatic pressure $\amalg$ can be read as

$$\Pi_P=\int_S \amalg w dS \tag{5.9}$$

Moreover, the external work done by Pasternak elastic foundation can be expressed as

$$\Pi_k=\int_S\left(\mathcal{K}_1w^2+\mathcal{K}_2\left(\left(\frac{\partial w}{\partial x}\right)^2+\left(\frac{\partial w}{\partial y}\right)^2\right)\right)dS \tag{5.10}$$

in which $\mathcal{K}_1$ and $\mathcal{K}_1$ are Winkler and shear stiffness constants, respectively.

Additionally, based upon the nonlocal exponential shear deformation shell model, the total strain energy of the hybrid FGM nanoshell can be expressed as

$$\begin{aligned}\Pi_s&=\frac{1}{2}\int_S\int_{-\frac{h}{2}}^{\frac{h}{2}}\sigma_{ij}\varepsilon_{ij}dzdS\\&=\frac{1}{2}\int_S\Big\{N_{xx}\varepsilon^0_{xx}+N_{yy}\varepsilon^0_{yy}+N_{xy}\gamma^0_{xy}+M_{xx}\kappa^{(1)}_{xx}+M_{yy}\kappa^{(1)}_{yy}+M_{xy}\kappa^{(1)}_{xy}+H_{xx}\kappa^{(2)}_{xx}\\&\qquad+H_{yy}\kappa^{(2)}_{yy},+H_{xy}\kappa^{(2)}_{xy},+Q_x\gamma_{xz},+Q_y\gamma_{yz}\Big\}dS\end{aligned} \tag{5.11}$$

where the stress resultants can be introduced as

$$\begin{Bmatrix} N_{xx} - e_0^2\theta^2\left(\dfrac{\partial^2 N_{xx}}{\partial x^2} + \dfrac{\partial^2 N_{xx}}{\partial y^2}\right) \\ N_{yy} - e_0^2\theta^2\left(\dfrac{\partial^2 N_{yy}}{\partial x^2} + \dfrac{\partial^2 N_{yy}}{\partial y^2}\right) \\ N_{xy} - e_0^2\theta^2\left(\dfrac{\partial^2 N_{xy}}{\partial x^2} + \dfrac{\partial^2 N_{xy}}{\partial y^2}\right) \end{Bmatrix} = \begin{bmatrix} A_{11}^* & A_{12}^* & 0 \\ A_{12}^* & A_{22}^* & 0 \\ 0 & 0 & A_{66}^* \end{bmatrix} \begin{Bmatrix} \varepsilon_{xx}^0 \\ \varepsilon_{yy}^0 \\ \gamma_{xy}^0 \end{Bmatrix}$$

$$+ \begin{bmatrix} B_{11}^* & B_{12}^* & 0 \\ B_{12}^* & B_{22}^* & 0 \\ 0 & 0 & B_{66}^* \end{bmatrix} \begin{Bmatrix} \kappa_{xx}^{(1)} \\ \kappa_{yy}^{(1)} \\ \kappa_{xy}^{(1)} \end{Bmatrix}$$

$$+ \begin{bmatrix} B_{11}^{**} & B_{12}^{**} & 0 \\ B_{12}^{**} & B_{22}^{**} & 0 \\ 0 & 0 & B_{66}^{**} \end{bmatrix} \begin{Bmatrix} \kappa_{xx}^{(2)} \\ \kappa_{yy}^{(2)} \\ \kappa_{xy}^{(2)} \end{Bmatrix}$$

$$\begin{Bmatrix} M_{xx} - e_0^2\theta^2\left(\dfrac{\partial^2 M_{xx}}{\partial x^2} + \dfrac{\partial^2 M_{xx}}{\partial y^2}\right) \\ M_{yy} - e_0^2\theta^2\left(\dfrac{\partial^2 M_{yy}}{\partial x^2} + \dfrac{\partial^2 M_{yy}}{\partial y^2}\right) \\ M_{xy} - e_0^2\theta^2\left(\dfrac{\partial^2 M_{xy}}{\partial x^2} + \dfrac{\partial^2 M_{xy}}{\partial y^2}\right) \end{Bmatrix} = \begin{bmatrix} B_{11}^* & B_{12}^* & 0 \\ B_{12}^* & B_{22}^* & 0 \\ 0 & 0 & B_{66}^* \end{bmatrix} \begin{Bmatrix} \varepsilon_{xx}^0 \\ \varepsilon_{yy}^0 \\ \gamma_{xy}^0 \end{Bmatrix}$$

$$+ \begin{bmatrix} D_{11}^* & D_{12}^* & 0 \\ D_{12}^* & D_{22}^* & 0 \\ 0 & 0 & D_{66}^* \end{bmatrix} \begin{Bmatrix} \kappa_{xx}^{(1)} \\ \kappa_{yy}^{(1)} \\ \kappa_{xy}^{(1)} \end{Bmatrix}$$

$$+ \begin{bmatrix} D_{11}^{**} & D_{12}^{**} & 0 \\ D_{12}^{**} & D_{22}^{**} & 0 \\ 0 & 0 & D_{66}^{**} \end{bmatrix} \begin{Bmatrix} \kappa_{xx}^{(2)} \\ \kappa_{yy}^{(2)} \\ \kappa_{xy}^{(2)} \end{Bmatrix}$$

$$\left\{\begin{array}{l} H_{xx}-e_0^2\theta^2\left(\dfrac{\partial^2 H_{xx}}{\partial x^2}+\dfrac{\partial^2 H_{xx}}{\partial y^2}\right) \\ H_{yy}-e_0^2\theta^2\left(\dfrac{\partial^2 H_{yy}}{\partial x^2}+\dfrac{\partial^2 H_{yy}}{\partial y^2}\right) \\ H_{xy}-e_0^2\theta^2\left(\dfrac{\partial^2 H_{xy}}{\partial x^2}+\dfrac{\partial^2 H_{xy}}{\partial y^2}\right) \end{array}\right\} = \begin{bmatrix} B_{11}^{**} & B_{12}^{**} & 0 \\ B_{12}^{**} & B_{22}^{**} & 0 \\ 0 & 0 & B_{66}^{**} \end{bmatrix} \left\{\begin{array}{l} \varepsilon_{xx}^0 \\ \varepsilon_{yy}^0 \\ \gamma_{xy}^0 \end{array}\right\}$$

$$+ \begin{bmatrix} D_{11}^{**} & D_{12}^{**} & 0 \\ D_{12}^{**} & D_{22}^{**} & 0 \\ 0 & 0 & D_{66}^{**} \end{bmatrix} \left\{\begin{array}{l} \kappa_{xx}^{(1)} \\ \kappa_{yy}^{(1)} \\ \kappa_{xy}^{(1)} \end{array}\right\}$$

$$+ \begin{bmatrix} G_{11}^{*} & G_{12}^{*} & 0 \\ G_{12}^{*} & G_{22}^{*} & 0 \\ 0 & 0 & G_{66}^{*} \end{bmatrix} \left\{\begin{array}{l} \kappa_{xx}^{(2)} \\ \kappa_{yy}^{(2)} \\ \kappa_{xy}^{(2)} \end{array}\right\}$$

$$\left\{\begin{array}{l} Q_x-e_0^2\theta^2\left(\dfrac{\partial^2 Q_x}{\partial x^2}+\dfrac{\partial^2 Q_x}{\partial y^2}\right) \\ Q_y-e_0^2\theta^2\left(\dfrac{\partial^2 Q_y}{\partial x^2}+\dfrac{\partial^2 Q_y}{\partial y^2}\right) \end{array}\right\} = \begin{bmatrix} A_{44}^{*} & 0 \\ 0 & A_{55}^{*} \end{bmatrix} \left\{\begin{array}{l} \psi_x \\ \psi_y \end{array}\right\} \tag{5.12}$$

in which

$$\left\{\begin{array}{l} N_{xx} \\ N_{yy} \\ N_{xy} \end{array}\right\} = \int_{-\frac{h}{2}}^{\frac{h}{2}} \left\{\begin{array}{l} \sigma_{xx} \\ \sigma_{yy} \\ \sigma_{xy} \end{array}\right\} dz, \quad \left\{\begin{array}{l} M_{xx} \\ M_{yy} \\ M_{xy} \end{array}\right\} = \int_{-\frac{h}{2}}^{\frac{h}{2}} \left\{\begin{array}{l} \sigma_{xx} \\ \sigma_{yy} \\ \sigma_{xy} \end{array}\right\} z dz$$

$$\left\{\begin{array}{l} H_{xx} \\ H_{yy} \\ H_{xy} \end{array}\right\} = \int_{-\frac{h}{2}}^{\frac{h}{2}} \left\{\begin{array}{l} \sigma_{xx} \\ \sigma_{yy} \\ \sigma_{xy} \end{array}\right\} z e^{-\frac{2z^2}{h^2}} dz, \quad \left\{\begin{array}{l} Q_x \\ Q_y \end{array}\right\} = \int_{-\frac{h}{2}}^{\frac{h}{2}} \left\{\begin{array}{l} \sigma_{xz} \\ \sigma_{yz} \end{array}\right\} \left(1-\frac{4z^2}{h^2}\right) e^{-\frac{2z^2}{h^2}} dz \tag{5.13}$$

and

$$\left\{\begin{matrix} A_{11}^{*}, B_{11}^{*}, D_{11}^{*} \\ B_{11}^{**}, D_{11}^{**}, G_{11}^{*} \end{matrix}\right\} = \left\{\begin{matrix} A_{22}^{*}, B_{22}^{*}, D_{22}^{*} \\ B_{22}^{**}, D_{22}^{**}, G_{22}^{*} \end{matrix}\right\}$$
$$= \int_{z_0}^{z_1} \left[Q_{11}^{p1}\right] \left\{\begin{matrix} 1, z, z^2 \\ ze^{-\frac{2z^2}{h^2}}, z^2 e^{-\frac{2z^2}{h^2}}, z^2 e^{-\frac{4z^2}{h^2}} \end{matrix}\right\} dz$$
$$+ \int_{z_1}^{z_2} \left[Q_{11}^{f}\right] \left\{\begin{matrix} 1, \bar{z}, \bar{z}^2 \\ \bar{z}e^{-\frac{2\bar{z}^2}{h^2}}, \bar{z}^2 e^{-\frac{2\bar{z}^2}{h^2}}, \bar{z}^2 e^{-\frac{4\bar{z}^2}{h^2}} \end{matrix}\right\} dz$$
$$+ \int_{z_2}^{z_3} \left[Q_{11}^{p2}\right] \left\{\begin{matrix} 1, z, z^2 \\ ze^{-\frac{2z^2}{h^2}}, z^2 e^{-\frac{2z^2}{h^2}}, z^2 e^{-\frac{4z^2}{h^2}} \end{matrix}\right\} dz$$
$$\left\{\begin{matrix} A_{12}^{*}, B_{12}^{*}, D_{12}^{*} \\ B_{12}^{**}, D_{12}^{**}, G_{12}^{*} \end{matrix}\right\} = \left\{\begin{matrix} A_{21}^{*}, B_{21}^{*}, D_{21}^{*} \\ B_{21}^{**}, D_{21}^{**}, G_{21}^{*} \end{matrix}\right\}$$
$$= \int_{z_0}^{z_1} \left[Q_{12}^{p1}\right] \left\{\begin{matrix} 1, z, z^2 \\ ze^{-\frac{2z^2}{h^2}}, z^2 e^{-\frac{2z^2}{h^2}}, z^2 e^{-\frac{4z^2}{h^2}} \end{matrix}\right\} dz$$
$$+ \int_{z_1}^{z_2} \left[Q_{12}^{f}\right] \left\{\begin{matrix} 1, \bar{z}, \bar{z}^2 \\ \bar{z}e^{-\frac{2\bar{z}^2}{h^2}}, \bar{z}^2 e^{-\frac{2\bar{z}^2}{h^2}}, \bar{z}^2 e^{-\frac{4\bar{z}^2}{h^2}} \end{matrix}\right\} dz$$
$$+ \int_{z_2}^{z_3} \left[Q_{12}^{p2}\right] \left\{\begin{matrix} 1, z, z^2 \\ ze^{-\frac{2z^2}{h^2}}, z^2 e^{-\frac{2z^2}{h^2}}, z^2 e^{-\frac{4z^2}{h^2}} \end{matrix}\right\} dz$$
$$\left\{\begin{matrix} A_{66}^{*}, B_{66}^{*}, D_{66}^{*} \\ B_{66}^{**}, D_{66}^{**}, G_{66}^{*} \end{matrix}\right\} = \int_{z_0}^{z_1} \left[Q_{66}^{p1}\right] \left\{\begin{matrix} 1, z, z^2 \\ ze^{-\frac{2z^2}{h^2}}, z^2 e^{-\frac{2z^2}{h^2}}, z^2 e^{-\frac{4z^2}{h^2}} \end{matrix}\right\} dz$$
$$+ \int_{z_1}^{z_2} \left[Q_{66}^{f}\right] \left\{\begin{matrix} 1, \bar{z}, \bar{z}^2 \\ \bar{z}e^{-\frac{2\bar{z}^2}{h^2}}, \bar{z}^2 e^{-\frac{2\bar{z}^2}{h^2}}, \bar{z}^2 e^{-\frac{4\bar{z}^2}{h^2}} \end{matrix}\right\} dz$$
$$+ \int_{z_2}^{z_3} \left[Q_{66}^{p2}\right] \left\{\begin{matrix} 1, z, z^2 \\ ze^{-\frac{2z^2}{h^2}}, z^2 e^{-\frac{2z^2}{h^2}}, z^2 e^{-\frac{4z^2}{h^2}} \end{matrix}\right\} dz \qquad (5.14)$$

$$\left\{\begin{matrix} A_{44}^{*} \\ A_{55}^{*} \end{matrix}\right\} = \left\{\begin{matrix} \int_{z_0}^{z_1} \left[Q_{44}^{p1}\right] \left(1 - \frac{4z^2}{h^2}\right) e^{-\frac{2z^2}{h^2}} dz + \int_{z_1}^{z_2} \left[Q_{44}^{f}\right] \left(1 - \frac{4\bar{z}^2}{h^2}\right) e^{-\frac{2\bar{z}^2}{h^2}} dz \\ + \int_{z_2}^{z_3} \left[Q_{44}^{p2}\right] \left(1 - \frac{4z^2}{h^2}\right) e^{-\frac{2z^2}{h^2}} dz \\ \int_{z_0}^{z_1} \left[Q_{55}^{p1}\right] \left(1 - \frac{4z^2}{h^2}\right) e^{-\frac{2z^2}{h^2}} dz + \int_{z_1}^{z_2} \left[Q_{55}^{f}\right] \left(1 - \frac{4\bar{z}^2}{h^2}\right) e^{-\frac{2\bar{z}^2}{h^2}} dz \\ + \int_{z_2}^{z_3} \left[Q_{55}^{p2}\right] \left(1 - \frac{4z^2}{h^2}\right) e^{-\frac{2z^2}{h^2}} dz \end{matrix}\right\}$$

Moreover, $\bar{z} = z - z'$ as z' is the z-coordinate of the physical neutral plane associated with FGM substrate which can be defined as

$$z' = \frac{\int_{-h_f/2}^{h_f/2} \left(\lambda_f(z) + 2\mu_f(z)\right) z dz}{\int_{-h_f/2}^{h_f/2} \left(\lambda_f(z) + 2\mu_f(z)\right) dz} \tag{5.15}$$

In accordance with the virtual work's principle as

$$\delta \int_{t_1}^{t_2} (\Pi_s - \Pi_P - \Pi_k) dt = 0 \tag{5.16}$$

and taking the variation of u, v, w, ψ_x, ψ_y and then integrating by parts, the size-dependent governing equations in terms of the stress resultants can be developed as

$$\frac{\partial N_{xx}}{\partial x} + \frac{\partial N_{xy}}{\partial y} = 0 \tag{5.17a}$$

$$\frac{\partial N_{xy}}{\partial x} + \frac{\partial N_{yy}}{\partial y} = 0 \tag{5.17b}$$

$$\begin{aligned} &\frac{\partial^2 M_{xx}}{\partial x^2} + 2\frac{\partial^2 M_{xy}}{\partial x \partial y} + \frac{\partial^2 M_{yy}}{\partial y^2} + \frac{N_{yy}}{R} + N_{xx}\frac{\partial^2 w}{\partial x^2} + 2N_{xy}\frac{\partial^2 w}{\partial x \partial y} + N_{yy}\frac{\partial^2 w}{\partial y^2} \\ &+ q - \mathcal{K}_1 w + \mathcal{K}_2\left(\frac{\partial^2 w}{\partial x^2} + \frac{\partial^2 w}{\partial y^2}\right) = 0 \end{aligned} \tag{5.17c}$$

$$\frac{\partial H_{xx}}{\partial x} + \frac{\partial H_{xy}}{\partial y} - Q_x = 0 \tag{5.17d}$$

$$\frac{\partial H_{xy}}{\partial x} + \frac{\partial H_{yy}}{\partial y} - Q_y = 0 \tag{5.17e}$$

Thereafter, through definition of Airy stress function $f(x, y)$ as below, the two first governing Eqs. (5.17a) and (5.17b) can be satisfied completely:

$$N_{xx} = \frac{\partial^2 f(x,y)}{\partial y^2} \quad , \quad N_{yy} = \frac{\partial^2 f(x,y)}{\partial x^2} \quad , \quad N_{xy} = -\frac{\partial^2 f(x,y)}{\partial x \partial y} \tag{5.18}$$

Furthermore, for a perfect nanoshell, the compatibility relation corresponding to the midplane strain components can be rewritten as

$$\frac{\partial^2 \varepsilon_{xx}^0}{\partial y^2} + \frac{\partial^2 \varepsilon_{yy}^0}{\partial x^2} - \frac{\partial^2 \gamma_{xy}^0}{\partial x \partial y} = \left(\frac{\partial^2 w}{\partial x \partial y}\right)^2 - \frac{\partial^2 w}{\partial x^2}\frac{\partial^2 w}{\partial y^2} - \frac{1}{R}\frac{\partial^2 w}{\partial x^2} \tag{5.19}$$

Now, by substituting Eq. (5.18) in the inverse of Eq. (5.12) and using Eqs. (5.17) and (5.19), the governing differential equations for a nonlocal hybrid FGM exponential shear deformable nanoshell can be established as

$$\varphi_1\frac{\partial^4 f}{\partial x^4}+(\varphi_7-2\varphi_2)\frac{\partial^4 f}{\partial x^2\partial y^2}+\varphi_1\frac{\partial^4 f}{\partial y^4}+\varphi_4\frac{\partial^4 w}{\partial x^4}+2(\varphi_3-\varphi_8)\frac{\partial^4 w}{\partial x^2\partial y^2}+\varphi_4\frac{\partial^4 w}{\partial y^4}$$
$$-\varphi_6\frac{\partial^3\psi_x}{\partial x^3}-(\varphi_5-\varphi_9)\frac{\partial^3\psi_x}{\partial x\partial y^2}-\varphi_6\frac{\partial^3\psi_y}{\partial y^3}-(\varphi_5-\varphi_9)\frac{\partial^3\psi_y}{\partial x^2\partial y}+\frac{1}{R}\frac{\partial^2 w}{\partial x^2}$$
$$=\left(\frac{\partial^2 w}{\partial x\partial y}\right)^2-\frac{\partial^2 w}{\partial x^2}\frac{\partial^2 w}{\partial y^2} \tag{5.20a}$$

$$\varphi_{10}\frac{\partial^4 w}{\partial x^4}+2(\varphi_{11}+2\varphi_{12})\frac{\partial^4 w}{\partial x^2\partial y^2}+\varphi_{10}\frac{\partial^4 w}{\partial y^4}+\varphi_{13}\frac{\partial^3\psi_x}{\partial x^3}+(\varphi_{14}+2\varphi_{15})\frac{\partial^3\psi_x}{\partial x\partial y^2}$$
$$+\varphi_{13}\frac{\partial^3\psi_y}{\partial y^3}+(\varphi_{14}+2\varphi_{15})\frac{\partial^3\psi_y}{\partial x^2\partial y}-\frac{1}{R}\frac{\partial^2 f}{\partial x^2}+\mathcal{K}_1 w-\mathcal{K}_2\left(\frac{\partial^2 w}{\partial x^2}+\frac{\partial^2 w}{\partial y^2}\right)$$
$$=\left(1-e_0^2\theta^2\nabla^2\right)\times\left(\frac{\partial^2 w}{\partial x^2}\frac{\partial^2 f}{\partial y^2}-2\frac{\partial^2 w}{\partial x\partial y}\frac{\partial^2 f}{\partial x\partial y}+\frac{\partial^2 w}{\partial y^2}\frac{\partial^2 f}{\partial x^2}+q\right) \tag{5.20b}$$

$$\varphi_{16}\frac{\partial^3 f}{\partial x^3}+\varphi_{17}\frac{\partial^3 f}{\partial x\partial y^2}+\varphi_{18}\frac{\partial^3 w}{\partial x^3}+(\varphi_{19}+2\varphi_{20})\frac{\partial^3 w}{\partial x\partial y^2}+\varphi_{21}\frac{\partial^2\psi_x}{\partial x^2}+\varphi_{22}\frac{\partial^2\psi_x}{\partial y^2}$$
$$+(\varphi_{23}+\varphi_{22})\frac{\partial^2\psi_y}{\partial x\partial y}-A_{44}^*\psi_x=0 \tag{5.20c}$$

$$\varphi_{16}\frac{\partial^3 f}{\partial y^3}+\varphi_{17}\frac{\partial^3 f}{\partial x^2\partial y}+\varphi_{18}\frac{\partial^3 w}{\partial y^3}+(\varphi_{19}+2\varphi_{20})\frac{\partial^3 w}{\partial x^2\partial y}+\varphi_{21}\frac{\partial^2\psi_y}{\partial y^2}+\varphi_{22}\frac{\partial^2\psi_y}{\partial x^2}$$
$$+(\varphi_{23}+\varphi_{22})\frac{\partial^2\psi_x}{\partial x\partial y}-A_{55}^*\psi_y=0 \tag{5.20d}$$

where the parameters φ_i $(i=1,\ldots,23)$ are defined in Appendix A.

Regarding the boundary conditions at the left and right ends of the hybrid FGM nanoshell, the clamped edge supports are considered based on which: $w=0$, $\frac{\partial w}{\partial x}=0$

Also, the equilibrium satisfaction for loading conditions along x-axis for axial compression and hydrostatic pressure loading cases yields, respectively, as

$$\int_0^{2\pi R} N_{xx}dy+2\pi Rh\sigma_{xx}=0 \tag{5.21a}$$

$$\int_0^{2\pi R} N_{xx}dy+\pi R^2 q=0 \tag{5.21b}$$

For a closed shell-type structure, the periodicity condition results in

$$\int_0^{2\pi R} \frac{\partial v}{\partial y} dy = 0 \tag{5.22}$$

which can be rewritten in the following form:

$$\int_0^{2\pi R} \left(\varphi_1 \frac{\partial^2 f}{\partial x^2} - \varphi_2 \frac{\partial^2 f}{\partial y^2} + \varphi_4 \frac{\partial^2 w}{\partial x^2} + \varphi_3 \frac{\partial^2 w}{\partial y^2} - \varphi_6 \frac{\partial \psi_x}{\partial x} - \varphi_5 \frac{\partial \psi_y}{\partial y} + \frac{w}{R} - \frac{1}{2}\left(\frac{\partial w}{\partial y}\right)^2 + \frac{d_{32}\mathcal{V}}{h_p} \right) dy = 0 \tag{5.23}$$

In addition, the unit shortening associated to the movable ends of the hybrid FGM exponential shear deformable nanoshell can be evaluated by

$$\begin{aligned} \frac{\Delta_x}{L} &= -\frac{1}{2\pi RL} \int_0^{2\pi R} \int_0^L \frac{\partial u}{\partial x} dx dy \\ &= -\frac{1}{2\pi RL} \int_0^{2\pi R} \int_0^L \left(\varphi_1 \frac{\partial^2 f}{\partial y^2} - \varphi_2 \frac{\partial^2 f}{\partial x^2} + \varphi_3 \frac{\partial^2 w}{\partial x^2} + \varphi_4 \frac{\partial^2 w}{\partial y^2} - \varphi_5 \frac{\partial \psi_x}{\partial x} - \varphi_6 \frac{\partial \psi_y}{\partial y} \right. \\ &\left. -\frac{1}{2}\left(\frac{\partial w}{\partial x}\right)^2 + \frac{d_{31}\mathcal{V}}{h_p} \right) dx dy \end{aligned} \tag{5.24}$$

5.3 Solving Process for Asymptotic Solutions

5.3.1 Boundary Layer Theory of Nonlocal Shell Buckling

In order to solve the problem in a more general framework, the following dimensionless parameters are taken into consideration:

$$X = \frac{\pi x}{L} \quad , \quad Y = \frac{y}{R} \quad , \quad \beta = \frac{L}{\pi R} \quad , \quad \eta = \frac{L}{\pi h} \quad , \quad \epsilon = \frac{\pi^2 R h}{L^2}$$

$$\{a_{11}^*, a_{12}^*, a_{44}^*, a_{55}^*, a_{66}^*\} = \left\{ \frac{A_{11}^*}{A_{00}}, \frac{A_{12}^*}{A_{00}}, \frac{A_{44}^*}{A_{00}}, \frac{A_{55}^*}{A_{00}}, \frac{A_{66}^*}{A_{00}} \right\}, \{g_{11}^*, g_{12}^*, g_{66}^*\}$$

$$= \left[\frac{G_{11}^*}{A_{00}h^2}, \frac{G_{12}^*}{A_{00}h^2}, \frac{G_{66}^*}{A_{00}h^2} \right]$$

$$\left\{ \begin{matrix} b_{11}^{*}, b_{12}^{*}, b_{66}^{*}, b_{11}^{**}, b_{12}^{**}, b_{66}^{**} \\ d_{11}^{*}, d_{12}^{*}, d_{66}^{*}, d_{11}^{**}, d_{12}^{**}, d_{66}^{**} \end{matrix} \right\} = \left\{ \begin{matrix} \frac{B_{11}^{*}}{A_{00}h}, \frac{B_{12}^{*}}{A_{00}h}, \frac{B_{66}^{*}}{A_{00}h}, \frac{B_{11}^{**}}{A_{00}h}, \frac{B_{12}^{**}}{A_{00}h}, \frac{B_{66}^{**}}{A_{00}h} \\ \frac{D_{11}^{*}}{A_{00}h^2}, \frac{D_{12}^{*}}{A_{00}h^2}, \frac{D_{66}^{*}}{A_{00}h^2}, \frac{D_{11}^{**}}{A_{00}h^2}, \frac{D_{12}^{**}}{A_{00}h^2}, \frac{D_{66}^{**}}{A_{00}h^2} \end{matrix} \right\} \tag{5.25}$$

$$W = \frac{\epsilon w}{h} \quad , \quad F = \frac{\epsilon^2 f}{A_{00}h^2} \quad , \quad \{\Psi_X, \Psi_Y\} = \frac{\epsilon^2 L}{\pi h}\{\psi_x, \psi_y\}$$

$$\wp_{\boldsymbol{x}} = \frac{\sigma_{xx}R}{2A_{00}} \quad , \quad \delta_x = \frac{\Delta_x R}{2Lh} \quad , \quad \wp_q = \frac{3^{3/4} q L R^{3/2}}{4\pi A_{00} h^{3/2}} \quad , \quad \delta_q = \frac{3^{3/4}\Delta_x \sqrt{R}}{4\pi h^{3/2}} \quad , \quad \mathcal{G} = \frac{e_0\theta}{L}$$

in which $A_{00} = (\lambda_m + 2\mu_m)h$. As a consequence, the dimensionless form of the nonlocal nonlinear governing differential equations can be obtained as

$$\begin{aligned} &\vartheta_1 \frac{\partial^4 F}{\partial X^4} + (\vartheta_7 - 2\vartheta_2)\beta^2 \frac{\partial^4 F}{\partial X^2 \partial Y^2} + \vartheta_1 \beta^4 \frac{\partial^4 F}{\partial Y^4} \\ &+ \epsilon\left(\vartheta_4 \frac{\partial^4 W}{\partial X^4} + 2(\vartheta_3 - \vartheta_8)\beta^2 \frac{\partial^4 W}{\partial X^2 \partial Y^2} + \vartheta_4 \beta^4 \frac{\partial^4 W}{\partial Y^4} \right) - \vartheta_6 \frac{\partial^3 \Psi_X}{\partial X^3} \\ &- (\vartheta_5 - \vartheta_9)\beta^2 \frac{\partial^3 \Psi_X}{\partial X \partial Y^2} - \vartheta_6 \beta^3 \frac{\partial^3 \Psi_Y}{\partial Y^3} - (\vartheta_5 - \vartheta_9)\beta \frac{\partial^3 \Psi_Y}{\partial X^2 \partial Y} + \frac{\partial^2 W}{\partial X^2} \\ &= \beta^2 \left(\frac{\partial^2 W}{\partial X \partial Y} \right)^2 - \beta^2 \frac{\partial^2 W}{\partial X^2} \frac{\partial^2 W}{\partial Y^2} \end{aligned} \tag{5.26a}$$

$$\begin{aligned} &\epsilon^2 \left(\vartheta_{10} \frac{\partial^4 W}{\partial X^4} + 2(\vartheta_{11} + 2\vartheta_{12})\beta^2 \frac{\partial^4 W}{\partial X^2 \partial Y^2} + \vartheta_{10}\beta^4 \frac{\partial^4 W}{\partial Y^4} + k_1 W - k_2 \left(\frac{\partial^2 W}{\partial X^2} + \frac{\partial^2 W}{\partial Y^2} \right) \right) \\ &+ \epsilon \left(\vartheta_{13} \frac{\partial^3 \Psi_X}{\partial X^3} + (\vartheta_{14} + 2\vartheta_{15})\beta \frac{\partial^3 \Psi_X}{\partial X^2 \partial Y} \right) \\ &+ \epsilon \left(\vartheta_{13}\beta^3 \frac{\partial^3 \Psi_Y}{\partial Y^3} + (\vartheta_{14} + 2\vartheta_{15})\beta^2 \frac{\partial^3 \Psi_Y}{\partial X \partial Y^2} \right) - \frac{\partial^2 F}{\partial X^2} \\ &= \left(1 - \pi^2 \mathcal{G}^2 \nabla^2\right) \times \left(\beta^2 \frac{\partial^2 W}{\partial X^2} \frac{\partial^2 F}{\partial Y^2} + 2\beta^2 \frac{\partial^2 W}{\partial X \partial Y} \frac{\partial^2 F}{\partial X \partial Y} + \beta^2 \frac{\partial^2 W}{\partial Y^2} \frac{\partial^2 F}{\partial X^2} + \epsilon^{3/2} \frac{4}{3} 3^{1/4} \wp_q \right) \end{aligned} \tag{5.26b}$$

$$\begin{aligned} &\vartheta_{16} \frac{\partial^3 F}{\partial X^3} + \vartheta_{17}\beta^2 \frac{\partial^3 F}{\partial X \partial Y^2} + \epsilon \left(\vartheta_{18} \frac{\partial^3 W}{\partial X^3} + (\vartheta_{19} + 2\vartheta_{20})\beta^2 \frac{\partial^3 W}{\partial X \partial Y^2} \right) + \vartheta_{21} \frac{\partial^2 \Psi_X}{\partial X^2} \\ &+ \vartheta_{22}\beta^2 \frac{\partial^2 \Psi_X}{\partial Y^2} + (\vartheta_{23} + \vartheta_{22})\beta \frac{\partial^2 \Psi_Y}{\partial X \partial Y} - a_{44}^{*} \eta^2 \Psi_X = 0 \end{aligned} \tag{5.26c}$$

$$\vartheta_{16}\beta^3\frac{\partial^3 F}{\partial Y^3}+\vartheta_{17}\beta\frac{\partial^3 F}{\partial X^2\partial Y}+\epsilon\left(\vartheta_{18}\beta^3\frac{\partial^3 W}{\partial Y^3}+(\vartheta_{19}+2\vartheta_{20})\beta\frac{\partial^3 W}{\partial X^2\partial Y}\right)$$
$$+\vartheta_{21}\beta^2\frac{\partial^2\Psi_Y}{\partial Y^2}+\vartheta_{22}\frac{\partial^2\Psi_Y}{\partial X^2}+(\vartheta_{23}+\vartheta_{22})\beta\frac{\partial^2\Psi_X}{\partial X\partial Y}-a_{55}^*\eta^2\Psi_Y=0 \tag{5.26d}$$

Furthermore, the dimensionless form of the clamped boundary conditions at the left ($X=0$) and right ($X=\pi$) ends of the hybrid FGM nanoshell can be given as $W=0$, $\frac{\partial W}{\partial X}=0$.

Also, the boundary layer-type equilibrium requirement for loading condition along x-axis corresponding to axial compression and hydrostatic pressure loading cases can be expressed as

$$\frac{1}{2\pi}\int_0^{2\pi}\beta^2\frac{\partial^2 F}{\partial Y^2}dY+2\epsilon\wp_x=0 \tag{5.27a}$$

$$\frac{1}{2\pi}\int_0^{2\pi}\beta^2\frac{\partial^2 F}{\partial Y^2}dY+\frac{2}{3}3^{1/4}\epsilon^{3/2}\wp_q=0 \tag{5.27b}$$

The dimensionless periodicity condition becomes

$$\int_0^{2\pi}\left\{\vartheta_1\frac{\partial^2 F}{\partial X^2}-\vartheta_2\beta^2\frac{\partial^2 F}{\partial Y^2}+\epsilon\left(\vartheta_4\frac{\partial^2 W}{\partial X^2}+\vartheta_3\beta^2\frac{\partial^2 W}{\partial Y^2}\right)-\vartheta_6\frac{\partial\Psi_x}{\partial X}-\vartheta_5\beta\frac{\partial\Psi_Y}{\partial Y}\right.$$
$$\left.+W-\frac{\beta^2}{2}\left(\frac{\partial W}{\partial Y}\right)^2+\frac{d_{32}R\mathcal{V}}{hh_p}\right\}dY=0 \tag{5.28}$$

Additionally, the unit shortening of the hybrid FGM exponential shear deformable nanoshell in dimensionless form can be introduced for axial compression and hydrostatic pressure loading cases, respectively, as

$$\delta_x=-\frac{1}{4\pi^2\epsilon}\int_0^{2\pi}\int_0^{\pi}\left\{-\vartheta_2\frac{\partial^2 F}{\partial X^2}+\vartheta_1\beta^2\frac{\partial^2 F}{\partial Y^2}+\epsilon\left(\vartheta_3\frac{\partial^2 W}{\partial X^2}+\vartheta_4\beta^2\frac{\partial^2 W}{\partial Y^2}\right)\right\}$$
$$-\vartheta_5\frac{\partial\Psi_X}{\partial X}-\vartheta_6\beta\frac{\partial\Psi_Y}{\partial Y}-\frac{1}{2}\left(\frac{\partial W}{\partial X}\right)^2+\frac{d_{31}R\mathcal{V}}{hh_p}\Bigg\}dXdY \tag{5.29a}$$

$$\delta_q=-\frac{3^{3/4}}{8\pi^2\varepsilon^{3/2}}\int_0^{2\pi}\int_0^{\pi}\left\{-\vartheta_2\frac{\partial^2 F}{\partial X^2}+\vartheta_1\beta^2\frac{\partial^2 F}{\partial Y^2}+\epsilon\left(\vartheta_3\frac{\partial^2 W}{\partial X^2}+\vartheta_4\beta^2\frac{\partial^2 W}{\partial Y^2}\right)\right.$$
$$\left.-\vartheta_5\frac{\partial\Psi_x}{\partial X}-\vartheta_6\beta\frac{\partial\Psi_y}{\partial Y}-\frac{1}{2}\left(\frac{\partial W}{\partial X}\right)^2+\frac{d_{31}R\mathcal{V}}{hh_p}\right\}\times dXdY \tag{5.29b}$$

5.3.2 Perturbation-Based Solution Methodology

In the preceding subsection, through definition of ϵ, namely, as the small perturbation parameter, the nonlocal governing differential Eqs. (5.26) were constructed in the form of boundary layer. At this step of the solving process, using the singular perturbation technique (Shen 2008; Shen 2009; Shen 2011a; b; Shen and Xiang 2014; Sahmani et al. 2016a; b; c; Sahmani and Aghdam 2017d; e; f; Sahmani and Aghdam 2018), the independent variables are considered as the summations of the regular and boundary layer solutions in the following forms:

$$W = \bar{W}(X,Y,\epsilon) + \tilde{W}(X,Y,\epsilon,\xi) + \hat{W}(X,Y,\epsilon,\varsigma) \tag{5.30a}$$

$$F = \bar{F}(X,Y,\epsilon) + \tilde{F}(X,Y,\epsilon,\xi) + \hat{F}(X,Y,\epsilon,\varsigma) \tag{5.30b}$$

$$\Psi_X = \overline{\Psi}_X(X,Y,\epsilon) + \tilde{\Psi}_X(X,Y,\epsilon,\xi) + \widehat{\Psi}_X(X,Y,\epsilon,\varsigma) \tag{5.30c}$$

$$\Psi_Y = \overline{\Psi}_Y(X,Y,\epsilon) + \tilde{\Psi}_Y(X,Y,\epsilon,\xi) + \widehat{\Psi}_Y(X,Y,\epsilon,\varsigma) \tag{5.30d}$$

where the accent character $\bar{\cdot}$ represents the regular solution and the accent characters $\tilde{}$ and $\tilde{}$ denote the boundary layer solutions associated with the left ($X=0$) and right ($X=\pi$) ends of piezoelectric nanoshell, respectively.

Now, each part of the solutions can be altered to the perturbation expansions in the following forms:

$$\begin{aligned}
\bar{W}(X,Y,\epsilon) &= \sum_{i=0} \epsilon^{i/2} \bar{W}_{i/2}(X,Y), \qquad \bar{F}(X,Y,\epsilon) = \sum_{i=0} \epsilon^{i/2} \bar{F}_{i/2}(X,Y) \\
\overline{\Psi}_x(X,Y,\epsilon) &= \sum_{i=1} \epsilon^{i/2} \overline{\Psi}_{xi/2}(X,Y), \qquad \overline{\Psi}_y(X,Y,\epsilon) = \sum_{i=1} \epsilon^{i/2} \overline{\Psi}_{yi/2}(X,Y) \\
\tilde{W}(\boldsymbol{X},\boldsymbol{Y},\boldsymbol{\epsilon},\boldsymbol{\xi}) &= \sum_{i=0} \epsilon^{i/2+1} \tilde{W}_{i/2+1}(\boldsymbol{X},\boldsymbol{Y},\boldsymbol{\xi}), \qquad \tilde{F}(\boldsymbol{X},\boldsymbol{Y},\boldsymbol{\epsilon},\boldsymbol{\xi}) \\
&= \sum_{i=0} \epsilon^{i/2+2} \tilde{F}_{i/2+2}(\boldsymbol{X},\boldsymbol{Y},\boldsymbol{\xi}) \\
\tilde{\Psi}_x(X,Y,\epsilon,\xi) &= \sum_{i=0} \epsilon^{i+3/2} \tilde{\Psi}_{xi+3/2}(\boldsymbol{X},\boldsymbol{Y},\boldsymbol{\xi}), \qquad \tilde{\Psi}_y(X,Y,\epsilon,\xi) \\
&= \sum_{i=0} \epsilon^{i/2+2} \tilde{\Psi}_{y_{i/2+2}}(\boldsymbol{X},\boldsymbol{Y},\boldsymbol{\xi}) \\
\hat{W}(X,Y,\epsilon,\varsigma) &= \sum_{i=0} \epsilon^{i/2+1} \hat{W}_{i/2+1}(X,Y,\varsigma), \qquad \hat{F}(X,Y,\epsilon,\varsigma) = \sum_{i=0} \epsilon^{i/2+2} \hat{F}_{i/2+2}(X,Y,\varsigma) \\
\widehat{\Psi}_x(X,Y,\epsilon,\varsigma) &= \sum_{i=0} \epsilon^{i+3/2} \widehat{\Psi}_{xi+3/2}(X,Y,\varsigma), \qquad \widehat{\Psi}_y(X,Y,\epsilon,\varsigma) = \sum_{i=0} \epsilon^{i/2+2} \widehat{\Psi}_{y_{i/2+2}}(X,Y,\varsigma)
\end{aligned} \tag{5.31}$$

where ξ and ς represent the boundary layer variables in the following forms:

$$\xi = \frac{X}{\epsilon^{1/2}}, \qquad \varsigma = \frac{\pi - X}{\epsilon^{1/2}} \tag{5.32}$$

In addition, it is assumed that

$$\epsilon^{3/2}\frac{4}{3}3^{1/4}q=\sum_{i=0}\epsilon^{i}\mathcal{Q}_{i} \tag{5.33}$$

Thereby, by substituting Eqs. (5.30) and (5.31) into the nonlocal governing differential Eqs. (5.26) and then collecting the expressions having the similar order of ϵ, the sets of perturbation equations can be extracted for both regular and boundary layer solutions. This procedure resumes until a maximum order of ϵ corresponding to which the convergence of the solving process is confirmed. For this purpose, a tolerance limit <0.001 is supposed, and it is indicated that the tolerance limit is achieved up to the forth order of the small perturbation parameter.

To continue the solution methodology, the initial buckling mode shape for the hybrid FGM nanoshell is defined corresponding to axial compression and hydrostatic pressure loading cases, respectively, as follows:

$$\bar{W}_2(X,Y)=\mathcal{A}_{00}^{(2)}+\mathcal{A}_{11}^{(2)}\sin(mX)\sin(nY)+\mathcal{A}_{02}^{(2)}\cos(2nY) \tag{5.34a}$$

$$\bar{W}_2(X,Y)=\mathcal{A}_{00}^{(2)}+\mathcal{A}_{11}^{(2)}\sin(mX)\sin(nY) \tag{5.34b}$$

Afterward, through performing some mathematical calculations, the asymptotic solutions can be extracted relevant to each independent variable as given in Appendix A for each loading case. By inserting them in Eqs. (5.27) and (5.29) and rearranging them in accordance with the order of the second perturbation parameter ($\mathcal{A}_{11}^{(2)}\epsilon$ for combination of axial compression with lateral electric field and $\mathcal{A}_{11}^{(2)}\epsilon^2$ for combination of hydrostatic pressure with lateral electric field), the explicit expressions for the nonlocal stability curves are obtained corresponding to each loading case as below:

- For combination of axial compression with lateral electric field:

$$\wp_x=\sum_{i=0,2,4,\ldots}\wp_x^{(i)}\left(\mathcal{A}_{11}^{(2)}\epsilon\right)^{i}=\wp_x^{(0)}+\wp_x^{(2)}\left(\mathcal{A}_{11}^{(2)}\epsilon\right)^{2}+\wp_x^{(4)}\left(\mathcal{A}_{11}^{(2)}\epsilon\right)^{4}+\ldots \tag{5.35}$$

$$\begin{aligned}\delta_x&=\sum_{i=0,2,4,\ldots}\delta_x^{(i)}\left(\mathcal{A}_{11}^{(2)}\epsilon\right)^{i}+\delta_x^{E}\\&=\delta_x^{(0)}+\delta_x^{E}+\delta_x^{(2)}\left(\mathcal{A}_{11}^{(2)}\epsilon\right)^{2}+\delta_x^{(4)}\left(\mathcal{A}_{11}^{(2)}\epsilon\right)^{4}+\ldots\end{aligned} \tag{5.36}$$

- For combination of hydrostatic pressure with lateral electric field:

$$\wp_q=\sum_{i=0,2,4,\ldots}\wp_q^{(i)}\left(\mathcal{A}_{11}^{(2)}\epsilon^2\right)^{i}=\wp_q^{(0)}+\wp_q^{(2)}\left(\mathcal{A}_{11}^{(2)}\epsilon^2\right)^{2}+\ldots \tag{5.37}$$

$$\delta_q=\sum_{i=0,2,4,\ldots}\delta_q^{(i)}\left(\mathcal{A}_{11}^{(2)}\epsilon^2\right)^{i}+\delta_q^{E}=\delta_q^{(0)}+\delta_q^{E}+\delta_q^{(2)}\left(\mathcal{A}_{11}^{(2)}\epsilon^2\right)^{2}+\ldots \tag{5.38}$$

The parameters presented in the above equations are defined in Appendix B. Now, it is supposed that the dimensionless coordinate of the point in which the maximum deflection occurs is in the form as $(X, Y) = (\pi/2m, \pi/2n)$. So, it yields:

- For combination of axial compression with lateral electric field:

$$\mathcal{A}_{11}^{(2)}\epsilon = \frac{w_m}{h} + \mathcal{S}_2 + \mathcal{S}_1\left(\frac{w_m}{h} + \mathcal{S}_2\right)^2 \tag{5.39}$$

- For combination of hydrostatic pressure with lateral electric field:

$$\mathcal{A}_{11}^{(2)}\epsilon^2 = \epsilon\frac{w_m}{h} + \mathcal{S}_4 + \mathcal{S}_3\left(\epsilon\frac{w_m}{h} + \mathcal{S}_2\right)^2 \tag{5.40}$$

where w_m represents the maximum deflection. Also, the symbols $\mathcal{S}_1, \mathcal{S}_2, \mathcal{S}_3$ and 4 are defined in Appendix B.

5.4 Numerical Results and Discussion

Herein, selected numerical results for nonlocal nonlinear instability of hybrid FGM exponential shear deformable nanoshells subjected to the two types of loading condition are presented. In the preceding presentation of the results, the left and right ends of nanoshell are supposed to be clamped, and $R/h = 50$, $L = 2R$. The properties of FGM substrate made of the mixture of silicon and aluminum and PZT-5H piezoelectric surface layers are tabulated in Table 5.1.

In Fig. 5.2, the nonlocal load-deflection equilibrium paths of hybrid FGM nanoshells under axial compression are depicted corresponding to various values of nonlocal parameter and thickness of FGM substrate. It can be seen that the influence of nonlocality causes to reduce the critical buckling compression, but it increases the minimum load relevant to the postbuckling regime. Furthermore, the width of the postbuckling domain decreases by taking the nonlocal effect into

Table 5.1 Material properties of different phases of hybrid FGM nanoshell (Miller and Shenoy 2000; Yan and Jiang 2011)

Aluminum <1 1 1>	
$E\ (GPa)$	70
ν	0.35
Silicon <1 0 0>	
$E\ (GPa)$	210
ν	0.24
PZT-5H piezoelectric	
$E\ (GPa)$	92.3
ν	0.30
$d_{31}\ (m/V)$	-2.65×10^{-10}
$d_{32}\ (m/V)$	-2.65×10^{-10}

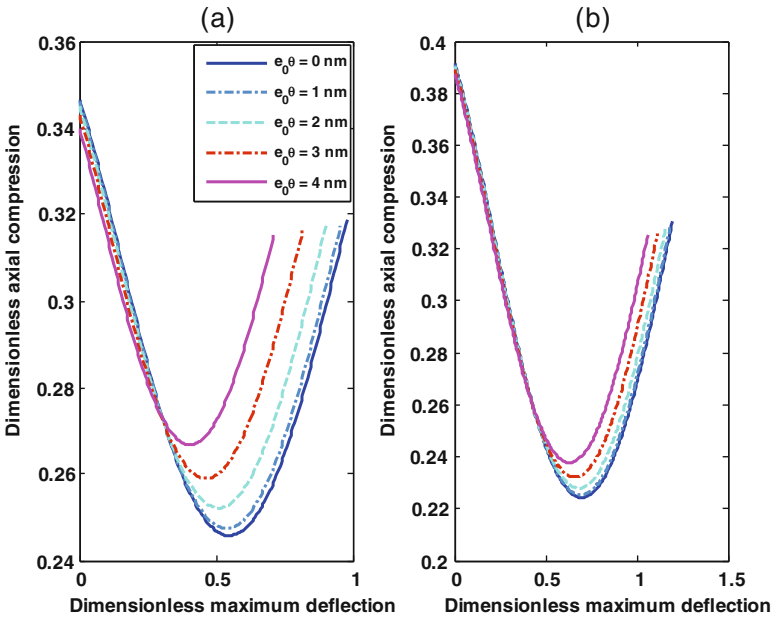

Fig. 5.2 Local and nonlocal load-deflection response of hybrid FGM nanoshells under axial compression corresponding to different nonlocal parameters ($k = 1, h_p = 0.25\ nm, V = k_1 = k_2 = 0$): (**a**) $h_f = 1\ nm$, (**b**) $h_f = 2\ nm$

consideration. These anticipations are more prominent for nanoshells with lower thickness of FGM substrate which indicates that the nonlocality size effect plays more important role in the nonlinear instability of thinner hybrid FGM nanoshells.

Figure 5.3 illustrates the nonlocal load-shortening equilibrium paths of hybrid FGM nanoshells with different nonlocal parameters and thickness of FGM substrate. It is observed that the nonlocal size dependency has a negligible influence on the slope of prebuckling part of the load-shortening equilibrium path of hybrid FGM nanoshell under axial compressive load. Moreover, it can be found that the depth of snap-through phenomenon related to the axial postbuckling behavior decreases due to the nonlocality influence. This pattern is more significant for thinner hybrid FGM nanoshell.

Displayed in Fig. 5.4 are the size-dependent load-deflection equilibrium curves of hybrid FGM nanoshells under hydrostatic pressure corresponding to various values of nonlocal parameter. It can be seen that by taking the influence of nonlocality into consideration, the hybrid FGM nanoshell buckles at lower hydrostatic pressure. Moreover, by moving to deeper part of the postbuckling domain, the size dependency of the nonlinear instability of nanoshell decreases. Additionally, it is found again that for hybrid FGM nanoshells with higher thickness of FGM substrate, the influence of nonlocality on the postbuckling behavior reduces.

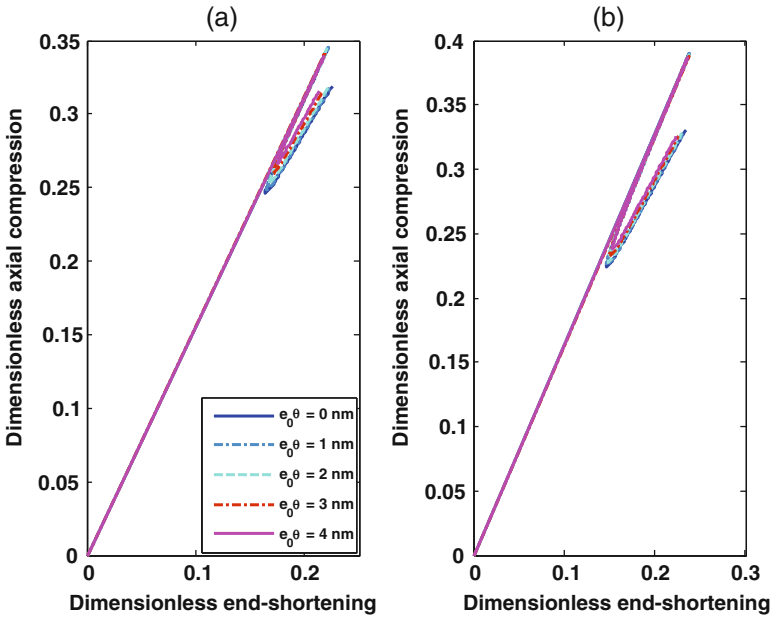

Fig. 5.3 Local and nonlocal load-shortening response of hybrid FGM nanoshells under axial compression corresponding to different nonlocal parameters ($k=1, h_p=0.25\ nm, V=k_1=k_2=0$): (**a**) $h_f=1\ nm$, (**b**) $h_f=2\ nm$

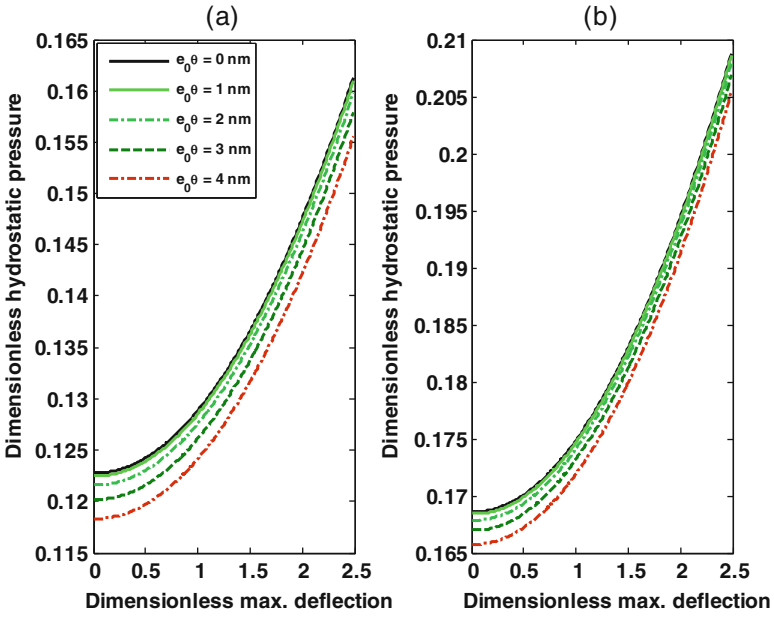

Fig. 5.4 Local and nonlocal load-deflection response of hybrid FGM nanoshells under hydrostatic pressure corresponding to different nonlocal parameters ($k=1, h_p=0.25\ nm, V=k_1=k_2=0$): (**a**) $h_f=1\ nm$, (**b**) $h_f=2\ nm$

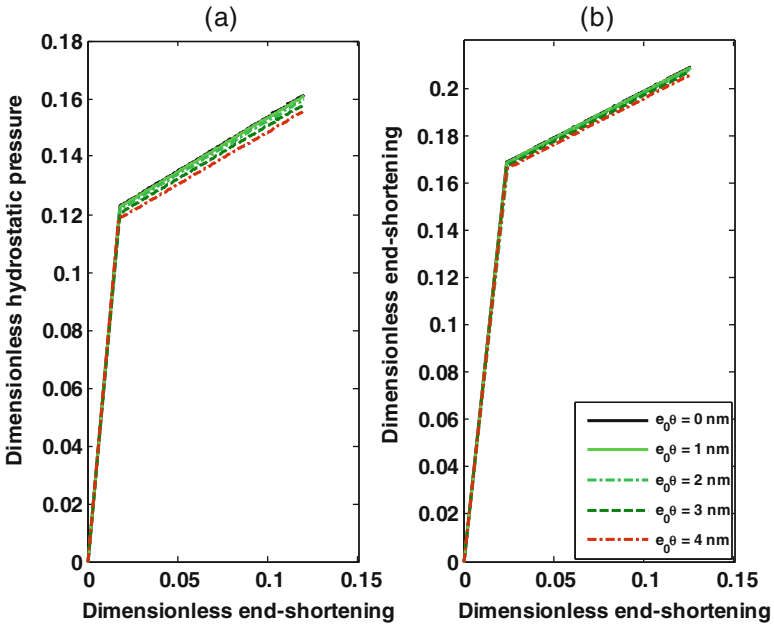

Fig. 5.5 Local and nonlocal load-shortening response of hybrid FGM nanoshells under hydrostatic pressure corresponding to different nonlocal parameters ($k=1, h_p=0.25$ *nm*, $V=k_1=k_2=0$): (**a**) $h_f=1$ *nm*, (**b**) $h_f=2$ *nm*

Figure 5.5 represents the size-dependent load-shortening equilibrium curves including both prebuckling and postbuckling regimes of hybrid FGM nanoshells under hydrostatic pressure with different nonlocal parameters. It is revealed that the nonlocal continuum elasticity has a negligible influence on the slope of prebuckling part of the load-shortening response of hybrid FGM nanoshells. Also, it is seen that the nonlocality size effect causes to decrease the critical hydrostatic pressure, but it leads to increase the associated shortening of the movable ends of nanoshells.

Plotted in Fig. 5.6 are the local and nonlocal load-deflection equilibrium paths of hybrid FGM nanoshells under axial compression with various material property gradient indexes. It is seen that the significance of the influence of material gradient index on the critical buckling compression is approximately the same for the local and nonlocal shell models. However, the reduction of minimum postbuckling load due to the increment in the value of material property gradient index is more considerable in the nonlocal shell model compared to the local one.

Figure 5.7 shows the local and nonlocal load-shortening equilibrium paths for both prebuckling and postbuckling domains of hybrid FGM nanoshells under axial compression with different material property gradient indexes. It is revealed that by moving from the ceramic-rich to metal-rich substrate, the slope of prebuckling part of the load-shortening equilibrium path decreases. Additionally, as it was mentioned before, the nonlocality leads to decrease the depth of the snap-through

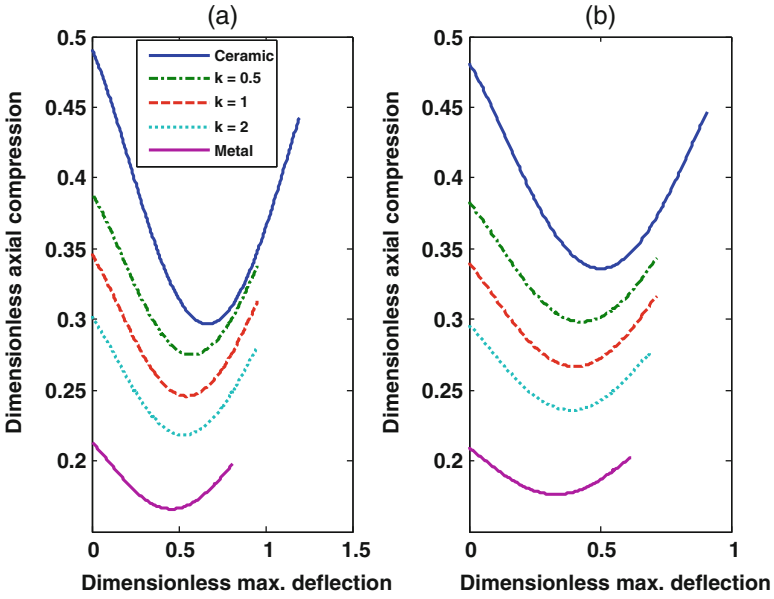

Fig. 5.6 Load-deflection response of hybrid FGM nanoshells under axial compression corresponding to different material property gradient indexes ($h_f = 1$ $nm, h_p = 0.25$ nm, $V = k_1 = k_2 = 0$): (**a**) $e_0\theta = 0$ nm, (**b**) $e_0\theta = 4$ nm

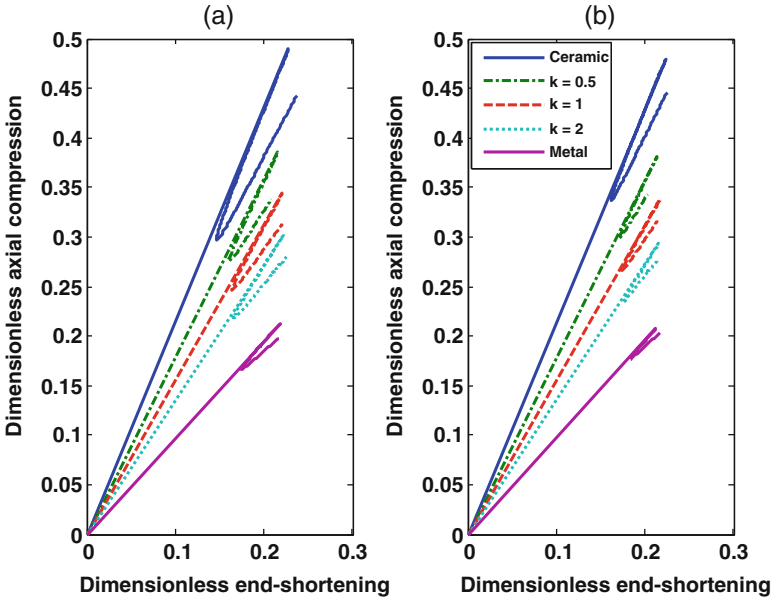

Fig. 5.7 Load-shortening response of hybrid FGM nanoshells under axial compression corresponding to different material property gradient indexes ($h_f = 1$ $nm, h_p = 0.25$ nm, $V = k_1 = k_2 = 0$): (**a**) $e_0\theta = 0$ nm, (**b**) $e_0\theta = 4$ nm

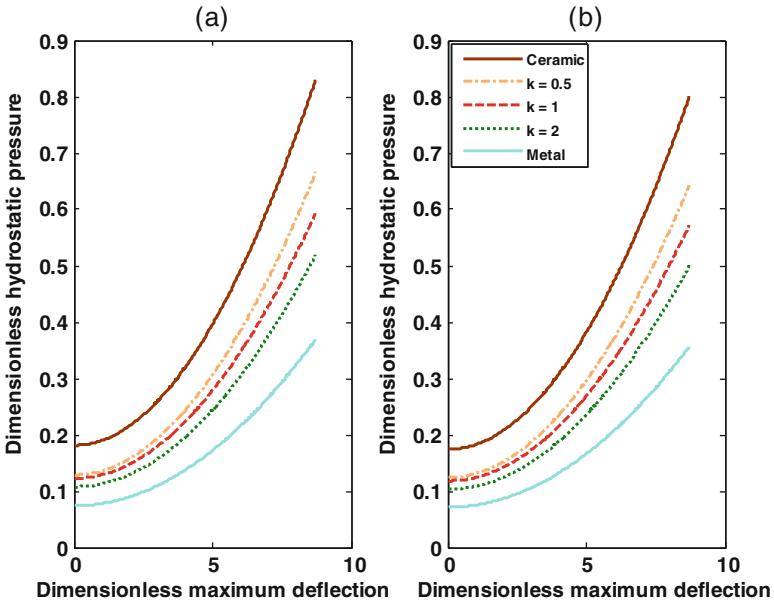

Fig. 5.8 Load-deflection response of hybrid FGM nanoshells under hydrostatic pressure corresponding to different material property gradient indexes ($h_f = 1\ nm, h_p = 0.25\ nm$, $V = k_1 = k_2 = 0$): (**a**) $e_0\theta = 0\ nm$, (**b**) $e_0\theta = 4\ nm$

phenomenon relevant to the postbuckling response of hybrid FGM nanoshell, and this pattern is more significant corresponding to lower value of material property gradient index.

In Fig. 5.8, the effect of material property gradient index on the local and nonlocal load-deflection responses of hybrid FGM nanoshells under hydrostatic pressure is depicted. It can be observed that by moving from the ceramic-rich hybrid nanoshell to metal-rich one, the critical hydrostatic pressure reduces. The intensity of this reduction is approximately the same for both local and nonlocal shell models. In addition, it can be found that by moving to the deeper part of the postbuckling domain, the gap between the load-deflection stability curves of axially loaded hybrid FGM nanoshells becomes more significant.

Plotted in Fig. 5.9 are the local and nonlocal load-shortening responses of hybrid FGM nanoshells under hydrostatic pressure with various material property gradient indexes. It is indicated that by increasing the value of material property gradient index, the slope of load-shortening equilibrium curves of hybrid FGM nanoshell decreases, but this reduction is more considerable in the postbuckling regime in comparison with the prebuckling one. These observations are similar corresponding to both local and nonlocal shell models.

In Fig. 5.10, the local and nonlocal load-deflection equilibrium paths of hybrid FGM nanoshells under combination of axial compression and lateral electric field

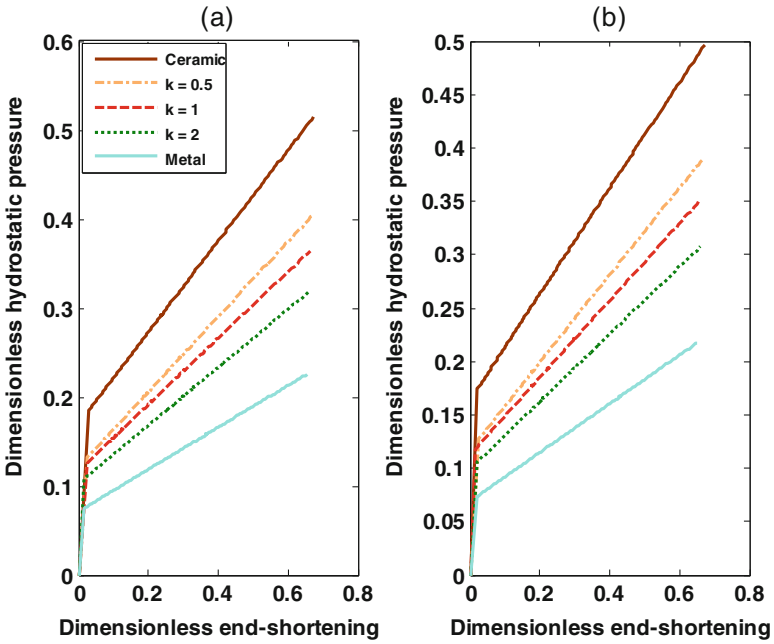

Fig. 5.9 Load-shortening response of hybrid FGM nanoshells under hydrostatic pressure corresponding to different material property gradient indexes ($h_f = 1\ nm, h_p = 0.25\ nm$, $V = k_1 = k_2 = 0$): (**a**) $e_0\theta = 0\ nm$, (**b**) $e_0\theta = 4\ nm$

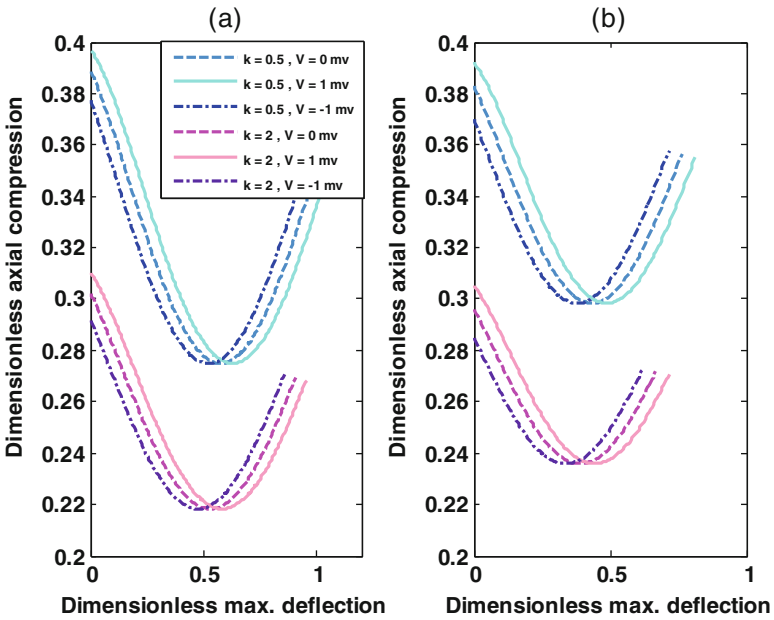

Fig. 5.10 Load-deflection response of axially loaded hybrid FGM nanoshells with different material gradient indexes subjected to various applied voltages ($h_f = 1\ nm, h_p = 0.25\ nm$, $k_1 = k_2 = 0$): (**a**) $e_0\theta = 0\ nm$, (**b**) $e_0\theta = 4\ nm$

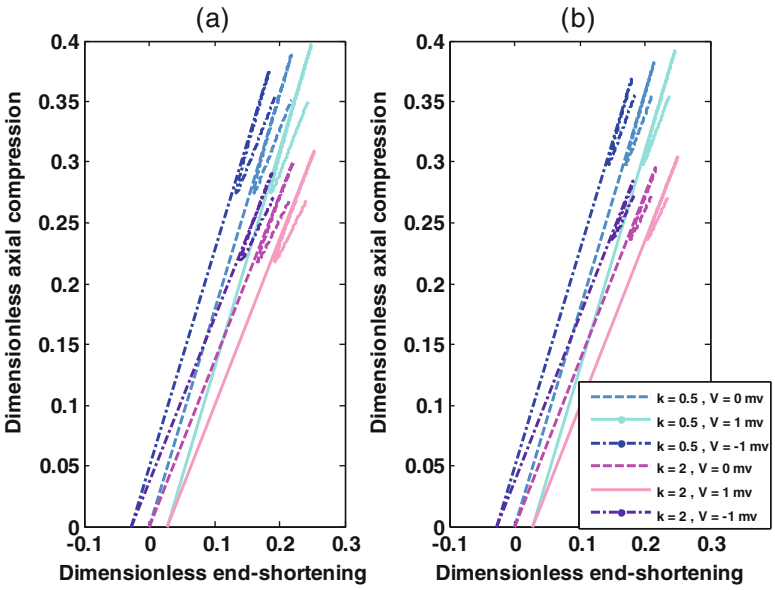

Fig. 5.11 Load-shortening response of axially loaded hybrid FGM nanoshells with different material gradient indexes subjected to various applied voltages ($h_f = 1$ *nm*, $h_p = 0.25$ *nm*, $k_1 = k_2 = 0$): (**a**) $e_0\theta = 0$ *nm*, (**b**) $e_0\theta = 4$ *nm*

created by various values of applied voltage are demonstrated. It can be observed that the lateral electric field created by a positive applied voltage leads to increase the critical buckling compression of an axially loaded hybrid FGM nanoshell, while the lateral electric field coming from a negative voltage causes to reduce it. However, no change occurs for the value of the minimum postbuckling load through applying the external lateral electric field. In addition, it is indicated that the significance in the influence of lateral electric field on the nonlinear instability characteristics of hybrid FGM nanoshell modeled via nonlocal shell model is more than its local counterparts.

Depicted in Fig. 5.11 are the local and nonlocal load-shortening equilibrium paths including both prebuckling and postbuckling domains for hybrid FGM nanoshells under combination of axial compression and lateral electric field coming from various values of applied voltage. It is found that positive and negative applied voltages cause, respectively, initial shortening and initial extension in the hybrid FGM nanoshell. As a result, the value of shortening associated with the critical point increases by applying a positive lateral electric field, and it decreases by a negative one. Also, it is seen that the initial shortening or extension are approximately the same for both local and nonlocal shell models and all values of material property gradient index.

In Fig. 5.12, the local and nonlocal load-deflection characteristics of hybrid FGM nanoshells with different material gradient indexes and subjected to combination of hydrostatic pressure and lateral electric field coming from various applied

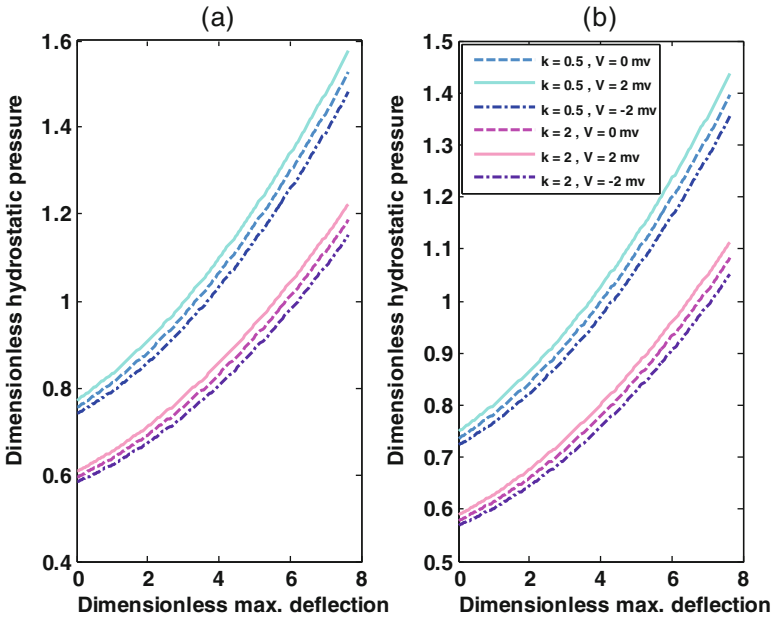

Fig. 5.12 Load-deflection response of hydrostatic pressurized hybrid FGM nanoshells with different material gradient indexes subjected to various applied voltages ($h_f = 1$ *nm*, $h_p = 0.25$ *nm*, $k_1 = k_2 = 0$): (**a**) $e_0\theta = 0$ *nm*, (**b**) $e_0\theta = 4$ *nm*

voltages are illustrated. It is demonstrated that an electric field coming from a positive voltage causes to increase the critical hydrostatic pressure of nanoshells, while negative electric fields lead to reduce it. By moving to the deeper region of the postbuckling regime, the difference between load-deflection equilibrium paths associated with various values of electric field increases. Furthermore, it can be seen that this pattern is somehow more significant in the local shell model compared to the nonlocal one.

Figure 5.13 shows the local and nonlocal load-shortening behavior of hybrid FGM nanoshells under combination of hydrostatic pressure and various lateral electric fields corresponding to different material property gradient indexes. It is observed that a positive value of applied voltage leads to an initial shortening, while a negative one causes an initial extension in the hybrid FGM nanoshell. These initial shortening and extension lead to, respectively, increase and decrease the value of shorting of the movable ends associated with the critical buckling point.

In Figs. 5.14 and 5.15, the influence of the elastic foundation on the load-deflection and load-shortening stability curves of hybrid FGM nanoshells under axial compression is demonstrated, respectively. It can be seen that by adding the Winkler elastic foundation, both the critical buckling load and minimum postbuckling load increase, but no change occurs for the width of the postbuckling regime. However, the Pasternak foundation including shear stiffness causes to enhance the buckling and minimum postbuckling loads, and also it increases the

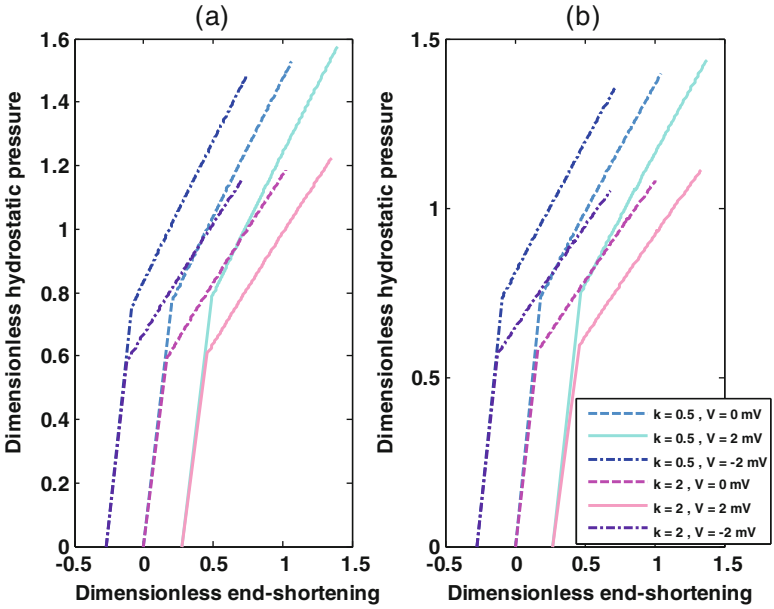

Fig. 5.13 Load-shortening response of hydrostatic pressurized hybrid FGM nanoshells with different material gradient indexes subjected to various applied voltages ($h_f = 1$ *nm*, $h_p = 0.25$ *nm*, $k_1 = k_2 = 0$): (**a**) $e_0\theta = 0$ *nm*, (**b**) $e_0\theta = 4$ *nm*

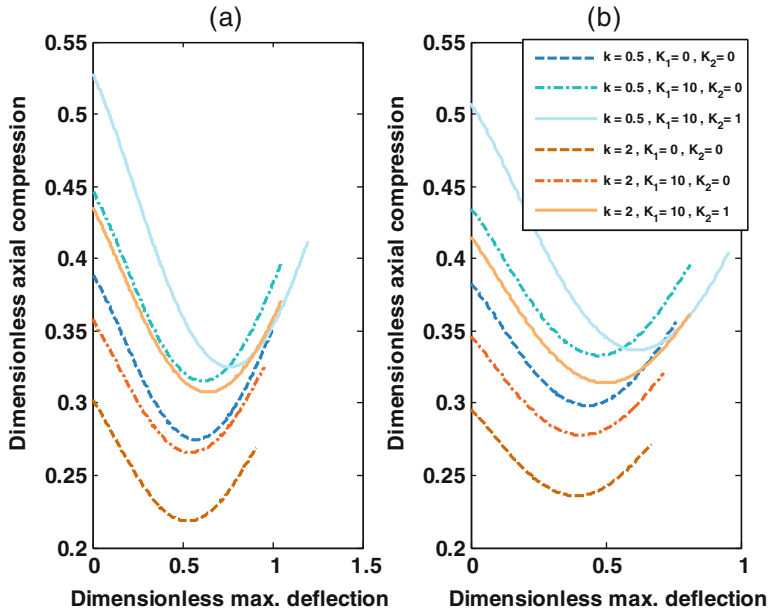

Fig. 5.14 Influence of the elastic foundation on load-deflection response of axially loaded hybrid FGM nanoshells with different material gradient indexes ($h_f = 1$ *nm*, $h_p = 0.25$ *nm*, $V = 0$): (**a**) $e_0\theta = 0$ *nm*, (**b**) $e_0\theta = 4$ *nm*

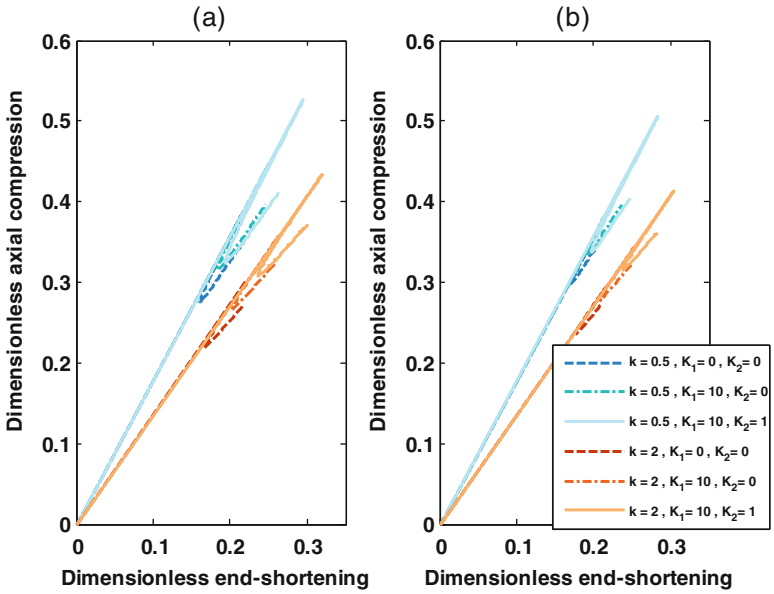

Fig. 5.15 Influence of the elastic foundation on load-shortening response of axially loaded hybrid FGM nanoshells with different material gradient indexes ($h_f = 1\ nm, h_p = 0.25\ nm, V = 0$): (**a**) $e_0\theta = 0\ nm$, (**b**) $e_0\theta = 4\ nm$

width of the postbuckling domain which leads to higher maximum deflection associated with the minimum postbuckling load. Moreover, it can be observed that the influence of the Pasternak elastic foundation on the value of minimum postbuckling load is less than its influence on the critical buckling load, and this pattern is more significant by taking nonlocal size dependency into account. Additionally, it is seen that the elastic foundation has no influence on the slope of prebuckling part of the load-shortening response, but it enhances the shortening of hybrid FGM nanoshell at the critical buckling point.

5.5 Conclusion

In the current study, the nonlocal size dependency in the nonlinear instability characteristics of FGM nanoshells integrated with piezoelectric face sheets and embedded in an elastic medium was investigated under two different loading conditions including axial compression and hydrostatic pressure combined with external lateral electric field. It was observed that the influence of nonlocality causes to reduce the critical buckling compression, but in the case of axially loaded, it increases the minimum load relevant to the postbuckling regime. Furthermore, the width of the postbuckling domain decreases by taking the nonlocal effect into

consideration. In addition, it was found that an electric field coming from a positive voltage causes to increase the critical load, while a negative electric field leads to reduce it. However, in the case of axially loaded, it was seen that the external electric field has no influence on the minimum postbuckling load. By moving to the deeper region of the postbuckling regime, the difference between load-deflection equilibrium paths associated with various values of electric field increases.

Also, it was indicated that by adding the Winkler elastic foundation, both the critical buckling load and minimum postbuckling load increase, but no change occurs for the width of the postbuckling regime. However, the Pasternak foundation including shear stiffness causes to enhance the buckling and minimum postbuckling loads, and also it increases the width of the postbuckling domain which leads to higher maximum deflection associated with the minimum postbuckling load. Moreover, it can be observed that the influence of the Pasternak elastic foundation on the value of minimum postbuckling load is less than its influence on the critical buckling load, and this pattern is more significant by taking nonlocal size dependency into account.

Appendix A

$$\varphi_1 = \frac{A_{11}^*}{\left(A_{11}^*\right)^2 - \left(A_{12}^*\right)^2}, \quad \varphi_2 = \frac{A_{12}^*}{\left(A_{11}^*\right)^2 - \left(A_{12}^*\right)^2}, \quad \varphi_3 = \frac{A_{11}^* B_{11}^* - A_{12}^* B_{12}^*}{\left(A_{11}^*\right)^2 - \left(A_{12}^*\right)^2}$$

$$\varphi_4 = \frac{A_{11}^* B_{12}^* - A_{12}^* B_{11}^*}{\left(A_{11}^*\right)^2 - \left(A_{12}^*\right)^2}, \quad \varphi_5 = \frac{A_{11}^* B_{11}^{**} - A_{12}^* B_{12}^{**}}{\left(A_{11}^*\right)^2 - \left(A_{12}^*\right)^2}, \quad \varphi_6 = \frac{A_{11}^* B_{12}^{**} - A_{12}^* B_{11}^{**}}{\left(A_{11}^*\right)^2 - \left(A_{12}^*\right)^2}$$

$$\varphi_7 = \frac{1}{A_{66}^*}, \quad \varphi_8 = \frac{B_{66}^*}{A_{66}^*}, \quad \varphi_9 = \frac{B_{66}^{**}}{A_{66}^*}$$

$$\begin{aligned}
&\varphi_{10} = D_{11}^* - B_{11}^* \varphi_3 - B_{12}^* \varphi_4, && \varphi_{11} = D_{12}^* - B_{11}^* \varphi_3 - B_{12}^* \varphi_4 \\
&\varphi_{12} = D_{66}^* - B_{66}^* \varphi_8, && \varphi_{13} = B_{11}^* \varphi_5 + B_{12}^* \varphi_6 - D_{11}^{**} \\
&\varphi_{14} = B_{12}^* \varphi_5 + B_{11}^* \varphi_6 - D_{12}^{**}, && \varphi_{15} = B_{66}^{**} \varphi_9 - D_{66}^{**} \\
&\varphi_{16} = B_{12}^{**} \varphi_1 - B_{11}^{**} \varphi_2, && \varphi_{17} = B_{11}^{**} \varphi_1 - B_{12}^{**} \varphi_2 - B_{66}^{**} \varphi_7 \\
&\varphi_{18} = B_{11}^{**} \varphi_3 + B_{12}^{**} \varphi_4 - D_{11}^{**}, && \varphi_{19} = B_{12}^{**} \varphi_3 + B_{11}^{**} \varphi_4 - D_{12}^{**} \\
&\varphi_{20} = B_{66}^{**} \varphi_8 - D_{66}^{**}, && \varphi_{21} = G_{11}^* - B_{11}^{**} \varphi_5 - B_{12}^{**} \varphi_6 \\
&\varphi_{22} = G_{66}^* - B_{66}^{**} \varphi_9, && \varphi_{23} = G_{12}^* - B_{11}^{**} \varphi_6 - B_{12}^{**} \varphi_5
\end{aligned} \tag{5.A1}$$

This point should be noted that the parameters of $\vartheta_i \quad (i = 1, \ldots, 23)$ are the dimensionless form of φ_i.

The solutions in asymptotic forms corresponding to each of independent variables are extracted as below:

- For combination of axial compression and lateral electric field loading case:

$$
\begin{aligned}
W = {} & \mathcal{A}_{00}^{(0)} + \epsilon \left[\mathcal{A}_{00}^{(1)} - \mathcal{A}_{00}^{(1)} \left(\sin\left(\frac{\Gamma_1 X}{\sqrt{\epsilon}}\right) + \cos\left(\frac{\Gamma_1 X}{\sqrt{\epsilon}}\right) \right) e^{-\frac{\Gamma_2 X}{\sqrt{\epsilon}}} \right. \\
& \left. - \mathcal{A}_{00}^{(1)} \left(\sin\left(\frac{\Gamma_1 (\pi - X)}{\sqrt{\epsilon}}\right) + \cos\left(\frac{\Gamma_1 (\pi - X)}{\sqrt{\epsilon}}\right) \right) e^{-\frac{\Gamma_2 (\pi - X)}{\sqrt{\epsilon}}} \right] \\
& + \epsilon^2 \left[\mathcal{A}_{00}^{(2)} + \mathcal{A}_{11}^{(2)} \sin(mX) \sin(nY) + \mathcal{A}_{02}^{(2)} \cos(2nY) \right. \\
& - \left(\mathcal{A}_{00}^{(2)} + \mathcal{A}_{02}^{(2)} \cos(2nY) \right) \left(\sin\left(\frac{\Gamma_1 X}{\sqrt{\epsilon}}\right) + \cos\left(\frac{\Gamma_1 X}{\sqrt{\epsilon}}\right) \right) e^{-\frac{\Gamma_2 X}{\sqrt{\epsilon}}} \\
& \left. - \left(\mathcal{A}_{00}^{(2)} + \mathcal{A}_{02}^{(2)} \cos(2nY) \right) \left(\sin\left(\frac{\Gamma_1 (\pi - X)}{\sqrt{\epsilon}}\right) + \cos\left(\frac{\Gamma_1 (\pi - X)}{\sqrt{\epsilon}}\right) \right) e^{-\frac{\Gamma_2 (\pi - X)}{\sqrt{\epsilon}}} \right] \\
& + \epsilon^3 \left[\mathcal{A}_{00}^{(3)} + \mathcal{A}_{11}^{(3)} \sin(mX) \sin(nY) + \mathcal{A}_{02}^{(3)} \cos(2nY) \right] \\
& + \epsilon^4 [\mathcal{A}_{00}^{(4)} + \mathcal{A}_{11}^{(4)} \sin(mX) \sin(nY) + \mathcal{A}_{20}^{(4)} \cos(2mX) + \mathcal{A}_{02}^{(4)} \cos(2nY) \\
& + \mathcal{A}_{13}^{(4)} \sin(mX) \sin(3nY) + \mathcal{A}_{22}^{(4)} \cos(2mX) \cos(2nY)] + O(\epsilon^5)
\end{aligned}
\tag{5.A2}
$$

$$
\begin{aligned}
F = {} & -\mathscr{B}_{00}^{(0)} \frac{Y^2}{2} + \epsilon^2 \left[-\mathscr{B}_{00}^{(2)} \frac{Y^2}{2} + \mathscr{B}_{11}^{(2)} \sin(mX) \sin(nY) + \mathscr{B}_{02}^{(2)} \cos(2nY) \right. \\
& + \mathcal{A}_{00}^{(1)} \left(\mathscr{k}_{10}^{(2)} \sin\left(\frac{\Gamma_1 X}{\sqrt{\epsilon}}\right) + \mathscr{k}_{01}^{(2)} \cos\left(\frac{\Gamma_1 X}{\sqrt{\epsilon}}\right) \right) e^{-\frac{\Gamma_2 X}{\sqrt{\epsilon}}} \\
& \left. + \mathcal{A}_{00}^{(1)} \left(\mathscr{k}_{10}^{(2)} \sin\left(\frac{\Gamma_1 (\pi - X)}{\sqrt{\epsilon}}\right) + \mathscr{k}_{01}^{(2)} \cos\left(\frac{\Gamma_1 (\pi - X)}{\sqrt{\epsilon}}\right) \right) e^{-\frac{\Gamma_2 (\pi - X)}{\sqrt{\epsilon}}} \right] \\
& + \epsilon^3 \left[-\mathscr{B}_{00}^{(3)} \frac{Y^2}{2} + \mathscr{B}_{02}^{(3)} \cos(2nY) \right. \\
& + \left(\mathcal{A}_{00}^{(2)} + \mathcal{A}_{02}^{(2)} \cos(2nY) \right) \left(\mathscr{k}_{10}^{(3)} \sin\left(\frac{\Gamma_1 X}{\sqrt{\epsilon}}\right) + \mathscr{k}_{01}^{(3)} \cos\left(\frac{\Gamma_1 X}{\sqrt{\epsilon}}\right) \right) e^{-\frac{\Gamma_2 X}{\sqrt{\epsilon}}} \\
& \left. + \left(\mathcal{A}_{00}^{(2)} + \mathcal{A}_{02}^{(2)} \cos(2nY) \right) \left(\mathscr{k}_{10}^{(3)} \sin\left(\frac{\Gamma_1 (\pi - X)}{\sqrt{\epsilon}}\right) + \mathscr{k}_{01}^{(3)} \cos\left(\frac{\Gamma_1 (\pi - X)}{\sqrt{\epsilon}}\right) \right) e^{-\frac{\Gamma_2 (\pi - X)}{\sqrt{\epsilon}}} \right] \\
& + \epsilon^4 \left[-\mathscr{B}_{00}^{(4)} \frac{Y^2}{2} + \mathscr{B}_{20}^{(4)} \cos(2\boldsymbol{m}\boldsymbol{X}) + \mathscr{B}_{13}^{(4)} \sin(mX) \sin(3nY) \right. \\
& \left. + \mathscr{B}_{22}^{(4)} \cos(2mX) \cos(2nY) \right] + O(\epsilon^5)
\end{aligned}
\tag{5.A3}
$$

$$\begin{aligned}\Psi_X = {} & \epsilon^{3/2}\left[\mathcal{A}_{00}^{(1)}c_{10}^{(3/2)}\sin\left(\frac{\Gamma_1 X}{\sqrt{\epsilon}}\right)e^{-\frac{\Gamma_2 X}{\sqrt{\epsilon}}}+\mathcal{A}_{00}^{(1)}c_{10}^{(3/2)}\sin\left(\frac{\Gamma_1(\pi-X)}{\sqrt{\epsilon}}\right)e^{-\frac{\Gamma_2(\pi-X)}{\sqrt{\epsilon}}}\right]\\ & +\epsilon^2\left[\boldsymbol{e}_{11}^{(2)}\cos(mX)\sin(nY)\right]\\ & +\epsilon^{5/2}\left[\left(\mathcal{A}_{00}^{(2)}+\mathcal{A}_{02}^{(2)}\cos(2nY)\right)c_{10}^{(5/2)}\sin\left(\frac{\Gamma_1 X}{\sqrt{\epsilon}}\right)e^{-\frac{\Gamma_2 X}{\sqrt{\epsilon}}}\right.\\ & \left.+\left(\mathcal{A}_{00}^{(2)}+\mathcal{A}_{02}^{(2)}\cos(2nY)\right)\rfloor_{10}^{(5/2)}\sin\left(\frac{\Gamma_1(\pi-X)}{\sqrt{\epsilon}}\right)e^{-\frac{\Gamma_2(\pi-X)}{\sqrt{\epsilon}}}\right]\\ & +\epsilon^3\left[\boldsymbol{e}_{11}^{(3)}\cos(mX)\sin(nY)\right]\\ & +\epsilon^4\left[\boldsymbol{e}_{11}^{(4)}\cos(mX)\sin(nY)+\boldsymbol{e}_{20}^{(4)}\sin(2mX)+\boldsymbol{e}_{13}^{(4)}\cos(mX)\sin(3nY)\right]\\ & +O(\epsilon^5)\end{aligned} \tag{5.A4}$$

$$\begin{aligned}\Psi_Y = {} & \epsilon^2\left[\mathcal{D}_{11}^{(2)}\sin(mX)\cos(nY)\right]\\ & +\epsilon^3\left[\mathcal{D}_{11}^{(3)}\sin(mX)\cos(nY)+\mathcal{D}_{02}^{(3)}\sin(2nY)\right.\\ & -2\mathcal{A}_{02}^{(2)}\beta n\sin(2nY)\left(d_{10}^{(3)}\sin\left(\frac{\Gamma_1 X}{\sqrt{\epsilon}}\right)+\boldsymbol{d}_{01}^{(3)}\cos\left(\frac{\Gamma_1 X}{\sqrt{\epsilon}}\right)\right)e^{-\frac{\Gamma_2 X}{\sqrt{\epsilon}}}\\ & \left.-2\mathcal{A}_{02}^{(2)}\beta n\sin(2nY)\left(\boldsymbol{d}_{10}^{(3)}\sin\left(\frac{\Gamma_1(\pi-X)}{\sqrt{\epsilon}}\right)+\boldsymbol{d}_{01}^{(3)}\cos\left(\frac{\Gamma_1(\pi-X)}{\sqrt{\epsilon}}\right)\right)e^{-\frac{\Gamma_2(\pi-X)}{\sqrt{\epsilon}}}\right]\\ & +\epsilon^4\left[\mathcal{D}_{11}^{(4)}\sin(mX)\cos(nY)+\mathcal{D}_{02}^{(4)}\sin(2nY)+\mathcal{D}_{13}^{(4)}\sin(mX)\cos(3nY)\right]\\ & +O(\epsilon^5)\end{aligned} \tag{5.A5}$$

- For combination of hydrostatic pressure and lateral electric field loading case:

$$\begin{aligned}W = {} & \mathcal{A}_{00}^{(0)}+\epsilon^{3/2}\left[\mathcal{A}_{00}^{(3/2)}-\mathcal{A}_{00}^{(3/2)}\left(\sin\left(\frac{\Gamma_1 X}{\sqrt{\epsilon}}\right)+\cos\left(\frac{\Gamma_1 X}{\sqrt{\epsilon}}\right)\right)e^{-\frac{\Gamma_2 X}{\sqrt{\epsilon}}}\right.\\ & \left.-\mathcal{A}_{00}^{(3/2)}\left(\sin\left(\frac{\Gamma_1(\pi-X)}{\sqrt{\epsilon}}\right)+\cos\left(\frac{\Gamma_1(\pi-X)}{\sqrt{\epsilon}}\right)\right)e^{-\frac{\Gamma_2(\pi-X)}{\sqrt{\epsilon}}}\right]\\ & +\epsilon^2\left[\mathcal{A}_{00}^{(2)}+\mathcal{A}_{11}^{(2)}\sin(mX)\sin(nY)-\mathcal{A}_{00}^{(2)}\left(\sin\left(\frac{\Gamma_1 X}{\sqrt{\epsilon}}\right)+\cos\left(\frac{\Gamma_1 X}{\sqrt{\epsilon}}\right)\right)e^{-\frac{\Gamma_2 X}{\sqrt{\epsilon}}}\right.\\ & \left.-\mathcal{A}_{00}^{(2)}\left(\sin\left(\frac{\Gamma_1(\pi-X)}{\sqrt{\epsilon}}\right)+\cos\left(\frac{\Gamma_1(\pi-X)}{\sqrt{\epsilon}}\right)\right)e^{-\frac{\Gamma_2(\pi-X)}{\sqrt{\epsilon}}}\right]\\ & +\epsilon^3\left[\mathcal{A}_{00}^{(3)}+\mathcal{A}_{11}^{(3)}\sin(mX)\sin(nY)\right]\\ & +\epsilon^4\left[\mathcal{A}_{00}^{(4)}+\mathcal{A}_{11}^{(4)}\sin(mX)\sin(nY)+\mathcal{A}_{20}^{(4)}\cos(2mX)+\mathcal{A}_{02}^{(4)}\cos(2nY)\right]+O(\epsilon^5)\end{aligned} \tag{5.A6}$$

$$
\begin{aligned}
F = \quad & -\mathscr{B}_{00}^{(0)}\left(\beta^2X^2+\frac{Y^2}{2}\right)+\epsilon\left[-\mathscr{B}_{00}^{(1)}\left(\beta^2X^2+\frac{Y^2}{2}\right)\right]\\
& +\epsilon^2\left[-\mathscr{B}_{00}^{(2)}\left(\beta^2X^2+\frac{Y^2}{2}\right)+\mathscr{B}_{11}^{(2)}\sin(mX)\sin(nY)\right]\\
& +\epsilon^{5/2}\left[\mathcal{A}_{00}^{(3/2)}\left(\mathscr{k}_{10}^{(2)}\sin\left(\frac{\Gamma_1X}{\sqrt{\epsilon}}\right)+\mathscr{k}_{01}^{(2)}\cos\left(\frac{\Gamma_1X}{\sqrt{\epsilon}}\right)\right)e^{-\frac{\Gamma_2X}{\sqrt{\epsilon}}}\right.\\
& \left.+\mathcal{A}_{00}^{(3/2)}\left(\mathscr{k}_{10}^{(2)}\sin\left(\frac{\Gamma_1(\pi-X)}{\sqrt{\epsilon}}\right)+\mathscr{k}_{01}^{(2)}\cos\left(\frac{\Gamma_1(\pi-X)}{\sqrt{\epsilon}}\right)\right)e^{-\frac{\Gamma_2(\pi-X)}{\sqrt{\epsilon}}}\right]\\
& +\epsilon^3\left[-\mathscr{B}_{00}^{(3)}\left(\beta^2X^2+\frac{Y^2}{2}\right)+\mathcal{A}_{00}^{(2)}\left(\mathscr{k}_{10}^{(3)}\sin\left(\frac{\Gamma_1X}{\sqrt{\epsilon}}\right)+\mathscr{k}_{01}^{(3)}\cos\left(\frac{\Gamma_1X}{\sqrt{\epsilon}}\right)\right)e^{-\frac{\Gamma_2X}{\sqrt{\epsilon}}}\right.\\
& \left.+\mathcal{A}_{00}^{(2)}\left(\mathscr{k}_{10}^{(3)}\sin\left(\frac{\Gamma_1(\pi-X)}{\sqrt{\epsilon}}\right)+\mathscr{k}_{01}^{(3)}\cos\left(\frac{\Gamma_1(\pi-X)}{\sqrt{\epsilon}}\right)\right)e^{-\frac{\Gamma_2(\pi-X)}{\sqrt{\epsilon}}}\right]\\
& +\epsilon^4\left[-\mathscr{B}_{00}^{(4)}\left(\beta^2X^2+\frac{Y^2}{2}\right)+\mathscr{B}_{20}^{(4)}\cos(2mX)+\mathscr{B}_{02}^{(4)}\cos(2nY)\right]\\
& +O\left(\epsilon^5\right)
\end{aligned}
\tag{5.A7}
$$

$$
\begin{aligned}
\Psi_X = \epsilon^2 & \left[\mathscr{C}_{11}^{(2)}\cos(mX)\sin(nY)+\left(c_{10}^{(2)}\sin\left(\frac{\Gamma_1X}{\sqrt{\epsilon}}\right)+c_{01}^{(2)}\cos\left(\frac{\Gamma_1X}{\sqrt{\epsilon}}\right)\right)e^{-\frac{\Gamma_2X}{\sqrt{\epsilon}}}\right.\\
& \left.+\left(c_{10}^{(2)}\sin\left(\frac{\Gamma_1(\pi-X)}{\sqrt{\epsilon}}\right)+c_{01}^{(2)}\cos\left(\frac{\Gamma_1(\pi-X)}{\sqrt{\epsilon}}\right)\right)e^{-\frac{\Gamma_2(\pi-X)}{\sqrt{\epsilon}}}\right]\\
& +\epsilon^3\left[\mathscr{C}_{11}^{(3)}\cos(mX)\sin(nY)\right]+\epsilon^4\left[\mathscr{C}_{11}^{(4)}\cos(mX)\sin(nY)+\mathscr{C}_{20}^{(4)}\sin(2mX)\right]\\
& +O\left(\epsilon^5\right)
\end{aligned}
\tag{5.A8}
$$

$$
\begin{aligned}
\Psi_Y = \epsilon^2 & \left[\mathcal{D}_{11}^{(2)}\sin(mX)\cos(nY)\right]+\epsilon^3\left[\mathcal{D}_{11}^{(3)}\sin(mX)\cos(nY)\right]\\
& +\epsilon^4\left[\mathcal{D}_{11}^{(4)}\sin(mX)\cos(nY)+\mathcal{D}_{02}^{(4)}\sin(2nY)\right]+O\left(\epsilon^5\right)
\end{aligned}
\tag{5.A9}
$$

in which

$$
\Gamma_1=\sqrt{\frac{\sqrt{\frac{1}{\vartheta_1\vartheta_{10}+\vartheta_4^2}}+\frac{\vartheta_4}{\vartheta_1\vartheta_{10}+\vartheta_4^2}}{2}}\qquad,\qquad \Gamma_2=\sqrt{\frac{\sqrt{\frac{1}{\vartheta_1\vartheta_{10}+\vartheta_4^2}}-\frac{\vartheta_4}{\vartheta_1\vartheta_{10}+\vartheta_4^2}}{2}}
\tag{5.A10}
$$

Appendix B

$$\wp_x^{(0)} = \frac{1}{2}\left\{\mathcal{U}_0\epsilon^{-1} + \mathcal{U}_3\epsilon\right\} \tag{5.B1}$$

$$\wp_x^{(2)} = -\frac{1}{2}\Bigg\{\left(\frac{6\mathcal{U}_0^2\mathcal{U}_8}{K_2}\right)\epsilon^{-1} - \left(2\mathcal{U}_6\mathcal{U}_8 + \frac{\mathcal{U}_0\mathcal{U}_4\mathcal{U}_8^2H_{20} + 4\mathcal{U}_0\mathcal{U}_5\mathcal{U}_8H_{20}}{2(\mathcal{U}_0H_{20} - \mathcal{U}_4)} + \frac{\mathcal{U}_0^2\mathcal{U}_8^2H_{20} + 4\mathcal{U}_0\mathcal{U}_5\mathcal{U}_8}{2(\mathcal{U}_0H_{20} - \mathcal{U}_4)} + \frac{\mathcal{U}_0^2\mathcal{U}_8^2 + 4\mathcal{U}_0\mathcal{U}_5\mathcal{U}_8}{2(\mathcal{U}_0 - \mathcal{U}_4)}\right)\epsilon\Bigg\} \tag{5.B2}$$

$$\wp_x^{(4)} = \frac{1}{2}\left\{\left(\frac{12\mathcal{U}_0^3\mathcal{U}_7\mathcal{U}_8\mathcal{U}_9H_{13}}{\mathcal{U}_2^2(\mathcal{U}_0H_{13} - \mathcal{U}_7)} + \frac{4\mathcal{U}_0^3\mathcal{U}_8\mathcal{U}_9(\mathcal{U}_0 + 2\mathcal{U}_7)}{\mathcal{U}_2^2(\mathcal{U}_0 - \mathcal{U}_7)} + \frac{16\mathcal{U}_0^3\mathcal{U}_8^2}{\mathcal{U}_2^2}\right)\epsilon^{-1}\right\} \tag{5.B3}$$

$$\delta_x^{(0)} = \wp_x\left(\vartheta_1 - \frac{2\vartheta_2^2\Gamma_2}{\pi\vartheta_1\left(\Gamma_1^2 + \Gamma_2^2\right)}\epsilon^{1/2}\right) + \frac{\left(\Gamma_1^2 + \Gamma_2^2\right)\vartheta_2^2\wp_x^2}{2\pi\Gamma_2}\epsilon^{1/2} \tag{5.B4}$$

$$\delta_x^{(2)} = \frac{m^2\epsilon}{16} \tag{5.B5}$$

$$\delta_x^{(4)} = \left[\frac{\left(\Gamma_1^2 + \Gamma_2^2\right)\mathcal{U}_0^2}{4\pi\Gamma_2\left(\mathcal{U}_5 + \mathcal{U}_2\mathcal{U}_6\right)^2}\right]\epsilon^{-3/2} + \frac{m^2}{4}\left(\frac{\mathcal{U}_0\mathcal{U}_8H_{20} + 4\mathcal{U}_5}{4(\mathcal{U}_0H_{20} - \mathcal{U}_4)}\right)^2\epsilon^3 \tag{5.B6}$$

$$\frac{\delta_x^E = \boldsymbol{d}_{31}R\mathcal{V}}{2hh_p} \tag{5.B7}$$

$$\wp_q^{(0)} = \mathcal{U}_0\mathcal{U}_1\mathcal{U}_8 + \mathcal{U}_2\mathcal{U}_8\epsilon^2 \tag{5.B8}$$

$$\begin{aligned}\wp_q^{(2)} = {} & 8\mathcal{U}_1\mathcal{U}_3\mathcal{U}_7\mathcal{U}_8 + \frac{8\mathcal{U}_1\mathcal{U}_3\mathcal{U}_8(\mathcal{U}_0\mathcal{U}_1\mathcal{U}_6\mathcal{U}_8H_{20} + \mathcal{U}_0\mathcal{U}_3\mathcal{U}_5H_{20})}{\mathcal{U}_0\mathcal{U}_1\mathcal{U}_8H_{20} - \mathcal{U}_5} \\ & + \frac{8\mathcal{U}_1\mathcal{U}_3\left(\mathcal{U}_0\mathcal{U}_6 + \mathcal{U}_0^2\mathcal{U}_3H_{20}\right)}{\mathcal{U}_0\mathcal{U}_1\mathcal{U}_8H_{20} - \mathcal{U}_5} + \frac{8\mathcal{U}_0\mathcal{U}_1\mathcal{U}_3(\mathcal{U}_6 + \mathcal{U}_0\mathcal{U}_3)}{\mathcal{U}_0\mathcal{U}_1\mathcal{U}_8 - \mathcal{U}_5} \\ & + 16\mathcal{U}_0\mathcal{U}_3\mathcal{U}_4\mathcal{U}_8\end{aligned} \tag{5.B9}$$

$$\begin{aligned}\delta_q^{(0)} = {} & \left[\frac{\vartheta_1}{2} - \vartheta_2 + \left(\frac{\left(2\vartheta_1\vartheta_2 - \vartheta_2^2\right)\Gamma_2}{\pi\vartheta_1\left(\Gamma_1^2 + \Gamma_2^2\right)}\right)\epsilon^{1/2}\right]\wp_q \\ & + \left[\left(\frac{3^{1/4}\left(\Gamma_1^2 + \Gamma_2^2\right)(2\vartheta_1 - \vartheta_2)^2}{6\pi\Gamma_2}\right)\epsilon\right]\wp_q^2\end{aligned} \tag{5.B10}$$

$$\delta_q^{(2)} = \left[\frac{3^{3/4}m^2}{32}\right]\epsilon^{-3/2} \tag{5.B11}$$

$$\delta_q^{E} = \left(\frac{\frac{3^{3/4}}{4}\boldsymbol{d}_{31}R\mathcal{V}}{hh_p}\right)\epsilon^{1/2} \tag{5.B12}$$

where

$$\begin{aligned} H_{11} &= 1+\pi^2\mathcal{G}^2\left(m^2+\beta^2n^2\right) \quad , \quad H_{02} = 1+4\pi^2\mathcal{G}^2\beta^2n^2 \\ H_{20} &= 1+4\pi^2\mathcal{G}^2m^2 \quad , \quad H_{13} = 1+\pi^2\mathcal{G}^2\left(m^2+9\beta^2n^2\right) \end{aligned} \tag{5.B13}$$

where $\mathcal{U}_i \quad (i=0,\ldots,9)$ are constant parameters extracted via the perturbation sets of equations.

$$\mathcal{S}_1 = -\frac{\mathcal{U}_0}{\mathcal{U}_5+\mathcal{U}_2\mathcal{U}_6}\epsilon^{-1} + 2\vartheta_2\wp_x^{(2)} \tag{5.B14}$$

$$\frac{\mathcal{S}_2 = 2\vartheta_2\wp_x^{(0)} + \boldsymbol{d}_{32}R\mathcal{V}}{hh_p} \tag{5.B15}$$

$$\mathcal{S}_1 = -\left[(2\vartheta_1-\vartheta_2)\left(\wp_q^{(2)}\right)\right] \tag{5.B16}$$

$$\mathcal{S}_2 = -(2\vartheta_1-\vartheta_2)\left(\wp_q^{(0)}\right) + \left(\frac{\boldsymbol{d}_{32}R\mathcal{V}}{hh_p}\right)\epsilon \tag{5.B17}$$

References

Ansari, R., & Sahmani, S. (2012). Small scale effect on vibrational response of single-walled carbon nanotubes with different boundary conditions based on nonlocal beam models. *Communications in Nonlinear Science and Numerical Simulation, 17*, 1965–1979.

Ansari, R., & Sahmani, S. (2013). Prediction of biaxial buckling behavior of single-layered graphene sheets based on nonlocal plate models and molecular dynamics simulations. *Applied Mathematical Modelling, 37*, 7338–7351.

Ansari, R., Sahmani, S., & Arash, B. (2010). Nonlocal plate model for free vibrations of single layered graphene sheets. *Physics Letters A, 375*, 53–62.

Ansari, R., Sahmani, S., & Rouhi, H. (2011). Axial buckling analysis of single-walled carbon nanotubes in thermal environments via the Rayleigh–Ritz technique. *Computational Materials Science, 50*, 3050–3055.

Chen, Y. H., Ma, J., & Li, T. (2004). Electrophoretic deposition and characterization of a piezoelectric FGM monomorph actuator. *Ceramics International, 30*, 1807–1809.

Dai, H.-L., Dai, T., & Zheng, H.-Y. (2013). Creep buckling and post-buckling analyses for a hybrid laminated viscoelastic FGM cylindrical shell under in-plane loading. *International Journal of Mechanics and Materials in Design, 9*, 309–323.

Donnell, L. H. (1976). *Beam, plates and shells* (pp. 377–445). New York: McGraw-Hill.

Duc, N. D., Cong, P. H., & Quang, V. D. (2016). Nonlinear dynamic and vibration analysis of piezoelectric eccentrically stiffened FGM plates in thermal environment. *International Journal of Mechanical Sciences, 115-116*, 711–722.

Eringen, A. C. (1972). Linear theory of nonlocal elasticity and dispersion of plane waves. *International Journal of Engineering Science, 10*, 425–435.

Es'haghi, M., Hosseini Hashemi, S., & Fadaee, M. (2011). Vibration analysis of piezoelectric FGM sensors using an accurate method. *International Journal of Mechanical Sciences, 53*, 585–594.

Farajpour, A., Rastgoo, A., & Mohammadi, M. (2017). Vibration, buckling and smart control of microtubules using piezoelectric nanoshells under electric voltage in thermal environment. *Physica B, 509*, 100–114.

Fares, M. E., Elmarghany, M. K., & Atta, D. (2009). An Efficient and simple refined theory for bending and vibration of functionally graded plates. *Composite Structures, 91*, 296–305.

Hao, M. J., Guo, X. M., & Wang, Q. (2010). Small-scale effect on torsional buckling of multi-walled carbon nanotubes. *European Journal of Mechanics – A/Solids, 29*, 49–55.

Hosseini-Hashemi, S., Fadaee, M., & Es'haghi, M. (2010). A novel approach for in-plane/out-of-plane frequency analysis of functionally graded circular/annular plates. *International Journal of Mechanical Sciences, 52*, 1025–1035.

Jun Yu, Y., Xue, Z.-N., Li, C.-L., & Tian, X.-G. (2016). Buckling of nanobeams under nonuniform temperature based on nonlocal thermoelasticity. *Composite Structures, 146*, 108–113.

Juntarasaid, C., Pulngern, T., & Chucheepsakul, S. (2012). Bending and buckling of nanowires including the effects of surface stress and nonlocal elasticity. *Physica E, 46*, 68–76.

Khorshidi, K., & Fallah, A. (2016). Buckling analysis of functionally graded rectangular nano-plate based on nonlocal exponential shear deformation theory. *International Journal of Mechanical Sciences, 113*, 94–104.

Kiani, K. (2010). A meshless approach for free transverse vibration of embedded single-walled nanotubes with arbitrary boundary conditions accounting for nonlocal effect. *International Journal of Mechanical Sciences, 54*, 1343–1356.

Li, Y. S., & Pan, E. (2015). Static bending and free vibration of a functionally graded piezoelectric microplate based on the modified couple-stress theory. *International Journal of Engineering Science, 97*, 40–59.

Li, H. B., Li, Y. D., Wang, X., & Huang, X. (2015). Nonlinear vibration characteristics of graphene/piezoelectric sandwich films under electric loading based on nonlocal elastic theory. *Journal of Sound and Vibration, 358*, 285–300.

Liew, K. M., He, X. Q., & Kitipornchai, S. (2004). Finite element method for the feedback control of FGM shells in the frequency domain via piezoelectric sensors and actuators. *Computer Methods in Applied Mechanics and Engineering, 193*, 257–273.

Liu, T.-J., & Zhang, C. (2016). Axisymmetric conducting indenter on a functionally graded piezoelectric coating. *International Journal of Mechanical Sciences, 115-116*, 34–44.

Liu, J. C., Zhang, Y. Q., & Fan, L. F. (2017). Nonlocal vibration and biaxial buckling of double-viscoelastic-FGM-nanoplate system with viscoelastic Pasternak medium in between. *Physics Letters A, 381*, 1228–1235.

Meng, F., Wang, H., Wang, X., & Li, Z. (2010). Elliptically delaminated buckling near the surface of piezoelectric laminated shells under electric and thermal loads. *Composite Structures, 92*, 684–690.

Mercan, K., & Civalek, O. (2017). Buckling analysis of Silicon carbide nanotubes (SiCNTs) with surface effect and nonlocal elasticity using the method of HDQ. *Composites Part B: Engineering, 114*, 34–45.

Miller, R. E., & Shenoy, V. B. (2000). Size-dependent elastic properties of nanosized structural elements. *Nanotechnology, 11*, 139–147.

Narendar, S., & Gopalakrishnan, S. (2011). Critical buckling temperature of single-walled carbon nanotubes embedded in a one-parameter elastic medium based on nonlocal continuum mechanics. *Physica E, 43*, 1185–1191.

Reddy, J. N. (2010). Nonlocal nonlinear formulations for bending of classical and shear deformation theories of beams and plates. *International Journal of Engineering Science, 48*, 1507–1518.

Sahmani, S., & Aghdam, M. M. (2017a). Nonlinear instability of hydrostatic pressurized hybrid FGM exponential shear deformable nanoshells based on nonlocal continuum elasticity. *Composites Part B: Engineering, 114*, 404–417.

Sahmani, S., & Aghdam, M. M. (2017b). Size dependency in axial postbuckling behavior of hybrid FGM exponential shear deformable nanoshells based on the nonlocal elasticity theory. *Composite Structures, 166*, 104–113.

Sahmani, S., & Aghdam, M. M. (2017c). Temperature-dependent nonlocal instability of hybrid FGM exponential shear deformable nanoshells including imperfection sensitivity. *International Journal of Mechanical Sciences, 122*, 129–142.

Sahmani, S., & Aghdam, M. M. (2017d). Size-dependent axial instability of microtubules surrounded by cytoplasm of a living cell based on nonlocal strain gradient elasticity theory. *Journal of Theoretical Biology, 422*, 59–71.

Sahmani, S., & Aghdam, M. M. (2017e). A nonlocal strain gradient hyperbolic shear deformable shell model for radial postbuckling analysis of functionally graded multilayer GPLRC nanoshells. *Composite Structures, 178*, 97–109.

Sahmani, S., & Aghdam, M. M. (2017f). Nonlinear instability of axially loaded functionally graded multilayer graphene platelet-reinforced nanoshells based on nonlocal strain gradient elasticity theory. *International Journal of Mechanical Sciences, 131*, 95–106.

Sahmani, S., & Aghdam, M. M. (2018). Nonlocal strain gradient shell model for axial buckling and postbuckling analysis of magneto-electro-elastic composite nanoshells. *Composites Part B: Engineering, 132*, 258–274.

Sahmani, S., Bahrami, M., & Aghdam, M. M. (2016a). Surface stress effects on the nonlinear postbuckling characteristics of geometrically imperfect cylindrical nanoshells subjected to axial compression. *International Journal of Engineering Science, 99*, 92–106.

Sahmani, S., Aghdam, M. M., & Bahrami, M. (2016b). Size-dependent axial buckling and postbuckling characteristics of cylindrical nanoshells in different temperatures. *International Journal of Mechanical Sciences, 107*, 170–179.

Sahmani, S., Aghdam, M. M., & Akbarzadeh, A. H. (2016c). Size-dependent buckling and postbuckling behavior of piezoelectric cylindrical nanoshells subjected to compression and electrical load. *Materials & Design, 105*, 341–351.

Sari, M. S. (2015). Free vibration analysis of non-local annular sector Mindlin plates. *International Journal of Mechanical Sciences, 96-97*, 25–35.

Selim, B. A., Zhang, L. W., & Liew, K. M. (2011). Active vibration control of FGM plates with piezoelectric layers based on Reddy's higher-order shear deformation theory. *Composite Structures, 155*, 118–134.

Shariyat, M. (2008). Dynamic buckling of suddenly loaded imperfect hybrid FGM cylindrical shells with temperature-dependent material properties under thermo-electro-mechanical loads. *International Journal of Mechanical Sciences, 50*, 1561–1571.

Shen, H.-S. (2005). Postbuckling of FGM plates with piezoelectric actuators under thermo-electro-mechanical loadings. *International Journal of Solids and Structures, 42*, 6101–6121.

Shen, H.-S. (2008). Boundary layer theory for the buckling and postbuckling of an anisotropic laminated cylindrical shell. Part I: Prediction under axial compression. *Composite Structures, 82*, 346–361.

Shen, H.-S. (2009). Postbuckling of shear deformable FGM cylindrical shells surrounded by an elastic medium. *International Journal of Mechanical Sciences, 51*, 372–383.

Shen, H.-S. (2011a). Postbuckling of nanotube-reinforced composite cylindrical shells in thermal environments, Part I: axial-loaded shells. *Composite Structures, 93*, 2096–2108.

Shen, H.-S. (2011b). Postbuckling of nanotube-reinforced composite cylindrical shells in thermal environments, Part II: Pressure-loaded shells. *Composite Structures, 93*, 2496–2503.

Shen, H.-S. (2013). Nonlocal shear deformable shell model for torsional buckling and postbuckling of microtubules in thermal environments. *Mechanics Research Communications, 54*, 83–95.

Shen, H.-S., & Xiang, Y. (2014). Postbuckling of axially compressed nanotube-reinforced composite cylindrical panels resting on elastic foundations in thermal environments. *Composites Part B: Engineering, 67*, 50–61.

Sheng, G. G., & Wang, X. (2010). Thermoelastic vibration and buckling analysis of functionally graded piezoelectric cylindrical shells. *Applied Mathematical Modelling, 34*, 2630–2643.

Şimşek, M. (2011). Nonlocal effects in the forced vibration of an elastically connected double-carbon nanotube system under a moving nanoparticle. *Computational Materials Science, 50*, 2112–2123.

Sofiyev, A. H., Kuruoglu, N., & Turkmen, M. (2009). Buckling of FGM hybrid truncated conical shells subjected to hydrostatic pressure. *Thin-Walled Structures, 47*, 61–72.

Wang, H. M., & Luo, D. S. (2016). Exact analysis of radial vibration of functionally graded piezoelectric ring transducers resting on elastic foundation. *Applied Mathematical Modelling, 40*, 2549–2559.

Wang, W., Li, P., Jin, F., & Wang, J. (2016). Vibration analysis of piezoelectric ceramic circular nanoplates considering surface and nonlocal effects. *Composite Structures, 140*, 758–775.

Wu, C.-P., & Lim, X.-F. (2016). Coupled electro-mechanical effects and the dynamic responses of functionally graded piezoelectric film-substrate circular hollow cylinders. *Thin-Walled Structures, 102*, 1–17.

Yan, Z., & Jiang, L. Y. (2011). The vibrational and buckling behaviors of piezoelectric nanobeams with surface effects. *Nanotechnology, 22*, 245703.

Yang, Y., & Lim, C. W. (2012). Non-classical stiffness strengthening size effects for free vibration of a nonlocal nanostructure. *International Journal of Mechanical Sciences, 54*, 57–68.

Yang, W. D., Yang, F. P., & Wang, X. (2016). Coupling influences of nonlocal stress and strain gradients on dynamic pull-in of functionally graded nanotubes reinforced nano-actuator with damping effects. *Sensors and Actuators A: Physical, 248*, 10–21.

Zhang, L. L., Liu, J. X., Fang, X. Q., & Nie, G. Q. (2014). Effects of surface piezoelectricity and nonlocal scale on wave propagation in piezoelectric nanoplates. *European Journal of Mechanics A/Solids, 46*, 22–29.

Zhang, Y., Zhang, L. W., Liew, K. M., & Yu, J. L. (2016). Buckling analysis of graphene sheets embedded in an elastic medium based on the kp-Ritz method and nonlocal elasticity theory. *Engineering Analysis with Boundary Elements, 70*, 31–39.

Part II
Vibrations and Automotive Applications

Chapter 6
Vibration Analysis of Oscillators with Generalized Inertial and Geometrical Nonlinearities

D. Younesian, E. Esmailzadeh, and H. Askari

6.1 Introduction

Significant attention has been devoted recently to the large-amplitude vibration analysis of continuous systems because of having wide range of applications in micro- and nanomechanics. Dynamic behavior of nano- and microsensors, resonators, power generators, and switches has been proved to be nonlinear. The significance of this research corresponds to the fact that the mechanical, transport, and electronic properties of these kind of structures are highly influenced by their vibration modes and resonant frequencies.

There is no doubt that closed-form solutions could promote the engineering foundation to have enhanced intelligence on the dynamic characteristic of such complicated systems. A number of researchers have proposed varieties of powerful and reliable approaches to elicit analytical solutions of such nonlinear systems (Nayfeh and Mook 1995). The homotopy perturbation method, variational approach, variational iteration method, max-min technique, frequency-amplitude formulation, energy balance method, Hamiltonian approach, simple approach, and parameter-expansion method have all been recently proposed in this line of

D. Younesian
School of Railway Engineering, Iran University of Science and Technology, Tehran, Iran

E. Esmailzadeh (✉)
Faculty of Engineering and Applied Science, University of Ontario Institute of Technology, Oshawa, ON, Canada
e-mail: ebrahim.esmailzadeh@uoit.ca

H. Askari
Department of Mechanical and Mechatronics Engineering, University of Waterloo, Waterloo, ON, Canada

L. Dai, R.N. Jazar (eds.), *Nonlinear Approaches in Engineering Applications*,
https://doi.org/10.1007/978-3-319-69480-1_6

research. Subsequently, several researchers have employed these methods to identify and model different phenomena in the nature (Askari et al. 2013; He 2006, 2010).

All the abovementioned methods are quite capable in solving different types of nonlinear differential equations. Variational approach, frequency-amplitude formulation, energy balance method, and Hamiltonian approach are effectively applicable for solving the nonlinear conservative oscillators, such as the relativistic oscillators, plasma physics equations, and the nonlinear oscillators with fractional power and Duffing-harmonic oscillators. Homotopy perturbation and variational iteration methods are powerful approaches that are applicable for solving both the nonlinear ordinary and partial differential equations.

Simple approach is also a new method, which has been developed based on the iteration perturbation method, and it is applicable of solving nonlinear differential equations of the oscillatory systems. Parameter expansion is a novel approach, which has been proposed by many researchers, that has been used for solving diverse types of nonlinear equations. Parameter-expansion method is a strong method in comparison with the Lindstedt-Poincaré method. Actually, it is a potent vehicle for investigating different types of nonlinear problems with strong nonlinearity. In the Lindstedt-Poincaré method, the solution of the nonlinear differential equation and also the natural frequency are expanded with respect to "small parameter, namely, epsilon." However, in the parameter-expansion method, all the coefficient of the elastic terms belonging to the nonlinear differential equation must be expanded.

Many types of the well-known nonlinear differential equations in physics and engineering have been analyzed by the abovementioned methods. Younesian et al. (2010a, b, 2011, 2012) considered three kinds of the generalized nonlinear oscillators supporting a wide range of applications in nonlinear mechanics as listed in Table 6.1. Cveticanin et al. (2010) have also pointed out several applications and also proposed a new sequence of generalized nonlinear system addressed in Table 6.1. Along the same track, Khan et al. (2011) considered a new path in this area to deal with another type of generalized nonlinear oscillators. Their progress on the area of generalized nonlinear oscillatory systems is also summarized in Table 6.1.

A new type of generalized nonlinear differential equation, which has been challenged in this chapter, could be represented in its most general form of

$$\ddot{u}+\sum_{\substack{j=0,1,2,3,..\\ q=2j+1}}^{n}\alpha_j u^q+\sum_{\substack{i=1,2,3,\dots\\ k=2i\\ p=k-1}}\beta_i\left[u^k\ddot{u}+ku^p\dot{u}^2/2\right]=0;u(0)=A \text{ and } \dot{u}(0)=0 \quad (6.1)$$

in which q and k are the two arbitrary indices. This equation can generally represent the dynamics of a wide range of oscillators with the geometrical and inertial nonlinearities. Geometric nonlinearity, which normally appears in the potential energy of the system, usually originates from the large deformations or deflections

Table 6.1 Generalized forms of nonlinear equations with their corresponding frequency-amplitude formulation

Generalized nonlinear equation	*Frequency-amplitude formulation*
$\ddot{u}+u+\alpha_3u^3+\alpha_5u^5+\alpha_7u^7+\ldots+\alpha_nu^n=0$ where $n=2k+1$ $k=0,1,2,3,\ldots$	Obtained using the variational approach (Younesian et al. 2011), the homotopy perturbation (Younesian et al. 2011), and the frequency-amplitude formulation (Younesian et al. 2010b) $\omega_{FAF}=\sqrt{1+2\sum_{n=2k+1}^{n}\frac{3\times5\times7\times\ldots\times n}{2\times4\times6\times\ldots\times n+1}\alpha_nA^{n-1}}$ Obtained using the energy balance method (Younesian et al. 2010b) $\omega_{EBM}=\lim_{\omega t\to\frac{\pi}{4}}\frac{1}{\sin\omega t}\sqrt{\frac{1}{2}+2\sum_{n=2k+1}^{n}\alpha_nA^{n-1}(1-\cos^{n-1}\omega t)}$
$\ddot{u}+\delta u+\Omega u^n+\frac{\gamma u^{m-1}}{\sqrt{u^m+\alpha}}=0 n=2k-1, m=2p$ $k=1,2,3,\ldots$ $p=1,2,3,\ldots$	Obtained using the energy balance method (Younesian et al. 2012) $\omega=\lim_{\omega t\to\frac{\pi}{4}\left(\frac{2}{\lambda}\right)}\sqrt{\frac{\delta A^2}{2}\left(1-\cos^2\omega t\right)+\frac{\Omega A^{n+1}}{n+1}\left(1-\cos^{n+1}\omega t\right)+\frac{2\gamma}{m}\left(\sqrt{A^m+\alpha}-\sqrt{A^m\cos^m\omega t+\alpha}\right)}$
$\ddot{u}+\sum_i c_i^2u\lvert u\rvert^{i-1}=0$ Where $i=$ Fractional number	Obtained using the simple approach (Cveticanin et al. 2012) $\omega=\sqrt{\sum_i c_i^2A^{i-1}\frac{\Gamma(i+2)}{2^{i-2}(i+2)^2\left(\Gamma\left(\frac{i+2}{2}\right)\right)^2}}$ Obtained by energy balance method (Cveticanin et al. 2012) $\omega=\sqrt{6\sum_i\frac{c_i^2A^{i-1}}{i+1}\left(1-\frac{\pi}{2^{i-2}(i+2)^2\left(\Gamma\left(\frac{i+2}{2}\right)\right)^2}\right)}$ Obtained using the frequency-amplitude formulation and the Hamiltonian approach (Cveticanin et al. 2010) $\omega_{FAF}=\sqrt{\sum_i\frac{c_i^2A^{i-1}\Gamma(i)}{2^{i-2}(i+1)\left(\Gamma\left(\frac{i+1}{2}\right)\right)^2}}$

(continued)

Table 6.1 (continued)

Generalized nonlinear differential equations	*Frequency-amplitude formulation*
$\ddot{u}+u^{\frac{2(m-n)+1}{2n+1}}=0$ For $m \geq n$ $m=0,1,2,3,\ldots$ $n=0,1,2,3,\ldots$	Obtained using the energy balance method (Younesian et al. 2010a) $\omega_{EBM}=\frac{2}{A}\left(\frac{2n+1}{2m+2}A^{\frac{2m+2}{2n+1}}\left(1-\left(\frac{\sqrt{2}}{2}\right)^{\frac{2m+2}{2n+1}}\right)\right)^{\frac{1}{2}}$ Obtained using modified energy balance method (Younesian et al. 2010a) $\omega_{EBM-PG}=\sqrt{\frac{12n+6}{2m+2}A^{\frac{2m}{2n+1}}\left(1-\frac{1}{2}\frac{\Gamma\left(\frac{1}{2}\right)\Gamma\left(\frac{2(m+n)+3}{2n+1}+1\right)}{\Gamma\left(\frac{2(m+n)+3}{4n+2}\right)}\right)}$ Obtained using the variational approach (Younesian et al. 2010a) $\omega_{VA}=\frac{1}{A^{\frac{(2n-m)}{2n+1}}}\left(\frac{2}{\pi}\frac{\Gamma\left(\frac{2(m+n)+3}{2(2n+1)}\right)}{\Gamma\left(\frac{m+2n+2}{2n+1}\right)}\right)^{\frac{1}{2}}$
$\ddot{u}+\beta u+u^{2n-1\sqrt{1+\varepsilon^2u^{4m}}}=0$ $m=1,2,3,\ldots$ $n=1,2,3,\ldots$	Obtained using the frequency-amplitude formulation (Khan et al. 2011) $\omega=\sqrt{\beta+A^{2n-2}\cos^{2n-2}\left(\frac{\pi}{6}\right)\sqrt{1+\varepsilon^2A^{4m}\cos^{4m}\left(\frac{\pi}{6}\right)}}$ Obtained using the modified frequency-amplitude formulation $\omega=\sqrt{\beta+A^{2n-2}\cos^{2n-2}(0.191\pi)\sqrt{1+\varepsilon^2A^{4m}\cos^{4m}(0.191\pi)}}$

Table 6.2 Special cases of the general forms of the differential Eq. (6.1)

Nonlinear vibration system	Governing differential equation of motion
Vibration of inextensible cantilever beam (Hamdan and Shabaneh 1997; Askari et al. 2015)	$\ddot{u} + \alpha_0 u + \alpha_1 u^3 + \alpha_2 u^5 + \beta_1 \left[u^2 \ddot{u} + u\dot{u}^2\right] + \beta_2 \left[u^4 \ddot{u} + 2u^3 \dot{u}^2\right] = 0$
Vibration of a microbeam (Younesian et al. 2014)	$\ddot{u} + \alpha_0 u + \alpha_1 u^3 + \beta_1 \left[u^2 \ddot{u} + u\dot{u}^2\right] = 0$
Vibration of embedded nanotubes and nanowires (Askari et al. 2014b, 2017; Jamshidifar et al. 2016)	$\ddot{u} + \alpha_0 u + \alpha_1 u^3 = 0$
Vibration of microtubules in the living cells (Shen 2011)	$\ddot{u} + \alpha_0 u + \alpha_1 u^3 + \alpha_1 u^5 = 0$
Motion of a particle on rotating parabola (Marinca and Herişanu 2010)	$\left(1 + 4q^2 u^2\right)\ddot{u} + 4q^2 \left(\dot{u}\right)^2 u + \Delta u = 0$

in flexible structures. Large deformations usually correspond to the nonlinear strain- and curvature-displacement relationships.

The kinetic energy of the system is the origin of the inertia nonlinearities. These nonlinear terms usually appear when the centripetal and Coriolis accelerations would exist. Dynamics of large number of systems in mechanics and physics can be physically described by Eq. (6.1). This equation becomes the well-known generalized Duffing equation when $\beta_i = 0$ and has been solved by several researchers (Younesian et al. 2010a, b, 2011, 2012, 2013; Esmailzadeh and Nakhaie-Jazar 1997; He 2002a; Askari et al. 2014a; Diba et al. 2014).

The main focus of this chapter is to find the analytical solutions of Eq. (6.1) and also investigate the accuracy of the obtained results. The energy balance method developed in 2002, the modified energy balance method published first in 2010, and the parameter-expansion method utilized in 2007 have all been considered in this chapter to determine the frequency-amplitude relationship in its most general form. Different applications of the proposed generalized equation are summarized in Table 6.2. It can be seen that this generic equation can formulate a wide range of dynamical systems from the classical discrete and distributed vibrating systems to the nano-mechanical structures and biomechanical systems.

6.2 Solution Procedure

In this section, the energy balance method (EBM), the modified energy balance method (MEBM), and the parameter-expansion method (PEM) (He 2002b) have been utilized to find the general solutions of Eq. (6.1).

6.2.1 Energy Balance Method

According to the energy balance method (EBM), initially the variational form of Eq. (6.1) should be constructed as shown below:

$$J(u)=\int_0^t\left(-\dot{u}^2\left(1+\sum_{\substack{i=1,2,3,\ldots\\k=2i}}^{n}\beta_i u^k\right)/2+\frac{1}{q+1}\sum_{\substack{j=0,1,2,3,..\\q=2j+1}}^{n}\alpha_j u^{q+1}\right)\mathrm{d}t \tag{6.2}$$

and subsequently, the Hamiltonian function of Eq. (6.1) can be derived as

$$H=\dot{u}^2\left(1+\sum_{\substack{i=1,2,3,\ldots\\k=2i}}^{m}\beta_i u^k\right)/2+\frac{1}{q+1}\sum_{\substack{j=0,1,2,3,..\\q=2j+1}}^{n}\alpha_j u^{q+1}=\frac{1}{q+1}\sum_{\substack{j=0,1,2,3,..\\q=2j+1}}^{n}\alpha_j A^{q+1} \tag{6.3}$$

The residual function for Eq. (6.3) can then be obtained as

$$R(t)=\dot{u}^2/2\left(1+\sum_{\substack{i=1,2,3,\ldots\\k=2i}}^{m}\beta_i u^k\right)+\left(\sum_{\substack{j=0,1,2,3,..\\q=2j+1}}^{n}\alpha_j u^{q+1}-\sum_{\substack{j=0,1,2,3,..\\q=2j+1}}^{n}\alpha_j A^{q+1}\right)/(q+1) \tag{6.4}$$

where $u=A\cos\omega t$ is considered as the initial guess for the solution of Eq. (6.1), and therefore, by substituting it into Eq. (6.4), one may arrive at

$$\begin{aligned}\underset{\omega t\to\frac{\pi}{4}}{R(t)}&=\frac{1}{2}A^2\omega^2\sin^2\omega t\left(1+\sum_{\substack{i=1,2,3,\ldots\\k=2i}}^{m}\beta_i A^k\cos^k\omega t\right)\\&+\frac{1}{q+1}\left(\sum_{\substack{j=0,1,2,3,..\\q=2j+1}}^{n}\alpha_j A^{q+1}\cos^{q+1}\omega t-\sum_{\substack{j=0,1,2,3,..\\q=2j+1}}^{n}\alpha_j A^{q+1}\right)=0\end{aligned} \tag{6.5}$$

Finally, one could obtain an expression for the frequency of the oscillation as

$$\omega = \frac{2}{A}\sqrt{\frac{\sum\limits_{\substack{j=0,1,2,3\ldots \\ q=2j+1}}^{n} \frac{1}{q+1}\left(\alpha_j A^{q+1}\right)\left(1-\left(\sqrt{2}/2\right)^{q+1}\right)}{1+\sum\limits_{\substack{i=1,2,3,.. \\ k=2i}}^{m} \beta_i A^k \left(\sqrt{2}/2\right)^k}} \tag{6.6}$$

6.2.2 Modified Energy Balance Method

The drawbacks of the classical energy balance method have been overcome by using a summation term in this updated procedure. In order to modify the classical EBM, Younesian et al. (2010a) combined the classical EBM with the Petrov-Galerkin method. They have stated that instead of setting the residual term to zero at a given collocation point, one should try to set its integration to zero. Hence, it may write

$$\tilde{R}(t) = \int_0^{T/4} R(t)\cos\omega t\,\mathrm{d}t = 0 \tag{6.7}$$

Substituting Eq. (6.5) into Eq. (6.7) would yield as

$$\begin{aligned}\tilde{R}(t) \quad &= \int_0^{T/4}\Big[\frac{1}{2}A^2\omega^2\sin^2\omega t\left(1+\sum_{\substack{i=1,2,3,.. \\ k=2i}}^{m}\beta_i A^k\cos^{k+1}\omega t\right) \\ &+\sum_{\substack{j=0,1,2,3,.. \\ q=2j+1}}^{n}\frac{\alpha_j}{q+1}A^{q+1}\left[\cos^{q+2}\omega t-\cos\omega t\right]\mathrm{d}t = 0\end{aligned} \tag{6.8}$$

and accordingly one could arrive at

$$\omega = \frac{2}{A}\sqrt{\frac{\int_0^{T/4}\sum\limits_{\substack{j=0,1,2,3,.. \\ q=2j+1}}^{n}\left\{\alpha_j A^{q+1}\left[\cos^{q+2}\omega t-\cos\omega t\right]/(q+1)\right\}\mathrm{d}t}{2\int_0^{T/4}\sin^2\omega t\left(1+\sum\limits_{\substack{i=1,2,3,\ldots \\ k=2i}}^{m}\beta_i A^k\cos^{k+1}\omega t\right)\mathrm{d}t}} \tag{6.9}$$

6.2.3 Parameter-Expansion Method

In this method, if one needs to solve Eq. (6.1) by the parameter-expansion method (PEM), the new form of Eq. (6.1) should be constructed as

$$\ddot{u} + 0.u + 1.\sum_{\substack{j=0,1,2,3,\ldots \\ q=2j+1}}^{n} \alpha_j u^q + 1.\sum_{\substack{1=1,2,3,.. \\ k=2i \\ p=k-1}}^{m} \beta_i \left[u^k \ddot{u} + \frac{k}{2} u^p \dot{u}^2 \right] = 0 \tag{6.10}$$

Actually, Eq. (6.1) is developed based on the parameter-expansion method, and the coefficients of zero (0) and one (1) must be replaced with the elastic force of the generalized nonlinear differential equation. Subsequently, the newly defined coefficients are expanded based on the small parameter ε. Accordingly, number (1) is expanded based on the small parameter ε for the nonlinear terms of the generalized nonlinear differential equation in order to find the natural frequency of the considered equation for this part of the equation.

Therefore, based on the parameter-expansion method, the following equations could be developed:

$$\begin{aligned} u &= u_0 + \varepsilon u_1 + \varepsilon^2 u_2 + \ldots \\ 0 &= \omega^2 + \varepsilon\omega_1 + \varepsilon^2\omega_2 + \ldots \\ 1 &= \varepsilon a_1 + \varepsilon^2 a_2 + \ldots \\ 1 &= \varepsilon b_1 + \varepsilon^2 b_2 + \ldots \\ 1 &= \varepsilon c_1 + \varepsilon^2 c_2 + \ldots \end{aligned} \tag{6.11}$$

Then one may substitute Eq. (6.11) into (6.10) in order to obtain

$$\begin{aligned} &\left(\ddot{u} + \varepsilon\ddot{u}_1 + \varepsilon^2\ddot{u}_2 + \ldots\right) + (\omega^2 + \varepsilon\omega_1 + \varepsilon^2\omega_2 + \ldots)(u_0 + \varepsilon u_1 + \varepsilon^2 u_2 + \ldots) \\ &+(\varepsilon a_1 + \varepsilon^2 a_2 + \ldots)\sum \alpha_j (u_0 + \varepsilon u_1 + \varepsilon^2 u_2 + \ldots)^q \\ &+(\varepsilon b_1 + \varepsilon^2 b_2 + \ldots)\sum \beta_i (u_0 + \varepsilon u_1 + \varepsilon^2 u_2 + \ldots)^k \left(\ddot{u}_0 + \varepsilon\ddot{u}_1 + \varepsilon^2\ddot{u}_2 + \ldots\right) \\ &+(\varepsilon c_1 + \varepsilon^2 c_2 + \ldots)\sum \frac{k}{2}\beta_i (u_0 + \varepsilon u_1 + \varepsilon^2 u_2 + \ldots)^p \left(\dot{u}_0 + \varepsilon\dot{u}_1 + \varepsilon^2\dot{u}_2 + ..\right)^2 = 0 \end{aligned} \tag{6.12}$$

By equating the terms of the identical powers for ε, one could arrive at

$$\begin{aligned} \varepsilon^0 &: \quad \ddot{u}_0 + \omega^2 u_0 = 0 \\ \varepsilon^1 &: \quad \ddot{u}_1 + \omega^2 u_1 + \omega_1 u_0 + a_1 \sum \alpha_j u_0^q + b_1 \sum \beta_i u_0^k \ddot{u}_0 + c_1 \sum \frac{k}{2}\beta_i u_0^p \dot{u}_0^2 = 0 \end{aligned} \tag{6.13}$$

where $u = A\cos\omega t$ is considered to be the initial guess for the solution.

$$\ddot{u}_1 + \omega^2 u_1 + \omega_1 A\cos\omega t + a_1 \sum \alpha_j A \cos^q \omega t + b_1 \sum \beta_i A^k \cos^k \omega t\left(-A\omega^2 \cos\omega t\right) + c_1 \sum \frac{k}{2} \beta_i u_0^p \dot{u}_0^2 = 0 \tag{6.14}$$

Using the Fourier expansion method and the definition of Gamma function Γ, one will obtain

$$\begin{aligned}
&\ddot{u}_1 + \omega^2 u_1 + \omega_1 A\cos\omega t + a_1 \sum \alpha_j A^q \frac{4\Gamma(2+q)/2}{\sqrt{\pi}(q+1)\Gamma(q+1)/2} \\
&-b_1 \sum \beta_i A^{k+1}\omega^2 \frac{4\Gamma(k+3)/2}{\sqrt{\pi}(k+2)\Gamma(2+k)/2} \\
&+c_1 \sum \frac{k}{2}\beta_i A^{p+2}\omega^2 \left[\frac{4\Gamma(3+k)/2}{\sqrt{\pi}(p+1)\Gamma(p+1)/2} - \frac{4\Gamma(4+p)/2}{\sqrt{\pi}(p+1)\Gamma(p+1)/2}\right]\cos\omega t + (\ldots) \\
&\times \cos 3\omega t + \ldots
\end{aligned} \tag{6.15}$$

Eliminating the secular terms would then yield to

$$\begin{aligned}
&\omega_1 A\cos\omega t + a_1 \sum \alpha_j A^q \frac{4\Gamma(2+q)/2}{\sqrt{\pi}(q+1)\Gamma(q+1)/2} \\
&-b_1 \sum \beta_i A^{k+1}\omega^2 \frac{4\Gamma(3+k)/2}{\sqrt{\pi}(k+2)\Gamma(k+2)/2} \\
&+c_1 \sum \frac{k}{2}\beta_i A^{p+2}\omega^2 \left[\frac{4\Gamma(3+k)/2}{\sqrt{\pi}(p+1)\Gamma(p+1)/2} - \frac{4\Gamma(4+p)/2}{\sqrt{\pi}(p+1)\Gamma(p+1)/2}\right] = 0
\end{aligned} \tag{6.16}$$

By considering the first approximation when $\varepsilon = 1$, one could write

$$\begin{gathered}
u = u_0 + u_1 \\
a_1 = 1, \quad b_1 = 1, \quad \text{and} \quad c_1 = 1 \\
0 = \omega^2 + \omega_1
\end{gathered} \tag{6.17}$$

Combining Eq. (6.16) and Eq. (6.17) would lead into the following expression:

$$\begin{aligned}
&-\omega^2 A\cos\omega t + \sum \alpha_j A^q \frac{4\Gamma(2+q)/2}{\sqrt{\pi}(q+1)\Gamma(q+1)/2} \\
&-\sum \beta_i A^{k+1}\omega^2 \frac{4\Gamma(3+k)/2}{\sqrt{\pi}(k+2)\Gamma(2+k)/2} \\
&+\sum \frac{k}{2}\beta_i A^{p+2}\omega^2 \left[\frac{4\Gamma(3+k)/2}{\sqrt{\pi}(p+1)\Gamma(p+1)/2} - \frac{4\Gamma(4+p)/2}{\sqrt{\pi}(p+1)\Gamma(p+1)/2}\right] = 0
\end{aligned} \tag{6.18}$$

6.3 Numerical Examples and Discussions

The general solutions for four special case studies are presented in this section. The results obtained using the three proposed solution methods were compared with those published in literature. The intention is to cover both the discrete dynamical systems and the continuous elastic systems. The nonlinear vibration of a tapered beam and also that of an inextensible cantilever beam have been considered here, and the corresponding frequency responses are obtained.

6.3.1 Nonlinear Vibration of Tapered Beam

The governing differential equation of motion, which corresponds to the fundamental vibration mode of a tapered beam, is presented by

$$\ddot{u} + \alpha_0 u + \alpha_1 u^3 + \beta_1 \left[u^2 \ddot{u} + u \dot{u}^2 \right] = 0 \tag{6.19}$$

By utilizing Eq. (6.6) and Eq. (6.18), it is found that the solutions using the energy balance method and the parameter-expansion method will give the same results as

$$\omega = \sqrt{\frac{\alpha_0 + 3\alpha_1 A^2/4}{1 + \beta_1 A^2/2}} \tag{6.20}$$

However, using Eq. (6.9) that is based on the modified energy balance method, one could obtain the frequency-amplitude relationship as

$$\omega = \sqrt{\frac{\alpha_0 + 7\alpha_1 A^2/10}{1 + 6\beta_1 A^2/15}} \tag{6.21}$$

The exact value of the natural frequency from Eq. (6.19) can be numerically obtained as

$$\omega_{ex} = \frac{2\pi}{T_e(A)} = \frac{\pi}{2\int_0^{\pi/2} \left[2\left(1 + \alpha A^2 \cos^2\theta\right) / \left(2 + \beta A^2 (1 + \cos^2\theta)\right) \right]^{1/2} \mathrm{d}\theta} \tag{6.22}$$

The accuracy of the presented results is evaluated numerically and illustrated in Fig. 6.1 for the sake of comparison. It can be seen that the reliability of the modified energy balance method (MEBM) is much higher in comparison with the other two procedures used, namely, the energy balance method (EBM) and the parameter-expansion method (PEM).

Figure 6.1 demonstrates that the extra improvement, which results from the MEBM, is quite remarkable. It is found that this modification would decrease the ultimate relative errors of up to 50%.

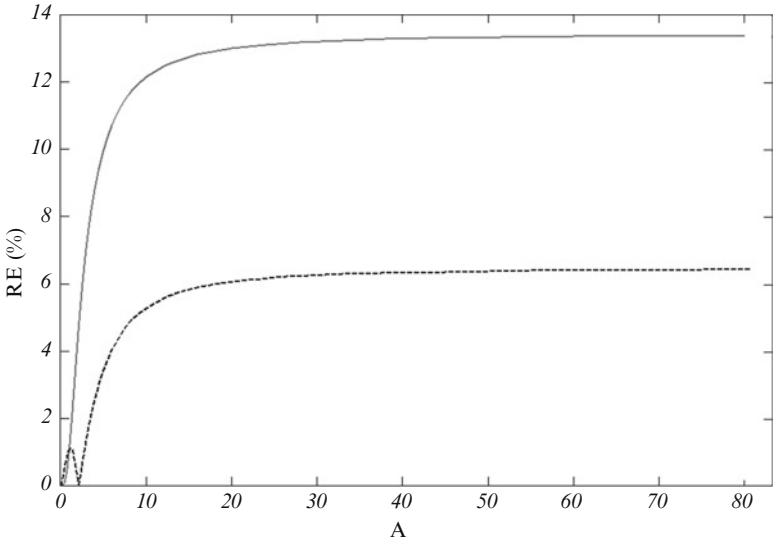

Fig. 6.1 Relative percentage errors for the natural frequencies obtained for very large amplitudes and amplitudes of less than 10

The ultimate relative error is defined to be

$$\lim_{A\to\infty} \frac{\omega_{\text{EBM, PEM}}(A)}{\omega_{\text{ex}}} = \frac{2\sqrt{3}}{\pi} \int_0^{\pi/2} \frac{\cos t}{\sqrt{1+\cos^2 t}} \mathrm{d}t \approx 0.8660 \tag{6.23}$$

and

$$\lim_{A\to\infty} \frac{\omega_{\text{MEBM}}(A)}{\omega_{\text{ex}}} = \frac{2\sqrt{3}}{\pi} \int_0^{\pi/2} \frac{\cos t}{\sqrt{1+\cos^2 t}} \mathrm{d}t \approx 0.9354 \tag{6.24}$$

The phase-plane trajectories of Eq. (6.19) are numerically plotted in Fig. 6.2 for various values of the initial conditions. This represents the important fact that the oscillation of the tapered beam is found to be periodic, and it represents like a Hamiltonian system.

The time history diagram of the oscillations of the system with respect to nondimensional parameter h or (t/T, time/period) is shown in Fig. 6.3. It can be seen that the results obtained are acceptable even when the system has strong nonlinearities and undergoes large amplitudes of vibration.

The frequency responses for the system with different nonlinearity indices are illustrated in Fig. 6.4. It is seen that the parameter β_1 plays an important role of either hardening or softening tuning parameter. Moreover, within its specific range of $\beta_1 \in [1.5\ 2.25]$, the system behaves similar to a linear oscillator, and hence, the natural frequency becomes independent of the initial amplitude.

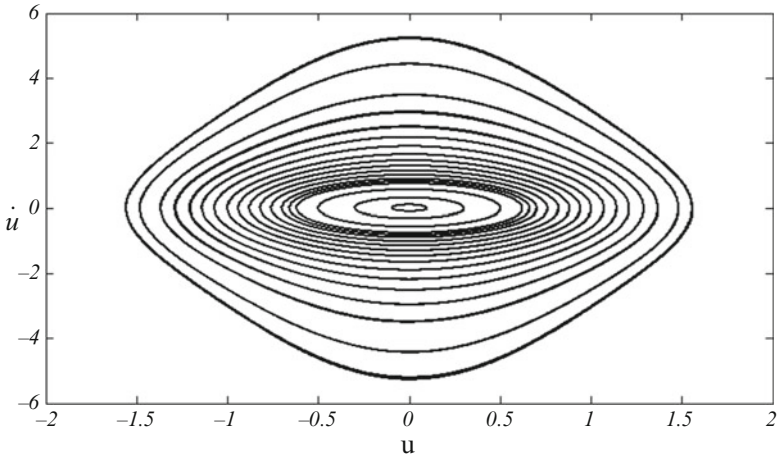

Fig. 6.2 Phase-plane trajectories for different initial amplitudes: $\alpha_1 = \beta_1 = 1$

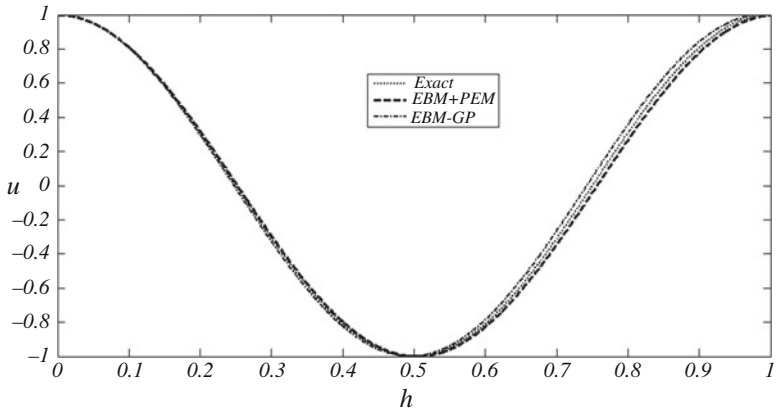

Fig. 6.3 Comparison of the solutions of exact method with those of EBM, MEBM, and PEM: $\alpha_1 = \beta_1 = 1$

6.3.2 *Nonlinear Vibration of Inextensible Cantilever Beam*

The nonlinear vibration of an inextensible cantilever beam is analyzed by Hamdan and Shabaneh (1997). Subsequently, other researchers made a good attempt to find the frequency-amplitude relationship of this system (Sfahani et al. 2011; Herişanu and Marinca 2010). The governing equation of motion corresponding to the fundamental vibration mode of such system is described by Hamdan and Shabaneh (1997):

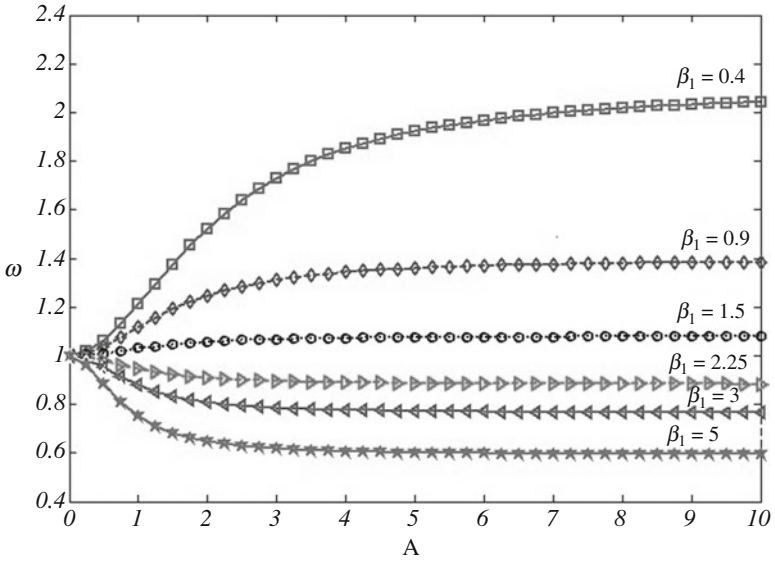

Fig. 6.4 Frequency-amplitude responses for different nonlinearity indices

$$\ddot{u} + \alpha_0 u + \alpha_1 u^3 + \alpha_2 u^5 + \beta_1 \left[u^2 \ddot{u} + u\dot{u}^2\right] + \beta_2 \left[u^4 \ddot{u} + 2u^3 \dot{u}^2\right] = 0 \tag{6.25}$$

The frequency-amplitude relationship, based on the solution method of parameter expansion, is obtained as Eq. (6.18):

$$\omega = \sqrt{\frac{\alpha_0 + 3\alpha_1 A^2/4 + 5\alpha_2 A^4/8}{1 + \beta_1 A^2/2 + 3\beta_2 A^4/8}} \tag{6.26}$$

The frequency-amplitude relationship, based on the solution method of energy balance, by means of Eq. (6.8), is obtained as

$$\omega = \sqrt{\frac{\alpha_0 + 3\alpha_1 A^2/4 + 15\alpha_2 A^4/32}{1 + \beta_1 A^2/2 + \beta_2 A^4/8}} \tag{6.27}$$

and eventually using the modified energy balance method (MEBM) for Eq. (6.9) will give

$$\omega = \sqrt{\frac{\alpha_0 + 7\alpha_1 A^2/10 + 19\alpha_2 A^4/35}{1 + 6\beta_1 A^2/15 + 24\beta_2 A^4/105}} \tag{6.28}$$

Table 6.3 Comparison of natural frequencies using different solution methods

Case	A	β_1	β_2	α_1	α_2	ω_{PEM} (RE%)	ω_{EBM} (RE%)	ω_{MEBM} (RE%)
1	1.0	0.3268	0.1295	0.2325	0.0878	1.007129 (0.299)	1.029511 (1.916)	1.021383 (1.112)
2	0.5	1.6420	0.9130	0.3135	0.2042	0.932556 (0.409)	0.953429 (1.819)	0.949704 (1.422)
3	0.2	4.0514	1.6652	0.2814	0.1496	0.965469 (0.121)	0.973067 (0.665)	0.972678 (0.624)
4	0.3	8.2055	3.1453	0.2723	0.1337	0.859702 (0.527)	0.885784 (2.490)	0.884388 (2.329)

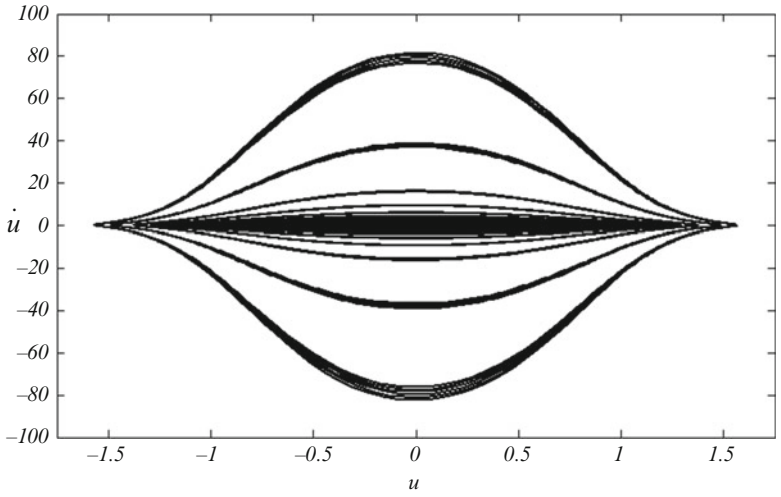

Fig. 6.5 Phase-plane trajectories for different initial conditions: $\alpha_1 = \beta_1 = 1$ and $\alpha_2 = \beta_2 = 1$

The validity of the obtained solution methods is evaluated at this stage. The nonlinear natural frequencies for four different real case studies are summarized in Table 6.3.

It can be seen that the parameter-expansion method (PEM) presents the most accurate responses in this case. In accordance with the results presented in Table 6.3, the modified energy balance method is far more accurate than the energy balance method.

The phase-plane trajectories and time history diagrams of Eq. (6.25) are illustrated in Figs. 6.5 and 6.6, respectively. Numerical approach is considered to plot phase-plane trajectories shown in Fig. 6.5. According to these figures, the model is classified as a harmonic Hamiltonian system, and the solution methods have all been proven to be satisfactory even for the large-amplitude oscillations and also in the presence of strong nonlinearities.

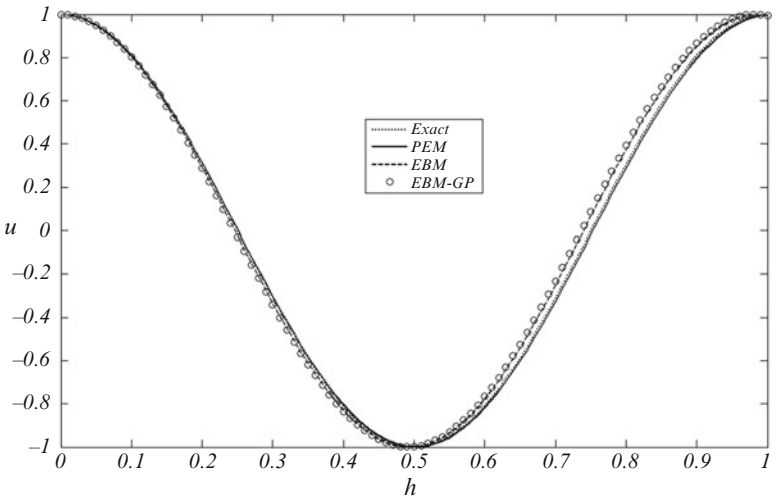

Fig. 6.6 Comparison of the exact solution with the EBM, MEBM, and PEM solutions: $\alpha_1 = \beta_1 = 1$ and $\alpha_2 = \beta_2 = 1$

6.3.3 Nonlinear Vibration of an Embedded Carbon Nanotube

Large-amplitude free-vibration equation of an embedded nanotube is modeled by (Askari et al. 2017):

$$EI\frac{\mathrm{d}^4 w}{\mathrm{d}x^4} + \rho A\frac{\mathrm{d}^2 w}{\mathrm{d}t^2} = \left[\frac{EA}{2L}\int_0^l \left(\frac{\partial w}{\partial x}\right)\mathrm{d}x\right]\frac{\partial^2 w}{\partial x^2} + p(x,t)\Big] \tag{6.29}$$

where $p(x,t)$ is the interaction pressure per unit axial length between the outer tube and the surrounding elastic medium, which is described by the Winkler model as

$$p = -kw \tag{6.30}$$

Substituting Eq. (6.30) into Eq. (6.29) gives

$$EI\frac{\mathrm{d}^4 w}{\mathrm{d}x^4} + \rho A\frac{\mathrm{d}^2 w}{\mathrm{d}t^2} + kw = \left[\frac{EA}{2L}\int_0^l \left(\frac{\partial w}{\partial x}\right)\mathrm{d}x\right]\frac{\partial^2 w}{\partial x^2} \tag{6.31}$$

Assuming the simply supported boundary conditions for the two ends of the proposed system, the unknown function $w(x,t)$ may be written as

$$w(x,t) = u(t)\sin\frac{\pi x}{l} \tag{6.32}$$

By substituting Eq. (6.32) into Eq. (6.31), the nonlinear differential equation for the time function $u(t)$ can be obtained as (Fu et al. 2006; Esmailzadeh and Nakhaie-Jazar 1998; Esmailzadeh et al. 1996)

$$\frac{\mathrm{d}^2u}{\mathrm{d}t^2}+\left(\frac{\pi^4EI}{l^4\rho A}+\frac{k}{\rho A}\right)u+\frac{\pi^4E}{4l^4\rho}u^3=0 \tag{6.33}$$

The frequency-amplitude relationship, based on the parameter-expansion method (PEM), is hence obtained from Eq. (6.18) as

$$\omega=\sqrt{\left(\frac{\pi^4EI}{l^4\rho A}+\frac{k}{\rho A}\right)+\frac{3}{4}\frac{\pi^4E}{4l^4\rho}A^2} \tag{6.34}$$

The frequency-amplitude relationship, based on the energy balance method (EBM), is obtained by using Eq. (6.8) as

$$\omega=\sqrt{\left(\frac{\pi^4EI}{l^4\rho A}+\frac{k}{\rho A}\right)+\frac{3}{4}\frac{\pi^4E}{4l^4\rho}A^2} \tag{6.35}$$

Finally, the modified energy balance method (MEBM) presented in Eq. (6.9) gives

$$\omega=\sqrt{\left(\frac{\pi^4EI}{l^4\rho A}+\frac{k}{\rho A}\right)+\frac{7}{10}\frac{\pi^4E}{4l^4\rho}A^2} \tag{6.36}$$

To analyze the proposed system, the effects of varying the initial conditions on the natural frequency of the system are illustrated in Fig. 6.7. The frequency ratio

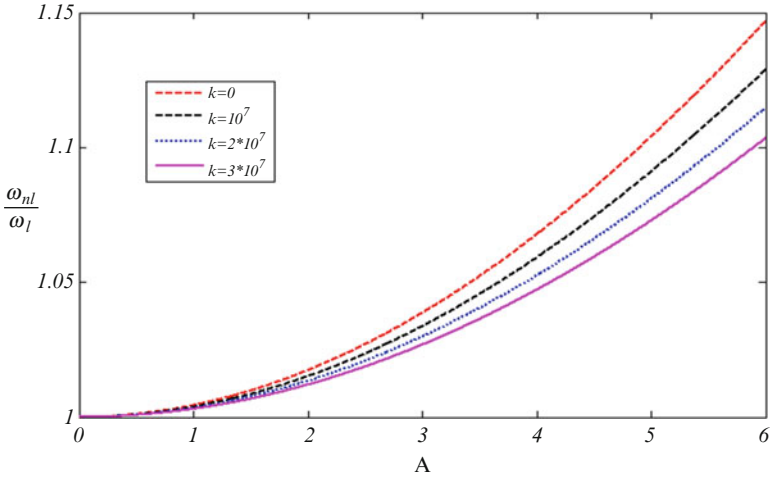

Fig. 6.7 Influences of the stiffness and initial condition on the frequency ratio

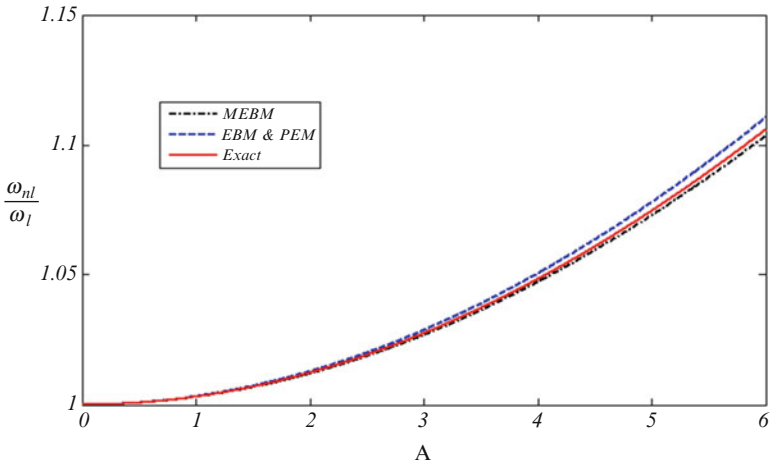

Fig. 6.8 Accuracy analysis of the three approaches with the exact method

increases by an increase of the initial conditions similar to a hardening system. However, it is seen that the value of nonlinear frequency decreases by an increase in the stiffness of the system for a given initial amplitude.

Figure 6.8 represents the accuracy of the different approaches. The modified energy balance method (MEBM) has the highest accuracy in comparison with the parameter-expansion method (PEM) and the energy balance method (EBM) for vibration analysis of an embedded carbon nanotube.

6.3.4 Motion of a Particle on Rotating Parabola

The motion of a particle on a rotating parabola is analyzed as an illustrative example in the dynamic analysis of discrete systems. Considering the governing differential equation of motion, developed earlier by Nayfeh and Mook (1995) and Marinca and Herişanu (2010):

$$\left(1+4q^2u^2\right)\ddot{u}+4q^2\left(\dot{u}\right)^2u+\Delta u=0 \tag{6.37}$$

The frequency-amplitude relationship based on the parameter-expansion method (PEM) is obtained as (Eq. 6.18):

$$\omega=\sqrt{\frac{\Delta}{1+2q^2A^2}} \tag{6.38}$$

The frequency-amplitude relationship, developed by means of Eq. (6.8), is obtained as

$$\omega = \sqrt{\frac{\Delta}{1 + 2q^2A^2}} \tag{6.39}$$

and the modified energy balance method (MEBM) solution given in Eq. (6.9) yields to

$$\omega = \sqrt{\frac{\Delta}{1 + 24q^2A^2/15}} \tag{6.40}$$

The relative errors of the three different solution methods are then been obtained as

$$\lim_{q^2A\to\infty} \frac{T_{\text{ex}}}{T_{\text{EBM, PEM}}} = \frac{4\int_0^{\frac{\pi}{2}} \sqrt{1 + 4q^2A^2\cos^2 t}\,\mathrm{d}t}{2\pi\sqrt{1 + 2q^2A^2}} = \frac{2\sqrt{2}}{\pi} \approx 0.9 \tag{6.41}$$

and

$$\lim_{q^2A\to\infty} \frac{T_{\text{ex}}}{T_{\text{MEBM}}} = \frac{4\int_0^{\frac{\pi}{2}} \sqrt{1 + 4q^2A^2\cos^2 t}\,\mathrm{d}t}{2\pi\sqrt{1 + 24q^2A^2/15}} = \frac{4}{\pi\sqrt{\frac{24}{15}}} = 1.0065 \tag{6.42}$$

In this case, one may conclude that in order to analyze the motion of a particle on a rotating parabola, the modified energy balance method (MEBM) has presented the highest accuracy in comparison with those obtained from the EBM and PEM.

6.4 Conclusion

A new class of generalized nonlinear oscillator has been investigated in detail. The applications of the generalized nonlinear equation in the structural dynamics and applied mathematics were then addressed. The governing dynamic equations were solved by means of three powerful approaches, namely, the energy balance method (EBM), the modified energy balance method (MEBM), and the parameter-expansion method (PEM). Utilizing these methods, the corresponding solutions were sought after, and three different general frequency-amplitude relationships in a closed-form format were obtained. It has been proved that the accuracy of these results is consistent. A tapered beam was chosen as a special case study, and the solution results showed that MEBM is the most accurate approach for the vibration analysis of a tapered beam; however, both the two methods of EBM and PEM could also present similar results for this system. The phase-plane trajectories demonstrated that this system is considered as the Hamiltonian type, which exhibits a periodic behavior. In spite of the nonlinear structure of the differential equation, for a specific range of $\beta_1 \in [1.5\ 2.25]$, the system performs similar to a linear oscillator, and the natural frequency shows to be independent of the initial amplitude. A

second special case in the form of an inextensible cantilever beam was considered. In accordance with the numerical results obtained for the cantilever beam, it is found that the PEM is the most accurate method to understand and analyze the vibration of such system. It is observed that the accuracy of the results found by using the MEBM is superior than those found using the classical EBM when obtaining the frequency-amplitude relationship. The nonlinear vibration of an embedded carbon nanotube was also investigated as the third special case. The results found for this case indicate that MEBM is the best choice to investigate the nonlinear natural frequency of that system. Finally, the motion of a particle on a rotating parabola to represent a discrete nonlinear dynamic system was studied. The solution results reveal that MEBM is a superior choice to analyze this system when compared with the other two methods of EBM and PEM.

References

Askari, H., Nia, Z. S., Yildirim, A., Yazdi, M. K., & Khan, Y. (2013). Application of higher order Hamiltonian approach to nonlinear vibrating systems. *Journal of Theoretical and Applied Mechanics, 51*(2), 287–296.

Askari, H., Saadatnia, Z., Esmailzadeh, E., & Younesian, D. (2014a). Multi-frequency excitation of stiffened triangular plates for large amplitude oscillations. *Journal of Sound and Vibration, 333*(22), 5817–5835.

Askari, H., Esmailzadeh, E., & Zhang, D. (2014b). Nonlinear vibration analysis of nonlocal nanowires. *Composites Part B: Engineering, 67*, 607–613.

Askari, H., Younesian, D., & Saadatnia, Z. (2015). Nonlinear oscillations analysis of the elevator cable in a drum drive elevator system. *Advances in Applied Mathematics and Mechanics, 7*(1), 43–57.

Askari, H., Younesian, D., Esmailzadeh, E., & Cveticanin, L. (2017). Nonlocal effect in carbon nanotube resonators: A comprehensive review. *Advances in Mechanical Engineering, 9*(2), 1–24.

Cveticanin, L., Kalami-Yazdi, M., Saadatnia, Z., & Askari, H. (2010). Application of Hamiltonian approach to the generalized nonlinear oscillator with fractional power. *International Journal of Nonlinear Sciences and Numerical Simulation, 11*(12), 997–1002.

Cveticanin, L., Kalami-Yazdi, M., & Askari, H. (2012). Analytical approximations to the solutions for a generalized oscillator with strong nonlinear terms. *Journal of Engineering Mathematics, 77*(1), 211–223.

Diba, F., Esmailzadeh, E., & Younesian, D. (2014). Nonlinear vibration analysis of isotropic plate with inclined part-through surface crack. *J Nonlinear Dynamics, 78*(4), 2377–2397.

Esmailzadeh, E., & Nakhaie-Jazar, G. (1997). Periodic solution of a Mathieu-Duffing type equation. *International Journal of Non-Linear Mechanics, 32*(5), 905–912.

Esmailzadeh, E., & Nakhaie-Jazar, G. (1998). Periodic behavior of a cantilever beam with end mass subjected to harmonic base excitation. *International Journal of Non-Linear Mechanics, 33*(4), 567–577.

Esmailzadeh, E., Mehri, B., & Nakhaie-Jazar, G. (1996). Periodic solution of a second order, autonomous, nonlinear system. *J Nonlinear Dynamics, 10*(4), 307–316.

Fu, Y. M., Hong, J. W., & Wang, X. Q. (2006). Analysis of nonlinear vibration for embedded carbon nanotubes. *Journal of Sound and Vibration, 296*(4–5), 746–756.

Hamdan, M. N., & Shabaneh, N. H. (1997). On the large amplitude free vibrations of a restrained uniform beam carrying an intermediate mass. *Journal of Sound and Vibration, 199*(5), 711–736.

He, J. H. (2002a). Preliminary report on the energy balance for nonlinear oscillations. *Mechanics Research Communications, 29*, 107–118.

He, J. H. (2002b). Modified Lindstedt-Poincare methods for some strongly non-linear oscillations – Part I: Expansion of a constant. *International Journal of Non-Linear Mechanics, 37*(2), 309–314.

He, J. H. (2006). Some asymptotic methods for strongly nonlinear equations. *International Journal of Modern Physics B, 20*(10), 1141–1199.

He, J. H. (2010). Hamiltonian approach to nonlinear oscillators. *Physics Letters A, 374*(23), 2312–2314.

Herişanu, N., & Marinca, V. (2010). Explicit analytical approximation to large-amplitude non-linear oscillations of a uniform cantilever beam carrying an intermediate lumped mass and rotary inertia. *Meccanica, 45*(6), 847–855.

Jamshidifar, H., Askari, H., & Fidan, B. (2016). Parameter identification and adaptive control of carbon nanotube resonators. *Asian Journal of Control, 19*(2), 1–10.

Khan, Y., Kalami-Yazdi, M., Askari, H., & Saadatnia, Z. (2011). Dynamic analysis of generalized conservative nonlinear oscillators via frequency amplitude formulation. *Arabian Journal for Science and Engineering, 38*(1), 175–179.

Marinca, V., & Herişanu, N. (2010). Determination of periodic solutions for the motion of a particle on a rotating parabola by means of the optimal homotopy asymptotic method. *Journal of Sound and Vibration, 329*(9), 1450–1459.

Nayfeh, A. H., & Mook, D. T. (1995). *Nonlinear oscillations*. Wiley-VCH, Germany.

Sfahani, M. G., Barari, A., Omidvar, M., Ganji, S. S., & Domairry, G. (2011). Dynamic response of inextensible beams by improved energy balance method. *Proceedings of the Institution of Mechanical Engineers – Part K: Journal of Multi-body Dynamics, 225*(1), 66–73.

Shen, H.-S. (2011). Nonlinear vibration of microtubules in living cells. *Current Applied Physics, 11*(3), 812–821.

Younesian, D., Askari, H., Saadatnia, Z., & Yildirim, A. (2010a). Periodic solutions for the generalized nonlinear oscillators containing fraction order elastic force. *International Journal of Nonlinear Sciences and Numerical Simulation, 11*(12), 1027–1032.

Younesian, D., Askari, H., Saadatnia, Z., & KalamiYazdi, M. (2010b). Frequency analysis of strongly nonlinear generalized Duffing oscillators using He's frequency–amplitude formulation and He's energy balance method. *Journal Computers and Mathematics with Applications, 59*(9), 3222–3228.

Younesian, D., Askari, H., Saadatnia, Z., & KalamiYazdi, M. (2011). Free vibration analysis of strongly nonlinear generalized Duffing oscillators using He's variational approach and homotopy perturbation method. *Nonlinear Science Letters A, 2*(1), 11–16.

Younesian, D., Askari, H., Saadatnia, Z., & KalamiYazdi, M. (2012). Analytical approximate solutions for the generalized nonlinear oscillator. *Applicable Analysis, 91*(5), 965–977.

Younesian, D., Marjani, S. R., & Esmailzadeh, E. (2013). Nonlinear vibration analysis of harmonically excited cracked beams on viscoelastic foundations. *J Nonlinear Dynamics, 71*(1–2), 109–120.

Younesian, D., Sadri, M., & Esmailzadeh, E. (2014). Primary and secondary resonance analyses of clamped-clamped micro-beams. *J Nonlinear Dynamics, 76*(4), 1867–1884.

Chapter 7
Quarter Car Suspension Model with Provision for Loss of Contact with the Road

Ali Khazaie, Najiullah Hussaini, Hormoz Marzbani, and Reza N. Jazar

7.1 Introduction

Suspension models are mathematical representations of automobile suspensions which can predict the behaviour of the vehicle suspension in response to a particular input; they are mainly used for ride analysis applications. Various models may differ in their detail and complexity depending on the requirements of a particular application.

7.1.1 Quarter Car Model

A quarter car model is used to model only one corner of the vehicle. It is a simple and effective tool to investigate basic ride behaviour of the vehicle. However, it only models the bounce movement of the chassis and the wheel and ignores pitch and roll. Commonly used quarter car ride models are mostly linear (Jazar 2013, 2014).

Linear quarter car models are the most frequently used ride models; these are fairly simple models which provide useful insight into the behaviour of a particular suspension system (Kim and Ro 2000). They are mostly represented in form of a

A. Khazaie (✉)
Department of Mechanical Engineering, Kennesaw State University, Kennesaw, GA, USA

N. Hussaini • H. Marzbani
School of Engineering, RMIT University, Melbourne, VIC, Australia

R.N. Jazar
School of Engineering, RMIT University, Melbourne, VIC, Australia

Xiamen University of Technology, Xiamen, China

L. Dai, R.N. Jazar (eds.), *Nonlinear Approaches in Engineering Applications*,
https://doi.org/10.1007/978-3-319-69480-1_7

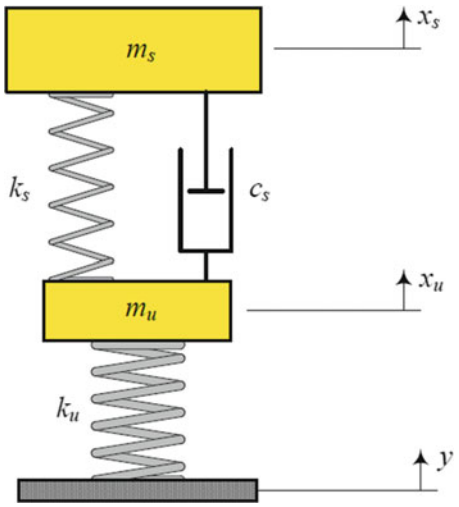

Fig. 7.1 Quarter car model (Jazar 2014)

two-mass model consisting of two point masses connected to each other through a spring and a damper and connected to the ground through a spring (Milliken and Milliken 1995).

When using two-mass models, designers may use component specifications to determine parameters such as sprung mass, unsprung mass and spring stiffness. Although this might be tempting, as Kim and Ro point out, this may not always lead to accurate representations of the real system (Kim and Ro 2000, 1999).

It must be noted that in reality, independent suspension for a single wheel (quarter car) is actually a multi-body system; having compliant rubber bushing means that the system is not limited to just two degrees of freedom. Approximating such a system to a simple system with only two point masses may not be very accurate, and the degree of accuracy may differ for each particular case (Kim and Ro 1999). Figure 7.1 shows the diagram of a simple two-mass quarter car model.

7.1.1.1 Linear Models

A linear quarter car model assumes that both tire and suspension springs are linear; this implies that the force acting through the springs is directly proportional to the vertical extension or compression of the springs. It does not account for variable motion ratios across the total range of wheel travel; motion ratios are rarely constant because of the geometry of suspension linkages. Damping in a linear model is assumed to be viscous (linear) with a constant damping coefficient across the range of wheel travel (Marzbani and Jazar 2014).

Tire damping is often ignored in linear models; however, some linear models may add viscous damping to the tire with very small damping ratios. A linear model also ignores any discontinuities such as asymmetric damping (different coefficients

in bump and rebound) or the case of tire losing contact with the ground or bump stops.

Maher and Young's study investigates the accuracy of linear models by comparing results of a linear model with experimental results and those of their own nonlinear model. They found that a linear quarter car model produced reasonably accurate results for unsprung mass acceleration over a wide frequency band; however it over-predicted acceleration of sprung mass. They developed their nonlinear model by using a trilinear damper model, a nonlinear tire model and inclusion of tire damping. Using their nonlinear model, Maher and Young found noticeable improvement in accuracy (Young and Maher 2011).

7.1.1.2 Nonlinear Models

A linear quarter car model is just an approximation of a real vehicle and is not an accurate representation of the real vehicle. The assumptions made to make the model linear are known to be untrue for a real car.

Major sources of nonlinearity in a quarter car suspension are:

- Geometric effects resulting in not linear effective springs
- Asymmetric damping
- Tire separation
- Bump stops

In actual cars the spring is often not mounted exactly vertically and often is mounted at some offset from the centre of the tire; moreover they are usually actuated by a set of suspension arms or linkages which rotate about a pivot and do not move in an exactly linear manner. All of this means that the motion ratio of spring and the wheel centre does not remain constant across the full range of wheel travel, and therefore the effective spring stiffness is not constant, and a linear spring model would be inaccurate.

Most automotive suspension dampers are not symmetric; this means the damping coefficient in bump is different to that in rebound. The damping coefficient also changes with speed; this can usually be approximated as a bilinear relation switching to a lower damping coefficient at a particular speed known as "knee speed". Figure 7.2 shows the characteristics of a typical automotive damper.

The continuous contact assumption for the tire is also untrue for a real car. The tire only rests on the road and is not held by the surface as such; therefore it cannot stretch beyond its geometric radius. This phenomenon is not very rare and can often be experienced when driving on rough road surfaces at high speeds. Maurice Olley refers to this phenomenon as "wheel hop" (Milliken and Milliken 2002), and Wong has also discussed the phenomenon in his book (Wong 2008). This will be discussed in detail in subsequent sections.

Bump stops are rubber blocks installed to restrict the wheel travel within safe limits. Although bump stops are placed beyond the normal operating range of the suspension, suspensions may hit bump stops under extreme conditions, such as

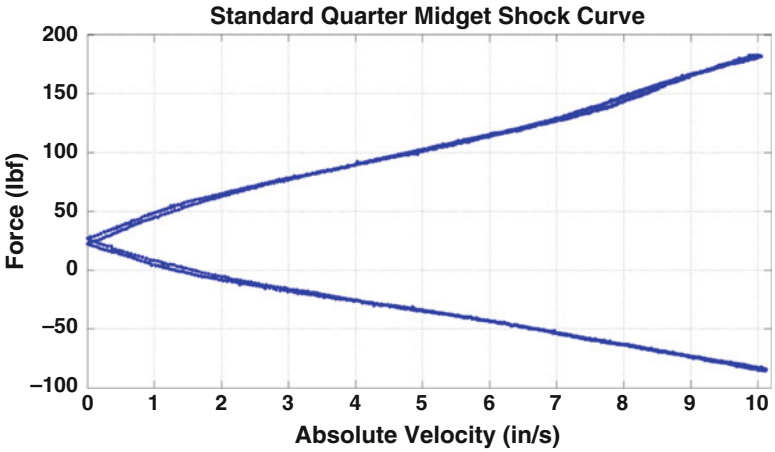

Fig. 7.2 Damper force plot for KAZ tech quarter midget (Courtesy: KAZ Technologies)

when carrying heavy loads or navigating uneven roads. Bump stops are significantly stiffer than the suspension spring; as the suspension impacts the bump stop, the stiffness of the system increases manifolds which may have significant effects on the behaviour of the suspension (Marzbani et al. 2013). Svahn, Jerrelind and Dankowicz have investigated the bump stop discontinuities in considerable detail in their work (Svahn et al. 2010).

7.1.2 Tire Separation

One major nonlinearity in vehicle ride behaviour is the possible separation of tire and the road. Physical observation suggests that this may occur at high frequencies or very large amplitudes of road undulations.

As the solution to the tire-road discontinuity results in piecewise functions for the system equations of motion and may require computer simulation to evaluate the response, therefore, many older texts chose to ignore this such as those by Gillespie and Giugianni (Gillespie 1992; Giugianni 2014).

Jazar mentions this shortcoming in his book while discussing limitations of popular linear quarter car models (Jazar 2014; Marzbani et al. 2012). Wong points out that the condition where tire leaves the road is significant from a roadholding point of view; the normal force through the contact patch governs the forces acting in the ground plane, i.e. tractive, braking and lateral forces; loss of contact implies that the normal force reduces to zero, and therefore the tire would not produce any forces in the ground plane either. He argues that tire separation is likely to occur close to the peak dynamic deflection of the tire; this implies that in passenger cars with low damping ratios, separation may occur close to sprung mass and unsprung mass natural frequencies; in performance cars with high damping ratios, tire

separation may occur at frequencies between sprung and unsprung mass natural frequencies (Wong 2008).

Maurice Olley, in his notes published by Milliken, also identifies this problem; he observes that the wheel may at times be thrown "clear of the ground"; once off the ground, it will return to the ground only under the effect of gravity. He also shows with the help of results from a bump test rig that the wheel may have different amplitudes at the same frequency depending on its frequency history (Milliken and Milliken 2002).

7.1.2.1 Separation Conditions

Wong and Olley have both recognized that the tire would cease to be in contact with the road when unsprung mass is deflected vertically upwards relative to the ground by a distance equal to the static compression of the tire. In other words the contact would break once the tire returns to its geometric radius (Wong 2008 ; Milliken and Milliken 2002). Svahn, Jerrelind and Dankowicz have used the same condition for transition between states of "contact" and "free flight" (Svahn et al. 2010).

7.1.2.2 Possible Effects of Tire Separation

As discussed previously, one major effect of loss of contact would be the loss of ground plane forces. This may have profound consequences in certain cases such as loss of grip during cornering or loss of braking force.

When going over large undulations at high speeds, the tire may actually be able to "jump" over the troughs resulting in smaller displacements of sprung mass and therefore a better ride.

As the system transitions between two different dynamic states, it may display erratic behaviour at certain frequencies (Milliken and Milliken 2002).

7.1.3 Computer Models for Quarter Car Simulation

Equations of motion of a linear quarter car form a system of linear ordinary differential equations; these can be analytically solved using method of undetermined coefficients (Jazar 2014; Gillespie 1992). The analytical solution can then be evaluated at any point of interest. However such an analytical solution may not be suitable for problems with discontinuities. These equations can also be solved numerically on MATLAB using one of the available ODE solvers (Young and Maher 2011).

Traditionally a discontinuous system such as a nonlinear quarter car model may be simulated using a multistep solution method. The system is evaluated at finite intervals after fixed time steps. This method is simple from a logical point of view;

however, it is prone to errors. If the discontinuity lies between two evaluation points, the solution would only transition once it reaches the end of that interval; such error may grow if the system is subject to multiple transitions. In order to minimize the error, smaller time steps may be used, but this improved accuracy comes at the cost of multiplied computational effort (Thomsen 2010).

7.1.4 Knowledge Gap

Based on the literature reviewed, we find that most authors who have investigated the subject have acknowledged the occurrence of the tire separation phenomenon but hold differing views about its effects on the results of ride simulation. We also find consensus about the conditions under which tire separation may occur. However, we find that the phenomenon has not been studied individually in isolation from other nonlinearities. The author believes that the tire separation effect when applied to an otherwise linear model may provide valuable insight into the tire separation phenomenon and would be a useful addition to the existing knowledge on the subject.

7.2 Model

The simulation is based on a model of a lightweight single seat race car. This vehicle is selected purely due to easy availability of data, and the model is essentially scalable to any size of vehicle (Table 7.1).

7.2.1 Separation Condition

When the vehicle suspension is subjected to periodic vertical inputs applied through the contact patch, it may break contact with the ground. Once the tire is no more in contact with the road, the tire spring becomes redundant, and the system will return to the ground only under the influence of gravity. Therefore we can describe the system as being in one of two distinct states, i.e.:

Table 7.1 Vehicle specifications for model

Sprung mass (quarter car)	49.5 kg
Unsprung mass (quarter car)	5.5 kg
Suspension spring stiffness	15,760 N/m
Tire vertical stiffness	197,900 N/m
Static tire deflection	6 mm
Critical damping	2000 Ns/m

- Contact
- Free fall

The two states are distinct physically and mathematically; therefore the equations of motion of the system would be discontinuous or piecewise (Jazar et al. 2007; Christopherson et al. 2005, 2006).

The argument for tire separation is based on the premise that the tire acts as a spring in compression, only it cannot be extended; it is also supported by intuition as there is no physical mechanism for the road to be able to "pull" the tire. Conversely the maximum radius that the tire can achieve is equal to the geometric radius of that tire when there is no vertical load on it. If the distance between the wheel centre and the road surface is larger than the geometric radius of unloaded tire, we can conclude that the tire is no more in contact with the road.

Therefore the "contact" and "free-fall" states are defined by the conditions given below:

$$\text{Contact Condition} : x_u - x_r < X_{T.stat}$$
$$\text{Free-Fall Condition } x_u - x_r \geq X_{T.stat}$$

7.2.2 *Governing Equations of Motion*

7.2.2.1 Sprung Mass

Figure 7.3 depicts the free-body diagram of sprung mass. It is assumed that unsprung mass has a larger displacement and velocity than the sprung mass at the instant when the equations of motion are derived; this is only to help us assign the appropriate signs to the variables; the resulting equation would be valid for any other values of these variables as well (Jazar 2011).

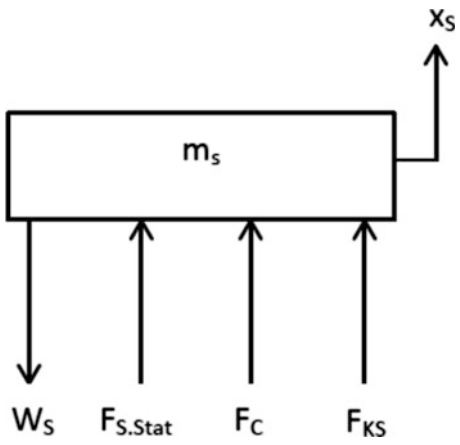

Fig. 7.3 Free-body diagram of sprung mass

$$
\begin{aligned}
F_{\mathrm{C}} &= c\left(\dot{x}_{\mathrm{U}} - \dot{x}_{\mathrm{S}}\right) \\
F_{\mathrm{KS}} &= k_{\mathrm{S}}(x_{\mathrm{U}} - x_{\mathrm{S}}) \\
F_{\mathrm{S.stat}} &= k_{\mathrm{S}} X_{\mathrm{S.stat}} = m_{\mathrm{S}} g \\
W_{\mathrm{S}} &= m_{\mathrm{S}} g \\
m_{\mathrm{S}}\ddot{x}_{\mathrm{S}} &= c\left(\dot{x}_{\mathrm{U}} - \dot{x}_{\mathrm{S}}\right) + k_{\mathrm{S}}(x_{\mathrm{U}} - x_{\mathrm{S}}) + m_{\mathrm{S}} g - m_{\mathrm{S}} g \\
m_{\mathrm{S}}\ddot{x}_{\mathrm{S}} &= -c\dot{x}_{\mathrm{S}} + c\dot{x}_{\mathrm{U}} - k_{\mathrm{S}} x_{\mathrm{S}} + k_{\mathrm{S}} x_{\mathrm{U}}
\end{aligned} \tag{7.1}
$$

where F_{C} is force across the damper.

F_{KS} is the force across suspension spring.
$F_{\mathrm{S.static}}$ is the static spring compressive force at ride height.
$X_{\mathrm{S.stat}}$ is the static compression (displacement) at ride height.
W_{S} is the weight of the sprung mass.
m_{S} is the sprung mass.
m_{U} is the unsprung mass.
x_{S} is the displacement of sprung mass.
x_{U} is the displacement of unsprung mass.
k_{S} is the equivalent stiffness of suspension spring.
c is the damping coefficient of the damper.

$$
\begin{gathered}
\omega_{\mathrm{s}} = \sqrt{\frac{k_{\mathrm{s}}}{m_{\mathrm{s}}}} \quad \text{and} \quad \omega_{\mathrm{u}} = \sqrt{\frac{k_{\mathrm{T}}}{m_{\mathrm{u}}}} \\
k_{\mathrm{s}} = \omega_{\mathrm{s}}^2 m_{\mathrm{s}} \quad \text{and} \quad k_{\mathrm{T}} = \omega_{\mathrm{u}}^2 m_{\mathrm{u}} \\
\xi = \frac{c}{2\sqrt{k_{\mathrm{s}} m_{\mathrm{s}}}} = \frac{c}{2 m_{\mathrm{s}} \omega_{\mathrm{s}}} \\
c = 2\xi\omega_{\mathrm{s}} \\
\epsilon = \frac{m_{\mathrm{s}}}{m_{\mathrm{u}}}
\end{gathered}
$$

where

ω_{s} is the sprung mass natural frequency
ω_{u} is the sprung mass natural frequency
ξ is the damping ratio

Substitute in (Eq. 7.1) and divide both sides by m_{s}:

$$
\ddot{x}_{\mathrm{S}} = -2\xi\omega_{\mathrm{s}}\dot{x}_{\mathrm{S}} + 2\xi\omega_{\mathrm{s}}\dot{x}_{\mathrm{U}} - \omega_{\mathrm{s}}^2 x_{\mathrm{S}} + \omega_{\mathrm{s}}^2 x_{\mathrm{U}} \tag{7.2}
$$

7.2.2.2 Unsprung Mass

Figure 7.4 depicts the free-body diagram of unsprung mass. Here it is assumed that the displacement of road is greater than the displacement of unsprung mass:

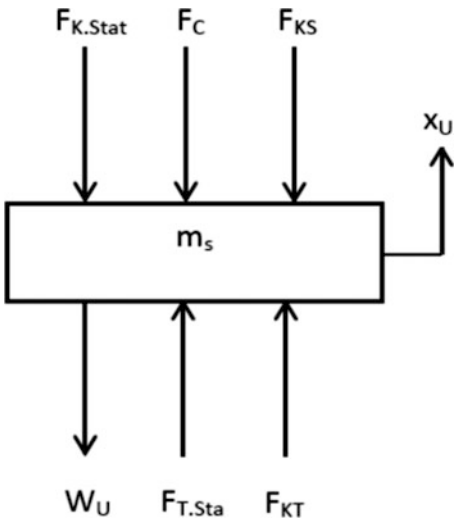

Fig. 7.4 Free-body diagram of unsprung mass

$$F_{\mathrm{KT}} = k_{\mathrm{T}}(x_{\mathrm{r}} - x_{\mathrm{U}})$$
$$F_{\mathrm{T.stat}} = k_{\mathrm{T}}X_{\mathrm{T.stat}} = (m_{\mathrm{S}} + m_{\mathrm{U}})g$$
$$W_{\mathrm{U}} = m_{\mathrm{U}}g$$

Contact state:

$$m_{\mathrm{U}}\ddot{x}_{\mathrm{U}} = -c\left(\dot{x}_{\mathrm{U}} - \dot{x}_{\mathrm{S}}\right) - k_{\mathrm{S}}(x_{\mathrm{U}} - x_{\mathrm{S}}) + k_{\mathrm{T}}(x_{\mathrm{r}} - x_{\mathrm{U}}) - m_{\mathrm{S}}g - m_{\mathrm{U}}g + (m_{\mathrm{S}} + m_{\mathrm{U}})g$$
$$m_{\mathrm{U}}\ddot{x}_{\mathrm{U}} = -c\left(\dot{x}_{\mathrm{U}} - \dot{x}_{\mathrm{S}}\right) - k_{\mathrm{S}}(x_{\mathrm{U}} - x_{\mathrm{S}}) + k_{\mathrm{T}}(x_{\mathrm{r}} - x_{\mathrm{U}})$$
$$m_{\mathrm{U}}\ddot{x}_{\mathrm{U}} = c\dot{x}_{\mathrm{S}} - c\dot{x}_{\mathrm{U}} + k_{\mathrm{S}}x_{\mathrm{S}} - (k_{\mathrm{S}} + k_{\mathrm{T}})x_{\mathrm{U}} + k_{\mathrm{T}}x_{\mathrm{r}}$$
$$\ddot{x}_{\mathrm{U}} = 2\xi\epsilon\omega_{\mathrm{s}}\dot{x}_{\mathrm{S}} - 2\xi\epsilon\omega_{\mathrm{s}}\dot{x}_{\mathrm{U}} + \epsilon\omega_{\mathrm{s}}^2 x_{\mathrm{S}} - \left(\epsilon\omega_{\mathrm{s}}^2 + \omega_{\mathrm{u}}^2\right)x_{\mathrm{U}} + \omega_{\mathrm{u}}^2 x_{\mathrm{r}} \tag{7.3}$$

Free-fall state (Fig. 7.4):

Under free-fall state, F_{T} and $F_{\mathrm{T.stat}}$ will be zero; therefore the equation of motion reduces to

$$m_{\mathrm{U}}\ddot{x}_{\mathrm{U}} = -c\left(\dot{x}_{\mathrm{U}} - \dot{x}_{\mathrm{S}}\right) - k_{\mathrm{S}}(x_{\mathrm{U}} - x_{\mathrm{S}}) - m_{\mathrm{S}}g - m_{\mathrm{U}}g$$
$$m_{\mathrm{U}}\ddot{x}_{\mathrm{U}} = c\dot{x}_{\mathrm{S}} - c\dot{x}_{\mathrm{U}} + k_{\mathrm{S}}x_{\mathrm{S}} - k_{\mathrm{S}}x_{\mathrm{U}} - (m_{\mathrm{S}} + m_{\mathrm{U}})g \tag{7.4}$$

Substitute ω_{s}, ω_{u} and ξ in (Eq. 7.3) and divide both sides by $\mathrm{m_u}$:

$$\ddot{x}_{\mathrm{U}} = 2\xi\epsilon\omega_{\mathrm{s}}\dot{x}_{\mathrm{S}} - 2\xi\epsilon\omega_{\mathrm{s}}\dot{x}_{\mathrm{U}} + \epsilon\omega_{\mathrm{s}}^2 x_{\mathrm{S}} - \epsilon\omega_{\mathrm{s}}^2 x_{\mathrm{U}} - (\epsilon + 1)g \tag{7.5}$$

where F_{KT} is the force across tire spring.
$F_{\mathrm{T.stat}}$ is the static compressive force of the tire.
$X_{\mathrm{T.stat}}$ is the static compression (displacement) of the tire.
m_{U} is the unsprung mass.
W_{U} is the weight of the unsprung mass.

K_T is the stiffness of tire spring.
x_r is the displacement of the road with respect to reference position (input signal).

When combined in matrix form, the equations can be represented as:
Contact state:

$$\begin{bmatrix}\ddot{x}_S \ddot{x}_U\end{bmatrix} = \begin{bmatrix}-2\xi\omega_s & 2\xi\omega_s \\ 2\xi\epsilon\omega_s & -2\xi\epsilon\omega_s\end{bmatrix}\begin{bmatrix}\dot{x}_S \\ \dot{x}_U\end{bmatrix} + \begin{bmatrix}-\omega_s^2 & \omega_s^2 \\ \epsilon\omega_s^2 & -\left(\epsilon\omega_s^2+\omega_u^2\right)\end{bmatrix}\begin{bmatrix}x_S \\ x_U\end{bmatrix} + \begin{bmatrix}0 \\ \omega_u^2 x_r\end{bmatrix} \quad (7.6)$$

Free-fall state:

$$\begin{bmatrix}\ddot{x}_S \ddot{x}_U\end{bmatrix} = \begin{bmatrix}-2\xi\omega_s & 2\xi\omega_s \\ 2\xi\epsilon\omega_s & -2\xi\epsilon\omega_s\end{bmatrix}\begin{bmatrix}\dot{x}_S \\ \dot{x}_U\end{bmatrix} + \begin{bmatrix}-\omega_s^2 & \omega_s^2 \\ \epsilon\omega_s^2 & -\epsilon\omega_s^2\end{bmatrix}\begin{bmatrix}x_S \\ x_U\end{bmatrix} + \begin{bmatrix}0 \\ (\epsilon+1)g\end{bmatrix} \quad (7.7)$$

State variables for state space formulation:

$$\begin{gathered} x_S = y_1 \\ x_U = y_2 \\ \dot{x}_S = \dot{y}_1 = y_3 \\ \dot{x}_U = \dot{y}_2 = y_4 \\ \ddot{x}_S = \dot{y}_3 \\ \ddot{x}_U = \dot{y}_4 \end{gathered}$$

Substituting state variables in (Eq. 7.6) and (Eq. 7.7)

$$\begin{gathered} \dot{y}_1 = y_3 \\ \dot{y}_2 = y_4 \\ \dot{y}_3 = -\omega_s^2 y_1 + \omega_s^2 y_2 - 2\xi\omega_s y_3 + 2\xi\omega_s y_4 \\ \text{For Contact}\, \dot{y}_4 = \epsilon\omega_s^2 y_1 - \left(\epsilon\omega_s^2 + \omega_u^2\right) y_2 + 2\xi\epsilon\omega_s y_3 - 2\xi\epsilon\omega_s y_4 + \omega_u^2 x_r \\ \text{For Free-Fall} : \dot{y}_4 = \epsilon\omega_s^2 y_1 - \epsilon\omega_s^2 y_2 + 2\xi\epsilon\omega_s y_3 - 2\xi\epsilon\omega_s y_4 + (\epsilon+1)g \end{gathered}$$

State-space equations in matrix form are given below:
For contact state:

$$\begin{bmatrix}\dot{y}_1 \\ \dot{y}_2 \\ \dot{y}_3 \\ \dot{y}_4\end{bmatrix} = \begin{bmatrix}0 & 0 & 1 & 0 \\ 0 & 0 & 0 & 1 \\ -\omega_s^2 & \omega_s^2 & -2\xi\omega_s & 2\xi\omega_s \\ \epsilon\omega_s^2 & -\left(\epsilon\omega_s^2+\omega_u^2\right) & 2\xi\epsilon\omega_s & -2\xi\epsilon\omega_s\end{bmatrix}\begin{bmatrix}y_1 \\ y_2 \\ y_3 \\ y_4\end{bmatrix} + \begin{bmatrix}0 \\ 0 \\ 0 \\ \omega_u^2 x_r\end{bmatrix} \quad (7.8)$$

For free-fall state:

$$\begin{bmatrix}\dot{y}_1 \\ \dot{y}_2 \\ \dot{y}_3 \\ \dot{y}_4\end{bmatrix} = \begin{bmatrix}0 & 0 & 1 & 0 \\ 0 & 0 & 0 & 1 \\ -\epsilon\omega_s^2 & \epsilon\omega_s^2 & -2\xi\omega_s & 2\xi\omega_s \\ \epsilon\omega_s^2 & -\epsilon\omega_s^2 & 2\xi\epsilon\omega_s & -2\xi\epsilon\omega_s\end{bmatrix}\begin{bmatrix}y_1 \\ y_2 \\ y_3 \\ y_4\end{bmatrix} + \begin{bmatrix}0 \\ 0 \\ 0 \\ (\epsilon+1)g\end{bmatrix} \quad (7.9)$$

7.2.3 Input Function

Input function used for this analysis is a sinusoidal function representing a corrugated road of the form:

$$x_r = X_r \sin(\omega t)$$

where X_r is the amplitude of input signal and ω is the angular frequency in rad/s.

7.2.4 Programme Structure

7.2.4.1 Time Response Programme

In order to compute the time response of the equations of motion presented above, they must be evaluated over a given time interval. The interval chosen must be long enough for the system to achieve steady state. The interval chosen for this analysis is equal to the time taken to complete 15 cycles of the input signal (Jazar 2013).

Because the system is discontinuous, the solution must determine the current state of the system at every instant. However it is practically impossible to determine the system state at infinitesimally small intervals. Therefore we need to set evaluation points at different times across the total time interval.

The programme uses MATLAB "ode45" ordinary differential equation solver to evaluate the equations of motion. The ode45 solver sets the resolution automatically over the total time interval with variable time steps in order to reduce computation time without compromising too much on the accuracy. Although ode45 also accepts a user-defined step size, it is still not straightforward to check separation condition within the ode45 function.

Therefore, the total time interval is divided into small time steps of 1/1000 s giving a finite number of evaluation points. The programme utilizes a loop to evaluate the equations of motion throughout the complete time interval. Each instance of the loop uses the initial conditions to check the separation condition and determine which set of equations must be used; the selected equation is then evaluated across the interval up to the next evaluation point. The end conditions are passed on to the next instance of the loop as initial conditions and are also saved in the result matrix.

The programme also has an "indicator" variable; this identifies which state the system is in at each evaluation point. 0 corresponds to the contact state while 1 corresponds to free-fall state.

Table 7.2 Conditions at which responses are calculated

Frequency ratios	0.2–5.0	Step size	0.05
Damping ratios	0.2, 0.4, 0.6, 0.8, 1.0		
Input amplitudes	0.01, 0.04, 0.07, 0.10		

7.2.4.2 Frequency Response Programme

The frequency response programme evaluates the time response over a range of input frequencies, input amplitudes and damping ratios. Table 7.2 below shows the conditions at which the response is evaluated.

Frequency response programme uses the same basic code as the time response programme; it is however evaluated multiple times at different conditions using loops. The time response is enclosed in the frequency ratio loop, which is enclosed in a damping ratio loop which in turn is enclosed in the input amplitude loop (Jazar 2013).

The amplitude is extracted from the time response result by first discarding the transient response. The time intervals used are sufficiently large that the transient response diminishes within 50% of the total time interval in most cases; therefore the first half of the time response is discarded as transient. The maximum and minimum values are then extracted from the steady-state result matrix, and their difference is calculated to obtain the output amplitude.

The result matrix is a three-dimensional matrix, for ease of manipulating this data; it is exported to a Microsoft Excel spreadsheet.

7.2.4.3 Model Response

Figure 7.5 shows an example of system response to a sinusoidal input with 0.04 m amplitude and a 2.5 frequency ratio when using the nonlinear model described above.

- *Point 1 to 2:* As the road (input) goes into a trough, the tire loses contact as it is unable to keep up with the road. Because at point 1 when the contact is lost, unsprung mass already has a small negative velocity, it continues to fall due to gravity between point 1 and 2; as it falls the suspension spring extends. As the road starts to rise, it catches up with the falling masses and contact is regained at point 2.
- *Point 2 to 3:* As the road continues to rise beyond after contact is regained, the tire is compressed which in turn applies a force (negative acceleration) on falling unsprung mass. Due to compression of tire spring, the unsprung mass decelerates and eventually turns around and starts rising. As the road reaches its crest at point 3, the unsprung mass still has a large positive velocity, and thus contact is lost again.
- *Point 3 to 4:* At point 3 the unsprung mass still has a positive velocity; as the contact is lost, it is thrown off the ground like a projectile. Unsprung mass

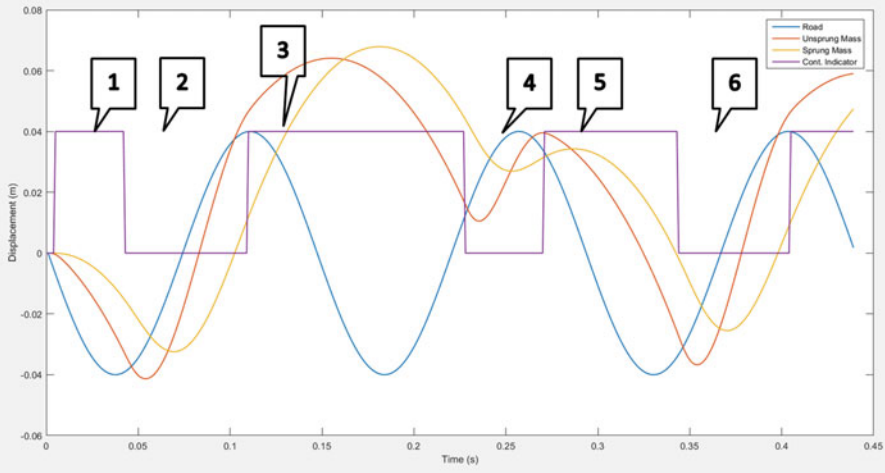

Fig. 7.5 Example of system behaviour (amplitude, 0.04 m; frequency ratio, 2.5; damping ratio, 1.0)

decelerates due to gravity and starts to fall; the rising road catches up with the falling mass at point 4 and contact is regained.

- *Point 4 to 5:* When contact is regained at point 4, the unsprung mass has a negative velocity while the road is rising; this compresses the tire spring which causes the unsprung mass to decelerate and eventually turn around. The road starts to drop before point 5 while the unsprung mass is still rising; as they move in opposite direction, contact is lost at point 5.
- *Point 5 to 6:* When the contact is lost at point 5, the vertical velocity of unsprung mass is almost zero; therefore beyond point 5, it falls due to gravity and eventually catches up with the rising road at point 6.

7.3 Results and Discussion

7.3.1 Separation Classification

Before the simulation results are analysed in detail, it needs to be established if the tire separation does mathematically happen and whether it has significant effects on simulation results.

All input frequencies in this report are shown as a ratio of sprung mass natural frequency. Frequency ratios are denoted by "*r*".

As we increase the input frequency for fixed damping ratio and amplitude values, we initially see transient separation; the system does change state in the first few cycles but eventually settles into a state of continuous contact. Figure 7.6

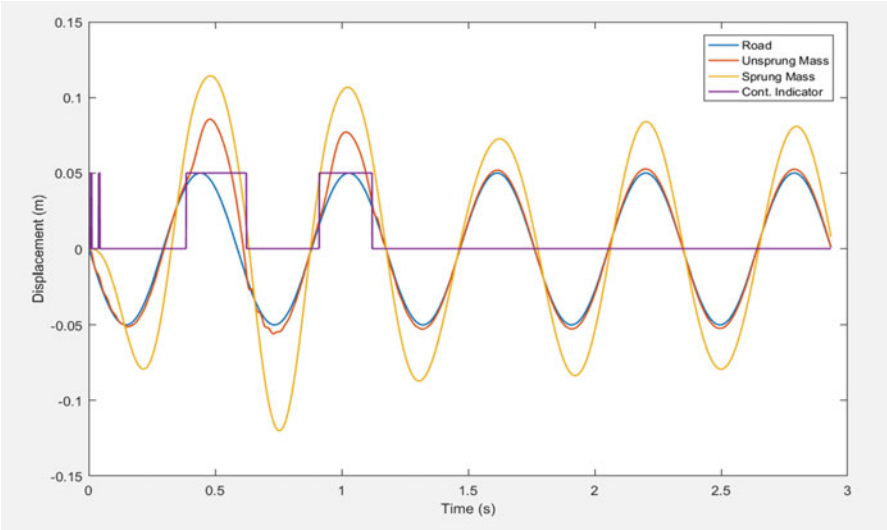

Fig. 7.6 Example of transient separation

shows an example of transient separation (amplitude 0.05, zeta 0.1, frequency ratio 0.60).

As the frequency is increased further at any given damping ratio and amplitude values, the system starts to exhibit repeated separation over a portion of each cycle; this could be termed as steady-state separation. Figure 7.7 shows an example of steady-state separation.

At some particular conditions, typically at high damping ratios and high amplitudes, the system exhibits non-uniform separation behaviour; in these cases the wheel is thrown clear off the ground with large velocities; as it travels back as a projectile, it passes multiple input cycles while it is airborne. An example of this case is shown in Fig. 7.8.

7.3.2 Separation Frequency

The frequency at which the tire loses contact with the road may be referred to as the separation frequency. At this frequency the tire is in the free-fall state for some interval in each cycle; separation in transient part of the response is ignored. The separation frequency is found to be a strong function of input amplitude especially at low amplitudes; it flattens out once the frequency ratio reduces to nearly 1 at higher amplitudes, which is when the frequency is close to the sprung mass natural frequency (Fig. 7.9).

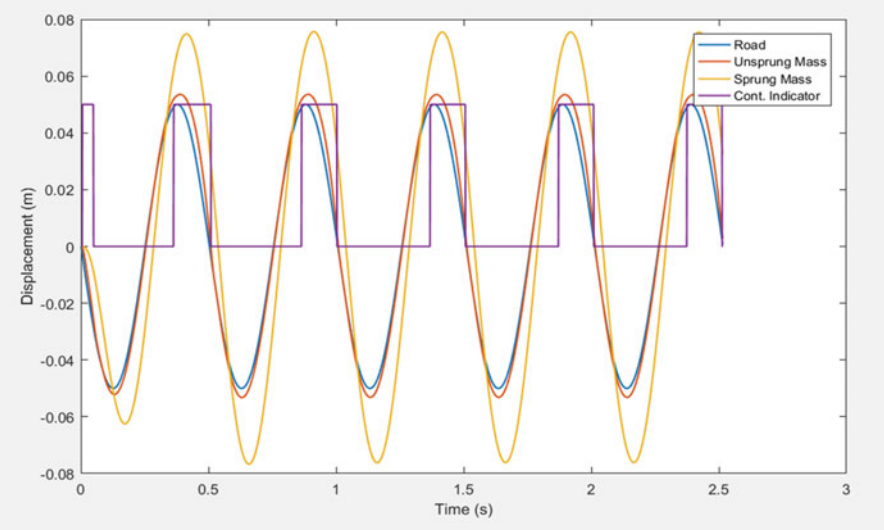

Fig. 7.7 Example of steady-state separation (amplitude 0.05, zeta 0.5 and frequency ratio 0.7)

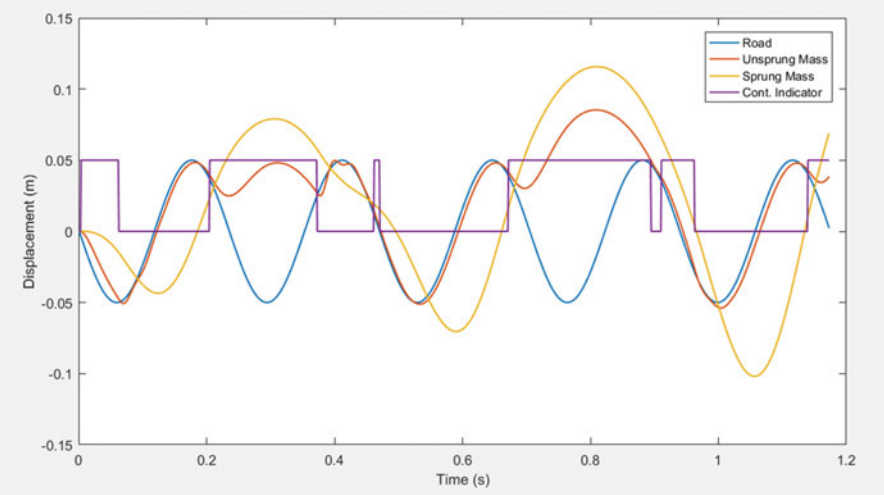

Fig. 7.8 Example of non-uniform separation (amplitude 0.05, zeta 0.2 and frequency ratio 1.5)

Separation frequency is also sensitive to damping ratio, but the effect is less significant compared to that of input amplitude; the effect diminishes at high amplitudes. At high damping ratios, the relation between input amplitude and separation frequency seems to follow a similar trend; however at very low damping ratios, they seem to deviate from the trend. One possible explanation for this deviation may be the influence of unsprung mass mode at higher frequencies.

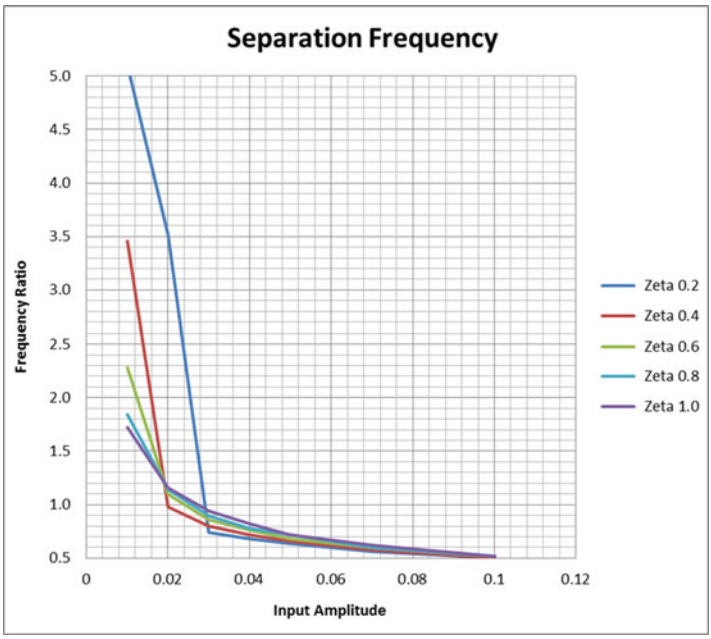

Fig. 7.9 Separation frequency curves

The separation frequency plot may be considered to define the limits of validity for a linear model; the linear model would remain valid for conditions below the separation curve. However it will not be accurate at conditions above the separation frequency curves; accuracy of a linear model will decrease as we move away from the separation frequency curves; this is demonstrated in subsequent sections of this report.

7.3.3 Time Responses

7.3.3.1 No Separation

At conditions under the corresponding separation curve shown in Fig. 7.10, both sprung and unsprung masses tend to follow the input excitation or road profile. Frequency of both the masses is same as the input excitation, amplitude of unsprung mass is close to the road undulation amplitude, and phase difference between unsprung mass and input is small. Figures 7.10 and 7.12 show time response of the system under two different sets of conditions with continuous contact.

Since there is no separation, the results are same as those obtained from a linear model; this implies that a linear model is valid under these conditions as discussed

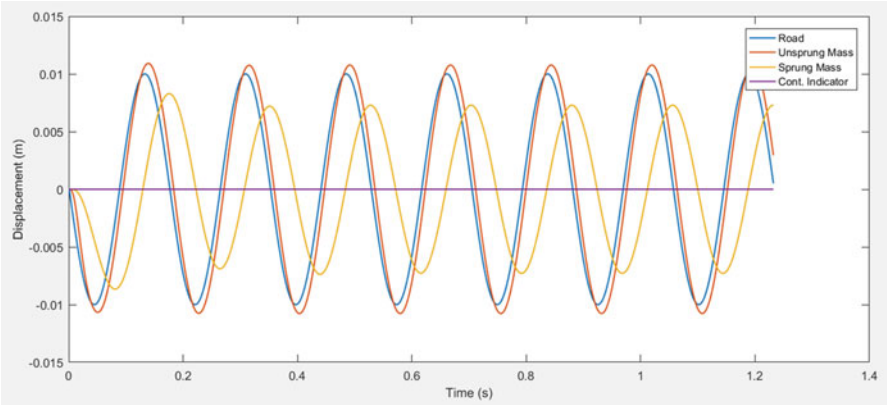

Fig. 7.10 Example of no separation time response (amplitude 0.01, zeta 0.6 and frequency ratio 2.0)

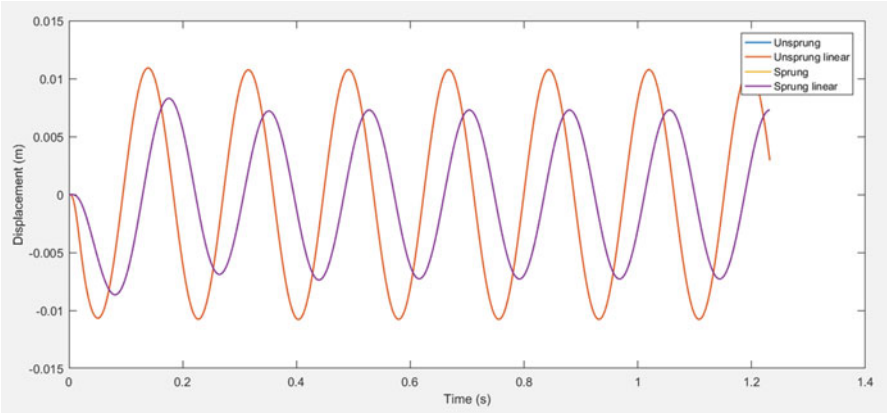

Fig. 7.11 Comparison with linear model results (amplitude 0.01, zeta 0.6 and frequency ratio 2.0)

above. Figures 7.11 and 7.13 show that the response of nonlinear model is exactly same as that of the linear model.

7.3.3.2 Transient Separation

Transient separation also occurs at conditions under the corresponding separation curves. Figures 7.14, 7.16, and 7.18 show examples of transient separation while Figs. 7.15, 7.17, and 7.19 compare the results at these conditions with a linear model. Results of the nonlinear model deviate slightly from those of the linear model as the tire breaks contact; however they do not converge immediately as the contact is regained. This shows that tire separation affects the entire response and

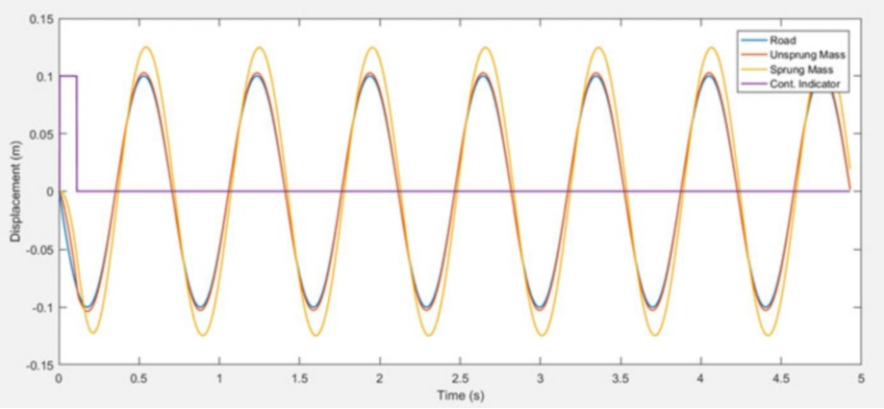

Fig. 7.12 Example of no separation time response (amplitude 0.1, zeta 0.6 and frequency ratio 0.7)

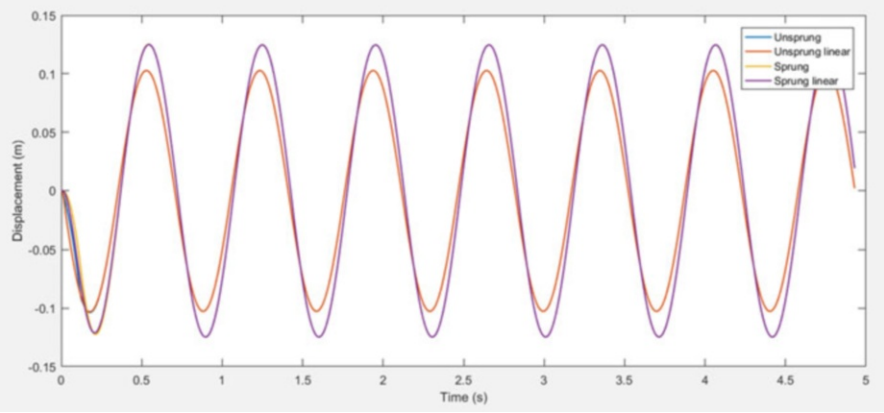

Fig. 7.13 Comparison with linear model results (amplitude 0.1, zeta 0.6 and frequency ratio 0.5)

not just the interval in which the tire is not in contact with the ground. However, the error is very small, and therefore a linear model can still be used under these conditions to give very accurate predictions of behaviour of a particular suspension.

7.3.3.3 Steady-State Separation

At conditions above the corresponding separation frequency curves, we can observe steady-state separation. With steady-state separation, the system is not in contact with the ground (free-fall state) for a certain period in each cycle; this interval of separation must remain nearly equal for each cycle after the system has settled into

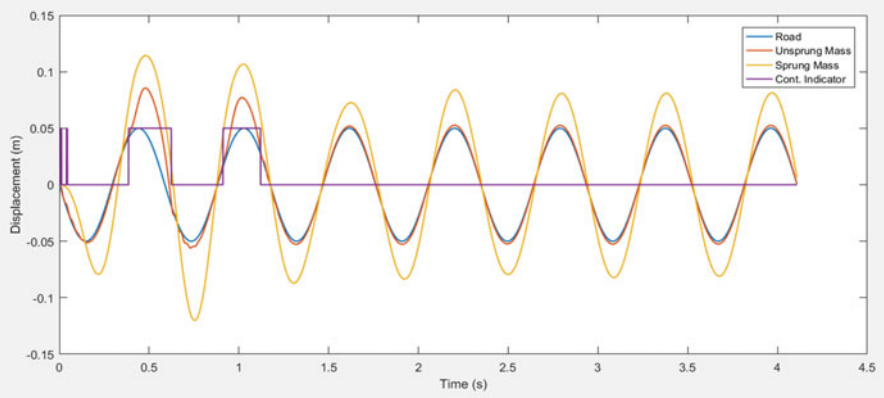

Fig. 7.14 Example of transient separation time response (amplitude 0.05, zeta 0.1 and frequency ratio 0.6)

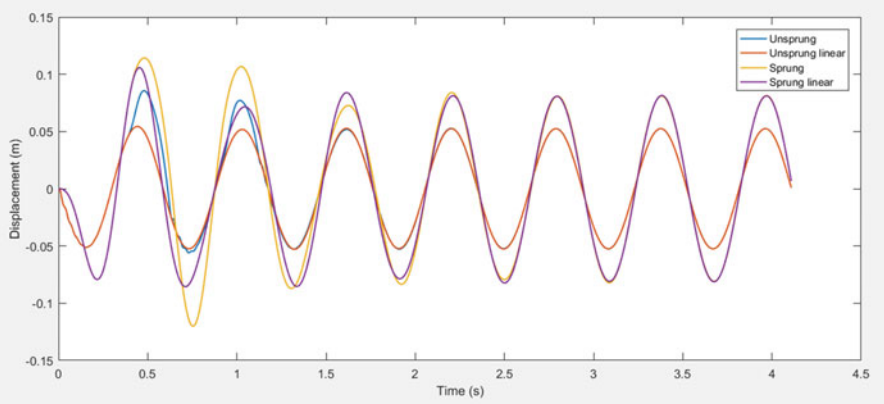

Fig. 7.15 Comparison with linear model results (amplitude 0.05, zeta 0.1 and frequency ratio 0.6)

steady state after passing through transient vibrations. The duration of separation may vary depending on frequency, amplitude and damping ratio.

At low frequency, close to sprung mass natural frequency, a linear model provides a good estimate of unsprung mass displacement; however sprung mass displacement is overestimated for low damping and underestimated for high damping scenarios.

At moderately high frequency ($r = 4$), linear model produces reasonable estimates for both sprung and unsprung mass displacements for systems with low damping, whereas for systems with high damping ratios, the linear model predictions are very large and cannot be considered as a useful approximation of the system behaviour. At this frequency a critically damped system with a high input

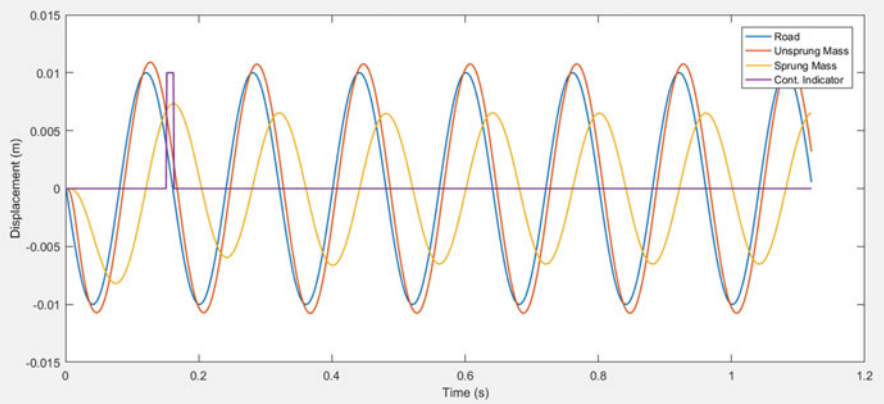

Fig. 7.16 Example of transient separation time response (amplitude 0.01, zeta 0.6 and frequency ratio 2.2)

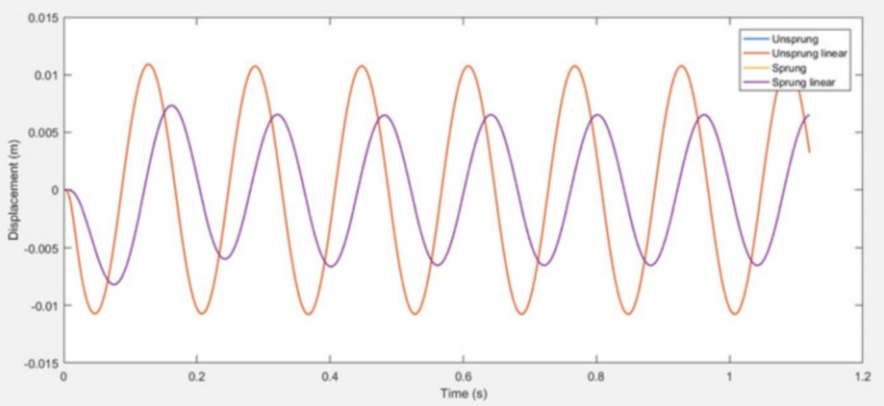

Fig. 7.17 Comparison with linear model results (amplitude 0.01, zeta 0.6 and frequency ratio 2.2)

amplitude tends to bounce high off the road; due to the long time taken by the system to return to surface, the response frequency does not remain the same as the input frequency, amplitudes are also exceptionally large, and very large forces may be transmitted to the body when the tire impacts the ground. An example of this phenomenon is shown in Fig. 7.20.

At very high frequency ($r = 7$), a system with low damping subjected to low input amplitude shows a response that is reasonably close to the estimate obtained from a linear model; with higher damping ratios, the error in linear model increases significantly. When the system is subjected to higher input, amplitudes at this frequency sprung mass exhibit a very small amplitude; this behaviour may be described as “float”; the sprung mass shows very small vertical displacements

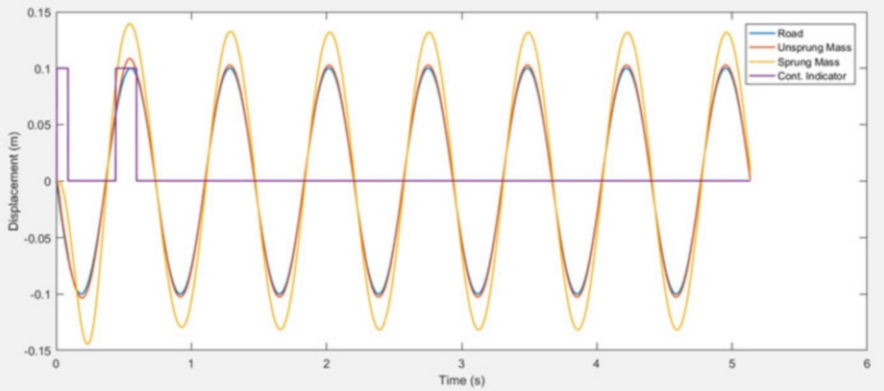

Fig. 7.18 Example of transient separation time response (amplitude 0.1, zeta 0.2 and frequency ratio 0.48)

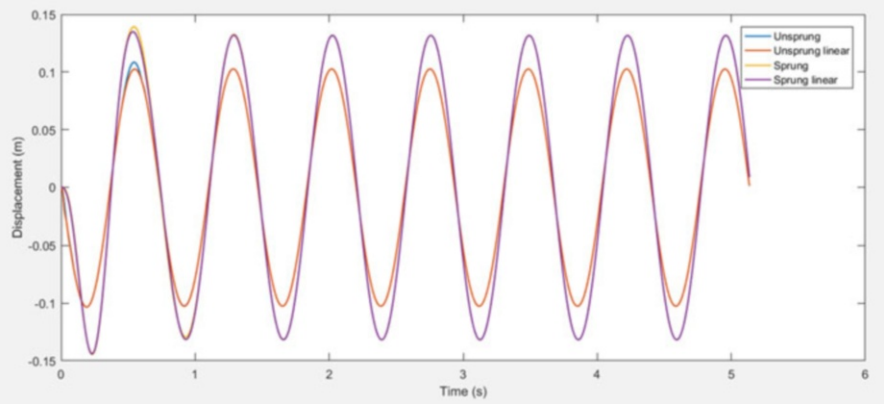

Fig. 7.19 Comparison with linear model results (amplitude 0.1, zeta 0.2 and frequency ratio 0.48)

and seems to float over the corrugations. An example of "float" is shown in Fig. 7.21.

Bounce and float phenomena are important from a ride perspective. Bounce may produce a very wobbly and soft ride quality which may be far worse than that predicted by the linear model. Float may produce a much harsher ride due to large forces transmitted to the body but more level due to smaller body displacements.

7.3.4 Frequency Responses

As observed in the previous section (see Sect. 7.3.3), the response of the system is sensitive to input frequency, input amplitude and system damping. Unlike linear

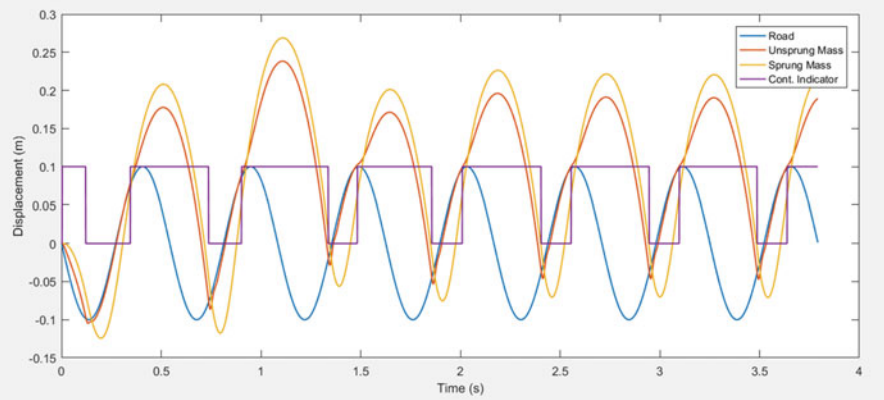

Fig. 7.20 Example of bounce phenomenon (amplitude, 0.1 m; frequency ratio, 0.65; damping ratio, 0.4)

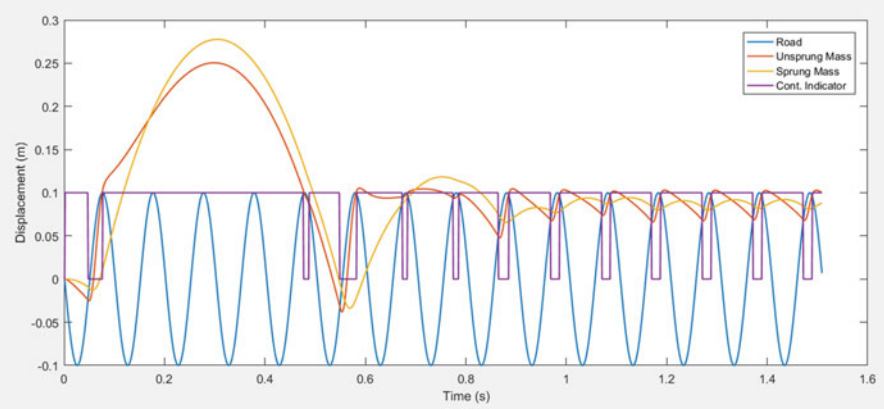

Fig. 7.21 Example of float behaviour (amplitude, 0.1 m; frequency ratio, 3.5; damping ratio, 0.6)

models the output amplitude is not directly proportional to the input amplitude; therefore the frequency responses cannot be represented as a ratio of input and output amplitudes. The system behaviour is unique at each different set of conditions; therefore frequency responses are shown at four distinct input amplitudes and five distinct damping ratios.

At very low amplitude (0.01 m), the response of the system is very similar to that of a linear model due to the fact that separation only starts at very high frequencies at this amplitude (see Sect. 7.2), and even when separation does occur, it is for a relatively short duration, and the response tends to deviate very slightly from the linear response. Figure 7.22 shows that the responses do not pass through a node at high frequencies as they would be expected to in a linear system; this can be

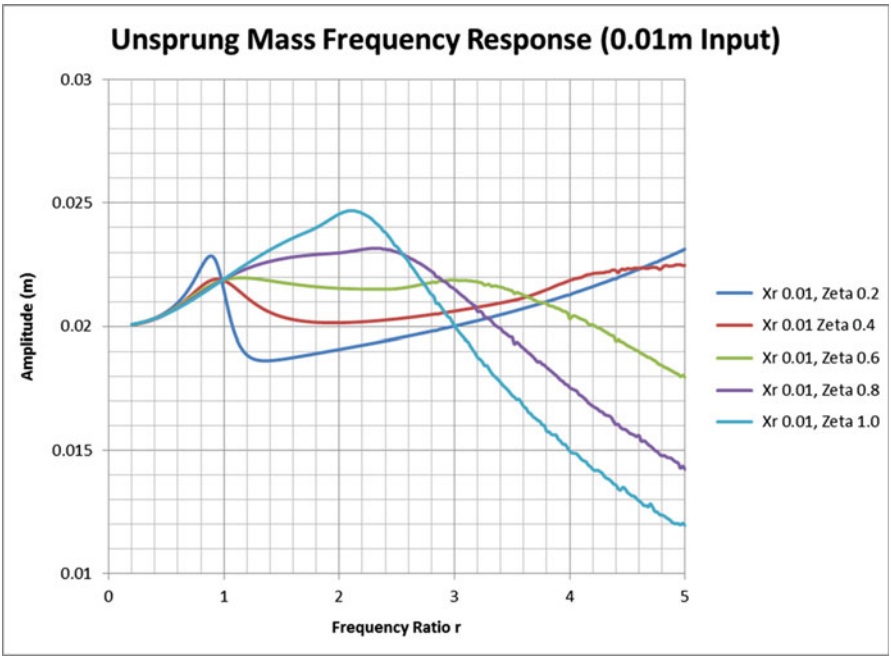

Fig. 7.22 Frequency response of unsprung mass to 0.01 m input

attributed to the fact that at high frequencies, the system tends to separate as shown in Fig. 7.9; therefore it starts to deviate from linear behaviour.

In Fig.7.23 we can observe that all the responses have a peak close to a frequency ratio of 1; this corresponds with resonance; at these frequencies the system may be separating, but the effect of separation on the overall response is small. As the frequency is increased, a secondary peak or plateau appears; this is visible in all of the responses; the top of the plateau corresponds to the bounce behaviour discussed in Sect. 7.3.3.3. At very high frequencies, all responses exhibit very low amplitudes which correspond to the float phenomenon discussed in Sect. 7.3.3.3.

Figure 7.26 shows how generic frequency response of a system with separation can be divided into different "regions" corresponding with the system time response behaviour. At low frequencies the system tends to follow the road and exhibits behaviour close to that of a linear system; the system then transitions from near-linear behaviour to bounce as the response approaches the secondary peak; following the second peak, the system exhibits pure bounce behaviour until the amplitude drops sharply and system transitions from bounce to float; at very high frequencies, the system settles to a consistent low amplitude and exhibits float behaviour. Figures 7.24, 7.25, 7.26, and 7.27 show examples corresponding to each of the regions of frequency response.

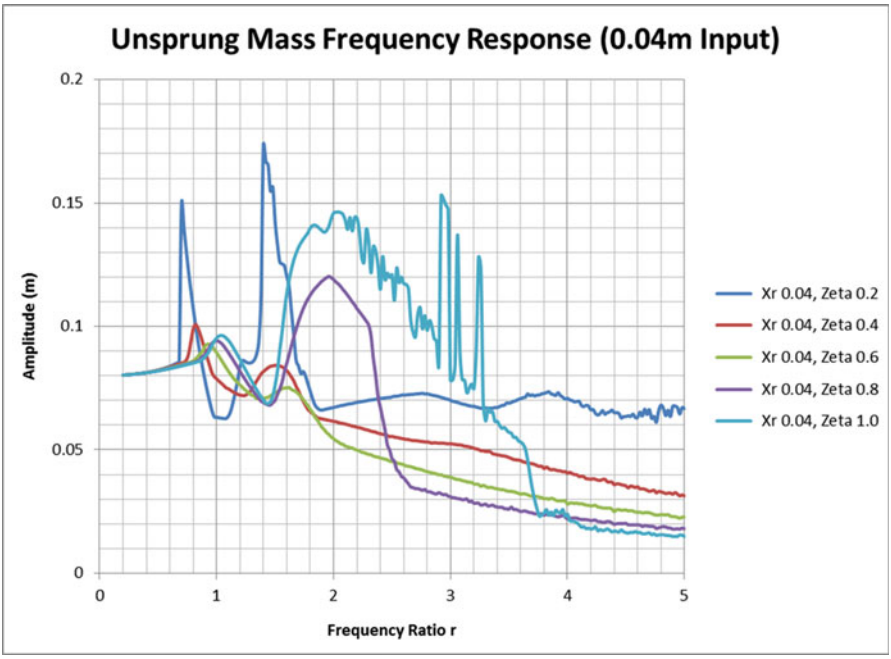

Fig. 7.23 Frequency response of unsprung mass to 0.04 m input

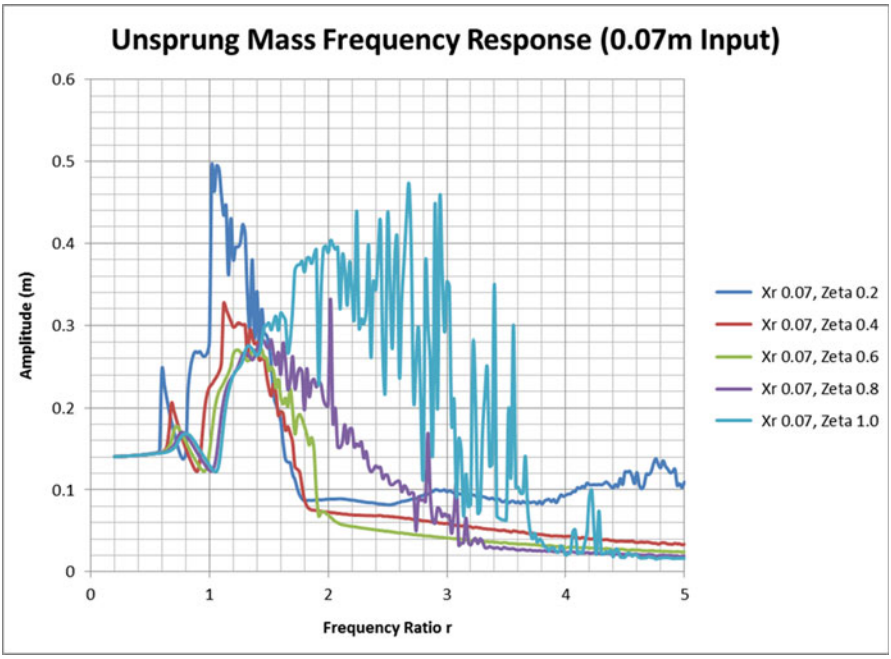

Fig. 7.24 Frequency response of unsprung mass to 0.07 m input

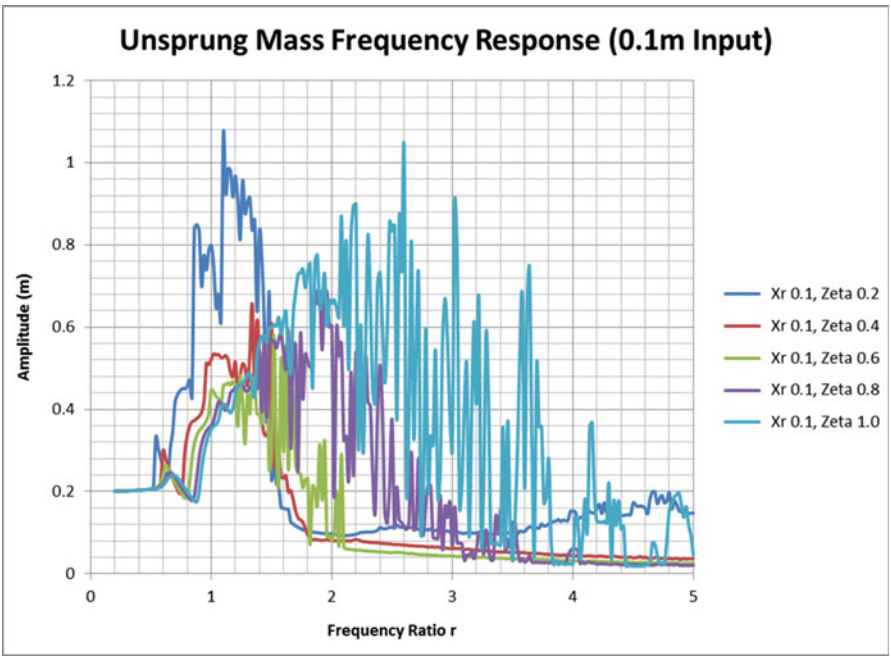

Fig. 7.25 Frequency response of unsprung mass to 0.1 m input

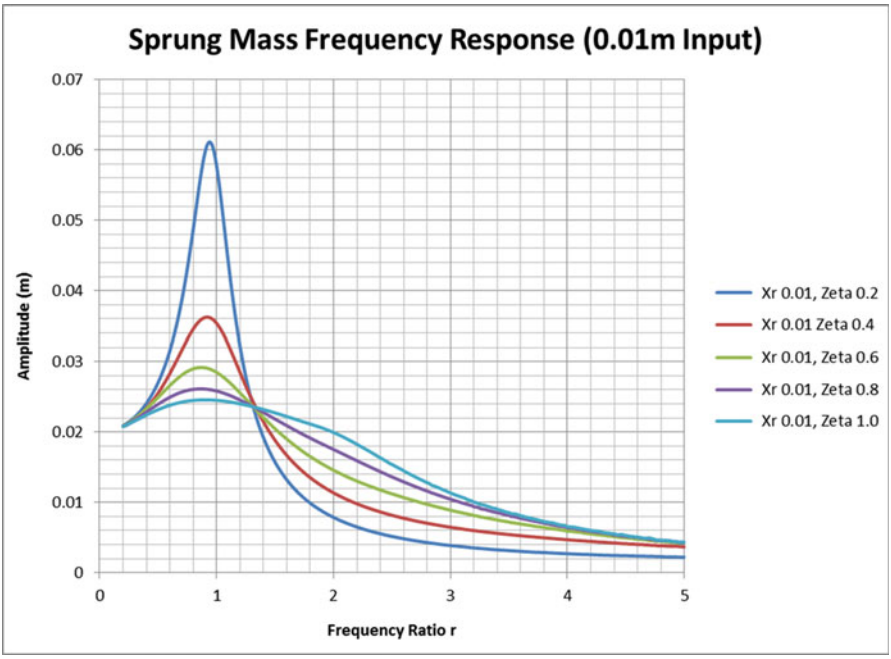

Fig. 7.26 Frequency response of sprung mass to 0.01 m input

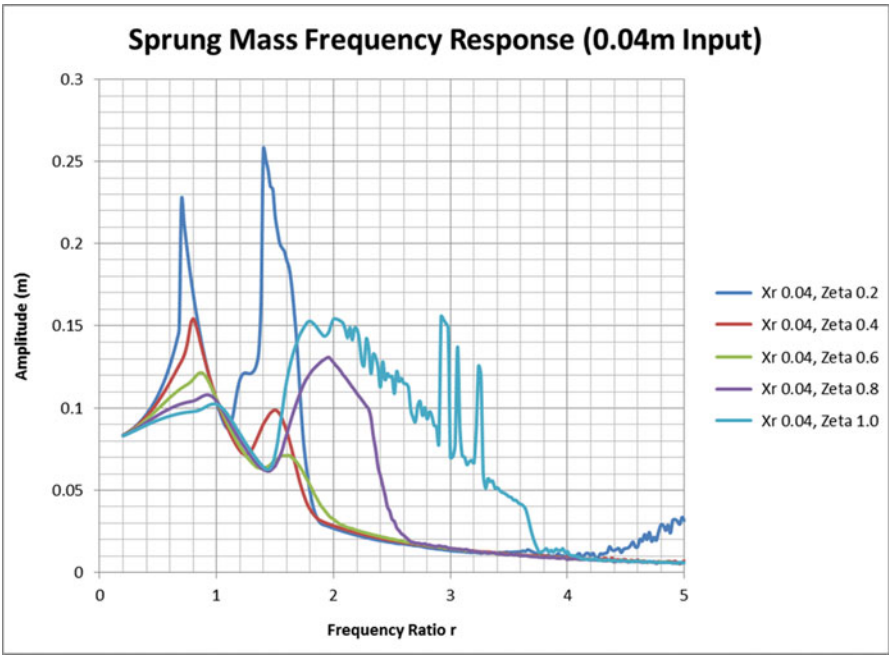

Fig. 7.27 Frequency response of sprung mass to 0.04 m input

At higher amplitudes this phenomenon can still be observed; however since the system is very unstable at high amplitudes, the responses show a lot of "noise", particularly in the bounce frequency range (Fig. 7.28).

Another noticeable trend is that the secondary peak reduces in height as damping is reduced from critical damping, but at very low damping ratios, the peak starts rise again; this indicates an opportunity for optimization of damping ratio to reduce displacement (Figs. 7.29, 7.30, 7.31, 7.32, 7.35).

7.3.5 Duration of No-Contact Condition

Duration of separation refers to the fraction of the oscillation time period in which the tire is not in contact with the road, i.e.

$$\text{Duration of Separation } (\%) = \frac{\text{Time in free fall state}}{\text{Total time}} \times 100$$

Duration of separation is calculated only for the steady-state response; the transient part is ignored. Cases where the entire response is unsteady appear as discontinuities or noise in the plots.

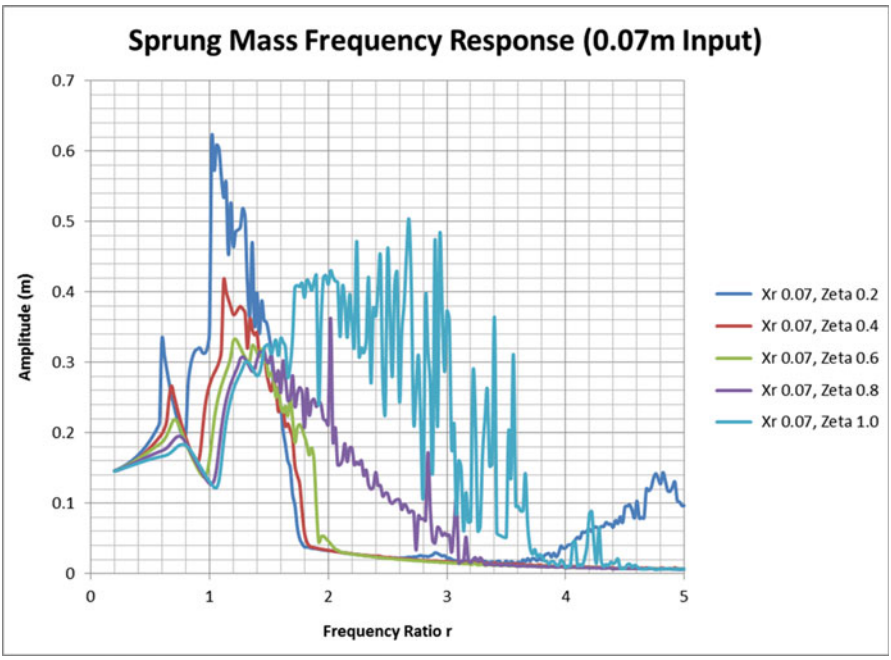

Fig. 7.28 Frequency response of sprung mass to 0.07 m input

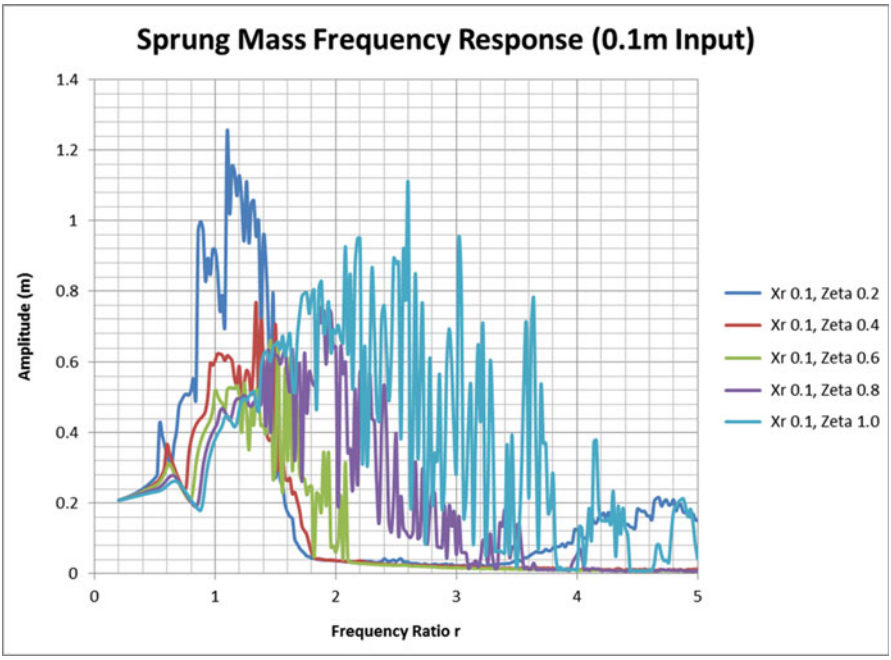

Fig. 7.29 Frequency response of sprung mass to 0.1 m input

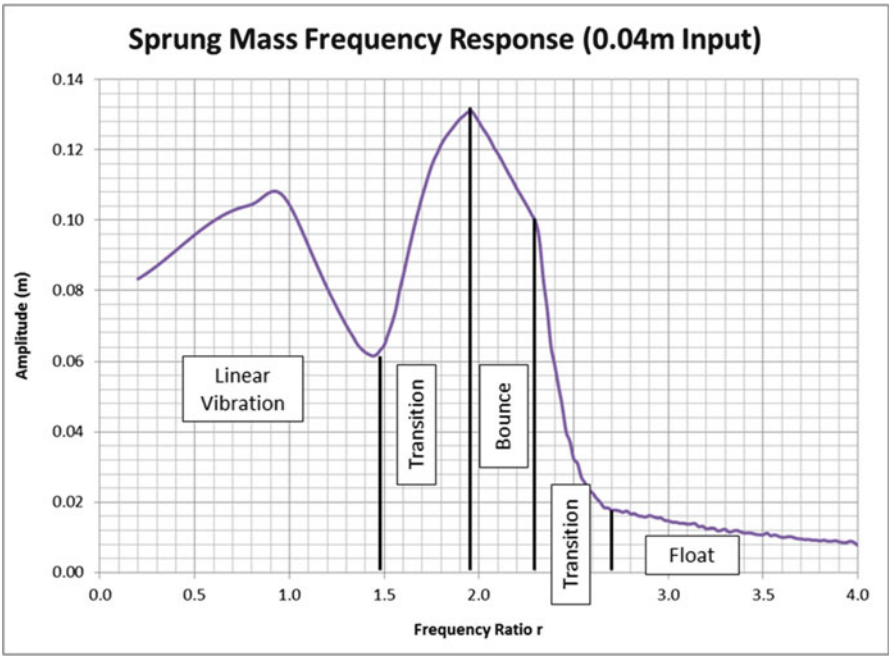

Fig. 7.30 System behaviour in different frequency ranges (zeta 0.8)

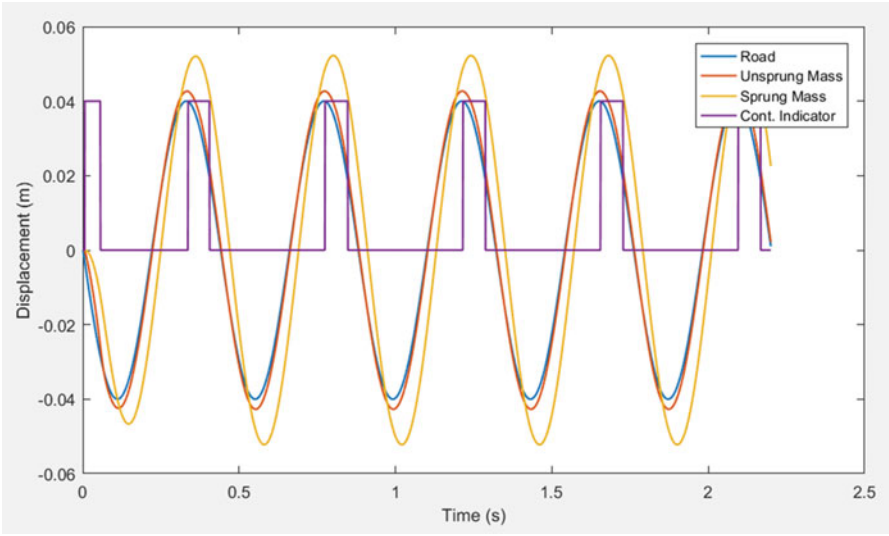

Fig. 7.31 Example of near-linear behaviour

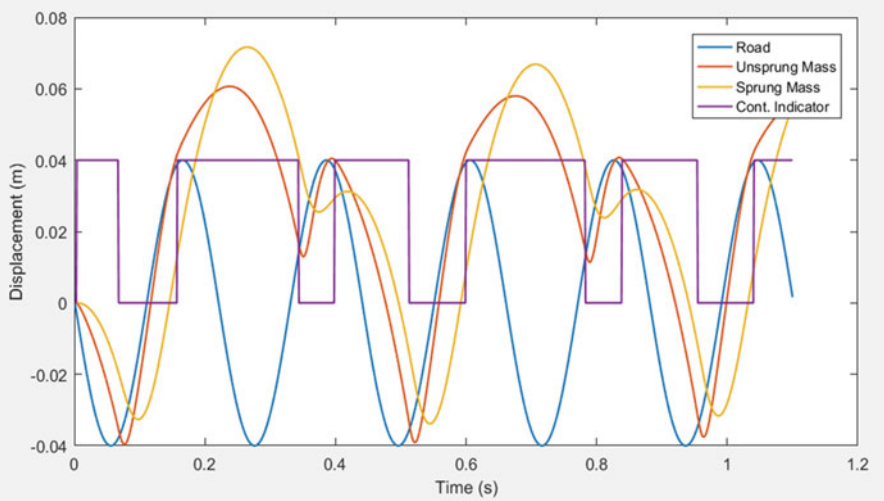

Fig. 7.32 Example of transition from linear to bounce

Tire separation duration plot provides some interesting insight into the behaviour of the system; this reconfirms the separation frequencies shown in Fig. 7.5; the projectile motion phenomenon discussed earlier can also be observed in Fig. 7.34 as the large plateau in the curve for critically damped system between $r = 2$ and $r = 3$.

It may be tempting to consider these plots as a measure of grip or handling performance; however this may not be entirely accurate as these plots show a ratio of time and do not show the instantaneous force; it only indicates the fraction of time when no grip will be available at all.

Figure 7.33 also shows that at low damping ratios the system may re-establish continuous contact at frequencies beyond the initial separation frequency (Fig. 7.36).

7.4 Nonlinear Damping

In order to visualize a more realistic response, a nonlinear damping scenario was also simulated. Actual automotive suspensions employ nonlinear or asymmetric dampers; in an asymmetric damper, the damping ratio in bump is not equal to that in rebound. In order to keep the model simple, damping coefficient in bump is zero, while that in rebound is a constant positive coefficient as shown in Fig. 7.40.

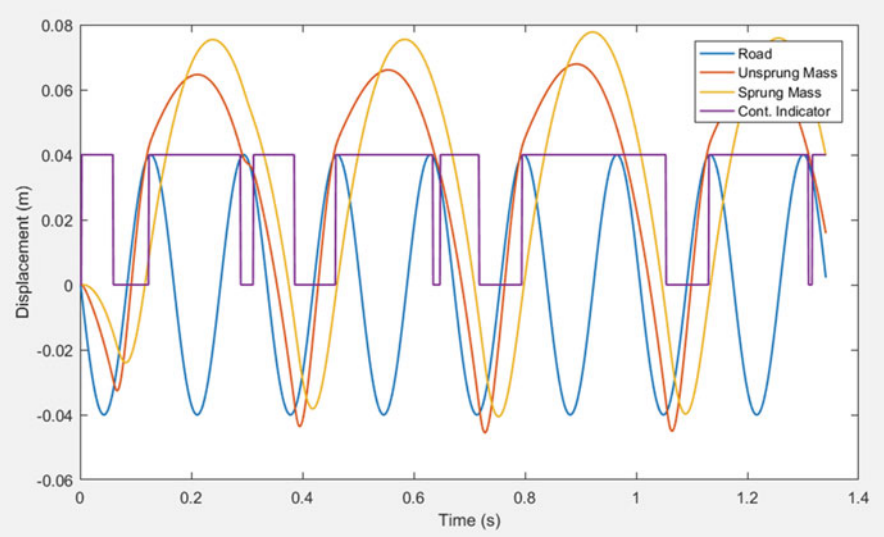

Fig. 7.33 Example of bounce behaviour

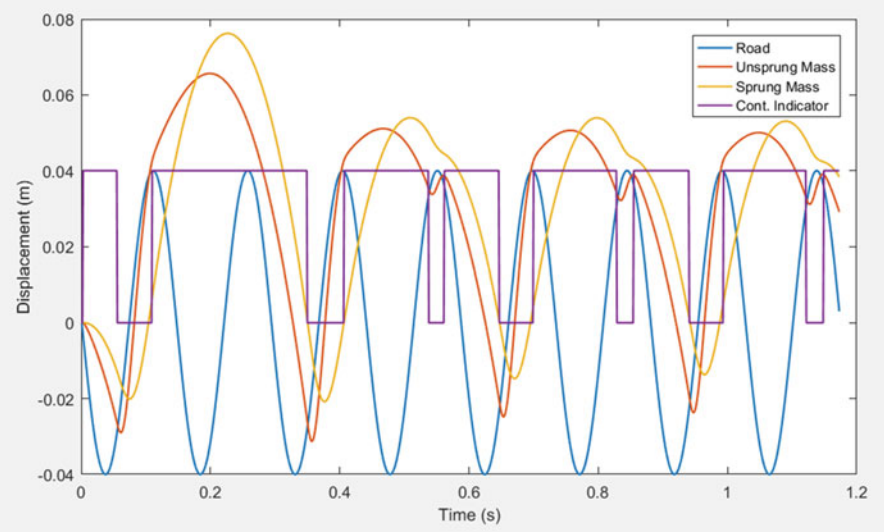

Fig. 7.34 Example of transition from bounce to float

7.4.1 Time Response with Nonlinear Damping

Figures 7.37, 7.38, and 7.39 show time response plots for systems with nonlinear damping as well as linear damping. Unsprung mass displacement for nonlinear

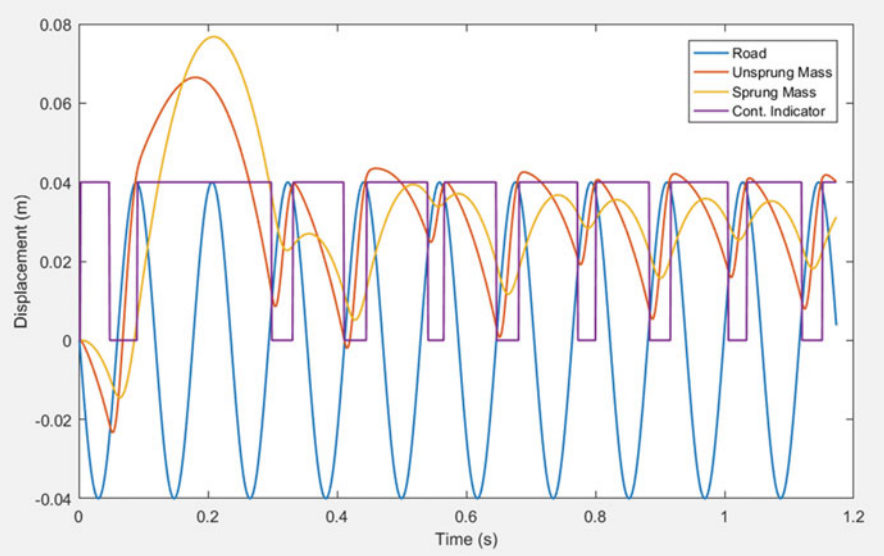

Fig. 7.35 Example of float behaviour

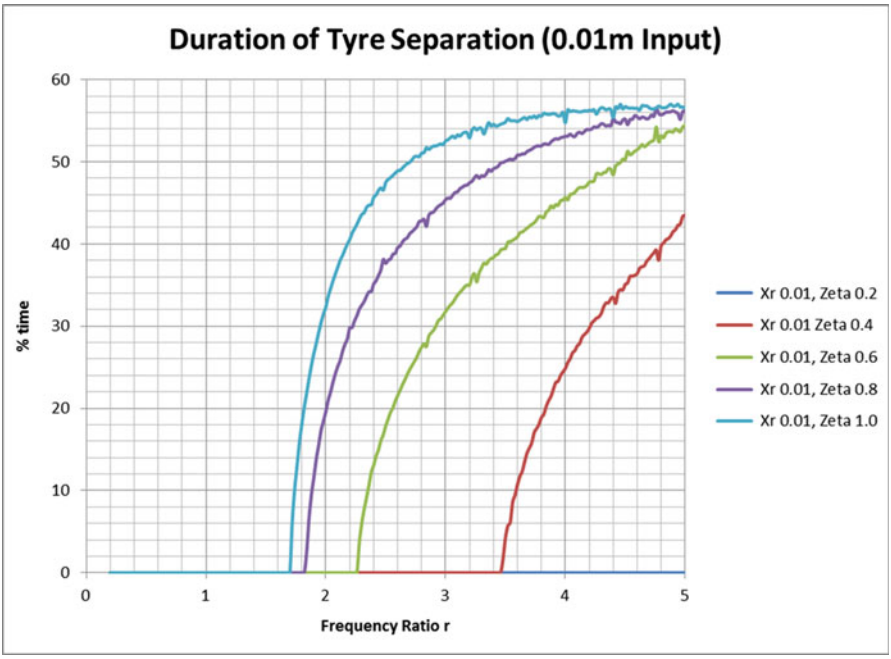

Fig. 7.36 Duration of tire separation in response to 0.01 m input

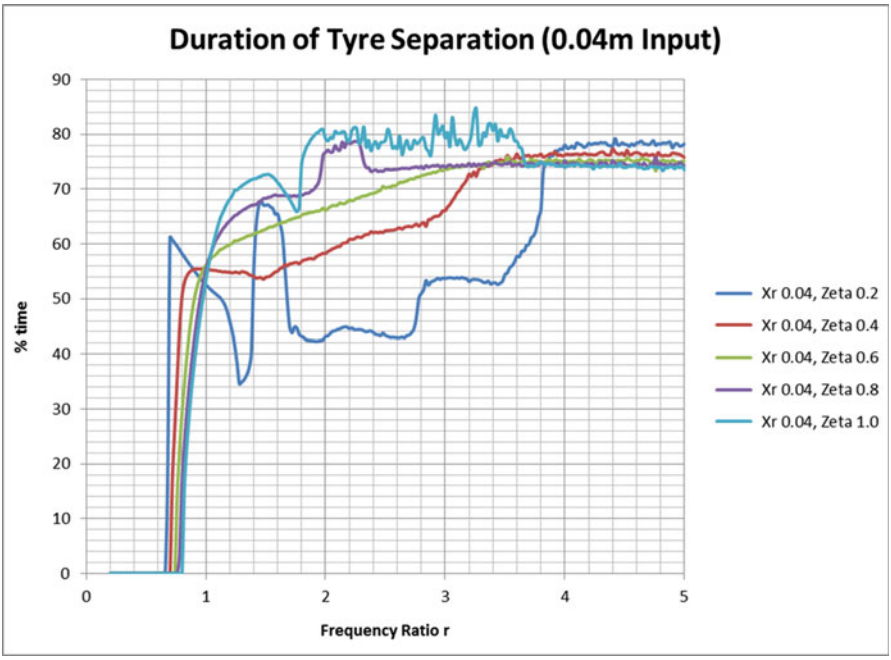

Fig. 7.37 Duration of tire separation in response to 0.04 m input

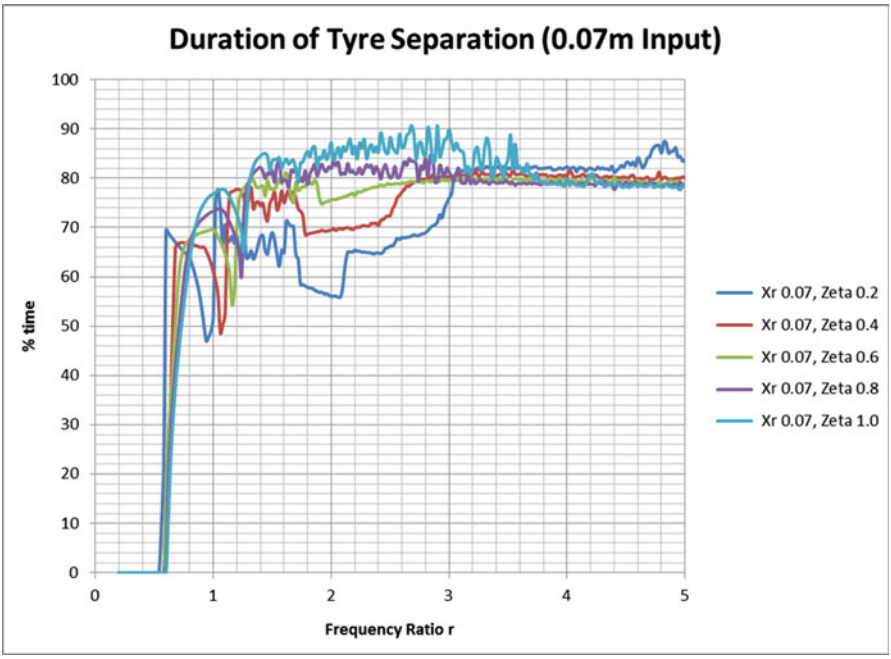

Fig. 7.38 Duration of tire separation in response to 0.07 m input

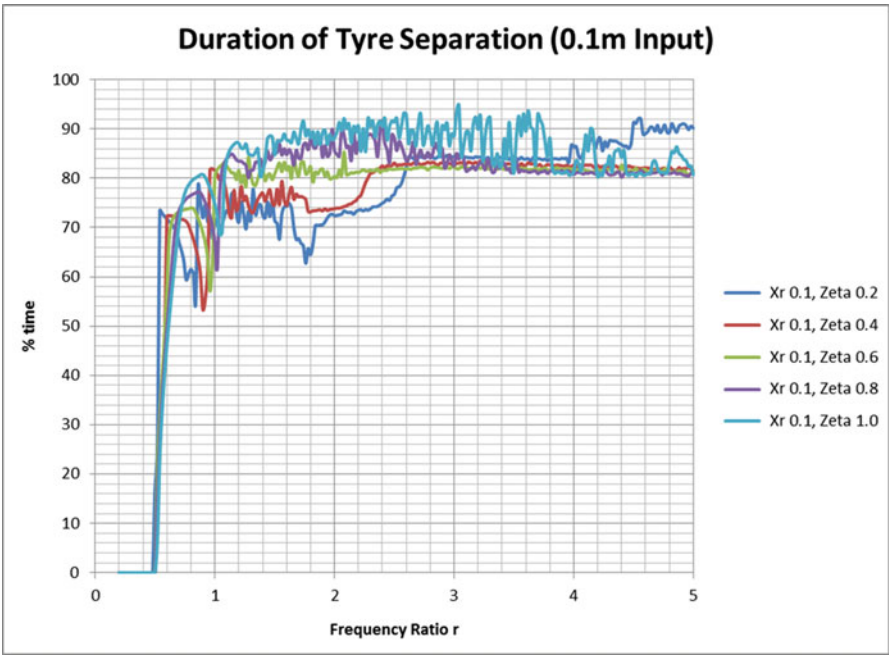

Fig. 7.39 Duration of tire separation in response to 0.1 m input

damping is similar to that with linear damping at most of the conditions; however, with nonlinear damping, unsprung mass sticks to the ground better and achieves steady state quicker in "bounce" conditions. Another phenomenon apparent in the figures below is that the sprung mass vibrates about a lower "mean" position with nonlinear damping than it does linear damping; the car hunkers down as it goes over successive bumps. The sprung mass response also shows a secondary frequency, much lower than the primary frequency which is equal to the road input frequency.

7.4.2 Frequency Response with Nonlinear Damping

Figure 7.40 shows the separation frequency plot for system with nonlinear damping; when compared with Fig. 7.9, separation frequencies for nonlinear damping are lower than those with linear damping throughout the amplitude range considered. This implies that the likelihood of loss of contact is increased when using nonlinear damping in a model.

Figures 7.41, 7.42, 7.43, and 7.44 show frequency responses for unsprung mass with nonlinear damping at different amplitudes; Figs 7.45, 7.46, 7.47, and 7.48 show the corresponding responses for sprung mass.

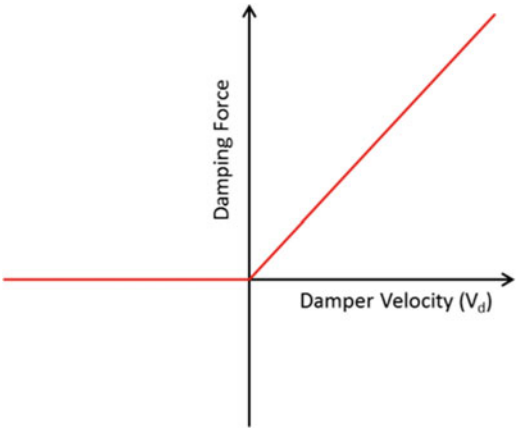

Fig. 7.40 Damper characteristic for nonlinear damper

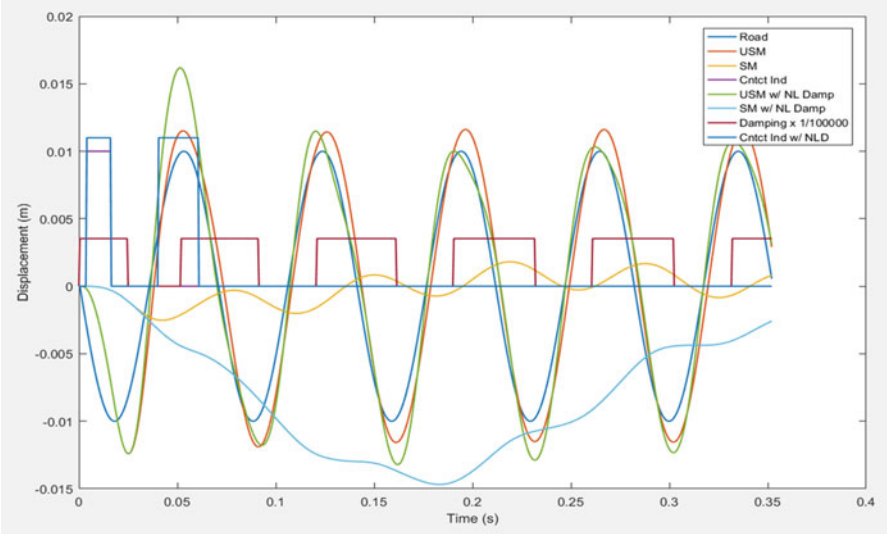

Fig. 7.41 Comparison between linear and nonlinear damping (amplitude, 0.01 m; frequency ratio, 5; damping ratio, 0.2)

The frequency responses show that the frequency range for "bounce" is much smaller with nonlinear damping than it is with linear damping and that it is almost equal for all damping values. The system with nonlinear damping becomes more stable (less noise) as damping is increased; in contrast the system with linear damping becomes more unstable as damping is increased. Sprung mass displacement is very low throughout the frequency range and follows the pattern of a linear (no separation) model except for the small frequency range where "bounce" phenomenon is seen (Figs. 7.49, 7.50, 7.51, and 7.52).

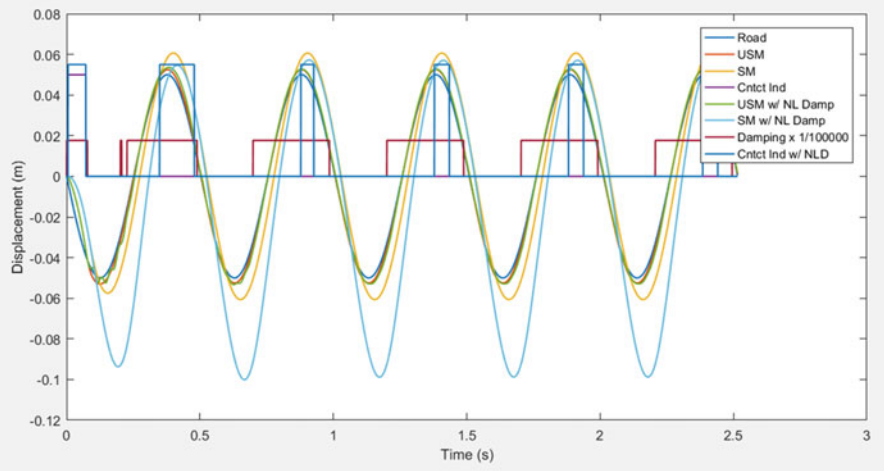

Fig. 7.42 Comparison between linear and nonlinear damping (amplitude, 0.05 m, frequency ratio, 0.7, damping ratio, 1.0)

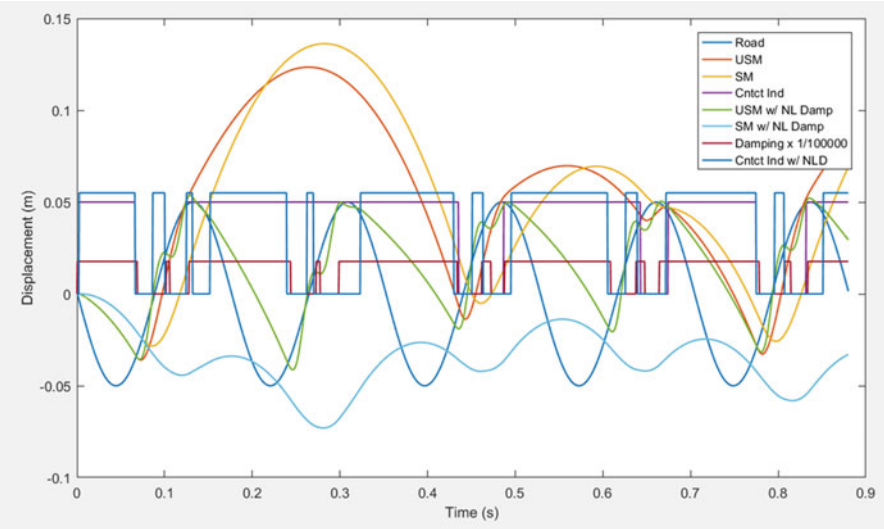

Fig. 7.43 Comparison between linear and nonlinear damping (amplitude, 0.05 m; frequency ratio, 2.0; damping ratio, 1.0)

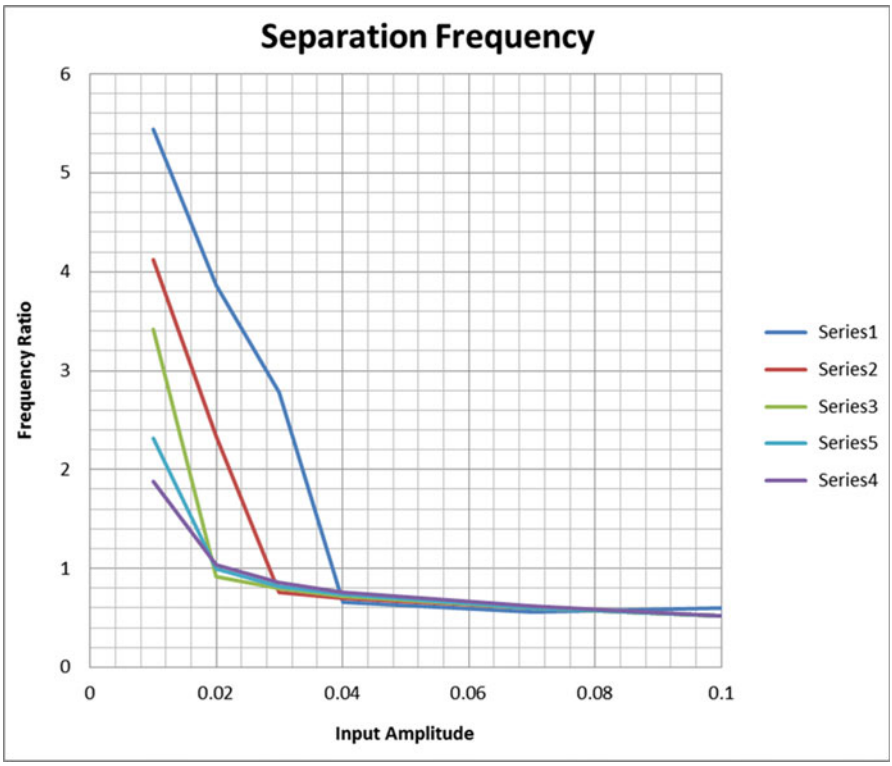

Fig. 7.44 Separation frequency plot with nonlinear damping

7.5 Conclusion

The results of this investigation have shown that the tire separation is mathematically detectable and is likely to occur within the normal range of operating conditions of common passenger and competition vehicles. Steady-state separation is initiated at a fixed set of conditions. Transient separation does affect the overall response of the system, but the deviation from linear response is very small and therefore insignificant.

Separation frequency curves can be regarded as the limits of accurate application of linear models; beyond this boundary the linear model may not yield an accurate approximation of system response. At low damping ratios, the linear model results may still be reasonable, but with higher damping ratios common in passenger and performance cars, linear models may produce very misleading results.

Linear models may still be useful for many applications, but this investigation shows that care should be taken when selecting an appropriate model for a specific application; the desired operating conditions of the application should be considered when making this decision.

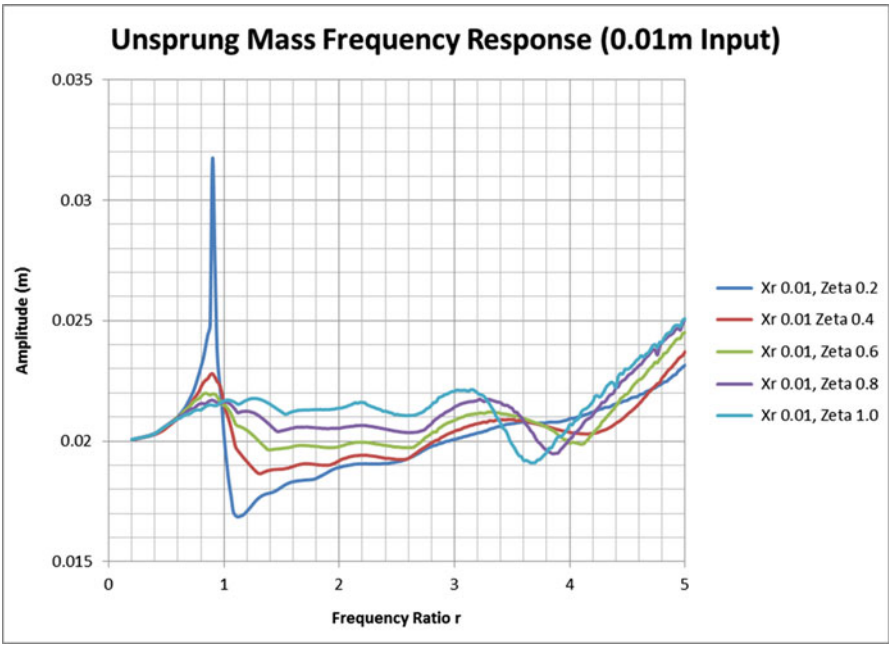

Fig. 7.45 Frequency response of unsprung mass with nonlinear damping to 0.01 m input

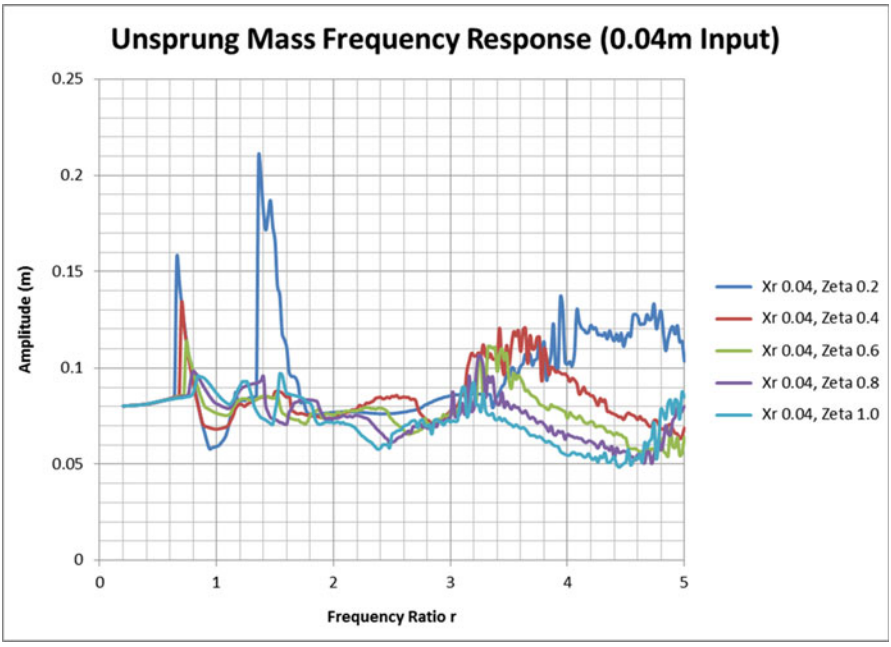

Fig. 7.46 Frequency response of unsprung mass with nonlinear damping to 0.04 m input

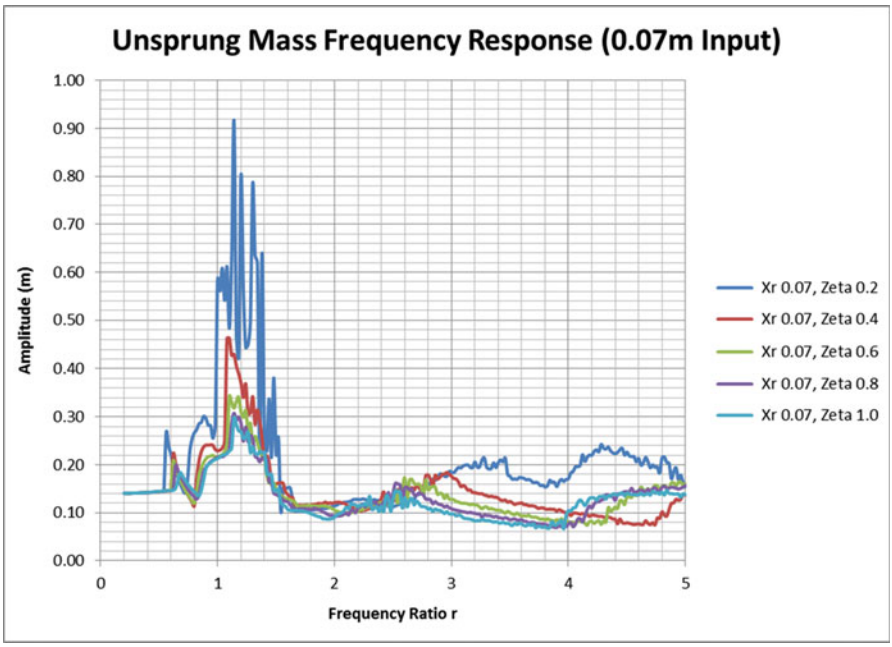

Fig. 7.47 Frequency response of unsprung mass with nonlinear damping to 0.07 m input

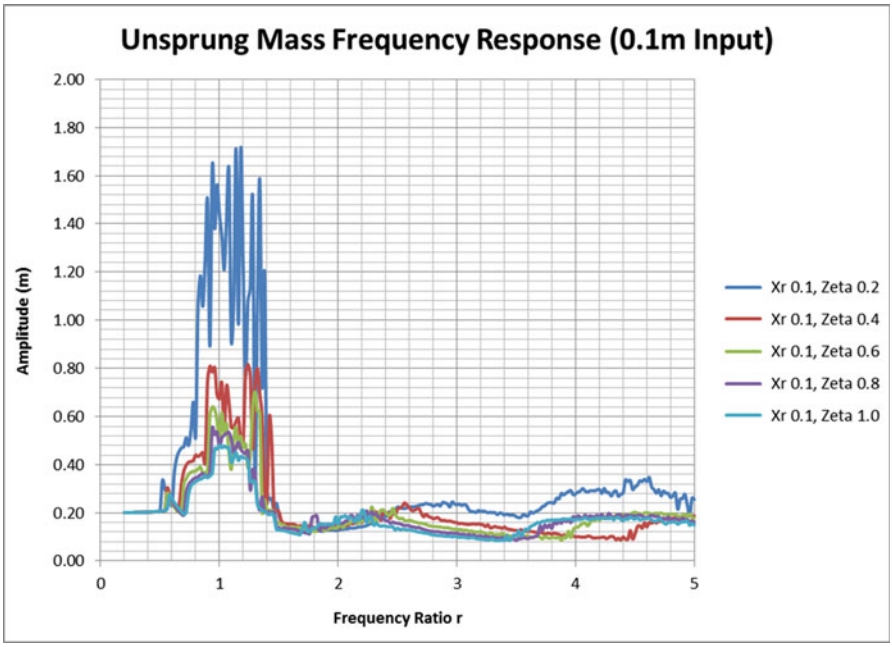

Fig. 7.48 Frequency response of unsprung mass with nonlinear damping to 0.1 m input

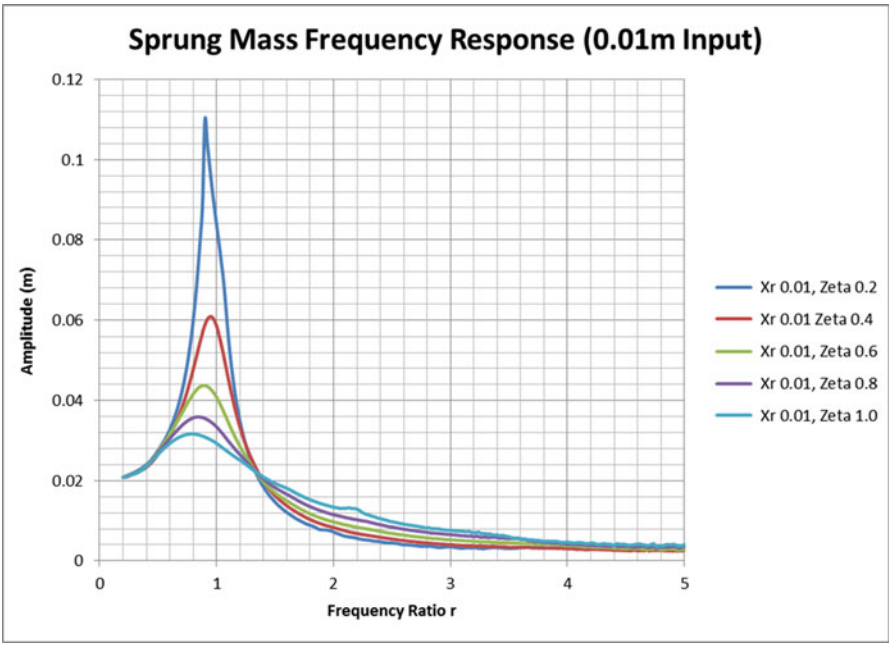

Fig. 7.49 Frequency response of sprung mass with nonlinear damping to 0.01 m input

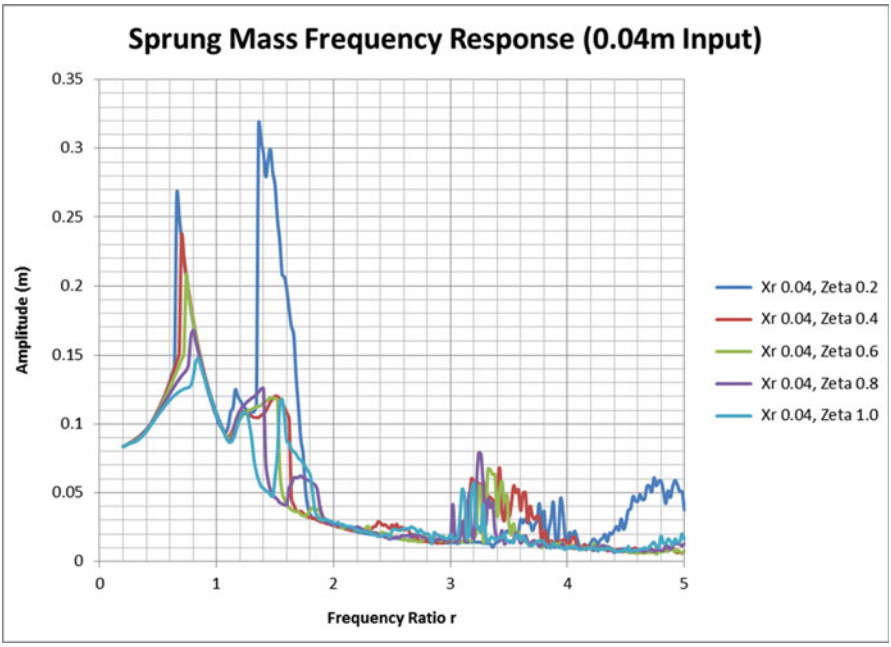

Fig. 7.50 Frequency response of sprung mass with nonlinear damping to 0.04 m input

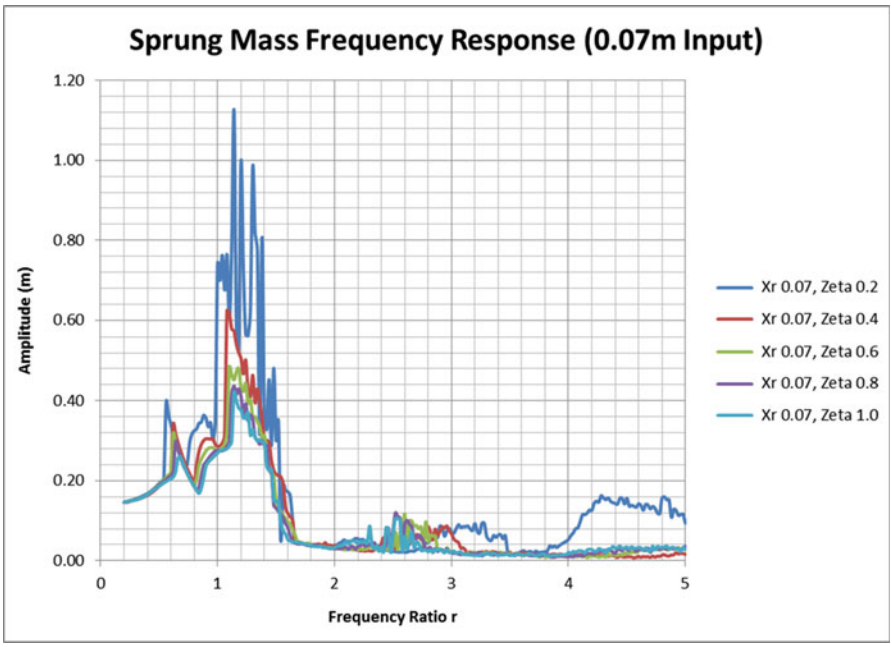

Fig. 7.51 Frequency response of sprung mass with nonlinear damping to 0.07 m input

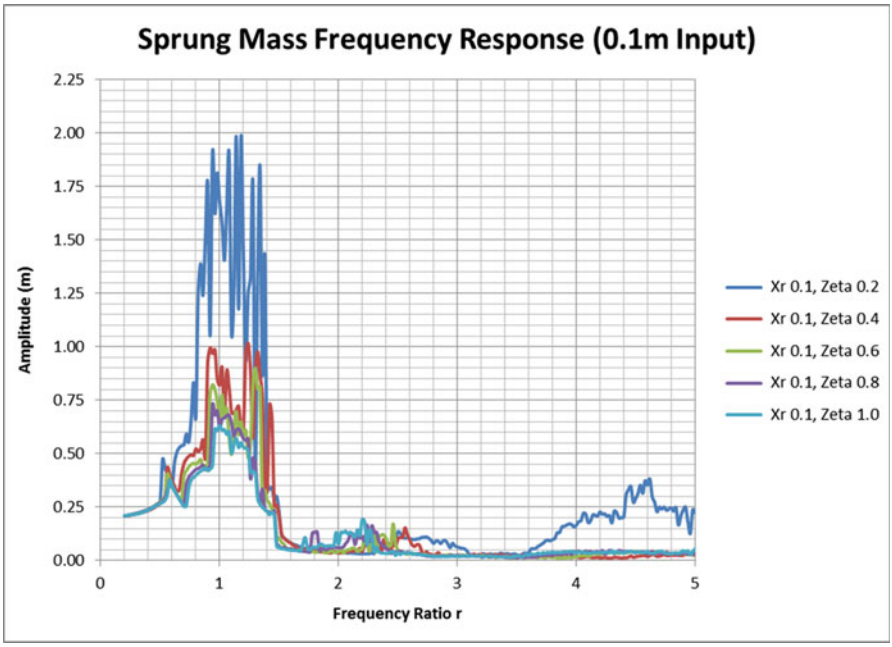

Fig. 7.52 Frequency response of sprung mass with nonlinear damping to 0.1 m input

Two very peculiar phenomena are seen in the results referred to in this report as bounce and float; these are important ride behaviours that may completely be absent in a linear simulation.

Frequency responses do show a certain consistent trend which suggests that mathematical equations governing frequency response could be defined. However, at high damping ratios and amplitudes, the frequency responses appear "noisy" as the system is very unstable; this needs to be further investigated before defining frequency responses mathematically.

As shown in Sect. 7.3.3, the interaction of separation with nonlinear damping significantly alters the response of the system; this suggests that the interaction of separation with other nonlinear phenomena may also alter system behaviour and therefore need to be investigated.

7.6 Future Work

This is considered a first step in investigation of the tire separation effects; this has opened new avenues for further research.

Results of this analysis are obtained using simulation; these have not been confirmed through physical testing or an alternate method of simulation. For these results to be reliable, they need to be validated through physical testing. Validation testing must use a rig that mimics the model used for simulation and not an actual vehicle suspension.

Additionally the results can also be compared to an actual "quarter car" rig with other nonlinearities involved in order to investigate the significance of the results as applied to an actual vehicle ride problem.

The possibility of non-dimensionalization of results also needs to be investigated in more detail as it would help in broadening their applicability to systems with varied characteristics.

A mathematical relation for separation frequency may also be sought in order to define the limits of applicability of linear models and provide designers with choice of models based on their specific application.

References

Christopherson, J., & Jazar, R. N. (2005). Optimization of classical hydraulic engine mounts based on RMS method. *Journal of the Shock and Vibration, 12*(2), 119–147.

Christopherson, J., & Jazar, R. N. (2006). Dynamic behavior comparison of passive hydraulic engine mounts, part 2: Finite element analysis. *Journal of Sound and Vibration, 290*, 1071–1090.

Gillespie, T. D. (1992). *Fundamentals of vehicle dynamics*. Warrendale: Society of Automotive Engineers.

Giugianni, M. (2014). *The science of vehicle dynamics: Handling, braking, and ride of road and race cars*. New York: Springer.

Jazar, R. N. (2011). *Advanced dynamics: Rigid body, multibody, and aerospace applications*. New York: Wiley.

Jazar, R. N. (2013). *Advanced vibrations: A modern approach*. New York: Springer.

Jazar, R. N. (2014). *Vehicle dynamics: Theory & application*. New York: Springer.

Jazar, R. N., Mahinfalah, M., & Deshpande, S. (2007). Design of a piecewise linear vibration isolator for jump avoidance IMechE. *Part K: Journal of Multi-Body Dynamics, 221*(K3), 441–450.

Kim, C., & Ro, P. (1999). Effect of suspension structure on equivalent suspension parameters. *Proceedings of Institution of Mechanical Engineers, 213*(5), 457–470.

Kim, C., & Ro, P. (2000). Reduced-order modelling and parameter estimation for a quarter-car suspension system. *Proceedings of Institution of Mechanical Engineers, 214*(8), 851–864.

Marzbani, H., Jazar, R. N., & Khazaei, A. (2012). Smart passive vibration isolation: Requirements and unsolved problems. *Journal of Applied Nonlinear Dynamics, 1*(4), 341–386. https://doi.org/10.5890/JAND.2012.09.002.

Marzbani, H., Jazar, R. N., & Fard, M. (2013). Hydraulic engine mounts: A survey. *Journal of Vibration and Control, 19*(16), 1439–1463. https://doi.org/10.1177/1077546312456724.

Marzbani, H., & Jazar, R. N. (2014). In R. N. Jazar & L. Dai (Eds.), *Smart flat ride tuning, nonlinear approaches in engineering applications 2*. New York: Springer. https://doi.org/10.1007/978-1-4614-6877-6_1.

Milliken, W. F., & Milliken, D. L. (1995). *Race car vehicle dynamics*. Warrendale: SAE International.

Milliken, W. F., & Milliken, D. L. (2002). *Chassis design: Principles and analysis*. Warrendale: SAE International.

Svahn, F., Jerrelind, J., & Dankowicz, H. (2010). *Suppression of bumpstop instabilities in a quarter-car model*. Berlin, Heidelberg: Verlag Springer.

Thomsen, P. G. (2010). *Discontinuities in ODEs: Systems with change of state*. Berlin/Heidelberg: Verlag Springer.

Wong, J. Y. (2008). *Theory of ground vehicles* (4th ed.). Hoboken: Wiley.

Young, D., & Maher, P. (2011). An insight into linear quarter car model accuracy. *Vehicle System Dynamics, 49*(3), 463–480.

Chapter 8
Friction Coefficient of Pneumatic Tires and Bitumen Roads

Jenelle C. Hartman, Hormoz Marzbani, Firoz Alam, M. Fard, and Reza N. Jazar

8.1 Introduction

Road surface friction is a significant factor in the slowing efficiency of a braking or sliding vehicle. Road authorities apply well-defined procedures in their design and production of roads in a quest for lower collision rates and safer roads. Globally, collision reconstructionists and investigators work to determine how and why motor vehicle collisions occur. A critical element of any analysis is to determine the friction coefficient of the vehicle tires and the road surface under rolling and sliding conditions. Due to the unexpected and dynamic nature of road trauma, it is not possible to determine the road surface friction in conditions identical to those occurring at the time of the collision. Post-collision skid resistance determination may be invalid or unreliable if sliding friction coefficient is affected by velocity, temperature and rainfall, subsequently resulting in fallacious collision analysis.

The effects of inaccurate collision analysis can be detrimental, potentially leading to prosecution of drivers for offences they did not commit or alternatively road development and design which is inappropriate or unsuitable for the location or conditions, making them unsafe or lethal.

Currently collision analysis relies on knowing or estimating the road surface friction skid resistance levels, which are determined post-incident/collision. If the conditions at the time of testing are different to those occurring at the time of the incident/collision, then the results may be inaccurate. This study will examine the effect of velocity, temperature and rainfall on the friction coefficient of pneumatic tires and road surfaces.

Where velocity, temperature or rainfall is determined to affect the sliding friction of pneumatic tires and road surfaces, then models will be developed

J.C. Hartman • H. Marzbani • F. Alam • M. Fard • R.N. Jazar (✉)
School of Engineering, RMIT University, Melbourne, VIC, Australia
e-mail: reza.jazar@rmit.edu.au

L. Dai, R.N. Jazar (eds.), *Nonlinear Approaches in Engineering Applications*,
https://doi.org/10.1007/978-3-319-69480-1_8

which will facilitate the ability to predict the friction coefficient for a given vehicle velocity or temperature using a result obtained at another velocity or temperature.

The ability to predict the friction coefficient will significantly improve the accuracy of collision reconstruction and analysis, and the increased understanding of road/tire surface friction will ensure that road design and construction become safer for all road users.

8.1.1 Prior Work

A thorough examination and review of literature related to the friction coefficient of pneumatic car tires and road surfaces highlighted a number of issues that were either contradictory or limited in their scope. The laws of friction often do not hold true for rubber products. Interest in the friction of pneumatic car tires and road surfaces is only new, and accordingly there are many areas that are simply not understood. The laws of friction developed by Coulomb told us that friction is independent of temperature and velocity. In 1952 Schallamach determined that rubber does not follow this rule. Multiple researchers who have identified that tire/road friction decreases non-linearly with increasing temperature have supported Schallamach (1952) and his findings. Heinrichs et al. (2003) and Shah and Henry (1978) have all performed extensive research specifically looking at the effects of vehicle velocity on road/tire friction coefficient, but their research is also contradictory (Jazar 2011).

What can be surmised from their work is the road/tire friction is dependent on vehicle velocity. Common sense would suggest that lubricants such as water would decrease the friction coefficient between two surfaces. However, in 2001, Claeys et al. identified that the depth of water is critical to establish what effect water will have as a lubricant on road/tire friction. Their work and results highlighted the need for further and more specific research relative to car tires and road surfaces (Jazar 2017). This was further supported using laboratory testing by Blythe in 2013. Blythe identified a need for real-world testing to validate their findings.

8.1.2 Significance

Essentially there remain two areas, which can be considered as gaps within the research area: contradiction and specificity. There is literature published which supports that velocity, temperature and rainfall do affect the friction coefficient of two surfaces, whilst there is equally published literature which identifies that the friction coefficient of two surfaces is not affected by velocity, temperature and rainfall. It is evident that the chemical makeup of the two surfaces in contact is the most important variable in determining the friction coefficient of any surfaces in contact. It is clearly apparent that to determine whether velocity, temperature or

rainfall affects the friction coefficient of pneumatic tires and bitumen road surfaces, the research must be performed using pneumatic tires and bitumen road surfaces. Current research by Blythe (2013) and using the two relevant surfaces is laboratory based, which always increases the risk of peripheral influences.

There is a need for research, which is conducted to determine the friction coefficient of pneumatic tires and road surfaces using a sliding actual motor vehicle on a used bitumen road surface to validate the previous findings.

The World Health Organization (WHO) reports that 1.27 million people are killed globally each year as a direct result of motor vehicle collisions. Motor vehicle accidents are the number one cause of death for those aged 10–24 years and the tenth highest cause of death behind natural causes such as heart disease and cancers. The impact of road safety and road deaths is increasing and is a global problem. An increased understanding of friction and how it impacts motor vehicle collisions will enable better understanding of how, when and why collisions occur and that in turn will assist in road design and road safety strategies aimed at reducing the associated devastate.

8.2 Literature Review

8.2.1 Friction

Friction is a surface force, which prevents or retards relative tangential interface motion between two surfaces or bodies studied within the field of tribology. Tribology is a multidisciplinary field based on fluid and machine dynamics, metallurgy, physical and surface chemistry, heat transfer and stress analysis (Quinn 1977). The specifics of a dynamic science devoted to the study of lubrication, friction and wear only evolved in 1966 when it was accepted by the government, of the Jost Committee Report and its recommendations (Persson 2001). Simply, tribology is the science of interacting solid surfaces in relative motion (Dowson 1979). Whilst the term tribology is relatively new, the study of friction is far from recent. Predominantly the interest in analysis and prediction of mechanisms that occur between two surfaces in relative motion is driven by industrial sectors, which is why the new interdisciplinary approach to subjects has become necessary in recent years. Whilst not called tribology specifically, the study of the subjects has a history dating back to the turn of the fifteenth century.

The effects of friction on machines and materials have been the source of study and contemplation for hundreds and even thousands of years, reaching as far back as Aristotle (384–322 BC) (Dowson 1979). Leonardo da Vinci first developed the laws of friction during the Renaissance in 1495. Leonardo formulated two basic laws of friction:

1. Friction is independent of contact area.
2. Friction is proportional to load.

Da Vinci never published or received credit for his work on friction for many years. In 1699, Guillaume Amontons rediscovered the two laws of friction earlier developed by da Vinci. The laws became known as Amontons Laws based on his reasoning that friction was primarily the result of work done to lift one surface over the roughness of the other, resulting in deformation and wear of the surfaces. In 1785 Charles Augustin Coulomb refined the concepts of Amontons. Coulomb redefined the second law of friction commonly referred to as Amontons-Coulomb Law asserting that the strength due to friction is proportional to compressive force. Whilst this law holds true for many materials even today, it is not a fundamental law. Laws of motion as devised by Sir Isaac Newton further considered friction. Newton asserted that moving friction is not dependent on speed or velocity. This became known as the third law of friction:

3. Friction is not dependent on velocity.

In recent years, Philip Bowden and David Tabor (1974) further explored the laws of friction and determined that the true area of contact is a very small percentage of the apparent area. Bowden and Tabor determined that as the normal force increases, more asperities come into contact and the area of asperity increases. As a result, a fourth law of friction was devised:

4. Friction is dependent on the adhesive interactions between contact surfaces.

Friction is a process where kinetic energy is converted into other forms of energy including heat energy, acoustic energy, optical energy, electric energy and mechanical energy. Eventually, virtually all the frictional work is converted into heat. However, some of the energy is lost due to adhesion and deformation. Adhesion is attributed to only a small proportion of the loss and occurs in the thin interface zones, whilst the great loss is due to deformation and occurs beneath the contact area in the larger volumes of material. The contact between rubbing surfaces may have a mechanical (deformation) or atomic (adhesive) nature, although simultaneous combination of both is also possible and indeed likely (Glaeser 2012).

Frictional phenomena, which occur at a given moment within a nominal contact area, constitute the physicochemical characteristics of friction processes which determine the magnitude of the friction force and the type and intensity of the resultant wear. Friction is based on three mechanical interactions including the normal force, tangential force and relative velocity of the two opposing asperities. The three parameters all alter during the friction phenomenon. There are three distinguishable stages in the friction phenomenon.

1. The establishment of the micro-contact between surface asperities
2. Physiochemical modifications of the micro-contact and the surrounding material
3. The breaking or rupturing of the micro-contact

Mechanical interactions result in a three-dimensional state of stress, which is both complex and variable. The state of stress is dependent upon the normal force, tangential force, relative velocity, the geometry of the micro-contact, the geometry of the interacting asperities, the material properties, temperature, heat and adhesive

intersections. The mechanical interactions produce elastic deformations followed by plastic deformations. Plastic deformation may produce work hardening of the material, whilst the frictional heat can induce recrystallisation, decrease the hardness and enhance diffusion and chemical interactions between the material and the surroundings (Persson 2001). In addition, plastic deformations facilitate the creation of bonds between atoms and molecules and release elastic strains. Due to the complexity of the mechanical interactions, rigorous analytical assessment is essentially impossible. In 1785 Charles Augustin Coulomb investigated the influence of five main factors, which affect friction. According to Coulomb the five main factors include:

- The nature of the materials in contact and their surface coatings
- The extent of the surface area
- The normal pressure
- The length of time that the surfaces remained in stationary contact
- Ambient conditions such as temperature, humidity and even vacuum

Coulomb was one of the first to consider the effects of tangential force on elastic fibres. In determining the friction law, Coulomb summarised many of his results using the friction law of

$$F = \mu L$$

where F is the load and L is the normal force. Coulomb surmised that the friction coefficient μ is usually almost independent of L, but also of the sliding velocity so long as the velocity is not particularly high or particularly low, the contact area and the surface roughness (Jazar 2011).

In 1979, Oliver reported that tire friction does not conform to the classical laws of friction. He identified two major components of tire surface/friction being adhesion and hysteresis. For a dry road surface, the adhesion component dominates the friction coefficients. When a road or surface is even moderately damp, the water prevents the formation of molecular bonds, and the hysteresis component is the primary source of tire/surface friction.

It is crucial to understand the contact mechanics of tires whilst sliding and to critically analyse the effects of water and rainfall on the friction coefficient of car tires and road surfaces. Performed recent research, which analyses the contact mechanics and the role of adhesion and hysteresis in rubber friction. Heinrich determined that a tire sliding on wet roads will have a lower friction coefficient as the contribution of energy dissipation due to tread deformation is smaller than for dry roads. A pioneer rubber friction researcher, Grosch, has shown that in many cases rubber friction is directly related to the internal friction of rubber (Grosch 1963). Based on the earlier work of Grosch, in 1997, Persson determined that the friction force between rubber and hard surfaces such as roads has two contributions being adhesion and hysteric components, respectively. The hysteric component comes from the internal friction of the rubber. When a tire is sliding, the asperities of the road exert oscillating forces on the rubber surface subsequently leading to

cyclic deformations of the rubber and energy dissipation due to the internal damping of the rubber. The friction of a sliding vehicle tire and road surface is also affected by adhesion. It is adhesion between the two surfaces that results in deformation of the tire tread, which increases the friction coefficient. If the adhesive interaction between two surfaces can be reduced, then the friction force will decrease. Since adhesion is reduced on wet surfaces, it can be concluded from the work of Persson that the friction coefficient of car tires and road surfaces should decrease when the road is wet. There is no discussion by Persson as to what the effect of heavy rainfall or a thick water layer in front of the tire will have on the friction of the two surfaces in contact.

Rubber is a polymer. Most polymers exhibit a sliding friction, which is much lower than rubber. Teflon has both a static and kinetic friction, which is typically below 0.1. Based on this it can be assumed that for most polymers, the internal friction contributes less to the sliding friction than it does for rubber.

8.2.2 Sliding Friction

W. B. Hardy studied the physics of friction at Cambridge from 1919 to 1933. Hardy claimed that friction phenomena are equally interesting for the physicist and the engineer: their investigation belongs to a most difficult field of boundary problem of physics (Blau 2012). Factors affecting friction vary from one tribosystem to another, and any modelling must be tailored to each specific circumstance. The physics of friction and its basic laws still remain elusive in many situations and simplified models. To accurately predict models for static or kinetic friction, it is necessary to understand the dominant interfacial processes of friction and its relative stability, know the size scale at which the processes operate and identify the rules that translate the external stimulus to the response of the tribosystem. The only way to accurately model the friction coefficient of motor vehicle tires and road surfaces is to research the two properties specifically and in relationship to each other (Jazar 2013).

The dynamics of the transition from static to kinetic friction remains mysterious although it is readily accepted that static friction varies but reaches maximum immediately before an object begins to move. Kinetic (sliding friction) is constant but a lower value than the maximum static friction. Static friction and kinetic friction are quite different (Fig. 8.1).

There are a number of elementary aspects of sliding friction, which have been researched and developed by Persson (2001). The work of Persson is particularly important due to his specific research into sliding car tires. The coefficient of friction (μ) between two solid objects is determined to be the force normal to the surface (F) divided by the load (L) (F/L). When considering sliding friction, generally the law that states that 'the coefficient of friction is independent of the apparent area of contact' is obeyed. That is, when the load remains the same, the friction force will be the same no matter what the contact area. According to

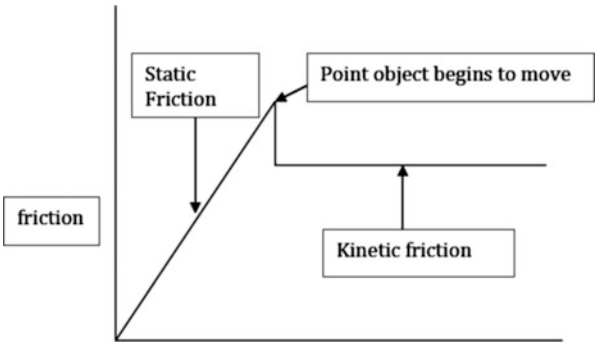

Fig. 8.1 Static and kinetic friction at work

Persson, the coefficient of friction is usually velocity independent, unless the sliding velocity is very low due to the role of thermal activation (Persson 2001). Persson supports the theory of friction of Bowden and Tabor. Around 1940, Bowden and Tabor presented a simple theory for the origin of the sliding friction for clean surfaces. They assumed that the friction force is the force required to shear cold-welded junctions formed between the solids (Persson 2001).

8.2.3 Rubber Friction

The vital role of friction in motor vehicle collisions and collision reconstruction and the applications of rubber tire and road friction have assumed increasing significance over the last few decades. John Boyd Dunlop introduced the first pneumatic rubber tire in 1888; however, it was not until 1947 that radial tires were then fitted to motor vehicles. The introduction of radial tires on vehicles has provoked a perpetual interest in the friction coefficient of motor vehicle tires and paired road surfaces. Literature specific to motor vehicle tires is limited. Primarily tire friction research is relevant to collision reconstruction experts and tire manufacturers with pivotal interest in vehicle and road safety. Tire manufacturers have a tendency to use methods and codes, which are kept confidential. Often university research is conducted in cooperation with tire manufacturers, again resulting in a degree of confidentiality.

Rubber products, both natural and synthetic, are elastomers. Elastomers are polymeric substances that possess elasticity. A material with elasticity has no permanent deformation or dissipation. Extensive research by Brown has identified that in general, polymers do not obey the long-standing laws of friction and the most used friction model is usually referred to as the Coulomb model. Experiments have supported the work of Brown and often show deviations from the basic Coulomb friction model. Friction of polymers is associated with their viscoelastic behaviour. The friction coefficient of polymers increases with sliding velocity until a maximum value is reached followed by a decrease of the friction coefficient. This

is due to the flexibility of polymer chains. Persson (1998) reported that rubber friction differs in many ways from the frictional properties of most other solids due to the very low elastic modulus of the rubber and the high internal friction exhibited in a wide frequency region.

Rubber used in motor vehicle tires is cross-linked polymer matrix, which typically contains only 10 per cent natural rubber (cis-1, 4-polyisoprene). Most general road tires are formed from a range of polymers including natural and synthetic polyisoprene, poly-(styrene-butadiene), polybutadiene and poly-(isoprene-isobutylene) which are then blended with reinforcing fillers (carbon black or silica), sulphur, antioxidants and processing oils. The reinforcing fillers like carbon black or silica produce two additional effects, the Payne effect and the Mullins effect, both of which are softening effects.

Friction of rubber is a complex phenomenon comprising two parts, adhesive friction and hysteresis friction. When a rubber tire slides on a road surface, molecular bonds between the surfaces are repeatedly broken and reformed. This is adhesive friction. The dynamic deformation of the rubber as energy is lost during sliding is hysteresis friction. The hysteric friction component results from the internal friction of the rubber. Rubber tire and road surface friction is dependent upon both the coarseness of the road surface and the viscoelastic properties of the tire rubber. The constitutive laws for large strains cannot be applied to the stress-strain relative to rubber since rubber does not follow reversible stress-strain relations. When rubber is dynamically stretched and released, the returned energy is less than the energy that is put into the rubber.

According to Persson, rubber friction differs in many ways from the frictional properties of most other solids due to the very low elastic modulus of rubber and the high internal friction exhibited by the rubber in a wide frequency region (Persson 1998). When an elastomer slides across another surface, true sliding at the interface will not always occur. Waves of detachment traverse the interface, and relative displacement will occur where contact is temporarily lost. Briggs and Briscoe identified that these waves are called Schallamach waves and resemble macro-dislocations where energy is dissipated by peeling the contact apart as the wave propagates.

Research into rubber friction changed in 1971 when Schallamach observed that when rubber moves over a hard surface, true sliding does not occur. Schallamach determined that the contact area is crossed by waves of detachment and it is only in this area that contact is lost and that relative motion between the two surfaces continues to occur.

Schallamach was one of the first researchers to seriously study rubber friction recognising that in relation to friction, rubber does not act in a way similar to other compositions such as metals, which form the basis for Amontons and Coulomb's laws. According to Rand and Crosby, Schallamach waves are a dominant mechanism in the friction of soft material interfaces. Schallamach waves are essentially air tunnels, which provide relative displacement between a sliding material and the substrate (Rand and Crosby 2006). For Schallamach waves to form, it is necessary that adhesive forces at the interface have enough strength to prevent movement at

the rear of the interface that subsequently creates a zone of tension. The interface will then begin to shear which causes compression in the front of the contact area. Critical compressive stress prior to slip will result in buckling of elastomers. If the adhesion energy that resists interfacial separation is greater than the stored elastic energy which causes buckle compression, then the buckle will attach to a slider and subsequently form a wave providing displacement between the substrate and the slider. There are three critical aspects relative to Schallamach's wave phenomenon:

1. How the waves form
2. The interfacial stress required to propagate them
3. Their regime of existence

Briggs and Briscoe took the work of Schallamach further. Schallamach developed the theory of Schallamach waves from models of rubber and smooth surfaces such as glass. Briggs and Briscoe then went on to consider the effects a rough surface had on waves of detachment. Their work determined that waves of detachment are also present when the surface is rough, and therefore, the same explanation of friction force that applies to smooth surfaces remains relevant. It is well established that when rubber slides over smooth and rough surfaces, the frictional force is accounted for in terms of network required to peel rubber away from the surface and then readhere to it. It is clear that during sliding the viscoelastic deformations of rubber induced by the adhesional interaction with the substrate increase the friction force. Therefore, if the adhesional interaction between a substrate and rubber can be reduced, then friction force will decrease. Persson (1998) states that if rubber is slid on a substrate covered by a thin layer of water, then sliding friction is reduced. This is because water is trapped in the surface cavities of the substrate, thereby leading to reduce viscoelastic deformations of the rubber.

Briggs and Briscoe also established that adhesion of rubber depends markedly on the roughness of the surface with which it is in contact. Road/tire friction is a function of tread depth, water depth and velocity.

8.2.4 Road Surface Texture

Road surface/tire friction is the result of the interaction between both the tire and the road surface and is not a property of the tire or the road surface individually. Tire/road surface friction is dominated by the texture of the road surface. Different road surface textures make different contributions. As discussed, skid resistance depends on the chemical bonding between the road stones and the tire rubber (adhesion) and the deformation and recovery of the tire as it passes over the projections and depressions in the road surface (hysteresis). When water is present between the road and tire, chemical bonding is affected. In wet conditions, the ability for chemical bonding to occur depends on the micro-texture.

8.2.5 Factors Affecting Friction

8.2.5.1 Velocity

In 1780, Coulomb identified a difference between static and dynamic friction coefficients. As a result of his work, he determined that the friction coefficient is independent of sliding speed (Schallamach 1952). A number of researchers have demonstrated that instantaneous tire/road friction decreases non-linearly with increasing speed (Takadoum 2007). Shah and Henry identified that the most significant decrease in friction will occur at vehicle speeds up to 30 km/h and then become more gradual as the speeds continue to increase (Heinrichs et al. 2004b). In 2002, Heinrichs identified that the road/tire friction coefficient was lower at 20 km/h compared to 40 km/h (Shah and Henry 1978a). Laws established by Coulomb were substantiated mostly with metals. More recent research has shown that highly elastic materials such as rubber do not agree with theoretical predictions relating to velocity. Although researchers generally agree that tire/road friction is affected by velocity, there is conflict in relation to where maximum and minimum speed thresholds occur when considering tire/road friction specifically.

8.2.5.2 Temperature

There is no general macroscopic theory of friction, which allows the prediction of the friction coefficient of two materials, since it is the nature of the two surfaces in contact, which has the greatest influence on the result (Butt and Kappl 2010). According to Coulomb's 'laws of friction', the coefficient of friction is independent of temperature (Wada and Uchiyama 1993). However, this theory has since been challenged with evidence that the coefficient of friction between pure metals is independent of temperature, whilst viscoelastic properties of rubber-like materials are strongly temperature dependent. Polymers do not obey Coulomb's laws (Schallamach 1952). The 'Williams-Landel-Ferry theory' identifies that rubber friction is essentially a viscoelastic phenomenon and very sensitive to temperature (Takadoum 2007). Research theories relating to the effects of temperature suggest friction coefficient increases as temperature increases, until the surface reaches maximum softening at which point the friction coefficient will begin to decrease (Wrobel and Szymiczek, 2008). Investigation into the effects of flash temperature on the friction coefficient of a rubber block sliding on a rough surface concluded that as localised temperature of rubber increases, the friction coefficient decreases (Persson 2006). The research considered the temperature of the rubber block only and not the temperature of the surfacing upon which it was sliding. Accordingly this research may not be relevant to the research proposed.

8.2.5.3 Lubrication

The mechanism of traction under dry conditions involves a complex interlocking between road surface texture and dynamic rubber properties (Moore 1967). Dry friction describes the reaction between two solid bodies in contact with each other when they are in motion and when they are not.

Lubricants will lower friction and reduce wear between two sliding solid bodies. Persson (1998) determined that a lubricant is used to lower the friction and reduce wear between two sliding bodies. Most surfaces will be covered with a layer of oil. Roads are certainly no exception. These oils will act as a lubricant and will lower the friction coefficient between car tires and road surfaces, but these oils are present on both dry and wet surfaces. Grease and oil are better lubricants than water as oil has a much higher viscosity. Fluid with a higher viscosity will reduce friction coefficient. If the depth of lubrication is sufficient to fully separate the two surfaces in contact, then the frictional interaction can be effectively modelled using lubrication theories. If despite lubrication the solid bodies remained in contact, then the characteristics of the bodies, the surface structure and any third bodies play a role.

'The single most important factor affecting tire friction force in practice is the presence of water in various forms including water, snow and ice. In most temperature climates on modern roads it has been shown that during a range of rainfall intensities normally encountered, the water rarely exceeds 2 mm and is typically 1 mm or less'. Experiments have shown that road/tire friction in low water depth conditions is a complex interaction between the road surfaces, tire construction and tread depth.

The depth of water on the road greatly influences tire/road friction (Claeys et al. 2001). There is a distinction between the effects of thin water layers and thick water layers. When there is a thin layer of water only, the contact between the tire and road is completely lost due to full contamination of the interface – viscous hydroplaning. When the layer of water becomes thick and extra force is generated in front of the tire due to the accumulation of water providing hydrodynamic forces, the water layer depth determines the magnitude of the force. It is important to be aware that once the tire rises to the top of the water surface then hydroplaning occurs and the friction force provided by the pushing of water is lost and friction force is subsequently reduced.

Rubber friction on wet rough substrates at low velocities is typically 20% to 30% smaller than for the corresponding dry surfaces (Persson et al. 2004). Persson has conducted extensive studies on sliding friction and suggests that rubber friction on wet road surfaces cannot be explained by a hydrodynamic effect but rather suggests that water pools within the road aggregate. As the rubber tire passes over the surface, the water is trapped within the aggregate fissure forming pools and creating a smoother surface and subsequently a lower friction coefficient. No matter what the reason, it is accepted strongly by tribologists and engineers that wet friction is typically lower than dry friction when comparing the same surfaces. Research conducted by both Persson and Schallamach does not perform rubber/road friction

testing on deep water pooling above the level of the aggregate. According to Moore (1967) at speeds up to 60 km/h, flooded roads consistently give higher sliding friction values. It was his belief that whilst there was evidence that this consistently occurs, there is no satisfactory explanation or theory for the phenomenon. Further investigations identified that wet rear tire friction coefficient is similar to the dry friction value, but the front tire traction is substantially below the dry value. The dry values have more variability than the wet results. This is most likely because the dry values represent variations associated with local differences in surface texture, whereas the presence of water in the wet tests appears to minimise texture variations.

Persson (1998) considered both the relevance of lubricant viscosity and depth when researching sliding friction. According to Persson when two layers separated by a layer of fluid are pushed together then the fluid will be pushed out. The higher the liquid viscosity, the longer this process will take. If viscosity of the separating fluid is low enough, then the fluid will be squeezed out rapidly leading to direct contact between the two surfaces. This is boundary lubrication and typically results in a very high sliding friction, which is independent of speed. Rainwater has a low viscosity.

Friction coefficient on a wet road decreases with increasing vehicle speed. At low travel speeds, road micro-texture is the primary contributor to friction coefficient. Macro-texture and water depth influence the extent to which friction decreases with increasing speed.

Micro-texture corresponds to asperities within a road surface where the individual pieces of aggregate are less than 0.5 mm. Macro-texture is measured as a texture depth and relates to the larger aggregate over 0.5 mm.

8.2.6 Hydroplaning

True contact between a vehicle tire and a road surface is established only at the rear of the nominal contact length. The front region of the contact length works to displace any fluid forward of the tire. As the amount of fluid to be displaced increases, the percentage of nominal contact area reduces until it becomes zero and at which time hydroplaning is said to be occurring. That is, the friction is almost zero and there is no ability to steer or brake the vehicle. The vehicle is essentially on top of the water with a complete layer of water between the tire and the road. ‘On a wet road surface, elastohydrodynamic effects attempt to entrain fluid across the individual asperities of the road texture thereby destroying intimate tread to surface contact and rapidly promoting the onset of the hydroplaning phenomenon’(Moore 1967). The mechanism of hydroplaning is characterised by a rapid spread of interfacial film of liquid from both ends of the contact length towards the centre. When hydroplaning occurs, the adhesion contribution to friction has been lost, and the hysteresis contribution is negligibly small. Hydroplaning does not occur instantaneously, but it occurs rapidly and seemingly sudden to a vehicle driver.

8.2.7 Friction and Collision Reconstruction

In Australia, the annual cost of motor vehicle collisions totals more than $17 billion. Whilst that figure alone is astounding, it does not recognise the emotional cost to those left grieving the fatally injured or those caring for the 25,000 who are seriously injured each year. No monetary figure can be put on the real cost of collisions in this country.

There are two methods used to estimate the cost of an accident: one economic and the other is comprehensive. Economic costs are a measure of the productivity lost and expenses incurred because of accidents. Comprehensive costs not only include the economic costs but also measure the value of lost quality of life associated with the deaths and injuries, that is, what is society prepared to pay to prevent them? Comprehensive costs are greater than economic costs.

Valuation of road crash costs involves an estimation of the total number of crashes and injuries, then quantifying the cost of specific crash components. There are human costs including loss of life, treatment of injuries and ongoing care of persons with disability, vehicle damage costs and general costs including insurance administration and emergency service costs. According to the Bureau of Infrastructure, Transport and Regional Economics, each fatality costs $2.4 million, each hospitalisation injury costs $214, 000 and each non-hospitalisation injury costs around $2100.00.

In road fatalities and collisions, the term collision or crash is typically used rather than accident as generally vehicle collisions are avoidable and not the result of chance. Collision reconstruction is the practice of determining the movement, relative positions and interaction of motor vehicles pre, post and during a collision event. After critical assessment of the human, environmental and vehicle factors available at a collision scene, a collision reconstructionist will use scientific and physics principles to determine how and why a collision has occurred, potentially also assigning liability. The determination of the friction coefficient of a road-tire surface is critical in most aspects of motor vehicle collision reconstruction. According to Warner et al. (1983), tire-road friction values are highly dependent on numerous physical factors including tire design, side force limitations, road surface wetness, vehicle speed and load shifting. It is the application of Coulomb's friction law

$$F = \mu L \text{ where } L = mg \text{ (vehicle weight)}$$

This allows the minimum speed of a vehicle to be determined from the length of a skid. This is a critical factor in collision reconstruction. The application relies upon the skid distance (d) being obtained and by the condition that the initial kinetic energy $mv^2/2$ is completely dissipated by the friction between the road and the vehicle tires during the skid.

8.3 Effect of Velocity on Friction

8.3.1 Introduction

Estimation of the friction coefficient of vehicle tires and paired road surfaces is necessary to determine pre- and postimpact vehicle velocities in motor vehicle collision reconstruction. Average friction values may be assumed for a range of surfaces based on previous research. Alternatively, accelerometers can provide more accurate values when used in testing conducted at the relevant collision site. Accelerometers require brake tests to be performed in test vehicles. Tests are usually performed at velocities determined to be safe for the conditions, often well below the velocities of vehicles being analysed. The use of the friction coefficient values obtained using accelerometers assumes that the average friction coefficient is independent of vehicle velocities.

Amontons' law of friction, which holds true for many material combinations, is not obeyed by elastomers such as rubber. Average tire/road friction coefficients have been shown to be dependent on vehicle velocities by a number of researchers (Heinrichs et al. 2004a; Leu and Henry 1978; Gunaratne et al. 2000). Therefore, the primary objective of this study is to experimentally determine the effects of vehicle velocities on the friction coefficient with and without antilock braking systems (ABS). Tests using actual vehicles not fitted with antilock braking systems (ABS) at a range of velocities from 20 to 80 km/h identified that as velocity increased, friction decreased non-linearly.

The most substantial decrease in friction coefficient results occurred in vehicles travelling up to 30 km/h with little significance in friction coefficient values recorded for vehicles travelling 60 to 80 km/h (Heinrichs et al. 2004a). ABS will not work if the vehicle velocity is below 25 km/h (Wu et al. 2010) Consequently comparison testing with and without ABS can only occur upwards of 30 km/h.

Friction coefficient (μ) is the maximum value of the frictional force divided by the normal force. An accelerometer calculates the friction coefficient 100 times per second from the commencement of braking, producing one average result. From the commencement of braking, friction coefficient increases until it reaches peak immediately prior to wheel lock-up when it then begins to decrease along the skid length. A vehicle travelling faster will produce a longer skid and subsequently a lower average friction coefficient. When emergency braking is applied to a vehicle, the peak friction coefficient is attained immediately before wheel lock. When a vehicle is fitted with ABS, the pressure on the hydraulics will reduce as the wheels begin to lock, aimed at keeping the friction coefficient near to peak. This will continue to occur up to 15 times per minute and is designed to increase braking efficiency and reduce the risk of vehicle loss of control (Erjavec, 2003). The friction coefficient of a vehicle under ABS braking is higher than a vehicle without ABS.

Study of friction relating to viscoelastic properties such as rubber is very new and research is limited in this area. The additional consideration of ABS further reduces the extent of research due to this introduction being only recent. It is

generally suggested in the literature that dry sliding frictional force of a tire decreases with increasing sliding velocity (Chowdury et al. 2011); however, there is some data that contradicts this. It is critical that friction coefficient of viscoelastic properties such as vehicle tires be determined specifically. In 2004, Cross considered the effect of velocity on the friction coefficient of an elastically soft material of tennis ball cloth sliding on smooth surfaces. He determined that sliding friction increases with velocity for the elastic material. Whilst vehicle tires have elastic properties, there is a stick-slip phenomenon caused when skidding.

According to Cross this will result in a decrease in friction coefficient with an increase in velocity contradicting other elastic and metal materials. The decrease in friction coefficient sometimes referred to as the velocity decrement of sliding friction has a relatively small effect for low and moderate highway velocities (Warner et al. 1983). Suggests that the variation in friction coefficient due to velocity is between 0.0017 and 0.005 mph^{-1}.

The objectives of this study were to identify how vehicle velocity affects the tire/road friction coefficient on dry asphalt roads using vehicles with and without ABS. We believed that as pre-skid vehicle velocity increases, the tire/road friction coefficient on dry bitumen would decrease in vehicles without ABS and increase in vehicles with ABS. The results of this study will increase the accuracy of vehicle velocity estimates in collision reconstruction for vehicles both with and without ABS, over a range of velocities. Will friction coefficient remain the same as velocity is increased? Is this the same for vehicles with and without ABS? This research will provide collision investigators and reconstruction experts worldwide a better understanding of the effects vehicle velocity has on the friction coefficient of the car tires and road surfaces specifically when ascertaining the road/tire friction coefficient of a collision scene using a vehicle travelling at a velocity considerably less than the subject vehicle.

8.3.2 Experimental Conditions

All preliminary ABS and non-ABS tests were conducted on 16 June 2011 between 3:03 and 3:56 pm. The road was dry and conditions were clear. No rain had been recorded in the 7 days prior. The ambient temperature was recorded at 13 °C (55 °F), which remained constant throughout the test period. Light winds only of less than 10 km/h were observed.

8.3.2.1 Location

Tests were performed in the service lane on the west side of Dorset Road, Bayswater, Victoria, Australia, between Allambanan Drive and Huntingdon Avenue. All tests were performed whilst travelling in a northerly direction. The geographic latitude, longitude and elevation are −37°49′41.49″ and

+145°17′14.90″. The service lane is privately owned and not open to the public. The road is not used as a thoroughfare and was developed in preparation for future industrial developments to the west. The road falls under the Roads Corporation Victoria jurisdiction and has not been resurfaced since 2003. The road is in excellent condition due to very low levels of vehicle traffic and essentially mild environmental conditions including temperature and rainfall. The area is well-drained. The service road in the direction of testing is shown in Fig. 8.2. The service lane aggregate is depicted in Fig. 8.3.

8.3.2.2 Test Vehicle

Tests were conducted in an Australian-built 2010 General Motors Holden (GMH) Commodore Omega four-door sedan. The 3.0 l V6 spark ignition direct injection vehicle was fitted with a six-velocity automatic transmission. Ventilated disc brakes were fitted to both the front and rear. In the rear wheel drive, the vehicle had antilock braking system (ABS) fitted as standard. The ABS was disengaged for non-ABS tests. No performance modifications had been made to the vehicle with all braking, steering and suspension components fitted by the manufacturer as standard. The vehicle's tested mass with two occupants was 1762 kg. The vehicle had travelled 21,091 km from new at the commencement of the first test. The vehicle type used in this study is depicted in Fig. 8.4.

8.3.2.3 Tires

The vehicle was fitted with four Bridgestone Turanza ER3HZ tires, which were fitted to the vehicle at new. The 225/60 R16 tubeless steel-belted radial tires are considered to be a mid-range touring model by the manufacturer. The minimum tire tread depth on any tire was 4 mm, and all tires were inflated to 34 PSI (2.3 × 105 Pa) prior to the commencement of testing. The tires have been used for both country and city driving, and no damage had been recorded or repairs carried out prior to the tests. Visual inspection showed no evidence of uneven wearing of the tires (Jazar 2017). Tread pattern of Turanza ER3HZ tire is shown in Fig. 8.5.

8.3.2.4 Brake Test Computer

The VC4000 Vericom brake test system was used on this experiment. The device has three major components, a crystal clock, an accelerometer and a microcontroller, which measures the instantaneous G-force 100 times per second and can measure the difference between ABS and standard brakes. The VC4000 is activated at a 0.2 g threshold upon initiation of the brake pedal load cell. The device is attached to the windscreen of the test vehicle and is considered one of the most modern and reliable test devices to determine G-force. The G-force is measured

Fig. 8.2 Service road on west side of Dorset Road, Bayswater, looking north in direction travelling by vehicle during testing

Fig. 8.3 Aggregate of service lane of Dorset Road, Bayswater, at location of testing

within 0.001 g providing accuracy of 1%. Distance is recorded at an accuracy of 1% over 400 m, and velocity is accurate within 1% up to 100 km/h. Therefore, the G-force will not change unless the velocity changes.

Vericom brake test computer is shown in Fig. 8.6.

Fig. 8.4 2010 Holden Omega sedan used for preliminary and verification testing

Fig. 8.5 Tread pattern of Bridgestone Turanza ER3HZ tire

8.3.2.5 Test Velocity

The series of skid tests, at a range of velocities, were performed in one vehicle. The friction coefficient of the vehicle tires and the road surface upon which it was travelling was determined during the tests. Tests were performed at 30 km/h, 40 km/h, 50 km/h, 60 km/h and 80 km/h. A passenger vehicle registered for general use on a true road with a human driver (author) was used for all tests.

Fig. 8.6 Vericom VC4000PC performance brake test computer with results displayed

8.3.3 Methodology

The test vehicle containing two adults (driver and observer/recorder) was driven in a northerly direction along Allambanan Drive, Bayswater. Once the vehicle test velocity was attained, the foot brake was activated with maximum pressure. Pressure remained 100% until the vehicle came to a complete stop, and the results were displayed on the Vericom brake testing computer display screen. The first series of tests were performed with the ABS on. The lowest velocity tests were conducted first, that is, two tests at 30 km/h were performed, then the velocity was increased from 10 km/h increments to 40 km/h, and two tests were again performed with continual velocity increases up to 80 km/h. At the completion of the ABS testing, removing the ABS fuse disabled the ABS, and the series was again repeated commencing at 30 km/h and increasing up to 80 km/h. Testing position on the roadway remained in the same general area but was gradually brought forward to prevent skids being consistently performed over the top of each other.

8.3.4 Results

8.3.4.1 Antilock Braking System (ABS) Enabled

When the vehicle, travelling at 35.6 and 32.8 km/h, was skidded with the antilock braking system enabled, the average friction coefficient was calculated at −0.885 g and −0.930 g. Deceleration experienced by an object is due to the vector sum of

non-gravitational forces acting on an object free to slow. The accelerations that are not produced by gravity are termed proper acceleration, and it is only these that are measured in G-force units.

When the tires of a vehicle are locked and sliding, the deceleration of the vehicle is due wholly to the friction coefficient of the car tires and road surfaces. By determining the G-force of a slowing vehicle, we know the friction coefficient. The mean of the two results was −0.907 g. At 42.6 and 41.9 km/h, the average friction coefficient was calculated at −0.895 g and −0.893 g. The mean average friction coefficient was −0.894 g showing a decrease of −0.013 g (1.44%) as the vehicle velocity increased. At 54.3, 52.9 km/h and 52.8 km/h, the average friction coefficient of the skidding vehicle with ABS enabled was calculated at −0.889, −0.948 g and −0.953 g.

The mean friction coefficient was −0.930 g. The mean average friction coefficient increased by −0.036 g from the lower vehicle travelling velocity at 42.2 km/h. In the vehicle that was skidded whilst the ABS was enabled, the average friction coefficient increased as the vehicle velocity increased from 42.2 to 83.1 km/h by −0.061 g (6.4%) as shown in Table 8.1. The lowest average friction coefficient was recorded at the tests conducted at 41.9 km/h. The highest average friction coefficient was recorded on the test conducted at 83.1 km/h. The test conducted at 32.8 km/h recorded a higher friction 4coefficient than the test conducted at 41.9 km/h (Fig. 8.7).

With the ABS disabled, the vehicle was skidded at 34.3 and 34.4 km/h. The average friction coefficient was calculated at −0.852 and −0.834 g. When the vehicle velocity was increased to 42.2 and 42.4 km/h, the average friction coefficient was calculated at −0.861 g and −0.834 g. The average friction coefficient increased by −0.004 g as the vehicle velocity was increased. When the vehicle velocity was further increased to 52.8 and 52.9 km/h, with the ABS disabled, the average friction coefficient was calculated to be −0.840 g and −0.823 g. As the velocity increased from 42 to 52 km/h, the mean average friction coefficient decreased by −0.063 g (1.89%). As the velocity further increased from 42.2 to 81.4 km/h, the average friction coefficient decreased by −0.070 (8.3%) (see Table 8.2).

The highest average friction coefficient was recorded in the tests conducted at 42.4 km/h. The lowest average friction coefficient was recorded on the test conducted at 81.4 km/h. The test conducted at 34.3 km/h recorded a higher friction coefficient than the test conducted at 42.4 km/h (Figs. 8.8 and 8.9).

8.3.5 Discussion

The velocity of a vehicle at the commencement of sliding will affect the friction coefficient of the vehicle tires and the road surfaces upon which it is travelling. As the velocity of the vehicle at commencement of skidding increased, the friction coefficient decreased when the vehicle ABS was disabled and increased when the

Table 8.1 Average friction coefficient of a vehicle sliding on bitumen with antilock braking system (ABS) enabled

Velocity (km/h)	Time (sec)	Distance (m)	Average G (g)	Mean G (g)
35.6	1.14	6.10	−0.885	−0.907
32.8	1.00	5.00	−0.930	
42.6	1.35	8.80	−0.895	−0.894
41.9	1.33	8.40	−0.893	
54.3	1.70	13.70	−0.889	−0.930
52.9	1.58	12.30	−0.948	
52.8	1.57	12.30	−0.953	
64.4	1.88	17.6	−0.970	−0.958
63.1	1.89	17.9	−0.946	
79.9	2.30	27.3	−0.955	−0.955
83.1	2.40	29.7	−0.956	

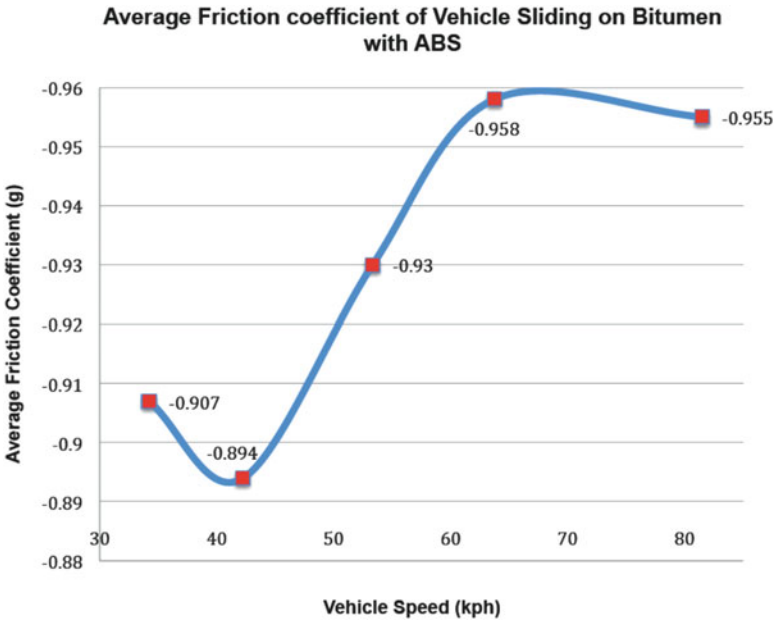

Fig. 8.7 Average friction coefficient of a vehicle sliding on bitumen with antilock braking system (ABS) enabled

vehicle ABS was enabled. However, this only occurred above 40 km/h. Below 40 km/h, the friction coefficient increased as velocity increased for vehicles without ABS and decreased as velocity increased for vehicle without ABS.

At 40 km/h, the difference in friction coefficient between a vehicle with and without ABS was −0.047 g. The friction coefficient remained higher in the vehicle with the ABS enabled at 40 km/h although the total stopping distance was equal in

Table 8.2 Average friction coefficient of a vehicle sliding on bitumen with antilock braking system (ABS) disabled

Velocity (km/h)	Time (sec)	Distance (m)	Average G (g)	Mean G (g)
34.3	1.14	5.9	−0.852	−0.843
34.4	1.17	5.9	−0.834	
42.2	1.39	8.5	−0.861	−0.847
42.4	1.44	8.7	−0.834	
52.8	1.78	13.2	−0.840	−0.831
52.9	1.82	13.7	−0.823	
61.6	2.23	18.9	−0.782	−0.802
61.5	2.12	18.0	−0.822	
81.4	2.93	32.5	−0.787	−0.777
81.4	3.00	33.5	−0.786	

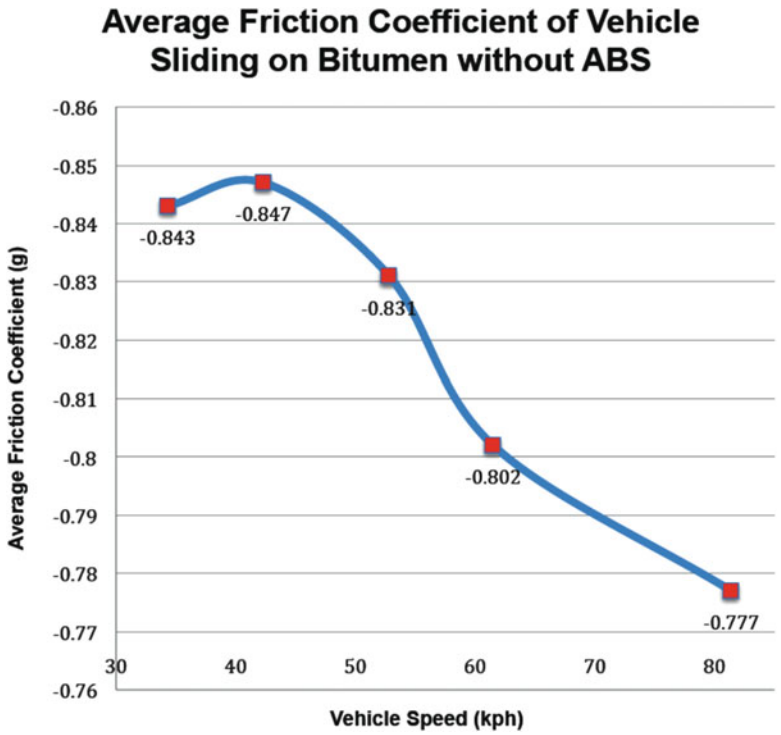

Fig. 8.8 Average friction coefficient of a vehicle sliding on bitumen with antilock braking system (ABS) disabled

both vehicles. At 80 km/h, the difference in the friction coefficient in the vehicle with and without ABS was −0.178 g and the average stopping distance of 4.5 m in the vehicle without ABS.

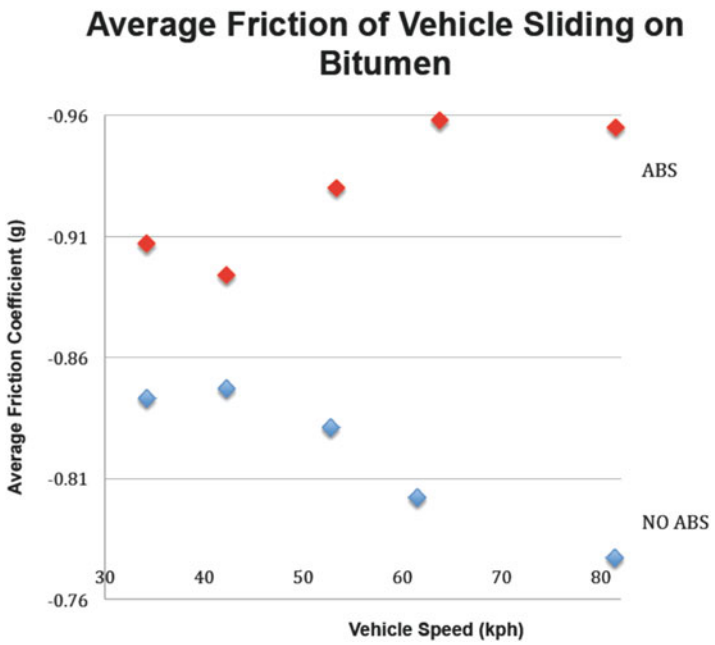

Fig. 8.9 Comparison of the average friction coefficient of a vehicle sliding on bitumen with and without ABS between 40 and 80 km/h

The effectiveness of ABS increases as velocity increases above 40 km/h. These on-road tests did not harmonise with the earlier research of in relation to non-ABS friction coefficient at lower velocities. Heinrich et al. identified that as velocity increased, friction decreased non-linearly with the most substantial decrease in vehicles travelling up to 30 km/h. The most substantial decrease in these results occurred between 50 and 60 km/h with an increase observed between 20 and 30 km/h.

Both series of tests support a peak at 40 km/h. With ABS enabled, the lowest friction coefficient between the vehicle tires and the road surface was observed at 40 km/h. With the ABS disabled, the highest friction coefficient between the vehicle tires and the friction coefficient was observed at 40 km/h. It is not possible to determine whether the friction coefficient peaks or plateaus at 70–80 km/h with the ABS enabled and disabled. Further tests need to be conducted at 70 km/h, 80 km/h, 90 km/h and 100 km/h to determine what trend occurs above 60 km/h.

There were only two tests that could be considered to be statistically significant. The test at 81.4 km/h and the test at 42.2 km/h when the ABS was off were the only results to fall within the 95% confidence interval range. Of the 11 tests performed with the ABS enabled, 8 fall within the 75% confidence range. With the ABS disabled, only half of the tests provided results that fell within the 75% confidence range.

$$v_i = \sqrt{v_e^2 - 2ad}$$

where v_i is initial velocity, v_e is end velocity, a is acceleration and d is distance.

Using the total braking distance of 33.5 m, it is possible to determine the effect of using an average g determined from a vehicle travelling at 40 km/h when the vehicle was travelling at a velocity above 80 km/h.

Friction coefficient determined at 40 km/h:

$$v_i = \sqrt{0^2 - (2 \times 9.81 \times -0.834 \times 33.5)} = 84.27 \text{ km/h}$$

Friction coefficient determined at 80 km/h:

$$v_i = \sqrt{0^2 - (2 \times 9.81 \times -0.768 \times 33.5)} = 80.89 \text{ km/h}$$

The Vericom brake test computers record the distance of braking using a multicontroller. This records braking distance from when the first application of braking is made by the driver. There is a delay between initial brake application and tire lock-up. Tire skid marks are rarely visible immediately upon tire lock-up. Test 10 with ABS disabled recorded a total braking distance of 33.5 m; however, physical measurements taken from the skid marks on the road were 29.1 m.

Using the total braking distance of 29.1 m, it is possible to determine the effect of using an average g determined from a vehicle travelling at 40 km/h when the vehicle was travelling at a velocity above 80 km/h. Friction coefficient determined at 40 km/h:

$$v_i = \sqrt{0^2 - (2 \times 9.81 \times -0.847 \times 29.1)} = 79.16 \text{ km/h}$$

Friction coefficient determined at 80 km/h:

$$v_i = \sqrt{0^2 - (2 \times 9.81 \times -0.777 \times 29.1)} = 75.82 \text{ km/h}$$

When using the physical marks left by a skidding vehicle (the evidence most readily available to collision investigators) rather than the total braking distance (calculated using a multicontroller), an underestimate of the vehicle travelling velocity will be made irrespective of what velocity the test vehicle was travelling to obtain the friction coefficient. All formulas for determining velocity that take into account braking distance were developed in reference to the total braking distance. Collision investigators can only rely upon the available physical evidence of braking such as skid marks which will be somewhat less than the total braking distance.

Whilst not considered statistically significant, the trend observed in the friction coefficient as velocity increases is well defined. The results are significant in relation to collision reconstruction. Based on the tests performed and the data

obtained, the relevance of the friction coefficient and its effect on vehicle velocity analysis can be identified. The highest friction coefficient result with the ABS disabled was recorded at the test performed at 42.2 km/h with an average friction coefficient of −0.861 g.

This result is below the lowest average friction coefficient obtained when the ABS was enabled. This result was obtained in a test performed at 35.6 km/h. From this it can be determined that any friction coefficient that is determined using a vehicle without ABS or a vehicle which has ABS which is disabled will provide a value which is below the true velocity for a vehicle with ABS. Using a friction coefficient obtained in a vehicle without ABS will result in an underestimate of the skidded vehicle velocity with ABS on.

The velocity at which friction tests are conducted to determine tire/road friction coefficients is a relevant consideration up to 80 km/h. As vehicle velocity increases, the significance of the results decreases. When friction coefficient tests are conducted in a vehicle without ABS to determine the velocity of a vehicle that does not have ABS, it is important to be aware that tests conducted below the velocity of the vehicle being analysed may result in an overestimate of vehicle velocity if using the total braking distance. Using the tests conducted without ABS, the mean average friction coefficient results at 34 km/h would result in an overestimate of velocity in the vehicle travelling at 81 km/h. Using the mean average friction coefficient obtained at 81.4 km/h provides a velocity estimate result of 81.3 km/h. All mean average friction coefficient results at 30 km/h, 40 km/h, 50 km/h and 60 km/h without ABS produce velocity overestimates of up to 4.0 km/h above the actual velocity of a vehicle which is travelling faster than that friction test vehicle velocity, at the commencement of braking. By neglecting pre-skid braking interval, the pre-braking vehicle velocity is underestimated by 5–15%. If using skid length only, then the velocity at which the friction coefficient testing occurs is irrelevant up to 80 km/h and will still provide an underestimate of the true vehicle velocity pre-braking.

Using a regression model it is possible to adjust measured friction coefficient values to account for the difference in vehicle velocity between the test vehicle velocity and the assessed vehicle velocity in vehicles without ABS. The Mehegan prediction model was developed to facilitate the ability to predict friction whilst accounting for a difference in vehicle velocity:

$$R^2 = 0.964$$
$$R = 0.982$$

To determine the friction coefficient at 81.4 km/h using the friction coefficient recorded at 42.3 km/h and using the Mehegan prediction model:

$$\mu_p = -0.982^{(n-m)/10} \times \mu^m$$
$$\mu_p = -0.982^{3.91} \times 0.847 = -788$$

Vehicle velocity determined using the Mehegan prediction model friction coefficient based upon braking distance of 32.5 m was obtained in tests performed at 81.4 km/h:

$$v_i = \sqrt{v_e^2 - 2ad}$$

$$v_i = \sqrt{0^2 - (2 \times 9.81 \times -0.788 \times 32.5)} = 80.62 \text{ km/h}$$

It was underestimated by 0.71 km/h.

Vehicle velocity determined using the Mehegan prediction model friction coefficient obtained at 42.3 km/h based upon braking distance of 32.5 m was obtained in tests performed at 81.4 km/h:

$$v_i = \sqrt{0^2 - (2 \times 9.81 \times -0.847 \times 32.5)} = 83.66 \text{ km/h}$$

It was underestimated by 2.26 km/h.

Using the adjusted friction coefficient, the vehicle velocity calculated was less than 1.0 km/h under the true velocity of the vehicle. When using the friction coefficient determined at 42.3 km/h, the calculated velocity overestimated the true velocity by 2.26 km/h. It should be noted that the calculations were based on the braking distance during testing not on the physical evidence of braking such as skid length. However, the adjusted friction coefficient most certainly provides very accurate results taking into account the difference in test vehicle velocity to assessment vehicle velocity when considering entire braking distance.

When determining the velocity of a vehicle fitted with ABS during skidding, care should be taken to ensure the velocity at which test skids are conducted to determine the friction coefficient is less than the predicted velocity of the vehicle being analysed. Using the results from these tests, the mean average friction coefficient obtained in the vehicle with ABS to determine the velocity of the vehicle that was known to be travelling at 83.1 km/h produced a range of over- and underestimates when using the total braking distance to determine the vehicle velocity. The mean average friction coefficient obtained at 30 and 40 km/h both underestimated the actual velocity. The mean average friction coefficient obtained at 50 km/h, 60 km/h and 80 km/h all produced overestimates.

The overestimates were not more than 1.91 km/h above the actual velocity and only occurred based on the total braking distance. When using the skid distance only, to determine pre-braking velocity, all calculations produced results that underestimated the true velocity.

8.3.6 Validation

To validate the accuracy of the Mehegan prediction model to predict the likely friction coefficient of a road surface and various vehicle velocities, we conducted a

Table 8.3 Predicted friction coefficient using Mehegan prediction model and modified Mehegan prediction model

Vehicle velocity km/h	Predicted result using Mehegan prediction model $\mu_p = -0.982^{(n-m)/10} \times \mu^m$	Predicted result using modified Mehegan prediction model $\mu_p = -0.982^{(n-m)/10} \times \mu^m \pm 0.95$
50.8	−0.825	−0.786 – 0.866
60.6	−0.810	−0.771 – 0.851
70.9	−0.797	−0.758 – 0.835
80.4	−0.782	−0.743 – 0.821

second series of tests. The tests were performed in the same vehicle at a different location. The tests were conducted in the driveway of Napier Park Nature Reserve, High Street, Road, Wheelers Hill, Victoria. The same procedure was followed as for series one with two tests being performed at 40 km/h, 50 km/h, 60 km/h, 70 km/h and 80 km/h with the ABS deactivated. No tests with ABS were performed (Tables 8.3 and 8.4).

Skid tests were performed at an average of 41.1 km/h, 50.8 km/h, 60.6 km/h, 70.9 km/h and 80.4 km/h to obtain the average friction coefficient at each velocity. The distance of each braking section was also recorded, which allows the vehicle velocity at the commencement of braking to be calculated using the velocity from skid formula. Using the known braking distance, the velocity at commencement of braking was calculated using the average friction coefficient obtained at 41.1 km/h. This was then used to determine the accuracy of this method when using a friction coefficient obtained at a lower test velocity compared to a subject vehicle velocity. At 51.8 km/h, 60.6 km/h and 80.4 km/h by using the friction obtained at 41.1 km/h, the calculated velocity was higher than the vehicle velocity at commencement of braking. The overestimate ranged between 0.92 and 1.71 km/h. At 70 km/h the velocity calculated was below the test vehicle velocity. It should be noted that the velocity from skid formula is based on using the length of a skid rather than braking distance. Braking distance is calculated using the Vericom brake test computer. Braking distance is longer than skid length. That is, a vehicle driver will always have applied braking prior to the commencement of a skid mark becoming visible on a road. Using the known braking distance, the velocity at commencement of braking the vehicle velocity was calculated using −0.840 g, the friction coefficient obtained at 41.1 km/h (Table 8.5).

Using the Mehegan prediction model formula designed and the friction coefficient −0.840 g obtained at 41.1 km/h, the expected friction coefficient values were calculated as shown in column 2 for values at 50.8 km/h, 60.6 km/h, 70.9 km/h and 80.4 km/h being the test velocities for which actual values were obtained. The purpose of using the Mehegan prediction model is to validate the formula for situations where a friction test cannot safely be conducted at the same velocity that a vehicle involved in a collision was travelling. For a collision reconstruction expert, the ability to adjust friction coefficient values obtained at low velocities will increase the accuracy of such work whilst allowing all testing to be safe. At 50 and

Table 8.4 Velocity calculations between 50 km/h and 80 km/h using friction coefficients obtained at 40 km/h

Velocity (km/h)	Test result	Error if using −0.840 g	Calculated velocity using −0.840 (km/h)	Error on calculated velocity (km/h)
50.8	−0.783	+0.057	52.45	+1.65
60.6	−0.786	+0.054	62.31	+1.71
70.9	−0.745	+0.095	70.04	−0.86
80.4	−0.732	+0.108	81.32	+0.92

Table 8.5 Velocity calculations between 50 km/h and 80 km/h using friction coefficient obtained at 40 km/h

Velocity (km/h)	Predicted result Mehegan prediction (g)	Calculated velocity using Mehegan prediction model (km/h)	Error on calculated velocity (km/h)
50.8	−0.825	51.99	+1.19
60.6	−0.810	61.18	+0.58
70.9	−0.797	68.23	−2.67
80.4	−0.782	78.59	−1.81

60 km/h, these prediction friction coefficient values resulted in estimated velocity calculations that were higher than the actual velocity by up to 1.19 km/h. At 70 km/h and 80 km/h, the estimated velocity calculations using the predicted friction coefficient values were lower than the actual velocity by up to 2.67 km/h. This margin of error is likely due to the non-linear decrease in friction coefficient as vehicle velocity increases, preventing a 'one-size-fits-all' approach as it occurs when one formula is devised using a regression model (Table 8.6).

For a collision reconstruction expert, friction remains an elusive phenomenon that can be a critical factor to any collision reconstruction. If a friction coefficient value that is higher than that relative to the subject vehicle is utilised in any calculation, then the end result will be a velocity that is higher than the actual velocity.

Preliminary testing identified that when a vehicle that is not fitted with ABS skids, then the friction coefficient will decrease as vehicle velocity increases above 40 km/h. Often a vehicle involved in a collision is travelling at a velocity that is dangerous or too high for the environment. This prevents the collision reconstruction expert from conducting road friction analysis at the relevant velocity. For every km the test vehicle is below the subject vehicle, the risk of overestimating velocity is increased.

Initial testing identified that the most significant decrease in friction coefficient occurred between 40 and 70 km/h. At 40 km/h a friction coefficient obtained at −0.847 g would result in an overestimate of velocity by 3.4 km/h if then used on a vehicle travelling at 80 km/h. Using mathematical modelling, the Mehegan prediction model formula was developed to allow predictions of friction coefficient at higher velocities based on results obtained at lower velocities. In the same series of

Table 8.6 Velocity calculations between 50 and 80 km/h using friction coefficient obtained at 40 km/h

Velocity (km/h)	Predicted result Mehegan prediction (g)	Calculated velocity using Mehegan prediction model (km/h)	Error on calculated velocity (km/h)
50.8	−0.786–0.866	50.74–53.26	−0.06 to +2.46
60.6	−0.771–0.851	59.69–62.34	−0.91 to +1.74
70.9	−0.758–0.835	66.54–69.84	−4.36 to −1.06
80.4	−0.743–0.821	76.48–80.39	−3.92 to −0.01

testing, the predicted friction at 80 km/h using the devised formula would be 0.788 g. By using the predicted friction coefficient, the calculated velocity would be −0.13 km/h below the actual vehicle velocity.

A complete second series of testing was then conducted at a second location to verify the accuracy of the mathematical Mehegan prediction model to predict the projection of friction coefficient as velocity increases. Determining the friction coefficient projections for 50 km/h, 60 km/h, 70 km/h and 80 km/h was done using the mathematical model based on the friction coefficient recorded at 40 km/h. The projected results were then compared against actual results recorded to verify the accuracy and validity of the model. At 50 km/h and 60 km/h, the calculated velocity when using the friction coefficient predicted using the model was between 0.58 and 1.19 km/h above the actual velocity. At 70 km/h and 80 km/h, the calculated velocity was between 1.81 and 2.67 km/h below the actual velocity, an error of ± 3%.

Two different locations were used to verify the model and its validity. There was a difference of 2% between the friction coefficients obtained at 40 km/h at the two sites. Taking this into account, the mathematical pro model was varied to incorporate a margin of error of 5%, which should be sufficient to incorporate the variation at most sites. Using the modified prediction model and the result obtained from the verification testing, the projection results are all an underestimate of the actual friction coefficient for that location. For a collision reconstruction expert, the use of a friction coefficient, which is lower than the actual friction coefficient, is acceptable, as it will result in a velocity which is lower than the actual velocity being analysed. Motor vehicle drivers who are involved in collisions whilst travelling at high velocity can be liable to both criminal and civil jurisdictions. For this reason it is not acceptable for a velocity to be calculated higher than the true velocity.

All velocity calculations in this research were based on the distance measured and recorded by the Vericom brake test computer. The distance is relative to the distance travelled by the vehicle from the initial application of braking. A collision reconstructionist is not provided with the total distance of braking but rather works with the tire marks visible on the road way. Tire marks are not left on the road immediately that braking is applied. The time from the brake application to the onset of visible skid marks on a road is defined as the transient period of the braking process. According to, the transient brake period is generally between 0.082 and

0.540 s with a vehicle velocity reduction of between 1% and 25%. This results in a velocity reduction of between 5% and 15%. Based on this, research using the friction coefficient obtained at 40 km/h can result in a velocity estimate, which is over by up to 4%. Therefore, if using visible tire marks to determine the velocity of a vehicle, the velocity should be an underestimate even if using a friction coefficient, which is obtained at a velocity lower than the subject vehicle. Using the mathematical projection model where velocity is being determined from tire marks would result in an underestimate of true vehicle velocity at the onset of braking at all velocities between 40 km/h and 80 km/h. The use of the modified projection model where the velocity is determined from tire marks will result in an estimate that could likely be between 11% and 21%. Whilst underestimates are acceptable estimates, up to 21% below are too low.

Where a velocity estimate is being performed using the friction coefficient values obtained from a test vehicle that is travelling considerably lower than the subject vehicle, then the projection model should be used in preference to the modified Mehegan prediction model.

8.3.7 Future Research

The vehicle velocities that were tested in this research limit the validity of the Mehegan prediction model for use in all collision reconstructions. It appears that a plateau occurs around 70–80 km/h for both vehicles with and without ABS. For conclusive validation of this model, testing would need to incorporate velocities up to 150 km/h. When using registered passenger vehicles and actual road surfaces, safety becomes paramount for this testing. Safety is compromised as vehicle velocity increases.

8.4 Effect of Temperature on Friction

8.4.1 Introduction

The friction coefficient of a particular road surface and car tire can be measured using a test vehicle and an accelerometer. However, the friction coefficient result can only be relevant to the conditions in which the testing occurred. This assumes that the friction coefficient of a road surface and paired car tire is not affected by temperature or otherwise provides nothing more than a ‘good estimate’.

When a motor vehicle collision is being reconstructed, the road surface friction needs to be either measured or estimated. Where precision is necessary, then tests should be performed. It is not possible to perform tests in identical weather conditions to what was occurring at the time of the collision. There will always be a delay between the collision and the subsequent friction testing. The delay may

be hours, days, weeks, months or even years. Despite the many other variables that may change between the collision and subsequent test due to time delay, consideration must be given to ambient temperature. A collision may occur at 2:00 am when the ambient temperature is near to 0 °C (32 °F). Due to the necessary scene examination and evidence preservation, it is reasonable that the friction testing may not occur until 2:00 pm later that day. The temperature could reasonably increase by up to 25 °C (77 °F) in that time.

If road surface/tire friction is not affected by temperature, then the temperature change will not be relevant; however, if it is relevant then it is critical to know what the effect is, to allow adjustment to friction test results to be made prior to reconstructing the collision and calculating vehicle velocity.

Early theories suggested that the coefficient of friction is independent of temperature. Coulomb included the nondependent relationship between temperature and rubber in his laws first published in 1785. However, more recently when polymers such as rubber have developed and more research has been performed, researchers now believe that rubber friction is very sensitive to temperature (Schallamach 1952, Takadoum 2007). The primary objective of this study is to experimentally determine the effects of ambient temperature on the friction coefficient of motor vehicle tires and road surfaces.

Predominantly, the research looking at the effects of temperature, which has been conducted, specific to car tires and road surfaces, has looked at extremely cold temperatures more prevalent in the United States and the United Kingdom. Australia experiences temperate weather for most of the year. However, due to the size and its position over the Tropic of Capricorn, the climate can vary throughout the continent. Typically, the northern states have warm weather throughout the entire year with the southern states having cooler temperatures in winter but still warm to hot in summer. Australia is one of the driest continents on earth with an annual rainfall of less than 600 millimetres. Due to its position in the southern hemisphere, Australia's seasons are opposite to the northern hemisphere where most research has been performed. December to February is summer; March to May is autumn; June to August is winter and September to November is spring. The testing for this research was performed over all seasons.

All research was performed in the State of Victoria where the climate is marked by a range of different climate zones. The northwest of the state has dry regions, whilst the northeast is covered in alpine snow regions.

Victoria has a reputation of forever changing weather, but as a general rule, the city has warm to hot summers, mild balmy spring and autumn and cool winters. Average temperatures are 25 °C in summer and 14 °C in winter. Rainfall is highest from May to October.

The objectives of this study are to identify how ambient temperature affects the tire/road friction coefficient on dry bitumen road surface using modern passenger vehicles. The results of this study will increase the accuracy of motor vehicle collision reconstruction in a range of environmental conditions worldwide. Will friction coefficient of car tires and road surfaces remain the same as ambient temperature increases?

This research will provide collision investigators and reconstruction experts worldwide a better understanding of the effects of vehicle velocity on the friction coefficient of the car tires and road surfaces, specifically when ascertaining the road/tire friction coefficient of a collision scene when testing is conducted after the collision is being analysed in substantially different ambient temperatures.

8.4.2 Experimental Conditions

The experimental testing phase was performed randomly between July 2012 and January 2014. Tests were performed randomly in a range of temperatures between 3 and 43 °C. Time of day was not a factor, and testing was based purely on ambient temperature with tests being performed both night and day. All tests were performed in dry conditions with no recent rainfall having been recorded in the preceding 12 h. All tests were performed with the ABS disabled as a result of fuse removal.

8.4.2.1 Location

All tests were performed at Attwood Victoria Police Driver Training Facility, 505 Mickleham Road, Attwood, Victoria, Australia (37.666°S 144.887°E). This is a private police facility, which is not open to the general public and primarily used to train members of Victoria Police in emergency driving techniques. The road is privately owned and has not been resurfaced since 2007. There were no resurfacing or significant repairs carried out on the road surface between July 2012 and January 2014. All tests were performed whilst driving the circuit in an anticlockwise direction. The dry tests were performed on the northern straight whilst travelling west. (See Fig. 8.10.) The bitumen road surface is in excellent condition due to very low levels of vehicle traffic and the high level of maintenance, due to the high-risk driving that occurs at the location. There were no noticeable condition changes during the period of testing. The area is well drained.

8.4.2.2 Test Vehicles

Tests were conducted in Australian-built General Motors Holden (GMH) Commodore Omega four-door sedans. There were two different vehicles used over the 3 years of testing. Both vehicles were of the same model having been built in 2010 and 2012 with no noted changes in production. The model, build and specifications of both vehicles were the same. The 3.0 l V6 spark ignition direct injection vehicles were fitted with six-velocity automatic transmissions. Ventilated disc brakes were fitted to both the front and rear. In the rear wheel drive, the vehicle had antilock braking system (ABS) fitted as standard. The ABS was disengaged for all tests. No

Fig. 8.10 Location of testing at Victoria Police Driver Training Facility, Attwood

performance modifications had been made to the vehicle with all braking, steering and suspension components fitted by the manufacturer as standard. The vehicle's tested mass with two occupants was 1762 kg. All vehicles had travelled less than 40,000 km at the time of tests. The vehicle type used in this study is depicted in Fig. 8.4.

8.4.2.3 Tires

At the time of testing, all vehicles were fitted with four Bridgestone Turanza ER3HZ tires that were fitted to the vehicle at new. The 225/60 R16 tubeless steel-belted radial tires were considered to be a mid-range touring model by the manufacturer. The minimum tire tread depth on any tire was 4 mm, and all tires were inflated to 34 PSI (2.3×105 Pa) prior to the commencement of testing. The tires on all vehicles had been used for both country and city driving, and no damage had been recorded or repairs carried out prior to the tests. Visual inspection showed no evidence of uneven wearing of the tires. Tread pattern of Turanza ER3HZ tire is shown in Fig. 8.5.

8.4.2.4 Brake Test Computer

The VC4000 Vericom brake test system was used on this primary research testing phase. The device has three major components, a crystal clock, an accelerometer and a microcontroller, which measures the instantaneous G-force 100 times per second and can measure the difference between ABS and standard brakes. The VC4000 is activated at a 0.2 g threshold upon initiation of the brake pedal load cell. The device is attached to the windscreen of the test vehicle and is considered one of the most modern and reliable test devices to determine G-force. The G-force is measured within 0.001 g providing accuracy of 1%. Distance is recorded at an accuracy of 1% over 400 m, and velocity is accurate within 1% up to 100 km/h. Therefore, the G-force will not change unless the velocity changes. Vericom brake test computer is shown in Fig. 8.5.

8.4.2.5 Test Velocity

The series of skid tests were all performed at as close to 60 km/h as possible. When the ABS fuse has been removed from the vehicle to disable the ABS, the cruise control function does not work. Once the Vericom brake test computer is activated, no application of braking can be made prior to the test braking application, or the Vericom will activate early and provide a false result. It is necessary for the driver to accelerate whilst observing the speedometer and activate braking as near as possible to 60 km/h. Due to the process for human velocity estimation and braking, no tests were conducted where braking was applied at 60.0 km/h precisely. The velocity ranges at which braking was activated were 47 and 62 km/h.

8.4.3 Methodology

Tests were performed randomly over a 21-month period. A total of 111 tests were conducted with a minimum of three tests at each temperature with less than 10% variance between the three tests required before results were accepted. Each vehicle had a driver and observer/recorder.

The author was the driver for most tests, although in one series of continuous 24 h testing, the driver was changed every 8 h due to fatigue considerations. Testing was conducted on the north side of the lap circuit whilst travelling west. Once the vehicle test velocity was attained (60 km/h), the foot brake was activated with maximum pressure. Pressure remained 100% until the vehicle came to a complete stop, and the results were displayed on the Vericom brake testing computer display screen. All tests were performed with the ABS off. Testing position on the roadway remained in the same general area but was gradually brought forward to prevent skids being consistently performed over the top of each other, particularly in the hot

weather conditions where considerable scuffing was occurring. Once ABS is disabled the speedometer in the vehicle does not always display, resulting in velocity estimation by the driver prior to braking application.

8.4.4 Results

As ambient temperature increased from 3 to 43 °C, the friction coefficient of car tires on a paired road surface increased from −0.630 g to −0.889 g. The increase was essentially linear with an average increase of −0.06 g for each increase of 10 °C. When observing the average of three results at each temperature, an inconsistent spike in results was observed at 26 °C−28 °C. The increase in friction coefficient from 25 to 26 °C was −0.029 g compared to the expected linear increase of −0.006 g. Although the three results at 26 °C were within 10% of each other, the initial test provided a friction coefficient of −0.801 g followed by the two more expected results of −0.771 g and −0.777 g. The results obtained at 26 and 27 °C are significantly above the line of best fit but still fell within the standard error (Fig. 8.11).

In 33 of the 37 series of tests for temperatures at which friction coefficient was tested, the friction coefficient observed in the third test was lower than the first test. The strength of the results is high providing clear evidence that for motor vehicle tires and the paired road surface, as ambient temperature increases, the friction

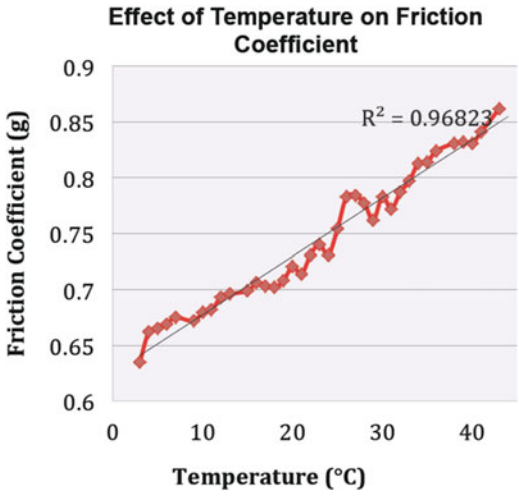

Fig. 8.11 Average friction coefficient of a vehicle sliding on bitumen with ABS disabled between 3 and 43 °C

coefficient also increases. There were seven instances where a very small reduction in the average friction coefficient over three tests was observed when the ambient temperature increased by 1 °C. However, this reduction was always immediately followed by an increase in friction coefficient as the ambient temperature was again increased by 1 °C. Where a decrease in friction coefficient was observed despite an increase in ambient temperature, the decrease was never less than the friction coefficient observed in the previous result (Table 8.7).

8.4.5 Discussion

The friction coefficient of motor vehicle tires and paired road surfaces will increase as the ambient temperature increases. There is a strong positive linear relationship between the two quantitative variables, temperature and friction coefficient, with minimal random variation. The correlation coefficient ($r = 0.983$) supports a high degree of correlation between the two variables with 1.0 the highest degree of relationship possible. The coefficient of determination ($r2 = 0.968$) suggests that 96.8% of the friction coefficient is directly accounted for by ambient temperature. There is a direct relationship between the independent (ambient temperature) and dependent (friction coefficient) variables.

The tests were all performed randomly over a 21-month period. At each temperature, the complete series of three tests were conducted in the same session. There was an unexpected escalation in friction coefficient results observed at 26 and 27 °C. Both these series of tests were conducted on the same day using the same vehicle and same driver.

The author was not the driver for these tests. These tests were not performed on the same day as the tests conducted at 25 °C or 28 °C. Whilst the results are not statistically inconsistent, they are certainly unexpectedly high. It is likely that these results were high due to a variable other than temperature. In 33 of 37 test series, the friction coefficient decreased from the first test to the third test despite the fact that the friction coefficient of the car tires and paired road surface increased as temperature increased. Friction always causes heat. The greater the friction that is required to stop a vehicle, the greater the amount of heat that is generated during braking. Therefore, the temperature of the brake components rises as the brakes are applied. Research has shown that one emergency stop at 96 km/h can raise brake lining temperatures by more than 70 °C (Friction Brake Theory). Repeated heavy stops such as that necessary to cause a vehicle to skid can continue to raise the temperature by equal amounts. The results are clear and provide strong evidence that the friction coefficient of car tires and road surfaces will increase as ambient temperatures increase. It is likely that the small decreases observed in most three test series are due to the increased heating of the braking components not any effects of ambient temperature.

Heat dissipation is the heat removed from brake friction surfaces by direct transfer to the surrounding air. Modern brake systems are designed to provide the

Table 8.7 Average friction coefficient of a vehicle sliding on bitumen with ABS disabled at a range of temperatures between 3 and 43 °C

Temperature (°C)	Average G (g)	Mean G (g)
3	−0.630 −0.634 −0.641	−0.635
4	−0.665 −0.663 −0.660	−0.662
5	−0.669 −0.666 −0.660	−0.665
6	−0.672 −0.671 −0.664	−0.669
7	−0.680 −0.677 −0.671	−0.675
9	−0.674 −0.674 −0.671	−0.672
10	−0.684 −0.681 −0.673	−0.680
11	−0.684 −0.684 −0.680	−0.682
12	−0.696 −0.687 −0.694	−0.693
13	−0.696 −0.698 −0.694	−0.696
15	−0.704 −0.701 −0.692	−0.699
16	−0.707 −0.704 −0.707	−0.706
17	−0.711 −0.704 −0.696	−0.703
18	−0.705 −0.704 −0.699	−0.702
19	−0.706 −0.712 −0.706	−0.708

(continued)

Table 8.7 (continued)

Temperature (°C)	Average G (g)	Mean G (g)
20	−0.734 −0.723 −0.708	−0.721
21	−0.721 −0.715 −0.708	−0.714
22	−0.745 −0.738 −0.710	−0.731
23	−0.747 −0.741 −0.732	−0.740
24	−0.740 −0.728 −0.725	−0.731
25	−0.748 −0.761 −0.753	−0.754
26	−0.801 −0.771 −0.777	−0.783
27	−0.799 −0.792 −0.761	−0.784
28	−0.782 −0.781 −0.768	−0.777
29	−0.778 −0.759 −0.749	−0.762
30	−0.784 −0.787 −0.778	−0.783
31	−0.774 −0.779 −0.763	−0.772
32	−0.794 −0.786 −0.781	−0.787
33	−0.798 −0.806 −0.787	−0.797
34	−0.815 −0.809 −0.815	−0.813
35	−0.816 −0.816 −0.810	−0.814

(continued)

Table 8.7 (continued)

Temperature (°C)	Average G (g)	Mean G (g)
36	−0.821 −0.828 −0.823	−0.824
38	−0.835 −0.829 −0.829	−0.831
39	−0.833 −0.840 −0.823	−0.832
40	−0.834 −0.835 −0.824	−0.831
41	−0.847 −0.846 −0.830	−0.841
43	−0.889 −0.860 −0.837	−0.862

best possible heat dissipation aimed to maintain the highest braking efficiency possible. Despite the design, friction always causes heat. Three heavy brake tests in fast succession will have an effect on the heat generated within the brakes and subsequently may be the cause for the reduction in friction coefficient of the car tires and road surfaces observed in sequential tests, therefore explaining the decrease in results.

With the results providing evidence of such a strong positive linear relationship between temperature and friction coefficient, the author believes that friction predictions for a range of ambient temperatures are possible using the carefully developed Hartman prediction model.

Based on a total braking distance of 30.0 m, it is possible to determine the effect of using a friction coefficient obtained at 3 °C compared to 43 °C by establishing the velocity of a vehicle at the commencement of braking.

1. Velocity of vehicle established using friction coefficient obtained at 3°C based on 30 m braking:

$$v_i = \sqrt{0^2 - (2 \times 9.81 \times -0.635 \times 30.0)} = 69.58 \text{ km/h}$$

2. Velocity of vehicle established using friction coefficient obtained at 13°C based on 30 m braking:

$$v_i = \sqrt{0^2 - (2 \times 9.81 \times -0.693 \times 30.0)} = 72.86 \text{ km/h}$$

3. Velocity of vehicle established using friction coefficient obtained at 23°C based on 30 m braking:

$$v_i = \sqrt{0^2 - (2 \times 9.81 \times -0.740 \times 30.0)} = 75.13 \text{ km/h}$$

4. Velocity of vehicle established using friction coefficient obtained at 33°C based on 30 m braking:

$$v_i = \sqrt{0^2 - (2 \times 9.81 \times -0.797 \times 30.0)} = 77.97 \text{ km/h}$$

5. Velocity of vehicle established using friction coefficient obtained at 43°C based on 30 m braking:

$$v_i = \sqrt{0^2 - (2 \times 9.81 \times -0.862 \times 30.0)} = 71.07 \text{ km/h}$$

When a collision reconstructionist is performing a collision analysis and velocity reconstruction, it is generally for a collision which has already occurred. Any type of test being used to determine the friction coefficient of the motor vehicle tires and paired road surface relative to the collision cannot be performed in identical conditions to what occurred at the time of the collision. If there is a substantial difference in the temperature at the time of the collision compared to the time of testing the temperature, then the difference must be considered and necessary adjustments made to the friction coefficient being used for speed determination. As ambient temperature increases, the relative friction coefficient increases.

A difference in ambient temperature between the time of a collision and the time of friction coefficient analysis of 10 °C will result in a velocity analysis, which is up to 3 km/h out. If it is warmer at the time of testing compared to the time of the collision, then the analysis will give a velocity estimation which is higher than the true velocity. If it is cooler at the time of testing compared to the time of the collision, then the velocity analysis will be too low. This is based on a vehicle analysis at around 70 km/h. As the velocity being analysed increases, then the margin of error will also increase. A temperature difference of 20 °C will result in a margin of error of around 5 km/h for a 70 km/h collision, and a 40 °C temperature difference from the time of the collision to the time of testing will result in a velocity analysis, which is up to 10 km/h incorrect. A collision analysis for a vehicle travelling around 120 km/h would be up to 17 km/h out if there was a temperature difference of up to 40 °C between the collision and subsequent testing.

In many instances collision reconstruction is being performed to provide critical evidence of the velocity of a vehicle prior to a collision. This evidence may be crucial for successful prosecution against drivers who are guilty of criminal offences, which have resulted in the death or serious injury of other road users. It is not acceptable for a collision reconstructionist to determine a vehicle travelling velocity which is either higher than the true velocity or lower. If friction tests are performed in significantly different temperatures from the temperature when the collision occurred, it is possible that the velocity determination could be out by more than 10 km/h. If it was cooler at the time of the collision compared to the tests, then the velocity analysis will be too high. If it was warmer at the time of the collision compared to the test time, then the velocity analysis will be too low. It is not possible to perform the tests in the same conditions as the collision conditions. It is however possible to determine the temperature at the time of the collision using recorded weather data. If ambient temperature at the time of the collision can be determined, then the Hartman prediction model can be used to determine the friction coefficient of the road surface and car tires relevant to the collision, using a friction coefficient result obtained at another time.

Hartman prediction model:

$$\mu_p = \mu_t \pm (0.007\mu_t \Delta t)$$

where μ_p is the predicted friction coefficient; μ_t measured friction coefficient, constant based on regression; and Δt difference in ambient temperature between the collision under analysis and the friction coefficient test.

Friction coefficient can be predicted for a range of temperatures using the Hartman prediction model.

6. Determining the friction coefficient at 3°C using a friction coefficient value obtained at 43°C:

$$\mu_p = -0.862 - [0.007 \times -0.862 \times (43 - 3)] = -0.618 \text{ g}$$

7. Vehicle velocity at 3°C determined using the adjusted friction coefficient based on braking distance of 30.0 m:

$$v_i = \sqrt{0^2 - (2 \times 9.81 \times -0.618 \times 30.0)} = 68.66 \text{ km/h}$$

8. Vehicle velocity at 3°C determined using the friction coefficient obtained at 3 °C based on braking distance of 30.0 m:

$$v_i = \sqrt{0^2 - (2 \times 9.81 \times -0.635 \times 30.0)} = 69.59 \text{ km/h}$$

9. Vehicle velocity at 3 °C determined using the friction coefficient obtained at 43 °C based on braking distance of 30.0 m:

$$v_i = \sqrt{0^2 - (2 \times 9.81 \times -0.862 \times 30.0)} = 71.07 \text{ km/h}$$

Using the friction coefficient obtained at 3 °C, the velocity of a vehicle which leaves 30.0 metres of skids when the ambient temperature is 3 °C can be determined to be about 69.59 km/h at the commencement of skidding. If the same skid marks of 30.0 metres, which were left in ambient temperature of 3 °C, were being assessed to determine velocity at the commencement of skid marks and the friction coefficient was determined using tests at 43 °C, then the velocity of the vehicle at the commencement of the marks would be calculated at 81.07 km/h. That is more than 10 km/h higher than the velocity of what the vehicle really would be.

Using the prediction model to determine the likely friction coefficient at 3 °C based on tests conducted at 43 °C, then the velocity at the commencement of skidding would be determined to be about 68.66 km/h. This is less than 1 km/h less than the true velocity of the vehicle.

For a collision reconstructionist, when determining vehicle velocity which is intended to prove or disprove the commission of a criminal offence, it is critical that the calculated velocity is not greater than the true velocity. Using the prediction model to determine the ambient temperature effect of friction coefficient will assist in ensuring that incorrectly high velocity determinations are not made.

8.4.6 Validation

The Hartman prediction model was used to determine the expected friction coefficient for a range of ambient temperatures. The greatest error was observed where there was a temperature difference of 37 °C when the observed error was −0.056 g. This margin of error falls well within acceptable levels of difference across a range of friction coefficient values for one variable. That is, if three results were recorded at one temperature, those three results would generally be considered accurate and reliable if they fell within a range of −0.06 g. This is an accepted difference between three tests where identical results are unlikely and not expected. When using the friction coefficient values to determine vehicle velocity, a difference of 0.056 g would affect the calculated velocity by less than 1 km/h. However, this difference was an underestimate, and therefore, the calculated velocity would be less than the true velocity by less than 1 km/h. For 6 of the 30 temperatures analysed, the predicted friction coefficient was identical to the measured friction coefficient; there was no margin of error. For 13 out of 37 tests, the prediction friction coefficient was higher than the measurement friction coefficient. The most significant difference was observed at 31 °C where the prediction friction coefficient was 0.013 higher than the actual measured friction coefficient (Table 8.8).

Table 8.8 Measured friction coefficient and predicted friction coefficient using the Hartman prediction model at a range of ambient temperatures between 3 and 43 °C

Ambient temperature (°C)	Friction coefficient test result (g)	Predicted friction coefficient using Hartman prediction model $\mu_p = \mu_t \pm (0.0071 \cdot \mu_t \Delta t)$	Calculated error
3	−0.635	−0.618	−0.017
4	−0.662	−0.624	−0.038
5	−0.665	−0.630	−0.035
6	−0.669	−0.636	−0.056
7	−0.675	−0.642	−0.033
9	−0.672	−0.654	−0.018
10	−0.682	−0.660	−0.020
11	−0.682	−0.667	−0.015
12	−0.693	−0.673	−0.020
13	−0.696	−0.679	−0.017
15	−0.699	−0.691	−0.008
16	−0.706	−0.697	−0.009
17	−0.703	−0.703	0.000
18	−0.702	−0.709	+0.007
19	−0.708	−0.715	+0.007
20	−0.721	−0.721	0.000
21	−0.714	−0.727	+0.013
22	−0.731	−0.734	+0.003
23	−0.740	−0.740	0.000
24	−0.731	−0.746	+0.015
25	−0.754	−0.752	−0.002
26	−0.783	−0.758	−0.025
27	−0.784	−0.764	−0.020
28	−0.777	−0.771	0.000
29	−0.762	−0.777	+0.015
30	−0.783	−0.783	0.000
31	−0.772	−0.789	+0.017
32	−0.787	−0.795	+0.008
33	−0.797	−0.801	+0.004
34	−0.813	−0.807	−0.006
35	−0.814	−0.813	−0.001
36	−0.824	−0.819	−0.005
38	−0.831	−0.832	+0.001
39	−0.832	−0.838	+0.006
40	−0.831	−0.844	+0.013
41	−0.841	−0.850	+0.009
43	−0.862	−0.862	0.000

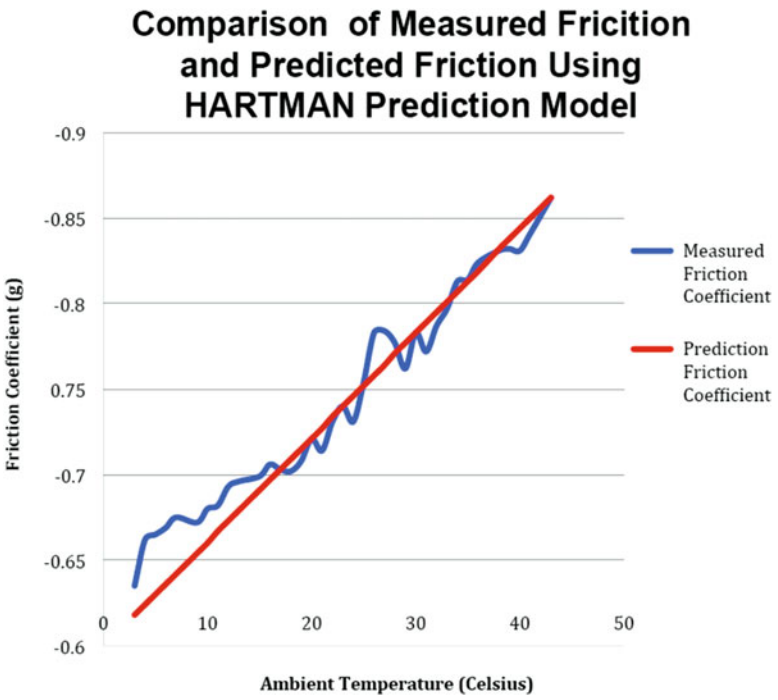

Fig. 8.12 Comparison of measured friction coefficient against predicted friction coefficient using Hartman prediction model

This difference is well within an expected range. A difference of 0.013 could overestimate the velocity by 0.6 km/h. Since it is best practice for collision reconstruction experts to round all calculations down, it is unlikely that this would have any effect on the overall result and subsequent collision analysis. Without the prediction formula, the calculation could be overestimated by more than 10 km/h if the ambient temperature is not taken into account when measuring the friction coefficient (Fig. 8.12).

The prediction model provides an ability to predict road/tire friction coefficient efficiently and reliably. The comparison graph highlights the strength of the formula and its application. The measured friction coefficient for any specific location and circumstance will vary slightly with identical results repeated rarely and almost never. The difference seen between the measured friction and predicted friction is within acceptable difference for two measured tests at all temperatures. That is, the difference between the measured and predicted friction coefficient is never more than 10%, which is the accepted difference. In this model the greatest difference between the measured friction and the predicted friction is less than 5% highlighting the strength of the reliability of this model and its application to friction coefficient prediction (Fig. 8.13).

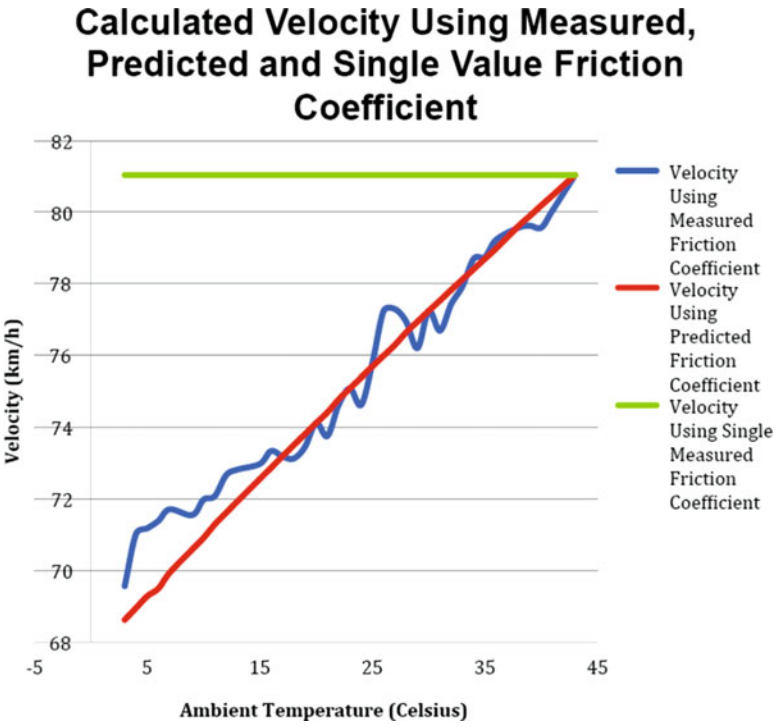

Fig. 8.13 Calculated velocity using measured, predicted and single-value friction coefficient

Vehicle velocity can be determined when a visible braking tire skid is evident. This is very common in motor vehicle collisions both pre-impact and postimpact. Whilst the method is regularly used to determine the pre-impact velocity of a vehicle, the travelling velocity of the vehicle will actually be higher due to the percentage of slowing which occurs between the initial application of braking and the subsequent onset of skidding once the wheels become locked. What is really being calculated is the velocity of the vehicle at the commencement of skidding. For a collision reconstructionist, the calculated velocity will be less than the travelling velocity, and therefore, it is a reliable method to be used to determine vehicle velocity even in criminal prosecution.

Vehicle speed can be determined using the velocity from skid formula:

$$\text{Speed} = \sqrt{254 \times d \times f}$$

where 254 is a constant, d is distance in metres and f is friction (g).

Figure 8.13 depicts the vehicle speed which can be determined for a 30.0-metre skid using the measured friction coefficient at each temperature range, the predicted friction coefficient using the Hartman prediction model for temperatures between 3 and 43 °C and the single friction coefficient measured at 43 °C. The effect of using

the single measured friction coefficient, irrespective of the difference between the temperatures at the time the skid was left and the time the subsequent test was performed, will vary depending on the difference between the two temperatures. The greater the difference between temperatures, the greater the inaccuracy in the velocity that is calculated. Figure 8.13 shows the effect of using a single measured friction coefficient for temperature differences up to 40 °C. If the temperature difference between the test and the analysed collision/skid is 40 °C, then the calculated velocity could be incorrect by over 11.4 km/h. If the test to determine the friction coefficient is performed in conditions, which are cooler than they were when the skid was left, then the calculated velocity will be an underestimate by up to 11.4 km/h. If the friction coefficient test is conducted in conditions which are warmer than they were when the skids were left, then the calculated velocity will be an overestimate by 11.4 km/h.

When using the Hartman prediction model to predict the friction coefficient at the time of a collision using a friction coefficient that was obtained at another time, the use of the velocity from skid formula to determine vehicle velocity is enhanced significantly. When using the prediction model to determine the likely friction, the calculated vehicle velocity was within 2 km/h at all temperatures.

Using the prediction model, the prediction friction coefficient was identical to the measured friction coefficient on 6 of 37 tests. The prediction model overestimated the friction coefficient in 13 of the 37 samples. Where the friction coefficient was overestimated, the subsequent vehicle velocity calculation was also overestimated. However, the overestimation was never more than 0.66 km/h. Where the friction coefficient was underestimated, the result was an underestimate of velocity by up to 2 km/h. When compared to the use of a single measured friction coefficient for all temperature conditions, the prediction model provides an accurate and very reliable method to determine the friction coefficient of the road surface and the car tires relevant to ambient temperature.

The use of the prediction model to determine friction coefficient is critical where the difference between the ambient temperatures at the time of testing is significantly different from the time which is being analysed. Where the difference in ambient temperature is within 5 °C, the difference in velocity calculation would be less than 2 km/h. If the ambient temperature at the time of testing is less than it was at the time of the collision/skidding, then the calculated velocity will be below the actual velocity, and therefore, the use of the prediction model is not so important. Where the ambient temperature is higher at the time of testing, then the prediction model should be used to ensure that any subsequent velocity calculation is not higher than the actual velocity. If the ambient temperature is different by more than 10 °C whether higher or lower, then the Hartman prediction model should be used to provide a more accurate and reliable friction coefficient and subsequent velocity determination.

8.4.7 Future Research

The research performed aspired to provide an analysis of the effect of ambient temperature on the friction coefficient of motor vehicle tires and paired road surfaces for an extensive range of temperatures prevalent in Australia and relevant to Australian conditions.

Based on the determination that the friction coefficient of car tires and road surfaces is affected by ambient temperature, the effects at below 0 °C temperatures would be relevant. Friction coefficient research relevant to car tires and road surfaces has predominantly been conducted in the United States and parts of Europe. Both regions are able to provide ideal conditions to perform such testing which most certainly would be relevant.

Further analysis could also be considered in relation to the observation of the decreasing friction coefficient observed between each series of tests. Based on this research, we know that as ambient temperature increases, the friction coefficient increases. However, in 30 of the 37 series of tests, the friction coefficient decreased from test one to test three. Ideally analysis could be performed to determine whether the reduction in friction coefficient is due to the heating of the rubber between tests or alternatively heating of braking components of the vehicle.

8.5 Effect of Rainfall on Friction

8.5.1 Introduction

Simplistic understanding of the friction phenomenon suggests that lubricants including water will lower the friction and reduce the wear between two sliding solid bodies. When considering roads, there is an expectation that most surfaces will be covered with a layer of oil deposited by both moving and stationary vehicles. The oil will act as a lubricant and lower the friction coefficient of car tires and road surfaces in both wet and dry conditions. But when combined with water in rainfall-type situations, the expectation is that the friction coefficient will be reduced significantly.

It is believed that the single most important factor effecting road-tire friction is the presence of water in various forms. Previous research suggests that it is the depth of the water that is crucial in determining the extent of the effect that the water has on the friction coefficient between car tires and road surfaces. There is clear distinction between the effects of thin water layers in comparison to thick water layers. During rainfall the depth of water rarely exceeds 2 mm and is typically 1 mm or less.

Dissipation of the water is facilitated by both the road and tire design. Until recent years, there has been an accepted belief that water as a lubricant reduces the friction coefficient of car tires and road surfaces. In 2001, Claeys identified that

specific to road-tire friction, the depth of the water layer is critical. Thin water layers most certainly reduce the friction coefficient by causing a complete loss in contact between the two surfaces. However, as the layer of water becomes thick, extra force is generated forward of the tire due to an accumulation of water. This increases the forces acting against the tire and subsequently increases the friction coefficient. This will occur until either the vehicle slows enough that the rate of dissipation increases or hydroplaning occurs. If hydroplaning does not occur, then the friction coefficient will increase as water depth increases.

It has been an expectation and a practice for a collision reconstructionist to reduce the measured friction coefficient obtained in dry conditions by −0.1 to −0.2 g if the collision being assessed had occurred in wet or raining conditions. The heavier the rain was reported to be, the greater the reduction in friction coefficient when adjusting dry result values. In 2013, since this research was conducted, a paper was published in SAE International. The paper titled *Friction, Tread Depth and Water:*

Laboratory Investigations of Passenger Car Tire Cornering Performance under Minimally – Wet Conditions (Blythe, Seguin) considered the effects of water depth on the friction coefficient of car tires and road surfaces.

The research was performed in laboratory conditions using three-dimensional dynamic vehicle simulations. The work concentrated on tread depth primarily but in addition did consider water depth. The work reported that at 64 km/h, with water depths greater than 1.27 mm, the friction coefficient of the car tire on the road surface was similar to dry friction results.

This research supports the work of Blythe and Seguin and relates the laboratory tire test results to real-world highway conditions as recommended in their paper published in 2013. The paper does suggest that as vehicle velocity increases, the friction coefficient will decrease even in deep water conditions. The effects of velocity in rainfall testing were not covered in this work.

The objectives of this study were to identify how rainfall affects the friction coefficient of motor vehicle tires and paired road surfaces without ABS. Simplistic approaches suggest that water, as a lubricant, will result in a reduction in friction coefficient. However, to the surprise of many, more recent and specific work suggests that in heavy rainfall, when water depths are greater than 1 mm above the level of asperities of the road surface, the friction coefficient may increase. The results of this study will increase the accuracy of vehicle velocity estimates in collision reconstruction for vehicles in raining and wet conditions. Will friction coefficient increase, decrease or remain the same in heavy rainfall conditions? This research will provide collision investigators and reconstruction experts world-wide a better understanding of the effects of rainfall and water on the friction coefficient of car tires and road surfaces specifically when a collision occurred in a period of heavy rainfall or post-rainfall.

8.5.2 Experimental Conditions

The experimental testing phase was performed on 12 August 2012. The entire test phase involved three series of tests with each series comprising a total of 20 tests. The three series of tests included pre-rainfall (dry), rainfall (rain) and post-rainfall (wet) tests. The ambient temperature was 13 °C with diminutive variation only. The entire testing phase was complete within 3 h between 9:40 am and 12:40 pm. The dry phase was completed first and was performed in an area with no rainfall recorded in the preceding 3 days. The rain phase was completed next using artificial rainfall. The wet phase was completed last on the area previously used for dry and rain testing. There was no notable wind recorded, and conditions were essentially mild to cool. Spatial cloud cover was evident.

8.5.2.1 Location

The test phase was performed at the Country Fire Authority (CFA) Training College, 4549 Geelong-Ballan Road, Fiskville, Victoria, Australia (37.683812°S 144.218707°E). This is a private training college for members of the CFA. The CFA is predominantly a volunteer fire and emergency service that has legislative responsibility for fire and emergencies in regional Victoria. The CFA, Fiskville, is used for general training including driver training. The road is privately owned and has not been resurfaced since 2001. The bitumen aggregate is in good condition with no obvious faults or defects. The area of testing is utilised as a thoroughfare with low-volume, low-speed traffic. The road runs in a general north-south direction with all tests performed whilst travelling in a northerly direction (Fig. 8.14).

Fig. 8.14 CFA Training College, Fiskville

Fig. 8.15 Holden Omega sedan used for dry, raining and wet friction testing (not actual vehicle)

8.5.2.2 Test Vehicle

Tests were conducted in an Australian-built General Motors Holden (GMH) Commodore Omega four-door sedan. One vehicle was used for the three series of tests. The vehicle was built in 2010 and first registered in 2011. The 3.0 l V6 spark ignition direct injection vehicle was fitted with a six-speed automatic transmission. Ventilated disc brakes were fitted to both the front and rear. In the rear wheel drive, the vehicle had antilock braking system (ABS) fitted as standard. The ABS was disengaged for all tests. No performance modifications had been made to the vehicle with all braking, steering and suspension components fitted by the manufacturer as standard. The vehicle's tested mass with two occupants was 1762 kg. The vehicle had travelled 12,755 km at the time of tests. The vehicle type used in this study is depicted in Fig. 8.15.

8.5.2.3 Tires

At the time of testing, the vehicle was fitted with four Bridgestone Turanza ER3HZ tires, which were fitted to the vehicle at new. The 225/60 R16 tubeless steel-belted radial tires were considered to be a mid-range touring model by the manufacturer. The minimum tire tread depth on any tire was 6 mm, and all tires were inflated to 34 PSI (2.3 $\times$ 105 Pa) prior to the commencement of testing. The tires had been used for both country and city driving, and no damage had been recorded or repairs carried out on any tire prior to the tests. Visual inspection showed no evidence of uneven wearing of the tires. The tires were all aged equally. The tires had travelled 12,755 km from new at the time of testing.

8.5.2.4 Brake Test Computer

All tests within this primary research testing phase were performed using a VC4000 Vericom brake test system. The device has three major components, a crystal clock, an accelerometer and a microcontroller which measures the instantaneous G-force 100 times per second and can measure the difference between ABS and standard brakes. The VC4000 is activated at a 0.2 g threshold upon initiation of the brake pedal load cell. The device is attached to the windscreen of the test vehicle and is considered one of the most modern and reliable test devices to determine G-force. The G-force is measured within 0.001 g providing accuracy of 1%. Distance is recorded at an accuracy of 1% over 400 m, and velocity is accurate within 1% up to 100 km/h. Therefore, the G-force will not change unless the velocity changes. The brake test computer was calibrated prior to each series of tests.

8.5.2.5 Test Velocity

The series of skid tests were all performed at as close to 60 km/h as possible. When the ABS fuse has been removed from the vehicle to disable the ABS, the cruise control function and speedometer display do not work. Once the Vericom brake test computer is activated, no application of braking can be made prior to the test braking application, or the Vericom will activate early and provide a false result. It is necessary for the driver to accelerate whilst estimating the vehicle speed and then activate braking as near as possible to 60 km/h. Due to the process for human velocity estimation and brake application timing, no tests were conducted where braking was applied at 60.0 km/h precisely. The velocity ranges at which braking was activated were 54 and 64 km/h.

8.5.3 Methodology

The testing phase to examine the effect of rainfall and wet roads on the friction coefficient of car tires and road surfaces was performed in one single session. All tests were performed at the same location in essentially the same conditions over a 3 h period. The first series of tests were performed on a dry road (Fig. 8.16). Twenty tests were performed over a 1 h period with approximately 3 min between tests to allow cooling of the vehicle braking system. All tests were performed whilst travelling north. The ABS was disabled.

The rainfall testing series was performed following the dry testing. Twenty tests were performed whilst travelling north in the same location as the dry testing. Rainfall was artificially replicated using the high-pressure hoses and recycled water from two firefighting Scania pumpers from either side of the roadway. Each pumper was capable of pumping 4000 litres of water per minute. The hoses pumped water

Fig. 8.16 CFA Training Facility, Fiskville, looking north on testing field

Fig. 8.17 Fire hose pumping water to simulate heavy rainfall conditions

continuously for the entire testing period (Figs. 8.17, 8.18, 8.19, 8.20 and 8.21). The testing period was performed over a 1 h period with approximately one test every 3 min providing a stationary period of at least 2 min to facilitate cooling of the braking system. The pumping of water replicated periods of very heavy rainfall. A thick layer of water was evident on the travelling path of the vehicle and in the braking location.

Fig. 8.18 Simulated rainfall direction and vehicle during braking

Fig. 8.19 Vehicle during braking throughout simulated rainfall testing

The third and final series of tests were performed in the same location following straight after the simulated rainfall testing. The hoses were turned off, and 20 consecutive tests were performed in the same location as the dry and rainfall testing. The series of 20 tests were performed over 1 h with the surface being lightly sprayed at 20 and 40 min to maintain a wet surface similar to what would be expected immediately following rainfall. There was a rest period of up to 3 min after each test to allow cooling of the braking components.

Fig. 8.20 Closer view of vehicle during braking in simulated rainfall testing

Fig. 8.21 Vehicle during skid resistance test on wet surface

8.5.4 Result

The average friction coefficient was calculated for 20 tests before, during and after rainfall. All tests were conducted consecutively for each series in the order of before (dry), during (rainfall) and after (wet) simulated rainfall. The average friction coefficient during rainfall over 20 tests was −0.816 g compared to −0.791 g in dry conditions and −0.709 g on the wet surface after rain. There were no results on

Table 8.9 Average friction coefficient before, during and after simulated rainfall

Test no.	Average friction coefficient rainfall (g)	Average friction coefficient dry (g)	Average friction coefficient wet (g)
1	−0.824	−0.788	−0.659
2	−0.834	−0.807	−0.731
3	−0.804	−0.823	−0.759
4	−0.784	−0.775	−0.74
5	−0.778	−0.796	−0.746
6	−0.835	−0.823	−0.679
7	−0.794	−0.773	−0.72
8	−0.844	−0.791	−0.726
9	−0.801	−0.807	−0.672
10	−0.823	−0.807	−0.699
11	−0.824	−0.794	−0.72
12	−0.814	−0.771	−0.751
13	−0.789	−0.799	−0.663
14	−0.827	−0.819	−0.668
15	−0.852	−0.752	−0.666
16	−0.811	−0.78	−0.734
17	−0.791	−0.784	−0.689
18	−0.83	−0.747	−0.72
19	−0.821	−0.806	−0.635
20	−0.810	−0.789	−0.644

the wet road, which had a higher friction coefficient to any result that was obtained during the simulated rainfall. That is, the highest friction coefficient recorded on the wet road was lower than the lowest friction coefficient recorded during rainfall. In three of the tests conducted in the wet, the results were higher than the three lowest results obtained in the dry. Eight of the results obtained in the simulated rain conditions were higher than the highest results obtained in the dry conditions (Table 8.9; Figs. 8.22, 8.23 and 8.24).

There were five results, which occurred, in the dry conditions, which were lower than the lowest result obtained in the raining conditions. When comparing the average of the full 20 results, the average friction coefficient measured in the raining conditions was 3.1% higher in the raining conditions compared to the dry conditions and 13.2% higher in the raining conditions compared to the wet conditions. The average friction coefficient in the dry conditions was 10.4% higher than the wet conditions. In the raining conditions the average g was more than −0.1 g higher compared to the wet conditions. The average g was −0.025 g more in the raining conditions compared to the dry.

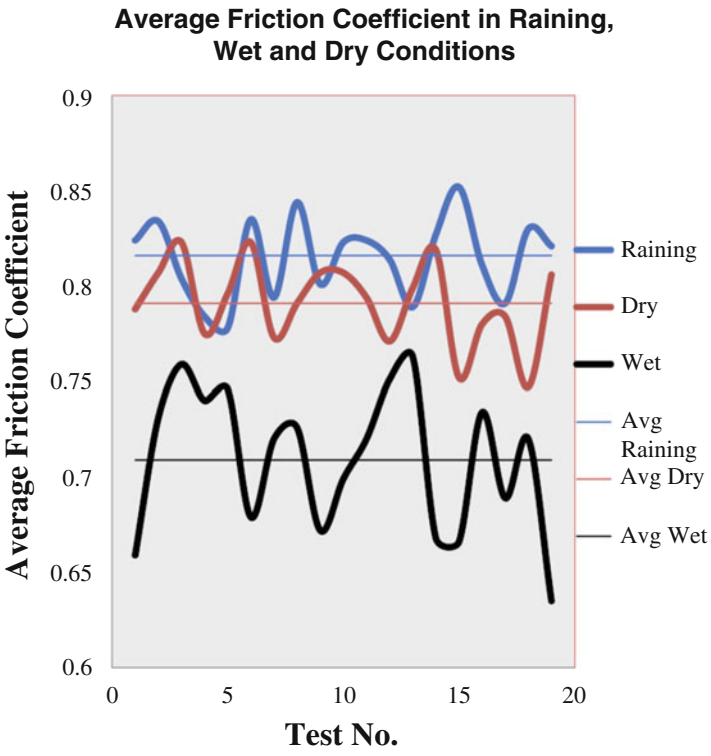

Fig. 8.22 Friction coefficient before, during and after simulated rainfall

8.5.5 Discussion

Contrary to significant volumes of research, the friction coefficient of a skidding vehicle tire on a road surface is not reduced during periods of high rainfall. Compared to a dry road, the friction coefficient is likely to be around 3% higher in heavy rain in a vehicle travelling at around 60 km/h. Consistent with previous research, the friction coefficient decreases significantly when the road is simply wet and there is no depth to the layer of water on the road. If the layer of water is below the level of asperity, then the road is regarded as wet.

The author believes the depth of the water is the critical factor in determining the effect of rainfall on the friction coefficient of car tires and road surfaces. Once the water in front of the sliding tire becomes so deep that dissipation does not occur at a rate fast enough to remove a build-up of water in the path ahead of the tire, a wedge occurs which increases the resistance against the tire as it slides. (See Fig. 8.25.) At very low water depths, the water between the tire and the road surface reduces the friction coefficient between the two solid surfaces by acting as a lubricant.

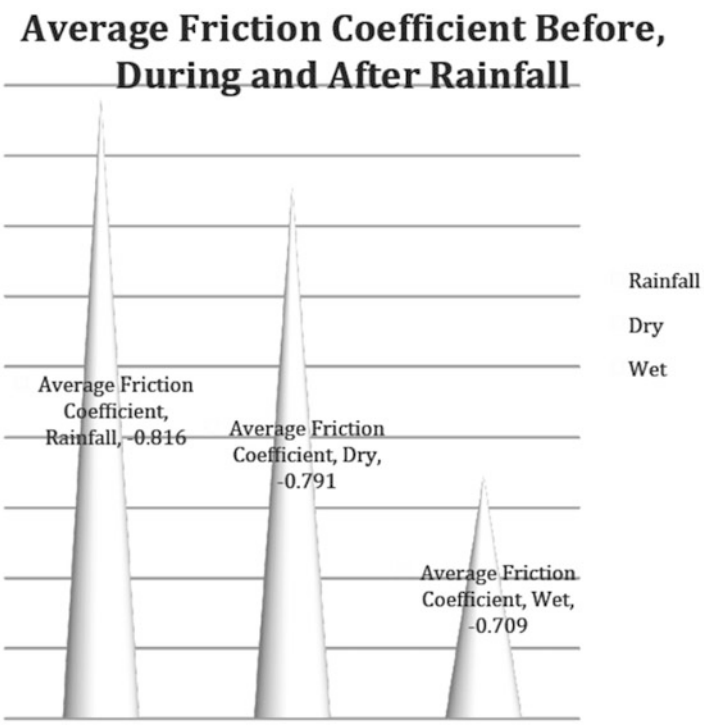

Fig. 8.23 Average of friction coefficient results before, during and after simulated rainfall

Once the layer becomes too deep to dissipate, the wedge will occur. Theoretically, if the friction coefficient is increased due to a wedge forming ahead of the tire as a result of an inability for the water to dissipate, then road design and tire tread also play key roles in determining whether the friction coefficient will increase or decrease in periods of rainfall. The water depth at which the friction coefficient increases is likely to be affected by these factors. Therefore, it is unlikely that simply determining a depth at which the friction coefficient will begin to increase would be possible. That is, a quality tire with good tread depth and good dissipation properties is likely to be more efficient in keeping the path ahead clear of water, and without the formation of the wedge, the friction coefficient will decrease in the same rainfall that another tire may fail to dissipate. As opposed to temperature where the temperature at the time of a collision can reasonably be estimated, it is not possible to estimate water depth. Apart from knowing the rate of rainfall, each road and each tire may vary the effect of the water build-up to some degree. The macro- and micro-textures of the road in addition to cross fall and gradient will further affect this. Prediction of friction coefficient of car tires and road surfaces based on the depth of water simply cannot possibly be used in collision reconstruction.

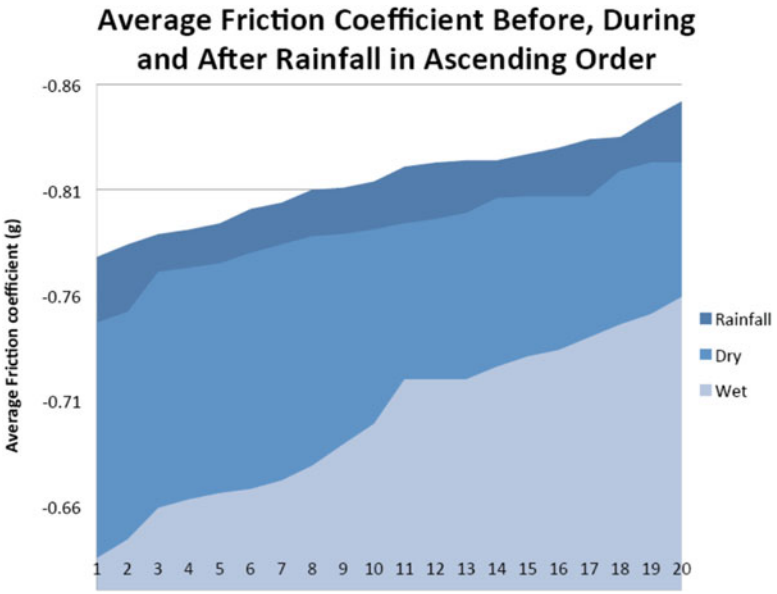

Fig. 8.24 Average of friction coefficient results before, during and after simulated rainfall in ascending order

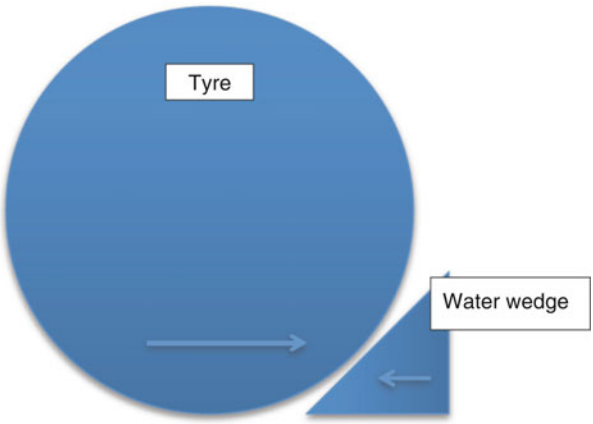

Fig. 8.25 Water wedge opposing direction of sliding tire

If analysing a collision, which has already occurred, quantifying the rainfall at the time of the collision in the exact location and the exact time is virtually impossible. Even if the quantity of rain could be determined, then it is basically impossible to determine what the dissipation properties of the tire and the road surface were, and therefore, it is very difficult to determine whether the wedge of water formed forward of the tire and if so what effect that wedge had (Fig. 8.26).

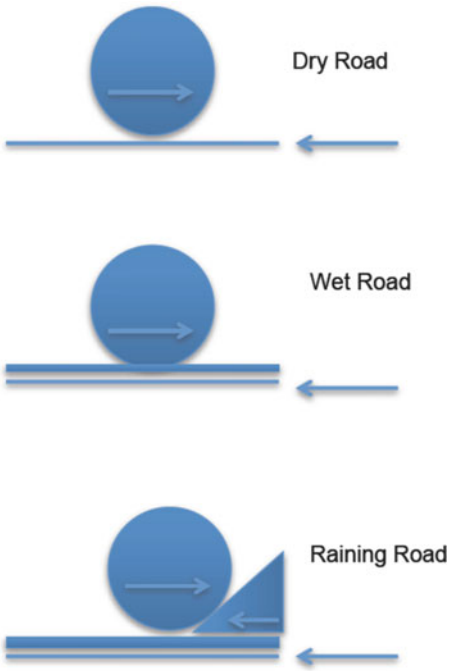

Fig. 8.26 Opposing forces in dry, wet and raining conditions

It should be possible in controlled laboratory testing to determine the effect of a water wedge and a range of depths for a range of tires and aggregate types and known velocities. It is unlikely that the findings could ever be used to validate friction coefficient prediction formulas for use in collision reconstruction based on the influence of rainfall on a skidding vehicle.

Based on the results of this research, the effect of using the friction coefficient obtained on a wet surface, for a tire that was locked and sliding on a road surface in heavy rainfall conditions, it is likely that a collision reconstructionist will underestimate the true speed of the vehicle by applying the friction coefficient obtained during testing on a wet surface.

Without knowing whether a wedge of water formed forward of the tire, it is not possible to know whether the friction coefficient will be affected by the rainfall, and therefore, the wet friction must be used. Based on a sliding distance of 30.0 m, the effect of using a friction coefficient obtained on a wet road to determine the velocity of vehicle sliding in heavy rain, if in fact the friction coefficient actually increased due to the wedge, could be up to 5 km/h.

Speed of vehicle sliding for 30.0 m on wet road:

$$\text{Speed} = \sqrt{254 \times d \times f}$$
$$\text{Speed} = \sqrt{254 \times 30 \times -0.709} = 73.5 \text{ km/h}$$

Speed of vehicle sliding for 30.0 m in heavy rainfall:

$$\text{Speed} = \sqrt{254 \times 30 \times -0.816} = 78.8 \text{ km/h}$$

If the sliding distance was double at 60.0 m, then the effect of using a friction coefficient obtained in wet conditions when it would be likely that friction coefficient was increased due to heavy rainfall could be as much as 8 km/h. In comparison to the effects of temperature, the effect is small, and whilst using the friction coefficient, which has been obtained on a wet road, a collision reconstructionist can be sure that the velocity, which is being analysed, is not an overestimate. That is, any calculated velocity would not be higher than the true speed that the vehicle was travelling. When a vehicle velocity is being presented in a court of law to prove or disprove the commission of a criminal offence, the most important consideration is that any vehicle velocity estimate is not higher than the true velocity. Although using a friction coefficient obtained on a wet surface to calculate the velocity of a vehicle sliding in a period of heavy rain is likely to result in an underestimate of speed, the margin of error is likely to be less than 7%. Given that it is impossible to determine the exact friction coefficient relative to any raining period with confidence, it is advisable to use wet friction rather than dry friction to ensure there is no possibility of providing an overestimate.

It is evident that the depth of any lubricant layer is the most relevant factor in determining whether the friction coefficient between car tires and road surfaces may actually be higher in periods of rainfall compared to dry friction. In periods of heavy rain, the friction coefficient between car tires and road surfaces is likely to increase. These results are surface specific to pneumatic tires and bitumen road surfaces, and without further research with other surfaces specifically, these results cannot be attributed to give similar results for other surfaces or objects. The viscoelastic properties of rubber make this substance unique, and any behaviours observed cannot reasonably be connected to other substances without further research.

Furthermore, when considering wet friction relative to car tires and road surfaces, consideration must be given to the fact that both tires and road surfaces are designed to dissipate water. The results observed in this research are surface specific.

In heavy rain the friction coefficient between car tires and road surfaces increased when the vehicle was travelling at about 60 km/h at the commencement of sliding. The phenomenon of hydroplaning is more likely to occur as speed increases, tire tread depth decreases and water depth increases. Hydroplaning is defined as friction coefficients at or below approximately −0.10 g, and essentially the surface of the tire loses complete contact with the surface of the road due to the layer of water between the two. Essentially the wedge of water, which has failed to dissipate and increases the force against the tire, provides a ramp upon which the tire can ride before continuing on top of the water (Fig. 8.27).

Wheel lock-up typically occurs as a result of severe braking. During wheel lock-up, a driver may lose steering control, and the friction coefficient is greatly reduced. A moving vehicle usually has a vehicle velocity which is equal to wheel velocity.

Fig. 8.27 Water wedge providing a ramp for tire to commence hydroplane

The speed of a vehicle can be calculated by measuring the speed of the wheel rotating and multiplying it by the nominal wheel radius. When a wheel becomes locked and slips, the vehicle velocity and wheel velocity will no longer be equal. Slip is a term commonly used to indicate the difference between wheel velocity and vehicle velocity:

$$\text{Slip} = v - \frac{\omega R}{v}$$

where v is vehicle velocity, ω is wheel velocity and R is radius of wheel and tire.

When a wheel is not locked or under braking, then slip $= 0$. In the incidence of severe braking likely to result in lock-up, $\omega = 0$ whilst slip $= 1$. There will be an optimum slip value between 0 and 1. That is a value where the friction coefficient is at maximum. Maximum or peak friction coefficient during braking is typically recorded immediately prior to lock-up.

It is likely that when a vehicle is sliding in deep water, peak friction is likely to be observed immediately prior to hydroplaning. Whilst assuming a friction coefficient of -0.1 or less when a vehicle is hydroplaning, it is likely that deceleration will have occurred prior to hydroplaning.

The friction theories of Amontons, Coulomb, Bowden and Tabor have dominated all others for many decades. However, the large variations in experimental values suggest that adhesion theory does not fully account for the phenomenon. In 1981 Suh suggested that there are three mechanisms involved in friction, namely, adhesion, asperity deformation and ploughing. According to Suh, frictional force is largely dependent upon ploughing of surface asperities.

Ploughing friction may be relevant to a soft wheel or tire which can be easily deformed or alternatively when the ground upon which it is sliding is relatively soft. When a wheel sinks into the soft material and pushes or ploughs its way through, this becomes the major source of friction. Ploughing is the likely explanation for the increase in friction coefficient when a vehicle slides across a road in heavy rainfall. This further supports the theory that the maximum of peak friction will occur immediately prior to hydroplaning. Whilst ploughing force can be calculated, it is necessary to know the depth of the soft surface, which is simply not possible when analysing a collision, which has already occurred.

When a tire slides on a road surface in heavy rain, the friction coefficient will be higher compared to a dry or wet surface. It is not possible to quantify the effect without determining the depth of the water, the tread depth of the tire and the road surface composition. When analysing a motor vehicle collision, which has occurred in periods of heavy rain, it is recommended that a ‘wet’ friction coefficient test is

performed to determine the friction coefficient relevant to the collision. However, this will certainly result in an underestimate of velocity. Although the friction coefficient in heavy rain may be higher than dry friction, it is possible that efficiency of dissipation may have been high and any ploughing effect minimal. The rate of dissipation cannot be quantified. By using a friction coefficient determined on a 'wet' but not raining road, there should be no risk of overestimating the velocity of a vehicle at the time of a collision. A friction coefficient determined on a wet road should not be lowered further to account for periods of heavy rainfall.

8.5.6 Future Research

Based on the earlier related laboratory research by Blythe and Seguin, which studied the effect of water depth on the friction coefficient of car tires and road surfaces, it would be beneficial to research the effect of vehicle velocity in heavy rainfall conditions in real-world environments. The work of Blythe would suggest that despite the friction coefficient being higher in rainfall, ideally knowing the water depth could also strengthen the validation of these results. However, it is difficult to determine such measurement in moving vehicles whilst maintaining conditions expected in periods of high rainfall. The ability to determine the actual water depth would be advantageous and may be an area of consideration for future research.

8.6 Conclusion

The study was set out to explore the effects of vehicle velocity, temperature and rainfall on the friction coefficient of pneumatic tires and bitumen road surfaces and has identified that all three elements will impact the friction coefficient between the two surfaces. The study also sought to identify whether friction coefficient of pneumatic tires and road surfaces could be predicted to account for the effects of the three variables. The general theoretical literature on the subject area of friction and how it is affected by velocity, temperature and rainfall, specifically in relation to pneumatic tires, is inconclusive within the diversification discourse.

8.6.1 Experimental Findings

Vehicle velocity, ambient temperature and rainfall were all determined to affect the friction coefficient of pneumatic tires and bitumen road surfaces.

1. Is the friction coefficient of pneumatic tires and bitumen road surfaces affected by velocity?

The velocity that a vehicle is travelling when it commences to slide on a bitumen road surface will affect the friction coefficient between the tires and the road surface. The effect will depend upon whether the vehicle is sliding with or without ABS braking. When a vehicle is sliding under the effects of ABS braking, the friction coefficient will decrease between 30 and 40 km/h and then increase from 40 km/h to where it begins to plateau around 80 km/h. When a vehicle is sliding without ABS, the friction coefficient will increase if the vehicle is travelling between 30 and 40 km/h before and then commence to decrease until around 80 km/h where it begins to plateau.

2. Is the friction coefficient of pneumatic tires and bitumen road surfaces affected by temperature?

The ambient temperature will affect the friction coefficient of pneumatic tires sliding on bitumen road surfaces. As the ambient temperature increases, the friction coefficient of the two sliding surfaces will increase. Between 3 and 43 °C, the effect is positive and linear with a very strong correlation. No plateau was observed between the experimental temperature ranges.

3. Is the friction coefficient of pneumatic tires and bitumen road surfaces affected by rainfall?

When a vehicle slides on a wet road, the friction coefficient between the pneumatic tires and the bitumen road surface will be lower when compared to the same tires sliding on the same road surface when dry. However, when the same vehicle slides during a period of rainfall, the friction coefficient of the tires sliding on the road surfaces will be higher compared to both the wet and dry road surfaces. The extent of the effect will be affected by the depth of the water layer forward of the sliding tire.

The volume of rainfall and the ability of both the tires and the road surface to dissipate the water will affect the depth of the water. The greater the depth of the water layers, the higher the friction coefficient between the tire and the road surface.

4. Can friction coefficient of pneumatic tires and bitumen road surfaces be predicted to account for any effect due to velocity, temperature or rainfall?

The friction coefficient of pneumatic tires and bitumen road surfaces can be predicted using the Mehegan prediction model to account for the effects of vehicle velocity. When the friction coefficient of a sliding tire on a road surface is determined using a vehicle which is travelling at a speed higher or lower than the speed of a vehicle being analysed, then the Mehegan prediction model can be used to predict the friction coefficient relevant to the vehicle being analysed using the friction coefficient determined at a different velocity. This allows skid resistance tests to be conducted and safe speeds even when analysing the travelling velocity of vehicles involved in collisions or incidents and much higher speeds.

The friction coefficient of pneumatic tires and bitumen road surfaces can also be predicted using the Hartman prediction model to account for the effects of ambient temperature. When there is a change in temperature between the time of a collision and the time of subsequent skid resistance temperature, then it is likely that there will be a change in ambient velocity.

The Hartman prediction model can be used to predict the friction coefficient of pneumatic tires sliding on bitumen road surfaces for any ambient temperatures higher or lower. Using experimental testing of actual cars sliding on road surfaces, it is not possible to quantify the depth of water forward of the sliding tire.

Therefore it is not possible to develop a model to facilitate the prediction of friction coefficient based on water depth. Whilst the experimental results identify that the greater the depth of water layer the higher the friction coefficient between the two sliding surfaces, it is not possible to quantify the effect.

8.6.2 Theoretical Implication

The theoretical cases for modification need to be reconsidered to further appreciate and recognise the effect of vehicle velocity, ambient temperature and rainfall on the friction coefficient of pneumatic tires and road surfaces.

The laws of friction are not relevant to the friction coefficient of pneumatic tires and bitumen road surfaces. The experimental result of a sliding tire without ABS is generally consistent with the suggestions of Takadoum (2010) in that the friction coefficient decreases with increasing speed. The velocity thresholds contradict the work of Heinrichs et al. (2004b). Whilst the pattern is consistent with most work presented since 2000, there is a need for further examination of minimum and maximum thresholds.

The framework suggests strongly that friction coefficient of pneumatic tires and bitumen road surfaces will decrease with increasing velocity. The Williams-Landel-Ferry theory already suggested that the friction coefficient of rubber and bitumen surfaces is affected by temperature which is supported by the experimental data. As recent as 2007, Takadoum indicated that as temperature increased, the friction coefficient of the two surfaces would increase only if the surface reaches maximum softening at which point the surface friction coefficient will begin to decrease. The research considered ambient temperatures up to 43 °C, and no decrease in friction was observed. It is noted from the study that in Australian conditions, there is no evidence to support the likelihood that there will be ambient temperatures observed which would result in maximum softening resulting in a decrease in friction coefficient. Whilst conditions above 43 °C do occur, it is not a common phenomenon over a sustained period of time and occurs seldom. There is no evidence to suggest when maximum softening will occur for pneumatic tires and bitumen road surfaces. There was evidence that skid resistance tests performed in quick succession will result in a reduction in friction coefficient. This is likely the

result of heating of the vehicle braking components as opposed to a reduction of friction coefficient between the tire and the road surface.

The experimental findings relating to rainfall are significant when considered in conduction with the laboratory research of Blythe (2013). The outline of the work of Blythe is that as water depth in the path of a sliding tire on a road surface the friction coefficient will increase. The empirical findings of Blythe are essentially the same as this study, and the research was performed over a similar time period, each without the knowledge of the other. The work of Blythe was performed in controlled laboratory circumstances and yielded the same findings as this study in real-world testing. Both these two studies highlight the necessity for the realisation that the simple presence of a lubricant is not sufficient to confirm a reduction in friction coefficient. This work supports significant early research that dry friction is higher than wet friction where there is no substantial depth to the lubricant layer.

8.6.3 Implication of Prediction Model

The use of the Mehegan prediction model to predict the friction coefficient is a valid method for prediction friction between pneumatic tires and bitumen road surface. This model was developed surface specific. It is reliable for predicting friction for any vehicle velocity using a known vehicle velocity between 40 and 80 km/h. Whilst the method is both valid and reliable, the effect when the friction coefficient is being determined for use in vehicle speed reconstruction is very minor and not necessary when the speed being analysed is higher than the speed at which the test skid was performed. Any speed determination is likely to result in a further underestimation of the true speed of the vehicle. This is due to any speed calculation being based upon physical evidence of tire marks which will already result in a speed underestimation.

The use of the Hartman prediction model to predict friction coefficient is both a valid and important model to be considered when contemplating the friction coefficient of pneumatic tires and bitumen road surfaces at a range of ambient temperatures. The effect of temperature on the friction coefficient of pneumatic tires and bitumen road surfaces is significant.

Where a vehicle speed is being analysed using a friction coefficient determined in different temperature conditions, the Hartman prediction model should be used to predict the actual friction relevant to the conditions which were occurring at the time which is being analysed. All collision reconstructionists should consider the use of the Hartman prediction model in any speed analysis. The model is validated for ambient temperatures between 3 and 43 °C.

8.6.4 Recommendation for Future Research

The scale of debate relating to this research and findings is complicated and multifaceted. To further validate the findings of this research and achieve solid understanding of the effects of velocity, temperature and rainfall, more case studies and research need to be performed specifically relating to pneumatic tires and bitumen road surfaces in controlled laboratory conditions.

The effect of ambient temperature was examined extensively but did not extend to temperatures below zero. Whilst it would be expected that friction coefficient will continue to decrease as the ambient temperature continues to decrease, it is not possible to validate the use of the Hartman prediction model without such research.

Development of a prediction model to account for the effects of rainfall would require an ability to measure rainfall and quantify water depth. There are a multitude of parameters, and it would be difficult to perform in real-world testing. Whilst laboratory testing should be able to identify the minimum and maximum thresholds in relation to water depth, it is likely to be difficult to attribute this relationship to rainfall due to the inability to quantify the exact rainfall conditions that were occurring at the time of a collision.

8.6.5 Deduction

In spite of what is often reported in relation to the phenomenon of friction, it is possible to predict friction. The friction coefficient of two surfaces is specific to the two surfaces in contact, and conclusions cannot be drawn from the results of two sliding surfaces and attributed to two different sliding surfaces. The friction coefficient of pneumatic tires and bitumen road surfaces is affected by velocity, temperature and rainfall. Using a known friction coefficient for a specific tire and road surface, it is possible to accurately predict the friction coefficient of the same tire and road surface for a range of velocities and temperatures.

Dedication This chapter is dedicated to all who have lost their lives or been seriously injured in motor vehicle collisions and their families and friends who live with the physical and emotional pain of their loss, every day. . .. . .. Jenelle C. Hartman.

References

Blau, P. (2012). *Friction science and technology: From concepts to applications* (2nd ed.). Ohio, USA: Taylor and Francis.

Blythe, W. & Seguin, D. (2013). "Friction, tread depth and water; Laboratory investigations of passenger car tire cornering performance under minimally-wet conditions", SAE Technical Paper 2013-01-0789, https://doi.org/10.4271/2013-01-0789

Bowden, F., & Tabor, D. (1974). *Friction: An introduction to tribology*. London: Heinemann Educational.

Butt, H., & Kappl, M. (2010). *Surface and interfacial forces*. Wiley-VCH Verlag GmbH & Co: Weinheim.

Chowdury, M. A., Khalil, M. K., Nuruzzaman, D. M., & Rahaman, M. (2011). The effect of sliding velocity and normal load on friction and wear property of aluminium. *International Journal of Mechanical and Mechatronics Engineering, 11*(1), 45–49.

Claeys, X., Yi, J., & Alvarez, L., et al. (2001). "A dynamic tire/road friction model for 3D vehicle control and simulation," Proceedings of IEEE Intelligent Transportation Systems Conference, pp: 483–488.

Dowson, D. (1979). *History of Tribology*. London: Longman.

Erjavec, J. (2003). TechOne automotive brakes. CengageBrain, Ch. 39, p. 359.

Glaeser, W. (2012). *Characterization of tribological materials*. New York: Momentum Press.

Gunaratne, M., Bandara, N., Medzorian, J., Chawla, M., & Ulrich, P. (2000). Correlation of tire wear and friction to texture of concrete pavements. *Journal of Materials in Civil Engineering, 12*, 46–54.

Grosch, K. A. (1963). The relation between the friction and visco-elastic properties of rubber. *Proc. R. Soc. Lond. A, 274*, 21–39. https://doi.org/10.1098/rspa.1963.0112.

Heinrichs, B. E., Allin, B., Bowler, J., & Siegmund, G. (2003). Vehicle speed affects both pre-skid braking kinematics and average tire/roadway friction. *Accident Analysis and Prevention, 36*, 829–840.

Heinrichs, B. E., Allin, B. D., Bowler, J. J., & Siegmund, G. P. (2004a). Vehicle velocity affects both pre-skid braking kinematics and average tire/roadway friction. *Accident Analysis and Prevention, 36*, 829–840.

Heinrichs, B. E., Boyd, D., & Allin, J. J. (2004b). Vehicle speed affects both pre-skid braking kinematics and average tire/roadway friction. *Accident Analysis and Prevention, 36*, 829–840.

Jazar, R. N. (2011). *Advanced dynamics: Rigid body, multibody, and aerospace applications*. New York: Wiley.

Jazar, R. N. (2013). *Advanced vibrations: A modern approach*. New York: Springer.

Jazar, R. N. (2017). *Vehicle dynamics: Theory and application* (3rd ed.). New York: Springer.

Leu, M. C., & Henry, J. J. (1978). Prediction of skid resistances as a function of velocity from pavement texture measurements. *Transportation Research Record, 666*, 7–13.

Moore, D. (1967). *The friction of pneumatic tires*. New York: Elsevier Scientific Pub.

Persson, B. (1998). On the theory of rubber friction. *Surface Science, 401*(3), 445–454.

Persson, B. (2001). Theory of Rubber Friction and Contact Mechanics. *The Journal of Chemical Physics, 115*, 3840.

Persson, B., Tartaglino, U., & Albohr, O. (2004). Rubber friction on wet and dry road surfaces: The sealing effect. *Physical Review B, 71*(3), 03542.

Perrson, B. (2006). Rubber friction: role of flash temperature. *J. Phys: Condens. Matter., 18*, 7789–7823.

Quinn, T. F. J. (1983). *Physical Analysis for Tribology*. Cambridge: Cambridge University Press.

Rand, C., & Crosby, A. (2006). Insight into the periodicity of Schallamach waves in soft material friction. *Applied Physics Letters, 89*, 261907.

Schallamach, A. (1952). The load dependence of rubber friction. *Proceedings of the Physical Society, 65*(9), 393.

Shah, V. R., & Henry, J. J. (1978). Determination of skid resistance-speed behaviour and side force coefficients of pavements. *Transportation Research, 666*, 13–18.

Takadoum, J. (2007). *Materials and surface engineering in tribology*. London: ISTE.

Takadoum, J. (2010). Tribology. In *Materials and surface engineering in tribology* (pp. 49–108). Wiley-ISTE.

Wada, N., & Uchiyama, Y. (1993). Friction and wear of short fibre reinforced rubber composites under various sliding speeds and loads. *Wear, 162–164*, 930–938.

Warner, C., Smith, G., James, M., & Germane, G. (1983). Friction Applications in Accident Reconstruction. SAE 830612.

Wrobel, G., & Szymiczek, M. (2008). Influence of temperature on friction coefficient of low density polyethylene. *JAMME, 28*(1), 31–34.

Wu, F., Li, J., Shu, X., Zha, X., & Xu, B. (2010). Test analysis and theoretical calculation on braking distance of automobile with ABS. *IFIP, 347*, 521–527.

Chapter 9
Solutions for Path Planning Using Spline Parameterization

M. Elbanhawi, M. Simic, and Reza N. Jazar

9.1 Introduction

Human drivers display remarkable abilities when controlling vehicles in a highly reactive manner and with impeccable precision. Even more impressive is the implicit consideration of the vehicle and road parameters. Researchers have shown that humans use specific visual cues to identify road curvature and endeavor to match it. Analysis that drew inspiration from the steering commands, used by operators of varying driving experience, is attempted to generate likewise natural paths. This approach can be combined with a path planning algorithm to generate paths with natural smooth trajectories for autonomous vehicles. This will circumvent the need to rely on computationally intensive planning algorithms that are based on forward model integration. Humans have been controlling the steering wheel for the past century. Currently self-driving is emerging as technology that promises to improve our lives greatly. Cars are underactuated systems designed to facilitate their control for operators. This simplification of actuation has adverse effects when attempting to automate such systems, leading to the appearance of nonholonomic constraints (Jazar 2008). Researchers have shown that drivers rely on certain visual landmarks to assess the path curvature prior to attempting to steer toward it (Land and Lee 1994; Land and Horwood 1995). The majority of studies, conducted on human steering, focus on modeling and predicating it, using control system theories (Donges 1978; MacAdam 1981; Prokop 2001). The aim of this chapter is to employ an efficient spline parameterization method to synthesize paths

M. Elbanhawi • M. Simic
School of Engineering, RMIT University, Melbourne, Australia

R.N. Jazar (✉)
School of Engineering, RMIT University, Melbourne, Australia

Xiamen University of Technology, Xiamen, China
e-mail: reza.jazar@rmit.edu.au

L. Dai, R.N. Jazar (eds.), *Nonlinear Approaches in Engineering Applications*,
https://doi.org/10.1007/978-3-319-69480-1_9

that mimic human steering controls, in order to generate motions that feel natural and familiar to human passengers. It is not uncommon for robotics researchers to draw inspiration by observing natural behavior (Donghyun et al. 2014; Lentink 2014). We hope that the results, presented in this chapter, can be employed in robotics to efficiently plan spline-based paths, similar to Yang et al. (2014), in addition to mimicking human steering, improving passenger comfort, and explicitly considering the limitations of the car.

Advances in sensing technology, computer vision, communications, and computational power have contributed toward the development of autonomous agents in a wide range of fields. Self-driving ground vehicles are used in military, urban transportation, and industrial and agricultural applications. Unmanned aerial vehicles (UAVs) and micro aerial vehicles (MAVs) are considered as a cost-effective, safe, and efficient choice for several military and civil applications. Robotic platforms are currently equipped with multiple sensors, which enable them to sense their surroundings and localize themselves in reference to their environment, goals, and obstacles. Path planning is a widely studied, fundamental task for mobile robots. Robot navigation mandates a strategy that steers it from its current location, through the environment while avoiding obstacles toward its goal.

Classical planning algorithms, such as A* algorithm (Hart et al. 1968), Voronoi diagrams (Canny 1985), visibility graphs (Asano et al. 1985), and cell decompositions (Brooks and Lozano-Perez 1985) produce piecewise linear paths. These paths consist of subsequent waypoints joined by straight lines. Potential field methods guide the robot toward its goal by applying attractive forces, toward the goal, and repulsive, away from obstacles (Khatib 1986). Potential field methods tend to produce oscillating paths in narrow passages (Koren and Borenstein 1991). Sampling-based motion planning algorithms, such as rapidly exploring random trees (RRT) (LaValle 2000) and probabilistic roadmap method (PRM) (Kavraki et al. 1996), rely on stochastic sampling to efficiently explore the search space. Resulting paths from randomization are suboptimal and require post-processing to improve their quality (Elbanhawi and Simic 2014c). Motion planning using state lattices is disadvantaged by discretization (Pivtoraiko et al. 2009; Pivtoraiko and Kelly 2011). Coarse discretization leads to loss of completeness, while high-fidelity subdivision increases the computational time of the planner, especially in highly dimensional scenarios. Homotopy class optimization of trajectories is proposed (Zucker et al. 2013). These methods do not discuss curvature continuity, and the performance is dependent on the optimization algorithm. Optimization methods are not immune from local minima and are not guaranteed to converge.

Agile robots, such as omnidirectional, differential-drive robots and quadrotors, are capable of traversing piecewise linear paths. Such paths require stationary turns, at every waypoint, to change heading toward the subsequent waypoint. This approach is inefficient with regard to time, energy, and jerk considerations. The motion of some robots, such as car-like vehicles and fixed-wing UAVs, is highly constrained. Nonholonomic robots must be considered in the planning procedure, as they cannot follow piecewise linear paths. Minimum turning radius constraints

impose further limitations on the path, which is often represented by maximum curvature restrictions.

Traditionally, Dubins paths or Reed's and Shepp's (Xuan-Nam et al. 1994; Reeds and Shepp 1990) are used in path smoothing for vehicles with minimum turning radius constraint in a two-dimensional space. Configurations are joined by sets of primitives consisting of circular arcs and straight lines. The amalgamation of circular arcs and lines results in discontinuities in curvature. Clothoids may appear to be suitable for path smoothing, as they are characterized by continuous curvature (Fraichard and Scheuer 2004). However, clothoid generation is challenging, as they have no closed-form expression. High-order splines (11th order) and polynomials (26th order) have been proposed for clothoid approximation (Wang et al. 2001; Meek and Walton 2004; Walton and Meek 2005; McCrae and Singh 2009; Montes et al. 2008). Recent work has enabled the real-time approximation of clothoids under bounded length and orientation limitations (Brezak and Petrovic 2013). Consequently, they are still not suited for real-time replanning and highly dimensional scenarios.

Curvature discontinuities result in overactuation, slipping, localization errors (Magid et al. 2006), passenger discomfort (Gulati and Kuipers 2008), mechanical wear and failure (Berglund et al. 2010; Maekawa et al. 2010), and control instability (Lau et al. 2009; Roth and Batavia 2002). Subsequently, achieving continuous curvature is advantageous in applications that involve carrying sensitive cargos such as human passengers (Gulati and Kuipers 2008) or heavy loads in mining applications (Berglund et al. 2010; Maekawa et al. 2010) and those which require precise localization such as agricultural applications to minimize the impact of the vehicle on crops (McPhee and Aird 2013; Sabelhaus et al. 2013; Alshaer et al. 2013) or energy loss minimization for MAVs with battery-size restrictions (Myung et al. 2007).

In our earlier work, we proposed an evaluating and bounding B-spline paths approximate solution. We show that humans control vehicles with continuous commands and generate paths that obey the vehicles kinematic constraints. We propose the premise of using a single B-spline curve to generate paths that resemble human driving and obey the vehicle's constraints. This is achieved by defining the curvature of a B-spline segment in terms of the parameters of its corresponding control polygon, which in this case is assumed to be a linear path generated by a path planning algorithm.

In this work we improve B-spline-based motion planning by proposing efficient methods for segment curvature evaluation and analytical bounding. The characteristics of B-splines are exploited to present two solutions for continuous curvature bounding, which can be combined together or used separately. The novelty of our proposal is that it is not limited to a plane or a dimension; it is not subject to orientation, length, or control polygon restrictions. It guarantees continuity throughout the path while preserving real-time performance. We also show that it is possible to plan the trajectory of a robot with nonholonomic constraints and maintain parametric continuity.

This chapter is organized as follows: Sect. 9.2 lists the current related research in path smoothing. The problem is formally described in Sect. 9.3. B-spline curve synthesis is introduced in Sect. 9.4. We address curvature continuity, segment curvature formulation, and curvature bounding in 2D in Sect. 9.5. Our findings are validated and compared with previous work using simulation experiments, as given in Sect. 9.6. The chapter is concluded in Sect. 9.7.

9.2 Related Work

There are two separate problems addressed in this chapter: firstly, planning a geometric curve with curvature bounds given in Sect. 9.4 and, secondly, maintaining parametric continuity of the generated trajectory. The authors could not ascertain any literature that combined these two problems. There are only approaches that address each issue separately. The benefits of synthesizing kinodynamically feasible and continuous paths are well studied in robotics (McPhee and Aird 2013; Magid et al. 2006; Gulati et al. 2009; Gulati and Kuipers 2008; Maekawa et al. 2010; Lau et al. 2009; Myung et al. 2007; Sabelhaus et al. 2013; Alshaer et al. 2013). However, current solutions given in the literature fail to guarantee C^2 continuity with curvature bounds for nonholonomic mobile robots.

Similarly, in trajectory generation literature, there are multiple solutions to optimally generate bounded trajectories for given geometric curves with regard to time (Balkcom and Mason 2002; Wu et al. 2000) and jerk considerations (Guarino Lo Bianco 2013). Other approaches considered curvature and acceleration bounds as parameters in optimization problems (Johnson and Hauser 2012; Kunz and Stilman 2013; Sachin et al. 2014). However these methods, adversely, provided no discussion on the parametric continuity problem and often led to C^1 continuity only. The approach developed by Velenis and Tsiotras (2008) for vehicles is limited to velocity continuity and acceleration bounds and ignored acceleration continuity which will undoubtedly lead to a jerky and uncomfortable ride (Gulati and Kuipers 2008; Guarino Lo Bianco 2013). Control laws proposed for unicycle robots ignored acceleration and curvature bounds (Lapierre et al. 2007; Sgorbissa and Zaccaria 2010; Morro et al. 2011).

Dubins paths and circular arcs were commonly used for robot planning despite their curvature discontinuity. Dubins paths were generated under the assumption that the vehicle maintains constant linear velocity. Multiple circular segments have been proposed for UAV path smoothing (Anderson et al. 2005). This approach was limited to planar scenarios and produces discontinuous paths. Bézier curves were commonly used for path smoothing. The order of Bézier is dependent on the number of control points, which resulted in limiting them to maintain a low-order curve (Jolly et al. 2009; Lau et al. 2009; Kwangjin and Sukkarieh 2010). A comparative navigational-based analysis showed that Bézier curves poorly interpolate a linear path as opposed to B-splines, (Elbanhawi et al. 2014). Limiting the

number of control points of Bézier curves results in the need to join multiple curve segments. Discontinuities arise at the joint of two Bézier segments.

A condition for Bézier curve geometric, G^2, continuity was presented in (Walton et al. 2003). However, this condition had no closed-form solution. Kwangjin et al. (Kwangjin and Sukkarieh 2010; Kwangjin et al. 2013) provided a solution for a particular case of the G^2 planar condition. This approach was used for upper-bounded curvature smoothing algorithms. It is still limited to a plane and, in fact, incapable of considering different curvature bounds in horizontal and vertical planes. Fixed-wing UAVs have different turning angle (horizontal plane) and climbing angle (vertical plane) limitations. Barsky and Derose (1990) proposed geometric continuity, G^k, as condition for ensuring that curve endpoints had the same directions, not the values. The work in (Kwangjin and Sukkarieh 2010; Kwangjin et al. 2013) fails to guarantee velocity and acceleration continuity, which are more realistic for robotics than geometric continuity. Pan et al. (2012) have shown that only C^2 parametric continuities of acceleration and velocity are suitable for real robots and provided a shortcutting algorithm that guarantees continuity in most scenarios but fails to address the maximum curvature constraint. Recent studies investigated trajectory planning for trailer cars with continuous velocities (Ghilardelli et al. 2014).

The advantages of B-splines for real-time planning have been shown (Dyllong and Visioli 2003; Elbanhawi and Simic 2012). A genetic algorithm was employed to select the location of a fixed number of control points, for a single B-spline curve (Nikolos et al. 2003). This guaranteed the continuity of the curve. However, having a constant number of control points reduced the robustness of the generated path. B-splines were used for generating smooth paths for passenger transporting robots (Gulati and Kuipers 2008). That approach is limited to a 2D setting and robots with no curvature bounds. Similarly, a 3D B-spline smoothing algorithm was presented that did not consider curvature continuity or upper bounds (Koyuncu and Inalhan 2008). Several optimization algorithms are limited to 2D offline B-spline smoothing and curvature bounding (Berglund et al. 2010; Maekawa et al. 2010). A B-spline shortcutting algorithm was proposed, which used multiple segments; however, it did not guarantee continuity in all segments and did not consider the maximum curvature (Pan et al. 2012). In our earlier work, we provided an approximate B-spline-based approach to the presented problem and did not consider acceleration and velocity bounds (Elbanhawi et al. 2014). Research findings were implemented, in real time, on experimental vehicle (Elbanhawi and Simic 2014b). On the other hand, in here we present solution of the problem analytically and consider kinodynamic constraints.

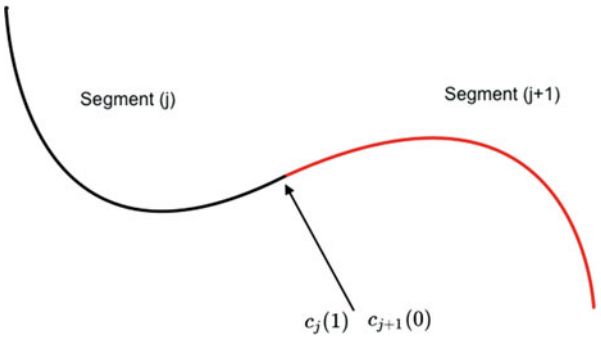

Fig. 9.1 Joining two path segments

9.3 Problem Statement

We consider front wheel-steered vehicles, referred to as car-like robots. It is common to model the vehicle using the bicycle model, which assumes identical steering angles on both sides (Jazar 2008), as shown in Fig. 9.1. This model has been shown to be adequate for modeling the global kinematic motion of front wheel-steered vehicles (Campion et al. 1996). The advantage of our approach is in solving two closely related problems simultaneously, which are generally decoupled in robotic literature. We aim to synthesize a curve that satisfies conditions given by Eqs. (9.1, 9.2, 9.3, and 9.4) and maintain parametric continuity. The vehicle's Cartesian coordinates (x, y) and heading angle θ are measured from the center of the rear axle relative to a global frame. The length between the front and back wheel is referred to as wheel base, W. The two actuation commands are linear velocity, v, and steering angle Φ. It is clear that the vehicle is underactuated as it has two controls and three degrees of freedom, i.e., it is not fully controllable (Ogata 2010). The velocity components in the x and y directions, v_x and v_y, are constrained as given in Eq. 9.1. This nonholonomic condition is often referred to as the rolling without slipping constraint.

$$v_x \sin(\theta) - v_y \cos(\theta) = 0 \tag{9.1}$$

Consider a planning algorithm that produces a path consisting of, $n-1$, straight lines joining successive, n, waypoints, $P = [P_1, \ P_2 . . . P_n]$, where $P_i = (P_{xi}, P_{yi}, P_{zi})$ for $i = [1, 2, .., n-1, n]$. It is required to generate a curve, $c(u)$, which closely follows straight-line path, where u is the normalized path length parameter. It is an independent variable in the range of [0,1] for any curve, $c(u)$. Parameter u takes the value $u = 0$ at the beginning of the segment and reached the value $u = 1$ at the end. The generated curve must satisfy the following imposed constraints.

Path continuity at the endpoints of two curve segments must be addressed; such a situation is illustrated in Fig. 9.1. For two consecutive curve segments $c_j(u)$ and $c_{j+1}(u)$, C^k parametric continuity could be then defined as shown in Eq. 9.2, according to Farin (2002), where k is a positive integer denoting the order of the parametric continuity.

$$\frac{\partial^i c_{j+1}(0)}{\partial u^i} = \frac{\partial^i c_j(1)}{\partial u^i}, \forall i = 1, 2, 3..k \tag{9.2}$$

The curvature of the path must not exceed the maximum curvature, K_{max}, at any point. The curvature, $k(u)$, along a path is defined as Eq. 9.3, where $c(u) = [x(u), y(u)]$ and the first- and second-order derivatives with respect to u are $c'(u) = [x'(u), y'(u)]$ and $c''(u) = [x''(u), y''(u)]$.

$$k(u) = \frac{x'(u)y''(u) - x''(u)y'(u)}{\left(x'(u)^2 + y'(u)^2\right)^{3/2}} \tag{9.3}$$

The minimum radius of curvature, r_{min}, in a plane restricts the curvature of the path to K_{max} in that plane. For car-like robots, the curvature constraint is a result of the maximum steering Φ_{max} angle due to the mechanical construction of the vehicle, as shown in Eq. 9.4. In three-dimensional scenarios for aerial vehicles, the maximum yaw and pitch angles in the horizontal and vertical planes must be considered separately (Fig. 9.2).

$$k_{\max} = \frac{1}{r_{\min}} = \frac{\tan(\phi_{\max})}{W} \tag{9.4}$$

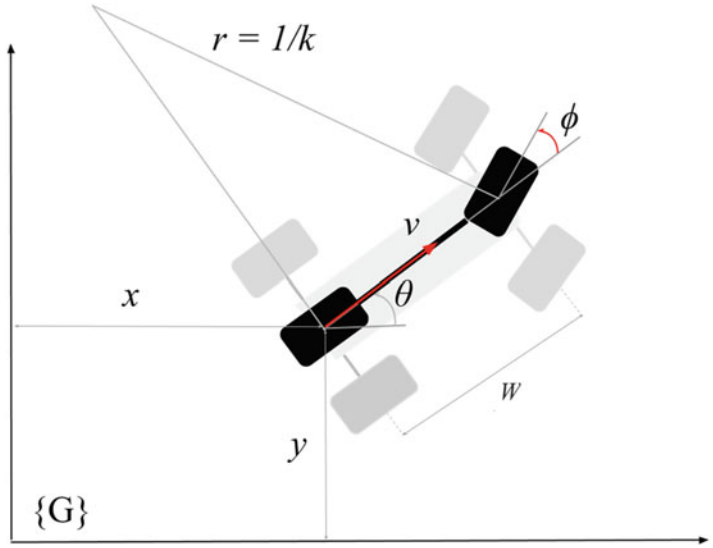

Fig. 9.2 Bicycle model for front wheel-steered vehicles

9.4 Spline Primitives

B-splines are vector-valued parametric curves, initially proposed by Schoenberg (1946). B-splines and nonuniform rational B-splines (NURBs) are commonly used for computer-aided design (CAD) applications as a result of their efficient synthesis and robustness (Farin 1992). In addition to CAD, they have been utilized in reverse engineering (Ma and Kruth 1998; Piegl and Tiller 2001), finite element analysis (Hughes et al. 2008), machining (Cheng et al. 2002; Sungchul and Taehoon 2003), medical imaging (Zhang et al. 2007), computer vision (Biswas and Lovell 2008), bio-inspired data fitting (Jones and Adamatzky 2014), and signal processing (Unser et al. 1993). As discussed in earlier sections, their use in robotics is fairly recent.

A p-th degree B-spline curve, $c(u)$, is defined by n control points and a knot vector $\hat{u}$, evaluated by Eq. 9.5. The length of the one-dimensional knot vector, m, is equal to $n + p + 1$. Normalized path length parameter, u, is simply referred to as the path parameter (Farin 2002).

$$c(u) = \sum_{i=0}^{n} N_{i,p}(u) P_i \tag{9.5}$$

P_i is the $i\text{-}th$ control point, which is in turn influenced by a corresponding basis functions. The number of basis functions therefore mirrors the number of control points, n. $N_{n,i}(u)$ is the $i\text{-}th$ B-spline basis function, which is defined using the Cox-de Boor recursive algorithm (De Boor 1972). First-order basis functions are evaluated using Eq. 9.6 based on the predefined knot vector. Higher-order functions are computed by the recursive substitution in Eq. 9.7.

$$N_{i,0}(u) = \begin{cases} 1 & u \in \left[\hat{u}_i, \hat{u}_{i+1}\right) \\ 0 & \text{else} \end{cases} \tag{9.6}$$

$$N_{i,p}(u) = \frac{u - \hat{u}_i}{\hat{u}_{i+p} - \hat{u}_i} N_{i,p-1}(u) + \frac{\hat{u}_{i+p+1} - u}{\hat{u}_{i+p+1} - \hat{u}_{i+1}} N_{i+1,p-1}(u) \tag{9.7}$$

We have previously shown B-spline properties that render them as superior to other parametric curves, for the task of robot navigation (Elbanhawi et al. 2014). The curve's degree, p, is independent of the number of control points, n. This allows the possibility of using a single curve for the entire path smoothing without imposing limitations on the number of control points. It is in contrast to Bézier curve methods (Jolly et al. 2009; Kwangjin and Sukkarieh 2010; Lau et al. 2009; Kwangjin et al. 2013) where the number of control points is predefined. Modification of control points affects the curve shape locally and does not change the rest of the path. This enables the local control of the path for smoothing or obstacle avoidance purposes. A clamped B-spline curve follows its control polygon more closely in comparison to a Bézier curve of the same order. Clamping is achieved by having $(p + 1)$ multiplicity of the initial and final knots, $\hat{u}$ (Farin 2002). Knot multiplicity ensures that the curve passes through the initial and final control points.

Despite the beneficial properties that characterize B-splines, maintaining path continuity and controlling its curvature are nontrivial issues. They continue to challenge the use of B-splines in robotic path planning applications (Lau et al. 2009; Elbanhawi and Simic 2014a; Pan et al. 2012). It must be noted that both Beziers and B-spline are essentially combinations of polynomials. In principal, there should exist control laws, or conditions, that are capable of generating parametrically continuous trajectories using Bezier curves as well. The authors could not identify such methods in literature. Consequently, we have utilized the existing benefits of B-splines for motion planning.

9.5 Curvature Bounding

9.5.1 Parametric Continuity

The challenge of path continuity stemmed from the linking of two separate path segments. Primitives such as circular arcs, polynomials, and clothoids were not flexible enough to represent a path using a single segment. The number of control points, which were usually predefined prior to smoothing, governs the order of a Bézier curve. Consequently, multiple Bézier curves must be linked for smoothing a single piecewise linear path.

The order of a B-spline curve is independent of the number of control points in the path, as already mentioned. In theory, it is possible to smooth a path using a single curve of a predefined order. The single B-spline curve approach was adopted for UAV planning; however, the number of control points was fixed (Nikolos et al. 2003). The region in which planning is conducted and path shape robustness are significantly limited by fixing the number of control points. The work by Jolly et al. (2009) is based on rapid replanning with a short planning horizon and relies on four control points. We did not pose any restrictions on the number of control points, apart from that the number of control points must exceed the degree of the curve, p. The local control property of B-spline enables the modification of a curve segment without changing the entire path. The necessity for rerouting commonly results from obstacle detection or smoothing purposes.

Despite the superiority of B-splines over a Bézier curve of the same order, in closely following the shape of a path, they still deviate from the original path (control polygon). Ideally, the curve would follow the original linear path and smoothly cut corners when turning is needed. It is desired to maintain proximity to the originally planned straight-line path as it is more likely to be collision-free. This was achieved by forcing the tangency of the curve to the sides of the control polygon. B-spline tangency to collinear control points is leveraged to ensure the close following of the original path. Systematic midpoint insertion, between every two successive points, effectively transformed control polygon edges into lines connecting three control points, thus forcing the curve's tangency to the edges. The effect of midpoint insertion is illustrated in Fig. 9.3. It is worth highlighting that in

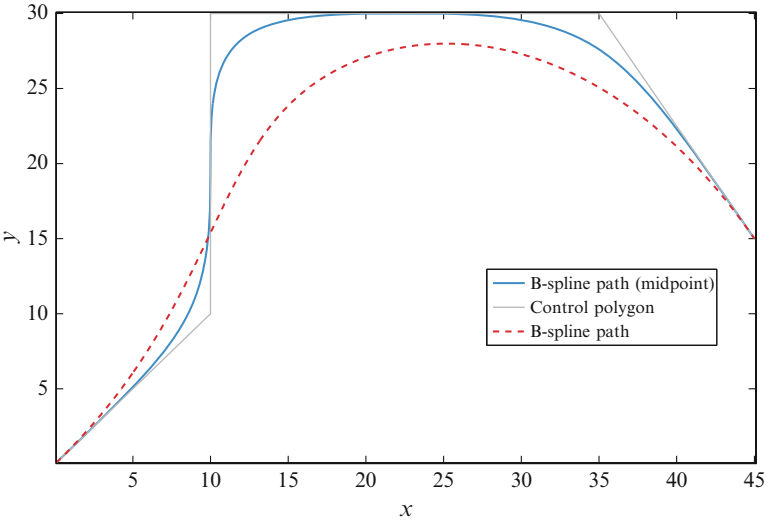

Fig. 9.3 Midpoint insertion improves the path proximity of B-splines without compromising parametric continuity. It forces the curve (*blue*) tangency to the edge of the control polygon (*black*) unlike the unmodified B-spline curve (*red*)

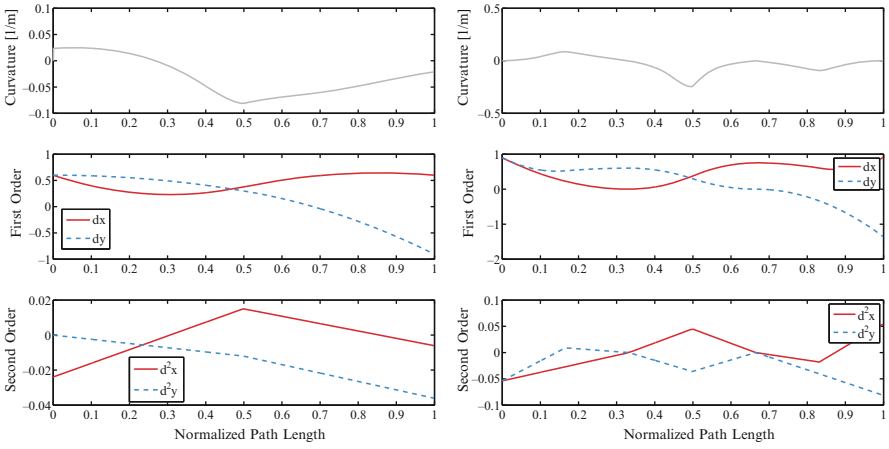

Fig. 9.4 Parametric continuity was maintained before (*left*) and after (*right*) midpoint insertion as a result of using a single B-spline segment

both cases, a single curve segment was used for smoothing. That guarantees continuity along the path. This avoids the need to address parametric continuity at union points, as illustrated in Fig. 9.1. The curvature and higher-order derivatives do not exhibit any abrupt changes after adding midpoints. This can be validated by comparing the resulting trajectories given in Fig. 9.4.

9.5.2 Curvature Evaluation

9.5.2.1 Path Segmentation

Our aim was to control the curvature, k, of a B-spline curve. Specifically, it was required to maintain the curvature below the maximum curvature bound, $K_{\max}$. Systematic midpoint insertion allowed for the definition of a repeated segment throughout the path (see for Fig. 9.5(a) illustration). The segment consists of two intersecting control edges and a total of five control points (including two midpoints). It was required to define B-spline paths curvature in terms of their corresponding segment parameters. This enabled the isolation of each segment and local modifications of its parameters by leveraging the local support property of B-splines. Smoothing modifications will be proposed to ensure maximum curvature bounds are obeyed.

The parameters of the reoccurring control segment are the side length, L, the angle between segment sides, α, and the length ratio of both sides, r, as illustrated in Fig. 9.5(b). In our earlier work (Elbanhawi et al. 2014), segments of equal sides were assumed, $r = 1$, which overestimated the curvature of the path and resulted in attaining approximate solutions. The use of the length ratio parameter, r, is presented to enable a more precise evaluation of the curvature. Position vectors describing the five control points of the segment can be defined with respect to the parameters of the same segment and are given in Eq. 9.8.

$$P\begin{pmatrix} P_x \\ P_y \end{pmatrix} = \begin{pmatrix} L, \frac{L}{2}, 0, r\frac{L}{2}\cos(\alpha), rL\cos(\alpha) \\ 0,\ 0,\ 0, r\frac{L}{2}\sin(\alpha), rL\sin(\alpha) \end{pmatrix} \tag{9.8}$$

The cubic B-spline curve, $p = 3$, has five control points, $n = 5$, and, $m = 9$, knots with four initial and final multiplicity for clamping, $\hat{u} = [0,0,0,0,0.5,1,1,1,1]$. Initial order basis functions were evaluated using Eq. 9.6. Following that, basis functions, $N(u)$, were computed, using the Cox-de Boor algorithm by recursive evaluation of

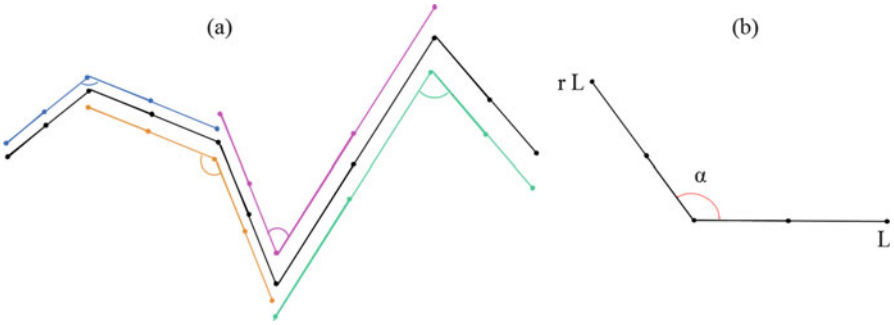

Fig. 9.5 (**a**) The notion of a reoccurring control segment through the path. A segment consists of two intersecting straight lines and five control points. (**b**) The parameters of a single segment

Eq. 9.7. The following third-order basis functions can be defined as given in the set of Eq. 9.9.

$$N_{0,3} = \frac{(1-2u)^3}{2} \tag{9.9a}$$
$$N_{1,3} = 6u^3 - 6u^2 + 1 \tag{9.9b}$$
$$N_{2,3} = -6u^2 + 6u - 1 \tag{9.9c}$$
$$N_{3,3} = -6u^3 + 12u^2 - 6u + 1 \tag{9.9d}$$
$$N_{4,3} = \frac{(2u-1)^3}{2} \tag{9.9e}$$

In order to define the curvature of a segment in terms of its parameters, $k = f(r, L, \alpha)$, the position vectors of the segment, Eq. 9.8, and basis functions, Eq. 9.9, were substituted in the curve Eq. 9.5. The curve was defined as a function of its corresponding segment parameters, $c(u) = \begin{bmatrix} x(u) \\ y(u) \end{bmatrix} = \begin{bmatrix} x(r, L, \propto) \\ y(r, L, \propto) \end{bmatrix}$; $x(u)$ and $y(u)$ are given in Eq. 9.10.

$$\begin{aligned} x(u) = {} & \tfrac{(1-2u)^3}{2} * L + (6u^3 - 6u^2 + 1) * \frac{L}{2} \\ & + (-6u^3 + 12u^2 - 6u + 1) * \frac{rL\cos(\alpha)}{2} \frac{(2u-1)^3}{2} * rL\cos(\alpha) \end{aligned} \tag{9.10a}$$

$$y(u) = \left(-6u^3 + 12u^2 - 6u + 1\right) * \frac{rL\sin(\alpha)}{2} + \frac{(2u-1)^3}{2} * rL\sin(\alpha) \tag{9.10b}$$

For a given segment, its parameters, r, L, and α, are constant and known prior to a curvature query. The first- and second-order derivatives with respect to the path parameter, u, are derived below from equations set (Eq. 9.11).

$$x'(u) = 3L\left(u^2(r\cos(\alpha) - 1) + 2u + 1\right) \tag{9.11a}$$
$$x''(u) = 6L(u(r\cos(\alpha) - 1) + 1) \tag{9.11b}$$
$$y'(u) = 3Lr\sin(\alpha)u^2 \tag{9.11c}$$
$$y''(u) = 6Lr\sin(\alpha)u \tag{9.11d}$$

The curvature expression, $k = f(r, L, \alpha)$, in Eq. 9.12 was obtained by substituting the curve and its first- and second-order derivatives from Eq. 9.11 into Eq. 9.3. It can be noted that when substituting by $r = 1$, in Eq. 9.12 we get the same expression derived in Elbanhawi et al. (2014). Prior to introducing the parameter, r, curvature evaluations were approximate, and the accuracy of the maneuvers could not be ascertained.

$$k(u) = \frac{2ru(u-1)\sin(\alpha)}{3L(u^4(r^2 - 2r\cos(\alpha) + 1) + 4u^3(r\cos(\alpha) - 1) - 2u^2(r\cos(\alpha) - 3 - 4u + 1))^{3/2}} \tag{9.12}$$

9.5.2.2 Segment Curvature Evaluation

Midpoint insertion ensured the curve's tangency to the polygon edges, which resembled paths generated by human operators in the experiments conducted by Elbanhawi et al. (2014). Subsequently, the curvature of the path started at $u = 0$ and finished at $u = 1$, with $k = 0$. Curvature peaked to k_{peak} at some point, u_{peak}, in between, $u = [0,1]$. In order to limit path curvature to the maximum value of $K_{\max}$, the peak curvature, k_{peak}, of the segments must be evaluated first. The point, u_{peak}, along the parametric path length, u, where the curvature peaks, was found by solving Eq. 9.13. Then k_{peak} was computed by substituting u_{peak} in Eq. 9.12.

$$\frac{dk(u)}{du} = 0 \tag{9.13}$$

For every path segment, there exists a singular curvature peak, as shown in Fig. 9.6. The red profiles show the influence of changing the segment angle while maintaining fixed length and ratio. The location of the peak curvature was entirely dependent on the length and ratio. For a large angle (blue) and fixed length, the ratio changed both the position and value of the peak curvature. Similarly, for a much smaller segment angle (gray), the length ratio was still influential on both the peak value and position.

Solving Eq. 9.13 for u_{peak} can prove to be a computationally intensive task, particularly when k_{peak} had to be evaluated multiple times during each query of the path planning procedure. One useful observation is that the location of u_{peak} is dependent on the segment angle, α, and length ratio, r, as highlighted in Fig. 9.7. We note that, while u_{peak} is dependent on r and α only, the peak curvature value, k_{peak}, is still dependent on r, α, and L. It was possible to store u_{peak} values in a lookup table of equal intervals from $r = 1$ to 10 and $\alpha = 0$ to π. The required values

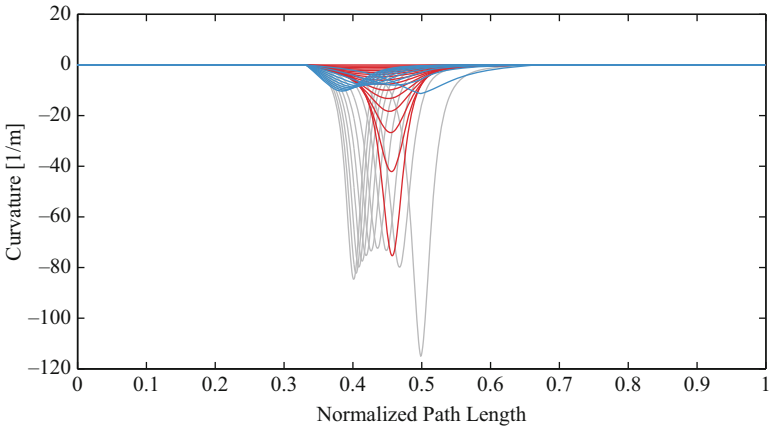

Fig. 9.6 Changing segment parameters shifts the position of the curvature peaks. In all cases, curvature profile is continuous with a singular peak

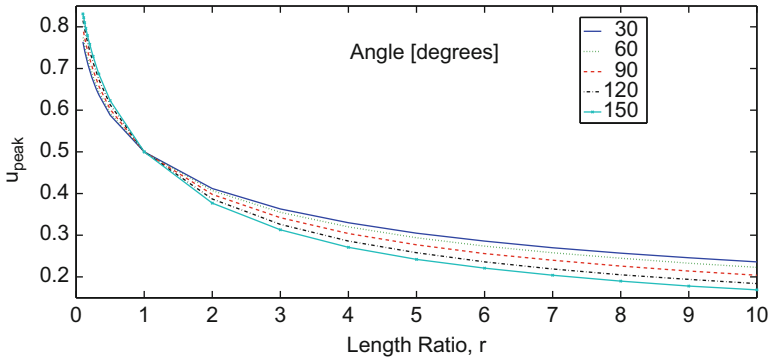

Fig. 9.7 Parametric length location, u_{peak}, of the peak curvature, k_{peak}, is dependent on the segment angle, α, and the length ratio, r. It can be noted that when length ratio is $0 < r < 1$, $u_{\text{peak}} > 0.5$ and when $r > 1$, $u_{\text{peak}} < 0.5$. This results from the observation that u_{peak} is shifted toward the shorter segment edge

can be interpolated. To maintain a sparse lookup table, we use the property in Eq. 9.14, which can be observed from Fig. 9.7. In our case, retaining a lookup table (*less than 10kB in size*) produced curvature values of 10^{-3} accuracy.

$$\text{If } 0 < r < 1, \text{then } u_{\text{peak}(r,\alpha)} = 1 - u_{\text{peak}(1/r,\alpha)} \tag{9.14}$$

9.5.3 Curvature Bounding

In this section, two analytical solutions for curvature bounding are presented. They ensured peak segment curvature does not exceed the maximum curvature, $k_{\text{peak}} \leq K_{\max}$. This confirms that the path is feasible, having shown in the previous section that each path segment has a single peak. The first solution was relaxed ensuring a smooth curvature. The second solution was strict to minimize deviation from the original control polygon. It was possible to combine both conditions in different segments, on account of B-spline local support property, with minimal effect on other segments. Both conditions were designed to make certain that the path was contained within the convex hull of the original control polygon to reduce the probability of the obstacle collision. Both solutions are essential homotopy class transformation to ensure feasibility. Nonetheless, the guarantee that the path is collision-free was not addressed in this work. We assume that this work will eventually be combined within a planning framework and will not be restricted to path smoothing.

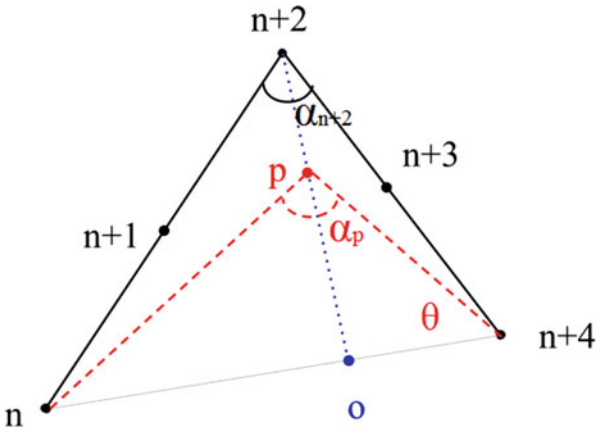

Fig. 9.8 First smoothing solution; it is required to find the point *(P)* along the line (dotted blue line), joining point *(n + 2)* and point *(o)*, that ensures the curvature, k_{peak}, does not exceed K_{max}

9.5.3.1 Single-Peak Solution

Consider the single control segment, shown in Fig. 9.8, whose corresponding B-spline curvature violates the maximum curvature condition. The segment consists of two lines $l_{n,n+2}$, joining point *(n)* and point *(n + 2)*, and $l_{n+2,\,n+4}$, joining point *(n + 2)* and point *(n + 4)*, shown as solid black lines. Point *(o)* is the intersection point between $l_{n,\,n+4}$ (thin gray line) and line $l_{o,n+2}$ (dotted blue line) which is passing through point *(n + 2)* and is orthogonal to $l_{n,\,n+4}$.

The current curvature, k_{n+2}, and segment angle, α_{n+2}, are known, and $k_{n+2} > K_{max}$. Assume that point *(n + 2)* is shifted toward point *(o)*, along the line, $l_{o,n+2}$, while points *(n)* and *(n + 4)* are unchanged and the midpoints *(n + 1)* and *(n + 3)* are recomputed accordingly. Finally at $\alpha_{n+2} = \pi$, $k_o = 0$. It is required to find the nearest point (p), at which $k_p = K_{max}$, as point *(n + 2)* is being shifted toward *(o)* along $l_{o,n+2}$. The minimum angle α_p lies between $\alpha_o = \pi$ and α_{n+2} as given by Eq. 9.15. We define $\overline{li,j}$ as the Euclidean distance between two points (i) and (j) whose Cartesian coordinates are known.

Assuming line $l_{o,n+2}$ is parameterized between P_{n+2} and P_o using $\hat{l} = [0,1]$, the value of $\hat{l}$ is required where the point (p) satisfies the curvature requirement. Firstly, P_p is given as follows:

$$P_p = P_{n+2}\left(1 - \hat{l}\right) + P_0\hat{l} \tag{9.15}$$

In every iteration, the curvature is evaluated until the $k_p = K_{max}$ condition is satisfied. To optimize the search, we can estimate the initial point where the curvature may be equal to K_{max}. This is achieved by knowing that, at $\hat{l} = 0$, $k = k_p$ and, at $\hat{l} = 1$, $k = 0$.

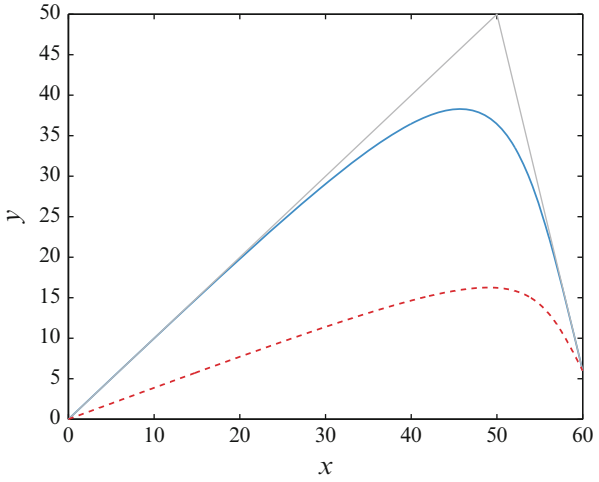

Fig. 9.9 Bounding using single-peak solution. The original path is *blue* and new path is *red*

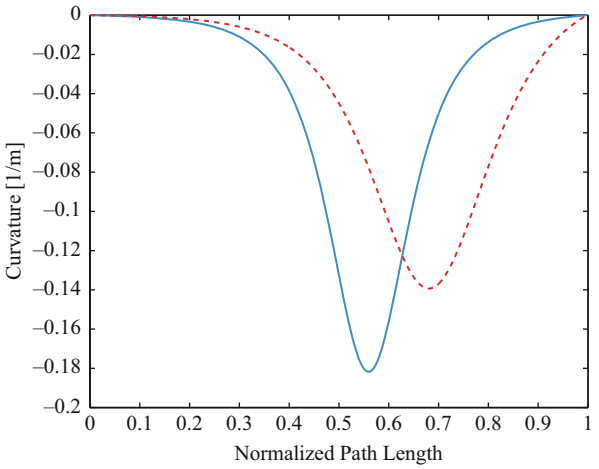

Fig. 9.10 Resulting curvature profiles before (*blue*) and after (*red*) bounding

$$\hat{l}_{\text{init}} = 1 - \left| \frac{K_{\max}}{K_p} \right| \tag{9.16}$$

An example of curvature bounding is shown in Fig. 9.9 using this solution. The resulting curvature has a single segment as shown in Fig. 9.10 and was bound to 0.14 m^{-1}. Curvature continuity was maintained in both cases.

9.5.3.2 Double-Peak Solution

In this section we proposed a different approach for the same problem considered in the previous section. The curvature of a control segment, P_1, P_0, P_5 and their

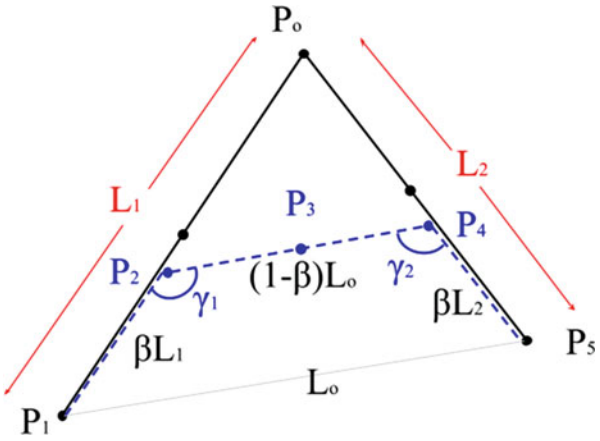

Fig. 9.11 Second smoothing solution; it is required to find the value of β that ensures curvature bounding in both segments and minimizes the total path length

Table 9.1 Comparing related methods

Method	Curvature bounds	Curve	Path	Continuity
Nikolos et al. (2003)	Yes	B-spline	3D	C^2
Anderson et al. (2005)	Yes	Arcs/line	2D	No
Gulati and Kuipers (2008)	No	B-spline	2D	No
Koyuncu and Inalhan (2008)	No	B-spline	3D	No
Jolly et al. (2009)	No	Bézier	2D	C^2
Lau et al. (2009)	No	Bézier	2D	No
Berglund et al. (2010)	Yes	B-spline	2D	No
Maekawa et al. (2010)	Yes	B-spline	2D	No
Pan et al. (2012)	No	B-spline	3D/2D	C^2/C^1
Kwangjin (2013)	Yes	Bézier	2D	G^2
Huh and Chang (2014)	No	Polynomial	2D	G^2
Proposed	Yes	B-spline	2D/3D	C^2

midpoints in Fig. 9.1 exceeds $K_{\max}$. Segment P_1, P_0, P_5 is decomposed into two segments, P_1, P_2, P_4 (segment 1) and P_2, P_4, P_5 (segment 2). Line segment $\overline{P_2P_4}$ is constructed to be parallel to edge $\overline{P_1P_5}$. As a result, triangles $\Delta P_1P_0P_5$ and $\Delta P_2P_0P_4$ are similar, and the ratio between their side lengths is $(1\text{-}\beta)$, where $0 < \beta < 1$ (Fig. 9.11). Segment 1 and 2 parameters can be described in terms of β, where segment angles are constant, as given in Table 9.1.

By substituting the segment parameters, given in Table 9.2, in Eq. 9.12, it is possible to find a range for β, subset of set [0,1), in which both segment curvatures are less than $K_{\max}$. Firstly, we compute a separate range for each segment 1 and 2 [βmin1, βmax1] and [βmin2, βmax2]. These computations are efficient by virtue of using the lookup table in the previous section. The allowable range for β is [max $(\beta_{\min 1}, \beta_{\min 2})$, min$(\beta_{\max 1}, \beta_{\max 2})$].

Table 9.2 Segment parameter

Parameter	Symbol	Segment 1	Segment 2
Length ratio	r	$\frac{(1-\beta)L_0}{\beta L_1}$	$\frac{(1-\beta)L_0}{\beta L_2}$
Edge length	L	βL_1	βL_2
Segment angle	α	γ_1	γ_2

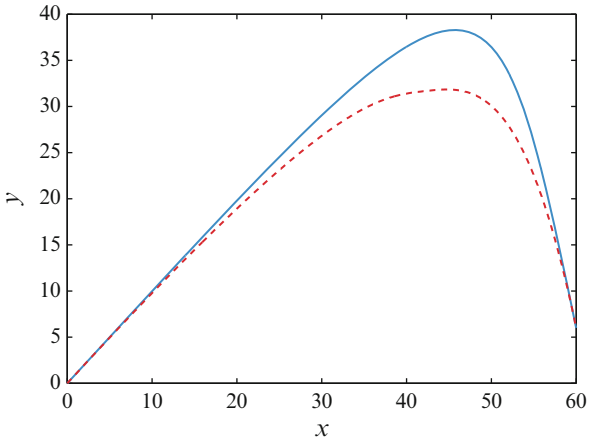

Fig. 9.12 Bounding using double-peak solution. The original path is *blue* and the feasible path is *red*

We nominate the β value that minimizes the total length. Now, new segment control points P_2, P_3, P_4 can be computed, where for any control point we have $P_i = (x_i, y_i)$.

$$\beta = \text{argmin}(\beta(L_1 + L_2 - L_0) + L_0), \beta \in [\beta_{\min}, \beta_{\max}] \tag{9.17}$$

$$P_2 = \beta P_1 + (1 - \beta)P_0 \tag{9.18}$$

$$P_4 = \beta P_5 + (1 - \beta)P_0 \tag{9.19}$$

A midpoint is inserted between the two added points based on the ratio between the lengths of both, such that if both lines are equal, $r = 1$; the midpoint is equidistant between them.

$$P_3 = \frac{r}{r+1}(P_4 - P_2) + P_2 \tag{9.20}$$

An example of curvature bounding is shown in Fig. 9.12 using this solution. The resulting curvature has two segments as shown in Fig. 9.13 and was bound to 0.14 m^{-1}. Curvature continuity was maintained in both cases.

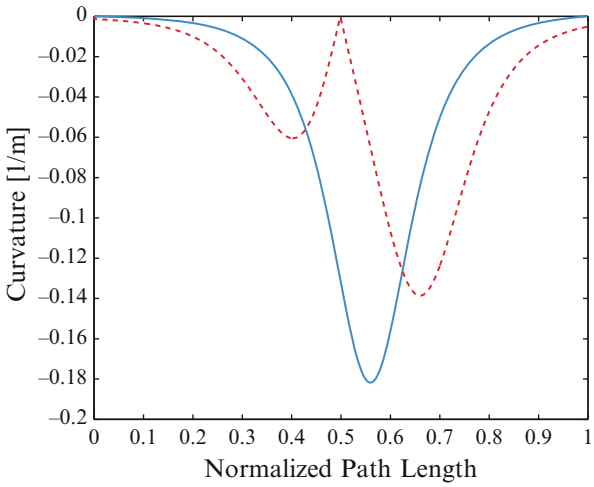

Fig. 9.13 Resulting curvature profiles before (*blue*) and after (*red*) bounding

Table 9.3 Curvature evaluation time performance for 1000 queries

Query time	Analytical solution	Lookup table
Mean (ms)	122.16	0.91
Standard deviation (ms)	6.95	0.34

9.6 Results

9.6.1 Curvature Evaluation

To efficiently evaluate a segment's curvature, we proposed storing the peak curvature position u_{peak} in a sparse lookup table and evaluating the curvature using the segment parameters. We conducted 1000 queries, for a range of segment parameters where r and $L = [1\text{ m}, 10\text{ m}]$ in steps of 1 m and α was $= [30°, 180°]$ in steps of 15°. The time performance of this evaluation method was compared with solving Eq. 9.13. From the results, given in Table 9.3, it is clear that this method is more efficient. Comparing with previously published research results Elbanhawi et al. (2014), which assumed equal segment length, we show that this approach has better accuracy. The results are illustrated in Fig. 9.14 and given in Table 9.4.

9.6.2 Curvature Bounding

In this section we compared the presented bounding solutions to our earlier work in Elbanhawi et al. (2014). Two different examples were used as shown in Figs. 9.15 and 9.18. The linear reference paths are assumed to result from a planning

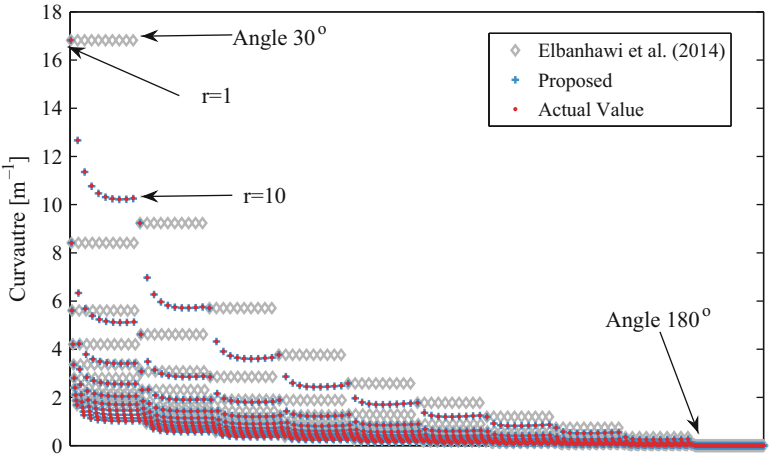

Fig. 9.14 Curvature evaluation errors of proposed lookup table compared to Elbanhawi et al. (2014)

Table 9.4 Curvature evaluation errors

Error [mm^{-1}]	Proposed	Elbanhawi et al. (2014)
Mean	0.87	384.25
Standard deviation	1.738	788.45
Maximum	19.34	6592.10

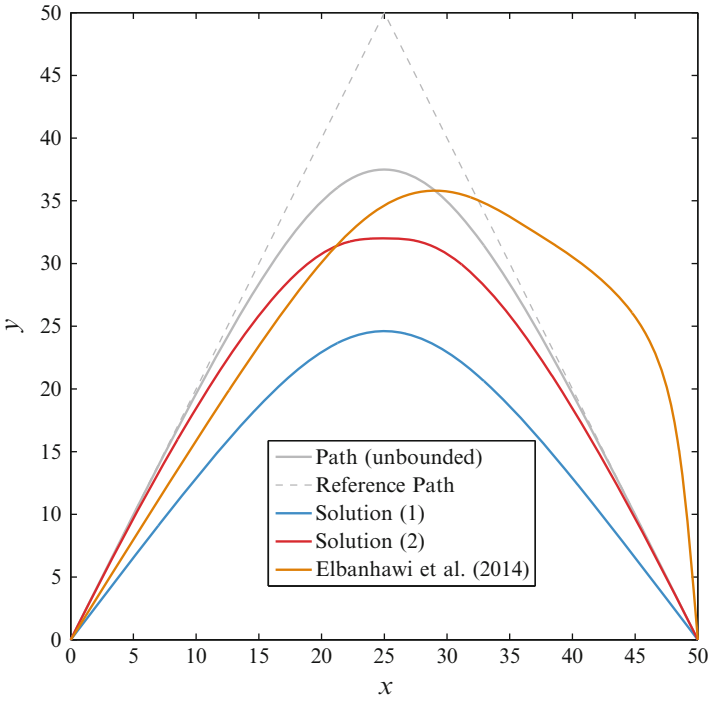

Fig. 9.15 Example 1: Bounding paths using different methods

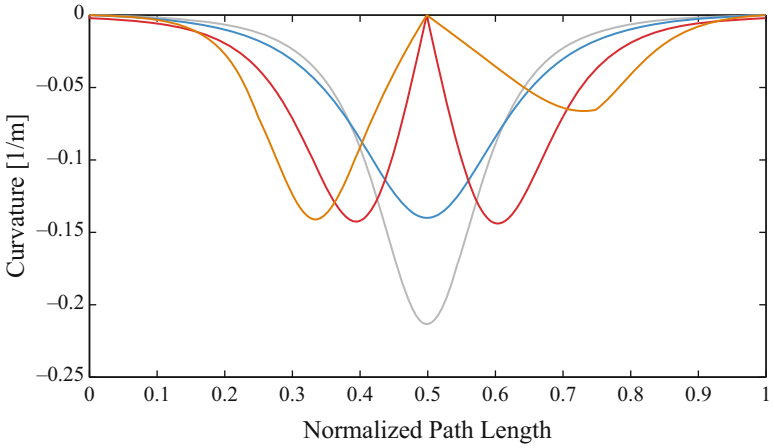

Fig. 9.16 Example 1: Resulting curvature profiles

algorithm. It can be noted that the proposed solutions maintain the curve within the convex hull of the original reference path. In both cases, the curvature is successfully bounded to 0.2 and 0.15 m^{-1} successively, and its continuity is maintained as shown in Figs. 9.16, 9.17, and 9.18. The proposed solutions reduce the deviation from the original path and the total path length, outperforming our earlier work as detailed in Tables 9.5 and 9.6. Solution (1) results in a low-frequency single-peak curvature profile as opposed to solution (2), which may have a better impact on passenger comfort in autonomous cars, as suggested in (Gulati and Kuipers 2008; Turner and Griffin 1999). On the other hand, solution (2) minimizes deviation from the reference paths and as a consequence minimizing the risk of collision.

Example (3) highlights the ability of the proposed method to generate a feasible path among obstacles. The benefit of maintaining the curve within the convex hull of the path is apparent in this example. The linear path was generated from a rapidly exploring random tree (RRT) algorithm (Elbanhawi and Simic 2014b). The resulting B-spline path among obstacles is illustrated in Fig. 9.19. Post-processing RRT algorithms have been shown to improve path quality and produce fairly consistent results. Nonetheless these methods do not guarantee that the path is collision-free. The resulting trajectory is given in Fig. 9.20. It is clear that the multi-segment path maintains curvature and parametric continuity.

9.7 Conclusion

An approach to continuous curvature robot path smoothing that satisfies the maximum curvature bounds and parametric continuity is presented here. B-spline curves have been proposed for this task. In this chapter we offer the following contributions:

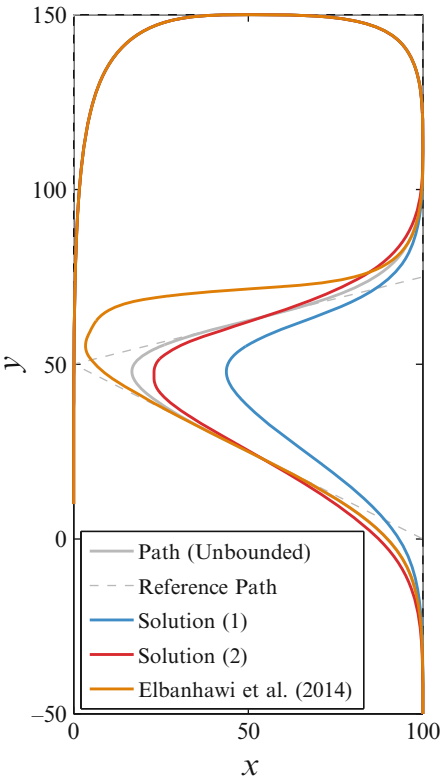

Fig. 9.17 Example 2: Bounding paths using different methods

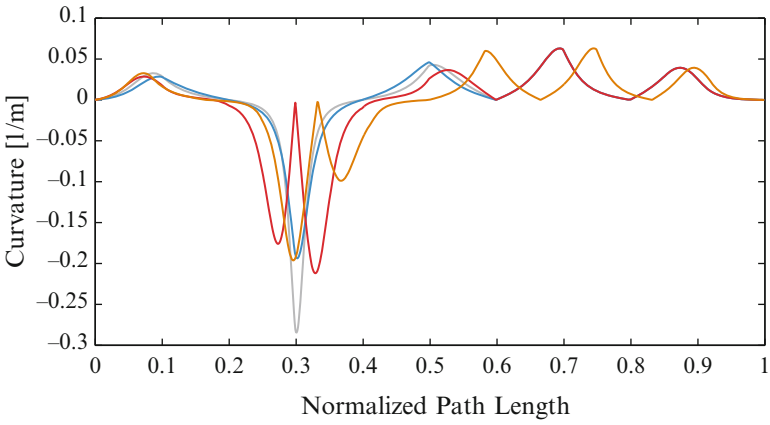

Fig. 9.18 Example 2:Resulting curvature profiles

Table 9.5 Example 1: Resulting path lengths and deviation

Path	Length [m]	Deviation mean [m]	Deviation maximum [m]
Linear path	94.33	–	–
Reference B-spline	92.28	–	–
Elbanhawi et al. (2014)	112.59	12.48	17.19
Solution (1)	71.78	8.58	12.89
Solution (2)	84.42	2.94	5.50

Table 9.6 Example 2: Resulting path lengths and deviation

Path	Length [m]	Deviation mean [m]	Deviation maximum [m]
Linear path	579.88	–	–
Reference B-spline	507.35	–	–
Elbanhawi et al. (2014)	535.28	20.15	45.04
Solution (1)	464.47	6.48	27.03
Solution (2)	506.27	6.04	23.99

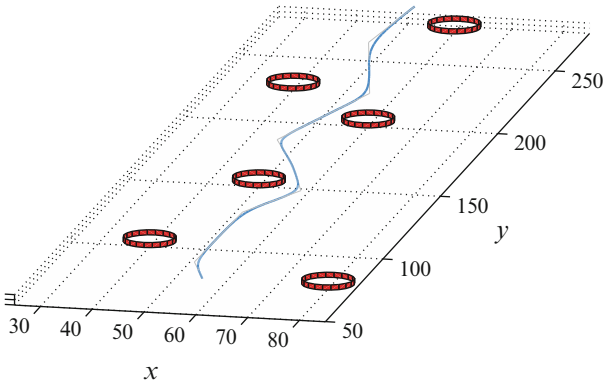

Fig. 9.19 Example 3: Kinodynamic motion among obstacles

- Maintaining path parametric C^2 continuity, by using a single B-spline curve segment with midpoint insertion, to generate more realistic robot paths (Pan et al. 2012). No limitations were posed on the number of control points, for the B-spline curve, enabling a more robust representation of the path, unlike the work in (Nikolos et al. 2003; Jolly et al. 2009).
- Two analytical solutions are offered, formulating the path curvature in terms of a predefined path segment's parameters. They modify the path to limit its curvature to the maximum kinodynamic curvature and satisfy the vehicle's constraints. Our previous publications presented an introduction to the more advanced solutions (Elbanhawi et al. 2014; Elbanhawi and Simic 2014b).

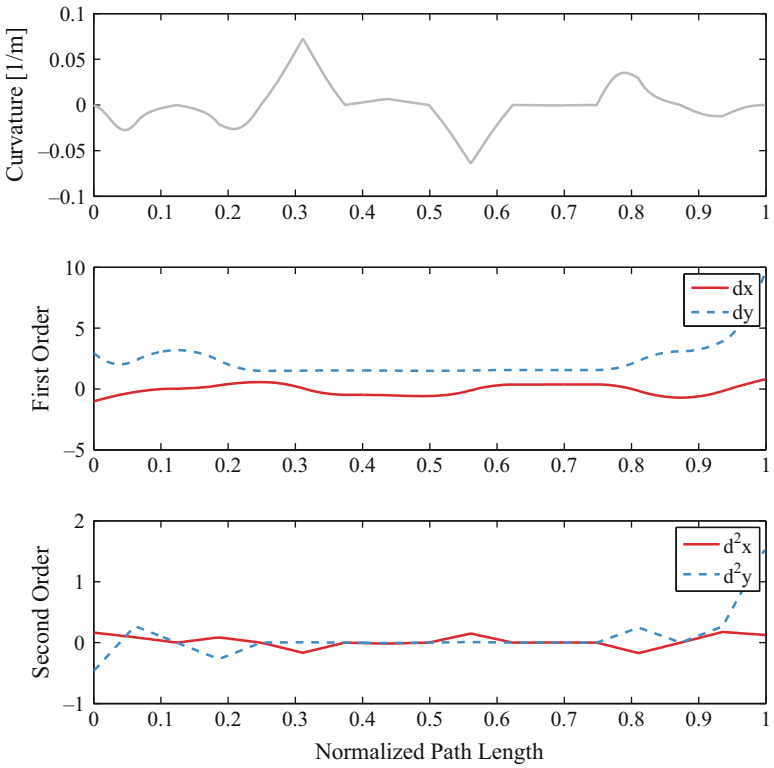

Fig. 9.20 Example 3: Resulting path maintains parametric continuity

Based on the presented numerical and experimental results, we show that this approach:

- Improved accuracy of segment curvature evaluation
- Accelerated segment curvature evaluation
- Decreased path length compared to reference spline and linear path
- Decreased deviation from reference path
- Bounded curvature to desired value while maintaining parametric continuity

The proposed method results in paths that lie within the convex hull of the linear path, with no undesirable oscillations in the path. This produced realistic commands with continuous velocity and acceleration.

This approach relies on smoothing a path defined by successive waypoints, which are generated by a planning algorithm. As presented here, smoothing is considered as a post-planning procedure. Consequently, obtaining an obstacle-free smooth path cannot be guaranteed. In many cases, when collision is detected, replanning is required (Koyuncu and Inalhan 2008). Several researchers examine collision detection for parametric curves (Kwangjin and Sukkarieh 2010; Pan et al. 2012). Circumventing the need for replanning can be achieved by incorporating the

smoothing process within the planning framework. The benefits of guiding the search by the reachability of the robot have been revealed (Shkolnik et al. 2009; Jaillet et al. 2011). In this context, the reachable set can be computed using the efficient curvature evaluation method presented here. Several comments have to be made regarding the presented contributions.

The benefit of solving C^2 parametric continuity problem with maximum curvature constraint and employing the results to mimic human steering is the possibility to combine this parameterization, within any planning framework, such as an RRT or A* algorithm for autonomous vehicles. We predict improvements in human comfort as a result of mimicking human steering, in addition to other claims made by researchers, with regard to continuous curvature paths.

The proposed midpoint insertion algorithm is used to simplify the smoothing algorithm; a more generalized approach would include the location of the inserted point, as a function of the segment angle, but the benefits of doing that are not clear. That could be the subject of other investigation.

In the practical implementation through experiments, we demonstrated that the closely following control polygon method is advantageous over the other algorithms. This benefit comes from the assumption that the path planning algorithm generates a collision-free piecewise linear path, which is then used by our smoothing algorithm, as shown in (Elbanhawi and Simic 2014b).The results can be developed within the context of a recently developed sampling-based algorithm (Elbanhawi and Simic 2014c), which employs efficient collision-checking procedures.

We expect that the outcomes of presented research can be integrated within an efficient planning framework, in which the spline-parameterized motions feel natural to passengers and improve their comfort. Passenger comfort and natural paths are obviously subjective terms that require a large sample of human volunteers for validation. The promising simulations' results, presented here, will be followed by field tests using prototype ground vehicles and UAVs. We plan to validate the concept of graceful motions and curvature continuity, with regard to passenger comfort, by conducting full-scale field experiments.

Acknowledgments M. Elbanhawi acknowledges the financial support of the Australian Postgraduate Award (APA) and Research Training Scheme (RTS).

References

Alshaer, B. J., Darabseh, T. T., & Alhanouti, M. A. (2013). Path planning, modeling and simulation of an autonomous articulated heavy construction machine performing a loading cycle. *Applied Mathematical Modelling, 37*(7), 5315–5325. doi:http://dx.doi.org/10.1016/j.apm.2012.10.042.

Anderson, E. P., Beard, R. W., & McLain, T. W. (2005). Real-time dynamic trajectory smoothing for unmanned air vehicles. *IEEE Transactions on Control Systems Technology, 13*(3), 471–477. https://doi.org/10.1109/TCST.2004.839555.

Asano, T., Guibas, L., Hershberger, J., & Imai, H. (1985). Visibility-polygon search and euclidean shortest paths. In: *26th Annual Symposium on Foundations of Computer Science*, 21–23 Oct 1985, pp 155–164. doi:https://doi.org/10.1109/SFCS.1985.65.

Balkcom, D. J., & Mason, M. T. (2002). Time optimal trajectories for bounded velocity differential drive vehicles. *The International Journal of Robotics Research, 21*(3), 199–217. https://doi.org/10.1177/027836402320556403.

Barsky, B. A., & Derose, T. D. (1990). Geometric continuity of parametric curves: Constructions of geometrically continuous splines. *Computer Graphics and Applications, IEEE, 10*(1), 60–68. https://doi.org/10.1109/38.45811.

Berglund, T., Brodnik, A., Jonsson, H., Staffanson, M., & Soderkvist, I. (2010). Planning smooth and obstacle-avoiding B-spline paths for autonomous mining vehicles. *IEEE Transactions on Automation Science and Engineering, 7*(1), 167–172. https://doi.org/10.1109/TASE.2009.2015886.

Biswas, S., & Lovell, B. C. (2008). *Bézier and splines in image processing and machine vision*. London: Springer.

Brezak, M., & Petrovic, I. (2013). Real-time approximation of clothoids with bounded error for path planning applications. *Robotics, IEEE Transactions on PP, 99*, 1–9. https://doi.org/10.1109/TRO.2013.2283928.

Brooks, R. A., & Lozano-Perez, T. (1985). A subdivision algorithm in configuration space for findpath with rotation. *IEEE Transactions on Systems, Man and Cybernetics, SMC-15*(2), 224–233. https://doi.org/10.1109/TSMC.1985.6313352.

Campion, G., Bastin, G., & Dandrea-Novel, B. (1996). Structural properties and classification of kinematic and dynamic models of wheeled mobile robots. *IEEE Transactions on Robotics and Automation, 12*(1), 47–62. https://doi.org/10.1109/70.481750.

Canny, J. (1985). Voronoi method for the piano-movers problem. In: *1985 I.E. International Conference on Robotics and Automation*, Mar 1985, pp. 530–535. doi:https://doi.org/10.1109/ROBOT.1985.1087297.

Cheng, M. Y., Tsai, M. C., & Kuo, J. C. (2002). Real-time NURBS command generators for CNC servo controllers. *International Journal of Machine Tools and Manufacture, 42*(7), 801–813. doi:http://dx.doi.org/10.1016/S0890-6955(02)00015-9.

De Boor, C. (1972). On calculating with B-splines. *Journal of Approximation Theory, 6*(1), 50–62.

Donges, E. (1978). A Two-Level Model of Driver Steering Behavior. *Human Factors: The Journal of the Human Factors and Ergonomics Society, 20*(6), 691–707. https://doi.org/10.1177/001872087802000607.

Donghyun, K., Cheongjae, J., & Frank, C. P. (2014). Kinematic feedback control laws for generating natural arm movements. *Bioinspiration & Biomimetics, 9*(1), 016002.

Dyllong, E., & Visioli, A. (2003). Planning and real-time modifications of a trajectory using spline techniques. *Robotica, 21*(05), 475–482. https://doi.org/10.1017/S0263574703005009.

Elbanhawi, M., & Simic, M. (2012). Robotics application in remote data acquisition and control for solar ponds. *Applied Mechanics and Materials, 253–255*, 705–715. https://doi.org/10.4028/http://www.scientific.net/AMM.253-255.705.

Elbanhawi, M., & Simic, M. (2014a). Examining the use of B-splines in Parking Assist Systems. *Applied Mechanics and Materials, 490–491*(1), 1025–1029. https://doi.org/10.4028/http://www.scientific.net/AMM.490-491.1025.

Elbanhawi, M., & Simic, M. (2014b). Randomised kinodynamic motion planning for an autonomous vehicle in semi-structured agricultural areas. *Biosystems Engineering, 126*(0), 30–44. doi:http://dx.doi.org/10.1016/j.biosystemseng.2014.07.010.

Elbanhawi, M., & Simic, M. (2014c). Sampling-based robot motion planning: A review. *Access, IEEE, 2*, 56–77. https://doi.org/10.1109/ACCESS.2014.2302442.

Elbanhawi, M., Simic, M., & Jazar, R. (2014). Continuous path smoothing for car-like robots using B-spline curves. *Journal of Intelligent and Robotic Systems*. (in press). https://doi.org/10.1007/s10846-014-0172-0.

Farin, G. (1992). From conics to NURBS: A tutorial and survey. *Computer Graphics and Applications, IEEE, 12*(5), 78–86. https://doi.org/10.1109/38.156017.

Farin, G. (2002). *Curves and surfaces for CAGD. Computing*. San Francisco: Morgan Kaufmann.

Fraichard, T., & Scheuer, A. (2004). From Reeds and Shepp's to continuous-curvature paths. *IEEE Transactions on Robotics, 20*(6), 1025–1035. https://doi.org/10.1109/TRO.2004.833789.

Ghilardelli, F., Lini, G., & Piazzi, A. (2014). Path generation using η4-Splines for a truck and trailer vehicle. *IEEE Transactions on Automation Science and Engineering, 11*(1), 187–203. https://doi.org/10.1109/TASE.2013.2266962.

Guarino Lo Bianco, C. (2013). Minimum-Jerk velocity planning for mobile robot applications. *IEEE Transactions on Robotics, 29*(5), 1317–1326. https://doi.org/10.1109/TRO.2013.2262744.

Gulati, S., & Kuipers, B. (2008). High performance control for graceful motion of an intelligent wheelchair. In: *ICRA 2008, IEEE International Conference on Robotics and Automation*, 19–23 May 2008, pp. 3932–3938. doi:https://doi.org/10.1109/ROBOT.2008.4543815.

Gulati, S., Jhurani, C., Kuipers, B., & Longoria, R. (2009). A framework for planning comfortable and customizable motion of an assistive mobile robot. In: *IROS 2009, IEEE/RSJ International Conference on Intelligent Robots and Systems*, 10–15 Oct 2009, pp. 4253–4260. doi:https://doi.org/10.1109/IROS.2009.5354172.

Hart, P. E., Nilsson, N. J., & Raphael, B. (1968). A formal basis for the Heuristic determination of minimum cost paths. *IEEE Transactions on Systems Science and Cybernetics, 4*(2), 100–107. https://doi.org/10.1109/TSSC.1968.300136.

Hughes, T. J. R., Reali, A., & Sangalli, G. (2008). Duality and unified analysis of discrete approximations in structural dynamics and wave propagation: Comparison of p-method finite elements with k-method NURBS. *Computer Methods in Applied Mechanics and Engineering, 197*(49–50), 4104–4124. doi:http://dx.doi.org/10.1016/j.cma.2008.04.006.

Huh, U.-Y., & Chang, S.-R. (2014). A G^2 continuous path-smoothing algorithm using modified quadratic polynomial interpolation. *International Journal of Advanced Robotic Systems, 11*(25). https://doi.org/10.5772/57340.

Jaillet, L., Hoffman, J., van den Berg, J., Abbeel, P., Porta, J. M., & Goldberg, K. (2011). EG-RRT: Environment-guided random trees for kinodynamic motion planning with uncertainty and obstacles. In: *2011 IEEE/RSJ International Conference on Intelligent Robots and Systems* (*IROS*), 25–30 Sept 2011, pp. 2646–2652. doi:https://doi.org/10.1109/IROS.2011.6094802.

Jazar, R. N. (2008). *Vehicle dynamics: Theory and application*. New York: Springer.

Johnson, J., & Hauser, K. (2012). Optimal acceleration-bounded trajectory planning in dynamic environments along a specified path. In: *2012 I.E. International Conference on Robotics and Automation* (*ICRA*), 14–18 May 2012, pp. 2035–2041. doi:https://doi.org/10.1109/ICRA.2012.6225233.

Jolly, K. G., Sreerama Kumar, R., & Vijayakumar, R. (2009). A Bezier curve based path planning in a multi-agent robot soccer system without violating the acceleration limits. *Robotics and Autonomous Systems, 57*(1), 23–33. doi:http://dx.doi.org/10.1016/j.robot.2008.03.009.

Jones, J., & Adamatzky, A. (2014). Material approximation of data smoothing and spline curves inspired by slime mould. *Bioinspiration & Biomimetics, 9*(3), 036016. https://doi.org/10.1088/1748-3182/9/3/036016.

Kavraki, L. E., Svestka, P., Latombe, J. C., & Overmars, M. H. (1996). Probabilistic roadmaps for path planning in high-dimensional configuration spaces. *IEEE Transactions on Robotics and Automation, 12*(4), 566–580. https://doi.org/10.1109/70.508439.

Khatib, O. (1986). Real-time obstacle avoidance for manipulators and mobile robots. *International Journal of Robotics Research, 5*(1), 90–98. https://doi.org/10.1177/027836498600500106.

Koren, Y., & Borenstein, J. (1991). Potential field methods and their inherent limitations for mobile robot navigation. In: *1991 I.E. International Conference on Robotics and Automation*, 9–11 Apr 1991, (Vol. 1392, pp. 1398–1404). doi:https://doi.org/10.1109/ROBOT.1991.131810.

Koyuncu, E., & Inalhan, G. (2008). A probabilistic B-spline motion planning algorithm for unmanned helicopters flying in dense 3D environments. In: *IROS 2008, IEEE/RSJ International Conference on Intelligent Robots and Systems*, 22–26 Sept 2008, pp. 815–821. doi: https://doi.org/10.1109/IROS.2008.4651122.

Kunz, T., & Stilman, M. (2013). Time-optimal trajectory generation for path following with bounded acceleration and velocity. *Robotics: Science and Systems, 8*, 209. Paper 27, July 9–13, University of Sydney, Sydney, NSW, Australia, 2012.

Kwangjin, Y. (2013). An efficient Spline-based RRT path planner for non-holonomic robots in cluttered environments. In: *2013 International Conference on Unmanned Aircraft Systems (ICUAS)*, 28–31 May 2013, pp. 288–297. doi:https://doi.org/10.1109/ICUAS.2013.6564701.

Kwangjin, Y., & Sukkarieh, S. (2010). An analytical continuous-curvature path-smoothing algorithm. *Robotics, IEEE Transactions on, 26*(3), 561–568. https://doi.org/10.1109/TRO.2010.2042990.

Kwangjin, Y., Jung, D., & Sukkarieh, S. (2013). Continuous curvature path-smoothing algorithm using cubic Bezier spiral curves for non-holonomic robots. *Advanced Robotics, 27*(4), 247–258. https://doi.org/10.1080/01691864.2013.755246.

Land, M., & Horwood, J. (1995). Which parts of the road guide steering? *Nature, 377*(6547), 339–340.

Land, M. F., & Lee, D. N. (1994). Where we look when we steer. *Nature, 369*(6483), 742–744.

Lapierre, L., Zapata, R., & Lepinay, P. (2007). Combined path-following and obstacle avoidance control of a wheeled robot. *The International Journal of Robotics Research, 26*(4), 361–375. https://doi.org/10.1177/0278364907076790.

Lau, B., Sprunk, C., & Burgard, W. (2009). Kinodynamic motion planning for mobile robots using splines. In: *IROS 2009, IEEE/RSJ International Conference on Intelligent Robots and Systems*, 10–15 Oct 2009, pp. 2427–2433. doi:https://doi.org/10.1109/IROS.2009.5354805.

LaValle, S. M., & Kuffner, J. J. (2000). *Rapidly-exploring random trees: A new tool for path planning*. In: Proceedings Workshop on the Algorithmic Foundations of Robotics, Iowa State University.

Lentink, D. (2014). Bioinspired flight control. *Bioinspiration & Biomimetics, 9*(2), 020301. https://doi.org/10.1088/1748-3182/9/2/020301.

Ma, W., & Kruth, J. P. (1998). NURBS curve and surface fitting for reverse engineering. *International Journal of Advanced Manufacturing Technology, 14*(12), 918–927. https://doi.org/10.1007/BF01179082.

MacAdam, C. C. (1981). Application of an Optimal Preview Control for Simulation of Closed-Loop Automobile Driving. *Systems, Man and Cybernetics, IEEE Transactions on, 11*(6), 393–399. https://doi.org/10.1109/TSMC.1981.4308705.

Maekawa, T., Noda, T., Tamura, S., Ozaki, T., & Machida, K. I. (2010). Curvature continuous path generation for autonomous vehicle using B-spline curves. *Computer-Aided Design, 42*(4), 350–359. doi:http://dx.doi.org/10.1016/j.cad.2009.12.007.

Magid, E., Keren, D., Rivlin, E., & Yavneh, I. (2006). Spline-based robot navigation. In: *2006 IEEE/RSJ International Conference on Intelligent Robots and Systems*, 9–15 Oct 2006, pp. 2296–2301. doi:https://doi.org/10.1109/IROS.2006.282635.

McCrae, J., & Singh, K. (2009). Sketching piecewise clothoid curves. *Computers & Graphics, 33*(4), 452–461. doi:http://dx.doi.org/10.1016/j.cag.2009.05.006.

McPhee, J. E., & Aird, P. L. (2013). Controlled traffic for vegetable production: Part 1. Machinery challenges and options in a diversified vegetable industry. *Biosystems Engineering, 116*(2), 144–154. https://doi.org/10.1016/j.biosystemseng.2013.06.001.

Meek, D. S., & Walton, D. J. (2004). An arc spline approximation to a clothoid. *Journal of Computational and Applied Mathematics, 170*(1), 59–77. https://doi.org/10.1016/j.cam.2003.12.038.

Montes, N., Herraez, A., Armesto, L., & Tornero, J. (2008). Real-time clothoid approximation by Rational Bezier curves. In: *ICRA 2008, IEEE International Conference on Robotics and*

Automation, 19–23 May 2008, pp. 2246–2251. doi:https://doi.org/10.1109/ROBOT.2008.4543548.

Morro, A., Sgorbissa, A., & Zaccaria, R. (2011). Path following for unicycle robots with an arbitrary path curvature. *Robotics, IEEE Transactions on, 27*(5), 1016–1023. https://doi.org/10.1109/TRO.2011.2148250.

Myung, H., Kuffner, J., & Kanade, T. (2007). Efficient two-phase 3D motion planning for small fixed-wing UAVs. In: *2007 I.E. International Conference on Robotics and Automation*, 10–14 April 2007, pp. 1035–1041. doi:https://doi.org/10.1109/ROBOT.2007.363121.

Nikolos, I. K., Valavanis, K. P., Tsourveloudis, N. C., & Kostaras, A. N. (2003). Evolutionary algorithm based offline/online path planner for UAV navigation. *Systems, Man, and Cybernetics, Part B: Cybernetics, IEEE Transactions on, 33*(6), 898–912. https://doi.org/10.1109/TSMCB.2002.804370.

Ogata K (2010) Modern Control Engineering. Prentice Hall,

Pan, J., Zhang, L., & Manocha, D. (2012). Collision-free and smooth trajectory computation in cluttered environments. *The International Journal of Robotics Research, 31*(10), 1155–1175. https://doi.org/10.1177/0278364912453186.

Piegl, L. A., & Tiller, W. (2001). Parametrization for surface fitting in reverse engineering. *Computer-Aided Design, 33*(8), 593–603. doi:http://dx.doi.org/10.1016/S0010-4485(00)00103-2.

Pivtoraiko, M., & Kelly, A. (2011). Kinodynamic motion planning with state lattice motion primitives. In: *2011 IEEE/RSJ International Conference on Intelligent Robots and Systems (IROS)*, 25–30 Sept 2011, pp. 2172–2179. doi:https://doi.org/10.1109/IROS.2011.6094900.

Pivtoraiko, M., Knepper, R. A., & Kelly, A. (2009). Differentially constrained mobile robot motion planning in state lattices. *Journal of Field Robotics, 26*(3), 308–333.

Prokop, G. (2001). Modeling human vehicle driving by model predictive online optimization. *Vehicle System Dynamics, 35*(1), 19–53. https://doi.org/10.1076/vesd.35.1.19.5614.

Reeds, J. A., & Shepp, L. A. (1990). Optimal paths for a car that goes both forward and backward. *Pacific Journal of Mathematics, 145*(2), 367–393.

Roth, S., & Batavia, P. (2002). *Evaluating path tracker performance for outdoor mobile robots* (pp. 26–27/07). Chicago, Illinois, USA: Paper presented at the Automation Technology for Off-Road Equipment.

Sabelhaus, D., Röben, F., Meyer zu Helligen, L. P., & Schulze Lammers, P. (2013). Using continuous-curvature paths to generate feasible headland turn manoeuvres. *Biosystems Engineering, 116*(4), 399–409. doi: http://dx.doi.org/10.1016/j.biosystemseng.2013.08.012.

Sachin, P., Jia, P., Abbeel, P., & Goldberg, K. (2014). Planning curvature and torsion constrained ribbons in 3D with application to intracavitary brachytherapy. Paper presented at the *International Workshop on the Algorithmic Foundations of Robotics* (*WAFR*), Boğaziçi University, İstanbul, Turkey, 3–5 August 2014.

Schoenberg, I. J. (1946). Contributions to the problem of approximation of equidistant data by analytic functions – A. On the problem of smoothing or graduations a 1st class of approximation formulae. *Quarterly of Applied Mathematics, 4*(1), 45–99.

Sgorbissa, A., & Zaccaria, R. (2010). 3D path following with no bounds on the path curvature through surface intersection. In: *2010 IEEE/RSJ International Conference on Intelligent Robots and Systems (IROS)*, 18–22 Oct 2010. pp. 4029–4035. doi:https://doi.org/10.1109/IROS.2010.5653235.

Shkolnik, A., Walter, M., & Tedrake, R. (2009). Reachability-guided sampling for planning under differential constraints. In: *ICRA '09, IEEE International Conference on, Robotics and Automation*, 12–17 May 2009, pp 2859–2865. doi:https://doi.org/10.1109/ROBOT.2009.5152874.

Sungchul, J., & Taehoon, K. (2003). Tool-path generation for NURBS surface machining. In: *American Control Conference*, 2003. Proceedings of the 2003, 4–6 June 2003 (Vol. 2613, pp. 2614–2619). doi:https://doi.org/10.1109/ACC.2003.1243471.

Turner, M., & Griffin, M. J. (1999). Motion sickness in public road transport: The effect of driver, route and vehicle. *Ergonomics, 42*(12), 1646–1664. https://doi.org/10.1080/001401399184730.

Unser, M., Aldroubi, A., & Eden, M. (1993). B-spline signal processing. I. Theory. *Signal Processing, IEEE Transactions on, 41*(2), 821–833. https://doi.org/10.1109/78.193220.

Velenis, E., & Tsiotras, P. (2008). Minimum-time travel for a vehicle with acceleration limits: Theoretical analysis and receding-horizon implementation. *Journal of Optimization Theory and Applications, 138*(2), 275–296. https://doi.org/10.1007/s10957-008-9381-7.

Walton, D. J., & Meek, D. S. (2005). A controlled clothoid spline. *Computers & Graphics, 29*(3), 353–363. doi:http://dx.doi.org/10.1016/j.cag.2005.03.008.

Walton, D. J., Meek, D. S., & Ali, J. M. (2003). Planar G2 transition curves composed of cubic Bézier spiral segments. *Journal of Computational and Applied Mathematics, 157*(2), 453–476. https://doi.org/10.1016/s0377-0427(03)00435-7.

Wang, L. Z., Miura, K. T., Nakamae, E., Yamamoto, T., & Wang, T. J. (2001). An approximation approach of the clothoid curve defined in the interval [0, π/2] and its offset by free-form curves. *Computer-Aided Design, 33*(14), 1049–1058. doi:http://dx.doi.org/10.1016/S0010-4485(00)00142-1.

Wu, W., Chen, H., & Woo, P.-Y. (2000). Time optimal path planning for a wheeled mobile robot. *Journal of Robotic Systems, 17*(11), 585–591. https://doi.org/10.1002/1097-4563(200011)17:11<585::AID-ROB1>3.0.CO;2-7.

Xuan-Nam, B., Boissonnat, J. D., Soueres, P., & Laumond, J. P. (1994). Shortest path synthesis for Dubins non-holonomic robot. In: *IEEE International Conference on Robotics and automation*, 8–13 May 1994, (Vol.1, pp. 2–7). doi:https://doi.org/10.1109/ROBOT.1994.351019.

Yang, K., Moon, S., Yoo, S., Kang, J., Doh, N., Kim, H., & Joo, S. (2014). Spline-Based RRT Path Planner for Non-Holonomic Robots. *Journal of Intelligent and Robotic Systems, 73*(1–4), 763–782. https://doi.org/10.1007/s10846-013-9963-y.

Zhang, Y., Bazilevs, Y., Goswami, S., Bajaj, C. L., & Hughes, T. J. R. (2007). Patient-specific vascular NURBS modeling for isogeometric analysis of blood flow. *Computer Methods in Applied Mechanics and Engineering, 196*(29–30), 2943–2959. doi:http://dx.doi.org/10.1016/j.cma.2007.02.009.

Zucker, M., Ratliff, N., Dragan, A. D., Pivtoraiko, M., Klingensmith, M., Dellin, C. M., Bagnell, J. A., & Srinivasa, S. S. (2013). CHOMP: Covariant Hamiltonian optimization for motion planning. *The International Journal of Robotics Research, 32*(9–10), 1164–1193. https://doi.org/10.1177/0278364913488805.

Part III
Modern Engineering Applications

Chapter 10
An Exact Solution Technique for Impact Oscillators

A. Banerjee, R. Das, and E.P. Calius

10.1 Introduction

In the real-life applications, vibrating systems with clearance between the two moving parts are very abundant due to its versatile applications. The impact occurs when either two nearby oscillators or an oscillator and a rigid obstacle come in contact. The physical process of impact is very complex and highly nonlinear. The velocity response of the impact event is discontinuous in nature; therefore, a multi-periodic response or a chaotic response generates during impact process. Due to the energy dissipation through the impact and the counteraction of the external excitation by the resulting impulsive force, the impacting system dissipates energy and subsequently attenuates the vibration of the main structure. In case of the realistic inelastic collision, the kinetic energy losses because the magnitude of the postimpact velocity gets reduced. On the other hand, the counteraction of the external excitation by the resulting impulsive force is not so straightforward to realize and depends on the natural and excitation frequency, amplitude of excitation and duration between two successive impacts.

Dated back to 1945, impact oscillators attract the attention of the researchers. The state of the art of the impacting oscillator can be subdivided into four main classes based on the studied system. These different classes of impacting oscillators

A. Banerjee
Department of Mechanical Engineering, University of Auckland, Auckland, New Zealand

Callaghan Innovation, Auckland, New Zealand

R. Das (✉)
Sir Lawrence Wackett Aerospace Centre, School of Engineering, RMIT University, Melbourne, VIC, Australia
e-mail: raj.das@rmit.edu.au

E.P. Calius
Callaghan Innovation, Auckland, New Zealand

L. Dai, R.N. Jazar (eds.), *Nonlinear Approaches in Engineering Applications*,
https://doi.org/10.1007/978-3-319-69480-1_10

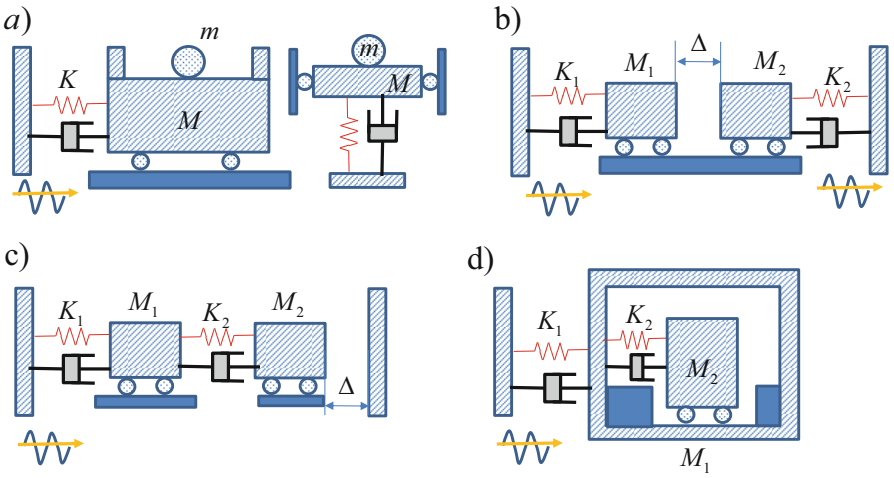

Fig. 10.1 Different sets of possible impacting oscillators. (**a**) Type A, one free oscillator is impacting with periodically exited forced limiter. (**b**) 2DOF structurally uncoupled but impacting coupled system. (**c**) 2DOF structurally coupled but impacting uncoupled system, (**d**) 2DOF all way coupled system

are illustrated in Fig. 10.1. The different forms of the impacting oscillators can be classified as:

Type A, impact oscillation of one free and one spring mass system (no coupling spring between auxiliary mass and main mass), having two-sided fenders (Masri and Caughey 1966; Warburton 1957; Grubin 1956; Viana et al. 2009; Masri 1970; Egle 1967; Popplewell et al. 1983) and one-sided stopper (Ding et al. 2004), which is shown in Fig. 10.1a.

Type B, two uncoupled spring mass systems impact with each other (Dongping and Haiyan 1997) as illustrated in Fig. 10.1b.

Type C, coupled multi-degree-of-freedom system (Pun et al. 1998) or two-degree-of-freedom system (Aidanpää and Gupta 1993; Blazejczyk-Okolewska et al. 2009; Luo 1999; Luo et al. 2001, 2006, 2007, 2008) where impact occurs at the only one mass with some external fixed obstacles as shown in Fig. 10.1c.

Type D, two coupled systems where impact occurs after closing the gap between them, as shown in Fig. 10.1d.

In type A system, internal mass is free; therefore, estimation of the impacting instance and the pre- and postimpact velocity at that moment is comparatively easier to determine than all the other cases. Type B system has two uncoupled vibrating components; thus computation of impacting instance and pre-impact velocity needs more computational efforts than the previous. In the contrary, type C system is coupled with an internal spring; thus, the conversion to the principal coordinate is essential to estimate the modal damping and to get an analytical

equation, which adds complexity in the equations due to shifting of coordinate system. On the other hand, the relative position of the impacting mass can be estimated with computationally much lower cost compared to all the other systems, because it is measured from the fixed rigid support, and postimpact velocity of the impacting mass depends only on the pre-impact velocity of the impacting mass and coefficient of restitution. However, in other cases, the postimpact velocity of each mass depends on the pre-impact velocity of that mass and the other mass as well; therefore, instead of a direct 1:1 relationship, there is a 2:2 relationship that exists which makes type C system computationally easier. From this discussion, it is evitable that the solution of the type D system is most complex among all other cases as shown in Fig. 10.1, because systems are coupled by an internal spring as well as the relative distance is not measured from a fixed support and the postimpact velocity also depends on the pre-impact velocity of each mass.

The main challenges lie in the prediction of duration between two successive impacts, frequency of the impacting response and the initial conditions after each impact for an impacting oscillator. Dynamics of impacting oscillator of type D was first analysed by Masri (1972), with the assumption of two equi-spaced impacts per cycle, which signifies that within a single time period of external force, internal mass hits successively at the outer and inner side of the main vibrating system. This consideration of equi-spaced impacts was overcome by Nigm and Shabana (1983), but the assumption of two impacts per cycles still remains which limits the solution capability of those solver to a certain ranges. Actually, in complete analytical solution, assumptions of periodic motion after a certain number of cycles help to reduce the equations of motion in realistic shape; otherwise, it is almost impossible to solve. Peterka (1998, 2005) solves the type D system considering damping and friction and finds out various types of n-p motions, where n is the number of forcing cycle and p is the number of impacts numerically. Phase portrait and bifurcation map for different excitation frequency motions for type D system is shown in Yue et al. (2012). Most recently, Yue (2016) identified period doubling bifurcation and torus bifurcation for the symmetric quasi-periodic motion of type D system.

From the application point of view, 2DOF impacting system, as shown in Fig. 10.1d, can be very effectively used as a unit of resonating metamaterial which is used as a mechanical filter or wave insulator or acoustic shield due to amazing damping property of impacting oscillators. Natural materials have their own excitation-independent mechanical properties, whereas the metamaterials (Banerjee 2011) can exhibit exotic behaviours, such as negative effective mass (Huang and Sun 2009, 2010, 2012; Yao et al. 2008; Sheng et al. 2003; Sun et al. 2011a, b, 2013; Pope and Laalej 2014; Calius et al. 2009; Huang et al. 2009; Lu et al. 2009; Hu et al. 2016), negative Poisson's ratio (Baughman et al. 1998; Friis et al. 1988; Kocer et al. 2009; Lakes 1987; 1993; Larsen et al. 1996) and negative stiffness (Huang and Sun 2012), in a certain range of frequencies due to the out-of-phase response of the multiple resonating units inside it. In fact, the presence of a resonating mass, inside each unit of a metamaterial, changes the effective dynamic mass of the full system. As the mass of a system has a considerable effect on the wave propagation, the transmission of a wave through the metamaterial becomes

frequency dependent. Each block of metamaterial exerts frequency-dependent impedance to the medium and confines energy from the transmitted wave at the resonating frequency range, which actually controls the wave propagation through the metamaterials (Huang and Sun 2010, 2012; Yao et al. 2008). However, the attenuation bandwidth is mostly independent of the number of repetitive units of the metamaterial, although the transmissibility decreases for higher number of units (Lei 2008; Banerjee et al. 2016a, 2017a).

In general, transmittance is used to quantify the wave transmission through the metamaterial (Hu et al. 2016; Banerjee et al. 2016a, b, 2017a, b). Experimental evidence of this concept is given by Yao et al. (2008); thus, in this chapter, the transmittance is plotted in the frequency domain to identify the attenuation and transmission bandwidth of the metamaterial.

The main challenges associated with the impact modelling are estimation of an exact postimpact velocity and computation of the energy loss due to impact for a specific coefficient of restitution. In this paper, the system is one dimensional; therefore, only the normal directional impact is considered. Normal directional impact can be modelled using Kelvin element (Brogliato 1999), nonlinear Hertz damped (Jankowski 2005) or undamped (Hertz 1881, 1882) model and stereo-mechanical (Newton 1999) or non-smooth unilateral model (Pfeiffer and Glocker 2000; Banerjee et al. 2016c, 2017c). Based on the critical review on various normal directional impacting models by Banerjee et al. (2016d), stereo-mechanical model is most accurate in terms of postimpact velocity estimation and computationally easiest among all other available impacting models; therefore, in this paper, stereo-mechanical model is adopted to compute the dynamic response of the system. The velocity response becomes discontinuous at the time of impact because the impact phenomenon is modelled as an instantaneous event in the stereo-mechanical model. In this paper, an analytical solution of the type D system is developed considering the modal damping after transforming the system to principal coordinate. Based on that analytical solution, a numerical scheme is developed to identify the impacting situation and then compute the postimpact initial conditions for the next impacting cycle. In general, during forced vibration, a linear system vibrates in the same frequency of the excitation, whereas, in case of impacting system, this phenomenon is no longer present. In some frequency range, the impacting motion becomes periodic after p numbers of impact, as described in the Sect. 10.2.1. To analyse this complex dynamic phenomena, (Zhang and Fu 2015) and Luo et al. (2006) used Peterka coefficient ($z = p/n$), positive real number, which is the ratio of the number of impact (p) and number of excitation force period (n) in the excitation time period. For complete analytical solution, such as $z = {}^{1}/_{n}$ where $n \in I$, Peterka coefficient is very effective, but for all the irrational values and rational values, where p and n are quite high, of z, the complexity of the solution increases; thus, the analytical solution of this becomes next to impossible; therefore, to compute all the possible solutions, a similar type of periodicity coefficient (λ) is proposed by Banerjee et al. (2017b). Using this proposed periodicity coefficient, the presented solver can detect all the types of impacting oscillations, namely, no impact, multi-periodic impact and chaotic impact. After that, transmittance for an excitation

frequency range is computed and compared with the equivalent linear system to elucidate the attenuation bandwidth increment of the metamaterial unit due to internal impact. Finally, a complete parametric study is carried out to get the best possible design of these systems for a specific requirement of bandwidth and excitation frequency.

10.2 An Exact Solution Scheme for Impacting Systems

The amplitude spectrum cannot be computed analytically for an impact oscillator; therefore, Banerjee et al. (2017b) developed a semi-analytical solution procedure to solve the impacting response and compute the periodicity. Mass and stiffness of the system, modal damping for the system, gap between the two fenders (or the impacting conditions), excitation amplitude and frequency are its input parameters. The displacement and velocity histories in time domain and the periodicity coefficient are the main output from this impacting simulation. The full solution scheme is illustrated in Fig. 10.2.

The algorithm flow chart of Fig. 10.2 can be summarized as follows:

1. From eigenvalue solution, natural frequencies and mode shapes of the system are computed from the model parameters, i.e. mass and stiffness.
2. The system is translated into the principal coordinate system for more than single degree of freedom, to uncouple the system and to introduce the modal damping into it.
3. The analytical solution of the system in principal coordinate can be obtained from which it is possible to identify whether impact is feasible or not. The instant of impact can also have computed from that.
4. The postimpact state in the principal coordinate system can be evaluated from Eq. (10.29) and use those as the initial condition for the next impacting cycle.
5. The check for identifying the chaos as described in Sect. 10.2.1 is implemented after that, and the periodicity of the impact oscillator is also computed.
6. The output of this scheme can be:
   (a) No impact occurs, because the relative displacement is less than the gap between the object and the fenders. The periodicity coefficient is one in this case, and the periodic solution of displacement and velocity is the two other outputs.
   (b) Impact occurs and steady state is also achieved. In this case, the solver yields the periodicity coefficient and response of the system.
   (c) The last case is chaos, in which impact occurs but steady-state response is not achieved; therefore, solution is not converged to a specific attractor.

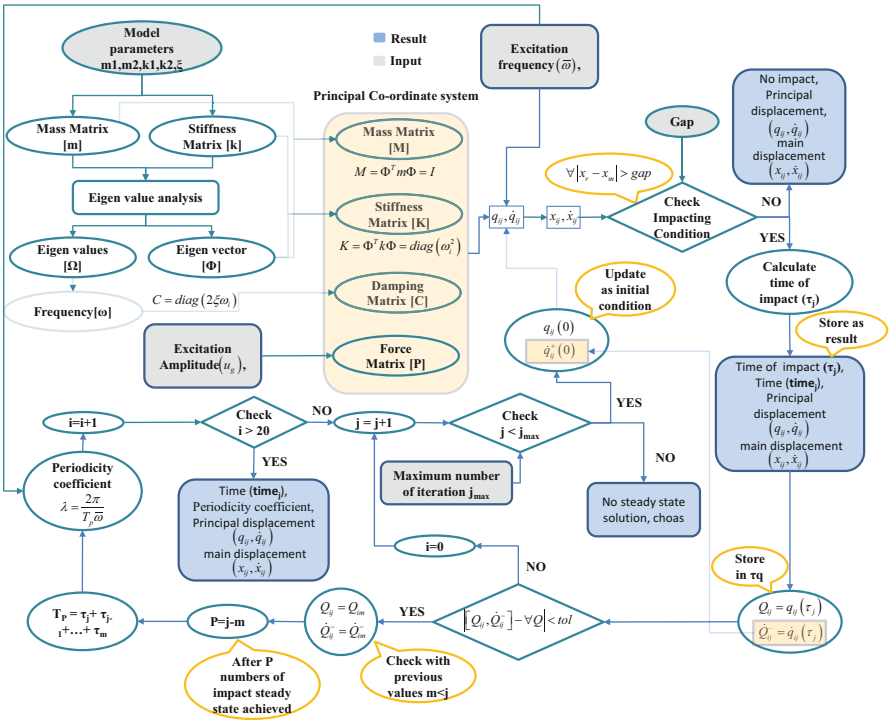

Fig. 10.2 Impact oscillator solution scheme (Banerjee et al. 2017b)

10.2.1 Identification of Different Periodic Motion, Chaos and Stopping Criteria

Most of the time after a few impacting cycles, the response of the impact system becomes steady, and the solution should stop to reduce computational cost. Besides that, identification of the various types of periodic response is also essential to estimate the effect of sub- and super-harmonic responses and chaos on the overall system dynamics. Along the time domain, several parallel planes which contain both the displacements and velocities of the impact oscillator, analogous to Poincare's plane, are chosen at the impacting time. Each plane contains both the post- and pre-impact velocities because impact is assumed to be instantaneous. Now, if the displacement and velocity response at plane after *j*th impact is identical with that of after *m*th impact, then it can be concluded that after $p = j - m$ numbers of impact, the response repeats or becomes periodic. The time differences between p numbers of consecutive planes (T_p) are checked, and when the last 20 values of T_p become equal, then it is assumed that the steady state is achieved and solution terminated. Otherwise, in case of the chaotic response, solution will not be

repeated; thus, it should continue up to a certain maximum number, for example, 5000 numbers of impacting cycles.

10.2.2 Periodicity Coefficient

Due to the counteraction of the external excitation by the resulting impulsive force, impact oscillators demonstrate discontinuous rich dynamics which is mostly multi-periodic or chaotic because of the presence of sub- and super-harmonics. In general, during the steady state of a forced vibration, a linear system vibrates in the external frequency, whereas, in the case of impact system, this phenomenon is no longer present. In some frequency range, the impacting motion becomes periodic after p numbers of impact; thus, the time period of the impact system changes to the time duration for the p steady-state impacts which can be assumed to be T_p. To encounter this issue, Banerjee et al. (2017b) defined periodicity as the ratio of the system's response frequency (ω_p) with excitation frequency $(\overline{\omega})$, which can be further simplified as

$$\lambda = \frac{\omega_p}{\overline{\omega}} = \frac{2\pi}{\overline{\omega} T_p} \tag{10.1}$$

This periodicity coefficient (λ) can help to identify the characteristics of the motion. The value of λ can be any positive real number, rational or irrational. For chaotic response, λ is assumed to be 0 as the chaotic system has no periodicity, and for the non-impacting case, it is assumed to be unity as the system vibrates in the excitation frequency during non-impacting linear motion.

To demonstrate how the solver works, a single-degree-of-freedom system and a mass-in-mass 2DOF system of type D are solved.

10.3 Single-Degree-of-Freedom System

Single-degree-of-freedom system with stopper can be considered as a piecewise linear system. The equation of motion can be written as

$$m\ddot{u} + c\dot{u} + ku = ku_g \sin \overline{\omega} t \tag{10.2}$$

The natural frequency is $\omega = \sqrt{k/m}$ and viscous damping is $c = 2\xi\omega$. As Eq. (10.2) is a single equation, therefore conversion to the principal coordinate is not required.

Now the transient part can be expressed as

$$
\begin{aligned}
{}_{\mathrm{t}}u &= e^{-\xi\omega t}[\sin(\omega_{\mathrm{d}}t)A + \cos(\omega_{\mathrm{d}}t)B] \\
{}_{\mathrm{t}}\dot{u} &= \omega_{\mathrm{d}}e^{-\xi\omega t}[\cos(\omega_{\mathrm{d}}t)A - \sin(\omega_{\mathrm{d}}t)B] - \xi\omega e^{-\xi\omega t}[\sin(\omega_{\mathrm{d}}t)A + \cos(\omega_{\mathrm{d}}t)B]
\end{aligned} \tag{10.3}
$$

where A and B are two unknowns based on the initial condition and damped natural frequency $\omega_{\mathrm{d}} = \omega\sqrt{1-\xi^2}$. On the other hand, the steady-state part can be written as

$$
\begin{aligned}
{}_{\mathrm{s}}u &= Z\sin\left(\overline{\omega}t - \gamma + \varphi\right) \\
{}_{\mathrm{s}}\dot{u} &= \overline{\omega}Z\cos\left(\overline{\omega}t - \gamma + \varphi\right)
\end{aligned} \tag{10.4}
$$

where $Z = \frac{ku_{\mathrm{g}}/\omega^2}{\sqrt{(1-\eta^2)^2+(2\xi\eta)^2}}$, $\gamma = \tan^{-1}\left(\frac{-2\xi\eta}{1-\eta^2}\right)$, $\eta = \dfrac{\overline{\omega}}{\omega}$ and φ are an unknown phase angle due to the impact, which represents the state when the impact occurs. Therefore, the displacement and the velocity of the system in the principal coordinate system can be expressed as

$$
\begin{aligned}
u &= e^{-\xi\omega t}[\sin(\omega_{\mathrm{d}}t)A + \cos(\omega_{\mathrm{d}}t)B] + Z\sin\left(\overline{\omega}t - \gamma + \varphi\right)\dot{u} \\
&= \omega_{\mathrm{d}}e^{-\xi\omega t}[\cos(\omega_{\mathrm{d}}t)A - \sin(\omega_{\mathrm{d}}t)B] - \xi\omega e^{-\xi\omega t}[\sin(\omega_{\mathrm{d}}t)A + \cos(\omega_{\mathrm{d}}t)B] \\
&+\overline{\omega}Z\cos\left(\overline{\omega}t - \gamma + \varphi\right) \\
&= e^{-\xi\omega t}\{[\omega_{\mathrm{d}}\cos(\omega_{\mathrm{d}}t) - \xi\omega\sin(\omega_{\mathrm{d}}t)]A - [\omega_{\mathrm{d}}\sin(\omega_{\mathrm{d}}t) + \xi\omega\cos(\omega_{\mathrm{d}}t)]B\} + \\
&\times\overline{\omega}Z\cos\left(\overline{\omega}t - \gamma + \varphi\right)
\end{aligned} \tag{10.5}
$$

Assigning the initial conditions, $u(0), \dot{u}(0)$, for the complete solution of Eq. (10.5), it can be derived that:

$$
\begin{aligned}
u(0) &= B + Z\sin(\varphi - \gamma) \\
\dot{u}(0) &= \omega_{\mathrm{d}}A - \xi\omega B + \overline{\omega}Z\cos(\varphi - \gamma) \\
&\rightarrow \begin{cases} B = u(0) - Z\sin(\varphi - \gamma) \\ A = \dfrac{\dot{u}(0)}{\omega_{\mathrm{d}}} + \dfrac{\xi\omega}{\omega_{\mathrm{d}}}u(0) - \dfrac{\xi\omega}{\omega_{\mathrm{d}}}Z\sin(\varphi - \gamma) - \dfrac{\overline{\omega}Z}{\omega_{\mathrm{d}}}\cos(\varphi - \gamma) \end{cases}
\end{aligned} \tag{10.6}
$$

Therefore, Eq. (10.5) can be rewritten in terms of the initial conditions by substituting the values of unknown A and B from Eq. (10.22) into Eq. (10.19):

$$
\begin{aligned}
u &= \underbrace{e^{-\xi\omega t}\left\{\cos(\omega_{\mathrm{d}}t)+\frac{\xi\omega}{\omega_{\mathrm{d}}}\sin(\omega_{\mathrm{d}}t)\right\}}_{S_{dd}(t)}u(0)\\
&+\underbrace{e^{-\xi\omega t}\frac{\sin(\omega_{\mathrm{d}}t)}{\omega_{\mathrm{d}}}}_{S_{dv}(t)}\dot{u}(0)-S_{dd}(t)Z\sin(\varphi-\gamma)-\\
&\quad S_{dv}(t)\overline{\omega}Z\cos(\varphi-\gamma)+Z\sin\left(\overline{\omega}t+\varphi-\gamma\right)\\
\dot{u} &= \underbrace{e^{-\xi\omega t}\left(-\left(\xi\omega\frac{\xi\omega}{\omega_{\mathrm{d}}}+\omega_{\mathrm{d}}\right)\sin(\omega_{\mathrm{d}}t)\right)}_{S_{vd}(t)}u(0)\\
&+\underbrace{e^{-\xi\omega t}\left(\cos(\omega_{\mathrm{d}}t)-\frac{\xi\omega}{\omega_{\mathrm{d}}}\sin(\omega_{\mathrm{d}}t)\right)}_{S_{vv}(t)}\dot{u}(0)-\\
&\quad S_{vd}(t)Z\sin(\varphi-\gamma)-S_{vv}(t)\overline{\omega}Z\cos(\varphi-\gamma)+\\
&\quad \overline{\omega}Z\cos\left(\overline{\omega}t+\varphi-\gamma\right)
\end{aligned}
\tag{10.7}
$$

Thus, the total response of the single-degree-of-freedom system can be expressed by summation of the transient and the steady-state part, in the following manner:

$$
\begin{aligned}
u &= S_{dd}(t)u(0)+S_{dv}(t)\dot{u}(0)-S_{dd}(t)Z\sin(\varphi-\gamma)\\
&\quad -S_{dv}(t)\overline{\omega}Z\cos(\varphi-\gamma)+Z\sin\left(\overline{\omega}t+\varphi-\gamma\right)\\
\dot{u} &= S_{vd}(t)u(0)+S_{vv}(t)\dot{u}(0)-S_{vd}(t)Z\sin(\varphi-\gamma)\\
&\quad -S_{vv}(t)\overline{\omega}Z\cos(\varphi-\gamma)+\overline{\omega}Z\cos\left(\overline{\omega}t+\varphi-\gamma\right)
\end{aligned}
\tag{10.8}
$$

In Eq. (10.8), d and v, which are used as the suffix of S, stand for displacement and velocity, respectively. Therefore, $S_{dd}(t)$ represents the coefficient of the displacement of the initial displacement of it.

The unknown phase is needed when the initial condition within an impacting cycle is unknown; however, in this case, the initial condition before an impacting cycle is known either from the postimpact velocity and displacement from the result of the previous cycle or from the assigned initial displacement and velocity if it is the first cycle. Therefore, the unknown phase of Eq. (10.7) can be eliminated which yields the modified form of Eq. (10.8):

$$
\begin{aligned}
u &= S_{dd}(t)u(0)+S_{dv}(t)\dot{u}(0)+S_{dd}(t)Z\sin(\gamma)\\
&\quad -S_{dv}(t)\overline{\omega}Z\cos(\gamma)+Z\sin\left(\overline{\omega}t-\gamma\right)\\
\dot{u} &= S_{vd}(t)u(0)+S_{vv}(t)\dot{u}(0)+S_{vd}(t)Z\sin(\gamma)-S_{vv}(t)\overline{\omega}Z\cos(\gamma)\\
&\quad +\overline{\omega}Z\cos\left(\overline{\omega}t-\gamma\right)
\end{aligned}
\tag{10.9}
$$

Now, if the gap between the fender and the initial position of the resonator is Δ, then impact occurs when

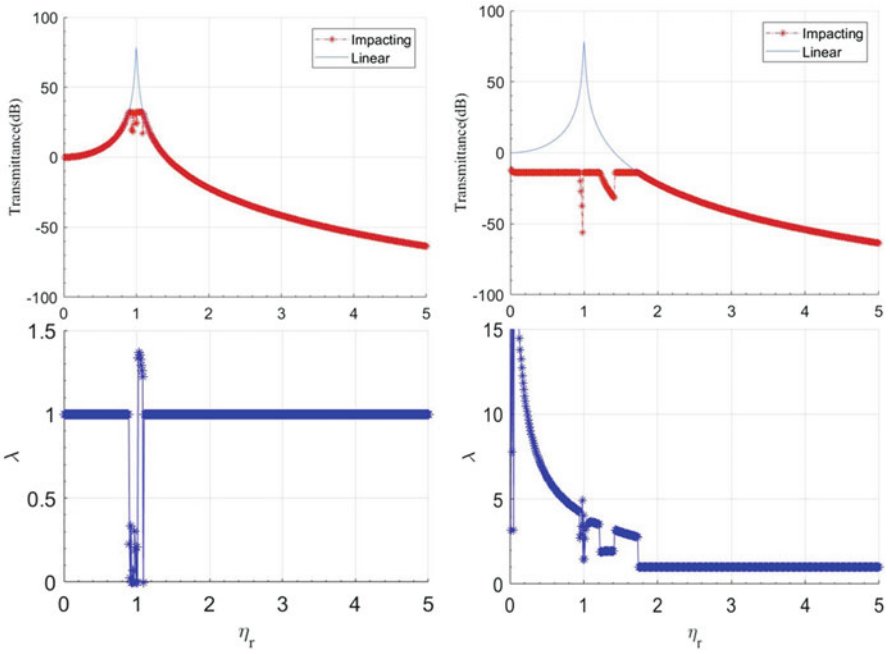

Fig. 10.3 Left and right columns show the transmittance spectrum at top row and periodicity number at the bottom row for gap = 5.0 and 0.5, respectively

$$u \pm \Delta = 0 \tag{10.10}$$

The first instant of impact (τ_1) can be estimated by substituting Eq. (10.9) into Eq. (10.10). Therefore, pre-impact velocity $\left(\dot{u}^{-}\right)$ can be calculated from Eq. (10.9) as

$$\dot{u}_1^{-} = \bar{S}_{vd} u(0) + \bar{S}_{vv} \dot{u}(0) + \bar{S}_{vd} Z \sin(\gamma) - \bar{S}_{vv} \overline{\omega} Z \cos(\gamma) + \overline{\omega} Z \cos\left(\overline{\omega}\tau_1 - \gamma\right) \tag{10.11}$$

where $\bar{S}_{xx} = S_{xx}\left(\tau_j\right)$. Postimpact velocity can be calculated according to Newton's law of impact:

$$\dot{u}_j^{+} = -\varepsilon \dot{u}_j^{-} \tag{10.12}$$

After each impact, the initial conditions of the equation of motion need to be updated. After jth impact, the pre-impact displacement and velocity would be $\left(\pm\Delta, \dot{u}_j^{+}\right)$which acts as the initial condition for the equation of motion.

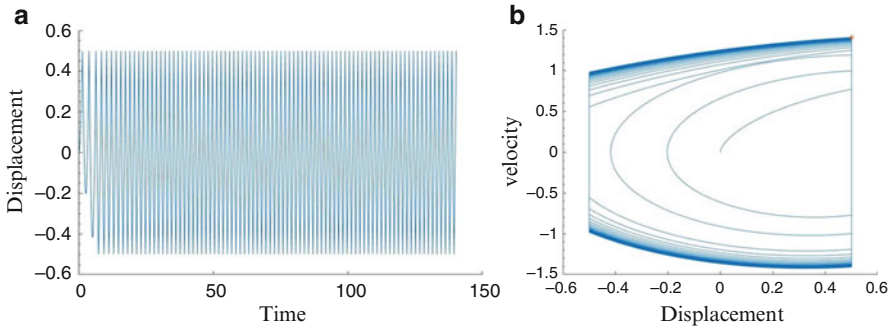

Fig. 10.4 (**a**) Time-domain displacement response of the system, (**b**) phase portrait of the velocity and displacement response of the single-degree-of-freedom system having mass 1, stiffness 1 and gap ratio 0.5

10.4 Case Studies for Impacting SDOF System

A SDOF impacting system having unit mass and stiffness with 1% modal damping is analysed to illustrate how the transmittance and periodicity number can vary throughout the frequency domain for two different gap ratios.

10.4.1 Response Spectrum

The transmittance and periodicity coefficient spectra for two different gaps are plotted in Fig. 10.3.

Transmittance diagram shows that impact occurs near the resonating frequency and impact band increases with the decreasing gap ratio. The amplitude of the impacting oscillation is limited to a specific value depending on the gap ratio. As the impacting amplitude is always less compared to the linear amplitude, thus transmittance reduces. Higher value of λ represents that the frequency of the impacting system increases. Lower gap ratio increases the numbers of impact in a specific time duration, and slowly the motion starts dominated by the impacting response. For higher gap ratio, super-harmonic motion, having $\lambda < 1$, can be perceived in some frequencies.

10.4.2 Time-Domain Data

To understand the multi-periodic response, time-domain response and the phase portrait are plotted for various frequencies.

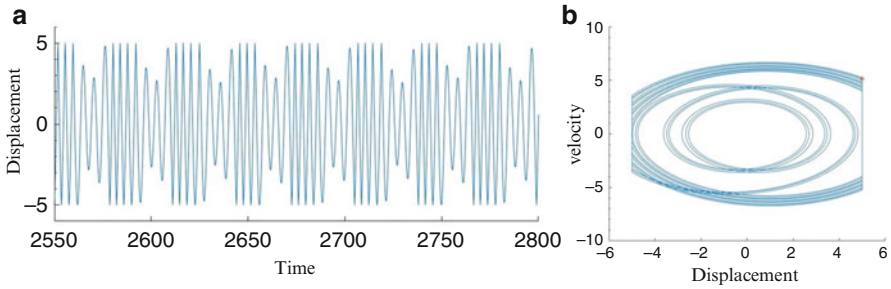

Fig. 10.5 (**a**) Time-domain displacement response and (**b**) phase portrait of the single-degree-of-freedom system having mass and stiffness unity and gap ratio of 5.0

Figure 10.4 illustrates that after few impacts, the response becomes steady and the phase portrait starts converging. In this case, the frequency of the response increases.

On the other hand, for gap ratio 5, the frequency of the system sometime decreases during impact. Time-domain plot of the displacement reveals the reason behind the frequency decrement as shown in Fig. 10.5a.

Figure 10.5 illustrates that the response repeats after 11 numbers of impacts in steady state and the total time for the 11 impacts is much more than the time period of the excitation.

10.5 Mass-in-Mass Impacting System

Banerjee et al. (2017b) has derived the full impact oscillation for mass-in-mass unit as shown in Fig. 10.1d. The analytical procedure is as follows:

The equation of motion of the linear system which is shown in Fig. 10.1d can be written as

$$\underbrace{\begin{bmatrix} m_1 & 0 \\ 0 & m_2 \end{bmatrix}}_{[m]} \underbrace{\begin{Bmatrix} \ddot{u}_1 \\ \ddot{u}_2 \end{Bmatrix}}_{\ddot{x}} + \underbrace{\begin{bmatrix} c_1 + c_2 & -c_2 \\ -c_2 & c_2 \end{bmatrix}}_{[c]} \underbrace{\begin{Bmatrix} \dot{u}_1 \\ \dot{u}_2 \end{Bmatrix}}_{\dot{x}} + \underbrace{\begin{bmatrix} k_1 + k_2 & -k_2 \\ -k_2 & k_2 \end{bmatrix}}_{[k]} \underbrace{\begin{Bmatrix} u_1 \\ u_2 \end{Bmatrix}}_{x} = \underbrace{\begin{Bmatrix} k_1 u_g \sin \overline{\omega} t \\ 0 \end{Bmatrix}}_{f} \tag{10.13}$$

where $[m]$, $[k]$ are, respectively, mass and stiffness matrix of the system and suffix 1 and 2 stand for the main and resonating unit, respectively. $[c]$ denotes the damping matrix, which cannot be predicted directly as there is no extra dampers attached to the system. Based on the concept that damping is proportional to the frequency, damping matrix $[c]$ can be calculated from the modal damping, according to

Felippa (2015). u_1, u_2 stand for the displacement of main and resonating units, respectively, and the dot denotes the time derivate. f is the force matrix, and $\overline{\omega}$ is the excitation frequency in rad/s.
The natural frequencies of the two-degree-of-freedom system can be expressed as

$$\omega_{1,2}^2 = \frac{k_2}{2m_2} + \left(\frac{k_1+k_2}{2m_1}\right) \pm \sqrt{-\frac{k_2}{m_2}\frac{k_1}{m_1} + \frac{1}{4}\left(\frac{k_1+k_2}{m_1} + \frac{k_2}{m_2}\right)^2} \tag{10.14}$$

and the modal matrix, which contains the mode shapes for each natural frequency, can be expressed as

$$\widetilde{\Phi} = \begin{bmatrix} a_1 & a_2 \\ 1 & 1 \end{bmatrix}; \quad a_n = -\frac{m_2}{k_2}\omega_n^2 + 1 \tag{10.15}$$

Now, Eq. (10.13) is a coupled second-order differential equation. To uncouple Eq. (10.13), the system $\{x\}$ is transferred to the principal coordinate $\{q\}$, by coordinate transformation, after assuming

$$\underbrace{\begin{Bmatrix} u_1 \\ u_2 \end{Bmatrix}}_{x} = \underbrace{\begin{bmatrix} \frac{a_1}{\sqrt{m_1 a_1^2 + m_2}} & \frac{a_2}{\sqrt{m_1 a_2^2 + m_2}} \\ \frac{1}{\sqrt{m_1 a_1^2 + m_2}} & \frac{1}{\sqrt{m_1 a_2^2 + m_2}} \end{bmatrix}}_{\Phi} \underbrace{\begin{Bmatrix} q_1 \\ q_2 \end{Bmatrix}}_{q} \tag{10.16}$$

where Φ is the mass normalized modal matrix. After shifting the coordinate system to principal coordinate, the mass, damping, stiffness and force matrix change to

$$\begin{aligned} M &= \Phi^T m \Phi = \begin{bmatrix} 1 & 0 \\ 0 & 1 \end{bmatrix}; \quad K = \Phi^T k \Phi = \begin{bmatrix} \omega_1^2 & 0 \\ 0 & \omega_2^2 \end{bmatrix} \\ C &= \Phi^T c \Phi = \begin{bmatrix} 2\xi\omega_1 & 0 \\ 0 & 2\xi\omega_2 \end{bmatrix}; \quad P = \Phi^T f \end{aligned} \tag{10.17}$$

where ξ is the modal damping coefficient and M, C, K and P are modal mass, damping, stiffness matrix and force vector, respectively. Actually, the unknown damping matrix of Eq. (10.13) can be calculated as $c = \Phi^{-T} C \Phi$ according to Felippa (2015). Therefore, Eq. (10.13) can be solved in two different modes as two uncoupled single-degree-of-freedom systems, and the equations of motion of the metamaterial unit in the principal coordinate system are

$$\begin{aligned} &\begin{bmatrix} 1 & 0 \\ 0 & 1 \end{bmatrix} \begin{Bmatrix} \ddot{q}_1 \\ \ddot{q}_2 \end{Bmatrix} + \begin{bmatrix} 2\xi\omega_1 & 0 \\ 0 & 2\xi\omega_2 \end{bmatrix} \begin{Bmatrix} \dot{q}_1 \\ \dot{q}_2 \end{Bmatrix} + \begin{bmatrix} \omega_1^2 & 0 \\ 0 & \omega_2^2 \end{bmatrix} \begin{Bmatrix} q_1 \\ q_2 \end{Bmatrix} = \begin{Bmatrix} P_1 \\ P_2 \end{Bmatrix} \sin\overline{\omega}t \\ &\rightarrow \ddot{q}_i + 2\xi\omega_i \dot{q}_i + \omega_i^2 q_i = P_i \sin\overline{\omega}t \quad i = 1, 2 \end{aligned} \tag{10.18}$$

where the force vector in principal coordinate system can be evaluated as

$$\begin{Bmatrix} P_1 \\ P_2 \end{Bmatrix} = \begin{bmatrix} \dfrac{a_1}{\sqrt{m_1 a_1^2 + m_2}} & \dfrac{1}{\sqrt{m_1 a_1^2 + m_2}} \\ \dfrac{a_2}{\sqrt{m_1 a_2^2 + m_2}} & \dfrac{1}{\sqrt{m_1 a_2^2 + m_2}} \end{bmatrix} \begin{Bmatrix} k_1 u_g \\ 0 \end{Bmatrix}$$
$$= \begin{Bmatrix} \dfrac{a_1}{\sqrt{m_1 a_1^2 + m_2}} \\ \dfrac{a_2}{\sqrt{m_1 a_2^2 + m_2}} \end{Bmatrix} k_1 u_g \tag{10.19}$$

The solution of the ith mode in Eq. (10.18) can be written as the summation of the transient and steady-state part. Now the transient part can be expressed as

$$\begin{aligned} {}_{\mathrm{t}}q_i &= e^{-\xi\omega_i t}[\sin(\omega_{di}t)A_i + \cos(\omega_{di}t)B_i] \\ {}_{\mathrm{t}}\dot{q}_i &= \omega_{di}e^{-\xi\omega_i t}[\cos(\omega_{di}t)A_i - \sin(\omega_{di}t)B_i] \\ &\quad -\xi\omega_i e^{-\xi\omega_i t}[\sin(\omega_{di}t)A_i + \cos(\omega_{di}t)B_i] \end{aligned} \tag{10.20}$$

where A and B are two 2×1 unknown vectors based on the initial condition and damped natural frequency $\omega_{di} = \omega_i\sqrt{1-\xi^2}$. On the other hand, the steady-state part can be written as

$$\begin{aligned} {}_{\mathrm{s}}q_i &= Z_i \sin(\overline{\omega}t - \gamma_i + \varphi) \\ {}_{\mathrm{s}}\dot{q}_i &= \overline{\omega}Z_i \cos(\overline{\omega}t - \gamma_i + \varphi) \end{aligned} \tag{10.21}$$

where $Z_i = \dfrac{P_i/\omega_i^2}{\sqrt{\left(1-\eta_i^2\right)^2 + (2\xi\eta_i)^2}}$, $\gamma_i = \tan^{-1}\left(\dfrac{-2\xi\eta_i}{1-\eta_i^2}\right)$, $\eta_i = \dfrac{\overline{\omega}}{\omega_i}$ and φ are an unknown phase angle due to the impact, which represents the state when the impact occurs.

Therefore, the displacement and the velocity of the system in the principal coordinate system can be expressed as

$$\begin{aligned} q_i &= e^{-\xi\omega_i t}[\sin(\omega_{di}t)A_i + \cos(\omega_{di}t)B_i] + Z_i \sin(\overline{\omega}t - \gamma_i + \varphi) \\ \dot{q}_i &= \omega_{di}e^{-\xi\omega_i t}[\cos(\omega_{di}t)A_i - \sin(\omega_{di}t)B_i] - \\ &\quad \xi\omega_i e^{-\xi\omega_i t}[\sin(\omega_{di}t)A_i + \cos(\omega_{di}t)B_i] + \overline{\omega}Z_i \cos(\overline{\omega}t - \gamma_i + \varphi) \\ &= e^{-\xi\omega_i t}\{[\omega_{di}\cos(\omega_{di}t) - \xi\omega_i \sin(\omega_{di}t)]A_i - \\ &\quad [\omega_{di}\sin(\omega_{di}t) + \xi\omega_i \cos(\omega_{di}t)]B_i\} + \overline{\omega}Z_i \cos(\overline{\omega}t - \gamma_i + \varphi) \end{aligned} \tag{10.22}$$

Assigning the initial conditions, $q_i(0), \dot{q}_i(0)$, for the complete solution of Eq. (10.22), it can be derived that

$$
\begin{aligned}
&q_i(0) = B_i + Z_i \sin(\varphi - \gamma_i) \\
&\dot{q}_i(0) = \omega_{di} A_i - \xi \omega_i B_i + \overline{\omega} Z_i \cos(\varphi - \gamma_i) \\
&\rightarrow \begin{cases} B_i = q_i(0) - Z_i \sin(\varphi - \gamma_i) \\ A_i = \dfrac{\dot{q}_i(0)}{\omega_{di}} + \dfrac{\xi \omega_i}{\omega_{di}} q_i(0) - \dfrac{\xi \omega_i}{\omega_{di}} Z_i \sin(\varphi - \gamma_i) - \dfrac{\overline{\omega} Z_i}{\omega_{di}} \cos(\varphi - \gamma_i) \end{cases}
\end{aligned} \tag{10.23}
$$

Therefore, Eq. (10.20) can be rewritten in terms of the initial conditions by substituting the values of unknown A and B from Eq. (10.23) into Eq. (10.20):

$$
\begin{aligned}
q_i = & \underbrace{e^{-\xi \omega_i t} \left\{ \cos(\omega_{di} t) + \frac{\xi \omega_i}{\omega_{di}} \sin(\omega_{di} t) \right\}}_{S_{idd}(t)} q_i(0) \\
& + \underbrace{e^{-\xi \omega_i t} \frac{\sin(\omega_{di} t)}{\omega_{di}}}_{S_{idv}(t)} \dot{q}_i(0) - S_{idd}(t) Z_i \sin(\varphi - \gamma_i) \\
& - S_{idv}(t) \overline{\omega} Z_i \cos(\varphi - \gamma_i) + Z_i \sin\left(\overline{\omega} t + \varphi - \gamma_i\right) \\
\dot{q}_i = & \underbrace{e^{-\xi \omega_i t} \left(- \left(\xi \omega_i \frac{\xi \omega_i}{\omega_{di}} + \omega_{di} \right) \sin(\omega_{di} t) \right)}_{S_{ivd}(t)} q_i(0) \\
& + \underbrace{e^{-\xi \omega_i t} \left(\cos(\omega_{di} t) - \frac{\xi \omega_i}{\omega_{di}} \sin(\omega_{di} t) \right)}_{S_{ivv}(t)} \dot{q}_i(0) \\
& - S_{ivd}(t) Z_i \sin(\varphi - \gamma_i) - S_{ivv}(t) \overline{\omega} Z_i \cos(\varphi - \gamma_i) \\
& + \overline{\omega} Z_i \cos\left(\overline{\omega} t + \varphi - \gamma_i\right)
\end{aligned} \tag{10.24}
$$

Thus, the total response in the principal coordinate can be expressed by summation of transient and the steady-state part, in the following manner:

$$
\begin{aligned}
q_i = & S_{idd}(t) q_i(0) + S_{idv}(t) \dot{q}_i(0) - S_{idd}(t) Z_i \sin(\varphi - \gamma_i) \\
& - S_{idv}(t) \overline{\omega} Z_i \cos(\varphi - \gamma_i) + Z_i \sin\left(\overline{\omega} t + \varphi - \gamma_i\right) \\
\dot{q}_i = & S_{ivd}(t) q_i(0) + S_{ivv}(t) \dot{q}_i(0) - S_{ivd}(t) Z_i \sin(\varphi - \gamma_i) \\
& - S_{ivv}(t) \overline{\omega} Z_i \cos(\varphi - \gamma_i) + \overline{\omega} Z_i \cos\left(\overline{\omega} t + \varphi - \gamma_i\right)
\end{aligned} \tag{10.25}
$$

In Eq. (10.25), d and v, which are used as the suffix of S, stand for displacement and velocity, respectively, and i represents the index of the mode, which can be 1 or 2. Therefore, $S_{1dd}(t)$ represents the coefficient of the displacement of the 1st mode with the initial displacement of it in principal coordinate system.

The unknown phase is needed when the initial condition within an impacting cycle is unknown; however, in this case, the initial condition before an impacting cycle is known either from the postimpact velocity and displacement from the result of the previous cycle or from the assigned initial displacement and velocity if it is the first cycle. Therefore, the unknown phase of Eq. (10.25) can be eliminated which yields the modified form of Eq. (10.25):

$$\begin{aligned} q_i &= S_{idd}(t)q_i(0) + S_{idv}(t)\dot{q}_i(0) + S_{idd}(t)Z_i \sin(\gamma_i) \\ &\quad - S_{idv}(t)\overline{\omega}Z_i \cos(\gamma_i) + Z_i \sin\left(\overline{\omega}t - \gamma_i\right) \\ \dot{q}_i &= S_{ivd}(t)q_i(0) + S_{ivv}(t)\dot{q}_i(0) + S_{ivd}(t)Z_i \sin(\gamma_i) \\ &\quad - S_{ivv}(t)\overline{\omega}Z_i \cos(\gamma_i) + \overline{\omega}Z_i \cos\left(\overline{\omega}t - \gamma_i\right) \end{aligned} \tag{10.26}$$

10.5.1 Identification of the Impact

As the gap between the two vibrating masses comes together, the impact can be described as follows:

$$\begin{aligned} &u_2 \pm \Delta - u_1 = 0 \\ &\Phi_{2i}q_i \pm \Delta - \Phi_{1i}q_i = 0 \\ &\underbrace{(\Phi_{21} - \Phi_{11})}_{\delta_1} q_1 + \underbrace{(\Phi_{22} - \Phi_{12})}_{\delta_2} q_2 \pm \Delta = 0 \\ &\delta_1 q_1(\tau_j) + \delta_2 q_2(\tau_j) \pm \Delta = 0 \\ &q_2(\tau_j) = \mp\frac{\Delta}{\delta_2} - \frac{\delta_1 q_1(\tau_j)}{\delta_2} \end{aligned} \tag{10.27}$$

The solution of Eq. (10.27) produces impacting time τ_j, and the substitution of τ_j in Eq. (10.26) yields the point of impact and the pre-impact velocity. Impact happens for a real-valued solution of τ_j; otherwise, when there is no real solution of τ_j, there is no impact, and the situation is purely linear.

10.5.2 Postimpact Velocity in Principal Coordinate System

When two approaching bodies come in contact, then impact occurs, and the velocity of both bodies changed to keep the total momentum constant. Assuming the resonating mass and the main mass are comparable, the postimpact velocity can be calculated as follows, from the stereo-mechanical model:

$$\underbrace{\begin{Bmatrix} \dot{u}_1^+ \\ \dot{u}_2^+ \end{Bmatrix}}_{\dot{x}^+} = \underbrace{\frac{1}{m_1+m_2}\begin{bmatrix} m_1-m_2\varepsilon & m_2(1+\varepsilon) \\ m_1(1+\varepsilon) & m_2-m_1\varepsilon \end{bmatrix}}_{G} \underbrace{\begin{Bmatrix} \dot{u}_1^- \\ \dot{u}_2^- \end{Bmatrix}}_{\dot{x}^-} \tag{10.28}$$

where + and – superscripts represent the post- and pre-impact cases, respectively, and ε denotes the coefficient of restitution. The postimpact velocity conversion factor in principal coordinate can be estimated as follows:

$$\begin{aligned} &x = \Phi q \rightarrow \dot{x} = \Phi\dot{q} \\ &\dot{x}^+ = G\dot{x}^- \rightarrow \Phi\dot{q}^+ = G\Phi\dot{q}^- \rightarrow \dot{q}^+ = \underbrace{\Phi^{-1}G\Phi}_{G_p}\dot{q}^- \\ &\dot{q}_i^+ = G_{pi1}\dot{q}_1^- + G_{pi2}\dot{q}_2^- \end{aligned} \tag{10.29}$$

where

$$\begin{aligned} G_p &= \Phi^{-1}G\Phi \\ G_p &= c\begin{bmatrix} R_{11o}m_1 + R_{11i}m_2 & \rho\{a_2R_{12o}m_1 + R_{12o}m_2\} \\ \rho\{-R_{11o}m_1 - R_{11i}m_2\} & R_{22o}m_1 + R_{22i}m_2 \end{bmatrix} \end{aligned} \tag{10.30}$$

where $R_{11o} = a_1 - a_2(a_1 + \varepsilon a_2 - \varepsilon)$, $R_{11i} = 1 + \varepsilon - \varepsilon a_1 - a_2$, $R_{12o} = 1 + \varepsilon - \varepsilon a_2 - a_2$, $R_{22o} = a_2 + a_1(a_2 + \varepsilon a_2 - \varepsilon)$, $R_{22i} = a_1 + 1 - \varepsilon - \varepsilon a_2$ and $c = (a_1 - a_2)^{-1}(m_2 + m_1)^{-1}$.

10.5.3 Postimpact Equation of Motion

To evaluate the complete time-domain response, it is essential to determine the postimpact equation of motion of the 2DOF system. After impact the velocity suddenly jumps, which induced discontinuity. The displacements and pre-impact velocities of the two-degree-of freedom system in principal coordinate can be determined from Eq. (10.26), after substituting the time of impact calculated from Eq. (10.27), as

$$\begin{aligned} Q_{ij} &= \bar{S}_{idd}q_i(\tau_j) + \bar{S}_{idv}\dot{q}_i(\tau_j) + \bar{S}_{idd}Z_i\sin(\gamma_i) \\ &\quad - \bar{S}_{idv}\overline{\omega}Z_i\cos(\gamma_i) + Z_i\sin(\overline{\omega}\tau_j - \gamma_i) \\ \dot{Q}_{ij}^- &= \bar{S}_{ivd}q_i(\tau_j) + \bar{S}_{ivv}\dot{q}_i(\tau_j) + \bar{S}_{ivd}Z_i\sin(\gamma_i) \\ &\quad - \bar{S}_{ivv}\overline{\omega}Z_i\cos(\gamma_i) + \overline{\omega}Z_i\cos(\overline{\omega}\tau_j - \gamma_i) \end{aligned} \tag{10.31}$$

where $\bar{S}_{xyz} = S_{xyz}(\tau_j)$. As the displacement response is continuous, the pre-impact displacement acts as postimpact displacement, whereas the postimpact velocity changes based on Eqs. (10.29) and (10.30) as

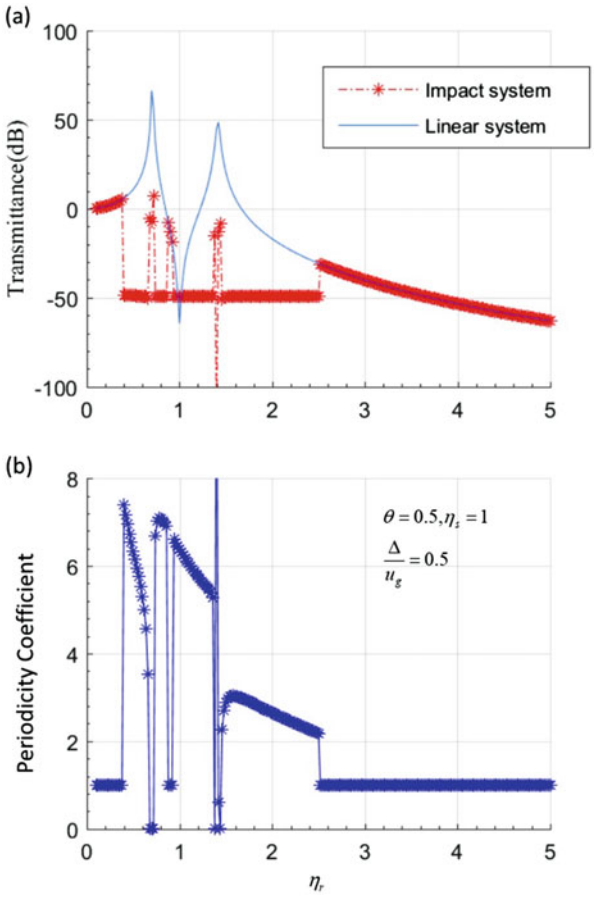

Fig. 10.6 Frequency domain plots of (**a**) transmittance for impacting and non-impacting systems and (**b**) periodicity number for an impacting system with elastic collisions (Banerjee et al. 2017b)

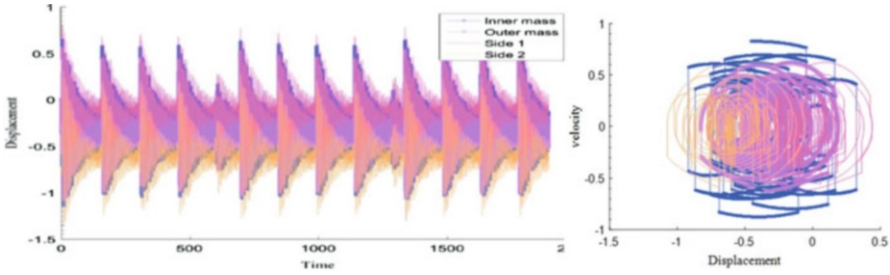

Fig. 10.7 Response of an impacting system in the presence of chaos. (**a**) Overall time-domain displacement response also showing the mean and RMS values, (**b**) phase portrait of the relative velocity and displacement for last 40 cycles (Banerjee et al. 2017b)

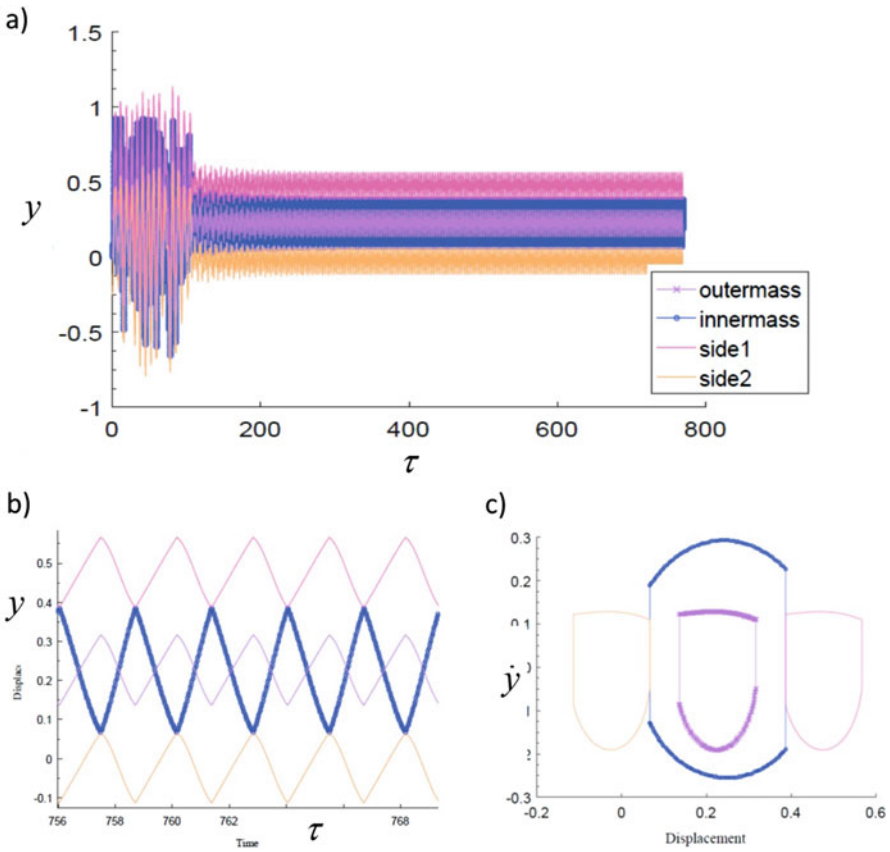

Fig. 10.8 Response of impacting system at $\eta_r = 0.6$. (**a**) Non-dimensional displacement as a function of non-dimensional time, (**b**) last seven impacting cycles of steady-state part of the full displacement response, (**c**) phase portrait of the inner and outer velocity and displacement of the steady-state part (Banerjee et al. 2017b)

$$\begin{aligned} q_{ij}(0) &= Q_{ij} \\ \dot{q}_{ij}^{+}(0) &= G_p \dot{Q}_{ij}^{-} \end{aligned} \tag{10.32}$$

The postimpact state acts as an initial condition for the postimpact equation of motion generation. The time scale also starts from zero for each impact, and the previous impacting time is stored and cumulated to get the final time-domain response. Therefore, the equation of motion after jth impact can be derived from Eq. (10.26) just by substituting the initial conditions $q_i(0), \dot{q}_i(0)$ with $q_{ij}(0), \dot{q}_{ij}(0)$.

10.6 Case Studies for Impact Mass-in-Mass System

10.6.1 Response Spectrum

A case study is performed in this section to illustrate the transmittance for a specific system, having $\eta_s = 1, \theta = 0.5$, and a specific gap ratio of $\Delta/u_g = 0.5$. In this section, the time histories of three different types of response categories, namely, no impact, periodic after impact and chaotic response, are elucidated.

Figure 10.6 illustrates the transmittance spectrum of the impact system in frequency domain in comparison with the linear oscillator. The transmittance in case of the impact oscillator is considerably less compared to an equivalent linear system. In the case of the linear oscillator, the existence of the two transmittance peaks limits the attenuation bandwidth, which is the most commonly encountered problem in the state of the art. Most interestingly, the two transmittance peaks drop due to the presence of impact; therefore, the attenuation band increases to a great extent.

10.6.2 Time Domain

The chaotic time-domain response of the system at $\eta_r = 2.0$ is illustrated in Fig. 10.7.

At frequency ratio $\eta_r = 2.0$, the vibration of the inner resonating mass is in out of phase with the external mass when the impact is not considered, and also the relative displacement can cross the boundary of the stoppers. From the time-domain response, as shown in Fig. 10.7a, it can be easily visualized that the response is shifted to the negative side; therefore, first the mean of the motion is computed, and then the RMS is calculated over the shifted coordinate system. The value of the mean is -0.3267, and the RMS is 0.2396 in non-dimensional displacement. The zoomed view of the chaotic response is depicted in Fig. 10.7b, which shows that the inner mass hits successively the fenders. The phase portrait of the chaotic response is shown in Fig. 10.6c which is not repeating in nature.

A time history response of the system at $\eta_r = 0.6$ is illustrated in Fig. 10.8, which gives a periodic response.

The amplitude of the inner mass of the equivalent linear system crosses the limit of the two fenders; therefore, an impact occurs. The impacting case is solved in the time domain using the proposed algorithm. In Fig. 10.8a, it can be found that the response gets stable and steady after few transient impacts, and this steady-state part is shown in Fig. 10.8b. Figure 10.8c depicts the phase portrait of the steady-state part. The steady-state response elucidates the following properties:

1. Two impacts, one with side A and another with side B, occur successively within a single period of the impacting motion.

2. The consecutive impacting events are not equi-spaced, which also supports the finding of Nigm and Shabana (1983). The time between two consecutive impacts, in this case, is 1.4524 s and 1.2160 s; therefore, the total duration of two-steady state impacts is $T_p = 2.6684$ s. Now, the excitation time period is $T_e = 2\pi/\overline{\omega} = 10.4720\,\text{s}$. Thus, the periodicity coefficient is $\lambda = \dfrac{\omega_p}{\overline{\omega}} = \dfrac{T_e}{T_p} = 3.9245$.
3. The response of the resonating unit is out of phase with the main unit although the linear response corresponding to that case is in the same phase. This out-of-phase phenomenon is very interesting from the perspective of wave propagation through these units.

The amplitude of the displacement of the outer unit is less in case of impact system compared to that of the linear response of non-impacting case.

10.7 Conclusions

This chapter presents an algorithm and associated numerical scheme to categorize all the discontinuous, non-smooth responses present in a mass-in mass impact system and compute its displacement transmittance spectrum. A periodicity coefficient (λ), which represents the ratio of impact frequency to the excitation, is proposed in this paper to identify and categorize the different types of non-smooth response. The presented algorithm can compute the response for every real positive value of λ, which explores the full frequency domain. Depending on the amplitude and frequency of excitation, coefficient of restitution, gap ratio, mass ratio and structural frequency ratio, the successive internal impact between the inner mass and the external cavity results in either multi-periodic, chaotic or sticking types of responses.

In case of SDOF system, multi-periodic response occurs due to the successive impact for small gap ratio, but for large gap ratio, chaotic response may occur. For small gap ratio, successive impacts dominate the response, whereas, in case of higher gap ratio, a coupling can be perceived between the forced vibration and impacting response. Therefore, the chance of going into chaotic state is more for high gap ratio.

For mass-in-mass impacting unit, the inner and outer masses are out of phase with each other irrespective of the phase of their linear responses, and the frequency of resulting motion increases during multi-periodic responses. As a result, the vibration of the main structure can be attenuated over a large range of excitation frequencies. The RMS value of the chaotic response is also less than that of the equivalent linear response.

It can then be concluded that the impact oscillator is attractive as vibration insulator because it has the potential to reduce the two transmittance peak characteristics of linear mass-in-mass resonant units. Multi-periodic motion necessarily

reduces the amplitude of the vibration of the outer mass; for some range, the chaotic vibration response is also less than the equivalent linear response. Sticking type of motion is undesirable for excitation frequencies below the first eigenfrequency of the system because in that range it increases the transmittance.

References

Aidanpää, J. O., & Gupta, R. B. (1993). Periodic and chaotic behaviour of a threshold-limited two-degree-of-freedom system. *Journal of Sound and Vibration, 165*(2), 305–327.

Banerjee, B. (2011). *An introduction to metamaterials and waves in composites*. Auckland: Taylor & Francis.

Banerjee, A., Das, R., & Calius, E. (2016a). A new approach for determination of the attenuation bandwidth of a resonating metamaterial. *Applied Mechanics and Materials, 846*, 264–269.

Banerjee, A., Calius, E. P., & Das, R. (2016b). The effects of cubic stiffness nonlinearity on the attenuation bandwidth of 1D elasto-dynamic metamaterials. In *IMECE 2016* (p. V013T01A020). Pheonix: ASME.

Banerjee, A., Chanda, A., & Das, R. (2016c). Oblique frictional unilateral contacts perceived in curved bridges. *Nonlinear Dynamics, 85*(4), 2207–2231.

Banerjee, A., Chanda, A., & Das, R. (2016). Historical origin and recent development on normal directional impact models for rigid body contact simulation: A critical review. *Archives of Computational Methods in Engineering, 24*(2), 397–422. https://doi.org/10.1007/s11831-016-9164-5.

Banerjee, A., Das, R., & Calius, E. P. (2017). Frequency graded 1d metamaterials: A study on the attenuation bands. *Journal of Applied Physics, 122*(7), 075101. https://doi.org/10.1063/1.4998446.

Banerjee, A., Das, R., & Calius, E. P. (2017b). Vibration transmission through an impacting mass-in-mass unit, an analytical investigation. *International Journal of Non-Linear Mechanics, 90*, 137–146.

Banerjee, A., Chanda, A., & Das, R. (2017c). Seismic analysis of a curved bridge considering deck-abutment pounding interaction: an analytical investigation on the post-impact response. *Earthquake Engineering & Structural Dynamics, 46*(2), 267–290.

Baughman, R. H., et al. (1998). Negative Poisson's ratios as a common feature of cubic metals. *Nature, 392*(6674), 362–365.

Błazejczyk-Okolewska, B., & Peterka, F. (1998). An investigation of the dynamic system with impacts. *Chaos, Solitons & Fractals, 9*(8), 1321–1338.

Blazejczyk-Okolewska, B., Czolczynski, K., & Kapitaniak, T. (2009). Dynamics of a two-degree-of-freedom cantilever beam with impacts. *Chaos, Solitons & Fractals, 40*(4), 1991–2006.

Brogliato, B. (1999). *Nonsmooth mechanics: models, dynamics and control*. London/New York: Springer.

Calius, E. P., et al. (2009). Negative mass sound shielding structures: Early results. *Basic Solid State Physics, 246*(9), 2089–2097.

Ding, W. C., Xie, J. H., & Sun, Q. G. (2004). Interaction of Hopf and period doubling bifurcations of a vibro-impact system. *Journal of Sound and Vibration, 275*(1–2), 27–45.

Dongping, J., & Haiyan, H. (1997). Periodic vibro-impacts and their stability of a dual component system. *Acta Mechanica Sinica, 13*(4), 366–376.

Egle, D. M. (1967). Discussion: On the stability of the impact damper (Masri, S. F., & Caughey, T.K. (1966). ASME Journal of Applied Mechanics, *33*, 586–592). *Journal of Applied Mechanics*, *34*(1), 253–253.

Pope, S. A., & Laalej, H. (2014). A multi-layer active elastic metamaterial with tuneable and simultaneously negative mass and stiffness. *Smart Materials and Structures, 23*(7), 075020.

Felippa, C. A. (2015). *Modal analysis of MDOF forced damped system*. Introduction to Aerospace Structures (ASEN 3112). Department of Aerospace Engineering Sciences, University of Colorado at Boulder, Epub date: 2015, Date Accessed: 5th July, 2016.

Friis, E., Lakes, R., & Park, J. (1988). Negative Poisson's ratio polymeric and metallic foams. *Journal of Materials Science, 23*(12), 4406–4414.

Grubin, C. (1956). On the theory of the acceleration damper. *Journal of Applied Mechanics, 23*(3), 373–378.

Hertz, H. (1881). On the contact of elastic solids. *Journal fur die Reine und Angewandte Mathematik, 92*(156–171), 110.

Hertz, H. (1882). *Über die Berührung fester elastischer Körper*.

Hu, G., et al. (2016). Metastructure with piezoelectric element for simultaneous vibration suppression and energy harvesting. *Journal of Vibration and Acoustics, 139*(1), 011012.

Huang, H. H., & Sun, C. T. (2009). Wave attenuation mechanism in an acoustic metamaterial with negative effective mass density. *New Journal of Physics, 11*(1), 013003.

Huang, G. L., & Sun, C. T. (2010). Band gaps in a multiresonator acoustic metamaterial. *Journal of Vibration and Acoustics, 132*(3), 031003.

Huang, H. H., & Sun, C. T. (2012). Anomalous wave propagation in a one- dimensional acoustic metamaterial having simultaneously negative mass density and Young's modulus. *The Journal of the Acoustical Society of America, 132*, 2887.

Huang, H. H., Sun, C. T., & Huang, G. L. (2009). On the negative effective mass density in acoustic metamaterials. *International Journal of Engineering Science, 47*(4), 610–617.

Jankowski, R. (2005). Non-linear viscoelastic modelling of earthquake-induced structural pounding. *Earthquake Engineering & Structural Dynamics, 34*(6), 595–611.

Kocer, C., McKenzie, D. R., & Bilek, M. M. (2009). Elastic properties of a material composed of alternating layers of negative and positive Poisson's ratio. *Materials Science and Engineering: A, 505*(1–2), 111–115.

Lakes, R. (1987). Foam structures with a negative Poisson's ratio. *Science, 235*(4792), 1038–1040.

Lakes, R. (1993). Advances in negative Poisson's ratio materials. *Advanced Materials, 5*(4), 293–296.

Larsen, U. D., Sigmund, O., & Bouwstra, S. (1996). Design and fabrication of compliant micromechanisms and structures with negative Poisson's ratio. In *Micro Electro Mechanical Systems, 1996, MEMS'96, Proceedings. An Investigation of Micro Structures, Sensors, Actuators, Machines and Systems*. IEEE, The Ninth Annual International Workshop on. 1996. IEEE.

Lei, Z. (2008). Effective 1-D material properties of coplanar-waveguide-based EBG- and metamaterials. In *Metamaterials, 2008,* International Workshop on. 2008.

Lu, M.-H., Feng, L., & Chen, Y.-F. (2009). Phononic crystals and acoustic metamaterials. *Materials Today, 12*(12), 34–42.

Luo, G. W. (1999). Periodic motions and transition phenomena in a two-degrees-of-freedom system with perfectly plastic impact. *Physics Letters A, 263*(1–2), 83–90.

Luo, G. W., Xie, J. H., & Guo, S. H. L. (2001). Periodic motions and global bifurcations of a two-degree-of-freedom system with plastic vibro-impact. *Journal of Sound and Vibration, 240*(5), 837–858.

Luo, G. W., Yu, J. N., & Zhang, J. G. (2006). Periodic-impact motions and bifurcations of a dual component system. *Nonlinear Analysis: Real World Applications, 7*(4), 813–828.

Luo, G., et al. (2007). Vibro-impact dynamics near a strong resonance point. *Acta Mechanica Sinica, 23*(3), 329–341.

Luo, G., et al. (2008). Periodic-impact motions and bifurcations of vibro-impact systems near 1:4 strong resonance point. *Communications in Nonlinear Science and Numerical Simulation, 13*(5), 1002–1014.

Masri, S. F. (1970). General motion of impact dampers. *The Journal of the Acoustical Society of America, 47*(1B), 229–237.

Masri, S. F. (1972). Theory of the dynamic vibration neutralizer with motion-limiting stops. *Journal of Applied Mechanics, 39*(2), 563–568.

Masri, S. F., & Caughey, T. K. (1966). On the stability of the impact damper. *Journal of Applied Mechanics, 33*(3), 586–592.

Newton, I. (1999). *The principia: Mathematical principles of natural philosophy*. California: University of California Press.

Nigm, M. M., & Shabana, A. A. (1983). Effect of an impact damper on a multi-degree of freedom system. *Journal of Sound and Vibration, 89*(4), 541–557.

Peterka, F., & Blazejczyk-Okolewska, B. (2005). Some aspects of the dynamical behavior of the impact damper. *Journal of Vibration and Control, 11*(4), 459–479.

Pfeiffer, F., & Glocker, C. (1996). *Multibody dynamics with unilateral contacts* (Vol. 9). John Wiley & Sons.

Pope, S. A., & Laalej, H. (2014). A multi-layer active elastic metamaterial with tuneable and simultaneously negative mass and stiffness. *Smart Materials and Structures, 23*(7), 075020.

Popplewell, N., Bapat, C. N., & McLachlan, K. (1983). Stable periodic vibroimpacts of an oscillator. *Journal of Sound and Vibration, 87*(1), 41–59.

Pun, D., et al. (1998). Forced vibration analysis of a multidegree impact vibrator. *Journal of Sound and Vibration, 213*(3), 447–466.

Sheng, P., et al. (2003). Locally resonant sonic materials. *Physica B: Condensed Matter, 338*(1–4), 201–205.

Sun, H., Du, X., & Frank Pai, P. (2011a). *Metamaterial broadband vibration absorbers by local resonance*. In Collection of Technical Papers – AIAA/ASME/ASCE/AHS/ASC Structures, Structural Dynamics and Materials Conference.

Sun, H., et al. (2011b). *Theory and experiment research of metamaterial beams for broadband vibration absorption*. In Collection of Technical Papers – AIAA/ASME/ASCE/AHS/ASC Structures, Structural Dynamics and Materials Conference.

Sun, H., et al. (2013). *Theory and experiment research of metamaterial panel for mechanical waves absorption*. In Collection of Technical Papers – AIAA/ASME/ASCE/AHS/ASC Structures, Structural Dynamics and Materials Conference.

Viana, R. L., De Souza, S. L. T., & Caldas, I. L. (2009). Multistability and self-similarity in the parameter-space of a vibro-impact system. *Mathematical Problems in Engineering, 2009*, 1–11.

Warburton, G. (1957). Discussion of "on the theory of the acceleration damper". *ASME Journal of Applied Mechanics, 24*, 322–324.

Yao, S., Zhou, X., & Hu, G. (2008). Experimental study on negative effective mass in a 1D mass–spring system. *New Journal of Physics, 10*(4), 043020.

Yue, Y. (2016). Bifurcations of the symmetric quasi-periodic motion and Lyapunov dimension of a vibro-impact system. *Nonlinear Dynamics, 84*(3), 1697–1713.

Yue, Y., Xie, J. H., & Gao, X. J. (2012). Capturing the symmetry of attractors and the transition to symmetric chaos in a vibro-impact system. *International Journal of Bifurcation and Chaos, 22*(05), 1250109.

Zhang, Y., & Fu, X. (2015). On periodic motions of an inclined impact pair. *Communications in Nonlinear Science and Numerical Simulation, 20*(3), 1033–1042.

Chapter 11
A Semi-analytical Solution for Bending of Nonlinear Magnetostrictive Beams

S.A. Sheikholeslami and M.M. Aghdam

11.1 Introduction

Magnetostrictive materials are a type of smart materials which produce strain when subjected to a magnetic field. This specification gives them a great importance to be used as sensors or actuators in various industries. Magnetostrictive materials are utilized for these purposes in some structural elements like rods, thin films, and beams. Although all magnetostrictive materials elongate in magnetic fields, some specific ones are of great importance. Terfenol-D ($Tb_{0.3}Dy_{0.7}Fe_2$) is one of these materials which produces strains of about 1500 ppm in a magnetic field intensity of 200 kA/m (Aboudi et al. 2014). Due to this high amount of strain, the material is called giant magnetostrictive material (GMM).

Many papers in the literature show the magnetization process in the magnetostrictive materials and prove the effects of stress on magnetization. Some notable works are the ones done by Bozorth and Williams (1945), Jiles and Atherton (1986), Sablik and Jiles (1993), Jiles (1995), and Smith et al. (2003). Experiments have shown that for giant magnetostrictive materials, such as Terfenol-D, the constitutive relations are nonlinear, coupled, and prestress sensitive (Clark et al. 1988; Moffett et al. 1991; Schatz et al. 1994; Liang and Zheng 2007). In order to model and analyze the magnetostriction phenomena, some nonlinear constitutive relations which account for magnetomechanical couplings have been presented in the literature. Carman and Mitrovic (1995) have proposed the standard square (SS) model and applied the model to 1-D problems. Wan et al. (2003) showed that the SS model is accurate for low and moderate magnetic fields, but the error increases in the high-field region. They also proposed two 1-D nonlinear models which describe the magnetic saturation trend. The first one is called the hyperbolic

S.A. Sheikholeslami • M.M. Aghdam (✉)
Department of Mechanical Engineering, Amirkabir University of Technology, Tehran, Iran
e-mail: aghdam@aut.ac.ir

L. Dai, R.N. Jazar (eds.), *Nonlinear Approaches in Engineering Applications*,
https://doi.org/10.1007/978-3-319-69480-1_11

tangent (HT) model, and the second one is based on density of domain switching (DDS). Comparing the results of the HT and DDS models with experiments, it has been shown that these two models can accurately predict the magnetostrictive strains for Terfenol-D in high magnetic fields, although they have still large deviations from experimental results in the region of high fields (with the error of about 30–40% for the compressive prestress of 65.4 MPa (Wan et al. 2003)). Another nonlinear coupled model called the D-H model is presented by Duenas et al. (1996). The D-H model can adequately predict the magnetostrictive strains in low and moderate fields, and likewise the HT and DDS models, can follow the saturation trend in high-field region, but fails to match the experimental results in this region. This is because in this model, the magnetostrictive strain is proportional to the square of the magnetization but is independent of the stress. Some other models which consider the hysteresis effects of magnetostrictive materials are proposed by Zheng et al. (2009) and Linnemann et al. (2009).

Based on the Gibbs free energy function, Liu and Zheng (2005) presented a multiaxial constitutive relation for magnetostrictive materials and showed that the model can accurately predict the magnetostrictive strains for low, moderate, and high values of magnetic field intensity under different prestresses. However, due to the simplification made in this model, a condition on the range of applied prestress must also be considered. Jin et al. (2012a, b) have generalized this model to consider the thermal effects.

There exist a large number of articles dealing with natural vibration and vibration suppression of homogeneous and laminated beam/plate structures in the literature, whereas few works are done on flexural bending of homogeneous magnetostrictive beams. In this paper, based on the model of Liu and Zheng (2005), a semi-analytical approach is used to analyze the bending of magnetostrictive beams under applied magnetomechanical loading. In the present work, the effects of mechanical bending moments and magnetic field intensities on deflection of homogeneous and isotropic nonlinear magnetostrictive beams are considered. For a given magnetic field intensity and bending moment, an algorithm is developed for computation of the magnetization, stress, and deflection for simply supported and cantilever beams. Due to the nonlinearity of constitutive relations, the magnetization values are found iteratively, and an analytic relation is derived for obtaining the deflection.

11.2 Formulation of the Problem

Figure 11.1 shows an isotropic and homogeneous magnetostrictive beam which is subjected to both mechanical and magnetic loadings.

Based on the Liu and Zheng (2005) model, the triaxial coupled constitutive relations for a magnetostrictive material can be written as

$$\varepsilon_{ij} = \frac{1}{E}\left[(1+\nu)\sigma_{ij} - \nu\sigma_{kk}\delta_{ij}\right] + \frac{\lambda_s}{\sigma_s}\widetilde{\sigma}_{ij} + \frac{1}{M_s^2}\left[\frac{3}{2}\lambda_s M_i M_j - M_k M_k\left(\frac{\lambda_s}{2}\delta_{ij} + \frac{\lambda_s\widetilde{\sigma}_{ij}}{\sigma_s}\right)\right] \tag{11.1a}$$

$$H_i = \frac{1}{k\bar{M}}L^{-1}\left(\frac{\bar{M}}{M_s}\right)M_i - \frac{\lambda_s}{\mu_0 M_s^2}\left[2\widetilde{\sigma}_{ij} - (I_\sigma^2 - 3J_\sigma)\frac{\delta_{ij}}{\sigma_s}\right]M_j\,, \quad i,j,k = 1,2,3 \tag{11.1b}$$

where δ_{ij} is the Kronecker delta; $\varepsilon_{ij}, \sigma_{ij}, E$, and ν are the strain components, stress components, Young modulus, and Poisson ratio, respectively; and $\tilde{\sigma}_{ij} = \left(3\sigma_{ij} - \sigma_{kk}\delta_{ij}\right)/2$. In addition, H_i, M_i, M_s, λ_s, and σ_s denote the magnetic field intensity components, magnetization components, saturation magnetization, saturation magnetostriction, and a stress parameter, respectively. $\bar{M} = \sqrt{M_1^2 + M_2^2 + M_3^2}$, $I_\sigma = \sigma_{kk}$, $J_\sigma = \left(I_\sigma^2 - \sigma_{ij}\sigma_{ij}\right)/2$, and L^{-1} represents the inverse of Langevin function $L(x) = \coth(x) - 1/x$. Finally, $\mu_0 = 4\pi \times 10^{-7}$ is the vacuum permeability, and $k = 3\chi_m/M_s$, where χ_m stands for the magnetic susceptibility of the material.

For the beam shown in Fig. 11.1, if the magnetic field intensity is applied in the beam longitudinal direction, Eqs. (11.1a) and (11.1b) can be simplified to

$$\varepsilon_x = \left(\frac{1}{E} + \frac{\lambda_s}{\sigma_s}\right)\sigma_x + \lambda_s\frac{M_x^2}{M_s^2} - \frac{\lambda_s\sigma_x}{\sigma_s}\frac{M_x^2}{M_s^2} \tag{11.2a}$$

$$H_x = \frac{1}{k}L^{-1}\left(\frac{M_x}{M_s}\right) - \frac{\lambda_s}{\mu_0}\left(2\sigma_x - \frac{\sigma_x^2}{\sigma_s}\right)\frac{M_x}{M_s^2} \tag{11.2b}$$

The second of Maxwell's equations of electromagnetism (called the Gauss law for magnetism) states that

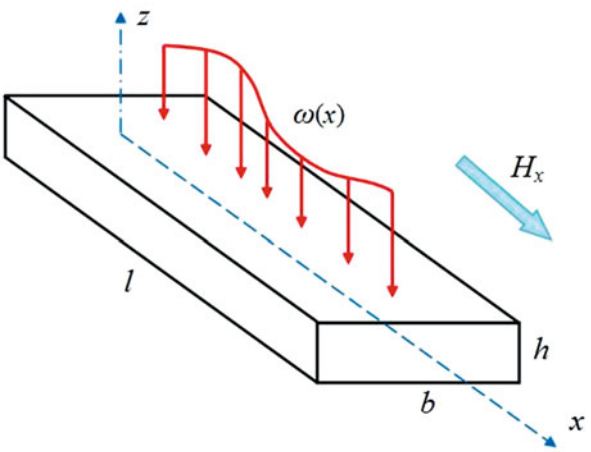

Fig. 11.1 Magnetostrictive beam and magnetomechanical loading

$$H_{x,x} + M_{x,x} = 0 \tag{11.3}$$

According to Eq. (11.3), for a magnetostrictive material in a constant magnetic field, the magnetization component in the direction of the field should also be constant. Therefore, the magnetization is a function of z only.

In the absence of any external longitudinal mechanical force, the force and moment resultants – which can be found in any mechanics of materials textbooks – are

$$\int_{-\frac{h}{2}}^{\frac{h}{2}} \sigma_x \mathrm{d}z = 0 \tag{11.4a}$$

$$\int_{-\frac{h}{2}}^{\frac{h}{2}} \sigma_x b z \mathrm{d}z = M \tag{11.4b}$$

where M is the external mechanical bending moment about the y-axis. For an Euler-Bernoulli beam with the coordinate system shown in Fig. 11.1, the total strain can be written as

$$\varepsilon_x = \varepsilon_0 - \kappa z \tag{11.5}$$

where ε_0 and κ denote the strain of the beam middle axis and the curvature of the beam, respectively. Rewriting Eq. (11.2a) and substituting in Eqs. (11.4a) and (11.4b) and using Eq. (11.5) yields

$$\int_{-\frac{h}{2}}^{\frac{h}{2}} \left[\varepsilon_0 - \kappa z - \lambda_s \frac{M_x^2}{M_s^2} - \frac{\lambda_s \sigma_x}{\sigma_s} \frac{M_x^2}{M_s^2}\right] \mathrm{d}z = 0 \tag{11.6a}$$

$$\frac{b}{\left(\frac{1}{E} + \frac{\lambda_s}{\sigma_s}\right)} \int_{-\frac{h}{2}}^{\frac{h}{2}} \left[\varepsilon_0 z - \kappa z^2 - \lambda_s \frac{M_x^2}{M_s^2} z - \frac{\lambda_s \sigma_x}{\sigma_s} \frac{M_x^2}{M_s^2} z\right] \mathrm{d}z = M \tag{11.6b}$$

Equations (11.6a) and (11.6b) can be integrated and rearranged to get

$$\varepsilon_0 = \frac{\lambda_s}{h M_s^2} \int_{-\frac{h}{2}}^{\frac{h}{2}} M_x^2 \left(1 - \frac{\sigma_x}{\sigma_s}\right) dz \tag{11.7a}$$

$$\kappa = \left(\frac{12}{h^3}\right) \left[\frac{M\left(\frac{1}{E} + \frac{\lambda_s}{\sigma_s}\right)}{b} - \int_{-\frac{h}{2}}^{\frac{h}{2}} M_x^2 \left(1 - \frac{\sigma_x}{\sigma_s}\right) z dz\right] \tag{11.7b}$$

Equation (11.2b) shows that the relation of magnetic field intensity with the corresponding component of magnetization is highly nonlinear. So the magnetization must be obtained numerically. For the case of pure bending, M is constant along the beam and, as a consequence, κ becomes constant. Therefore, the strain ε_x will be a function of z only. For this case, the deflection is obtained analytically with two successive integrations. The boundary conditions for a simply supported

(SS) or cantilever (C) beam can be found in any mechanics of materials book. Thus, the deflection can be written as

$$w(x) = \begin{cases} \frac{\kappa}{2}(x^2 - lx), & \text{for SS} \\ \frac{\kappa x^2}{2}, & \text{for C} \end{cases} \tag{11.8}$$

where l is the length of the beam and the cantilever beam is supposed to be clamped at $x = 0$. For the general loading case (bending due to transverse mechanical loading), the function $\kappa(x)$ can be determined, and two successive integrations yield the equation of the beam elastic curve.

11.3 Solution Algorithm

The following algorithm is utilized for solving the problem. First, with a given mechanical moment, an initial guess for $\sigma_x(z)$ is considered in the thickness direction. With a prescribed magnetic field intensity H_x, the magnetization component M_x can be obtained iteratively in each point through the thickness using Eq. (11.2b). The total strain profile $\varepsilon_x(z)$ is then achieved using Eqs. (11.7a), (11.7b), and (11.5). Then, using the obtained strain profile, the stress profile can be calculated using the rearranged form of Eq. (11.2a), which is a better estimation for the stress profile. The iteration follows up until a desired value of convergence is reached. The beam deflection is then found with twice integration of the curvature κ, along with application of the boundary conditions. This method is illustrated with a flowchart in Fig. 11.2.

11.4 Verification, Numerical Results, and Discussions

In order to validate the present method and obtain numerical results, the following values are considered for a Terfenol-D beam with a 10 cm × 10 cm rectangular cross section: $l = 1$m, $E = 110$ GPa, $M_s = 796$ kA/m, $\chi_m = 25$, $\sigma_s = 200$ MPa, and $\lambda_s = 1550$ ppm. Since there is no direct experimental work in the literature for bending of homogeneous magnetostrictive beams and because of the fact that for small deformations, a beam can be considered as several rods bonding together, it is possible to compare the results of a certain point in the thickness direction (e.g., the top point $z = 5$ cm) with those of a rod. Figure 11.3 shows the comparison of present results with the experimental results of Liang and Zheng (2007). The data used in this figure is tabulated in Table 11.1. The magnetostrictive strain (the contribution of magnetization to strain, denoted by λ) is plotted versus the longitudinal magnetic field intensity. As it can be observed, the present results match well with

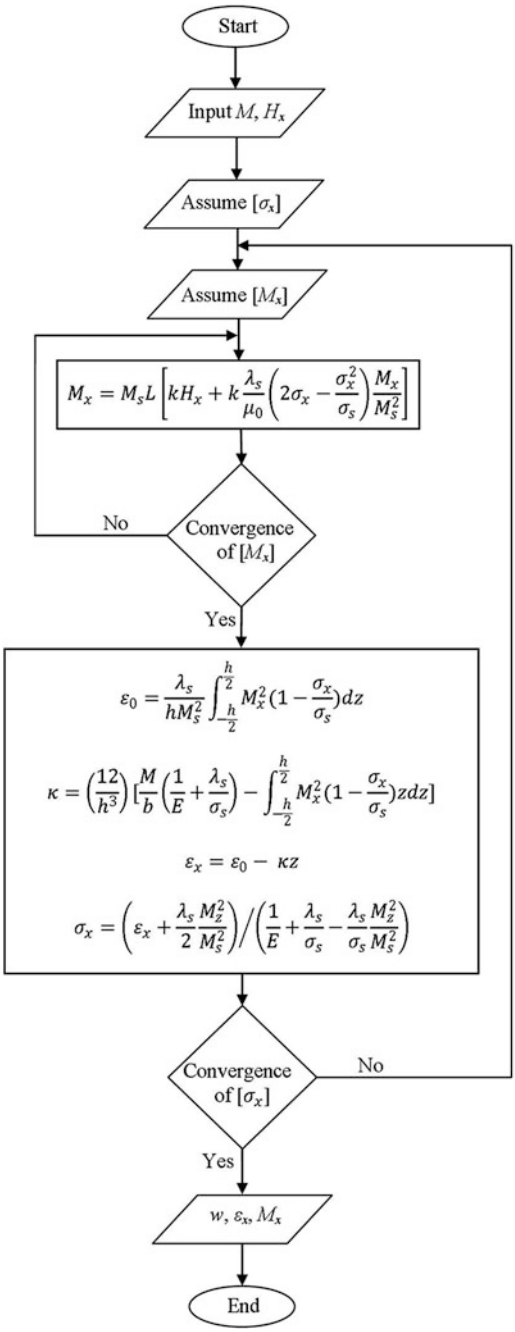

Fig. 11.2 Flowchart of the solution algorithm for bending of a magnetostrictive beam in longitudinal magnetic field

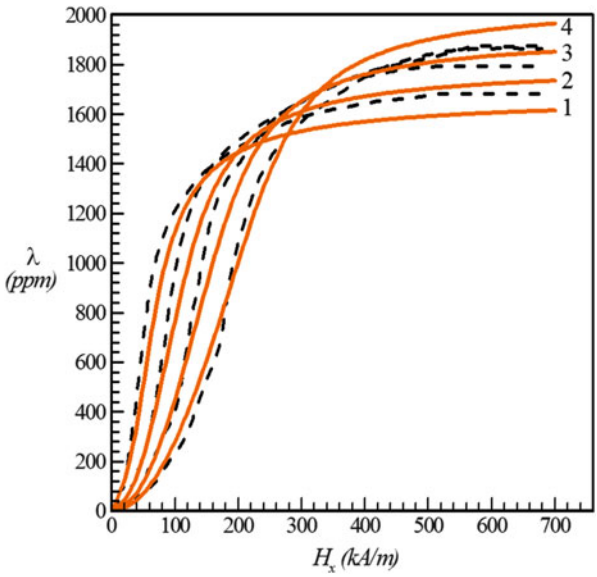

Fig. 11.3 Comparison of the present results (solid lines) with the experimental results (dashed lines) of Liang and Zheng (2007) using the data of Table 11.1

Table 11.1 The data corresponding to Fig. 11.3

Line number	Prestress (MPa)	Corresponding bending moment (kN.m)
1	−15.3	2.55
2	−32	5.33
3	−48.7	8.12
4	−65.4	10.9

experimental data in low, moderate, and high fields, which implies effectiveness of the model used in the present work for magnetostrictive beams.

In order to investigate the effect of pure magnetic field on the Terfenol-D beam, the magnetostrictive strain is plotted versus the magnetic field intensity in Fig. 11.4. In this case, the beam acts like a rod, and no deflection occurs due to the absence of prestress. It can be seen that the longitudinal magnetization tends to stretch the beam. This phenomenon happens due to the rotation of small magnetic domains and is discussed in detail in the literature.

The variation of maximum deflection with magnetic field for a cantilever beam subjected to a constant bending moment ($M = 5$ kN.m) is plotted in Fig. 11.5. As it can be seen, in the region of low fields, the maximum beam deflection increases rapidly due to magnetic domain anisotropy. As the magnetic field intensity grows, the magnetostriction effect dominates the deflection variations and the magnetic domains rotate almost uniformly in the thickness direction, which in turn decrease the curvature of the beam and, as a consequence, the deflection. In the high-field region, the deflection becomes less sensible to the magnetic field variations due to the magnetic saturation phenomena. It should be noted that the bending moment

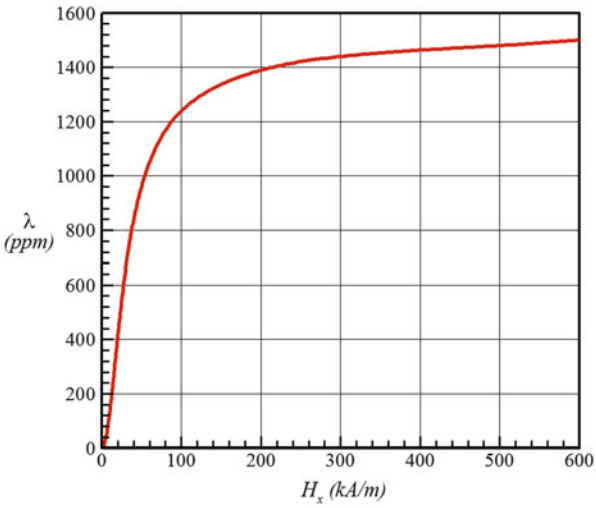

Fig. 11.4 Magnetostrictive strain versus magnetic field intensity for a cantilever beam, $M = 0$

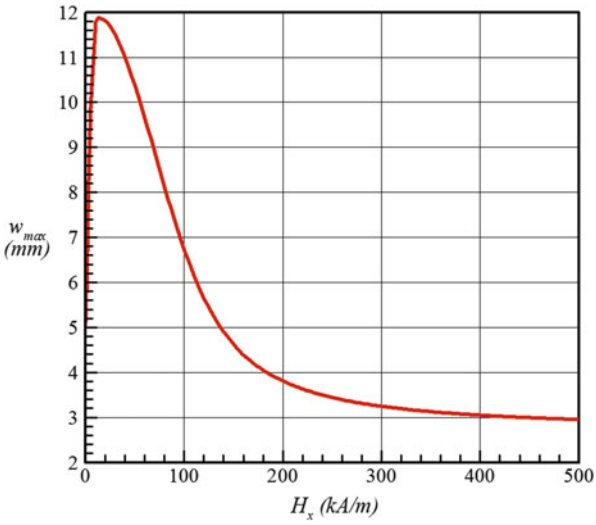

Fig. 11.5 Variation of maximum deflection with magnetic field intensity for a cantilever magnetostrictive beam, $M = 5$ kN.m

must be chosen in such a way that the condition $-\sigma_s/2 \leq \sigma_x \leq \sigma_s$ holds for prestress throughout the beam thickness. Otherwise, some enormous errors and physically impossible results may occur (Liu and Zheng 2005).

One of the most important properties of magnetostrictive materials is their change in magnetic domain alignment. The stress tends to align the magnetic domains perpendicular to the axis of the beam, and thus, a pre-strain is produced in the material before the beam is magnetized. This property is reported and discussed in some references (Liu and Zheng 2005; Jin et al. 2012a, b; Zheng and Sun 2007). In order to show this effect on beam deflections, two plots are presented in Fig. 11.6 for simply supported and cantilever beams. It can be seen that the

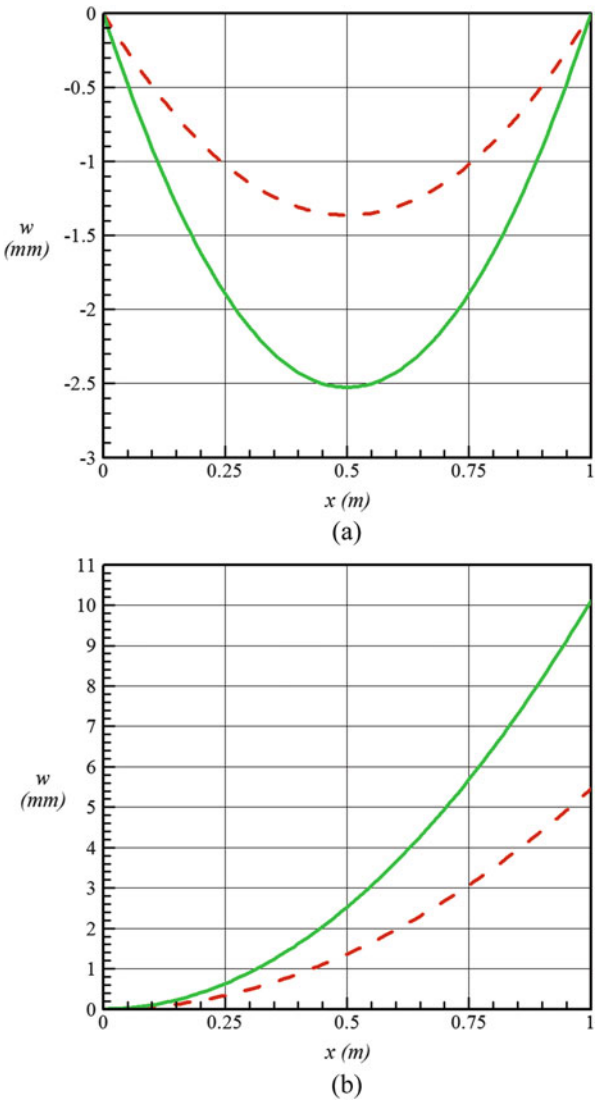

Fig. 11.6 Deflection of (**a**) simply supported and (**b**) cantilever beam for $M = 10$ kN.m and $H = 0$

maximum deflection of a magnetostrictive beam is about two times larger than the same beam made of conventional materials (with the same elastic modulus).

Solid lines represent $\lambda_s = 1700$ ppm and dashed lines represent $\lambda_s = 0$.

Figure 11.7 shows the variation of magnetization through the thickness of the beam in a constant magnetic field intensity. Although the magnetic field is constant, the magnetization varies nonlinearly through the thickness. This is because of the stress-magnetization coupling of magnetostrictive materials. When a beam is subjected to bending, the stress varies in the thickness direction and, as a consequence, the magnetization varies in that direction. This fact can be seen from the

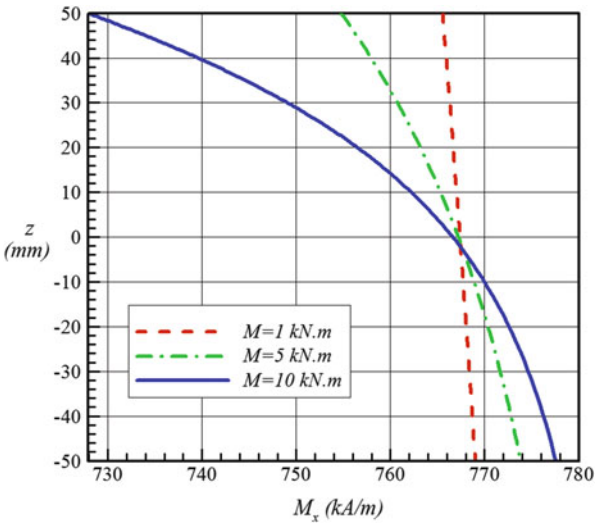

Fig. 11.7 Variation of magnetization through the thickness of the beam for $H_x = 300$ kA/m

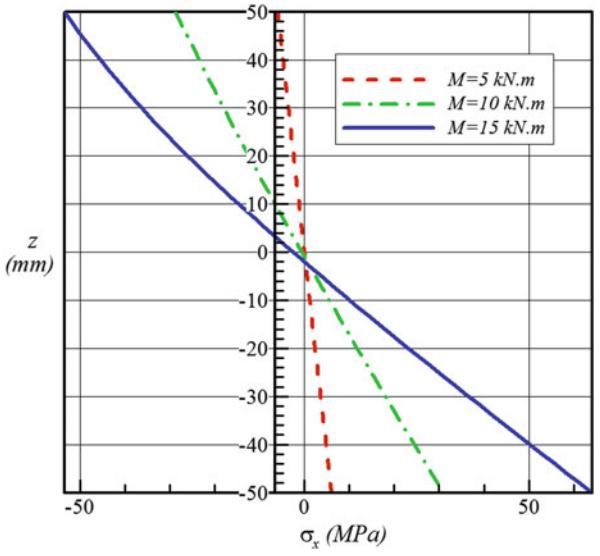

Fig. 11.8 Variation of stress through the thickness of the beam for $H_x = 300$ kA/m

Langevin function in Eq. (11.1b). When the bending moment is low (under 1.5 kN. m), the variation of magnetization through the thickness is approximately linear, but in higher bending moments, due to the effect of stress in either Eqs. (11.2b) or (11.3), the variation becomes nonlinear.

Both Eqs. (11.2a) and (11.2b) show that while the total strain is assumed to vary linear in z-direction, the stress varies nonlinearly due to the magnetization. Thus, the stress neutral axis will not coincide with the strain neutral axis. As an example, the variation of stress through the beam thickness is plotted in Fig. 11.8 for a beam subjected to uniform longitudinal magnetic field.

11.5 Conclusions

In the present chapter, a semi-analytical solution was proposed for bending analysis of magnetostrictive materials, based on the Liu and Zheng nonlinear constitutive model. Through the mechanical loading, a linear prestress was introduced to the beam. A longitudinal magnetic field intensity was applied to the beam uniformly. In this model, the Langevin function is used to relate the magnetic field intensity and magnetization, so the magnetization components were obtained iteratively through the well-known Newton-Raphson method. The middle axis strain and the curvature were next computed to obtain the linear strain profile. Next, a better estimation for stress profile was found using the rearranged form of the constitutive relation. The procedure then continued until a desired value of convergence was reached. As a special case, the magnetostrictive beam subjected to pure bending was considered, and the numerical results were obtained for two cases of simply supported and cantilever beams. In order to validate the present results, a comparison was done between the magnetostrictive strains obtained in the present work and those of experimental analysis of magnetostrictive rods. In order to do the comparison, the beam was considered to consist of several rods bonding together. So, one of these rods was compared with experimental rod analysis in various loading conditions. Next, the nonlinear stress and magnetization profiles and the variation of beam deflection versus magnetic field intensity were plotted and discussed as the results. It has been discussed that with the increase in magnetic field intensity, the beam deflection firstly increases in the range of low to moderate fields and then decreases smoothly until the saturation value in high-field region. It has been shown that the Liu and Zheng nonlinear model can accurately catch the experimental results and is suitable in one-dimensional form for beam analysis as well as rod analysis. This method can be extended to thermal analysis of nonlinear magnetostrictive beams, plates, and shells either in homogeneous forms or composites.

References

Aboudi, J., Zheng, X., & Jin, K. (2014). Micromechanics of magnetostrictive composites. *International Journal of Engineering Science, 81*, 82–99.

Bozorth, R. M., & Williams, H. J. (1945). Effect of small stresses on magnetic properties. *Reviews of Modern Physics, 17*(1), 72.

Carman, G. P., & Mitrovic, M. (1995). Nonlinear constitutive relations for magnetostrictive materials with applications to 1-D problems. *Journal of Intelligent Material Systems and Structures, 6*(5), 673–683.

Clark, A. E., Teter, J. P., & McMasters, O. D. (1988). Magnetostriction "jumps" in twinned Tb0.3Dy0.7Fe1.9. *Journal of Applied Physics, 63*(8), 3910–3912.

Duenas, T. A., Hsu, L., & Cakman, G. P. (1996). Magnetostrictive composite material systems analytical/experimental. In *MRS Proceedings* (Vol. 459, p. 527). New York: Cambridge University Press.

Jiles, D. C. (1995). Theory of the magnetomechanical effect. *Journal of Physics D: Applied Physics, 28*(8), 1537.

Jiles, D. C., & Atherton, D. L. (1986). Theory of ferromagnetic hysteresis. *Journal of Magnetism and Magnetic Materials, 61*, 48–60.

Jin, K., Kou, Y., & Zheng, X. (2012a). A nonlinear magneto-thermo-elastic coupled hysteretic constitutive model for magnetostrictive alloys. *Journal of Magnetism and Magnetic Materials, 324*(12), 1954–1961.

Jin, K., Kou, Y., & Zheng, X. (2012b). The resonance frequency shift characteristic of Terfenol-D rods for magnetostrictive actuators. *Smart Materials and Structures, 21*(4), 045020.

Liang, Y., & Zheng, X. (2007). Experimental researches on magneto-thermo-mechanical characterization of Terfenol-D. *Acta Mechanica Solida Sinica, 20*(4), 283–288.

Linnemann, K., Klinkel, S., & Wagner, W. (2009). A constitutive model for magnetostrictive and piezoelectric materials. *International Journal of Solids and Structures, 46*(5), 1149–1166.

Moffett, M. B., Clark, A. E., Wun-Fogle, M., Linberg, J., Teter, J. P., & McLaughlin, E. A. (1991). Characterization of Terfenol-D for magnetostrictive transducers. *The Journal of the Acoustical Society of America, 89*(3), 1448–1455.

Sablik, M. J., & Jiles, D. C. (1993). Coupled magnetoelastic theory of magnetic and magnetostrictive hysteresis. *IEEE Transactions on Magnetics, 29*(4), 2113–2123.

Schatz, F., Hirscher, M., Schnell, M., Flik, G., & Kronmüller, H. (1994). Magnetic anisotropy and giant magnetostriction of amorphous TbDyFe films. *Journal of Applied Physics, 76*(9), 5380–5382.

Smith, R. C., Dapino, M. J., & Seelecke, S. (2003). Free energy model for hysteresis in magnetostrictive transducers. *Journal of Applied Physics, 93*(1), 458–466.

Wan, Y., Fang, D., & Hwang, K. C. (2003). Non-linear constitutive relations for magnetostrictive materials. *International Journal of Non-Linear Mechanics, 38*(7), 1053–1065.

Liu, X., & Zheng, X. (2005). A nonlinear constitutive model for magnetostrictive materials. *Acta Mechanica Sinica, 21*(3), 278–285.

Zheng, X., & Sun, L. (2007). A one-dimension coupled hysteresis model for giant magnetostrictive materials. *Journal of Magnetism and Magnetic Materials, 309*(2), 263–271.

Zheng, X., Sun, L., & Jin, K. (2009). A dynamic hysteresis constitutive relation for giant magnetostrictive materials. *Mechanics of Advanced Materials and Structures, 16*(7), 516–521.

Chapter 12
Limited Data Modelling Approaches for Engineering Applications

Hamid Khayyam, Gelayol Golkarnarenji, and Reza N. Jazar

12.1 Introduction

Over the past several years, the study of various complex systems has been of great interest to researchers and scientists. Complex systems and problems are very pervasive and appear in different application areas including education, healthcare, medicine, finance, marketing, homeland security, defense, and environmental management, among others. In these systems, many components are involved with nonlinear interactions. Forecasting the future state of a complex system and designing such a system are very costly, time consuming, and compute intensive due to project times and technical constraints in industry. To overcome these complexities and save considerable amount of cost, time, and energy, modelling can be utilized. Modelling is generally defined as mathematical realization and computerized analysis of abstract representation of real systems. It helps achieve comprehensive insight into the functionality of the modelled systems, investigate the performance and behavior of processes, and finally optimize the process control. Mathematical modelling is an inexpensive and a powerful paradigm to deal with real-world complex problems. It comprises a wide range of computational methods. This technique can lower the costs by reducing the number of experiments and increasing the safety by forecasting the events, the results of laboratory tests, or the industrial data (Dobre and Sanchez Marcano 2007; Pham 1998; Rodrigues and Minceva 2005).

H. Khayyam (✉) • R.N. Jazar
School of Engieering, RMIT University, Melbourne, VIC, Australia
e-mail: hamid.khayyam@rmit.edu.au

G. Golkarnarenji
Institute for Frontier Materials, Carbon Nexus, Deakin University, Waurn Ponds, VIC, Australia

L. Dai, R.N. Jazar (eds.), *Nonlinear Approaches in Engineering Applications*,
https://doi.org/10.1007/978-3-319-69480-1_12

It is difficult to classify mathematical modelling. Any classifications depend directly on the subject of the study. According to Rasmuson et al. (2014a), mathematical modelling is divided into two main categories: deterministic (based on physical and chemical structure of the problem) and heuristic (based on experimental results). Deterministic mathematical models are based on physical and chemical theories and equations including rate of chemical reactions, mass balance, heat balance, and momentum-energy balance (Navier-Stokes equations). This model is constructed entirely from the prior knowledge and physical insight. Since there are not sufficient theoretical support and experiments by deterministic models to especially analyze complex systems, this type of problems can be solved by heuristic modelling techniques. In cases when little is known about the actual system process and no or some physical insight is available, these techniques are solutions to obtain models. These models are used when the system is very complicated; time, resources, and theory are limited; and developing analytical models is very difficult and even impossible. Although the development of these models may require less effort and is simpler, they are the only relevant methods for restricted range of operation and scale-up. These techniques are highly developed technologies and effective modelling tools that can be used to deal with complexity and vague parts of a system process. Heuristic modelling is to predict the probability of a result. To build an accurate data model, sufficient amount of data is needed. The number of data depends on the nature of the problem, the quality of the data, and the proportion between the numbers of instances and the number of attributes. One of the basic principles in classical statistics is the law of large numbers. Based on this principle, the empirical distribution function $F_l(x)$ converges to the distribution of $F(x)$ when the number of data tends to infinity. In other words, in order to get a reliable mathematical model using machine learning methods, the training set should include infinite number of samples. Algorithms use data to find the patterns and the more data advances the accuracy of the model. In many situations in real world, however, it is not possible to have so many samples for training and mathematical modelling. In these situations, the enterprises must deal with a small number of data, such as dealing with pilot production of a new product in the early stages of a system, small number of customers, and some rare diseases when a few medical records are available (Ruparel et al. n.d.). Small data set conditions exist in many fields, such as fault diagnosis, disease diagnosis, or deficiency detection in manufacturing industry, mechanics, aviation, and many more (Mao et al. 2006; Li and Wen 2014a). One main problem with small data set is overfitting in model development which gives good results on training data and poor performance on testing data (Ali 2009).

There are various definitions regarding small sample size. According to one study, small data is rarely less than 5, sometimes between 5 and 20, often between 30 and 50 or 50 and 100, and some cases between 1000 and 3000. Small data are rows of observations and columns of variables which do not include statistical outliers and influential points (Ratner 2011). Based on central limit theorem (Ross 2009) which is one of the basic theories in statistics, when the size of a sample is large ($\geq$25 or 30), the x-bar distribution is almost normal without the

population distribution being considered. Hence, the sample size less than 25 (or 30) is considered as small. According to Huang (2002), the definition of concept "small" is as follows.

Suppose $X = \{x_i | \, i = 1, 2, \ldots, n\}$ is employed as a sample from a population. In order to determine a relationship R defined on Ω, X is employed. Γ is defined as the operator space, which can be used to estimate R with a given sample. To indicate the value of R at a point $x \in \Omega$, $r(x)$ is used. $r_x^{\gamma}(x)$ is the estimate with X by γ, and $\left| r_x^{\gamma}(x) - r(x) \right|$ is the estimate bias, $\forall \, \gamma \in \Gamma$, $\exists \, x \in \Omega$.

X is called small if and only if its size n is too small to obtain the required accuracy which is the similarity between $r_x^{\gamma}(x)$ and $r(x)$ for identifying a relationship of the population from which X is employed. Hence, based on different applications, the definition of sample size varies due to the level of required accuracy.

In order to describe or explain the establishment of validity, statistical reliability, and replicability to deal with real-world applications for small sample size, design of experiment (DOE) methods including factorial, response surface, and Taguchi are used (Davim 2015). Researchers and engineers construct the suitable DOE methods that are best for predicting the outcome data.

Some developed DOE based on Taguchi method to reduce experimental tests and useful for data modelling have been constructed (Khayyam et al. 2015a, 2017). Developing an appropriate forecasting model with smaller variance of forecasting error and good accuracy based on small data sets will boost the management effectiveness and help the enterprises to meet the competitive environment (Li et al. 2012). In data modelling, the most prevailing categories of machine learning techniques and different types of prediction for system identification are classification and regression. These methods are supervised learning problems, where a system is presented with input and outputs, and the aim is to map inputs to outputs through learning a function. Classification is one of the most commonly used prediction methods. In this method, an observation needs to be assigned to a predefined class or group. Many industrial problems are recognized as classical problems which can be solved mathematically in a nonlinear method. A regression problem is a type of classification except when the output variable is a real value instead of a category (Ali and Smith 2006). In addition, it is used to understand and explore the forms of the relationships between independent variables that are related to the dependent variable.

These techniques and methods have been described in the following sections. It must be noted that the categorization of these techniques is barely based on their ubiquity in industry. Many of the methods mentioned below can be applied to both classification and regression problems. This section is organized as follows. Sections 12.2 and 12.3 present the data modelling techniques including classification and regression. Section 12.4 describes the resampling techniques used in these modelling techniques for data modelling. Section 12.5 presents some of the applications of these methods for limited data. Conclusion remarks are given in the last section.

12.2 Classification Techniques

Classification is one of the most used machine learning methods. Classification is the prediction of categorical (discrete or unordered) class labels for unlabeled patterns based on the observations. Models or classifiers are constructed to describe important data classes in classification. Classification assists in better understanding of the data (Han et al. 2011). Let $\{(\boldsymbol{x}_1, y_1), \ldots, (\boldsymbol{x}_N, y_N\}$ be training set of q-dimensional patterns $\mathbf{X}=\{x\}_{i=1}^{N} \subset R^q$ and a corresponding set of lables $\mathbf{Y}=\{y\}_{i=1}^{N} \subset R$. The aim of classification is to predict the class label y' for an unseen pattern $\boldsymbol{x}'$ by constructing a model f. The classifier should be able to assign patterns without labels to labels of patterns with identified assignment that are alike.

12.2.1 LDA and QDA and PCA

In order to improve the generalization ability and robustness of a classifier, various methods can be used. Principal component analysis (PCA) and linear discriminant analysis (LDA) are two frequently used feature extraction methods. LDA is a supervised technique. In discriminant analysis, various classes belong to a known probability density function. The covariance matrix and mean of classes are estimated, and the new sample belongs to the class with the highest probability. In LDA, the covariance matrix and mean of the distribution of class models are the same. However, in quadratic discriminant analysis (QDA), the covariance and mean of various classes are different (Sharma and Paliwal 2015). PCA is an efficient unsupervised technique to analyze the data of high dimension and to find a smaller number of unrelated variables called principal components from a large set of correlated variables without loss of information. The aim of this method is to describe the maximum amount of variance with the fewest number of principal components. In general, in terms of classification performance, LDA outperforms PCA (Ilin and Raiko 2010).

LDA method for limited data can be found in many application areas including bioinformatics, text and face recognition, etc. The PCA method can also be found in many application fields including petroleum, nano-material manufacturing, and nuclear power plant industries.

12.2.2 K-Nearest Neighbor Algorithm (K-NN)

One of the famous classification methods which is simple yet powerful is K-NN classifier. It can be used for both classification and regression problems. However, it is more widely used in classification problems in the industry. Based on the idea behind the K-NN classifier, useful label information can be obtained from the

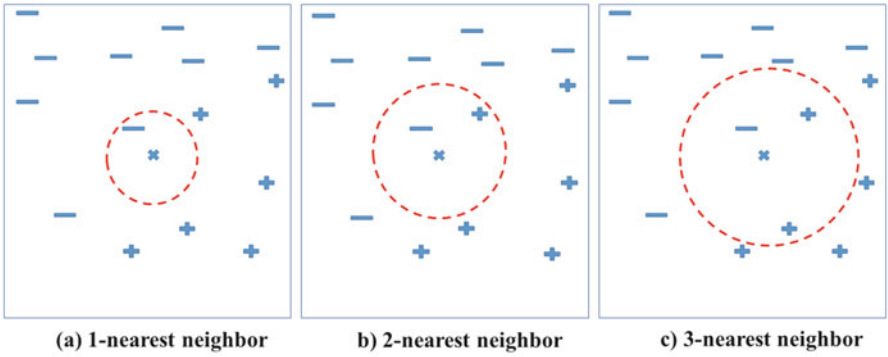

Fig. 12.1 K-nearest neighbor algorithm for (**a**) $k = 1$, (**b**) $k = 2$, and (**c**) $k = 3$ (Ertekin 2012)

nearest patterns to a target pattern $\boldsymbol{x}'$. The class labels of most of the K-nearest patterns in data space are predicted with this class (Fig. 12.1).

A similarity measure should be defined in data space, and Minkowski metric is employed for this purpose:

$$\left\|\boldsymbol{X}' - \boldsymbol{X}_j\right\|^p = \left(\sum\nolimits_{i=1}^{q} \left|(x_i)' - (x_i)_j\right|^p\right)^{1/p} \tag{12.1}$$

which is the Euclidean distance when $p = 2$. In the case of binary classification, $\{1,-1\}$ are used as labels, and K-NN is as follows:

$$f_{\mathrm{K-NN}}(\boldsymbol{x}') = \begin{cases} 1 & \text{if } \sum_{i\in \mathrm{N}_K(x')} y_i \geq 0 \\ -1 & \text{if } \sum_{i\in \mathrm{N}_K(\boldsymbol{x}')} y_i < 0 \end{cases} \tag{12.2}$$

where K is the neighbor size and $\mathrm{N_K}(\mathbf{x}')$ is the set of indices of the K-nearest patterns.

In the case of multi-class classification, K-NN gives the class label of most of the K-nearest patterns in data space for an unseen pattern $\mathbf{x}'$:

$$f_{\mathrm{K-NN}}\left(\boldsymbol{X}'\right) = \arg\max \quad y = Y \sum\nolimits_{i\in \mathrm{N}_K(\boldsymbol{x}')} L(y_i = y) \tag{12.3}$$

When the argument of indicator function L(•) is true, it returns 1; else it returns zero.

The selection of value of k which determines the locality of K-NN is of myriad importance. Smoother decision regions and probabilistic information are obtained by large K values. However, it has a damaging effect when too large values of K are selected due to destroying the locality of the estimation. Odd numbers are usually chosen for values of K. The value of K can be grid searched by determining the classification error rate using a test set (Peng et al. 2017). K-NN has been used in many fields of application including computer vision, pattern recognition, image classification, intrusion, and fraud detection.

12.2.3 Support Vector Machine (SVM)

SVM is a fairly new powerful intelligent and flexible supervised learning algorithm used classification problems and pattern recognition. It was developed by Vapnik (Kulkarni and Harman 2011; Vapnik 1999; Burges 1998) and is based on structural risk minimization. Global optimal points can be reached using this method, and it does not have the local minimum problem. SVM can be used for both regression and classification. In problems of small data sets, it has special generalization ability (Chen 2004).

Support vector machine (SVM) forms hyperplanes in a multidimensional space that draws a boundary between cases of different class labels (Chapelle et al. 2002). SVM builds an optimal hyperplane by minimizing an error function using an iterative training algorithm. SVM models can be divided into four different categories based on the error function (Abd and Abd 2017):

- Classification SVM Type 1 (C-SVM classification)
- Classification SVM Type 2 (nu-SVM classification)
- Regression SVM Type 1 (epsilon-SVM regression)
- Regression SVM Type 2 (nu-SVM regression)

SVM is part of maximum margin classifiers which define a boundary hypersurface with maximum distance from the training points of the two classes (Fig. 12.2).

A traditional SVM boundary is a vector $\boldsymbol{w} \in R^q$ and an offset b which constructs a hyperplane $(\boldsymbol{w},b)$ in R^q:

$$W^T \boldsymbol{Z} + b = 0 \qquad Z \in R^q \tag{12.4}$$

Space R^q is divided into two regions $\hat{z}_+$ and $\hat{z}\_$ by the hyperplane $(\boldsymbol{w},b)$:

$$\hat{z}_+ = \{Z \in R^q : W^T \boldsymbol{Z} + b < 0)$$

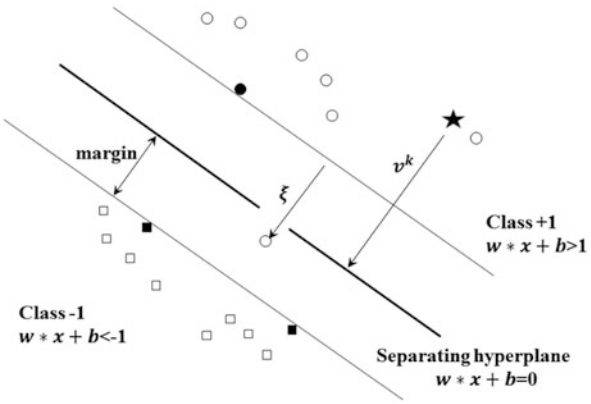

Fig. 12.2 A separating hypersurface with maximum distance from the training points of the two classes (Leopold and J. Kindermann 2006)

$$\hat{z}_{-=} \{Z \in R^q : W^T \mathbf{Z} + b > 0)$$

However, only plane boundaries are constructed with this hyperplane which makes it inadequate for many highly nonlinear engineering problems $f(x) = V_0$. This problem can be solved by selecting a suitable nonlinear transformation $Z = \phi(x) : R^s \rightarrow R^q$ which makes it possible to define curved boundaries in R^s by using the same approach. The separation of R^s is performed based on the sign of the decision value $d(x)$ in this case.

$$d(x) = TW\phi(x) + b \tag{12.6}$$

Classes X_- and X_+ can be predicted as follows:

$$\begin{aligned} \hat{C}_+ &= \{X \in R^q : W^T \phi(x) + b < 0\} \\ \hat{C}_{-=} &\left\{Z \in R^q : W^T \phi(x) + b > 0\right\} \end{aligned} \tag{12.7}$$

SVM parameters for a good approximation of the boundary B must be selected to separate the sets C_- and C_+ (defined by the sign of $f(x) - V_0$) and $\hat{C}_+$ and $\hat{C}_-$ (defined by the decision value $d(x)$). The SVM boundary B can then approximate the limit hypersurface:

$$\hat{B} = \{\mathbf{z} : \mathrm{d}(\mathbf{z}) = 0\}$$

The optimal values of $\mathbf{w}$ and b can be obtained using the training set $\mathrm{D_N}$ defined as

$$D = \{(x_i, c_i)\} \text{ with } c_i = c(x_i), i = 1, 2, .., N$$

and the optimization problem:

$$\begin{aligned} \arg\min_{w,b,\xi} &= \frac{1}{2}\|w\|^2 + C\sum_{i=1}^{N} \xi_i \\ \text{Subject to} &= c_i\left(w^T \phi(x_i) + b\right) \geq 1 - \xi_i = \xi_i \geq 0, i = 1, \ldots\ldots, N \end{aligned} \tag{12.8}$$

A minimum of $\mathbf{w}$ is the classification margin (maximum distance between the boundaries and the separated classes). The combination of the other term with the first constraint is the classification error for the training set ($x_i \in \hat{C}_-$ and $x_i \notin C_-$, or $x_i \in \hat{C}_+$ and $x_i \notin C_+$). Hence, the conflicting objectives of minimizing the misclassification error and maximizing the classification margin are defined by Eq. (12.8). In order to find a favorable trade-off between these two objectives, parameter C should be tuned. High C will increase the misclassification error and decrease the classification margin. A low value of C decreases the misclassification error and increases the classification margin. The optimal value of $\mathbf{w}$ depends on the weighted sum of the transform of the training set $\phi(x_i)$:

$$w = \sum_{i=1}^{N} c_i \alpha_i \phi(x_i \ ) \tag{12.9}$$

The sign of $c_i = \pm 1$ and the magnitude of the Lagrange multipliers $\alpha_i \geq 0$ in the first constraint of Eq. (12.8) define the weighting coefficients of each summation term in Eq. (12.9). By combining Eqs. (12.6) and (12.9), the kernel-based SVM is presented as

$$d(x) = \sum_{i=1}^{N} c_i \alpha_i k(x, x_i) + b \tag{12.10}$$

where the kernel function is $k(x, y) = \phi T(x)\phi(y)$.

Typically, $\alpha_i > 0$ only for a subset of the N training data points, adequately close to the boundary. The points in this subset $V \subset D$ are support vectors, and the summation of Eq. (12.8) is limited to less than N terms due to their definition:

$$d(x) = \sum_{(x_i c_i) \in V} c_i \alpha_i k(x, x_i) + b \tag{12.11}$$

C has a great effect on the number of support vector set. The number of support vectors increases with high C and results in high-curvature sections in the boundary; however, low C decreases the number of the support vectors and smooths the surface. Many kernel functions can be used for $k(x, y)$. The most frequently used one is radial basis function kernel which is defined as

$$k(x, y) = e^{-\gamma \|x-y\|^2} \tag{12.12}$$

SVM has been used in many fields of applications, including image classification and recognition, fraud detection, and text categorization (Cholette et al. 2017).

12.2.4 Decision Tree (DT)

A decision tree is a flowchart-like tree structure with many branches and nodes. It is a very fast and easy method to be used. Trees can be used for both classification and regression problems. However, it is widely used in classification problems. Large dimensional data can be handled by decision trees. The non-leaf nodes (internal nodes) are tests on an attribute, the branches denote the result of the test, and each leaf node (or terminal node) represents label of a class and the predictions. The root node is the attribute that performs the best classification on data. To split the data, the second best attribute is used. The issue at each node is to choose the variable and how to split. The decision tree algorithms are due to the method of attribute selection used to test the instances at each node. In order to improve accuracy of the classification on unknown data, many branches which are outliers or noise should be removed by tree pruning (Han et al. 2011) (Fig. 12.3).

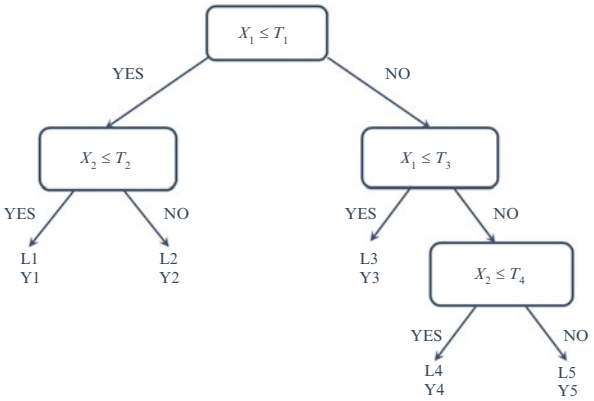

Fig. 12.3 An example of a decision tree (Ghiasi and Mohammadi n.d.)

Decision tree generation algorithm is as follows:

Input:

- *Data partition*, D, the training sets and their class labels
- *Attribute list*, the candidate attribute sets
- *Attribute selection method*, a method which best divides the data sets into separate classes by a splitting criterion. Split point or splitting subset and splitting attribute are parts of this criterion. The common method used is information gain or Gini index. Gini index method results in binary trees. Information gain allows growth of two or more branches from a tree.

Output Decision tree

Method

Generate node N
If all the tuples in D belong to class C,

N is a leaf node with label of class C.

If attribute-list is empty then

Assign N as a leaf node with the label of the majority class in D

Apply attribute-selection-method to find the best splitting-criterion and label node N
If splitting-attribute has a separate value and it is not just a binary tree then

Attribute-list = attribute-list-splitting –attribute

For each result j from splitting–criterion

Assign the set of data in D which satisfy the outcome j as Dj
If Dj is empty

Let node N be a leaf labeled with the label of majority class in D

Else let node N be the node returned by generate–decision tree (Dj, attribute list)

End for
Return N

Decision tree has been used in different application areas such as financial analysis, manufacturing and production, astronomy, and many more (Rokach and Maimon 2014).

12.2.5 Bayesian Approaches

Bayesian classification is a probabilistic model which learns the distribution of the instances with different class values to solve the classification problem.

12.2.5.1 Bayesian (Naive Bayes)

Naive Bayesian (simple Bayesian) classification is one of the most easy and efficient classification methods. Let X be a sample of data without any labels. H is a hypothesis that X is a part of a specified class, C. The aim is to determine $P(H|X)$ showing our confidence in the hypothesis after X is given. To calculate the posterior probability $P(H \mid X)$ using $P(H)$, $P(X)$, and P(X|H), Bayesian theorem is used. The posterior probability is calculated as follows (Shatovskaya et al. 2006):

$$P(H|X) = \frac{P(X|H).P(H)}{P(X)} \tag{12.13}$$

Assume that we have a set of m samples $S = \{S1, S2, \ldots, Sm\}$. Each sample is an n-dimensional feature vector $\{X1, X2, \ldots, Xn\}$ which is the training data set. Xi values are related to attributes $A1, A2, \ldots, An$, respectively. Suppose that $c1, c2, \ldots, ck$ are k existed classes and each sample belongs to one of these classes. The aim is to predict the class for sample X with an unlabeled class. This is possible by using the highest conditional probability $P(C_i|X)$, $i = 1, 2\ldots, k$.

The naive Bayesian theorem is calculated as given below:

$$P\ (C_i|X) = \frac{P(x|C_i).P(C_i)}{P(X)} \tag{12.14}$$

In order to maximize $P\ (C_i|X)$, $P(X|\,C_i)$. $P(C_i)$ should be maximized as $P(X)$ is constant for all the classes.

$P(C_i)$ is calculated as follows:

$$P(C_i) = \frac{\text{number of trainning samples in class } C_i}{m} \tag{12.15}$$

where m is the total number of training samples.

As there is a conditional independence between attributes, we can calculate $P\ (C_i|X)$ as follows:

$$P(Ci \mid X) = \prod_{t=1}^{n} P(X_t|\ Ci) \tag{12.16}$$

where X_t are attribute values in sample X.

The probabilities $P(X_t|C_i)$ can be estimated from the training data set calculating for each attribute columns. In order to calculate $P(X_t|C_i)$, density functions such as Gauss, lognormal, gamma, and Poisson distributions can be used. $P(X_t|C_i)$ is calculated as follows with the assumption of Gauss distribution for data:

$$P(X_t|C_i) = \frac{1}{\sqrt{2\pi\sigma_i^2}} e^{-\frac{(x_t-\mu_i)^2}{2\sigma_i^2}} \tag{12.17}$$

where μ is the mean and $-\infty < \mu < +\infty$ and σ is the standard deviation and $\sigma > 0$ (Catal et al. 2011).

Naive Bayes has been used in many fields of application including text classification, anomaly, fraud, and fault detection in engineering.

12.2.5.2 Bayesian Belief Network (BBN)

This method is a probabilistic graphical model which finds the dependencies among variables (Pearl 2014). BBN is used when available data is incomplete, uncertain, and inaccurate. It is based on directed acyclic graph (DAG) with nodes denoting the variables and directed links presenting the probabilistic conditional dependence. In this method, the variables are related in a family relationship. Suppose x_1 and x_2 are the parents and y is a child. x_1 is a parent of y if a link connects x_1 to y. Mutual excusive states define the variables, and conditional probabilities quantify their relations for each feasible combination of these states.

For N mutually exclusive hypotheses ($i = 1, 2, \ldots, n$), Bayes theorem determines the unknown parameter as follows:

$$p(H_i|E) = \frac{p(E|H_i) * p(H_i)}{\sum_{i=1}^{n} p(E|H_i) * p(H_i\ )} \tag{12.18}$$

where $p(H_j|E)$ is the posterior probability for the hypothesis $H(j = 1, 2, \ldots, n)$ based on the acquired evidence E. $p(H_i)$ is the prior probability. $p(E|H_j)$ shows conditional probability. When H_j is true, the denominator which is a constant value shows the total probability. Unconditional or prior probability is the likelihood of an event before any evidence is given. Posterior probability is the likelihood after the observation. This equation is used in BBN (Janssens et al. 2006).

BBN is created as follows:

1. Identifying variables that have effect on the response variable.
2. The conditional dependence of the variables is shown by arrows. It is important that the connection of variables is based on cause-effect assumption and not on the correlation.
3. By determining prior probability of each state, the mutually exclusive and collectively exhaustive states are given to parent variables. Unknown apriority is for the unconditional probability of variables with no parent nodes. In this case for each state $1/n$ probability is assigned where n is the total number of states of variables.

BBN has been used in many fields of application including accident modelling and risk analysis in chemical and process industry, fault diagnosis, pattern recognition, and knowledge discovery.

12.2.6 Ensemble Method

Ensemble method is a combination of multiple models such as classifiers to create an improved learning method which is high in performance. In this method, the unseen data is passed to each base classifier which returns a vote. The ensemble method returns the final class prediction based on the majority of the votes of the classification models. This method is suitable when there is not enough data available to present the distribution of the data. This method is chosen when there is uncertainty of choosing the computational model to solve the problem. This method is also used when the given classifier is not capable of solving the problem due to the complexity of the method. The ensemble methods such as bagging, boosting, and random forests are to process the multiple votes to reach the final prediction (Cosma et al. 2017) (Fig. 12.4).

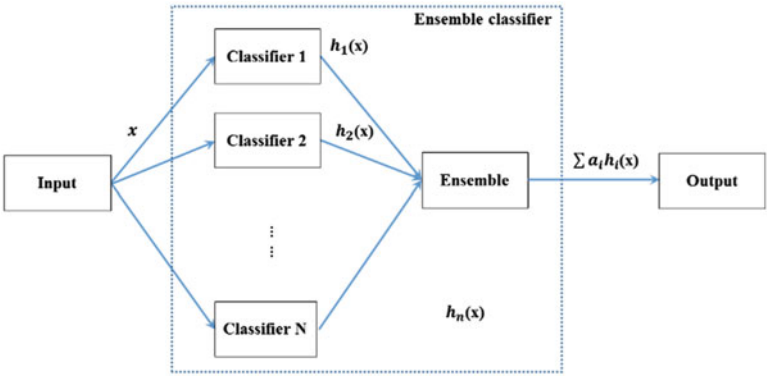

Fig. 12.4 An example of ensemble learning (Xu et al. 2015)

This method has been used in many application areas such as malware fraud and intrusion detection, remote sensing, speech, person recognition, and many more.

12.2.6.1 Random Forest (RF)

RF is an efficient ensemble method and is a cluster (ensemble) of many decision trees where each tree is built by bootstrap sampling (sampling with replacement) (Breiman 2001; Datla 2015). It can be used for both classification and regression problems. However, it is extensively used in classification problems. It was derived from concepts of bagging (bootstrap aggregating) introduced by Breiman (1996). RF adds randomness to bagging. In a traditional tree, best split among all variables is selected to split each node. In a random forest, the split occurs by randomly choosing the best among a subset of predictors. This approach is very user-friendly, performs well, and avoids overfitting. Two parameters are involved in this method: the number of trees in the forest and the number of variables in the random subset at each node (Fig. 12.5).

The algorithm of random forests is given below:

- Select ntree bootstrap samples from the data set.
- Construct an unpruned tree for each bootstrap sample as follows: at each node, the best split is chosen among randomly sampled mtry of the predictors. Predict the unknown data by combining the predictions (majority votes for classification, average votes for regression) of the ntree trees (Liaw and Wiener n.d.).

This method has been used in many application areas such as fault detection, remote sensing, wind power prediction, mineral processing, and many more.

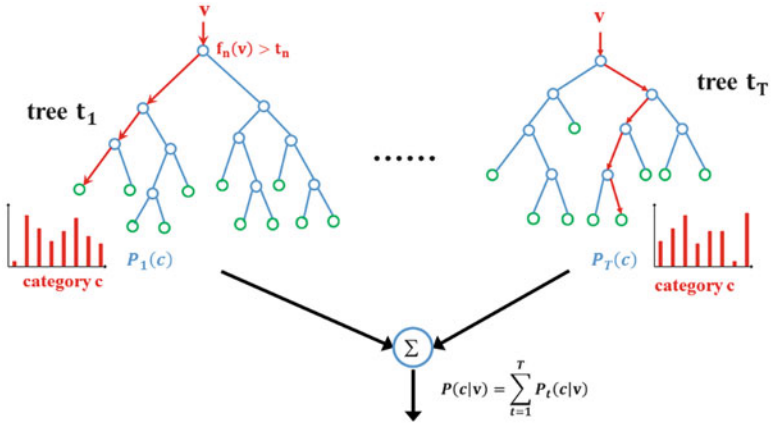

Fig. 12.5 An example of random forest (Stenger n.d.)

12.2.6.2 Adaptive Boosting (AdaBoost)

In order to improve the classification accuracy of classification problems, boosting method is used. A weak learning algorithm is converted into a strong learning algorithm with good classification performance. The original boosting approach is boosting by filtering which requires a large amount of training data. AdaBoost has solved this problem. AdaBoost is an ensemble method boosting algorithm that can be used for classification or regression problems. Nonetheless, it is usually used in classification problems. In this method, the misclassified training samples are given high weights in the next iteration.

The generic algorithm of AdaBoost for classification problems is given below (Freund and Schapire 1997; Zhang et al. 2008; Schapire 2003):

Set of training samples: $(x_1, y_1), \ldots, (x_m, y_m)$; $x_i \in \mathrm{X}, y_i \in \{-1, +1\}$

Initial weights $D_1(i) = \frac{1}{m}$

For $t = 1, 2, \ldots, T$,

$$\text{Find } h_t = \arg\min_{h_j \in H} \varepsilon_j = \sum_{i=1}^{m} D_t(i) y_i \neq h_j(x_i) \tag{12.19}$$

If $\varepsilon_t \geq 1/2$ then stop

$$\text{Set } \alpha_t = \frac{1}{2}\log\left(\frac{1-\varepsilon_t}{\varepsilon_t}\right) \tag{12.20}$$

$$\text{Assign } D_{t+1}(i) = \frac{D_t(i)\exp(-\alpha_t y_i h_t(x_i))}{z_t} \tag{12.21}$$

where z_t is the normalization factor.

Result of the ultimate classifier

$$H(x) = \text{sign}\left(\sum_{t=1}^{T} \alpha_t h_t(x)\right) \tag{12.22}$$

This method is widely used in many application areas including computer vision, image retrieval, facial recognition, and many more.

12.2.7 Kernel Logistic Regression (KLR)

KLR is the kernel and nonlinear form of logistic regression, which is a recognized classifier in the field of statistic leaning. The KLR algorithm is a method which reduces the dimension and is used for data with high dimensionality and small data sets. KLR overcomes the limitation of logistic regression with nonlinear boundaries by using kernel trick. Kernel trick maps original data of X into high-dimensional feature space of F. Then it detects the relations by using linear pattern analysis.

Let $D = \{(x_i, t_i)\}_{i=1}^{l}, x_i \in X \in R^d \quad , t_i \in [0, 1]$ is the labeled data training set.

A kernel function $K{:}X \times X\text{-} > R$ defines the feature space $F(\phi{:}X\text{-} > \mathrm{F})$. In the feature space, the kernel function defines the inner product of the images of input vectors. The most common kernel function is the radial basis function (RBF),

$$k\left(x, x^{'}\right) = \exp\left\{\gamma \parallel x - x^{'}\parallel^2\right\} \tag{12.23}$$

A typical logistic regression model is built in the feature space as follows:

$$\mathrm{logit}\{y(x)\} = w.\phi(x) + b \qquad \mathrm{logit}(p) = \log\frac{p}{1-p} \tag{12.24}$$

By minimizing a cost function signifying the regularized negative log likelihood of the data, the optimal model parameter (w, b) is determined as follows:

$$L = \lambda\|w\|^2 - \sum\nolimits_{i=1}^{l} t_i \log\mu_i + (1 - t_i)\log(1 - \mu_i) \tag{12.25}$$

where λ (regularization parameter) is controlling the bias-variance trade-off. The optimization problem can be written as

$$w = \sum\nolimits_{i=1}^{l} \alpha_i \phi(x_i) \Rightarrow \mathrm{logit}\{y(x)\} = \sum\nolimits_{i=1}^{l} \alpha_i k(x_i, x) + b \tag{12.26}$$

By using Newton method or a least-square procedure, the optimal model parameter (α,b) can be found (Cawley and Talbot 2004).

This method has many applications in aerospace, pattern recognition, signal processing, and many more.

12.3 Regression Techniques

The regression method is similar to classification methods. The only difference is that instead of finding patterns that determine a class, it finds patterns that determine numerical values.

The aim of regression is modelling the effect of independent variables $x_1, \ldots, x_k$ on a response or dependent variable y. In regression modelling, the aim is to develop a model in order to make predictions about the response variables, based on independent variables.

12.3.1 Linear Regression

It is one of the most widely known modelling techniques. This method is massively used for fitting a quantitative response variable as a function of one or more predicator variables. One of the most common methods used for fitting a regression

line is the least-square regression (Powell 1965; Motulsky and Ransnas 1987; Rasmuson et al. 2014b). This method is called least square as it minimizes the sum of the square of the distances of the training data points to the prediction curve. The problem should be solved iteratively for nonlinear systems. In order to do this, the parameters should be initiated (i.e., best guess values should be provided). The nonlinear regression then improves the initial parameter values until the iteration does not further improve the fit.

To perform these iterations at low computational cost, many algorithms can be used. The most common algorithms include the steepest descent, GNA, and Levenberg-Marquardt algorithm (LMA) (Rasmuson et al. 2014b).

12.3.2 Artificial Neural Network (ANN)

Artificial neural network is considered as a highly developed technology extended to all kinds of areas in prediction, control, and process identification (Li and Pengfei 2013). ANNs are being increasingly used for nonlinear regression and classification problems. Nonetheless, it is massively used in regression problems in the industry. When a complex nonlinear relationship exists in given data sets, ANN may provide a more competitive model than the conventional least-square methods (Hunter et al. 2012). It can compute values from inputs, and due to its adaptive nature, it is capable of machine learning.

The ANN consists of neurons connected to each other with a collection of links called synapses. Neurons are positioned in layers and each layer's neurons work in parallel. It consists of an input layer, hidden layers, and an output layer (Davim 2012) (Fig. 12.6). This method provides poor insight into the modelled relationship and significance of many inputs due to the black box nature (Lawal 2011).

The interconnection of different neuron layers, updating the weights of the interconnections, and the activation function are the three types of parameters in ANN. In addition, the training algorithms are the key parameters in neural network applications. The training is to find appropriate weights such that the neural network not only fits the known data but also predicts new inputs. A good artificial network should be able to minimize both the learning error and the prediction error. Most of the algorithms used in training ANNs employ some form of gradient descent, using backpropagation to calculate the gradients. The training algorithms for ANN are scaled conjugate gradient (SCG), Bayesian regularization (BR), and LM (Kermani et al. 2005; Cherkassky and Mulier 2007). SCG algorithm takes less memory; however, it has good generalization for noisy data sets. Training automatically stops in relation to adaptive weight minimization (regularization). BR typically takes more time. According to several researchers (Kermani et al. 2005; Hagan and Menhaj 1994), LM algorithm has good convergence properties. It takes more memory but less time. When the generalization is no longer improved, the training automatically stops. The amount of oscillation in learning procedure is

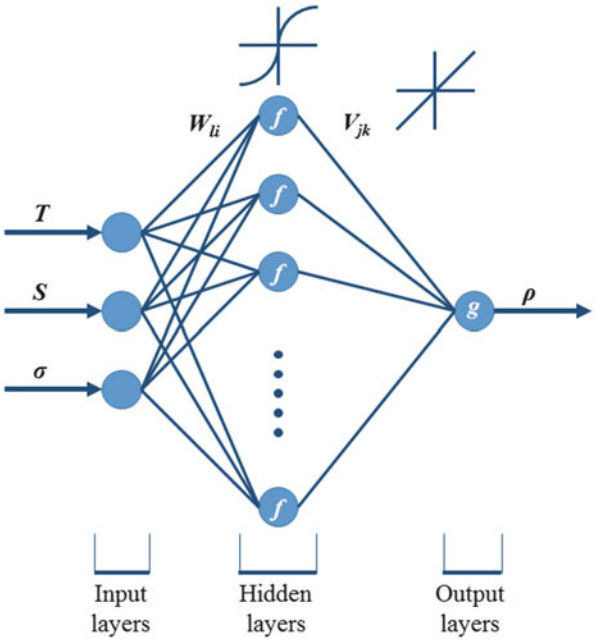

Fig. 12.6 An example of neural network

reduced by this method. It can fit any practical functions since it is the fastest backpropagation algorithm for training and prediction purposes.

Artificial neural networks have been applied successfully to many manufacturing and engineering areas including image processing, information retrieval, remote sensing, energy cost prediction, and chemistry-related problems.

12.3.3 Support Vector Regression (SVR)

SVR is a specific class of SVM. In this method, we embed the data into a higher-dimensional feature space, and the data is fitted to a linear function with minimum complexity to the feature space (Gunn 1998; Vapnik et al. 1996). In other words, a nonlinear regression problem is mapped into a linear regression problem. This is done by applying the kernel functions. Three common kernel functions are the polynomial sigmoid and the Gaussian radial basis function (RBF) kernel. The Gaussian kernel is perhaps the most frequently used kernel function due to its excellent prediction performance and less free variables to be adjusted (Keerthi and Lin 2003).

Given train data set $\{(x_1,y_1), (x_2,y_2), ..., (x_n,y_n)\}$, SVR method finds a function which describes the relationship between x and y. Equation (12.27) presents the function:

$$f(x) = \sum_{i=1}^{n} w\varphi(x) + b \tag{12.27}$$

where $\varphi(x)$ maps x to a new space when the relations between x and y are nonlinear. The relationship of $\varphi(x)$ and y is linear in the new space. A linear hyperplane is determined by the variables w and b that can fit the training data set.

The aim of SVR is to lower the expected risk. This has been shown in Eq. (12.28):

$$R_{\text{emp}} = \frac{1}{n} \sum_{i=1}^{n} L_{\varepsilon}(y_i, f(x_i)) \tag{12.28}$$

where L_{ε} is the ε-insensitive loss function in Eq. (12.29).

$$L_{\varepsilon}\,(y, f(x)) = \begin{cases} 0, & \text{if } |y - f(x)| \le \varepsilon \\ |y - f(x)| - \varepsilon, & \text{Otherwise} \end{cases} \tag{12.29}$$

In order to minimize the expected risk using ε-insensitive loss function, SVR uses linear regression and minimizes $\|w^2\|$ to decrease the complexity of the model. This has been shown in Eq. (12.30):

$$\min_{w,b,\xi,\xi^*} \frac{1}{2}\|w^2\| + C\sum_{i=1}^{n} \left(\xi_i + \xi_i^*\right)$$

Subject to:

$$\begin{cases} w\phi(x_i) + b - y_i \le \varepsilon + \xi_i \ , \\ y_i - w\phi(x_i) - b \le \varepsilon + \xi_i^*, \\ \xi_i^*, \xi_i \ \ge 0, \qquad i = 1, 2, \ldots, n. \end{cases} \tag{12.30}$$

where ξ_i, ξ_i^* $(i = 1,\ldots,n)$ are the slack variables which are nonnegative and show the difference between the real value and $f(x)$ of training data.

This optimization problem can be changed to a dual problem and can be solved using Eq. (12.31):

$$f(x) = \sum_{i=1}^{n} \left(a_i^* - a_i\right) K(x_i, x) + b \tag{12.31}$$

Subject to:

$$0 \le a_i^* \le C, 0 \le a_i < C$$

where a_i and a_i^* are the Lagrange multipliers obtained from the dual problem. The inner product of $\varphi(x_i)$ and $\varphi(x_j)$ determines $k(x_i, x_j)$ which is the kernel function.

In this study RBF was selected as the kernel function which is represented by Eq. (12.32):

$$k(x,z) = \exp\left(\frac{\| x - z\|^2}{2\gamma^2}\right) \tag{12.32}$$

where γ should be set correctly as well as C and ε in Eqs. (12.26) and (12.27) (Hu et al. 2016). The general ability of SVR method is highly affected by fitting parameters. Inappropriate selection of parameters in SVR causes under-fitting or overfitting (Cai et al. 2009). The main parameters that should be carefully tuned are the C which is the trade-off between error minimization and margin maximization, the value of ε to build the regression function by managing the number of support vectors, and the parameter γ in RBF (Eq. 12.28). However, no common rules are presented to determine these parameters (Vapnik and Vapnik 1998).

SVR has been applied successfully to many application areas including signal processing, aerospace, environment and urban systems, petroleum science, and many more.

12.3.4 Gaussian Process Regression (GPR)

GPR models are kernel-based probabilistic and nonparametric models. It can produce a stochastic function with probability distribution as the output (Rasmussen 2004). The properties of a Gaussian process model are controlled by the covariance function. A Gaussian process is defined by mean function *m(x)* and its covariance function *k (x, x')* of a real *f(x)* as follows:

$$m(\mathbf{x}) = \mathbb{E}[f(\mathbf{x})] \tag{12.33}$$

where is the expectation.

$$k(\mathbf{x},\mathbf{x}') = \mathbb{E}[(f(\mathbf{x}) - m(x))(f(\mathbf{x}') - m(x'))] \tag{12.34}$$

and Gaussian process will be

$$f(\mathbf{x}) \equiv \mathcal{GP}\left(m(\mathbf{x}), k\left(\mathbf{x},\mathbf{x}^{'}\right)\right) \tag{12.35}$$

Commonly used covariance functions are the following equations:

$$\text{Constant} : k_C(x,x') = \mathrm{C} \tag{12.36}$$

$$\text{Linear} : k_L(x,x') = x^T x' \tag{12.37}$$

$$\text{Squared exponential} : k_{SE}(x,x') = \exp\left(-\frac{||d||^2}{2l^2}\right) \tag{12.38}$$

$$\text{Matern}: k_{\text{Matern}}(x,x') = \frac{2^{1-\upsilon}}{\Gamma(\nu)}\left(\frac{\sqrt{2\nu}\mid x-x'\mid}{l}\right)^{\nu} k_{\nu}\left(\frac{\sqrt{2\nu}\mid x-x'\mid}{l}\right) \tag{12.39}$$

$$\text{Periodic}: k_P(x,x') = \exp\left(-\frac{2\sin^2\left(\frac{d}{2}\right)}{l^2}\right) \tag{12.40}$$

$$\text{Polynomial}: k_{\text{Poly}}(x,x') = \sigma^2\left(x^T x' + C\right)^d \tag{12.41}$$

where $d = x - x'$ and σ^2 is the variance. The parameter l is the characteristic length scale of the process. k_ν is the modified Bessel function of order ν and $\Gamma(\nu)$ is the gamma function evaluated at ν. Moreover, different combinations of covariance functions can be defined in order to include various understanding about the data set (Rasmussen 2004). Several types of GPs can be applied in order to find the most appropriate covariance and mean functions based on negative log likelihood and root-mean-square error (RMSE) results.

Gaussian process has been applied successfully to many engineering areas such as wind speed prediction, modelling, and control in process engineering.

12.3.5 Thin-Plate Spline (TPS)

TPS is a popular technique used in data fitting and prediction as it is insensitive to noise (Bookstein 1989). These splines are the generalization of the natural cubic splines in 1D. The term "thin-plate spline" is based on choosing a function that minimizes an integral that represents the bending energy of a surface (Bookstein 1989):

$$\frac{1}{n}\sum_{i=1}^{n}\left(\left\|f\left(x_i - y_i\right\|^2\right) + \lambda\text{BendingEnergy}\right. \tag{12.42}$$

where

$$\text{Bending Energy } 2D = \iint\left(\left(\frac{\partial^2 f}{\partial x^2}\right)^2 + 2\left(\frac{\partial^2 f}{\partial x \partial y}\right)^2 + \left(\frac{\partial^2 f}{\partial y^2}\right)^2\right)dxdy \tag{12.43}$$

Any radial basis function can be the choice of the above function $f(x_i)$, but a common choice is as follows:

$$f(x) = \sum_{i=1}^{n}\alpha_i k_i(x) + \sum_{j=1}^{m}\alpha_{n+j}\varphi_j(x) \tag{12.44}$$

$$k_i(x) = \|x - x_i\|^2 \ln\left(\|x - x_i\|\right) \tag{12.45}$$

where $x = [x, y, z]$ and $\phi(x) = [1, x, y, z]$.

The spline parameters (vector a) can be assessed by solving the linear equations below:

$$Aa = y \tag{12.46}$$

$$A = \begin{bmatrix} k - \alpha^2 & \lambda I(n) & p \\ p' & & 0 \end{bmatrix} \tag{12.47}$$

$$a = [a_1 \ldots . a_{n+3}]'; y = \; [y_1 \ldots \ldots . y_n \;\; 0_{1\times m}]' \tag{12.48}$$

$$k = \begin{bmatrix} k_1(x_1) & \ldots & k_n(x_1) \\ \ldots & \ldots & \ldots \\ k_1(x_n) & \ldots & k_n(x_n) \end{bmatrix}; p = \begin{bmatrix} 1 & \ldots & x_1 \\ 1 & \ldots & x_n \end{bmatrix} \tag{12.49}$$

$$\alpha = \text{mean}(k(:))$$

and $I(n)$ is the n by n identity matrix.

TPS has been used in many application areas such as remote sensing, composites, pattern recognition, environmental modelling, and many more.

12.3.6 Taylor Polynomial (TP)

Another method for data modelling in which nonlinear models are to be fitted to data is Taylor polynomials.

Taylor polynomial is a suitable method in interpolation curve fitting. Supposing f is a function which is differentiable at 0, the nth Taylor polynomial of f at 0, shown as p_n, is defined as

$$p_n(x) = \sum\nolimits_{k=0}^{n} \frac{f^k(0)}{k!} x^k \tag{12.50}$$

where $f^k(0)$ shows the kth derivative of f at 0. In particular, $f^0(0)$ is the value of f at 0. Explicitly

$$p_n(x) = f(0) + f'(0)x + \frac{f''(0)}{2}x^2 + \frac{f'''(0)}{6}x^3 + \ldots + \frac{f^{(n)}(0)}{n!}x^n \tag{12.51}$$

Taylor polynomials have been used in many application areas such as computational and physical science, control engineering, heat and mass transfer, pattern recognition, and many more.

12.3.7 Deep Learning (DL)

Deep learning is a method in which the representations of data with many levels of abstractions are learned by computational models with several processing layers (LeCun et al. 2015). As the definition of sample size varies depending on the application, deep learning has been mentioned here. It is being used for nonlinear regression and classification problems. Nonetheless, it is used in regression problems in the industry. Deep learning is comparable with artificial neural network with more complex training structure and architecture. An ordinary neural network comprises of three layers: one input layer, one hidden layer, and one output layer. However, deep learning models may have many hidden layers with various functions performing convolution operations or nonlinear transformations. In order to ensure the robustness of these models, new parameters such as dropout have been defined which determine the part of the neurons not to be considered randomly during the training. This method overcomes the limitations of conventional methods which is the lack of ability to process raw data (Fan et al. 2017). The nonlinear relationship between parameters h_l and h_{l+1} is specified by neural network through a function which is defined as below:

$$h_{l+1} = \delta(Wh_l + b) \tag{12.52}$$

where δ is the activation function and vector b and matrix W are model parameters.

When there is one layer between the variables, h_l and h_{l+1} form one layer called a single-layer neural network. Deep neural network (DNN) is a multilayer neural network with advanced learning methods. To construct DNN for $y = f(u)$, the network functions are serially stacked as follows:

$$h_1 = \delta_1(W_1 u + b_1) \tag{12.53}$$

$$h_2 = \delta_2(W_2 h_1 + b_2) \tag{12.54}$$

$$\vdots$$

$$y = \delta_L(W_L h_{L-1} + b_L) \tag{12.55}$$

where L is the number of layers.

Assume $\{u^n, \tau^n\}_{n=1}^N$ is the data set of inputs and outputs and $\varepsilon\,(y^n, \tau^n)$ is the error function that estimates the difference between the output of $y^n = f(u^n)$ and the target T^n. The model parameters for the whole network, $\theta = \{W_1, \ldots, W_L, b_1, \ldots, b_L\}$, can be selected to minimize the sum of the errors:

$$\min_\theta \left[J = \sum\nolimits_{n=1}^{N} \varepsilon(y^n, \tau^n) \right] \tag{12.56}$$

The minimization problem above can be solved analytically through its gradient being acquired through error backpropagation if suitable choice of $E(.)$ is given (Chong et al. 2017).

Deep learning has many applications in computer vision, image classification, pattern recognition, robotics, and many more.

12.3.8 Kernel Ridge Regression (KRR)

KRR method is the combination of ridge regression and ordinary least-square (OLS) regression. This method employs a set of nonlinear prediction functions and uses penalization to avoid overfitting. This is performed through mapping predictors into a high-dimensional space of nonlinear functions of the predictors. The overfitting then is avoided by estimating a linear forecast equation in this high-dimensional space, using a penalty (ridge or shrinkage). This method is very flexible in model development. However, the researchers should decide regarding the choice of kernel. Moreover, parameters should be tuned in this method, and their interpretation is not always clear (Exterkate 2013). This method includes in many application areas including pattern recognition, signal processing, aerospace, and many more.

In order to obtain more accuracy and lower error, some resampling methods can be applied before using above methods.

12.3.9 Model Performance

Model performance is the comparison of predictions from a mathematical model and new experimental tests. It shows whether the computer model is an accurate representation of the real system. Model validation (goodness of fit) is determined by coefficient of determination (R^2), adjusted-R^2, RMSE, sum of squared errors (SSE), mean squared error (MSE), and standard error of prediction (SEP). R^2 should be close to 1; however, it does not always indicate that the model is a good one. It has been shown that by adding new variables to the model regardless of whether the variable is statistically significant or not, R^2 always increases. Hence, adjusted-R^2 is preferred to be calculated as it is adjusted for the number of terms in the model. The adjusted-R^2 should be over 90% to show the strong synergy between the observed and predicted values. SSE, MSE, and SEP are also used for model validation. Values closer to 0 are desirable. In addition, analysis of variance (ANOVA) helps to find the significant factors affecting the objective function. ANOVA is used to measure the F-ratio which helps to calculate the probability (the p-value). When p-value is less than 0.05, the controlling factor has a significant effect on the dependent variable. If the p-value is greater than 0.05, the factor has no significant effect on the dependent variable. The controlling factors are significant at a 95% confidence level (Montgomery 2008; Barrett 2007).

Statistically, the performance of the models was assessed by measuring R^2, SEP, adjusted- R^2, MSE, and SSE from the following equations:

$$R^2 = 1 - \frac{\sum \left(y_{\text{exp}} - y_{\text{pred}}\right)^2}{\sum \left(y_{\text{exp}} - y_{\text{m}}\right)^2} \tag{12.57}$$

$$\text{Adjusted } R^2 = 1 - \frac{\left(1 - R^2\right)(N-1)}{N - P - 1} \tag{12.58}$$

$$\text{SEP} = \sqrt{\frac{\sum \left(y_{\text{exp}} - y_{\text{pred}}\right)^2 - N\left(\sum \left(y_{\text{exp}} - y_{\text{pred}}\right)\right)^2}{N-1}} \tag{12.59}$$

$$\text{MSE} = \frac{\sum \left(y_{\text{exp}} - y_{\text{pred}}\right)^2}{N} \tag{12.60}$$

$$\text{SSE} = \sum\nolimits_{i=1}^{n} \left(y_{\text{pred}} - y_{\text{exp}}\right)^2 \tag{12.61}$$

where y_{exp}, y_{pred}, and y_{m} show the experimental, predicted, and the mean of dependent variable, respectively. P is the number of predicators (coefficients) in the model and N is the total size of the sample.

12.4 Resampling and Virtual Data Generation

Resampling methods are very popular due to their robustness, accuracy, great generalizability, and simplicity. Resampling happens when a data generating technique is used to generate new data without being related to a theoretical distribution. Resampling is used when the distribution of the data is unknown or the data set is too small to use the standard methods (Hoffman 2015). Resampling can be used to make comparison such as median or ratios which cannot be answered with traditional parametric or nonparametric methods. The samples can be generated many times with or without replacement. Randomization is an example of sampling without replacement. Bootstrapping is a resampling method with replacement. Resampling method is related to Monte Carlo simulation in which the data is produced, and based on many possible scenarios, the final decision is made. In resampling, all possible combination can be used. However, it is compute intensive and time consuming. The main resampling techniques are bootstrapping, jackknife, Monte Carlo, and exact test method. With these techniques thousands of samples can be generated rapidly.

12.4.1 Monte Carlo Simulation (MCS)

MCS makes random sampling repeatedly from populations with known characteristics and test statistics calculated in each case. With this multiple resampling, sampling distributions for the statistics of interest can be constructed. The *p*-value is

then found from this distribution. Randomization and bootstrap tests are special cases of Monte Carlo tests.

The procedure of MCS can be summarized as follows (Crowley 1992):

- Observation simulation based on a hypothetical distribution.
- Multiple calculation of the statistic of interest to generate the distribution of the statistic.
- Find the *p*-value or other necessary values based on the distribution of the statistic.

12.4.2 Randomization Exact Test (Permutation Test)

Permutation test is a resampling test without replacement and it is a nonparametric method. Exact test simulates all possible permutations. In this method, the sampling distribution can be constructed for any statistic of interest without any assumptions regarding the shape and other parameters of the population distributions due to randomization. It can be used without normal assumption of distribution of data under the null hypothesis. In this method, the observations will be rearranged, and the corresponding statistic of interest will be calculated for each permutation. After permuting all the possibilities, all the statistics of interest can be put together, to construct the distribution curve under null hypothesis (Curran-Everett 2012). The null hypothesis is rejected if the observed result belongs to a relatively higher probability under the alternative hypothesis. With small samples, we can construct the sampling distribution by estimating the statistic of interest for each possible order.

12.4.3 Cross-Validation (CV)

CV is a method of performance evaluation of a model on an unknown data set. In a *k*-fold cross-validation method, the training data set is divided into *k* equally sized subsets, and one of the subsets is kept for testing and the rest are used for training purpose. This process is done *k*-times with each *k* subsets being used just once as the testing data set. The final estimation of the accuracy is performed by averaging the results of each *k* subset. The size of *k* varies from 2 to 10. The most common *k*-fold cross-validation methods are leave-one-out and stratified cross-validation. In leave-one-out cross-validation, *n*-1 out of the *n* training vectors is selected as a training set, and one vector which is left out is treated as the testing data. This applies to every fold. In a stratified cross-validation method, the training set is divided into homogeneous groups, and the folds contain approximately the same proportions as the training data set (Kohavi n.d.).

12.4.4 Jackknife Method (JK)

JK technique is used when the distribution of the parameter is unknown and difficult to compute or has no analytic distribution. The JK (delete-1) is to leave out one observation at a time from the data set and calculate the parameter of interest (e.g., variance or bias) for the remaining n-1 observations and repeat the process until each of the n observations is deleted. All the results obtained from the n different observations will be averaged. The procedure is able to remove bias. This method is a limited version of the bootstrap. The effect on a statistical estimate is quantified when each observation is left out one at a time. If the parameter of interest is discontinuous such as median, this method does not work (Efron 1992).

Suppose $\widehat{\theta}$ is the calculated estimator of the parameter of interest based on all n observations.

$$\text{Let}\,\widehat{\theta}_{(.)} = \frac{1}{n}\sum\nolimits_{i=1}^{n}\widehat{\theta}_{(i)} \tag{12.62}$$

where $\widehat{\theta}_{(i)}$ is the estimate of interest based on the sample when the ith observation is removed, and $\widehat{\theta}_{(.)}$is the average of all the estimates.

Variance is calculated as follows:

$$\text{Var}\left(\widehat{\theta}\right)_{\text{Jack}} = \frac{n-1}{n}\sum\nolimits_{i=1}^{n}\left(\widehat{\theta}_{(i)} - \widehat{\theta}_{(.)}\right)^2 \tag{12.63}$$

The estimate of the bias of $\widehat{\theta}$ is

$$\widehat{\text{Bias}_{(\text{Jack})}} = (n-1)\left(\widehat{\theta}_{(.)} - \widehat{\theta}\right) \tag{12.64}$$

12.4.5 Bootstrap

The bootstrap is another nonparametric resampling method for estimating the sampling distribution of an estimator. It is for evaluating the variance of the estimator. It was described by Bradley Efron (1992). It uses Monte Carlo method for the resampling process which consists of randomly sampling a data set with replacement. The bootstrap estimator is the average of all parameter estimates obtained from different samples (Efron and Tibshirani 1994; Davison and Hinkley 1997). Robust estimates of point variables (e.g., median, mean, regression coefficient) with their standard errors and confidence limits can be obtained using this method with no limits to the number of resampling runs.

The algorithm is given below:

- Suppose data set $X = \{X_1 \ldots Xn\}$.
- Calculate function $\widehat{\theta}(X)$ that estimates parameter θ of the model.

- For $i = 1$ *to* s (s is the generated number of bootstrap samples):
  - By sampling with replacement, produce a bootstrap sample $X^l = \{x_1{}^i \ldots x_n{}^i\}$ from the data set.
  - Calculate $\widehat{\theta}^i = \widehat{\theta}^i\left(X^i\right)$ similar to the original estimate $\widehat{\theta}$.
- Calculate the sample mean and sample variance of the θ^is:

$$\overline{\widehat{\theta}} = \frac{1}{s}\sum\nolimits_i \widehat{\theta}^i \quad \text{and } b = \frac{1}{s-1}\sum\nolimits_i \left(\widehat{\theta}^i - \overline{\widehat{\theta}}\right)^2 \tag{12.65}$$

- $\widehat{\theta}$ is the estimate of θ and $\sqrt{b}$ is bootstrap estimate of its standard error.

Bootstrap method has this advantage of modelling the effects of the real sample size compared to other methods as every resampling has the same number of observations as the real data set. Bootstrapping method considers a small sample size as a virtual population to produce more data (Fan and Wang 1996).

When data do not follow the prerequisite for parametric regression analysis, the bootstrapping method can also be used to determine the regression coefficients. When there is no correlation between X and Y, any xi can be related to any yi . In this way, bootstrapping method can be used to randomly select all possible combination of X and Y (Hoffman 2015).

12.4.6 Subsampling

In order to estimate the sampling distribution of an estimator, an alternative to bootstrapping is subsampling. Two fundamental differences between bootstrapping and subsampling are that in subsampling the sample size is bigger than the resample size and the resampling occurs without replacement. In subsampling, the rate of convergence of the estimator is known and the distribution is continuous. Hence, subsampling is used when the rate of convergence is not the square root of the sample size and when the distribution is not normal. It can also be used for time series data as well (Politis et al. 1999).

12.4.7 Virtual Sample Generation (VSG)

Another way of solving the problem of small sample size is to produce virtual samples to increase the robustness of the learning algorithm and improve the learning accuracy and prediction.

One way to generate virtual samples is to use prior knowledge regarding the target function to enlarge the data set. VSG fills in the information gaps in sparse data to make learning methods perform well (Niyogi et al. 1998).

Another approach to deal with small data sets is using virtual attributes. The data is extended into a high-dimensional space in this method to get a better performance in classification (Li and Wen 2014a).

12.5 Engineering Approaches and Applications

Heuristic techniques have been applied successfully to many manufacturing and engineering areas. In this section some of the applications of these methods have been mentioned.

12.5.1 Mechanical and Industrial Engineering

In one study, a support vector model and an optimization method were presented for microwave filter manufacturing. Due to the scarcity of the collected data set, the data was expanded using obtained experiments from physical knowledge available, and a support vector machine was developed (Zhou and Huang 2012).

In 2006, Li et al. (2006) used a data fuzzification method (mega-fuzzification) with a data trend estimation procedure to increase the amount of data in the early stages of manufacturing. The adaptive-network-based fuzzy inference system (ANFIS) was applied to neuro-fuzzy learning in this study to improve the accuracy of learning. In another study, a new method of virtual sample generation named genetic algorithm-based virtual sample generation (GABVSG) was used in multilayer ceramic capacitors (MLCC) which are passive components in modern electronics with costly pilot runs. The results of BPNN (backpropagation neural network), SVR model, and mega trend diffusion (MTD) methods were compared. The result showed that the proposed method had good performance in BPNN and SVR and was better than that of MTD method. The average error in SVR using GABVSG is less than that of BPNN (Li and Wen 2014b).

In another study, bootstrapping method was used to generate virtual data in multilayer ceramic capacitors (MLCC) using ANN method. The results revealed better performance with the proposed procedure. Using the combination of ANN and bootstrapping method reveals lower and stable learning errors (Tsai and Li 2008).

12.5.2 Chemical and Process Engineering

In one study, SVM was used for pattern recognition based on a small data set to predict corrosion rate of injecting water pipeline. This study in Shengli Oil Field showed that SVM had a greater accuracy in prediction of corrosion rate than the

neural network and is reliable and easy to be used in petroleum engineering. All absolute errors were less than 5% in model testing. This indicates that SVM can be used in many applications due to high precision and generalization (Zhen et al. 2010). In another study, the skin-core morphology was studied by optical microscopic (OM) images and Fourier transform infrared attenuated total reflectance mapping (FTIR-ATR mapping) and modelled with limited data set using Gaussian process model and polynomial equations (Golkarnarenji et al. 2017).

In another paper, the carbon fiber thermal stabilization process was studied and analyzed using various dynamic models to predict the process using small data sets. The Levenberg-Marquardt algorithm (LMA)-neural network (LMA-NN), Gauss-Newton (GN)-curve fitting, Taylor polynomial method, and a genetic algorithm were employed in the study. The results showed that the Taylor polynomial method performs significantly better with higher accuracy than other methods in small data sets (Khayyam et al. 2015b).

12.5.3 Material and Textile Engineering

SVM and BPNN models were compared in a study to predict the yarn properties. The parameters of SVM model were optimized using genetic algorithm. The mean error (%) of two predictive indices was 22.80% and 13.67% for ANN model and 12.71% and 5.52% for SVM. The result showed that SVM had stability of predictive accuracy when compared to BP neural network in small and noisy data sets (Lu et al. 2015).

12.5.4 Electrical Engineering

To analyze faulty analogue circuits, a bagging ensemble system was proposed and employed. Cross-validation technique was also used to improve the accuracy and generalization ability of the circuit (Liu et al. 2009). Fault diagnosis results of radial basis function (RBF) and radial basis function artificial neural network (RBFNN) without and with cross-validation showed that the ensemble system combined with cross-validation improved the diagnosis correction rate (%). An integration of particle swarm optimization (PSO) and virtual sample generation was also proposed in MLCC and purified terephthalic acid (PTA) to improve the accuracy of the developed forecasting model. The accuracy and performance of foresting model improved with the proposed tool (Chen et al. 2017).

12.5.5 Civil and Environmental Engineering

In one study, SVM was used for image classification with limited remotely sensed data sets. This method was compared to relevance vector machine (RVM) and sparse multinomial logistic regression (SMLR). For these data, RVM and SMLR were able to classify data with similar accuracy to SVM using less training data sets (Pal and Foody 2012).

In another study, the groundwater pollution sensitivity was estimated using decision tree and rule induction method using small data sets. The training data was collected from the Woosan Industrial Complex, Korea. The result showed that the decision tree and rule induction methods show better consistency and prediction accuracy than the other methods with small data sets (Yoo et al. 2016).

Landslide susceptibility mapping was studied in Hendek region in Turkey comparing neural network and logistic regression using small data sets. Comparing two methods, neural network predicted higher percentages of landslides than logistic regression method in high and very high zones (Yesilnacar and Topal 2005).

In order to use ANN for small data sets, a diffusion neural network (DNN) was developed by Huang and Moraga (2004) which is a combination of ANN and the principle of information diffusion. This method improved the prediction accuracy of ANN by generating new samples via applying fuzzy theories. The error was reduced about 48% in this case.

In another study, two wood pulp applications were used with small data sets. Various methods based on feed-forward neural network (FFNN) and RBFNN were tested. Data sets were obtained using D-optimal design and random selection and compared for their ability to develop a suitable model. The result showed improvement using D-optimal design when compared to a randomly selected training data set (Lanouette et al. 1999). This study also reveals that the RBFNN performs better than FFNN. The thin-plate spline activation function performed better than the Gaussian activation function in this study.

12.6 Conclusion

Developing a reliable model using limited and small data is a challenging task specially when the process to be modelled is highly nonlinear and many inputs and outputs are involved.

Although machine learning from small data sets makes the modelling procedure difficult and prone to overfitting, in real world, there are many situations when organization must work with small data sets.

Hence, the study of different techniques and methods suitable for small data sets is of myriad importance and was reviewed and described here.

According to the "no free lunch" theorem (Wolpert and Macready 1997), no model exists that works best for every problem, and it is impossible to develop a data model that is universally better than all others. As a result, it is usual in machine learning to try to use many models and find the best method for a particular problem (Khayyam et al. 2015b; Balabin and Lomakina 2011). However, generally, it can be concluded that data models such as SVM and SVR have high precision and accuracy in small and noisy data sets. In addition, ensemble methods combined with cross-validation improve the error rate. Combination of data models such as ANN with methods such as principle of information diffusion can also reduce the error significantly. Finally, we recommend the use of more than one method for classification and regression problems in different engineering areas, so that the best technique can be chosen to be a strong support for these problems.

References

Abd, A. M., & Abd, S. M. (2017). Modelling the strength of lightweight foamed concrete using support vector machine (SVM). *Case Studies in Construction Materials, 6*, 8–15.

Ali, A. B. M. S. (2009). *Dynamic and advanced data Mining for Progressing Technological Development: Innovations and systemic approaches: Innovations and systemic approaches*. Information Science Reference.

Ali, S., & Smith, K. A. (2006). On learning algorithm selection for classification. *Applied Soft Computing, 6*, 119–138.

Balabin, R. M., & Lomakina, E. I. (2011). Support vector machine regression (SVR/LS-SVM)—An alternative to neural networks (ANN) for analytical chemistry? Comparison of nonlinear methods on near infrared (NIR) spectroscopy data. *Analyst, 136*, 1703–1712.

Barrett, J. D. (2007). *Taguchi's quality engineering handbook*. Taylor & Francis.

Bookstein, F. L. (1989). Principal warps: Thin-plate splines and the decomposition of deformations. *IEEE Transactions on Pattern Analysis and Machine Intelligence, 11*, 567–585.

Breiman, L. (1996). Bagging predictors. *Machine Learning, 24*, 123–140.

Breiman, L. (2001). Random forests. *Machine Learning, 45*, 5–32.

Burges, C. J. (1998). A tutorial on support vector machines for pattern recognition. *Data Mining and Knowledge Discovery, 2*, 121–167.

Cai, Z.-j., Lu, S., & Zhang, X.-b. (2009). Tourism demand forecasting by support vector regression and genetic algorithm. In *Computer science and information technology, 2009. ICCSIT 2009. 2nd IEEE international conference on* (pp. 144–146).

Catal, C., Sevim, U., & Diri, B. (2011). Practical development of an eclipse-based software fault prediction tool using naive Bayes algorithm. *Expert Systems with Applications, 38*(3), 2347–2353.

Cawley, G. C., & Talbot, N. L. (2004). Efficient model selection for kernel logistic regression. In *Pattern recognition, 2004. ICPR 2004. Proceedings of the 17th international conference on* (pp. 439–442).

Chapelle, O., Vapnik, V., Bousquet, O., & Mukherjee, S. (2002). Choosing multiple parameters for support vector machines. *Machine Learning, 46*, 131–159.

Chen, N. (2004). *Support vector machine in chemistry*. World Scientific Pub.

Chen, Z.-S., Zhu, B., He, Y.-L., & Yu, L.-A. (2017). A PSO based virtual sample generation method for small sample sets: Applications to regression datasets. *Engineering Applications of Artificial Intelligence, 59*, 236–243.

Cherkassky, V., & Mulier, F. M. (2007). *Learning from data: Concepts, theory, and methods*. Chichester: Wiley.

Cholette, M. E., Borghesani, P., Gialleonardo, E. D., & Braghin, F. (2017). Using support vector machines for the computationally efficient identification of acceptable design parameters in computer-aided engineering applications. *Expert Systems with Applications, 81*, 39–52.

Chong, E., Han, C., & Park, F. C. (2017). Deep learning networks for stock market analysis and prediction: Methodology, data representations, and case studies. *Expert Systems with Applications, 83*, 187–205.

Cosma, G., Brown, D., Archer, M., Khan, M., & Graham Pockley, A. (2017). A survey on computational intelligence approaches for predictive modeling in prostate cancer. *Expert Systems with Applications, 70*, 1–19.

Crowley, P. H. (1992). Resampling methods for computation-intensive data analysis in ecology and evolution. *Annual Review of Ecology and Systematics, 23*, 405–447.

Curran-Everett, D. (2012). Explorations in statistics: Permutation methods. *Advances in Physiology Education, 36*, 181–187.

Datla, M. V. (2015). Bench marking of classification algorithms: Decision trees and random forests - a case study using R. In *2015 international conference on trends in automation, communications and computing technology (I-TACT-15)* (pp. 1–7).

Davim, P. (2012). *Computational methods for optimizing manufacturing technology models and techniques*. Hershey: Engineering Science Reference.

Davim, J. P. (2015). *Design of Experiments in production engineering*. Springer International Publishing.

Davison, A. C., & Hinkley, D. V. (1997). *Bootstrap methods and their application* (Vol. 1). New York: Cambridge university press.

Dobre, T. G., & Sanchez Marcano, J. G. (2007). *Chemical engineering: Modelling, simulation and similitude*. Weinheim: Wiley-VCH Verlag GmbH & KGaA.

Efron, B. (1992). Bootstrap methods: Another look at the jackknife. In *Breakthroughs in statistics* (pp. 569–593). Springer.

Efron, B., & Tibshirani, R. J. (1994). *An introduction to the bootstrap*. CRC press.

Ertekin, S. (2012). *K-NN*. Available: https://ocw.mit.edu/courses/sloan-school-of-management/15-097-prediction-machine-learning-and-statistics-spring-2012/lecture-notes/MIT15_097S12_lec06.pdf.

Exterkate, P. (2013). Model selection in kernel ridge regression. *Computational Statistics & Data Analysis, 68*, 1–16.

Fan, X., & Wang, L. (1996). Comparability of jackknife and bootstrap results: An investigation for a case of canonical correlation analysis. *The Journal of Experimental Education, 64*, 173–189.

Fan, C., Xiao, F., & Zhao, Y. (2017). A short-term building cooling load prediction method using deep learning algorithms. *Applied Energy, 195*, 222–233.

Freund, Y., & Schapire, R. E. (1997). A decision-theoretic generalization of on-line learning and an application to boosting. *Journal of Computer and System Sciences, 55*, 119–139.

Ghiasi, M. M., & Mohammadi, A. H. (n.d.). Application of decision tree learning in modelling CO2 equilibrium absorption in ionic liquids. *Journal of Molecular Liquids*.

Golkarnarenji, G., Naebe, M., Church, J. S., Badii, K., Bab-Hadiashar, A., Atkiss, S., et al. (2017). Development of a predictive model for study of skin-core phenomenon in stabilization process of PAN precursor. *Journal of Industrial and Engineering Chemistry, 49*, 46–60.

Gunn, S. R. (1998) Support vector machines for classification and regression.

Hagan, M. T., & Menhaj, M. B. (1994). Training feedforward networks with the Marquardt algorithm. *IEEE Transactions on Neural Networks, 5*, 989–993.

Han, J., Pei, J., & Kamber, M. (2011). *Data mining: Concepts and techniques*. Elsevier.

Hoffman, J. I. E. (2015). Chapter 37 - resampling statistics. In *Biostatistics for medical and biomedical practitioners* (pp. 655–661). Academic Press.

Hu, W., Yan, L., Liu, K., & Wang, H. (2016). A short-term traffic flow forecasting method based on the hybrid PSO-SVR. *Neural Processing Letters, 43*, 155–172.

Huang, C. (2002). Information diffusion techniques and small-sample problem. *International Journal of Information Technology & Decision Making, 1*, 229–249.

Huang, C., & Moraga, C. (2004). A diffusion-neural-network for learning from small samples. *International Journal of Approximate Reasoning, 35*, 137–161.

Hunter, D., Yu, H., Pukish, M. S., III, Kolbusz, J., & Wilamowski, B. M. (2012). Selection of proper neural network sizes and architectures—A comparative study. *IEEE Transactions on Industrial Informatics, 8*, 228–240.

Ilin, A., & Raiko, T. (2010). Practical approaches to principal component analysis in the presence of missing values. *Journal of Machine Learning Research, 11*, 1957–2000.

Janssens, D., Wets, G., Brijs, T., Vanhoof, K., Arentze, T., & Timmermans, H. (2006). Integrating Bayesian networks and decision trees in a sequential rule-based transportation model. *European Journal of Operational Research, 175*, 16–34.

Keerthi, S. S., & Lin, C.-J. (2003). Asymptotic behaviors of support vector machines with Gaussian kernel. *Neural Computation, 15*, 1667–1689.

Kermani, B. G., Schiffman, S. S., & Nagle, H. T. (2005). Performance of the Levenberg–Marquardt neural network training method in electronic nose applications. *Sensors and Actuators B: Chemical, 110*, 13–22.

Khayyam, H., Naebe, M., Bab-Hadiashar, A., Jamshidi, F., Li, Q., Atkiss, S., et al. (2015a). Stochastic optimization models for energy management in carbonization process of carbon fiber production. *Applied Energy, 158*, 643–655.

Khayyam, H., Naebe, M., Zabihi, O., Zamani, R., Atkiss, S., & Fox, B. (2015b). Dynamic prediction models and optimization of Polyacrylonitrile (PAN) stabilization processes for production of carbon fiber. *IEEE Transactions on Industrial Informatics, 11*, 887–896.

Khayyam, H., Fakhrhoseini, S. M., Church, J. S., Milani, A. S., Bab-Hadiashar, A., Jazar, R. N., et al. (2017). Predictive modelling and optimization of carbon fiber mechanical properties through high temperature furnace. *Applied Thermal Engineering, 125*, 1539–1554.

Kohavi, R. (n.d.). A study of cross-validation and bootstrap for accuracy estimation and model selection.

Kulkarni, S., & Harman, G. (2011). *An elementary introduction to statistical learning theory* (Vol. 853). Wiley.

Lanouette, R., Thibault, J., & Valade, J. L. (1999). Process modeling with neural networks using small experimental datasets. *Computers & Chemical Engineering, 23*, 1167–1176.

Lawal, I. A. (2011). Predictive modeling of material properties using GMDH-based Abductive networks. In Y. O. Mohammed (Ed.), *Modelling symposium (AMS), 2011 fifth Asia* (pp. 3–6).

LeCun, Y., Bengio, Y., & Hinton, G. (2015). Deep learning. *Nature, 521*, 436–444., 05/28/print.

Leopold, E., & Kindermann, J. (2006). Content classification of multimedia documents using partitions of low-level features. *JVRB - Journal of Virtual Reality and Broadcasting, 3*, 2007.

Li, F., & Pengfei, L. (2013). *The research survey of system identification method*. presented at the 2013 5th International Conference on Intelligent Human-Machine Systems and Cybernetics (IHMSC).

Li, D.-C., & Wen, I. H. (2014a). A genetic algorithm-based virtual sample generation technique to improve small data set learning. *Neurocomputing, 143*, 222–230.

Li, D.-C., & Wen, I.-H. (2014b). A genetic algorithm-based virtual sample generation technique to improve small data set learning. *Neurocomputing, 143*, 222–230.

Li, D.-C., Wu, C., & Chang, F. M. (2006). Using data continualization and expansion to improve small data set learning accuracy for early flexible manufacturing system (FMS) scheduling. *International Journal of Production Research, 44*, 4491–4509.

Li, D.-C., Chang, C.-J., Chen, C.-C., & Chen, W.-C. (2012). A grey-based fitting coefficient to build a hybrid forecasting model for small data sets. *Applied Mathematical Modelling, 36*, 5101–5108.

Liaw, A., & Wiener, M. (n.d.). Classification and regression by randomForest.

Liu, H., Chen, G., Song, G., & Han, T. (2009). Analog circuit fault diagnosis using bagging ensemble method with cross-validation. In *Mechatronics and automation, 2009. ICMA 2009. International conference on* (pp. 4430–4434).

Lu, Z. J., Xiang, Q., Wu, Y. m., & Gu, J. (2015). Application of support vector machine and genetic algorithm optimization for quality prediction within complex industrial process. In *2015 I.E. 13th international conference on industrial informatics (INDIN)* (pp. 98–103).

Mao, R., Zhu, H., Zhang, L., & Chen, A. (2006). A new method to assist small data set neural network learning. In *Intelligent systems design and applications, 2006. ISDA'06. Sixth international conference on* (pp. 17–22).

Montgomery, D. C. (2008). *Design and analysis of experiments*. Wiley.

Motulsky, H. J., & Ransnas, L. A. (1987). Fitting curves to data using nonlinear regression: A practical and nonmathematical review. *The FASEB Journal, 1*, 365–374.

Niyogi, P., Girosi, F., & Poggio, T. (1998). Incorporating prior information in machine learning by creating virtual examples. *Proceedings of the IEEE, 86*, 2196–2209.

Pal, M., & Foody, G. M. (2012). Evaluation of SVM, RVM and SMLR for accurate image classification with limited ground data. *IEEE Journal of Selected Topics in Applied Earth Observations and Remote Sensing, 5*, 1344–1355.

Pearl, J. (2014). *Probabilistic reasoning in intelligent systems: Networks of plausible inference*. Morgan Kaufmann.

Peng, X., Cai, Y., Li, Q., & Wang, K. (2017). Control rod position reconstruction based on K-nearest neighbor method. *Annals of Nuclear Energy, 102*, 231–235.

Pham, Q. T. (1998). Dynamic optimization of chemical engineering processes by an evolutionary method. *Computers & Chemical Engineering, 22*, 1089–1097.

Politis, D. N., Romano, J. P., & Wolf, M. (1999). *Subsampling*. New York: Springer.

Powell, M. (1965). A method for minimizing a sum of squares of non-linear functions without calculating derivatives. *The Computer Journal, 7*, 303–307.

Rasmuson, A., Andersson, B., Olsson, L., & Andersson, R. (2014a). *Mathematical modeling in chemical engineering*. New York: Cambridge University Press.

Rasmuson, A., Andersson, B., Olsson, L., & Andersson, R. (2014b). *Mathematical modeling in chemical engineering*. New York: Cambridge University Press.

Rasmussen, C. E. (2004). Gaussian processes in machine learning. In *Advanced lectures on machine learning* (pp. 63–71). Berlin: Springer.

Ratner, B. (2011). *Statistical and machine-learning data mining: Techniques for better predictive modeling and analysis of big data*. CRC Press.

Rodrigues, A. E., & Minceva, M. (2005). Modelling and simulation in chemical engineering: Tools for process innovation. *Computers & Chemical Engineering, 29*, 1167–1183.

Rokach, L., & Maimon, O. (2014). *Data mining with decision trees: Theory and applications*. World scientific.

Ross, S. M. (2009). *Introduction to probability and statistics for engineers and scientists*. Elsevier Science.

Ruparel, N. H., Shahane, N. M., & Bhamare, D. P. (n.d.). Learning from small data set to build classification model: A survey.

Schapire, R. E. (2003). The boosting approach to machine learning: An overview. In *Nonlinear estimation and classification* (Vol. 171, p. 149). Springer.

Sharma, A., & Paliwal, K. K. (2015). Linear discriminant analysis for the small sample size problem: An overview. *International Journal of Machine Learning and Cybernetics, 6*, 443–454.

Shatovskaya, T., Repka, V., & Good, A. (2006). Application of the Bayesian networks in the informational modeling. In *2006 international conference - modern problems of radio engineering, telecommunications, and computer science* (pp. 108–108).

Stenger, T. -K. K. B. Available: http://www.iis.ee.ic.ac.uk/icvl/iccv09_tutorial.html.

Tsai, T.-I., & Li, D.-C. (2008). Utilize bootstrap in small data set learning for pilot run modeling of manufacturing systems. *Expert Systems with Applications, 35*, 1293–1300.

Vapnik, V. N. (1999). An overview of statistical learning theory. *IEEE Transactions on Neural Networks, 10*, 988–999.

Vapnik, V. N., & Vapnik, V. (1998). *Statistical learning theory* (Vol. 1). New York: Wiley.

Vapnik, V., Golowich, S. E., & Smola, A. (1996). Support vector method for function approximation, regression estimation, and signal processing. In *Advances in neural information processing systems* (Vol. 9).

Wolpert, D. H., & Macready, W. G. (1997). No free lunch theorems for optimization. *IEEE Transactions on Evolutionary Computation, 1*, 67–82.

Xu, J., Yao, L., & Li, L. (2015). Argumentation based joint learning: A novel ensemble learning approach. *PLoS One, 10*, e0127281.

Yesilnacar, E., & Topal, T. (2005). Landslide susceptibility mapping: A comparison of logistic regression and neural networks methods in a medium scale study, Hendek region (Turkey). *Engineering Geology, 79*, 251–266.

Yoo, K., Shukla, S. K., Ahn, J. J., Oh, K., & Park, J. (2016). Decision tree-based data mining and rule induction for identifying hydrogeological parameters that influence groundwater pollution sensitivity. *Journal of Cleaner Production, 122*, 277–286.

Zhang, C.-X., Zhang, J.-S., & Zhang, G.-Y. (2008). An efficient modified boosting method for solving classification problems. *Journal of Computational and Applied Mathematics, 214*, 381–392.

Zhen, H., Hong, L., Mujiao, F., & Chunbi, X. (2010). Application of statistical learning theory to predict corrosion rate of injecting water pipeline. In *Cognitive informatics (ICCI), 2010 9th IEEE international conference on* (pp. 132–136).

Zhou, J., & Huang, J. (2012). Support-vector modeling and optimization for microwave filters manufacturing using small data sets. In *Industrial informatics (INDIN), 2012 10th IEEE international conference on* (pp. 202–207).

Chapter 13
Theoretical and Numerical Investigation of the Elastic-Plastic Behavior of Thick-Walled Cylinders

Monir Takla

13.1 Introduction

Extremely loaded cylindrical pressure vessels used in nuclear power plants as well as in chemical and oil-related industries have to sustain reliably the design loads, keeping in mind the potentially dangerous consequences of overloading nuclear reactors. As a result, it became necessary to investigate the behavior of extremely loaded pressure vessels undergoing plastic or elastic-plastic deformations.

13.1.1 Background

Accurate calculation of the distribution of stresses and large strains leads to improved accuracy when calculating the maximum sustainable loads, as well as bifurcation limits, which mark the onset of irregular deformations. Therefore, the correctness of failure analysis is based on the validity and accuracy of the fundamental solution, which describes the development of the regular stable unique deformations.

Available literature does not provide accurate prediction for the distribution of stresses and strains in metallic pressure vessels under excessive combined radial and axial loading when the elastic limit is exceeded and large elastic-plastic deformations occur.

Inspired by the desire to enhance the safety of pressure vessels, a reliable solution, adequately addressing the nonhomogeneous stress, strain, and velocity fields in thick-walled cylindrical pressure vessels, is needed to be investigated.

M. Takla (✉)
School of Engineering, RMIT University, Melbourne, VIC, Australia
e-mail: monir.takla@rmit.edu.au

L. Dai, R.N. Jazar (eds.), *Nonlinear Approaches in Engineering Applications*,
https://doi.org/10.1007/978-3-319-69480-1_13

13.1.2 Historical Overview

A first closed solution was provided by Lame (1852) for small elastic deformations of a closed cylinder under internal and external pressure. Small elastic-plastic deformations of thick-walled cylinders were first investigated by Turner (1909), adopting the Tresca yield criterion. Other researchers followed the same approach to provide solutions for various boundary conditions, materials, etc. Their works, however, were limited to the theory of small deformations.

The first solution that used the von Mises yield criterion was provided by Belayev et al. (1938) and Sokolovskij (1955). MacGregor et al. (1948) and Hodge et al. (1950) provided some solutions for special cases considering small deformations.

Celep (1971) described the large deformations of a cylinder constrained in the axial direction and obtained a numerical solution by applying the von Mises yield criterion with linear material hardening. Fischer (1977) applied the Tresca yield criterion together with the normality rule to a state of plane strain, taking linear material hardening into consideration. Oeynhausen (1981) also adopted the same approach for cylinders loaded by internal pressure and small axial force, considering nonlinear hardening. The validity of the analysis was limited to small axial loads due to the singularities resulting from applying the Tresca yield criterion together with the normality rule.

Imaninejad and Subhash (2005) investigated small plastic deformations of thick-walled cylinders subjected to internal pressure and proportional axial loading, assuming constant strain ratios throughout the cylinder wall. This assumption violates the basic principle that the axial strain is independent of the radial location, in contrast with the other two strain components. Accordingly, it resulted in an inaccurate solution including singularity. In a correct solution, the strain ratios should be treated as functions of the radial location and cannot be assumed constant.

13.1.3 Assumptions

The material is elastic-plastic, with small elastic and large plastic, constant volume deformations. The material is assumed homogeneous and isotropic with isotropic plastic hardening, excluding time, temperature, and inertia effects. The deformation is axially symmetric and is merely a function of the radial coordinates. Stresses and strains are uniquely defined in the deformed state and are functions of the radial location.

13.2 Theoretical Analysis

A theoretical solution is generally based on substituting a constitutive law into the equilibrium equations, taking into consideration that the geometric compatibility is maintained. In the developed solution, large elastic-plastic deformations are considered, while a thick-walled cylinder is loaded by combined large hydrostatic pressure and axial force, considering nonlinear isotropic hardening. The adopted constitutive law is based on applying the von Mises yield criterion in association with its normality rule. An algorithm for calculating the stress and strain distributions is developed, and the applied loads are calculated for prescribed states of large deformation.

13.2.1 Geometric Relations

The large deformations of the cylinder are described using spatial and material cylindrical coordinate systems. Deformations are assumed to remain independent of the axial position. The developed geometric expressions provide the relationships between the geometric variables in the initial configuration and those in the deformed configuration.

13.2.1.1 Coordinate Systems

The initial undeformed configuration is selected as the reference configuration. A cylindrical coordinate system is selected for both spatial and material coordinate systems. The coordinates are respectively defined by

$$x^j = (r, \phi, z) \tag{13.1}$$

$$X^\alpha = (R, \Phi, Z) \tag{13.2}$$

The metric tensors of the curvilinear coordinate system are

$$g_{ik} = \begin{bmatrix} 1 & 0 & 0 \\ 0 & r^2 & 0 \\ 0 & 0 & 1 \end{bmatrix} \tag{13.3}$$

$$g^{ik} = \begin{bmatrix} 1 & 0 & 0 \\ 0 & \frac{1}{r^2} & 0 \\ 0 & 0 & 1 \end{bmatrix} \tag{13.4}$$

13.2.1.2 Basic Deformations

The derivatives with respect to the reference coordinates are denoted by

$$(\cdot)' = \frac{\partial}{\partial R}(\cdot) \quad , \quad (\cdot)^* = \frac{\partial}{\partial \Phi}(\cdot) \quad , \quad (\cdot)^+ = \frac{\partial}{\partial Z}(\cdot) \tag{13.5}$$

The material points move only in the radial and axial directions. However, deformations are only a function of the radial coordinate (Fig. 13.1), i.e.,

$$\phi = \Phi \quad , \quad (\cdot)^* = 0, \tag{13.6}$$

$$z^+ = \frac{l}{l_o}, \quad \dot{z} = \frac{\dot{l}}{l_o}, \quad \frac{\dot{z}^+}{z^+} = \frac{\dot{l}}{l}, \tag{13.7}$$

where

$$l\,(t_o) = l_o \tag{13.8}$$

Accordingly, plane cross sections remain plane, and the circular cylindrical lateral surfaces remain circular cylindrical. Since the deformations contain no rotations, the strain rate tensor in the deformed state is directly obtained as

$$d_k^i = \left. v^i \right|_k = \begin{bmatrix} \dfrac{\dot{r}'}{r'} & 0 & 0 \\ 0 & \dfrac{\dot{r}}{r} & 0 \\ 0 & 0 & \dfrac{\dot{l}}{l} \end{bmatrix} \tag{13.9}$$

The assumption of incompressibility results in the condition:

$$d_s^s = \frac{\dot{r}'}{r'} + \frac{\dot{r}}{r} + \frac{\dot{l}}{l} = 0, \tag{13.10}$$

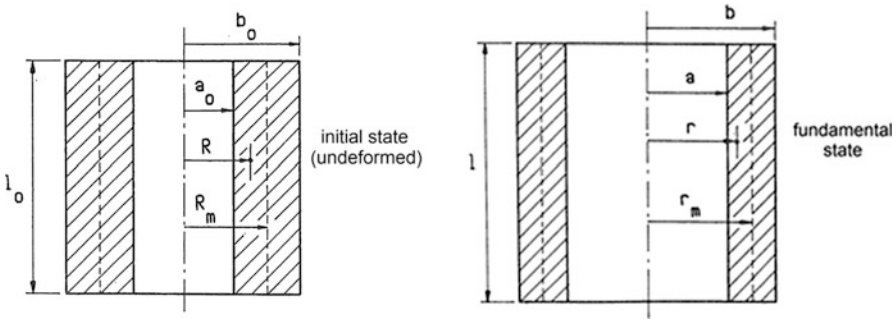

Fig. 13.1 Fundamental Deformations

the integration of which leads to the relationship

$$R^2 = \frac{l}{l_o}\left(r^2 - C_1\right) \tag{13.11}$$

where the initial conditions at $t = t_o$ are given by

$$r(t_o) = R \tag{13.12}$$

The integration constant C_1 in (13.11) and the homogeneous axial strain are independent of the loading or the material properties.

The components of the strain rate tensor are obtained from

$$d_1^1 = \frac{1}{2r^2}\dot{C}_1 - \frac{1}{2}\left(1 + \frac{C_1}{r^2}\right)\frac{\dot{l}}{l}, \tag{13.13}$$

$$d_2^2 = \frac{1}{2r^2}\dot{C}_1 - \frac{1}{2}\left(1 - \frac{C_1}{r^2}\right)\frac{\dot{l}}{l}, \tag{13.14}$$

$$d_3^3 = \frac{\dot{l}}{l} \tag{13.15}$$

The time integration of the components of the strain rate tensor results in the components of the HENCKY (logarithmic) strain tensor:

$$\varepsilon_1^1 = -\frac{1}{2}\ln\left(\frac{l}{l_o}\right) + \frac{1}{2}\ln\left(1 - \frac{C_1}{r^2}\right), \tag{13.16}$$

$$\varepsilon_2^2 = -\frac{1}{2}\ln\left(\frac{l}{l_o}\right) - \frac{1}{2}\ln\left(1 - \frac{C_1}{r^2}\right), \tag{13.17}$$

$$\varepsilon_3^3 = \ln\left(\frac{l}{l_o}\right) \tag{13.18}$$

The strains and strain rates are functions of the radial location, independent of the cylinder geometry. The inner radius in the deformed state is designated as a, and the outer radius as b. The radius of middle surface is

$$r_m = \frac{a+b}{2} \tag{13.19}$$

In the initial state ($t = t_o$),

$$a(t_o) = a_o \tag{13.20}$$

$$b(t_o) = b_o \tag{13.21}$$

$$r_m(t_o) = R_m \tag{13.22}$$

The following geometric expression provides the relationships between the geometric variables in the initial state and those in the deformed state:

$$\frac{b_o}{a_o} = \left[\frac{(b/a)^2 - L_1}{1 - L_1}\right]^{\frac{1}{2}} \tag{13.23}$$

$$L_1 = \frac{C_1}{a^2} \tag{13.24}$$

The dimensionless quantity L_1 is identified as the "radial loading parameter" and will be used as a measure of the radial deformation.

13.2.2 Stress Distribution in the Elastic Range

Due to elastic incompressibility, Hooke's law for small elastic deformations becomes

$$t_j^i = 2G\,\varepsilon_j^i \ , \tag{13.25}$$

a linear relationship between the components of the Hencky strain tensor (13.16, 13.17, and 13.18) and those of the stress deviator. Accordingly, the stress differences become

$$\sigma_2^2 - \sigma_1^1 = -2G \ln\left(1 - \frac{C_1}{r^2}\right), \tag{13.26}$$

$$\sigma_2^2 - \sigma_3^3 = -G\left[3 \ln\left(\frac{l}{l_o}\right) + \ln\left(1 - \frac{C_1}{r^2}\right)\right], \tag{13.27}$$

$$\sigma_3^3 - \sigma_1^1 = G\left[3 \ln\left(\frac{l}{l_o}\right) - \ln\left(1 - \frac{C_1}{r^2}\right)\right] \tag{13.28}$$

13.2.3 Stresses in the Elastic-Plastic Range

Due to the applied nonlinear constitutive law, which is based on the von Mises yield criterion, a fast iterative algorithm is developed to calculate the stress distribution throughout the cylinder wall. Incompressible small elastic but large plastic deformations together with an almost-proportional load path are assumed in the analysis. Radial and tangential stresses are calculated as functions of the radial position.

13.2.3.1 Application of Nonlinear Constitutive Law

Applying the von Mises yield criterion with the normality rule necessitates utilizing an iterative approach to the solution, based on assuming incompressible small elastic and large plastic deformations together with an almost-proportional load path. Also, the state of stress depends not only on the state of strain but also on the state of the strain rate.

13.2.3.2 Basic Equations

For the Hencky strain tensor $\varepsilon_{\sim}$,

$$\dot{\underset{\sim}{\varepsilon}} = \underset{\sim}{D}\,, \tag{13.29}$$

and accordingly

$$\underset{\sim}{\varepsilon} = \int_{t_o}^{t} \underset{\sim}{D}\ \mathrm{d}\tau \qquad \text{if} \qquad \underset{\sim}{\varepsilon}\Big|_{t_o} = \underset{\sim}{0} \tag{13.30}$$

The equivalent stress and strain rates are scalar quantities defined by

$$\overline{\sigma} = \left[\frac{3}{2}\mathrm{Tr}\left(\underset{\sim}{T}^2\right)\right]^{\frac{1}{2}}, \tag{13.31}$$

$$\dot{\overline{\varepsilon}} = \left[\frac{2}{3}\mathrm{Tr}\left(\underset{\sim}{D}^2\right)\right]^{\frac{1}{2}}, \tag{13.32}$$

where $\underset{\sim}{T}$ is the Cauchy stress deviator and $\underset{\sim}{D}$ is the strain rate tensor.

It should be noted that the Cauchy stress tensor coincides with the symmetric Kirchhoff stress tensor for incompressible material behavior. The value of the equivalent strain is obtained by the integration:

$$\overline{\varepsilon} = \int_{t_o}^{t} \dot{\overline{\varepsilon}}\,\mathrm{d}\tau \tag{13.33}$$

For proportional loading, this leads to

$$\overline{\varepsilon} = \left[\frac{2}{3}\mathrm{Tr}\left(\underset{\sim}{\varepsilon}^2\right)\right]^{\frac{1}{2}} \tag{13.34}$$

Dividing the strain rate tensor into elastic and plastic components results in

$$\underset{\sim}{D} = \underset{\sim}{D}_{\mathrm{e}} + \underset{\sim}{D}_{\mathrm{p}}, \tag{13.35}$$

where

$$\underset{\sim}{D}_{\mathrm{e}} = \frac{1}{2\mathrm{G}}\ \overset{\cdot}{\underset{\sim}{T}}\,, \tag{13.36}$$

$$\underset{\sim}{D}_{\mathrm{p}} = \ \delta \frac{\mathrm{Tr}\left(\underset{\sim}{T}\ \underset{\sim}{D}\right)}{\mathrm{Tr}\left(\underset{\sim}{T}^2\right)}\ \underset{\sim}{T} = \ \delta\left[\frac{\mathrm{Tr}\left(\underset{\sim}{T}\ \underset{\sim}{D}\,\mathrm{e}\right)}{\mathrm{Tr}\left(\underset{\sim}{T}^2\right)} + \frac{\mathrm{Tr}\left(\underset{\sim}{T}\underset{\sim}{D}_{\mathrm{p}}\right)}{\mathrm{Tr}\left(\underset{\sim}{T}^2\right)}\right]\underset{\sim}{T} \tag{13.37}$$

The hardening parameter δ is a dimensionless material property function of the tangent modulus:

$$\delta\left(W_{\mathrm{p}}\right) = 1 - \frac{E_{\mathrm{t}}}{E} \tag{13.38}$$

13.2.3.3 Material Model

The selected material characteristic law is similar to that of RAMBERG-OSGOOD (Bruhns 1974).

$$\varepsilon = \frac{\sigma}{E} + \ \frac{\sigma_{\mathrm{o}}}{B}\ \left(\frac{\sigma}{\sigma_{\mathrm{o}}} - 1\right)^{\mathrm{n}} \qquad \sigma\ \geq\ \sigma_{\mathrm{o}}, \tag{13.39}$$

$$\varepsilon = \frac{\sigma}{E} \qquad \sigma\ \leq\ \sigma_{\mathrm{o}}, \tag{13.40}$$

where σ and ε are the axial true stress and the HENCKY (logarithmic) strain, respectively, obtained from a uniaxial tension or compression test. The true stress at the transition from the linear elastic into the nonlinear plastic range is given by σ_o, resulting in the tangent modulus

$$E_t = \frac{\mathrm{d}\sigma}{\mathrm{d}\varepsilon} = \frac{\mathrm{E}}{1 + \frac{E}{B} n \left(\frac{\sigma}{\sigma_o} - 1\right)^{n-1}} \qquad \sigma\ \geq\ \sigma_o, \tag{13.41}$$

$$E_t = \frac{\mathrm{d}\sigma}{\mathrm{d}\varepsilon} = E \qquad \sigma\ \leq\ \sigma_o \tag{13.42}$$

and the curvature

$$\frac{dE_t}{\mathrm{d}\varepsilon} = \frac{\mathrm{d}^2\sigma}{\mathrm{d}\varepsilon^2} = \frac{E^3 n\ (n-1)\ \left(\frac{\sigma}{\sigma_{\mathrm{o}}} - 1\right)^{n-2}}{\sigma_{\mathrm{o}} B\left[1 + \frac{E}{B} n \left(\frac{\sigma}{\sigma_{\mathrm{o}}} - 1\right)^{n-1}\right]^3} \qquad \sigma \geq \sigma_o \tag{13.43}$$

$$\frac{dE_t}{\mathrm{d}\varepsilon} = \frac{\mathrm{d}^2\sigma}{\mathrm{d}\varepsilon^2} = 0 \qquad \sigma \leq \sigma_o \tag{13.44}$$

Such material model implies continuous transition and provides a continuous tangent modulus at the elastic-plastic interface.

13.2.3.4 First Iteration

Due to the assumption of elastic incompressibility,

$$E = 3\mathrm{G} = \frac{\overline{\sigma}}{\overline{\varepsilon}_\mathrm{e}} \tag{13.45}$$

As a first iteration, the elastic component of the strain rate tensor is

$$\underset{\sim}{D}_\mathrm{e} = \frac{3}{2}\,\frac{\overline{\varepsilon}_\mathrm{e}}{\overline{\sigma}}\,\underset{\sim}{\dot{T}} \tag{13.46}$$

Integration leads to

$$\underset{\sim}{\varepsilon}_\mathrm{e} = \frac{3}{2}\,\frac{\overline{\varepsilon}_\mathrm{e}}{\overline{\sigma}}\,\underset{\sim}{\mathrm{T}} \tag{13.47}$$

Along the entire load path, it is valid that

$$\underset{\sim}{D}_\mathrm{e} = \frac{\dot{\overline{\varepsilon}}_\mathrm{e}}{\overline{\varepsilon}_\mathrm{e}}\,\underset{\sim}{\varepsilon}_\mathrm{e} \tag{13.48}$$

and

$$\overline{\varepsilon}_\mathrm{e} = \left[\frac{2}{3}\mathrm{Tr}\left(\underset{\sim}{\varepsilon}_\mathrm{e}^{\,2}\right)\right]^{\frac{1}{2}} \tag{13.49}$$

This leads for elastic and plastic incompressible material behavior to

$$\underset{\sim}{D} = \left[\frac{\mathrm{Tr}\left(\underset{\sim}{D}^2\right)}{\mathrm{Tr}\left(\underset{\sim}{T}^2\right)}\right]^{\frac{1}{2}}\underset{\sim}{T}\,, \tag{13.50}$$

a simple linear constitutive law, which also describes accurately rigid plastic material behavior. For a proportional loading path, Eq. (13.50) contains no approximations. However, when there are deviations from proportionality, it implies an approximation to the elastic part of the strain rate tensor.

13.2.3.5 Second Iteration

For deformations without rotation, a special nonlinear constitutive law can be given by

$$\underset{\sim}{T} = \frac{1}{\delta} \frac{\mathrm{Tr}\left(\underset{\sim}{T}^2\right)}{\mathrm{Tr}\left(\underset{\sim}{T}\underset{\sim}{D}\right)} \left[\underset{\sim}{D} - \frac{1}{2\mathrm{G}}\dot{\underset{\sim}{T}}\right] \tag{13.51}$$

From the first iteration (13.50),

$$\underset{\sim}{T} = \frac{\frac{2}{3}\overline{\sigma}}{\dot{\overline{\varepsilon}}} \underset{\sim}{D} = \overset{(1)}{\underset{\sim}{T}} \tag{13.52}$$

The material time derivative provides

$$\dot{\underset{\sim}{T}} = \frac{2}{3}\left[\underset{\sim}{D}\, E_t + \overline{\sigma}\left\{\frac{\bar{D}}{\overline{\varepsilon}}\right\}\right] \tag{13.53}$$

The second term depends merely on the change of the strain rate tensor but does not exist for proportional deformations. Substituting (13.53) in the constitutive law (13.51),

$$\overset{(2)}{\underset{\sim}{T}} = \overset{(1)}{\underset{\sim}{T}} - \frac{2}{9\mathrm{G}\delta}\left(\overline{\sigma}^2 \frac{1}{\dot{\overline{\varepsilon}}}\dot{\left[\frac{\underset{\sim}{D}}{\dot{\overline{\varepsilon}}}\right]}\right) \tag{13.54}$$

The second term can only be calculated if a specific load path is defined.

The outcome of the first iteration is very accurate for small deformations with small deviations from proportionality. However, an improvement by the second iteration becomes impossible as the second term in (13.54) becomes very large. This is because the hardening parameter δ is reduced to zero at the elastic-plastic transition point in the adopted material model. In this case, the second iteration cannot improve the results. Therefore, the influence of this term is needed to be modified, e.g., through multiplying it by a factor "η" defined by

$$\eta = \left(\frac{\overline{\varepsilon}_p}{\overline{\varepsilon}}\right)^2, \tag{13.55}$$

so that

$$\overset{(2)}{\underset{\sim}{T}} = \overset{(1)}{\underset{\sim}{T}} - \frac{2}{9\mathrm{G}\delta}\left(\overline{\sigma}^2 \frac{1}{\dot{\overline{\varepsilon}}}\dot{\left[\frac{\underset{\sim}{D}}{\dot{\overline{\varepsilon}}}\right]}\right).\eta \tag{13.56}$$

This factor maintains the validity of the solution for small plastic deformations in the elastic-plastic transition zone.

13.2.4 Description of the Load Path

According to Eq. (13.54), it is necessary to specify a load path in the calculation of the second approximation.

Radial and tangential stresses and strains are both functions of the radial position, while the axial strain remains constant throughout the wall thickness. Therefore, while it may be theoretically possible to keep constant strain ratios at one radial position, it is impossible to keep the same strain ratios throughout the cylinder wall. Accordingly, an exactly proportional relationship, between the applied pressure and the axial force, would not lead to consistent strain ratios throughout the cylinder.

Also, enforcing an exactly proportional loading path leads to unnecessarily significant complications. Therefore, an alternative approach is introduced, in which the description of the loading path is implicitly expressed through the description of the deformation path.

The dimensionless geometrical quantity γ is introduced at an arbitrarily selected material point, which has the radius $r = m$ in the deformed configuration, defined by

$$\gamma = \frac{m}{a} \tag{13.57}$$

This material point is located at the position "$R = m_o$," in the reference configuration. It has to be noted, however, that

$$\gamma_o = \frac{m_o}{a_o} \neq \gamma \tag{13.58}$$

The integrated strain component in the circumferential direction for the radius m is calculated directly from (13.17):

$$\varepsilon_{2m} = \varepsilon_2\big|_{(r=m)} = \ln\left[\left(1 - \frac{C_1}{m^2}\right) e^{\varepsilon_3}\right]^{-\frac{1}{2}} \tag{13.59}$$

The following geometric relationship

$$\dot{\varepsilon}_{2m} = \left(\frac{3}{4\psi} e^{2\varepsilon_{2m}} - \frac{1}{2}\right) \dot{\varepsilon}_3 \tag{13.60}$$

is proposed to remain satisfied along the loading path at the selected position $r = m$, where the parameter ψ remains constant. It provides an exactly proportional relationship between the applied pressure and the externally applied axial force when m is selected to be the middle radius of a rigid plastic, closed thin-walled tube. For thick-walled cylinders or for large elastic deformations, the resulting load path becomes approximately proportional.

Integration results in

$$\varepsilon_3 = \ln\left(\frac{3\,e^{2\varepsilon_{2m}} - 2\psi}{3 - 2\psi}\right) - 2\,\varepsilon_{2m} \tag{13.61}$$

The initial conditions were utilized to determine the integration constants; the expression for ψ can be expressed as

$$\psi = \frac{3m^2}{2C_1}(1 - e^{-\varepsilon_3}) \tag{13.62}$$

The relationship between the components of the velocity field is directly obtained from

$$\dot{\varepsilon}_2 = \frac{m^2}{r^2}\left(\frac{\dot{\varepsilon}_3}{2} - \dot{\varepsilon}_m\right) - \frac{\dot{\varepsilon}_3}{2} \tag{13.63}$$

The second term of Eqs. (13.54) and (13.56), needed for the second iteration, is obtained after short calculation as

$$\dot{\left[\frac{\dot{\varepsilon}_2}{\dot{\bar{\varepsilon}}}\right]} = -\frac{3}{8}\,\frac{\left[1 + 2\left(\frac{\dot{\varepsilon}_3}{\dot{\varepsilon}_2}\right)\right]}{\left[1 + \left(\frac{\dot{\varepsilon}_3}{\dot{\varepsilon}_2}\right) + \left(\frac{\dot{\varepsilon}_3}{\dot{\varepsilon}_2}\right)^2\right]^2}\left(\frac{\dot{\bar{\varepsilon}}}{\dot{\varepsilon}_2}\right)\dot{\left[\frac{\dot{\varepsilon}_3}{\dot{\varepsilon}_2}\right]}, \tag{13.64}$$

$$\dot{\left[\frac{\dot{\varepsilon}_3}{\dot{\bar{\varepsilon}}}\right]} = -\frac{3}{8}\,\frac{\left[1 + 2\left(\frac{\dot{\varepsilon}_2}{\dot{\varepsilon}_3}\right)\right]}{\left[1 + \left(\frac{\dot{\varepsilon}_2}{\dot{\varepsilon}_3}\right) + \left(\frac{\dot{\varepsilon}_2}{\dot{\varepsilon}_3}\right)^2\right]^2}\left(\frac{\dot{\bar{\varepsilon}}}{\dot{\varepsilon}_3}\right)\dot{\left[\frac{\dot{\varepsilon}_2}{\dot{\varepsilon}_3}\right]} \tag{13.65}$$

The third component can be obtained from the incompressibility condition.

Consequently, further material time derivatives of the velocity field components are necessary. They are obtained from

$$\dot{\left(\frac{\dot{\varepsilon}_2}{\dot{\varepsilon}_3}\right)} = A_2\dot{\varepsilon}_2 + A_3\dot{\varepsilon}_3, \tag{13.66}$$

with

$$A_2 = 2A_oM, \tag{13.67}$$

$$A_3 = A_oM\frac{(r^2 - C_1)}{r^2} - \frac{M}{r^2}\gamma^2, \tag{13.68}$$

where

$$A_o = 2\left(1 - \gamma_o{}^2\right) + \frac{m^2\gamma_o{}^2}{m^2 - C_1} - \frac{m^2}{r^2}\left(1 - \frac{r_o{}^2}{a_o{}^2}\right), \tag{13.69}$$

$$M = \frac{1}{2} + \left(\dot{\varepsilon}_2/\dot{\varepsilon}_3\right)_m \tag{13.70}$$

The time derivative of the inverse of the left side of (13-66) is obtained from

$$\frac{\cdot}{\left(\dot{\varepsilon}_3/\dot{\varepsilon}_2\right)} = \left(\dot{\varepsilon}_3/\dot{\varepsilon}_2\right)^2 \frac{\cdot}{\left(\dot{\varepsilon}_2/\dot{\varepsilon}_3\right)} \tag{13.71}$$

Substituting from (13.71) into (13.64) and (13.65), the required expression of Eqs. (13.52) and (13.54) can be obtained, so that the stress tensor can be determined.

13.2.5 Equilibrium Condition

The equilibrium condition is given by

$$\frac{\partial \sigma_1^1}{\partial r} + \frac{1}{r}\left(\sigma_1^1 - \sigma_2^2\right) = 0 \tag{13.72}$$

Integration leads directly to

$$\sigma_1^1 = \int_a^r \left(\sigma_2^2 - \sigma_1^1\right) \frac{\mathrm{d}r}{r} - \mathrm{p} \tag{13.73}$$

where p is the internal pressure. The integration constants are determined from the boundary conditions at the inner and outer boundaries. The values of the other components of the stresses are obtained by utilizing the expressions of the stress differences.

13.2.6 External Loads in the Fundamental State

With the obtained stress distribution across the tube wall, it becomes possible to determine the external loads. From the boundary conditions in conjunction with Eq. (13.73), the expression for the internal pressure can be given as

$$p = \int_a^b \left(\sigma_2^2 - \sigma_1^1\right) \frac{\mathrm{d}r}{r} \tag{13.74}$$

An expression for the axial force is reached by integrating the axial stresses over the tube cross section:

$$N = 2\pi \int_a^b \sigma_3^3 \, r \, \mathrm{d}r \tag{13.75}$$

Taking into consideration the axial stress component resulting from the internal pressure, the expression for the externally applied force F is obtained as

$$F = 2\pi \int_a^b \sigma_3^3 \, r \, \mathrm{d}r \quad - \pi \, a^2 p \tag{13.76}$$

Since the stresses are available only numerically, numerical integration is therefore necessary to determine the external loads (13.74 and 13.76).

13.3 Results and Validation

A cylinder with an initial diameter ratio of 1.6 is considered thick enough to represent reasonably the thick-walled cylinder, which would expose any inaccuracies in the theoretical analysis when validating the results.

13.3.1 Material Properties

The material model presented in Sect. 13.2.3.3 is used in the analysis. The arbitrarily selected material is an aluminum alloy AlMgCuPb (Zander 1981). The characteristic material values defined in Eq. (13.39) are given by

$$\begin{aligned} \sigma_o &= 240 \ \mathrm{N/mm^2} \\ E &= 59500 \ \mathrm{N/mm^2} \\ B &= 4875.5 \ \mathrm{N/mm^2} \\ n &= 2.79865 \end{aligned}$$

The characteristic material curve is shown in Fig. 13.2, which is used in all theoretical calculations and numerical validations.

13.3.2 Approach to the Presentation of Results

The load path to any combined load can be fully defined through the selection of the parameter "γ," defined in Eq. (13.57), which can be determined from

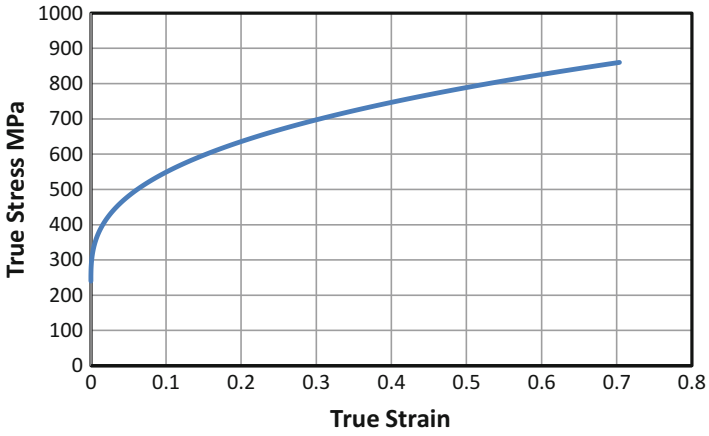

Fig. 13.2 Characteristic material curve

$$\gamma = \left(\frac{b_o}{a_o}\right)^j \tag{13.77}$$

For an almost-proportional relationship between the applied radial pressure and the integrated axial force, the value of j is selected as 0.5.

In the theoretical analysis, a state of deformation is defined by the radial loading parameter and the axial strain. Therefore, it is appropriate to represent the loading via the deformations. In a "deformation diagram," the axial strain "ε_3" is plotted against the radial loading parameter "L_1," while in a "load diagram," the internal pressure is plotted against the external axial force.

To standardize the results, the internal pressure and the axial force are normalized into dimensionless stress variables defined as

$$F_n = \frac{F}{\pi\sigma_o\left(b_o{}^2 - a_o{}^2\right)}, \tag{13.78}$$

$$p_n = \frac{p\, a_o}{\sigma_o(b_o - a_o)} \tag{13.79}$$

13.3.3 Loading by an Almost-Proportional Load Path

In the presented case study, a load combination of $L_1 = 0.2$ and $\varepsilon_3 = 0.1$ is reached through an almost-proportional load path along which $j = 0.5$ (Eq. 13.77). The load path is represented in Fig. 13.3 for the selected cylinder geometry. The selected loading parameters resulted in a normalized pressure of 1.1947 (Eq. 13.78) and a

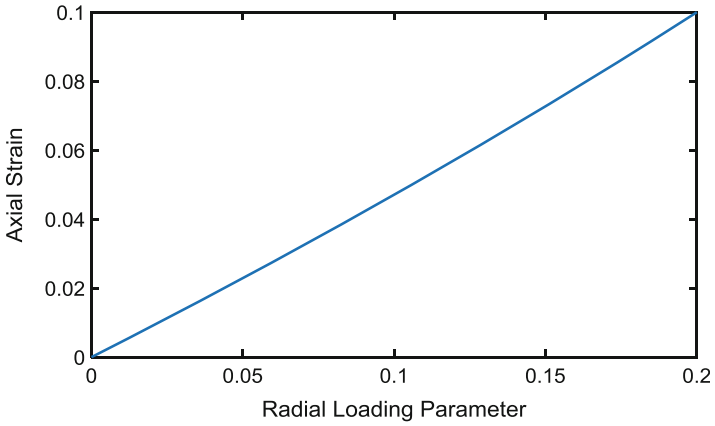

Fig. 13.3 Load path – deformation diagram

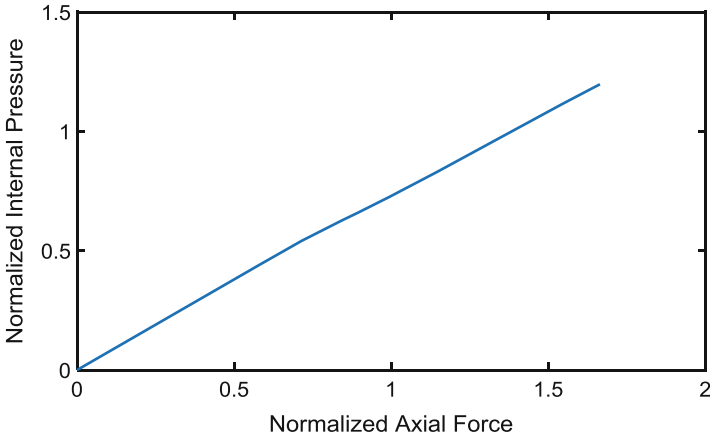

Fig. 13.4 Load path – load diagram

normalized axial force of 1.66 (Eq. 13.79). Figure 13.4 shows the resulting load path represented on the load diagram.

13.3.4 Validation Using Finite Element Analysis

The theoretical analysis is validated by comparing the theoretically obtained results with those obtained numerically using nonlinear finite element simulation, which takes into consideration elastic-plastic material behavior with nonlinear hardening. The nonlinear FEA program ABAQUS V. 6–14 was utilized as the platform for the

numerical FEM analysis. The program is adequately equipped with the tools needed to model large elastic-plastic deformations.

13.3.4.1 Model Setup

The arbitrarily selected dimensions of the cylinder are 10 mm for the internal diameter and 16 mm for the external diameter. The end boundary conditions are modeled so that they result in axially homogeneous fundamental deformation conforming to the theoretical assumptions.

In order to minimize computational cost, an axisymmetric modeling technique has been adopted, in which only a cross section of the cylinder is modeled. Also, due to the axial symmetry of geometry, loading, and boundary conditions, a symmetry boundary condition was introduced at the middle plane of the cylinder so that only half the cylinder is needed to be modeled. These simplifications provided significant improvements to the computational efficiency without any sacrifice of the accuracy of the results. Figure 13.5 shows a comparison between the theoretical model and the actual FEA model. The material model presented in Sect. 13.2.3.3 and the material characteristics presented in Sect. 13.3.1 have been used in the numerical simulation. The material characteristic curve used in the theoretical analysis is discretized and introduced as an array to the model.

13.3.4.2 Element Selection

Axisymmetric solid elements are utilized. In order to avoid shear locking and hourglass effects, second-order quadratic elements were selected for the analysis, which provides parabolic distribution of the deformations and results in high degree of accuracy of the model stiffness. Mesh sensitivity analysis was conducted to ensure that the selected mesh size is adequate for providing high degree of accuracy.

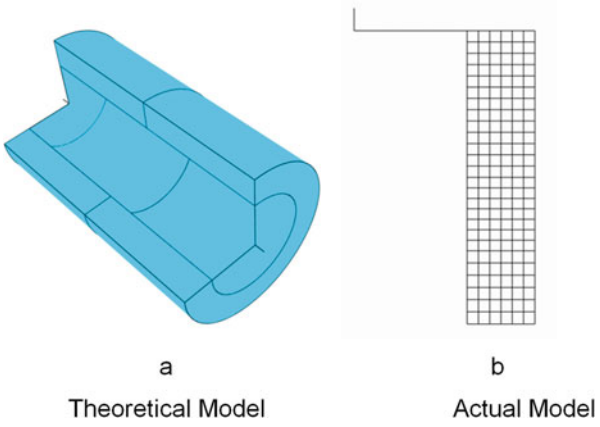

Fig. 13.5 Finite element model

13.3.4.3 Load Application

Hydrostatic pressure was applied to both the cylinder walls and the closed ends of the tube. The pressure is applied so that it acts on the deformed configuration, i.e., not limited to the initial configuration.

In order to validate the theory, the values of the theoretically calculated, normalized loading components were used with Eqs. (13.78) and (13.79) to calculate the loads. An internal pressure of 172.0 MPa and an externally applied force of 195.333 kN are applied simultaneously, which provides an exact ratio between the applied pressure and the axial force in the incremental finite element analysis. This is close to having $j = 0.5$ (Eq. 13.77) in the theoretical analysis. The external axial load is applied to the cylinder end so that it does not cause any localized stresses or deformations.

13.3.4.4 Analysis Techniques

The nonlinear incremental static analysis takes into consideration large deformations and material nonlinearities. The Newton-Raphson method was adopted for the analysis.

13.3.5 Numerical Validation

The stress and strain distributions calculated in Sect. 13.2 are compared with those from finite element simulations. Figure 13.6 shows comparison of the distribution of the radial, hoop, and axial strain components obtained from the developed theory with those calculated independently from the finite element analysis for the same loading combination, following the load path presented in Sect. 13.3.3.

The results show outstanding agreement between all strain components obtained by adopting both theoretical and FEM approaches as they effectively coincide. This agreement represents validation of both the completely different approaches.

The results show clearly that the ratios between the strain components vary considerably throughout the cylinder wall. This explains the incorrect outcome presented in literature (Imaninejad et al. 2005) when constant strain ratios were assumed throughout the cylinder.

The distribution of the von Mises equivalent strain is displayed in Fig. 13.7. The corresponding von Mises equivalent stress distribution is presented in Fig. 13.8. Both theoretical and numerical FEM results are presented showing, again, outstanding agreement.

The deviatoric stress components, which are solely responsible of distortion, yielding, and plastic deformations, are presented in Fig. 13.9. Once again, the agreement between theoretical and numerical FEM results is outstanding.

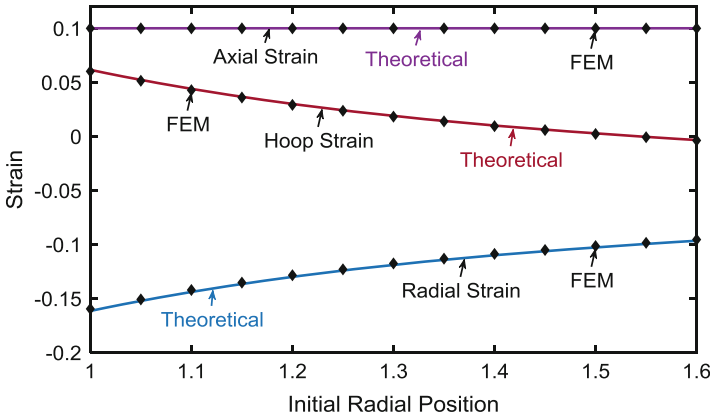

Fig. 13.6 Strain components

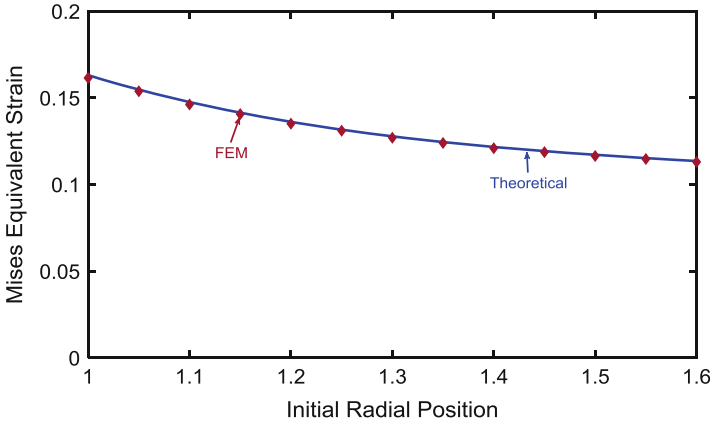

Fig. 13.7 Von Mises equivalent strain

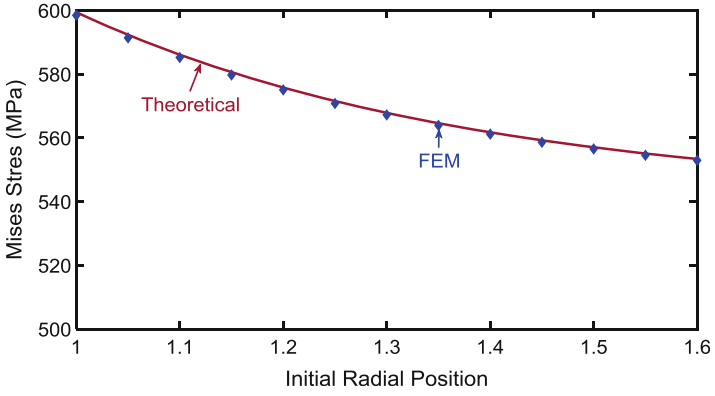

Fig. 13.8 Von Mises equivalent stress

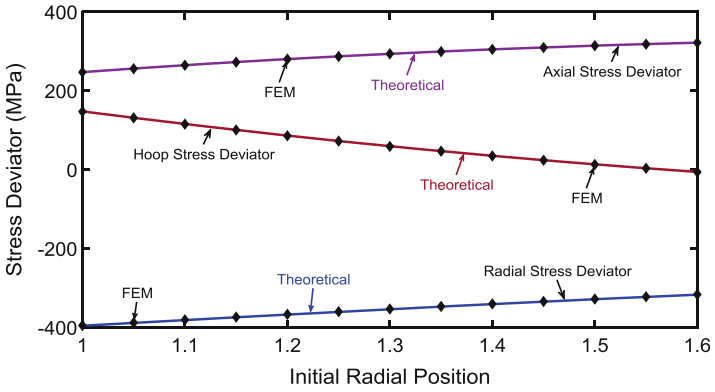

Fig. 13.9 Deviatoric stress components

Comparing the deviatoric stress distributions (Fig. 13.9) with the distribution of the strain components (Fig. 13.6) shows that the ratios between the deviatoric stress components are effectively the same as those of the strain components. These ratios, however, vary throughout the cylinder wall.

The finite element simulations are completely numerical, and the results obtained from the theoretical solution are also calculated through numerical integration using a Runge-Kutta algorithm. Therefore, such outstanding agreement between the solution obtained from the developed theory and that obtained from finite element analysis, utilizing a completely independent commercial program, actually exceeds accuracy expectations and proves beyond doubt the correctness of the developed theory.

The results also show a smooth continuous distribution of stresses and strains, which confirms resolving the long-standing, persisting issues cited in literature (Oeynhausen 1981; Imaninejad and Subhash 2005), where the presented solutions contained either singularity or discontinuity in the resulting stress and strain fields. Therefore, the outcome of this research represents an achievement and a large step forward in the safety analysis of pressure vessels.

13.4 Conclusion

A general theory was developed for large elastic-plastic deformations of thick-walled cylindrical pressure vessels loaded by combined large hydrostatic pressure and axial force, considering nonlinear isotropic hardening. The adopted constitutive law is based on applying the von Mises yield criterion in association with its normality rule. The deformation of the cylinder is assumed to remain axially symmetric, i.e., deformations are independent of the axial position. Stress and strain distributions are obtained and presented for a case study of combined internal pressure and axial tensile load.

The theoretical analysis is validated by comparing the theoretically obtained results with those obtained numerically using nonlinear finite element simulation, which satisfies the theoretical boundary conditions.

The nonlinear incremental finite element simulation takes into consideration large elastic-plastic material behavior with nonlinear isotropic hardening. An almost-proportional load path is assumed in the theoretical analysis, while exactly proportional loading is adopted in the finite element simulations.

The numerical results obtained from the finite element simulations effectively coincide with those obtained from the theoretically developed solutions, although the theoretically assumed load path is not exactly proportional. This validates both the developed theory and the finite element simulation and confirms the viability of all assumptions.

This investigation addressed and resolved a persisting unresolved problem, presented a novel approach, and provided a validated accurate solution to the problem, which results in continuous and accurate stress and strain fields throughout the cylinder wall. It rectifies outcomes from earlier attempts cited in literature over decades, which contained inaccuracies, discontinuities, and singularities due to invalid assumptions and/or inadequate selection of the yield criterion.

The findings provide valuable information in the safety design of extremely loaded pressure vessels. The presented approach also establishes the basis for further research in the stability investigations and bifurcation analysis of thick-walled pressure vessels.

References

Belayev, N. M., & Sinltsklj, A. K. (1938). Stresses and deformations in thick-walled cylinders on the plastic-elastic state of material. *Bulletin of the Academy Science of the U.R.S.S.*

Bruhns, O. T. (1974). *Einige Bemerkungnen zur Bestimmung von Verzweigungslasten elastoplastisch derformierter Kontinua*, Mitteilung Nr. 74–9 des Inst. f. konstr. Ing.bau, Ruhr-Univ. Bochum.

Celep, Z. (1971). *Beitrag zur Theorie dicker Kreiszylinder- und Kugelschalen unter innerem Druck*. Diss. TU Hannover.

Fischer, B. (1977). *Zur zyklischen, elastoplastischen Beanspruchung eines dickwandigen Zylinders bei endlichen Verzerrungen*, Mitteilungen aus dem Institut für Mechanik Nr. 9, Ruhr-Universität Bochum.

Hodge, P. G., & White, G. N. (1950). A quantitative comparison of flow and deformation theories of plasticity. *Journal of Applied Mechanics, 17*, 180–184.

Imaninejad, M., & Subhash, G. (2005). Proportional loading of thick-walled cylinders. *International Journal of Pressure Vessels and Piping, 82*, 129–135.

Lame, M. G. (1852). *Lecons sur la Theorie Mathematique de l'Elasticite des Corps Solides*. Paris: Imprimeur-Libraire.

MacGregor, C. W., Coffin, L. F., Jr., & Fisher, J. C. (1948). Partially plastic thick-walled tubes. *Journal of Franklin Institute, 245*, 135–158.

Oeynhausen, H. (1981). *Verzweigungslasten elastoplastisch deformierter, dickwandiger Kreiszylinder unter Innendruck und Axialkraft*, Mitt. Institut f. Mechanik, No. 29, RU Bochum.

Sokolovskij, V. V. (1955). *Theorie der Plastizität*. Berlin: VEB Verlag Technik.

Turner, L. B. (1909). The stresses in a thick hollow cylinder subjected to internal pressure. *Transactions of the Cambridge Philosophical Society, 21*, 377–396.

Zander, G. (1981). *Zur Bestimmung von Verzweigungslasten dünner Kreiszylinder unter kombinierter Längs- und Torsionsbelastung*, Mitteilungen aus dem Institut für Mechanik Nr. 27 Ruhr-Universität Bochum.

Chapter 14
A Complex Variable Method to Predict an Aerodynamics of Arbitrary Shape Ballistic Projectiles

Sayavur I. Bakhtiyarov, Jimmie C. Oxley, James L. Smith, and Philipp M. Baldovi

14.1 Introduction

Explosive ballistic projectiles (EBPs) can be described as fragments of various sizes, masses, compositions, and shapes that formed from explosive devices. They follow almost parabolic trajectories before they impact the targets. EBPs represent a significant hazard that can potentially cause damage to natural and man-made structures, fatal injury to people, and damage to the environment. These hazardous effects originate from the high-impact energy and elevated temperature of the EBPs. EBPs are capable of penetrating all building materials. The studies show that they reach initial (detonation) velocities up to several kilometers per second.

When an explosive detonates the expansion of the extremely pressurized gas products (the Taylor wave) fragment any casing the charge may have had. The resulting fragments have different masses, shapes, and velocities. Understanding their distributions is key to evaluating the level of resultant damage. After achieving their initial velocity, the fragments continue their lethal ballistic trajectory through the air. Their final velocities necessarily are less than their initial velocities due to gravity and drag forces.

S.I. Bakhtiyarov (✉) • P.M. Baldovi
Mechanical Engineering Department, New Mexico Institute of Mining and Technology, Socorro, NM, USA
e-mail: sayavur.bakhtiyarov@nmt.edu

J.C. Oxley • J.L. Smith
Department of Chemistry, DHS Center of Excellence in Explosives, University of Rhode Island, Kingston, RI, USA

L. Dai, R.N. Jazar (eds.), *Nonlinear Approaches in Engineering Applications*,
https://doi.org/10.1007/978-3-319-69480-1_14

14.1.1 Gurney Equations

When a cased explosive detonates, the outer shell is accelerated due to the initial shock wave and the expansion of the gaseous products. Ronald Gurney (1943) first modeled the energy distributed between the solid (metal) shell and the detonation gases and developed a set of mathematical equations to define (i) the detonation velocities of fragments generated by the explosive, (ii) the explosives forces, and (iii) the accelerations of shaped charge explosives. In his models, which are based on the principle of energy conservation, Gurney made simplifying assumptions that the velocity gradient (e.g., particle velocity distribution) in the explosive detonation product gases was linear and that the density was uniform throughout the explosive product. These assumptions simplify integration of the kinetic energy of the explosive and that of the internal energy over the explosive. The Gurney model assumes that the change in the internal energy is equal to the kinetic energy of the metal liner and produced explosive gases:

$$CE_0 - \int_{\text{gas}} EdC = \frac{1}{2}MV_0^2 + \frac{1}{2}\int_{\text{gas}} V^2 dC \tag{14.1}$$

where M and C are the masses of the metal liner and the charge, respectively, E is the internal energy of explosive, E_0 is the initial value of the explosive's internal energy, V_0 is the velocity of the metal liner, and V is the particle velocity within the explosive products. Gurney suggested that the explosive products expand adiabatically according to the ideal gas law. Then the following energy-density relationship can be used:

$$E = E_0\left(\frac{\rho}{\rho_0}\right)^{\gamma-1}, \tag{14.2}$$

where ρ and ρ_0 are the current and initial explosive densities.

The fragment velocities determined in many experimental studies showed a good agreement with Gurney's formula (Bola et al. 1992). An analytical method for the evaluation of the detonation velocity of fragments was proposed by Zhang et al. (2003). The latter method was based on the equation of motion of the fragment and the gas pressure inside the casing. Another analytical formula for the detonation velocity (cylindrical metal casing) was proposed by Elek et al. (2013). In their studies, the casing was treated as a deforming body. Pearson (1990) divided the dynamics of the fragment motion into the following phases:

- Phase 1: the case expansion is considered as elastic-plastic.
- Phase 2: the plastic expansion continues with further development of fractures.
- Phase 3: the fragmentation process starts.
- Phase 4: each fragment continues its terminal movement.

Pearson calculated the velocity in each phase and compared it with Gurney's velocity. Velocities in phases 3 and 4 were lower than Gurney velocity by 4% and 9%, respectively.

Gurney equations have been used successfully in many applications (Nystrom and Gylltoft 2009). However, the assumptions used in the Gurney formulae (uniform density and linear velocity distribution in the products) are over simplifications. Over the years, various improvements have been offered. A simple model suggested by Thomas (1944) assumed that, once the liner expanded to a certain multiple of its initial radius, it was no longer accelerated; any internal energy remaining in the products did not contribute to the final velocity of the liner. Hirsch (1986, 1995) showed that when the total energy partitioned between the flyer plate and gases exceeded unity, the Gurney assumptions failed. Hirsch established a range of $\frac{M}{C}$ values where the Gurney assumptions would not work (anomalous region). *Hydrocode* simulations have been conducted by Flis (1996) to take into the account both density nonuniformity and velocity nonlinearity distributions.

The equations proposed by Gurney to calculate the velocity of an accelerated flyer after detonation (V) for simple charge geometries is as follows:

$$\frac{V}{\sqrt{2E}} = \left(a\frac{M}{C} + b\right)^{-\frac{1}{2}}. \tag{14.3}$$

Here, $\sqrt{2E}$ is an empirical Gurney velocity constant of the explosive charge. The values of the empirical constants a and b depend on the charge geometry and can be found in Table 14.1.

An approximate technique was proposed by Kamlet and Jacobs (1968) to calculate the Gurney velocity as a function of the detonation velocity and the pressure. The initial density of the explosives ρ_0 and a parameter Φ was used to correlate detonation velocity and the pressure. The introduced parameter Φ was considered as a function of the released energy and the amount of the produced gases.

Hardesty and Kennedy (1977) showed that the internal energy remaining in the product gases late in their expansion does not contribute to the acceleration of the casing. Therefore, the effective specific energy of an explosive is less than that measured by detonation calorimetry. The authors proposed an expression for Gurney velocity using parameter Φ and density ρ_0:

$$\sqrt{2E} = 0.6 + 0.54\sqrt{1.44\,\rho_0\Phi}. \tag{14.4}$$

Another correlation using parameters Φ and ρ_0 was proposed by Kamlet and Fioger (1979):

Table 14.1 Empirical constants in Gurney equation for different charge geometries

Charge geometry	a	b
Cylindrical	1	0.5
Spherical	1	0.6
Symmetrical sandwich	2	0.33

$$\sqrt{2E} = 0.887\, \Phi^{0.5} \rho^{0.4}. \tag{14.5}$$

Some of the proposed correlations used only the detonation velocity. For example, the following expression for the Gurney velocity was proposed by Cooper (1996):

$$\sqrt{2E} = \frac{v_{\mathrm{D}}}{2.97}. \tag{14.6}$$

Based on gas dynamic analysis another formula for the Gurney velocity has been proposed (Kennedy, 1998):

$$\sqrt{2E} = \frac{0.605\, v_{\mathrm{D}}}{\gamma - 1} \tag{14.7}$$

where γ is a Poisson constant (a ratio of the heat capacity at constant pressure to the heat capacity at constant volume) at the detonation.

In contrast to the assumptions of the Gurney equations and other analytical models described above, Cullis et al. (2014) and Predebon et al. (1977) showed that the velocity distribution along the longitudinal axis of a cylinder is not constant. Experimental results obtained by Charron (1979), Li et al. (2015), and Huang et al. (2015) showed a nonuniform reduced velocity distribution near the edges of the cylindrical casing. Therefore, an introduction of the reduction factors to the Gurney equations has been recommended. To find a nonuniform velocity distribution, Szmelter et al. (2007) proposed to substitute complex shapes of casing with sphere. The maximum velocity was in good agreement with the experiments; however, the overall distribution did not agree well. Resolving fragment velocity into the radial and the axial components and using empirical constants, Smit et al. (2001) proposed a multidimensional model with equivalent masses in radial and axial directions. A nonuniform velocity distribution predicted by the 2D finite difference code HEMP (Anderson et al. 1985; Karpp and Predebon 1975) was in good agreement with experimental results. Some researchers tried to introduce correction factors into the Gurney equation to account for the reduced velocity at the cylindrical casing edges (Zulkonski 1976; Charron 1979; Mock and Holt 1983; Wang et al. 2013; Xiangshao et al. 2013). The proposed correction formulae yield zero velocity at the detonated edge which does not agree with experimental results. Huang et al. (2010, 2015) proposed another empirical formula which was calibrated with experimental results and did not yield zero velocity at the detonation end. Grisaro and Dancygier (2015) developed 2D and 3D models to predict a nonuniform velocity distribution (normalized by shape function) along the longitudinal axis of the cylinder and near its edges. The simulation results were in good agreement with available experimental data.

14.1.2 Projectile Initial Launch Angle (Projection Angle)

One of the assumptions of the Gurney equations is the liners (fragments) which move perpendicular to the surface of the casing (initial angle of launch $\theta = 0^{\circ}$). However, in a real situation, the direction of the fragment motion depends on the approaching angle of the detonation to the fragment. If the detonation propagates parallel to the metal surface, the metal fragment will move in the direction of detonation propagation under the angle of projection $\theta = \frac{\alpha}{2}$, where α is the angle between the normal to the initial position of the plate and the normal to the deflection angle of the plate (Taylor 1963). Thus, the projection angle can be estimated by the following equation (Taylor 1963):

$$\theta = \sin^{-1}\left(\frac{v}{2v_{\mathrm{D}}}\right) \tag{14.8}$$

where v_{D} and v are the detonation velocity and the velocity of the fragment, respectively. This formula is valid also for the oblique shock waves relative to the metal surface. In this case, the phase velocity of detonation along the plate surface will be considered as v_{D}.

For the unsteady motion where the liner did not reach the final velocity, Chou et al. (1983) proposed the following equation for the launch angle:

$$\theta = \frac{v}{v_{\mathrm{D}}} - \frac{t}{2}\frac{dv}{ds} + \frac{v}{4}\frac{dt}{ds} \tag{14.9}$$

where v is the final velocity of the liner, v_{D} is the phase velocity of the detonation wave along the metal surface, t is the acceleration time, and s is the position along the liner. Eq. (14.8) can be obtained as a special case (steady motion case) from Eq. (14.9) $\left(\frac{dv}{ds} = \frac{dt}{ds} = 0\right)$.

The analysis of the witness panels used during the fragment recovery field tests showed that the initial launch angles of the fragments are small (Oxley et al. 2001; Oxley, 2003).

14.1.3 Fragment Size

Detonation fragments the casing of an explosive as the rapid expansion of product gases reaches the ductility limit of the casing material (up to 50% expansion in some cases). Observations show that for steel casings, fractures occur due to the cracks developed parallel to the axis of the cylindrical casing. A model for breakup of the cylindrical metal case was proposed by Mott (1947). This model predicted the length of the average fragment as a function of the mechanical properties of the case material, its breakup radius, and velocity.

Grady (1981) analyzed fragmentation of one-dimensional bodies due to the dynamic stress loading and proposed analytic functions for the fragment size distribution for both ductile and brittle fractures. He showed that the fragment distribution is a function of the stress-loading conditions and the material properties. The predicted fragment distribution curve was compared to the experimental data obtained by Wesenberg and Sagartz (1977) for aluminum rings, and a good agreement was found.

14.1.4 Fragment Range

Several studies have been conducted to predict the dynamics of the motion of the primary fragments. Since an exact analytical solution of the motion of the projectile including gravity, drag, and lift forces is not possible, several approximations were made to solve the problem. Davis (2003) proposed the following formula to calculate the fragment velocity with the assumption that a drag coefficient is the velocity independent:

$$V = V_0 e^{-\frac{x}{L}} \tag{14.10}$$

where V is the velocity of the fragment, V_0 is the initial (detonation) velocity, $x = n$ L is a number in L multiples, and L is the characteristic length defined as:

$$L = \frac{h\rho_{\mathrm{m}}}{\frac{1}{2}C_{\mathrm{D}}\rho_{\mathrm{a}}} \tag{14.11}$$

where h is the thickness of the fragment in the direction of motion, ρ_{m} and ρ_{a} are densities of metal casing and air, respectively, and C_{D} is the drag coefficient.

Bishop (1958) proposed a chart to estimate maximum fragment range as a function of the fragment thickness for steel and aluminum cubes. Due to the density variations, the chart shows a significant difference in maximum ranges for steel and aluminum fragments. Using Bishop's chart and converting the fragment thickness to the function of density and maximum fragment weight, Kelleher (2002) proposed the following equation to estimate the maximum fragment range (in *meters*):

$$R_{\max} = 190\,\rho^{-0.112}W + 52\,\rho^{0.858} \tag{14.12}$$

where ρ is the fragment density in gcm^{-3} and W is the maximum fragment weight in kg. However, the proposed equation does not account for the explosive type and the charge amount and the wind speed and direction. Figure 14.1 shows a variation of the horizontal range vs. maximum fragment weight predicted by Kelleher (2002) for steel ($\rho = 7.86$ kg m^{-3}), aluminum ($\rho = 2.70$ kg m^{-3}), and plastic ($\rho = 0.80$ kg m^{-3}) casings. As seen in Fig. 14.1, for fragments of small weight, there is a horizontal range which depends on the casing density. It is almost independent of the casing density for large mass fragments. As in non-drag case, the maximum horizontal range takes place when an initial launch angle $\theta = 45^{\circ}$.

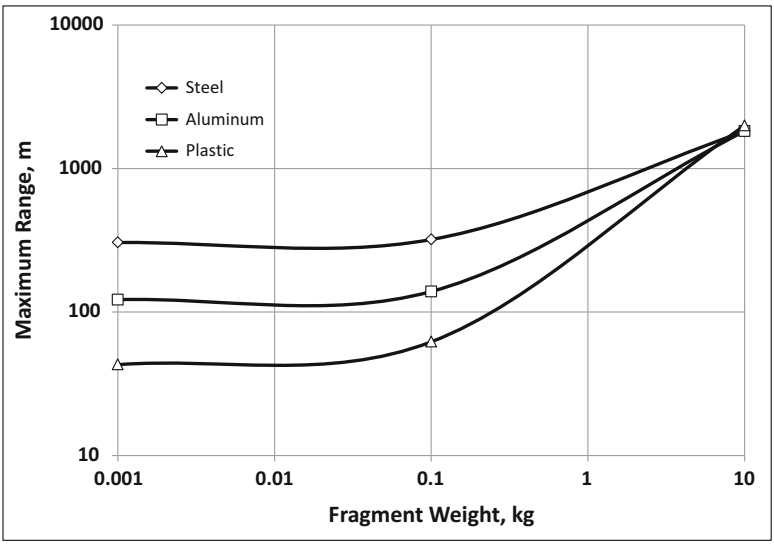

Fig. 14.1 Variation of maximum horizontal range with fragment weights predicted by Kelleher (2002)

Davis (1978) proposed a critical length of the fragment (in *meters*) in the direction of flight:

$$L = \frac{2h\rho_{\mathrm{m}}}{C_{\mathrm{D}}\rho_{\mathrm{a}}} \cdot h, \tag{14.13}$$

where ρ_{m} and ρ_{a} are densities of metal and air (in g cm^{-3}), respectively, C_{D} is the drag coefficient, and h is the thickness of the fragment (in mm). The safe distances for the equipment and personnel are recommended as 5 L and 8 L, respectively. The critical length of the fragment can be used to calculate a horizontal range of the fragment. Neglecting the gravity and the lift forces, it can be determined as:

$$R = L\ln\frac{V_0}{V}. \tag{14.14}$$

The problem of the fragment motion was numerically solved by Baker et al. (1983) for different lift-to-drag coefficient ratios. The maximum ranges of the fragments were obtained as a result of their simulations.

Kinney and Graham (1985) proposed another empirical formula for the fragment range as a function of the TNT equivalent (e.g., energy released in the detonation of 1000 kg of TNT) of the explosive mass:

$$R = am_{\mathrm{TNT}}^{\frac{1}{3}} \tag{14.15}$$

where m_{TNT} is the TNT equivalent mass of explosive (kg) and $a = 45$. The ratio $\frac{R}{m^{\frac{1}{3}}}$ is called a "scaled distance" (e.g., fragments are expected to be thrown 45 m per cube root kg TNT). However, according to the standard bomb disposal (SBD) practice, for a safety distance from the detonation center, the coefficient a should be $a = 120$ (Lenz 1965).

14.2 Objectives and Goals

The objective of this study was to develop an engineering method to predict the aerodynamics of explosive ballistic projectiles (EBPs) of arbitrary shapes. The approach was to combine a complex variable method ("linearization of single-bonded area") with the numerical analysis of the projectile motion dynamics in order to predict the motion of EBPs of arbitrary shapes, sizes, and masses.

14.3 Methods

14.3.1 Projectile Motion with Quadratic Air Resistance

Consider a projectile of mass m that is launched with an initial (detonation) velocity v_0 at an initial launch angle of θ to the horizon in the uniform gravitational field g (Fig. 14.2.).

The equation of the projectile motion can be written as:

$$m\frac{d\vec{v}}{dt} = \vec{G} + \vec{F}_{\mathrm{D}} + \vec{F}_{\mathrm{L}} \tag{14.16}$$

where m is the mass of the projectile, $\vec{v}$ is the projectile velocity, $\vec{G}$ is the force of gravity (projectile weight), $\vec{F}_{\mathrm{D}}$ is the drag force, $\vec{F}_{\mathrm{L}}$ is the lift force, $\frac{d\vec{v}}{dt} = \vec{a}$ is an acceleration of the projectile, and t is a time. Drag and lift are two components of the aerodynamic force F_{A}.

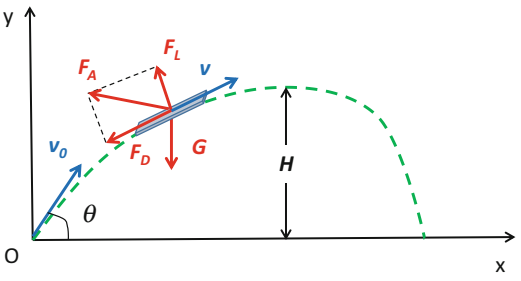

Fig. 14.2 Projectile motion

A drag force is the most important physical parameter in aerodynamic analysis. Drag force consists of two force components: friction (viscous) drag (F_f or F_v) acting tangent to the surface and pressure drag (F_p) acting normal to the surface. These components are determined by the following formula:

$$F_p = \int_S dA(p - p_0) \text{ and } F_f = \int_S dA\tau_w \tag{14.17}$$

where p and p_0 are pressures at the surface and away from the surface, respectively, and τ_w is a wall shear stress. The shape of the object and its angle of attack determine which drag is dominant. Depending on domination of a friction or a pressure drag, the objects are called *streamlined* or *blunt*, respectively. Drag coefficient is a function of flow velocity and direction, object position, object size, and fluid density and viscosity. The flow velocity and fluid properties (density and viscosity) can be incorporated into the nondimensional criterion called Reynolds number (*Re*), which defines the ratio of inertial forces to viscous forces. If we assume that the drag force is approximately proportional to the square of the speed of the projectile relative to the air, then we can write:

$$\vec{F}_D = -\frac{C_D A_F \rho}{2} v\vec{v} \tag{14.18}$$

where C_D is the drag coefficient, ρ is the mass density of the fluid, and A is the reference area (usually the face area A_F).

Lift force is the component of the aerodynamic force which is perpendicular to the approaching flow direction. It can be estimated using the following formula:

$$\vec{F}_L = \frac{C_L A \rho}{2} v\vec{v} \tag{14.19}$$

where A is the area normal to the lift force and C_L is the lift coefficient which is a function of the angle of attack, which is an angle between the fragment reference line (chord) and the oncoming flow, Mach number, and Reynolds number. The analyses showed that the maximum lift coefficient would be at 15° angle of attack. Some studies show relationship between drag and lift forces. For example, Küchemann (2012) proposed the following empirical relationship for predicting a lift force to drag force ratio:

$$\frac{F_L}{F_D} = \frac{4(M+3)}{M} \tag{14.20}$$

where M is the Mach number. The formula (20) was verified by wind tunnel tests, and it is considered a quite accurate.

The analysis of the shapes and sizes of the fragments recovered from field test conducted by Oxley et al. (2001) showed that there is asymmetry between the top and bottom surfaces of the explosive fragments and their thicknesses are up to 50 times less than their lengths. This would suggest these fragments could be

considered as cambered airfoils; thus, lift force must be taken into the consideration. Eq. (14.16) can be written in algebraic form in *2D* Cartesian coordinate system as:

$$m\frac{dv_x}{dt} = -F_{Dx} + F_{Lx}, \tag{14.21}$$

$$m\frac{dv_y}{dt} = -G - F_{Dy} + F_{Ly}. \tag{14.22}$$

Substituting Eq. (14.18) in Eqs. (14.21) and (14.22), we obtain:

$$\frac{dv_x}{dt} = -\frac{(C_\mathrm{D}A_\mathrm{F} - C_\mathrm{L}A)\rho}{2mg} v v_x, \tag{14.23}$$

$$\frac{dv_y}{dt} = -g - \frac{(C_\mathrm{D}A_\mathrm{F} - C_\mathrm{L}A)\rho}{2mg} v v_y. \tag{14.24}$$

14.3.2 Complex Variable Method Analysis

Generally, ballistic projectile motion must be considered as a motion with six degrees of freedom (6DoF). *Pitch*, *roll*, and *yaw* are three dynamic parameters which characterize the angles of rotation of ballistic projectile motion in three dimensions about its center of mass (Fig. 14.3.). They define the rotations about the corresponding axes relative to the steady equilibrium state. These rotational motions are caused by forces (or moments) applied in different directions from the center of the projectile.

To measure the ability of ballistic projectiles to overcome air resistance in flight, the ballistic coefficient, which is inversely proportional to the negative acceleration, is usually used. The ballistic coefficient is related to the drag coefficient as:

$$C_\mathrm{B} = \frac{m}{C_\mathrm{D}A} = \frac{\rho l}{C_\mathrm{D}} \tag{14.25}$$

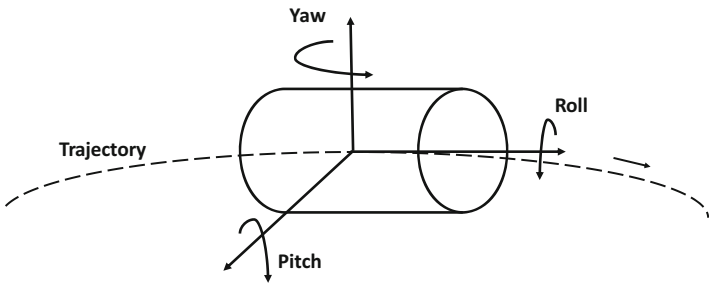

Fig. 14.3 Angles of rotation of ballistic projectile motion

where l is the length of the projectile. A ballistic coefficient for the projectiles by action of explosive can be defined as:

$$C_{\mathrm{B}} = \frac{m}{D_{\mathrm{e}}^2 i} \tag{14.26}$$

where D_{e} is the effective diameter of the projectile and i is a coefficient of form. There are different formulae to determine a coefficient of form. Theoretical studies of projectile motion traditionally focus on regularly shaped object such as uniform spheres or cylinders. The dynamics of more asymmetric objects subjected to both force and torque is more complicated as it usually includes coupling between translational and rotational motions. The problem is more complicated if we do not know the orientation alignment of asymmetric objects under external forces. In most calculations, the reference area is the projected frontal area of the object (e.g., $A = \pi\, r^2$ for spherical shape object). If the area of contact of the fluid with the surface area of the object is bigger than the frontal area (e.g., airfoils), the reference area will be the nominal area of the object. Volumetric drag coefficient ($C_{\mathrm{V}} = \sqrt[3]{\forall^2}$) is used for objects of revolution (where $\forall$ is the volume of the object). Some calculations use a wetted surface area, which is applicable for submerged streamlined objects. However, 3D motion of the projectile about its center of mass with six degrees of freedom (6DoF) requires a different approach to estimate both the drag coefficient C_{D} and the reference area A. Bakhtiyarov (2013, 2017) proposed a complex variable method ("linearization of single-bonded area") which can be used in developing a universal formula for the velocities of the projectiles of arbitrary shapes, sizes, and masses. This method introduces a function:

$$\psi = u + \frac{\Delta p}{4\mu l}\left(x^2 + y^2\right), \tag{14.27}$$

which can be transformed to a Laplace equation with the boundary condition $\psi = \frac{\Delta p}{4\mu l}(x^2 + y^2)$, on the stream contours. The proposed technique has the following hydrodynamic interpretation: The problem of determination of the projectile velocities in the viscous fluid medium (in our case, it is air) is reduced to the problem of determination of the fluid flow around a prism with the same cross-section area rotating with the angular velocity $\omega = \frac{\Delta p}{2\mu l}$. In order to find the function $\psi\,(x, y)$ for arbitrary cross-section area, an interior of this area in z-plane ($z = x + iy$) is reflected into the interior of the unique circle $\xi - plane$ ($\zeta = \xi + i\eta = \rho e^{i\theta}$) using the following power series:

$$z = a_0 + a_1\zeta + a_2\zeta^2 + \ldots + a_n\zeta^n + \ldots. \tag{14.28}$$

Using Schwarz's integral, the function $f(\zeta)$ will be determined in a unit circle by the given real part on the contour. Taking into the account the boundary conditions, both the function $f(\zeta)$ and the flow function $\psi = \frac{1}{2}\omega z \cdot \bar{z}$ can be determined:

$$\psi = \omega\left[\frac{1}{2}\sum_{k=0}^{\infty} a_k^2 + \sum_{k=1}^{\infty} \rho^k \cos k\theta \sum_{s=0}^{\infty} a_s a_{s+k}\right]. \tag{14.29}$$

Combining (14.27) and (14.29), we can find the projectile velocities in the ζ-plane:

$$\psi = \frac{\Delta p}{2\mu l}\left[\frac{1}{2}\sum_{k=0}^{\infty} a_k^2\left(1-\rho^{2k}\right) + \sum_{k=1}^{\infty} \rho^k \cos k\theta \sum_{s=0}^{\infty} a_s a_{s+k}\left(1-\rho^{2s}\right)\right]. \tag{14.30}$$

The distribution of velocities *u(x, y)* in *z*-plane will be constructed according to the method proposed by Lavrentyev and Shabat (1973):

$$x = \sum_{k=0}^{\infty} a_k \rho^k, \tag{14.31}$$

$$y = \sum_{k=1}^{\infty} a_k \rho^k \sin k\theta. \tag{14.32}$$

The results of numerical calculations of ψ for the ballistic projectiles with various cross sections are validated by formula for geometrical shapes given in literature. The equivalent radius of the object of arbitrary shape will be defined by the method suggested by Polya and Szego (1962):

$$r'_e = \frac{S^3}{4\pi^2 J_0 r_H} = \frac{2r_H}{\xi'}, \tag{14.33}$$

where $\xi' = \frac{8\pi^2 J_0}{S\chi^2}$ is the shape coefficient and I_0 is the moment of inertia. As an example, for the right *n*-angle shape object:

$$\xi' = \frac{\pi^2}{3n^2}\left(1 + 3\cot^2\frac{180^\circ}{n}\right). \tag{14.34}$$

In the proposed method, the linear size characteristics of the cross section of the arbitrary shape objects could be determined by different ways, such as an exact solution of the Eq. (14.30), based on Boussinesq's equation, using *a conform representation* method, etc. A *conform representation* method was applied in these simulations. The turbulent flow of air was studied using a model of superposition of the molecular and turbulent viscosities (Schiller 1936):

$$\overline{\tau}_w(1-y) = (\mu + \mu_t)\frac{du}{dy}. \tag{14.35}$$

It is assumed that the turbulent flow occurs by the two-layered Prandtl-Taylor structure model. The equivalent viscosity of fluid is determined as $\mu = \mu_{equiv} = \overline{\tau}_w/\dot{\gamma}_{st}$, where $\overline{\tau}_w$ is the shear stress at the wall and $\dot{\gamma}_{st}$ is the shear rate. The flow resistance is estimated by the Blasius formula (Loitsyansky 1973). The following parameters were used to describe the ballistic projectile resulting

from the case breakup: mass, shape, dimensions, projected areas, ballistic coefficient (subsonic, supersonic) vs. Mach number, drag coefficient, lift-to-drag force ratio $\left(\frac{F_L}{F_D}\right)$, and imparted velocity (speed, direction, etc.).

14.3.3 Numerical Analysis

Since an exact solution to Eqs. (14.23) and (14.24) cannot be found analytically, we will solve them numerically. As we know, the acceleration components a_x and a_y are continuously changing as the velocity components v_x and v_y change. A basic concept of the numerical simulation is that over an adequately short time interval Δt, we can consider the acceleration as a constant. If we know the initial coordinates and velocity components of the projectile at some time $t = t_0$ (usually $t_0 = 0$), we can find their values at a time $t + \Delta t$ using the formulae for the constant acceleration. During a time interval Δt, the average changes of the x and y components of the acceleration and the velocity of the projectile will be:

$$a_x = \frac{\Delta v_x}{\Delta t}, a_y = \frac{\Delta v_y}{\Delta t}, \Delta v_x = a_x \Delta t, \Delta v_y = a_y \Delta t. \tag{14.36}$$

The values of x and y components of the velocity at a time $t + \Delta t$ will be:

$$v_x + \Delta v_x = v_x + a_x \Delta t \text{ and } v_y + \Delta v_y = v_y + a_y \Delta t. \tag{14.37}$$

The average of the velocity components during the time interval Δt will be:

$$v_x + \frac{\Delta v_x}{2} \text{ and } v_y + \frac{\Delta v_y}{2}.$$

Then, during a time interval Δt, the coordinates x and y change as:

$$\Delta x = \left(v_x + \frac{\Delta v_x}{2}\right)\Delta t = v_x \Delta t + \frac{a_x \Delta t^2}{2} \text{ and} \Delta y = \left(v_y + \frac{\Delta v_y}{2}\right)\Delta t$$
$$= v_y \Delta t + \frac{a_y \Delta t^2}{2}. \tag{14.38}$$

The initial conditions can be stated as:

$$\text{At } t = 0: \quad x = 0, y = 0, v_x = v_0 \cos\theta, \quad v_y = v_0 \sin\theta. \tag{14.39}$$

Using Eqs. (14.37) and (14.38), we can find the position and the velocity of the projectile at the end of each interval in terms of their values at the beginning. A general algorithm of the simulations is presented in Fig. 14.4.

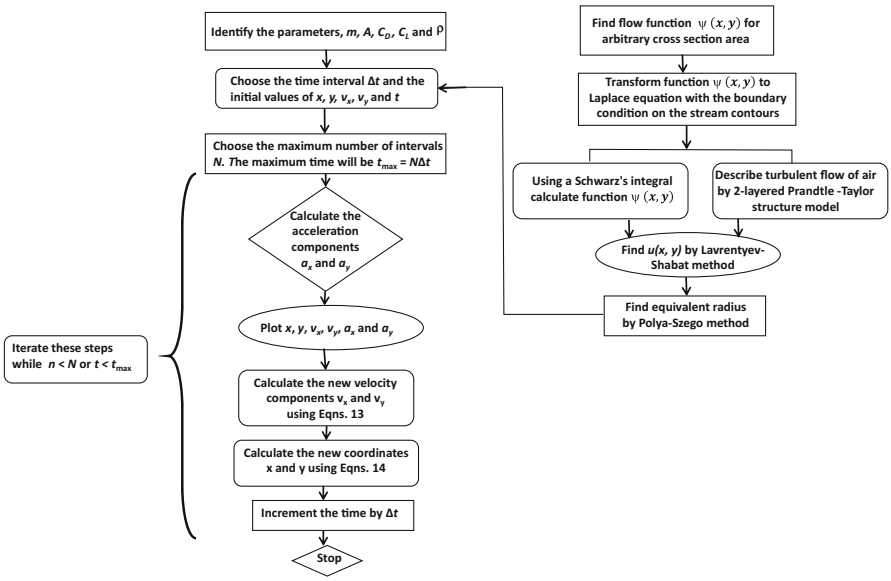

Fig. 14.4 General algorithm of complex variable method incorporated with numerical analysis

14.4 Results

Projectile trajectories were numerically simulated according to the algorithm of simulations shown in Fig. 14.4. Simulations were performed with time interval $\Delta t = 1\ s$ for the fragments recovered from previous pipe bomb tests by Oxley et al. (2001). The recovered masses of the randomly selected fragments for these analyses varied between 5 g and 115 g, and the surface areas varied between 0.5 and 100 cm^2. Preliminary simulations were performed to define a qualitative impact of each parameter on the fragment range. As an example, Figs. 14.5, 14.6, 14.7, and 14.8 are provided to show a variation of numerically simulated projectile trajectories for different variables. Figure 14.5 shows projectile trajectories simulated at different drag coefficients (C_D) and parameter $k = \sqrt{\frac{2mg}{C_D A \rho}}$ at $m = 11\ g, v_0 = 1,000 \frac{m}{s}$, and $\theta = 45^\circ$. Figure 14.6 shows the predicted projectile trajectories for different launch velocities at $m = 11\ g, C_D = 0.7, k = 33$, and $\theta = 45^\circ$. Figure 14.7 depicts projectile trajectories simulated at different launch angles at $m = 11\ g, v_0 = 1{,}000$ m/s, $C_D = 0.7, k = 33$. The projectile trajectories simulated at different masses of the fragments at $\theta = 45^\circ, v_0 = 1{,}000$ m/s, and $C_D = 0.7, k = 33$ are shown in Fig. 14.8.

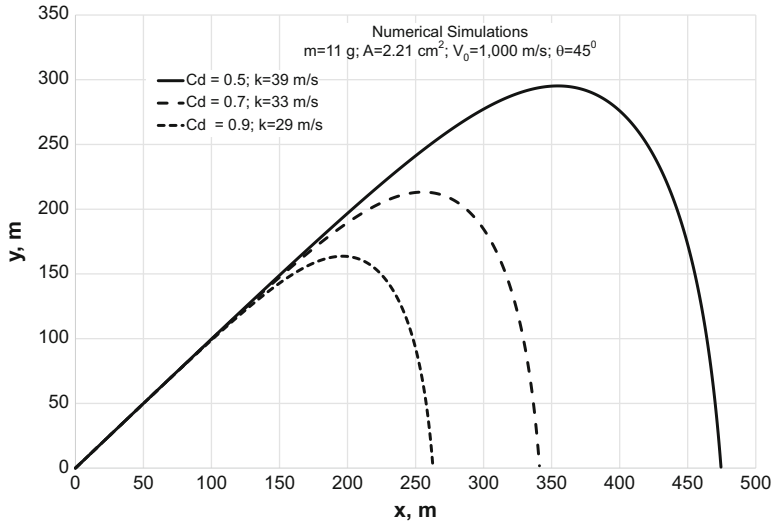

Fig. 14.5 Variation of numerically simulated projectile trajectories with drag coefficient

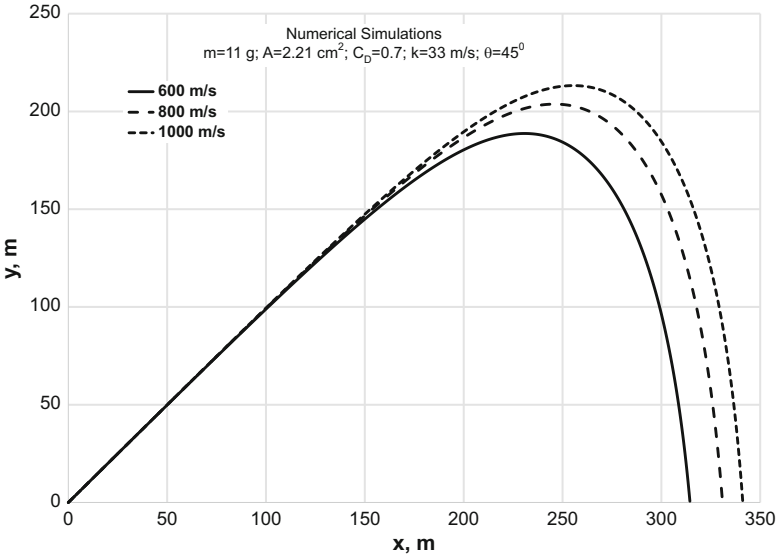

Fig. 14.6 Variation of numerically simulated projectile trajectories with initial launch velocities

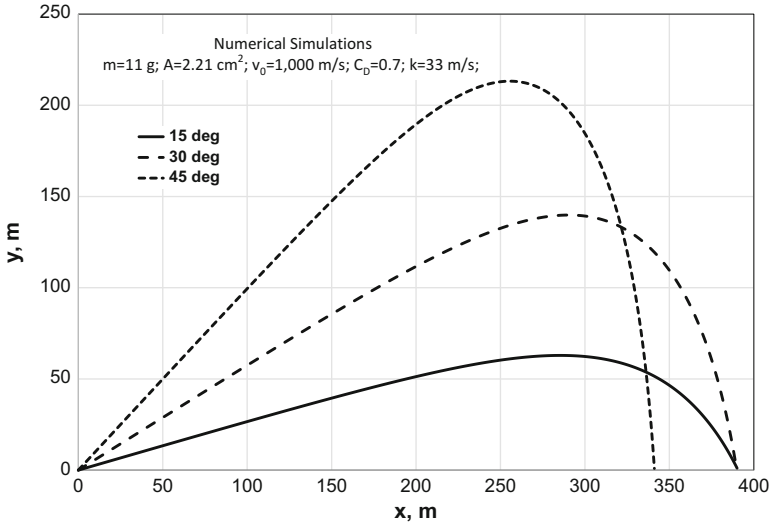

Fig. 14.7 Variation of numerically simulated projectile trajectories with initial launch angles

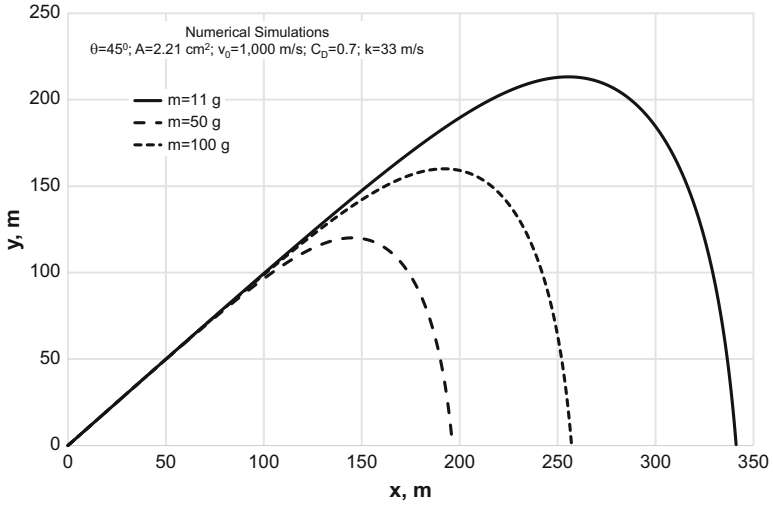

Fig. 14.8 Variation of numerically simulated projectile trajectories with fragment mass

14.5 Discussions

The analyses of the simulations show that the fragment range decreases as the drag coefficient (C_D) increases (or parameter k decreases) (e.g., see Fig. 14.5). One would expect the fragment range increases as the launch velocity increases (e.g., see Fig. 14.6) and the launch angle decreases (e.g., see Fig. 14.7). The fragment range decreases as the fragment mass increases for the same face areas (e.g., see Fig. 14.8).

The projectile ranges were numerically simulated for the fragments recovered during the pipe bomb tests conducted by Oxley et al. 2001), and the results were compared to those predicted by the models proposed by Kelleher (2002), Kinney and Graham (1985), Lenz (1965), and Bomb Disposal Guide (BDG). To find the initial launch angles (θ), we numerically simulated the variation of this angle vs. maximum projectile range using Eqs. (14.8) and (14.9) for the fragments recovered from the pipe bomb tests. The results of the comparison as an example are shown in Fig. 14.9 for $m = 5.28$ g, $v_0 = 1,237\frac{\text{m}}{\text{s}}, C_D = 0.7$. The simulations for all selected fragments along with the predictions made by prior proposed models are shown in Table 14.2. The percent and the standard deviations of the projectile ranges calculated by various models for fragments recovered during the pipe bomb tests (Oxley et al. 2001) are depicted in Figs. 14.10 and 14.11, respectively. It is worthwhile to mention that most of those models neglected the drag and lift forces. As seen from these figures, the numerical model developed in this study is the best to describe the actual test results obtained during the field pipe bomb tests.

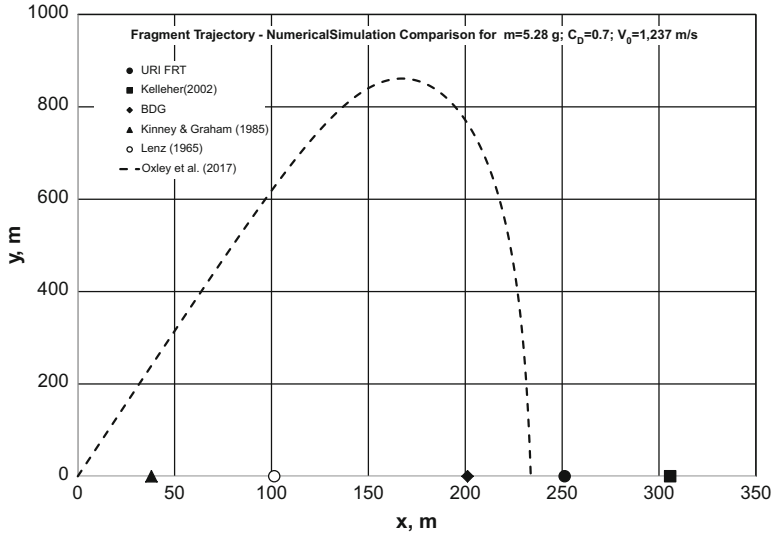

Fig. 14.9 A comparison of the maximum fragment range (in meters) determined from the fragment recovery tests (FRT) conducted at the University of Rhode Island (URI) with simulated predictions ($m = 5.28$ g)

Table 14.2 Comparison of the maximum fragment range (meters) determined from fragment recovery tests (FRT) conducted by Oxley et al. (2001)

Source	$m = 5.28$ g	$m = 5.42$ g	$m = 5.84$ g	$m = 22.32$ g	$m = 64.04$ g	$m = 114.74$ g
FRT URI DHS COE	251.330	200.620	184.700	192.044	50.81	26.74
Kelleher (2002)	305.780	305.800	305.864	308.350	314.61	322.29
Bomb Disposal Guide (BDG)	201.198	201.198	201.198	201.198	201.198	201.198
Kinney & Graham (1985)	38.039	38.039	38.039	38.039	38.039	38.039
Lenz (1965)	101.436	101.436	101.436	101.436	101.436	101.436
Oxley et al. (2017)	233.807	189.308	172.786	190.700	51.137	26.883

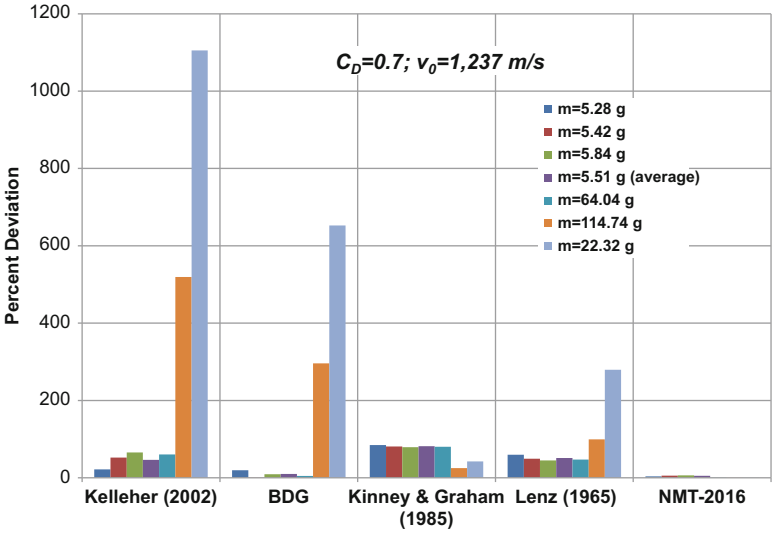

Fig. 14.10 Comparison of percent deviations of projectile ranges calculated by various models

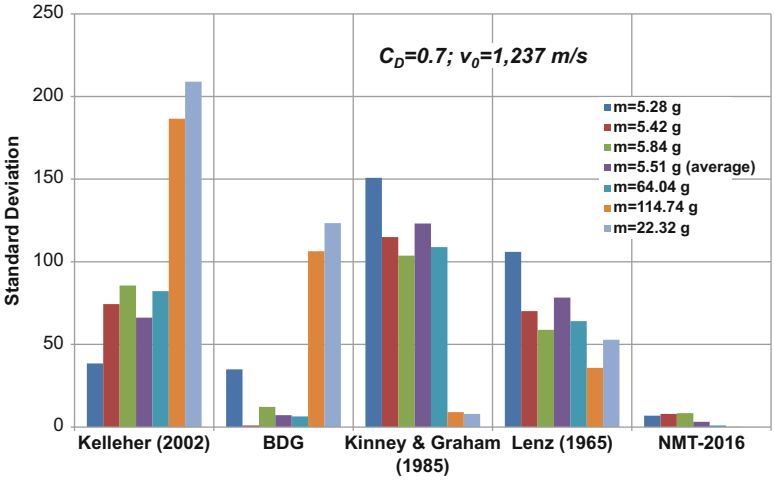

Fig. 14.11 Comparison of standard deviations of projectile ranges calculated by various models

14.6 Conclusions

An engineering method to predict aerodynamics of explosive ballistic projectiles (EBPs) of arbitrary shapes has been developed. Incorporating the numerical solution of the equations of the dynamic motion of projectile with a complex variable method ("linearization of single-bonded area"), the velocities and the trajectories of

arbitrary shape EBPs have been determined. The developed simulation technique was applied to predict the trajectories and velocities of the fragments recovered during a previous pipe bomb tests. The results of the simulations were compared to prior developed model predictions. It appears that the developed numerical model is the best to describe the actual test results if compared to other model predictions.

Acknowledgments This study was performed under an appointment to the US Department of Homeland Security (DHS) Science & Technology (S&T) Directorate Office of University Programs Summer Research Team Program for Minority Serving Institutions, administered by the Oak Ridge Institute for Science and Education (ORISE) through an interagency agreement between the US Department of Energy (DOE) and DHS. ORISE is managed by ORAU under DOE contract number DE-SC0014664. All opinions expressed in this paper are the author's and do not necessarily reflect the policies and views of DHS, DOE, or ORAU/ORISE.

References

Anderson, C. E., Predebon, W. W., & Karpp, R. R. (1985). Computational modeling of explosive filled cylinders. *International Journal of Impact Engineering, 23*, 1317–1330.

Baker, W. E., Cox, P. A., Westine, P. S., Kulesz, J. J., & Strehlow, R. A. (1983). *Explosion hazards and evaluation*. Amsterdam: Elsevier.

Bakhtiyarov, S. I. (2017). Complex variable method to predict aerodynamics of arbitrary shape fragmentation. In *Proceedings of ISEE 43rd annual conference on explosives & blasting technique*, Orlando, 29 January–1 February 2017 (accepted).

Bakhtiyarov, S. I. (2013). A complex variable method to predict an aerodynamics of arbitrary shape debris. In *Proceedings of 6th IAASS conference "Safety is not an option"*, Montreal, 21–23 May 2013, pp. 51–52.

Bishop, R. H. (1958). *Maximum missile ranges from cased explosive charges*. SC-4205 (TR). Albuquerque: Sandia National Laboratories.

Bola, M. S., Madan, A. K., Singh, M., & Vasudeva, S. K. (1992). Expansion of metallic cylinders under explosive loading. *Defence Science Journal, 42*, 157–163.

Charron, Y. J. (1979). *Estimation of velocity distribution of fragmenting warheads using a modified gurney method*. MSc thesis, USA Air Force Inst. of Tech., Ohio.

Chou, P. C., Carleone, J., Hirsch, E., Flis, W. J., & Ciccarelli, R. D. (1983). Improved formulas for velocity, acceleration, and projection angle of explosively driven liners. *Propellants, Explosives, and Pyrotechnics, 8*, 175–183.

Cooper, P. W. (1996). *Explosives engineering*. New York: Wiley-VCH.

Cullis, I. G., Dunsmore, P., Harrison, A., Lewtas, I., & Townsley, R. (2014). Numerical simulation of the natural fragmentation of explosively loaded thick walled cylinders. *Defense Technology, 10*, 198–210.

Davis, W. C. (1978). *Fragments hazard zone for explosives shots, Los Alamos Internal Report, M-3-78-4*. Los Alamos.

Davis, W. C. (2003). Introduction to explosives. In J. A. Zukas & W. P. Walters (Eds.), *Explosive effects and applications* (pp. 1–22). New York: Springer.

Elek, P., Jaramaz, S., & Mickovic, D. (2013). Modeling of the metal cylinder acceleration under explosive loading. *Scientific and Technical Review, 63*, 39–46.

Flis, W. J. (1996). Gurney formulas for explosive charges surrounding rigid cores. In: *Proceedings of 16th international symposium on ballistics,* San Francisco, 23–28 September 1996, pp. 1–11.

Grady, D. E. (1981). Fragmentation of solids under impulsive stress loading. *Journal of Geophysical Research, 86*(B2), 1047–1054.

Grisaro, H., & Dancygier, A. N. (2015). Numerical study of velocity distribution of fragments caused by explosion of a cylindrical cased charge. *International Journal of Impact Engineering, 86*, 1–12.

Gurney, R. W. (1943). *The initial velocities of fragments from bombs, shells, and grenades, BRL-405*. Aberdeen: Ballistic Research Laboratory.

Hardesty, D. R., & Kennedy, J. E. (1977). Thermochemical estimation of explosive energy output. *Combust and Flame, 28*, 45–59.

Hirsch, E. (1986). Improved gurney formulas for exploding cylinders and spheres using 'Hard Core' approximation. *Propellants, Explosives, Pyrotechnics, 11*, 81–84.

Hirsch, E. (1995). On the inconsistency of the Asymmetric-Sandwich Gurney Formula when used to model thin plate propulsion. *Propellants, Explosives, Pyrotechnics, 20*(4), 178–181.

Huang, G., Li, W., & Feng, S. (2010). Fragment velocity distribution of cylindrical rings under eccentric point initiation. *Propellants, Explosives, Pyrotechnics, 35*, 1–7.

Huang, G. Y., Li, W., & Feng, S. S. (2015). Axial distribution of fragment velocities from cylindrical casing under explosive loading. *Internatinal Journal of Impact Engineering, 76*, 20–27.

Kamlet, M. J., & Fioger, M. (1979). An alternative method for calculating gurney velocities. *Combustion and Flame, 34*, 213–214.

Kamlet, M. J., & Jacobs, S. J. (1968). Chemistry of detonations. I. A simple method for calculating detonation properties of C-H-N-O explosives. *The Journal of Chemical Physics, 48*, 23–35.

Karpp, R. R., & Predebon, W. W. (1975). *Calculations of fragment velocities from naturally fragmenting munitions*, *BRL Report No. 2509*. Aberdeen Proving Ground, Maryland: Ballistic Research Laboratories (BRL).

Kelleher, J. (2002). Explosive residue: Origin and distribution. *Forensic Science Communications, 4*(2), 1–11.

Kennedy, J. E. (1998). Chapter 7 The gurney model of explosive output for driving metal. In J. A. Zukas & W. P. Walters (Eds.), *Explosive effects and applications* (pp. 221–257). New York: Springer.

Kinney, G. F., & Graham, K. J. (1985). *Explosive shocks in air* (2nd ed.). New York: Springer.

Küchemann, D. (2012). *The aerodynamic design of aircraft. AIAA Education series*. Reston: American Institute of Aeronautics & Astronautics.

Lavrentyev, M. A., & Shabat, B. V. (1973). *The methods of complex variable functions theory*. Moscow: Nauka. 736p (in Russian).

Lenz, R. R. (1965). *Explosives and bomb disposal guide*. Springfield: Thomas Books.

Li, W., Huang, G. Y., & Feng, S. S. (2015). Effect of eccentric edge initiation on the fragment velocity distribution of a cylindrical casing filled with charge. *International Journal of Impact Engineering, 80*, 107–115.

Loitsyansky, L. G. (1973). *Mechanics of fluids and gases*. Moscow: Nauka. 848p.

Mock, W., Jr., & Holt, W. H. (1983). Fragmentation behavior of armco iron and HF-1 steel explosive-filled cylinders. *Journal of Applied Physics, 54*(5), 2344–2351.

Mott, N. F. (1947). Fragmentation of shell cases. *Proceedings of the Royal Society of London, 300*, 300–308.

Nystrom, U., & Gylltoft, K. (2009). Numerical studies of the combined effects of blast and fragment loading. *International Journal of Impact Engineering, 36*, 995–1005.

Oxley, J. C., Smith, J. L., Bakhtiyarov, S. I., & Baldovi, P. M. (2017). A complex variable method to predict a range of arbitrary shape ballistic projectiles. *Journal of Applied Nonlinear Dynamics, 6*(4), 521–530.

Oxley, J. C., Smith, J. L., Resende, E., Rogers, E., Strobel, R. A., & Bender, E. C. (2001). Improvised explosive devices: Pipe bombs. *Journal of Forensic Sciences, 46*(3), 510–534.

Oxley, J. C. (2003). The chemistry of explosives. In J. A. Zukas & W. P. Walters (Eds.), *Explosive effects and applications* (pp. 137–172). New York: Springer.

Pearson, J. (1990). *Fragmentation model for cylindrical warheads*, *Report No. NWC TP 7124*. China Lake: Naval Weapons Center.

Polya, G., & Szego, G. (1962). *Izoperimetric inequalities in mathematical physics* (p. 336). Moscow: Nauka. (in Russian).

Predebon, W. W., Smothers, W. G., & Anderson, C. E. (1977). *Missile warhead modeling: Computations and experiments*, *Report No. 2796*. Aberdeen Proving Ground, Maryland: USA Ballistic Research Laboratory.

Schiller, L. (1936). *Fluids flow in pipes*. Moscow: ONTI-NKTp. 230p (in Russian).

Smit, G. J. F., & Mostert, F. J. P. D. P. (2001). A novel approach to the multidimensional nature of velocities of fragments originating from convex shaped warheads. In R. C. Iris (Ed.), *19th international symposium of ballistics* (pp. 655–661). Thun/Interlaken: RUAG Land Systems.

Szmelter, J., Davies, N., & Lee, C. K. (2007). Simulation and measurement of fragment velocity in exploding shells. *Journal of Battlefield Technology, 10*, 1–7.

Taylor, G. I. (1963). Analysis of the explosion of a long cylindrical bomb detonated at the end. In G. Batchelor (Ed.), *Scientific papers of G. I. Taylor* (Vol. III, pp. 277–286). Cambridge: Cambridge University Press.

Thomas, L. H. (1944). *Theory of the explosion of cased charges of simple shape*, *BRL Report No. 475*.

Wang, M., Lu, F., Li, X., & Cao, L. (2013). A formula for calculating the velocities of fragments from velocity enhanced warhead. *Propellants Explosives Pyrotechnics, 38*, 232–237.

Wesenberg, D. L., & Sagartz, M. J. (1977). Dynamic fracture of 6061-T6 aluminum cylinders. *Journal of Applied Mechanics, 44*, 643–646.

Xiangshao, K., Weiguo, W., Jun, L., Fang, L., Pan, C., & Ying, L. (2013). A numerical investigation on explosive fragmentation of metal casing using smooth particle hydrodynamic method. *Materials and Design, 51*, 729–741.

Zhang, Q., Miao, C. Q., Lin, D. C., & Bai, C. H. (2003). Relation of fragment with air shockwave intensity for explosion in a shell. *International Journal of Impact Engineering, 28*, 1129–1141.

Zulkonski, T. (1976). *Development of optimum theoretical warhead design criteria*, *Report No. ADB015617*. China Lake: Naval Weapons Center.

Chapter 15
Extension of Substructuring Technique in the Nonlinear Domain

Mladenko Kajtaz

Conventional finite element models based on substructures allow only linear analysis. Some load-bearing structures such as energy absorbers and impact attenuators are designed to perform their useful functions in the nonlinear domain. Evaluating engineering design concepts of those structures objectively and with a certain rigour is challenging. Finite element analysis (FEA) as a potentially suitable tool for the evaluation typically is not computationally efficient and affordable in the conceptual design phase. An idea of extending the substructuring technique to be used for the concept evaluation by allowing substructures to exhibit a nonlinear response and use them in finite element models to reduce the computational cost is investigated in this chapter. For this reason, it was necessary to introduce a new algorithm capable of substructuring nonlinear structural models with sufficient accuracy. The main requirement for successful application of substructuring to this class of design problems is the definition of structural stiffness within an engineering design concept, which is, in fact, the minimal requirement for FEA functionality as well. In this work, the expansion of the substructuring technique beyond the linear response expectancy application is achieved by employing a scalar qualifier to economically modify original substructure matrix for substructures to exhibit a nonlinear response. This extension and integration of substructuring are crucial in allowing FEA to become more computationally efficient and affordable in the conceptual design phase. This chapter provides a comprehensive overview of the traditional substructuring process, followed by a detailed description of the developed method that extends substructures beyond the linearity domain. The implementation of the extended substructures within a commercial FEA code (ABAQUS) is then presented.

M. Kajtaz (✉)
School of Engineering, RMIT University, Melbourne, Australia
e-mail: mladenko.kajtaz@rmit.edu.au

L. Dai, R.N. Jazar (eds.), *Nonlinear Approaches in Engineering Applications*,
https://doi.org/10.1007/978-3-319-69480-1_15

15.1 Substructuring

Structural alternations as a result of an engineering design search imply modifications to their finite element models which are usually reflected as changes in member size, material, and general modifications of the finite element mesh. However, the loads on the structure are unaffected by the alternations and as they remain unchanged. The situation can symbolically be described as:

$$\text{Initial system} : \mathbf{KU} = \mathbf{F} \tag{15.1}$$

$$\text{Altered system} : \mathbf{K}^*\mathbf{U}^* = \mathbf{F} \tag{15.2}$$

$$\text{where } \mathbf{K}^* = \mathbf{K} + \Delta\mathbf{K} \tag{15.3}$$

$$\mathbf{U}^* = \mathbf{U} + \Delta\mathbf{U} \tag{15.4}$$

In order to obtain desired unknowns **U***, an obvious approach is a complete resolution of the altered system or alternatively to obtain **U*** with less computational effort than complete resolution by utilising information available from the initial system. The alternative, called *reanalysis approach*, was a very attractive solution approach in the infancy of computational engineering because of then limited computational resources. Arora (Arora 1976) in his comprehensive review of reanalysis approaches lists over 80 references describing the reanalysis methods. The reanalysis approaches continued to intrigue researchers for decades later, and many new approaches have been proposed (Abu Kassim and Topping 1987; Barthelemy and Haftka 1993). The various approaches may be categorised as follows (Kirsch 2008):

1. *Direct methods*, giving exact closed-form solutions and applicable to situations where a relatively small part of the structure is changed. They are usually based on the Sherman-Morrison (Sherman and Morrison 1949) and Woodbury (Woodbury 1950) formulas for the update of the inverse of a matrix.
2. *Iterative methods*, based on convergence from **U** towards **U*** at a rate that is case dependent. The iterative methods work best when alterations are small since large differences between **K** and **K*** make the iterations converge slowly or even diverge.
3. *Approximate methods*, giving approximate solutions, with the accuracy being dependent on the type of changes. They are usually based on a truncated series expansion or on a reduced set of structural equations, and they are generally suitable for situations where changes occur for large parts of the structure. The common approximations can be further divided into local approximations (the Taylor series expansion or the binomial series expansion), global approximations (polynomial fitting, response surface or reduced basis methods) and combined approximation ((Kirsch and Rubinstein 1972) improvements of the iterative method).

The reanalysis approach presented here is referred to as substructuring technique, and it is categorised as a direct method of reanalysis. Mathematically,

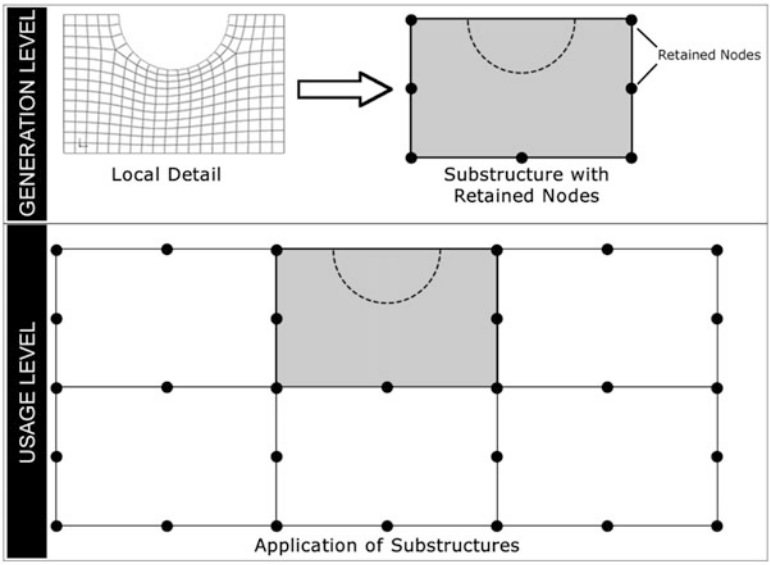

Fig. 15.1 Schematics of substructures

substructuring is considered as a partial solution of the complete set of structural equations. Physically, substructuring is considered as a division of a structure or a finite element mesh into multiple nonoverlapping domains (Fig. 15.1). In other contexts, substructuring is also known as *blocking* or *dissection* (numerical analysis) and *diakoptics* or *tearing* (electrical engineering). The substructuring process includes the following steps (Cook et al. 2001):

- Condensation of degrees of freedom (DOF) and the loads of a substructure to the retained nodes. The substructure is then treated as a traditional finite element connected to other elements via the retained nodes.
- Assembly of the stiffness and nodal force contributions from the substructure into the global stiffness matrix and the force vector.
- Evaluation of the system's equilibrium equations.
- Recovery of displacements of the condensed nodes from the retained nodes and followed by an evaluation of strains and stresses for the substructure.

15.1.1 Nodal Condensation

A nodal condensation, or a reduction of the number of element degrees of freedom (DOF), is utilised to perform a partial evaluation of the total finite element system equilibrium equations prior to assembling the structure stiffness and force matrices.

Originally, it was used to eliminate the internal degrees of freedom in a quadrilateral finite element constructed from four triangles (Wilson 1965). The process consists of employing Gauss elimination to eliminating DOF associated with the condensed, also known as slave, nodes until only DOF associated with the retained, or master, nodes remain. As the global stiffness matrix is obtained by direct addition of the element stiffness matrices, the nodal condensation implies that some of the total Gauss solution is already accomplished on the element level which reduces the overall size and bandwidth of the global stiffness matrix.

In order to establish the equations used in the nodal condensation and further illustrate this technique, let $\mathbf{ku} = \mathbf{f}$ be a linear problem of a substructure under consideration requiring a solution (Wilson 1974). Let m be the set of all indices of DOF associated with the retained (master) nodes. Grouping DOF corresponding to m in the vector $\mathbf{u}_m$ and those corresponding to the slave nodes, s, in $\mathbf{u}_s$, the original problem expression is partitioned into the form:

$$\begin{bmatrix} \mathbf{k}_{mm} & \mathbf{k}_{ms} \\ \mathbf{k}_{sm} & \mathbf{k}_{ss} \end{bmatrix} \times \begin{Bmatrix} \mathbf{u}_m \\ \mathbf{u}_s \end{Bmatrix} = \begin{Bmatrix} \mathbf{f}_m \\ \mathbf{f}_s \end{Bmatrix} \tag{15.5}$$

By mimicking Gauss elimination, which is assuming that $\mathbf{k}_{ss}$ is invertible, vector $\mathbf{u}_s$ is obtained using the second row of Eq. (15.1) as:

$$\mathbf{u}_s = -\mathbf{k}_{ss}^{-1}\mathbf{k}_{sm}\mathbf{u}_m - \mathbf{f}_s \tag{15.6}$$

Substituting this into the first row of Eq. (15.1) yields:

$$\bar{\mathbf{k}}_{mm}\mathbf{u}_m = \bar{\mathbf{f}}_m \tag{15.7}$$

where

$$\begin{aligned} \bar{\mathbf{k}}_{mm} &= \mathbf{k}_{mm} - \mathbf{k}_{ms}\mathbf{k}_{ss}^{-1}\mathbf{k}_{sm} \\ \bar{\mathbf{f}}_m &= \mathbf{f}_m - \mathbf{k}_{ms}\mathbf{k}_{ss}^{-1}\mathbf{f}_s \end{aligned}$$

In mathematics, the stiffness matrix $\bar{\mathbf{k}}_{mm}$ from Eq. (15.7) is referred to as the Schur complement of the matrix $\mathbf{k}_{mm}$ in $\mathbf{k}$, and it inherits all properties of $\mathbf{k}$ (Fuzhen 2005). This important quality enables a substitution of an unreduced matrix with a condensed matrix, thus allowing all consequent matrix operations to uninterruptedly execute. Therefore, the condensed matrices are treated as ordinary matrices of any traditional finite element, and they are assembled into the global stiffness matrix and the equivalent nodal force vector in the standard manner. If required, the condensed DOF, $\mathbf{u}_s$, are recovered using Eq. (15.6) which may be further simplified if the loads act on the master nodes only, then $\mathbf{f}_s = 0$, and Eq. (15.6) simplifies to:

$$\mathbf{u}_s = -\mathbf{k}_{ss}^{-1}\mathbf{k}_{sm}\mathbf{u}_m = \mathbf{L}\mathbf{u}_m \tag{15.8}$$

where matrix **L** is a linear transformation between the master and the slave DOF of a substructure (Guyan 1965; Vorob'ev et al. 1994). The stresses at any point are computed from the retained displacements $\mathbf{u}_m$ as follows:

Given the stress vector:

$$\boldsymbol{\sigma} = [\mathbf{S}_m \ \mathbf{S}_s][\mathbf{u}_m \quad \mathbf{u}_s]^T - \mathbf{C}\boldsymbol{\varepsilon}_0 + \boldsymbol{\sigma}_0 \tag{15.9}$$

where

$$\mathbf{S}_m = \mathbf{C}\mathbf{B}_m$$
$$\mathbf{S}_s = \mathbf{C}\mathbf{B}_m$$
with
$$\mathbf{B} = [\mathbf{B}_m \quad \mathbf{B}_s]$$

B – strain-displacement matrix that transforms nodal displacements to strains at any point in the substructure

C – constitutive matrix that transforms effective strains to stresses at any point in the substructure

Substituting $\mathbf{u}_s$ from Eq. (15.6) into Eq. (15.9) yields:

$$\boldsymbol{\sigma} = \mathbf{S}^*\mathbf{u}_m + \boldsymbol{\tau}^* \tag{15.10}$$

where

$$\mathbf{S}^* = \mathbf{S}_m - \mathbf{S}_s\mathbf{Q}$$
$$\mathbf{t}^* = \mathbf{C}\boldsymbol{\varepsilon}_0 + \boldsymbol{\sigma}_0 + \mathbf{S}_m\mathbf{R}$$
$$\mathbf{Q} = \mathbf{k}_{ss}^{-1}\mathbf{k}_{sm}$$
$$\mathbf{R} = \mathbf{k}_{ss}^{-1}\mathbf{f}_s$$

In a special case when $\mathbf{u}_s$ contains a single DOF, the described condensation process coincides with the standard Gauss elimination technique for solving system of algebraic equations (Bathe and Wilson 1976), implying that the technique can be interpreted as the partial solution of the global assembled system $\mathbf{KU} = \mathbf{F}$.

15.1.2 Benefits and Limitations of Substructures

Substructuring is a computationally efficient way of handling complex finite element models because it reduces the total number of DOF by at least 10 percent and even more than 30 percent depending on a problem, without compromising analysis accuracy (Chandrupatla and Belegundu 2002; Kajtaz et al. 2010). These benefits originate from their generation which is based on the standard Gauss elimination technique whereby the nodal condensation performs part of the solution of the total finite element system equilibrium equations on the element level (Bathe 1996). This partial solution of the global system of equilibrium equation is external and

independent from the remaining equilibrium equations, which can be figuratively interpreted as a reuse of the computational time and effort invested in generating a substructure at every inclusion of the substructure in a finite element model. The benefits of this type are most evident in the case of modelling repetitive geometries as the condensed DOF are processed only once. Consequently, the reduced model size leads to a more efficient allocation of computational resources due to benefits in shorter computational time and smaller storage requirements per analysis step. There is also a more pragmatic advantage in breaking a large problem into smaller and more tractable parts allowing for different substructures to be studied simultaneously by different design groups.

Failing to utilise a substructure more than once also fails to produce the desired computational savings as the total effort of producing substructures would be equal to that of using uncondensed elements. Hence, the potential computational benefits are only attainable by problems that repeatedly employ a single substructure. From the perspective of accuracy, in a static linear analysis, substructuring is strictly a manipulation of stiffness matrices based on the Gauss elimination and therefore introduces no approximations. Consequently, as indicated in Eq. (15.7), the response within a substructure is always linear, which is one of the crucial limitations of the traditional substructuring technique – hence their behaviour as predefined constant stiffness and their traditional application in practice (Postnov and Rodionov 1982; Singh et al. 1989; Kammer and Flanigan 1991; Wu et al. 1991; Burton 1997; Yiu 1997; Palekar et al. 2003).

15.1.3 Application of Substructures

In the early days of FEA, utilisation of substructures was more frequent, whereby their primary purpose was to overcome computer memory limitations by dividing a complex elastic structure into a multiple of more manageable smaller sections (Araldsen 1974; Petersson and Popov 1977; Gurujee 1978). Substructuring as a parallel computing technique was very attractive for distributed computing in networks of workstations working in parallel, as well as in shared memory parallel computers. Today, when the computer memory is more abundant and less of a performance critical issue, their application shifted to speeding up natural frequency extraction, frequency response and eigenvalue analyses (Bennighof et al. 2000; Gibson 2000; Elssel and Voss 2006; Swenson and Bennighof 2006; Floersheim et al. 2009; Thomas et al. 2009). In these areas of the application, the substructuring was established as an unavoidable and dominant technique. In particular, Bennighof and Lehoucq (Bennighof and Lehoucq 2004) developed automated multilevel substructuring (AMLS) method which was successfully further generalised and commercialised by Voss (Elssel and Voss 2005, 2006; CDH AG 2012) to become a part of many major FEA software packages capable of performing a frequency response and eigenvalue analysis. On the other hand, the application of substructuring in the other FEA areas is very marginal and, if present,

always tied to an analysis of elastic structures due to their mentioned limitation. The literature review revealed that there were no prior attempts to expand substructures in the nonlinear domain as proposed in this research. For particular nonlinear problems which require the application of substructures, a roundabout approach was devised whereby linearly responding parts of a structure were converted to substructures and the nonlinearly responding parts remained meshed by traditional finite elements (Dodds and Lopez 1980; Bathe and Gracewski 1981; Owen and Goncalves 1983; Wu et al. 1991; Burton 1997; Palekar et al. 2003; Labeas and Belesis 2011). This hybrid solution was widely accepted as the main approach for solving such rare problems as there was no strong demand to develop a better solution. However, in the context of the engineering design concept evaluation, design concept alternatives of complex load-bearing structures frequently exhibit nonlinear stiffness responses, and hence, neither substructuring technique in its original formulation nor the mentioned workaround approach would be a viable solution.

15.2 Extending Substructures

In general, nonlinearity involves stiffness or load dependences on displacements which adds complexity that the traditional substructures are incapable of managing. In order to improve this limitation and expand the substructuring technique beyond the linear response expectancy application, the substructuring technique requires an adaptation to the principles of nonlinearity and an incremental numerical analysis. This section summarises the fundamental principles of the nonlinear finite element analysis and presents the theory behind the novel concept of expanding the substructuring technique into nonlinearity adopted here.

15.2.1 Nonlinearity and Incremental Solutions

In linearity, it is assumed that displacements and rotations are small, stress is directly proportional to strain, the loads maintain their original direction as the structure deforms and supports remain unchanged (Bathe 1996). With these assumptions, the response is directly proportional to load, and the solution to the finite element equilibrium equation, $\mathbf{KU} = \mathbf{F}$, is obtained in a single step of equation solving as $\mathbf{U} = \mathbf{K}^{-1}\,\mathbf{F}$. Linearity may be a good representation of reality or a result of the assumptions made for analysis purposes, but with this not being the case, a problem becomes nonlinear. Based on a disagreement with a particular basic assumption used in linearity, nonlinearity in structures can be classed as (Bathe 1996):

(i) *Material nonlinearity* – associated with changes in material properties: material not being linearly elastic.
(ii) *Geometric nonlinearity* – associated with changes in configuration: displacements of the finite elements not being infinitesimally small.
(iii) *Boundary condition nonlinearity* – associated with changes in boundary conditions: DOF become free or restrained at certain load level.

In general, a problem is nonlinear if stiffness or load depends on the displacements which adds complexity as equations that describe the solution must incorporate conditions not fully known until the solution is known. For a time-independent problem described by the finite element equilibrium equation, $\mathbf{KU} = \mathbf{F}$, $\mathbf{K}$ and/or $\mathbf{F}$ is regarded as functions of $\mathbf{U}$ in which, unlike in linearity, the solution cannot be obtained explicitly nor in a single step of an analysis. Therefore, the solution is obtained iteratively in a number of incremental linear steps whereby the tentative solution is updated after each step until a convergence test is satisfied (Bathe et al. 1973, 1978; Bathe and Wilson 1976; Bathe 1979). Crisfield (2000) exhaustively reviews many such solution procedures, but the most commonly applied implicit procedure in structural analysis is Euler's method of solving first-order differential equations (Butcher 2003) as the underlying incremental method coupled with the Newton-Raphson method for the equilibrium iterations (Bathe and Cimento 1980; Kojic and Bathe 2005; Strang 2010). The Newton-Raphson method solves the governing equations by applying the unbalanced forces of externally applied nodal loads and nodal point forces that are equivalent to the element stresses. The method is summarised by the following sequence of equations (Bathe 1996):

$$G^{i-1} = F - \int_v B\left(U^{i-1}\right)^T \sigma\left(U^{i-1}\right) dV = 0 \tag{15.11}$$

$$K\left(U^{i-1}\right)\Delta U = G^{i-1} \tag{15.12}$$

$$U^i = U^{i-1} + \Delta U \tag{15.13}$$

where $\mathbf{G}^{i-1}$, $\boldsymbol{\sigma}$, $\mathbf{B}$, $\mathbf{K}$, and $\mathbf{U}^{i-1}$ are, respectively, the unbalanced forces, stresses, strain-displacement matrix, tangential stiffness and displacements at the start of the ith iteration, $\mathbf{F}$ are the external forces at the end of the current load increment and $\Delta\mathbf{U}^i$ are the iterative displacements for the ith iteration. Tangential stiffness being a function of displacement is iteration specific and therefore computed and assembled repeatedly.

15.2.1.1 Principal Theory of Extended Substructuring Technique

One of the essential aspects of the finite element theory is the calculation of finite element matrices. For that purpose, the most practical traditional finite element is the isoparametric finite element which defines both element geometry and the

unknown field variables directly through the application of the interpolation or shape functions. The unknown field variable in structural mechanics is the displacement field. The strain vector is defined in terms of derivatives of the element displacements with respect to the coordinates, and a transformation of the effective strains to the stresses at any point in the element is performed through the constitutive matrix, which is constant in linear elasticity, whereas in nonlinearity, it is the consistent tangent matrix defined as:

$$\mathbf{C}^{\tan} = \left.\frac{\partial \sigma}{\partial \varepsilon}\right|_{(u_i)} \tag{15.14}$$

The strain-displacement matrix, including the shape function matrix, and the constitutive matrix are required for construction of the element stiffness matrix which is defined from the principle of virtual work for an individual element to be:

$$\mathbf{k}_e = \int_V \left(B^T C B\right) dV \tag{15.15}$$

As the equation indicates, the nature of **k** depends on the material property matrix, and it is governed by the element's shape functions. In linearity, in order for the basic assumptions of linearity to remain valid, both of these entities are constant and independent of the element displacements. In nonlinearity, this stiffness formulation also allows for the stiffness adjustments at every increment of the iterative process in order to capture variations in matrices **B** and **C** as a result of the nonlinear changes.

By contrast, traditional substructures have an explicitly defined stiffness matrix, shown in Eq. (15.16), as a result of Gauss elimination which prevents any modifications during an incremental analysis. In order to extend substructuring into the nonlinearity, a scalar qualifier is employed to economically modify the original substructure matrix at every increment and, thus, allows substructures to exhibit a nonlinear response. The expression in Eq. (15.17) for stiffness matrix of the extended substructure is therefore a modification of Eq. (15.16):

$$\bar{\mathbf{k}}_{mm} = \begin{bmatrix} a_{11} & \cdots & a_{1n} \\ \vdots & \ddots & \vdots \\ a_{n1} & \cdots & a_{nn} \end{bmatrix} \tag{15.16}$$

$$\mathbf{k}_{xss} = m_i \bar{\mathbf{k}}_{mm} = m_i \begin{bmatrix} a_{11} & \cdots & a_{1n} \\ \vdots & \ddots & \vdots \\ a_{n1} & \cdots & a_{nn} \end{bmatrix} \tag{15.17}$$

The scalar qualifiers m_i are determined at the substructure generation level or in an intermediate phase between the generation and their usage. An approach and effort required for a successful evaluation of the qualifiers depend on availability of the numerical code and accessibility to the main procedure of a finite element solver. In the case when a full access to a finite element solver is available, the

qualifiers may theoretically be incorporated into the incremental solution in a form of the modified incremental equation (Eq. 15.18), which is shown in Eq. (15.13); however, a more detail study and validation are required:

$$m_i \bar{\mathbf{k}}_{mm} \Delta \mathbf{u} = \mathbf{F}^{ext} - m_i \bar{\mathbf{k}}_{mm} \mathbf{u}_{i-1} \tag{15.18}$$

On the other hand in cases of commercial and proprietary finite element solvers when access to their code is limited, determining the qualifiers may be more challenging, and that is the focus of this research with the goal of producing a practical and *user-friendly* approach. The following sections of this chapter are concerned with the detailed development of this approach.

15.2.2 Determining the Qualifiers

Theoretically, as Eq. (15.18) indicates, there would be one qualifier m for each analysis increment step. This ideal solution becomes feasible and practical only if the qualifiers could be determined in an analytical or in an economically viable empirical approach. Unfortunately, none of the approaches are possible when using commercial finite element solvers. It is impossible to obtain a single parameter from the information produced after a substructure generation to analytically predict nonlinear response of all elements condensed into the substructure. By contrast, the empirical approach would be possible, but due to prohibitively high associated computational costs, which may exceed the computational cost of running a finite model without substructures, this approach is not practical.

In order to produce a practically feasible empirical solution, the ideal theoretical proposition needs to be approximated. Therefore, instead of having a qualifier for every incremental step of the analysis, the solution is approximated by assigning a qualifier for multiple incremental steps. In this research, a concept of bilinear stiffness was utilised to mimic the linear and nonlinear behaviour, analogous to elastic and plastic material properties. Therefore, Eq. (15.17) becomes:

$$\mathbf{k}_{xss} = \begin{cases} \bar{\mathbf{k}}_{mm} & a \leq t \\ m\bar{\mathbf{k}}_{mm} & a > t \end{cases} \tag{15.19}$$

where a is a timing feedback variable such as the total strain energy.

As Eq. (15.19) indicates, there would only be one qualifier for the entire analysis, that is, assuming all nonlinearity to occur at a uniform gradient. The nonlinear behaviour is, then, defined by setting two parameters: (1) m, the scalar qualifier itself, and (2) t, timing of the modification occurrence. Hence, a complex and nonlinear force-displacement curve degenerates into a pair of straight lines meeting at the point defined by the parameter t. While the first part of Eq. (15.19), that is, describing the liner response, remained accurate and without further approximations, the second part, that is, describing the nonlinear response, introduces

approximations. The approximations are observed to be within 80 percent of the accuracy for most of the test cases because the developed approach is based on an interpolation principle whereby three test runs with different combinations of the qualifier m and its timing t are used as the basis of the interpolation. The resulting expression is then used to correlate the qualifier m with the desired stiffness slope. Similarly, the timing t is correlated with the desired timing of the stiffness change.

15.2.2.1 Parameters, Feedback Variables and their Correlations

Prior to developing the interpolation method to determine the parameters m and t, a correlation study was undertaken to determine the influence of the qualifier m on stiffness manifested as a gradient of a force-displacement chart. A power law-like relationship between the parameter m and the gradient S was determined in a mathematical form as follows:

$$m = aS^b \tag{15.20}$$

where a and b are problem specific and unknown values and S gradient (stiffness slope) as a feedback variable.

In order to find the unknowns in Eq. (15.20), the power law is expanded using the natural logarithm:

$$\ln(m) = b\ln(S) + \ln(a) \tag{15.21}$$

Equation (15.20) is modelled using the linear regression approach by fitting a straight line through a set of data produced by three calibration runs with different values for the qualifier m. Given that the qualifier m is in the range between 0 and 1, suggested calibration values would be the extremes and the median. However, in a few rare occasions, the natural log relationship may not always be linear (Fig. 15.2), which may lead to incorrect predictions of the qualifier m if the test case values are not carefully chosen. With reference to the problem shown in Fig. 15.2, a percentage for a correct prediction would decrease if all three calibration values for m are not higher or lower than 0.1. Having a wide range that covers values on either side of this boundary will significantly reduce the chance for a correct prediction. This suggests that although a wide range is possible, it may not always be suitable. A successfully obtained relationship between the qualifier m and the gradient provides means for determining a qualifier m for any desired gradient. The same approach is also used to determine the timing of the stiffness modification for any desired force or displacement value used as an indicator for change. With an aim to analytically correlate the parameters with their respective feedback variables, a methodology based on an interpolation of these values was developed. The complete interpolation process of determining m and t is fully automated and programmed into a programming routine, which requires a limited user interaction that does not go beyond providing of required inputs. The inputs are usually

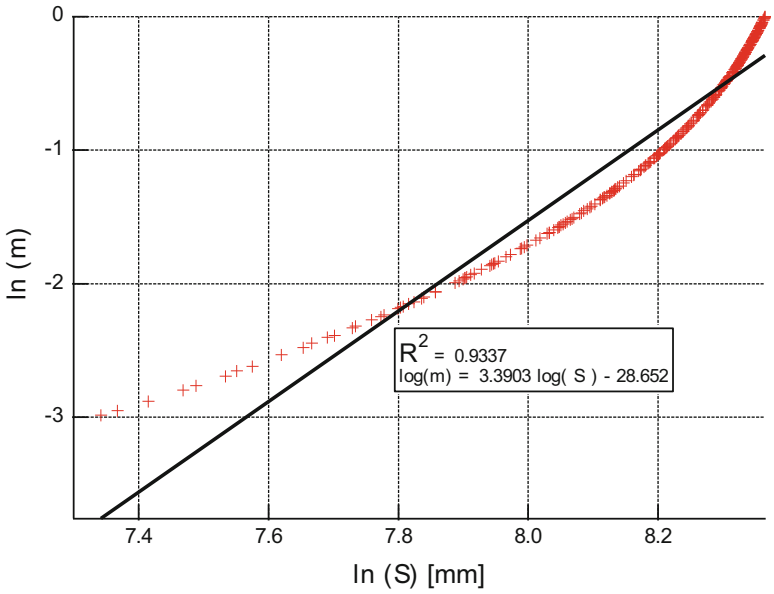

Fig. 15.2 Linear regression

associated with defining environment variables and specifying expected ranges for the parameters *m* and *t*. Details of the computer programme and the underlying methodology are presented in the following sections.

15.2.2.2 Interpolation Method for Determining M and T

Two preparatory activities are required in order to commence with the interpolation. The first consists of determining the desired values for the interpolation, and the second involves determining suitable ranges of values for the parameters. The former is used as the input for the software, whereas the latter is fully concealed from the end user by the software. In order to determine the desired values, the overall response of the finite element model that was previously traditionally meshed using standard finite elements needs to be divided into linear segments. The number of segments is generally optional and depends on complexity of the nonlinear response. However, the maximum number of segments is determined by a number of present substructures plus the initial linear segment. Any method can be used for this linearisation, and the method that has been built into the computer programme is based on the principle of the linear regression with the objective to concurrently maximise the determination coefficients (the R^2 values) of all linear segments. Through a search process driven by a genetic algorithm, the best end points of the linear segments and their respective gradients (slopes) are determined, whereby they represent the desired values for the subsequent interpolation.

Although the suitable ranges for the parameters are user-specified inputs, there is a suggested procedure that ensures an effective choice of the values. As discussed before, the widest range for the parameter m is from 0 to 1, but narrowing of the range is also possible, and it may depend on amounts of observed deformation and nonlinearity. On the other hand, determining the range for the timing parameter t is more involving due to the nature of the parameter itself. Since the strain energy has been used here as the timing parameter, the suitable range for this parameter was determined from an aggregation of the total strain energies in all elements of the traditionally meshed model. The following code sample shows commands for a total strain energy output request in ABAQUS:

```
*OUTPUT, HISTORY
*ELEMENT OUTPUT, ELSET=COMPONENT_SET
 ELSE,
```

A careful examination of the produced output reveals the required range. As the interpolation operates in the natural log space, the third value that is used in the interpolation is the average of the min and max logarithmic values as per Eq. (15.22). The third value for the parameter m is obtained in the same fashion:

$$\ln(\text{third}) = \frac{\ln(\text{min}) + \ln(\text{max})}{2} \tag{15.22}$$

Once the preparatory activities are completed, the interpolation process commences. This is analytically performed, and it is concealed from the end user by the developed software.

Algorithm 1 – Determining the parameters *m* and *t* algorithm

Knowing: environment variables; ranges of the parameters m and t
Step 1. Initialise parameters and variables
Step 2. Plot the nonlinear response of the finite element model that had been traditionally meshed using standard finite elements
Step 3. Linearise the nonlinear force-displacement plot by utilising Genetic
do while the fittest individual is not found
Step 3a. Segment the nonlinear plot with the desired number of linear
Step 3b. Create a population of individuals consisting of data points representing the beginnings and ends of the linear segments
Step 3c. Grade the individuals by the objective function which is defined as maximisation of all coefficients of determination (R^2) values of the simple linear regression model (Montgomery *et al.* 2012)
Step 3d. Produce a new population from the fittest individuals by crossover mutation
end do while
Step 4. Output the fittest individual as the result of linearisation
Step 5. Obtain desired values for the feedback variables slope and knee.
Step 6. Obtain the correlations via a calibration
for each segment / UEL:
for each calibration run corresponding to different combinations of the parameters *m* and *t*:
Create relevant UEL by generating a FORTRAN file
Run ABAQUS analysis
Obtain corresponding feedback variable values
end for each
Obtain relationship between the parameters and their feedback
Use the desired values as inputs to the relationship to obtain the candidate parameter values
Run ABAQUS to validate the values and setup the next segment
end for each
Step 7. Graph the history

15.2.3 Algorithm of the Interpolation Method

The complete automation of the interpolation process for determining *m* and *t* is summarised in the flowchart shown in Fig. 15.3. It is based on establishing correlations between the parameters and their feedback variables which are readily obtainable. Although the algorithm is presented in a sequential order, its implementation is parallelised. In particular, the steps of establishing the correlation between the parameters and their feedback variables are performed concurrently with the linearisation (see Fig. 15.3).

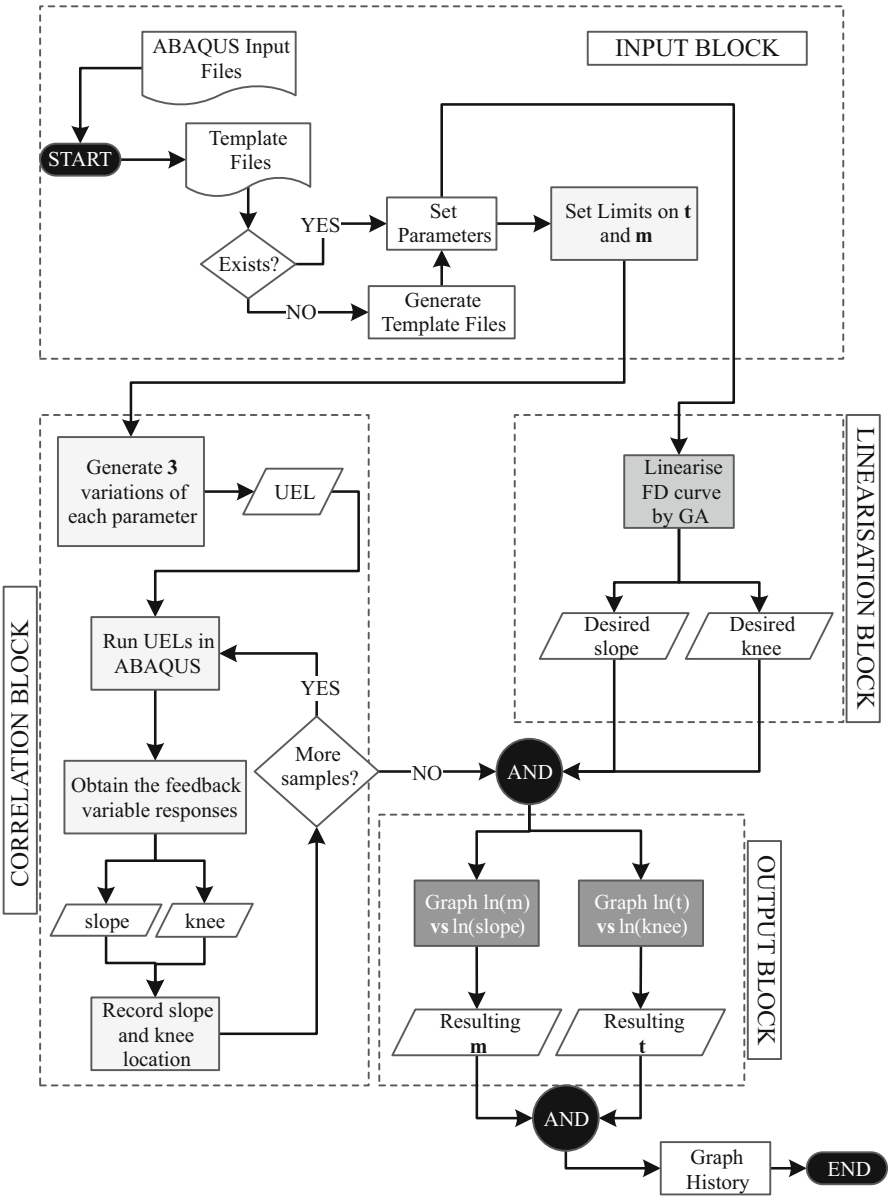

Fig. 15.3 Algorithm of the interpolation method

15.3 Implementation Within a Commercial Finite Element Code

Although a more thorough implementation of the extended substructures would be possible if a custom FEA code was to be developed, there are also some advantages of implementing them within a commercial code as a subroutine. From the programming and development perspective, the most important advantage is the ease of maintaining and porting subroutines in comparison with maintaining and porting a complete finite element programme. However, from the perspective of an end user, the most important advantage is convenience and familiarity with the existing commercial codes whereby the extended substructuring is only a complementary implement to a spectrum of the existing features, rather than a separate and diverse product. Finally, from the perspective of the author, this strategy has been selected in order to satisfy the projected outcome of this research which requires the practical and user-friendly application of the proposed methodology to an efficient and effective evaluation of load-bearing engineering concepts. In this research, the commercial finite element solver ABAQUS was used. To obtain the required access and customisation of the stiffness matrix, the substructure extension was implemented using the user element definition subroutines called UEL whereby the extended substructure was defined as a multi-node finite element with a fully customised element formulation. The ABAQUS user subroutine UEL needs to be coded to define the contribution of the element to the model, and depending on its purpose, the subroutine must define the contribution of the element to the residual force vector and the global stiffness matrix, update the solution-dependent state variables associated with the element, form the mass matrix and so on. Often, several of these functions must be performed in a single call to the subroutine. The element principal contributions to the model during general analysis steps are contribution to the residual force vector and the global stiffness matrix. The contribution to the global stiffness matrix is the actual element stiffness matrix as defined in Eq. (15.16). Modifying it by an appropriate qualifier m will actually yield a desired extended substructure. The actual process can be summarised by the following steps:

1. Generate a traditional substructure
2. Output a stiffness matrix
3. Store the stiffness matrix in primary or secondary memory storage
4. Multiply each matrix value with a qualifier m
5. Use the result as the extended substructure stiffness matrix

15.3.1 ABAQUS User Element Subroutine

In order for a UEL to be imported into ABAQUS, it must be written in a separate FORTRAN file. The UEL subroutine interface is given as follows:

```
SUBROUTINE UEL(RHS,AMATRX,SVARS,ENERGY,NDOFEL,NRHS,NSVARS,
1 PROPS,NPROPS,COORDS,MCRD,NNODE,U,DU,V,A,JTYPE,TIME,DTIME,
2 KSTEP,KINC,JELEM,PARAMS,NDLOAD,JDLTYP,ADLMAG,PREDEF,
3 NPREDF,LFLAGS,MLVARX,DDLMAG,MDLOAD,PNEWDT,JPROPS,NJPROP,
4 PERIOD)
```

Quantities such as coordinates, displacements, increments, element properties, load types, procedure type, etc. are contained in the interface parameters which are fully detailed in the ABAQUS manual (Simulia 2009). However, for coherence, some are mentioned here:

COORDS	Array in which the original coordinates of the elements are stored
U	Array that contains the total values of all variables (DOFs)
DU	Incremental values of all variables
DTIME	Increment of time
PROPS	Material properties like Young's modulus
NNODE	Numbers of nodes and in element
NDOFEL	Numbers of degrees of freedom element
LFLAGS	An array containing the flags that define the current solution procedure and requirements for element calculations

For static analyses, indicated by LFLAGS(1) = 1,2, the stiffness matrix **K** of the element and the residual vector **f** must be returned to Abaqus in AMATRX and RHS, respectively. In SVARS, user-defined variables like stresses, temperature, damage, etc. can be stored and returned to Abaqus; and PNEWDT can be used to set a new time increment. This variable, PNEWDT, allows for an input to be provided to the automatic time incrementation algorithms in Abaqus by specifying a ratio of a new time increment to the time increment currently being used (DTIME).

The user element behaviour is defined by its main contribution to the finite element model during an analysis that is reflected as loads **F** at the element nodes which depend on the displacement values **u** at the element nodes. In nonlinear user elements, the forces are also dependant on the internal state variables, H, which must be updated at the end of each increment through SVARS parameter. Therefore, the solution of the nonlinear system of equations requires that the stiffness matrix **K** includes all direct and indirect dependencies of the load and displacement, which may be expressed as manipulated in Eq. (15.8) in the form:

$$\mathbf{K} = -\frac{\partial F}{\partial H}\frac{\partial H}{\partial \mathbf{u}} \tag{15.23}$$

where

$\partial F = \partial F^{ext} - \partial F^{int}$ is an incremental residual quantity similar to **G** in Eq. (15.12).

To define a user element, an instruction through the command ∗USER ELEMENT is given in the preprocessing stage. This command must appear in the input file before the user element is invoked with the ∗ELEMENT option. For the purpose of a unique identification, the command ∗USER ELEMENT assigns an element type key to a user-defined element which is in the form *Un*. The unique identifier *n* needs to be a positive integer smaller than 10,000 because of the limitation on the number of user elements. Since each user element can have any number of nodes, their number needs to be declared through this command too. Furthermore, the number of the activated degrees of freedom associated with each node must also be declared. If the system variable array is to be used, this is where its size is declared too. In the current UEL implementation, the size of the system variable array is dependent on the number of degrees of freedom and the total number of element nodes; thus, it is defined according to the following relation: VAR = 2*(DOF*NODES + 1). The user element is then introduced to the model as any other ABAQUS element by specifying the Un type identification. Unlike the traditional ABAQUS elements that get their properties assigned through the *section* command, the user elements get their properties through *UEL PROPERTY command. The following code sample shows a simple example of the user element usage in ABAQUS:

```
*USER ELEMENT, TYPE=U100, NODES=5, COORDINATES=6, VAR=32
  1,2,3,4,5,6
*ELEMENT, TYPE=U100, ELSET=MY_UEL
100,
 1000, 1001, 1002, 1003,  1004, 1005
*UEL PROPERTY, ELSET=MY_UEL
```

In order to compile and include user subroutines in an analysis, the name of a file with the user definitions needs to be included in the ABAQUS execution command:

abaqus job=my_analysis user=my_subroutine.for

15.3.2 Extended Substructure as ABAQUS User Element

The unique implementation of extended substructures as an ABAQUS user element via UEL subroutine is summarised in algorithm 2. The algorithm is based on the mandatory requirements for a definition of the element behaviour whereby the stiffness contribution is provided by modifying the original substructure stiffness matrix by an appropriate qualifier at applicable time; and the force contribution is adjusted with a force correction to ensure continuity at any point of the applied load history profile. In particular, the modified stiffness of the underlying substructure unbalances the governing constitutive equilibrium equation whereby the externally

applied loads also require adjustments to return the system to an equilibrium. Unless a force correction is implemented, the analysis would result in an undesirable abrupt load change. The essential code snippets are addressed and briefly explained now.

Algorithm 2 – Implementation of extended substructuring in ABAQUS

Knowing: stiffness matrix of a traditional substructure; parameter m and parameter t
Step 1. Initialise parameters and variables
Step 2. Read in the stiffness matrix of a traditional substructure from a file and store AMATRX[]
Step 3. Define UEL contribution to stiffness:
    if total strain energy greater than parameter t **then:**
        if nodal force correction is required now **then:**
            Calculate the nodal force correction to ensure the continuity by by multiplying the force residual of the previous increment with the difference of the parameters m
            Store the nodal force correction for each node in in SVARS[] at locations starting from NDOFEL+1
            Set a flag indicating the nodal force correction was evaluated
    else:
        Recall the nodal force correction from SVARS[] and store in a new
Step 4. Modify AMATRX[]: AMATRX[] = m * AMATRX[]
Step 5. Calculate UEL contribution to force residual and store in SVARS[]
Step 6. Update the total strain energy and store in SVARS[]
Step 7. Reduce increment size if the gradient change is surpassed in the current increment and repeat the increment with the new increment size

```
c ...
c ... SNIPPET 1
c ...

      if(svars(2*(NDOFEL+1)).gt.t1) then
         mm=m1
c ...
c ... SNIPPET 2
c ...
          do k1=1, NDOFEL
            ff(k1,1) = (mm-one)*svars(k1)
            svars(NDOFEL+1+k1) = ff(k1,1)
c ...
c ... SNIPPET 3
c ...
        amatrx(k1,k2) = amatrx(k1,k2)*mm
c ...
c ... SNIPPET 4
c ...
        a_force(k1,1) = a_force(k1,1) + amatrx(k1,k2)*u(k2)
        rhs(k1, 1) = rhs(k1, 1) - (a_force(k1,1)+ff(k1,1))
c ...
c ... SNIPPET 5
c ...
        d_energy = d_energy     + (a_force(k1,1)+ff(k1,1))*du(k1,1)
        d_energy = d_energy     + half*(d_force(k1,1))*du(k1,1)
c ...
c ... SNIPPET 6
c ...
        svars(2*(NDOFEL+1))= svars(2*(NDOFEL+1))+d_energy
```

Snippet 1 ABAQUS subroutines do not transfer variable values between increments unless they are stored in the system variable array, SVARS[]. Therefore, for the purpose of determining if the change of the stiffness is required, a value of the total strain energy is stored at the particular location in the array. The total strain energy is the parameter $\underline{a}$ in Eq. (15.19).

Snippet 2 A force correction per a degree of freedom is calculated to ensure continuity and a smooth transition between two modes of the stiffness as per Eq. (15.19).

Snippet 3 The original substructure stiffness is modified which represents the implementation of the second part of Eq. (15.19) that describes the nonlinear response.

Snippet 4 The contributions to the residual force vector and the global stiffness matrix are defined and updated.

Snippet 5 The total strain energy as the timing parameter is calculated for the updated state of the system with purpose of progress tracking and safekeeping.

Snippet 6 The state variable array is updated with the new total strain energy value to allow for a continuous transition to the next increment.

15.4 Summary

The substructuring technique as a reanalysis approach has been introduced in this chapter, and a comprehensive discussion on development of the method which allows the substructures to exhibit a nonlinear response has been given. The principal theory of the novel idea whereby a scalar qualifier has been employed to economically modify original substructure matrix to enable substructures to exhibit a nonlinear response has been described, and its unique integration into the algorithm has been documented. Furthermore, the insight into implementation of the extended substructures as an integral part of a commercial finite element solver was also provided. A methodology for establishing a scalar qualifier to economically modify the original substructure matrix has been presented as an algorithm, and its implementation as a computer programme was demonstrated.

References

Abu Kassim, A. M., & Topping, B. H. V. (1987). Static reanalysis: A review. *Journal of Structural Division, 113*(5), 1029–1045.

Araldsen, P. O. (1974). An example of large-scale structural analysis of an oil tanker. *International Journal of Computational Structures, 4*(1), 69–93.

Arora, J. S. (1976). Survey of structural reanalysis techniques. *Journal of Structural Division, 102* (4), 783–802.

Barthelemy, J. F. M., & Haftka, R. T. (1993). Approximation concepts for optimum structural design — a review. *Structural optimization, 5*(3), 129–144.

Bathe, K.-J., & Gracewski, S. (1981). On nonlinear dynamic analysis using substructuring and mode superposition. *Computers & Structures, 13*(5–6), 699–707.

Bathe, K. J. (1979). Finite element formulation, modelling and solution of nonlinear dynamic problems. In K. J. Bathe (Ed.), *Numerical methods for partial differential equations* (pp. 1–40). Cambridge MA: Academic Press.

Bathe, K. J. (1996). *Finite element procedures*. Upper Saddle River: Prentice-Hall.

Bathe, K. J., Bolourchi, S., Ramaswamy, S., & Snyder, M. D. (1978). Some computational capabilities for nonlinear finite element analysis. *Journal of Nuclear Engineering and Design, 46*, 429–455.

Bathe, K. J., & Cimento, A. P. (1980). Some practical procedures for the solution of nonlinear finite element equations. *Computer Methods in Applied Mechanics and Engineering, 22*(1), 59–85.

Bathe, K. J., Ramm, E., & Wilson, E. L. (1973). Finite element formulations for large deformation dynamic analysis. *International Journal for Numerical Methods in Engineering, 9*, 353–386.

Bathe, K. J., & Wilson, E. L. (1976). *Numerical methods in finite element analysis*. Englewood Cliffs: Prentice-Hall.

Bennighof, J. K., Kaplan, M. K., & Muller, M. B. (2000). Extending the frequency response capabilities of automate multi-level substructuring. *AIAA* **AIAA-2000-1574**.

Bennighof, J. K., & Lehoucq, R. B. (2004). An automated multilevel substructuring method for eigenspace computation in linear elastodynamics. *Journal on Scientific Computing, 25*(6), 2084–2106.

Burton, T. D. (1997). Reduced models of structural systems with isolated nonlinearities. *AIAA* **AIAA-1997-787-293**.

Butcher, J. C. (2003). *Numerical methods for ordinary differential equations*. New York: Wiley.
CDH AG. (2012). CDH AG. Retrieved 12 Sept 2012, from http://www.cdh-ag.com
Chandrupatla, T. R., & Belegundu, A. D. (2002). *Introduction to finite elements in engineering*. Upper Saddle River: Prentice Hall.
Cook, R. D., Malkus, D. S., Plesha, M. E., & Witt, E. J. (2001). *Concepts and applications of finite element analysis*. New Jersey: Wiley.
Crisfield, M. A. (2000). *Non-linear finite element analysis of solids and structures*. Chichester: Wiley.
Dodds, R. H., & Lopez, L. A. (1980). Substructuring in linear and nonlinear analysis. *International Journal for Numerical Methods in Engineering, 15*(4), 583–597.
Elssel, K., & Voss, H. (2005). Solving nonlinear eigenproblems by AMLS. *Proceedings in Applied Mathematics and Mechanics, 5*, 765–766.
Elssel, K., & Voss, H. (2006). An a priori bound for eigenvalue computation by AMLS. *Proceedings in Applied Mathematics and Mechanics, 6*, 715–716.
Floersheim, R. B., Hou, G. J.-W., & Thornburgh, R. P. (2009). Predictive analysis with random variables in a bolted helicopter tailcone substructure. *AIAA* **AIAA-2009-2272**.
Fuzhen, Z. (2005). *The schur complement and its applications. Numerical methods and algorithms*. Boston: Springer.
Gibson, T. L. (2000). Life cycle assessment of advanced materials for automotive applications. *Society of Automotive Engineers (SAE)* **2000–01-1486**.
Gurujee, C. S. (1978). An improved method of substructure analysis. *Computers & Structures, 8*, 147–152.
Guyan, R. J. (1965). Reduction of stiffness and mass matrices. *AIAA, 3*, 380.
Kajtaz, M., Subic, A., & Takla, M. (2010). A collaborative FEA platform for rapid design of lightweight vehicle structures. *International Journal of Vehicle Design, 53*(1/2), 110–131.
Kammer, D. C., & Flanigan, C. C. (1991). Development of test-analysis models for large space structures using substructure representations. *Journal of Spacecraft, 28*(2), 244–250.
Kirsch, U., & Rubinstein, M. F. (1972). Structural reanalysis by iteration. *Computers & Structures, 2*(4), 497–510.
Kirsch, U. (2008). *Reanalysis of structures: A unified approach for linear, nonlinear, static, and dynamic systems*. New York: Springer.
Kojic, M., & Bathe, K. J. (2005). *Inelastic analysis of solids and structures*. New York: Springer.
Labeas, G. N., & Belesis, S. D. (2011). Efficient analysis of large-scale structural problems with geometrical non-linearity. *International Journal of Non-Linear Mechanics, 46*, 1283–1292.
Owen, D. R. J., & Goncalves, O. J. A. (1983). Substructuring techniques in material nonlinear analysis. *Computers & Structures, 15*(3), 205–213.
Palekar, S. M., Subramanian, K. V., & Bavare, M. S. (2003). Super-Elements – A remedy for non-linear analyses of large-sized models. In *17th international conference on structural mechanics in reactor technology (SMiRT 17)*, Prague, Czech Republic.
Petersson, H., & Popov, E. P. (1977). Substructuring and equation system solutions in finite element analysis. *Computers & Structures, 7*, 197–206.
Postnov, V. A., & Rodionov, A. A. (1982). Using the superelement method to solve elastoplastic problems. *International Applied Mechanics, 18*(2), 149–153.
Sherman, J., & Morrison, W. J. (1949). Adjustment of an inverse matrix corresponding to changes in the elements of a given column or a given row of the original matrix. *Annals of Mathematical Statistics, 20*, 124–127.
Simulia. (2009). Simulia Products – Abaqus FEA. From http://www.simulia.com/products/abaqus_fea
Singh, Y. P., Ball, J. H., Rouch, K. E., & Sheth, P. N. (1989). A finite element approach for analysis and design of pumps. *Finite Elements in Analysis and Design, 6*, 45–58.
Strang, G. (2010). *Calculus*. Cambridge, MA: Wellesley-Cambridge Press.
Swenson, E. D., & Bennighof, J. K. (2006). Efficient frequency response analysis of structures with viscoelastic materials. *AIAA* **AIAA-2006-2236**.

Thomas, H., Mandal, D., & Pagaldipti, N. (2009). Structural-acoustic optimisation using CMS super elements. *AIAA* **AIAA-2009-2209**.

Vorob'ev, Y. S., Kanilo, S. P., Shepel, A. I., & Sapelkina, Z. V. (1994). Evaluation of static condensation method effectiveness in calculating natural vibrations of turbomachine blades. *Strength of Materials, 26*(1), 73–78.

Wilson, E. L. (1965). Structural analysis of axisymmetric solids. *AIAA Journal, 3*(12), 2269–2274.

Wilson, E. L. (1974). The static condensation algorithm. *International Journal for Numerical Methods in Engineering, 8*(1), 198–203.

Woodbury, M. A. (1950). *Inverting modified matrices*, *Technical Report 42*. Princeton: Statistical Research Group, Princeton University.

Wu, H. T., Diep, S. Q., & Gupta, V. K. (1991). *Nonlinear static analysis of McDonnell Douglas MD90 aircraft using MSC/NASTRAN superelement database*. MSC 1991 World Users' Conference.

Yiu, Y. C. (1997). Substructure and finite element formulation for linear viscoelastic materials. *AIAA* **AIAA-97-1517-CP**.

Index

L. Dai, R.N. Jazar (eds.), *Nonlinear Approaches in Engineering Applications*,
https://doi.org/10.1007/978-3-319-69480-1